Strategies for Development and Investigation of Chemoresistive Gas Sensors

Dissertation

der Mathematisch-Naturwissenschaftlichen Fakultät
der Eberhard Karls Universität Tübingen
zur Erlangung des Grades eines
Doktors der Naturwissenschaften
(Dr. rer. nat.)

vorgelegt von

Benjamin Junker-Reiss

geb. Junker

aus Albstadt

Tübingen

2026

Gedruckt mit Genehmigung der Mathematisch-Naturwissenschaftlichen Fakultät der Eberhard Karls Universität Tübingen.

Tag der mündlichen Qualifikation:	15.05.2026
Dekan:	Prof. Dr. Thilo Stehle
1. Berichterstatter:	Prof. Dr. Udo Weimar
2. Berichterstatter:	Prof. Dr. Günter Gauglitz
3. Berichterstatter:	Prof. Dr.-Ing. Ralf Moos

"Remember kids, the only difference between science and screwing around is writing it down."

- Adam Savage

Contents

Abbreviations and Symbols

Table 1: Abbreviations, Acronyms and Chemical Symbols

Abbreviation	**Meaning**
AC	Alternating Current
AI	Artificial Intelligence
ALD	Atomic Layer Deposition
CB	Conduction Band
CPD	Contact Potential Difference
D	Deuterium ($^{2}_{1}$H)
DC	Direct Current
DFT	Density Functional Theory
DRIFTS	Diffuse Reflectance Infrared Fourier Transformation Spectroscopy
e^-	Electron
EDX	Energy-Dispersive X-ray Spectroscopy
EXAFS	Extended X-ray Absorption Fine Structure
FTIR	Fourier Transformation Infrared (Spectroscopy)
HAADF-STEM	High Angle Annular Dark Field Scanning Transmission Electron Microscopy

Abbreviation	Meaning
HERFD-XANES	High Energy Resolved Fluorescence Detection X-ray Absorption Near Edge Structure
IPC450, IPC1000	SnO_2, calcined at 450/1000 °C at the Institute of Physical Chemistry, Tübingen
KP	Kelvin Probe
LED	Light Emitting Diode
Ln	Lanthanoid
NAP-XPS	Near-Ambient Pressure X-ray Photoelectron Spectroscopy
PCA	Principal Component Analysis
RH, r.h.	Relative Humidity
RT	Room Temperature
S	Site, Surface
SEM	Scanning Electron Microscopy
SiNWs	Silicon Nanowires
SMOX	Semiconducting Metal Oxide
STEM	Scanning Transmission Electron Microscopy
UHV	Ultra High Vacuum
UL	unloaded
UV-vis	Ultraviolet and Visible (spectroscopy)
V	Vacancy
VB	Valence Band
VOC	Volatile Organic Compound
XANES	X-ray Absorption Near Edge Structure
XAS	X-ray Absorption Spectroscopy
XPS	X-ray Photoelectron Spectroscopy
XRD	X-ray Diffraction

For selected reactions, the Kröger-Vink notation is used. The expression A_X^b indicates that atom A occupies the site of atom X. b denotes the relative charge of A compared to X, with $\cdot$ representing positive, $\times$ neutral, and $'$ negative relative charge.

Note that due to different style guidelines of journals and individual preferences of co-authors, reviewers and editors, abbreviations and symbols are not used consistently throughout all attached manuscripts.

Zusammenfassung

Chemoresistive Gassensoren auf der Basis halbleitender Metalloxide (semiconducting metal oxides, SMOX) sind vielseitig und einfach herzustellen. Der Sensorprozess beginnt mit der Rezeption, d.h. der chemischen Wechselwirkung von Analyt und Oberfläche, gefolgt von der Transduktion, welche die Übersetzung dieser Wechselwirkungen in messbare elektrische Signale beschreibt. Deren grundlegendes Verständnis ist, ebenso wie das der Reaktionen von Sauerstoff und Wasser, die Voraussetzung für die Untersuchung weiterer Analyte.

Ein gravierender Nachteil der SMOX-Sensoren ist ihr Mangel an Selektivität. Deshalb werden in dieser Arbeit verschiedene Strategien zur Abmilderung dieses Defizits vorgestellt. Die Eigenschaften von NiO, $LaFeO_3$/$SmFeO_3$, Sn_3O_4 und Silizium-Nanodrähten als alternative Materialien werden erforscht. Auch die häufig verwendeten Materialien SnO_2, WO_3 und In_2O_3 werden durch Dotieren und Beladen verändert. Außerdem wird der Einfluss der Struktur besprochen. Darüber hinaus wird die Aktivierung durch Licht und ihr Effekt auf verschiedene SMOX untersucht und mit thermischer Aktivierung verglichen. Die Auswirkungen jeder Strategie auf Rezeption und Transduktion, sowie praktische Gesichtspunkte werden diskutiert.

Schließlich wird eine Übersicht über Forschungsmethoden gegeben. Diese schließt eine kurze Beschreibung der Apparate, deren Vorteile und Einschränkungen und deren Rolle in den vorgestellten Studien mit ein.

Summary

Chemoresistive gas sensors based on semiconducting metal oxides (SMOX) are versatile and easy to manufacture. The sensing process begins with the reception, i.e. the chemical interaction between analytes and surface, followed by transduction, which describes the conversion of these interactions into measurable electrical signals. Their fundamental understanding, along with the reactions of oxygen and water, is prerequisite for the study of other analytes.

A major drawback of SMOX sensors is their lack of selectivity. Therefore, different strategies to mitigate this shortcoming are presented in this work. The properties of NiO, $LaFeO_3$/$SmFeO_3$, Sn_3O_4, and silicon nanowires as alternative materials are explored. Also the commonly used materials SnO_2, WO_3, and In_2O_3 are modified by doping and loading. In addition, the influence of structure is discussed. Moreover, light activation and its effect on several SMOX materials is investigated and compared to thermal activation. Each strategy's implications on reception and transduction, as well as practical considerations are discussed.

Finally, an overview on investigation methods is presented. This includes a brief description of the instrumentation, their advantages and drawbacks, and their role in the presented studies.

List of Publications and Own Share

Accepted Publications referred to in this Thesis

[BJR01] Rhodium Oxide Surface-Loaded Gas Sensors

by Anna Staerz†, Inci Boehme†, David Degler, Mounib Bahri, Dmitry E. Doronkin, Anna Zimina, Helena Brinkmann, Sina Herrmann, Benjamin Junker, Ovidiu Ersen, Jan-Dierk Grunwaldt, Udo Weimar, and Nicolae Barsan.

Nanomaterials 2018, 8, 892.

DOI: 10.3390/nano8110892

Accepted: 2018-10-25

Own share: B. Junker-Reiss was involved in preparation and execution of XAS experiments at DESY as student research assistant. Even though the actual contribution to the final publication was rather low, plenty of knowledge and experience in X-ray spectroscopy could be gained.

- Scientific ideas: 5%
- Data generation: 10%
- Analysis & interpretation: 5%
- Paper writing: 5%

[BJR02] Microfluidically synthesized Au, Pd and AuPd nanoparticles supported on SnO_2 for gas sensing applications

by Ghazal Tofighi[†], David Degler[†], Benjamin Junker, Sabrina Müller, Henning Lichtenberg, Wu Wang, Udo Weimar, Nicolae Barsan, and Jan-Dierk Grunwaldt.

Sensors and Actuators B: Chemical, 292:48–56, 2019.

DOI: 10.1016/j.snb.2019.02.107

Accepted: 2019-02-22

Own share: B. Junker-Reiss prepared sensors from provided powders and conducted electrical and spectroscopic experiments, for which he also assisted in data evaluation.

- Scientific ideas: 5%
- Data generation: 50%
- Analysis & interpretation: 25%
- Paper writing: 5%

[BJR03] Investigations on the Temperature-Dependent Interaction of Water Vapor with Tin Dioxide and Its Implications on Gas Sensing

by David Degler, Benjamin Junker, Frank Allmendinger, Udo Weimar, and Nicolae Barsan.

ACS Sensors 2020, 5, 3207–3216

DOI: 10.1021/acssensors.0c01493

Accepted: 2020-09-11

Own share: B. Junker-Reiss was involved in preparation, conduction and evaluation of the experiments. Also, he was summarizing, describing and visualizing different of mechanisms based on literature review.

– Scientific ideas: 10%

– Data generation: 40%

– Analysis & interpretation: 25%

– Paper writing: 25%

[BJR04] NAP-XPS as a new tool for in-situ studies of SMOX gas sensors

by Benjamin Junker, Marco Favaro, David E Starr, Michael Hävecker, Udo Weimar, and Nicolae Barsan.

Journal of Physics D: Applied Physics. 55 (2022) 064002.

DOI: 10.1088/1361-6463/ac3283

Accepted: 2021-12-14

Own share: B. Junker-Reiss prepared the samples and conducted all of the electrical measurements and laboratory XPS characterization experiments. NAP-XPS experiments were prepared, conducted and evaluated together with Marco Favaro at BESSY II. The manuscript was written mainly by B. Junker-Reiss. The publication is based on the results of Benjamin Junker-Reiss' Master thesis, entitled *The application of high pressure XPS in SMOX gas sensor research.*

– Scientific ideas: 40%

– Data generation: 75%

– Analysis & interpretation: 75%

– Paper writing: 90%

[BJR05] The Role of Different Lanthanoid and Transition Metals in Perovskite Gas Sensors

by Abdulaziz Alharbi†, Benjamin Junker†, Mohammad Alduraibi, Ahmad Algarni, Udo Weimar, and Nicolae Bârsan

Sensors 2021, 21, 8462.

DOI: 10.3390/s21248462

Accepted: 2021-12-14

Own share: Benjamin Junker-Reiss suggested substituting the elements of already well investigated $LaFeO_3$. He prepared sensors from powders provided by Abulaziz Alharbi. He conducted all of the electrical and DRIFTS characterization as well as part of the XRD characterization. He was writing the corresponding parts of the manuscript and, together with Abdulaziz Alharbi and Nicolae Bârsan, proposed interpretations.

- Scientific ideas: 50%
- Data generation: 50%
- Analysis & interpretation: 50%
- Paper writing: 50%

[BJR06] Proof of Concept for Operando Infrared Spectroscopy Investigation of Light-Excited Metal Oxide-Based Gas Sensors

by Xiao-Xue Wang, Benjamin Junker, Carolin Ewald, Udo Weimar, Xin Guo, and Nicolae Bârsan

Journal of Physical Chemistry Letters 2022, 13, 3631-3635.

DOI: 10.1021/acs.jpclett.2c00480

Accepted: 2022-04-14

Own share: Benjamin Junker-Reiss was, together with Xiao-Xue Wang, developing and building a test setup for Operando DRIFTS experiments. He was assisting in writing and interpretation of the results.

- Scientific ideas: 25%
- Data generation: 10%
- Analysis & interpretation: 10%
- Paper writing: 10%

[BJR07] Sensing mechanisms of CO and H_2 with NiO material – DRIFTS investigations

by Cristian Eugen Simion†, Benjamin Junker†, Udo Weimar, Adelina Stanoiu, and Nicolae Bârsan

Sensors & Actuators: B. Chemical 390 (2023) 134028

DOI: 10.1016/j.snb.2023.134028

Accepted: 2023-05-24

Own share: Benjamin Junker-Reiss was preparing sensors from powders provided by Cristian E. Simion, with whom he was conducting the operando DRIFTS experiments. Analysis and interpretation was done together with Nicolae Bârsan. Benjamin Junker-Reiss was also visualizing and describing the results.

- Scientific ideas: 25%
- Data generation: 50%
- Analysis & interpretation: 50%
- Paper writing: 75%

[BJR08] Modeling the Conduction Mechanism in Chemoresistive Gas Sensor Based on Single-Crystalline Sn_3O_4 Nanobelts: A Phenomenological In Operando Investigation

by Pedro H. Suman, Benjamin Junker, Udo Weimar, Marcelo O. Orlandi, and Nicolae Bârsan

ACS Sensors 2024, 9, 1, 149–156.

DOI: 10.1021/acssensors.3c01810

Accepted: 2023-12-22

Own share: Benjamin Junker-Reiss was assisting Pedro H. Suman in performing Kelvin probe experiments. He was advising in data analysis and writing the manuscript.

- Scientific ideas: 10%
- Data generation: 25%
- Analysis & interpretation: 10%
- Paper writing: 5%

[BJR09] Multivariate Analysis of Light-Activated SMOX Gas Sensors

by Benjamin Junker, Arne Kobald, Carolin Ewald, Peter Janoschek, Malte Schalk, Udo Weimar, Lutz Mädler, and Nicolae Barsan

ACS Sensors 2024, 9, 1584–1591.

DOI: 10.1021/acssensors.4c00078

Accepted: 2024-02-27

Own share: Experimental data was collected by Benjamin Junker-Reiss and Carolin Ewald using sensors prepared by Malte Schalk. Inspired by Nicolae Bârsan, Benjamin Junker-Reiss and Arne Kobald performed the data analysis and interpretation. Benjamin Junker-Reiss did the majority of

writing and visualization, assisted by Arne Kobald and Peter Janoschek.

- Scientific ideas: 25%
- Data generation: 50%
- Analysis & interpretation: 50%
- Paper writing: 75%

[BJR10] Ultra Responsive NO_2 silicon nanowires gas sensor

by Rachel Elizabeth Brophy, Benjamin Junker, Elham Aghabalei Fakhri, Hákon Örn Árnason, Halldór Guðfinnur Svavarsson, Udo Weimar, Nicolae Bârsan, and Andrei Manolescu

Sensors & Actuators: B. Chemical 410 (2024) 135648.

DOI: 10.1016/j.snb.2024.135648

Accepted: 2024-03-14

Own share: Benjamin Junker-Reiss was adapting the sensors, prepared by Rachel E. Brophy to the experimental setup, suggested experiments and performed the sensor characterization. The analysis was done jointly with Rachel E. Brophy, Nicolae Bârsan, and Andrei Manolescu. Writing and visualizing was done mainly by Rachel E. Brophy.

- Scientific ideas: 25%
- Data generation: 50%
- Analysis & interpretation: 25%
- Paper writing: 25%

[BJR11] Operando DRIFTS Proof of Visible-Light-Activated Surface Reduction of WO_3: Implication for Gas Sensing

by Benjamin Junker†, Xiao-Xue Wang†, Udo Weimar, and Nicolae Barsan

Journal of Physical Chemistry C 2025, 129, 21, 9795–9800.

DOI: 10.1021/acs.jpcc.5c01808

Accepted: 2025-05-07

Own share: Benjamin Junker-Reiss was, together with Xiao-Xue Wang planning and conducting the experimental work, except UV-vis spectroscopy. Visualization and writing was also shared between Xiao-Xue Wang and Benjamin Junker-Reiss. Nicolae Bârsan assisted in data analysis and editing the manuscript.

- Scientific ideas: 25%
- Data generation: 50%
- Analysis & interpretation: 50%
- Paper writing: 75%

[BJR12] Investigation on the Structure – Function Relationship of Atomic-Layer-Deposited Platinum Additives on Tungsten Trioxide Gas Sensor Materials

by David Degler, Ugur Geyik, Benjamin Junker-Reiss, Muhammad Hamid Raza, Patrick Amsalem, Norbert Koch, Blanka Detlefs, Nicola Pinna, Udo Weimar, and Nicolae Barsan.

Journal of Physical Chemistry C 2025, 129, 34, 15301-15308

DOI: 10.1021/acs.jpcc.5c05000

Accepted: 2025-08-07

Own share: Benjamin Junker-Reiss was, together with David Degler, Blanka Detlefs and Ugur Geyik, planning, executing and analyzing XAS experiments. He was also assisting David Degler, Ugur Geyik and Nicolae Bârsan in writing the manuscript and visualizing the results.

- Scientific ideas: 5%
- Data generation: 10%
- Analysis & interpretation: 10%
- Paper writing: 20%

[BJR13] Unraveling the gas sensing mechanism of single-crystalline Sn_3O_4 nanobelts using operando DRIFT spectroscopy and isotopically labeled gases

by Pedro H. Suman, Benjamin Junker-Reiss, Udo Weimar, Marcelo O. Orlandi, and Nicolae Barsan

Sensors & Actuators: B. Chemical 447 (2026) 138909.

DOI: 10.1016/j.snb.2025.138909

Accepted: 2025-10-03

Own share: Benjamin Junker-Reiss was assisting Pedro H. Suman in the execution of DRIFTS experiments and was editing the manuscript.

- Scientific ideas: 5%
- Data generation: 10%
- Analysis & interpretation: 20%
- Paper writing: 10%

[†]These authors contributed equally.

Other accepted Publications

- **Near ambient pressure photoelectron spectro-microscopy: from gas–solid interface to operando devices**

  by Matteo Amati, Luca Gregoratti, Patrick Zeller, Mark Greiner, Mattia Scardamaglia, Benjamin Junker, Tamara Ruß, Udo Weimar, Nicolae Barsan, Marco Favaro, Abdulaziz Alharbi, Ingvild J T Jensen, Ayaz Ali, and Branson D Belle

  J. Phys. D: Appl. Phys. 54 (2021) 204004 (14pp).

  DOI: 10.1088/1361-6463/abe5e2

- **Operando Investigation of the Aging Mechanism of Lead Sulfide Colloidal Quantum Dots in an Oxidizing Background**

  by Tamara Russ, Zhixiang Hu, Benjamin Junker, Huan Liu, Udo Weimar, and Nicolae Barsan

  J. Phys. Chem. C 2021, 125, 19847–19857.

  DOI: 10.1021/acs.jpcc.1c04045

- **AI-enabled rapid method for complex quality assessment of edible oils**

  by Asia Kalinichenko, Nicolae Bârsan, Benjamin Junker, André Sackmann, and Udo Weimar

  EUROSENSORS XXXVI

  DOI: 10.5162/EUROSENSORSXXXVI/PT5.149

- **Rapid Determination of Hexane Residues in Refined Vegetable Oils Using Semiconducting Metal Oxide-Based Sensors**

  by Asia Kalinichenko, Benjamin Junker , Udo Weimar, and Nicolae Bârsan

  Proceedings 2024, 97, 122.

DOI: 10.3390/proceedings2024097122

- **Novel method for monitoring residual hexane in refined oils using semiconducting metal oxide-based gas sensors**

  by Asia Kalinichenko, André Sackmann, Benjamin Junker, Udo Weimar, and Nicolae Bârsan

  Sensors & Actuators: B. Chemical 434 (2025) 137616

  DOI: /10.1016/j.snb.2025.137616

Conference Talks

- **Hydrocarbon gas sensing with perovskite structured SMOX materials**

  presented at PhD GOSPEL Workshop 2021/2022, 2022-06-09, Virtual Edition.

- **Neuartige Reaktionswege bei Halbleiter-Metalloxid-Sensoren bei niedriger Temperatur für neue Applikationsfelder**

  presented at 16. Dresdner Sensor-Symposium 2022, 2022-12-06, Dresden, Germany. DOI: 10.5162/16dss2022/3.5

- **Complementary operando DRIFTS and XAS investigations for the understanding of gas sensing with semiconducting metal oxides (SMOX)**

  presented at ACS Fall 2024, 2024-08-19, Denver CO, USA.

- **Spectroscopic investigations on the effect of light on gas sensing with semiconducting metal oxides**

  presented at International Meeting on Chemical Sensors (IMCS) 2025, 2025-06-25, Freiburg, Germany.

Chapter 1

Introduction

Gas sensors are required for numerous applications such as air quality control, detection of harmful or combustible gases or breath analysis in healthcare [1]. Among different types of gas sensors, chemoresistive gas sensors have the advantages of low cost, longevity, high sensitivity, fast response and high potential for miniaturization, compared to their electrochemical or optical counterparts [2, 3]. The most versatile materials used are semiconducting metal oxides (SMOX). Their operating principle could be summarized in one sentence: "Gas molecules react with the SMOX and change its resistivity". Yet, many details about the process and the influencing factors are still insufficiently understood. Consequently, SMOX gas sensors are in the focus of both academic research and industrial development. The goal of researchers is to unravel the sensing mechanism, i.e. the understanding of the entire process from the chemical reaction to the readout and of relevant factors.

Figure 1.1 illustrates several aspects of the construction, operation, investigation and application of chemoresistive SMOX gas sensors: The sensing layer itself, if not homogeneous, may consist of particles of different sizes, shapes, phases or even of different compounds [BJR08],[4, 5, 6, 7]. The semiconducting metals can be doped, loaded or mixed with additives, often noble metals [BJR01], [BJR02], [BJR12], [8, 9]. Chemical reactions of gas

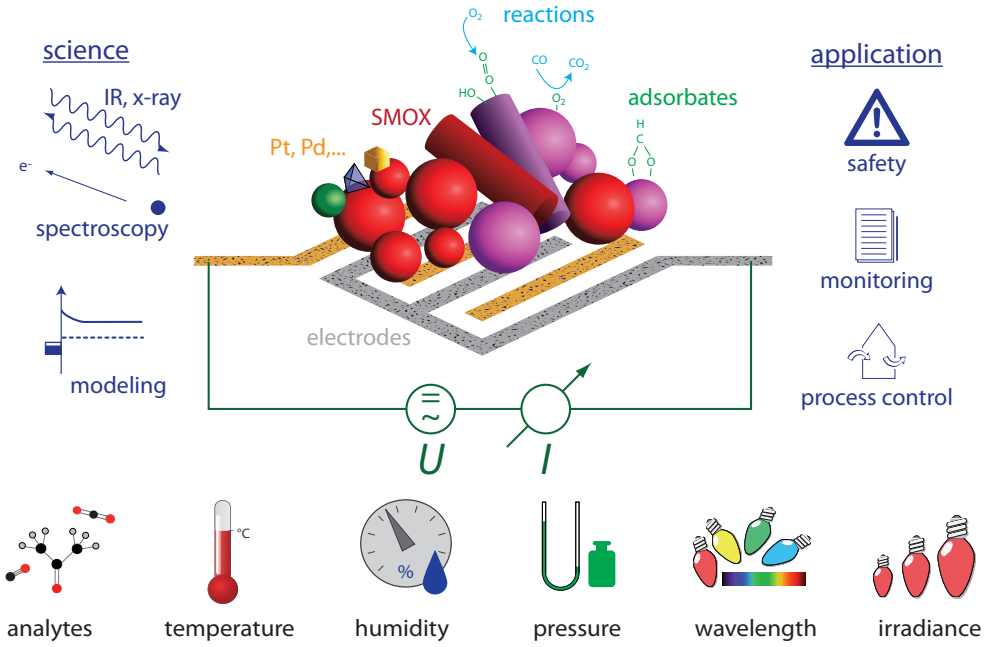

Figure 1.1: Illustration of materials, processes, stimuli, probe techniques and applications of chemoresistive gas sensors.

molecules at the surface create or consume species at the surface, e.g. hydroxyl groups or formates, and new molecules are formed. Temperature, pressure, humidity and illumination at different wavelength and irradiance affect the gas phase, the SMOX, and their interaction. In case of chemoresistive sensors the measured quantity is ohmic resistance, which requires at least two electrodes for establishing electrical contact. Different electrode materials, geometry and spacing are possible, with implications for their catalytic properties and local electric field strength [10]. The polarization of the electrodes (constant voltage, constant current, pulsed, alternating current at different frequencies) is another variable [11, 12]. Academic research often involves the acquisition of more information than resistance, e.g. spectroscopic investigations (infrared, UV-vis, X-ray absorption, photoelectron spectroscopy), work function changes or mass spectrometry. All

of these techniques provide insights into the chemical and physical processes. Finally, the entire sensor assembly from sensing layer to electronics and housing is customized for its respective application, e.g. safety, data logging or process control.

1.1 Reception

The detection of gases requires some form of interaction between the target molecules and the sensor surface. A distinction is made between physisorption, where only weak Van-der-Waals forces are involved and chemisorption, where chemical bonds are formed [13]. Therefore, Gao et al. describe reception as "how the sensing materials recognize gas molecules through adsorption or reaction" [14].

Probably the most relevant reaction for any sensor operated in ambient air is the chemisorption of oxygen [15]:

$$\frac{1}{2}\,\mathrm{O_2} + \mathrm{V_O}^{\cdot\cdot} + 2\,\mathrm{e}^- \rightleftharpoons \mathrm{O_O}^{\times} \tag{1.1}$$

The reception of other analytes may shift the equilibrium of (1.1) in either direction or take place independently. **Figure 1.2a** illustrates the reception process of CO on a generic n-type SMOX on a molecular level: The chemical reaction of CO with an oxygen ion at the surface yields CO_2 and an oxygen vacancy. The electrons localized at the oxygen ions are released into the conduction band:

$$\mathrm{CO} + \mathrm{O_O}^{\times} \longrightarrow \mathrm{CO_2} + \mathrm{V_O}^{\cdot\cdot} + 2\,\mathrm{e}^- \tag{1.2}$$

In ambient air, chemisorption of oxygen induces a space charge layer and upwards band bending of the valence and conduction bands. In **Figure 1.2b** the implication of the reception of CO on the electronic structure of the SMOX is shown: The presence of a rather low concentration of CO counteracts the chemisorption of O_2, therefore diminishing the band bending eV_S and the work function Φ of the SMOX. Moreover, the electron depletion layer created by the chemisorption of O_2 is decreased and becomes more shallow (**Figure 1.2c**) [15].

The unraveling of the reception processes is probably the most challenging aspect in the elucidation of the entire sensing mech-

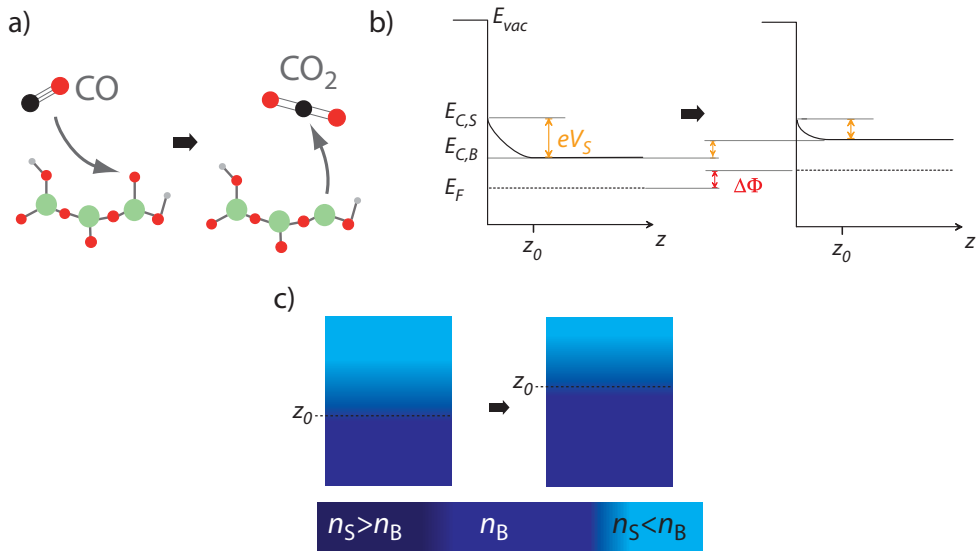

Figure 1.2: Reception of CO on a generic *n*-type SMOX in air. a) Oxidation of CO to CO_2 on a molecular level. b) Band structure and electronic states. c) Charge carrier density in microscopic scale.

anism, not only because it is unique for each analyte – SMOX combination, but also because many factors such as temperature, concentration, presence of humidity and other interfering analytes, additives, phase or crystal facet impact the molecular interaction [16].

1.2 Transduction

Complementing the reception, transduction describes "how the interaction of gas-solid translates into macroscopically measurable electrical signal changes" [14]. Basically, the localization of free charge carriers is sufficient to change the SMOX' conductance and therefore the sensor's resistance. However, the details of the transduction process highly depend on the structure of the sensing layer: **Figure 1.3a** shows a compact *n*-type sensing layer with an electron depletion layer at the surface, created by the chemisorp-

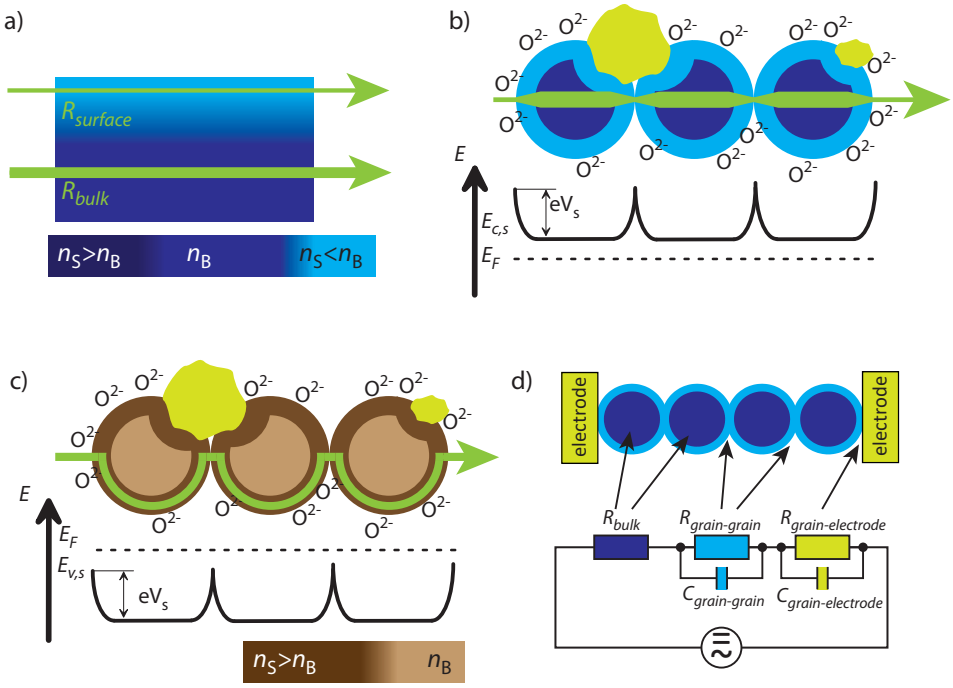

Figure 1.3: Charge transport in SMOX sensing layers. Thicker arrows indicate sections of higher resistivity in the conductive path. a) *n*-type compact layers b) *n*-type porous layer. Additives decrease the local electron density of the SMOX. c) *p*-type porous layers. Additives increase the local hole density of the SMOX. d) Equivalent circuit of the entire sensor including resistive and capacitive elements.

tion of oxygen. Two parallel paths for the electrical current are depicted with green arrows: The depletion layer just beneath the surface has a decreased conductivity, whereas the bulk remains unaffected. While the chemical reactions control the charge separation, the material's Debye length L_D determines how far the depletion layer penetrates the material, denoted with z_0. For a shorter Debye length, the contribution of the unaffected bulk increases.

As shown in **Figure 1.3b**, in porous layers consisting of loosely sintered grains with $r > z_0$, the depletion layers form a potential barrier at each grain – grain contact, dominating the overall resis-

tance. This effect may be enhanced by noble metals loadings with higher work function than the SMOX [8]. In good approximation, the resistance change is determined by the fraction of electrons whose thermal energy is higher than the barrier height eV_S and can be described using the Boltzmann equation [17]:

$$\frac{R}{R_0} \propto e^{\frac{-e\Delta V_S}{kT}} \tag{1.3}$$

The exponential relationship between band bending and resistance change according to (1.3) makes transduction in n-type SMOX with porous layers highly efficient compared to compact layers.

In contrast, for p-type SMOX (**Figure 1.3c**), the presence of a highly conductive hole accumulation layer prevents the formation of potential barriers. In fact, the current bypasses the more resistive bulk regions of the grains entirely [18]. Beyond these three examples, more factors like grain size, contact area, aspect ratio, heterojunctions, additives etc. affect the actual transduction. Often, the complex structure of the sensing layer can be approximated by equivalent circuits. In the example given in **Figure 1.3d**, three resistors in series are used to describe the contributions of bulk, grain—grain contacts and electrode–grain contacts. The space charge layers can be approximated by capacitors in parallel to the respective resistor. Experimentally, these circuits are accessible via AC and DC measurements [19].

Transduction itself only depends on the amount of charge carriers that is exchanged during the reception and is therefore independent of the analyte gas. Chemoresistive sensors are measured as resistors, but SMOX sensors can also be constructed as capacitors, diodes or transistors, where other transduction principles apply [20].

1.3 Materials

Even though the sensitive layer of chemoresistive gas sensors can be made from numerous materials, e.g. sulfides, halides, carbon-derived structures, or (metal-)organic compounds, the most prominent class of materials is semiconducting metal oxides (SMOX), with SnO_2 as the most widespread representative. The reason is the oxides' compatibility with the reaction of ambient oxygen according to (1.1). A well-suited gas sensitive material needs to fulfill some requirements on gas sensing performance: sensitivity, selectivity, speed, chemical stability etc. For mass production of sensors, more criteria become relevant, e.g. price, ease of manufacturing, toxicity and mechanical stability [21]. There is no single material to meet all of these criteria, hence trade-offs are made depending on the application's needs.

1.4 Additives

The performance of SMOX gas sensors can be greatly enhanced by the addition of small amounts of other compounds, often noble metals in their metallic or oxidized form. In general one can distinguish between doping and loading. Doping refers to "the addition of a small amount of foreign atoms [...] in the lattice" [13]. Doping of SMOX gas sensors works best for combinations where the crystal structures of SMOX and additive are compatible, e.g. Pt in SnO_2 [22]. The concentration of dopants in SMOX sensors is usually much higher than in electronic semiconductors, therefore, in poorly matched combinations, a separate phase can be formed by the dopant over time. In contrast, loading or decoration refers to the addition of noble metals to the surface of the SMOX. The size of the additives goes from single ionic or atomic sites to large clusters [8]. Finally, physical mixtures of SMOX and noble metal particles are possible [6]. Loadings provide new reac-

tion sites where analyte molecules are either activated and "spill over" to the SMOX or the reaction takes place entirely on the loading [8]. The other important function of loadings is electronic interaction. Depending on size and distribution of the additive, this interaction affects band bending, as shown in **Figure 1.3b** or results in the formation of heterojunctions.

1.5 Analytical Challenges

With thousands of possible applications for gas sensors, it is evident that there is no such thing as *the best* sensor. Apart from obvious boundary conditions such as size, cost, ease of manufacturing or longevity, power consumption and selectivity of SMOX remain two of the major challenges.

Decreased power consumption is achieved in different ways: Miniaturization of the sensing element, more efficient materials and catalysts which allow for lower temperatures of operation or entirely different modes of operation [23, 24, 25]. These can be for example a sleep mode at low temperature between short sampling times or the introduction of light as a low power energy source. While miniaturization is a challenge of engineering, the development of alternative materials and modes of operation is driven mainly by chemists.

The human (not to mention some animals') nose excels in the recognition and classification of complex gas mixtures and can easily tell if a person is in a forest, a bakery, a public swimming pool, a mechanical workshop or next to a fireplace. For sensors, the ability to distinguish between different analytes and to quantify them independently is a formidable challenge. Also here, different approaches can be found: On the one hand, multiple different sensing materials can be combined in an array, which calls for materials with different selectivities [26]. On the other hand, multiplexing can also be achieved with a single sensor, that is operated

in temperature modulation. In both cases, the raw data is evaluated using different algorithms and machine learning approaches to extract the composition of a gas mixture [27].

Light activation is actually a key to both of these issues: The energy consumption of sensors can be decreased, while adjusting the photon energy and irradiance changes selectivity and sensitivity [25, 28].

Chapter 2

Objective

This thesis seeks to provide strategies for the development of advanced chemoresistive gas sensors with enhanced selectivity and decreased power consumption. Therefore new materials as well as variations of commonly used SMOX, including doping and loading, are proposed. These materials are investigated and evaluated for their potential applications. Besides, improved sensing systems are also accessible by changing their mode of operation: low temperature, temperature modulation or light activation.

On top of that, methods for the investigation of chemoresistive SMOX gas sensors are presented. There are still gaps in the knowledge on common basic materials and reactions that need investigation. With the development and application of advanced operando characterization techniques, e.g. DRIFTS or NAP-XPS, a better understanding of both material-specific as well as universal concepts is gained. Each stage of the investigation requires special experimental and theoretical methods, whose potentials and limitations are presented.

Chapter 3

Results and Discussion

3.1 Universal Concepts in Cemoresistive Gas Sensors

Gas sensors that are operated in ambient indoor or outdoor air are all subject to similar environmental conditions, i.e. temperature, pressure, and atmospheric composition. Air consists of around 78% low-reactive nitrogen, however, both oxygen (21%) and water vapor are highly reactive and omnipresent compounds of ambient air. Other constituents of the atmosphere are either rather inert (9934 ppm Ar, 420 ppm CO_2, 18 ppm Ne, 5.2 ppm He) or present permanently in concentrations low enough to be generally neglected (1.92 ppm CH_4, 0.55 ppm H_2, 0.33 ppm N_2O)[29].

Prior to the study of other analytes, a fundamental understanding of the reactions of both O_2 and H_2O is crucial. Conveniently, there are many similarities between different materials and universal concepts to explain their behavior.

3.1.1 Adsorption of Atmospheric Oxygen

The response of some materials towards 20.5% O_2, i.e. a change in the atmosphere from dry nitrogen to dry air, is presented in **Figure 3.1a**. At a first glance, there is no correlation between the sensor signal and temperature, material, or type of semiconductor.

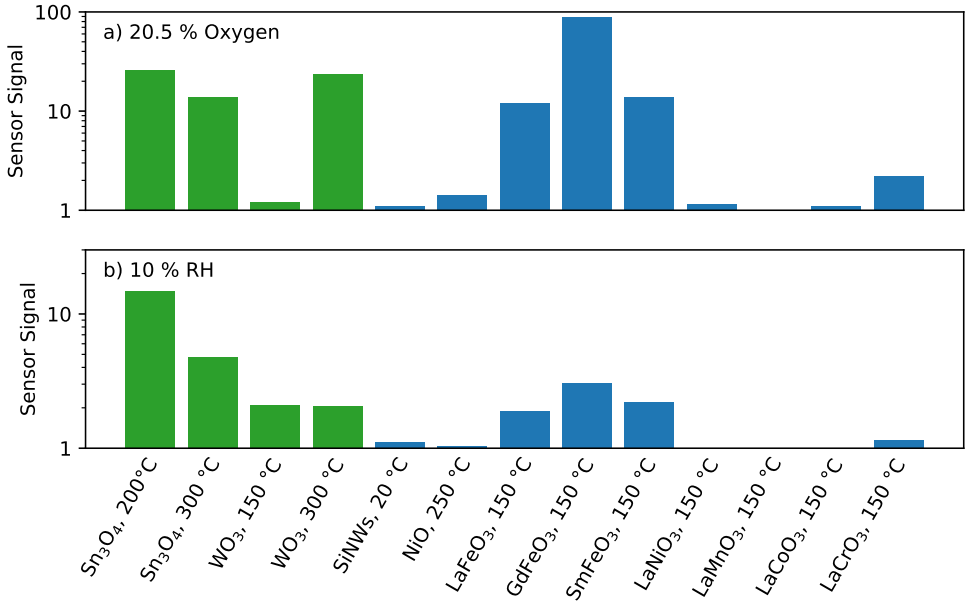

Figure 3.1: Sensor signals of various materials at different temperatures for the exposure to 20.5 % oxygen in a background of nitrogen (a) and 10 % RH in a background of dry air (b). The signals were calculated as $S = R_{\text{air}}/R_{\text{N2}}$ and $S = R_{\text{dry}}/R_{\text{humid}}$ for *n*-type semiconductors (green). For *p*-type semiconductors (blue) the reciprocal definitions are used [BJR05],[BJR07],[BJR10],[BJR11],[BJR13].

The first step of the interaction of oxygen with the SMOX surface is physisorption, involving only on weak Van-der-Waals type forces, at a not further specified site S:

$$O_2 + S + \rightleftharpoons (O_2)_S{}^{\times} \tag{3.1}$$

This site can be an oxygen vacancy, e.g. as found on NiO [BJR07] or Sn_3O_4 [BJR13].

The high electronegativity of oxygen drives the ionization of the dioxygen molecule to a superoxo-ion $O_2{}^-$:

$$(O_2)_S{}^{\times} + e^- \rightleftharpoons (O_2{}^-)_S{}' \tag{3.2}$$

This step marks the transition from physisorption to chemisorption with charge transfer and the formation of a space charge layer. It may result in a sensor signal.

The superoxo ion can subsequently be split and the ions are further oxidized until oxide ions O^{2-} are obtained:

$$(O_2{}^-)_S{}' \overset{e^-}{\rightleftharpoons} (O_2{}^{2-})_S{}'' \overset{S}{\rightleftharpoons} 2\,(O^-)_S{}' \overset{2e^-}{\rightleftharpoons} 2\,(O^{2-})_S{}'' \tag{3.3}$$

The stability of the individual oxygen species and therefore the coverage of the SMOX surface depends on the SMOX itself and the temperature. However atomic oxygen ions O^{2-} are the most abundant species [30]. The reaction sequence also elucidates that the molecular species serve as precursors for the atomic ones.

These processes can be traced with DRIFT spectroscopy; a few examples are given in **Figure 3.2**: On many materials, superoxo-ions (marked in blue) can be observed between 1030 and 1072 cm^{-1}. For Sn_3O_4, WO_3, and In_2O_3, the peaks related to the respective metal-oxygen bonds point to a complete reaction to oxide ions and therefore high sensor signals [BJR13], [BJR11].

In case of NiO, however, the superoxide-ions are rather dominant compared to the peaks for oxides (1257, 1296 cm^{-1}). This

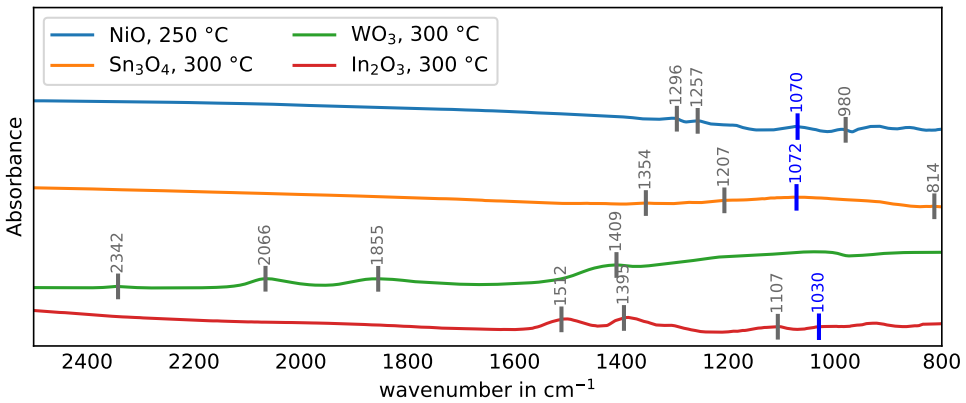

Figure 3.2: DRIFT absorbance spectra of several materials for the exposure to 20.5 % O_2 [BJR07],[BJR11],[BJR13]. Wavenumbers for O_2^- are marked in blue.

might contribute to the low sensor signal, because the additional charge transfer from (3.3) is of minor relevance [BJR07].

The effect of temperature can be seen for WO_3 and Sn_3O_4. In the first case, the signal increases with temperature because more activation energy for chemisorption of oxygen is available [BJR11]. For Sn_3O_4 the signal decreases with increasing temperature, probably due to a higher concentration of charge carriers already in N_2 [BJR13]. Given the low temperature and the almost absent sensor response, presumably the interaction of O_2 and SiNWs only involves physisorption according to (3.1).

Among the investigated perovskites, $LaNiO_3$, $LaMnO_3$ and $LaCoO_3$ show almost no response. Their resistivity is very low, almost comparable to metals [BJR05]. If reactions occur, their impact on the charge carrier density might thus be negligible.

3.1.2 Physisorption and Associative Adsorption of Water

Water vapor can interact with a SMOX surface in multiple ways. Not only will these reactions differ in the resulting surface species,

but also in their electrical effects. Among the relevant parameters are surface termination and reconstruction, defects, presence of other adsorbates, loadings, electron density, acidity and basicity, temperature, and pressure.

At low temperature, weak interactions based on Van-der-Waals forces are found. Water molecules in the gas phase are in a dynamic adsorption equilibrium with the surface. This interaction itself does not involve any exchange of electric charges, but may indirectly affect the resistance by competition with oxygen for the same sites according to (3.4).

$$O_O{}^{\times} \underset{O_2,\,2\,e^-}{\rightleftharpoons} V_O{}^{\cdot\cdot} \overset{H_2O}{\rightleftharpoons} (H_2O)_O{}^{\cdot\cdot} \tag{3.4}$$

An oxygen vacancy is either occupied by an oxygen molecule (reaction to the left) or a water molecule (to the right). The left part of the reaction also requires two electrons per half oxygen molecule. Both sides of the equation are linked and an increase in H_2O concentration, decreases the coverage with $O_O{}^{\times}$.

This competition between H_2O and O_2 is found at room temperature on SiNWs [BJR10]. In fact, the response to humidity is entirely based on this mechanism. With increasing surface coverage, the adsorbed water molecules will interact with surface oxygen via their hydrogen bonds [BJR03].

3.1.3 Chemisorption and Dissociative Adsorption of Water

Associatively adsorbed water molecules form an intermediate from physisorbed water to hydroxyl groups, where the water molecules are dissociated. A possible reaction is the formation of two terminal hydroxyl groups, i.e. monodentate OH ligands added to an existing metal cation [BJR03], [31, 32]. The $M-OH$ group can be regarded as an electron donor, since the metal ion remains oxidized.

$$H_2O + 2\,M_M{}^{\times} + O_O{}^{\times} \rightleftharpoons 2\,(M^{\delta+} - OH^{\delta-})_M{}^{\times} + V_O{}^{\cdot\cdot} + 2\,e^- \quad (3.5)$$

Another possibility is the formation of rooted hydroxyl groups, which can be treated as as protonated oxygen ions [BJR03], [BJR07], [31]. In this case, the negative charge of the reactant $O_O{}^{\times}$ is distributed across the two $(OH)_O{}^{\cdot}$ and therefore remains localized.

$$H_2O + O_O{}^{\times} + V_O{}^{\cdot\cdot} \rightleftharpoons 2\,(OH)_O{}^{\cdot} \pm 0\,e^- \quad (3.6)$$

Moreover, a reaction leading to a mixture of both types of OH groups is possible [BJR07], [BJR03], [31, 32]:

$$H_2O + M_M{}^{\times} + O_O{}^{\times} \rightleftharpoons (M^{\delta+} - OH^{\delta-})_M{}^{\times} + (OH)_O{}^{\cdot} + 1\,e^- \quad (3.7)$$

Assuming that the metal cation on which the hydroxyl group is formed conserves its oxidation state, the reaction provides one electron to the conduction band.

Both DRIFTS as well as resistance measurements indicate, which of the processes dominates. For WO_3, Sn_3O_4, and SnO_2, a decrease in resistance and well defined peaks above $3300\,cm^{-1}$ can be observed, indicating the formation of isolated hydroxyl groups via reactions (3.5) and (3.7). In contrast, on NiO there is barely an electrical effect and the aforementioned peaks are not observed, hence, reaction (3.6) is more likely to take place.

The previously discussed reactions of water were either neutral or reducing. In contrast, under certain conditions such as high temperature or illumination, an oxidizing effect of water was observed on WO_3 [BJR06], [33]. Following (3.8), water is reduced to hydrogen gas and the WO_3 surface is oxidized.

$$H_2O + V_O{}^{\cdot\cdot} + 2\,e^- \longrightarrow O_O{}^{\times} + H_2 \quad (3.8)$$

Finally, it is worth mentioning that in hot and humid climates the molar concentration of water, i.e. absolute humidity, can be as high as 40 000 ppm and therefore also the molar fraction of oxygen is decreased significantly, with implication on (1.1) [29].

3.2 Development of alternative Sensor Systems

As outlined in the previous section, commonly used pristine SMOX operated at high temperature, are based on the same principles and are often insufficient in terms of selectivity. Thus, different strategies towards sensors with new properties are followed.

3.2.1 Material Selection

An obvious way towards new properties is to explore other materials as sensing layers. Due to their different chemical and physical parameters some reactions are favored, others are hindered. The expected outcome is altered selectivity, along with potential benefits in response time, temperature of operation, sensitivity, stability etc.

Perovskites

While the term *Perovskite* generally refers to any compound ABX_3 resembling the crystal structure of $CaTiO_3$, within this work it is restricted to mixed oxides of lanthanoids and transition metals: $LnMO_3$. A well investigated representative of this class is $LaFeO_3$ [BJR05], [34, 35, 36]. Not only does $LaFeO_3$ show an excellent response to ethylene and acetylene at low temperature (150 °C), but it also has a pronounced inherent selectivity, especially when compared to SnO_2 or WO_3. Sensors signals towards various analytes are visualized in **Figure 3.3**.

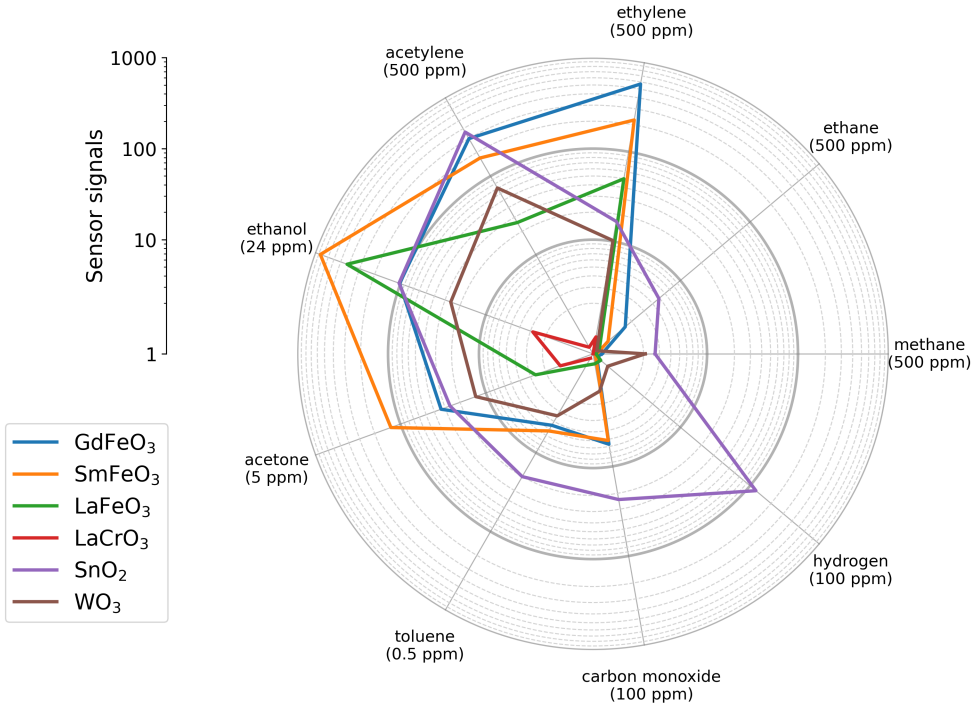

Figure 3.3: Sensor signals for different target gases in dry air for several $LnMO_3$ (operated at 150 °C), SnO_2 (300 °C), and WO_3 (250 °C)

From an application point of view, also other perovskites are promising, e.g. $SmFeO_3$ and $GdFeO_3$, which show higher responses than $LaFeO_3$ towards many of the analytes at the expense of selectivity. However, the higher baseline resistance is a challenge for the readout electronics. For all compounds, in which the Fe atoms were replaced by other transition metals (Cr, Mn, Co, Ni), the gas sensitive properties are almost absent and some of the materials show metallic properties (low resistance, positive temperature coefficient of resistance, dark color) [BJR05].

Concerning the sensing mechanism of these materials, the results suggest that the Fe-site plays a crucial role in the surface reactions. This is especially interesting, since for the detection of ethylene, both metallic Pt and Fe cations in the SMOX are required [BJR05],[10]. The C-C bond of ethylene is probably split

on Pt and the fragments are adsorbed at an Fe-site of the perovskite. If either component is missing, the reaction is prevented.

Moreover, $LaFeO_3$ and $SmFeO_3$ show their highest sensor signals around 150 °C. DRIFTS investigations reveal that high sensor signals are linked to surface formates [BJR05], [34].

Combined DRIFTS and gas phase analysis investigations provide more insights: Figure **3.4** presents the results obtained for $SmFeO_3$ on Au-electrodes, exposed to 500 ppm acetylene in dry air.

In the DRIFT absorbance spectra (**Figure 3.4a** and **c**) a shift from formate to carbonate adsorbates with increasing temperature can be observed. Combustion products and consumption of the analyte (acetylene) was analyzed by transmission gas phase FTIR spectroscopy of the upstream and downstream gas flows. The spectra are presented in **Figure 3.4b**, along with a quantification of the main peaks in **Figure 3.4d**. Up to 150 °C (where the highest signal is observed), no significant consumption of acetylene or any reaction products are found. From 200 °C upward on, where also the carbonates can be seen in DRIFTS, a conversion of C_2H_2 to CO and CO_2 is evident. The unstable level of residual humidity in the spectrometer hinders the quantification of the reaction product H_2O. In case of $SmFeO_3$, the creation of surface species (in this case: formates) is therefore much more efficient in evoking a sensor signal than the combustion of the analyte to CO_2 and H_2O.

Nickel Oxide

Nickel oxide sensors, investigated by Simion et al. [BJR07] exhibit a rare, but highly useful property: Their response to CO and H_2 is almost independent of the background humidity. The underlying mechanism was investigated via operando DRIFT spectroscopy, including O_2, H_2O and D_2O exposures. As already described in the previous section, the formation of superoxo-ions O_2^- as pre-

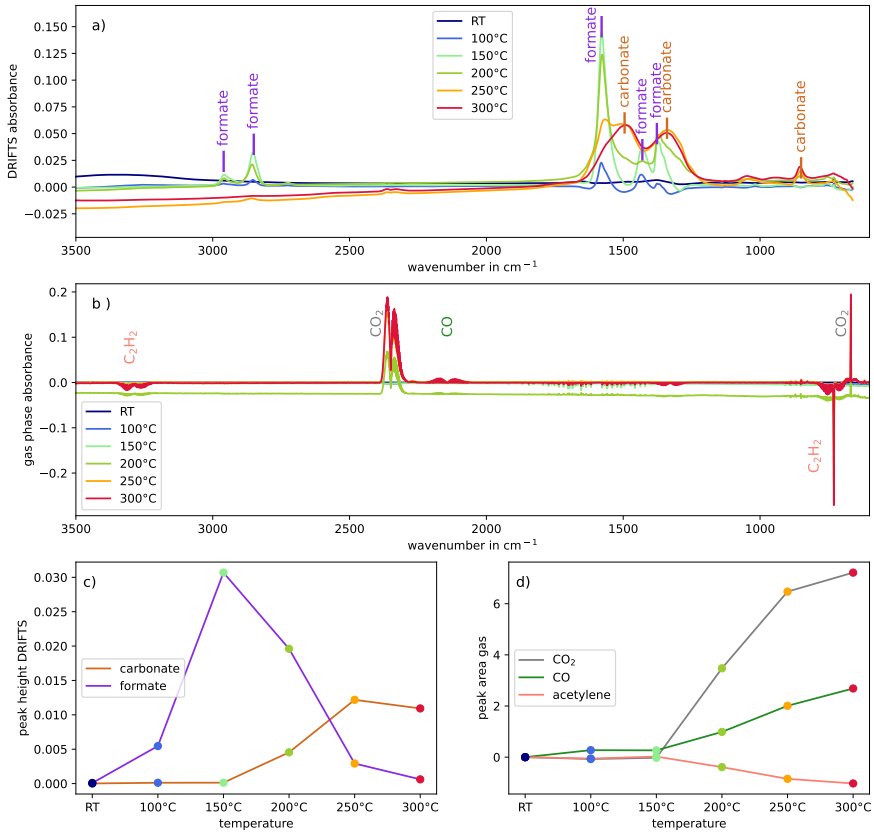

Figure 3.4: Temperature dependent reactions of acetylene on $SmFeO_3$ based sensors. a) DRIFT absorbance spectra and assignment of main peaks. b) Gas phase absorbance spectra of downstream air. c) and d) quantification of peaks in DRIFT and gas phase spectra, respectively.

cursors for oxide-ions O^{2-} according to (3.3) is the foundation for the subsequent reactions. For NiO, the equilibrium is more on the side of O_2^-. Interestingly, the reaction of both CO and H_2 with NiO yields OH groups, even though CO cannot provide H-atoms. Therefore a mechanism is proposed, in which the NiO surface is reduced and then immediately reacts with atmospheric water vapor, even if only present as residuals [BJR07]. The processes are

described as:

$$CO + H_2O + 2\,O_O{}^{\times} \longrightarrow 2\,(OH)_O{}^{\cdot} + CO_2 + 2\,e^- \quad (3.9)$$

$$H_2 + 2\,O_O{}^{\times} \longrightarrow 2\,(OH)_O{}^{\cdot} + 2\,e^- \quad (3.10)$$

In case of H_2, the OH groups are formed directly. All in all, the sensing mechanism of NiO is based on oxidation and reduction of the NiO surface, in contrast to the perovskites where adsorbates are formed during the reception process. For a holistic understanding, also other temperatures and other analytes still need to be investigated.

NiO can be used in applications where humidity is unknown and where the distinction between CO and H_2 is not required.

Tin Oxide

Tin(IV)-oxide (SnO_2) is the most commonly used and best understood SMOX material. Surprisingly, the related compounds SnO and Sn_3O_4 have only been investigated to a limited extent. In these compounds (at least part of) the Sn(IV) ions are reduced to Sn(II), which has several implications for its properties: new reactions sites, altered electron density and electronic states, and different surface termination.

Their oxidation state was investigated using XAS. **Figure 3.5** shows XANES spectra at the Sn-L_3 and Sn-L_1 edges of tin oxides, measured as fluorescence at the Lα_1 and Lβ_3 emission lines, respectively [37]. For comparison, XANES spectra of commercial tin compounds with known oxidation state have been recorded as well. While there is a very good agreement between the commercial and home made SnO_2, the SnO nanobelts show contributions of SnO_2, probably because the nanobelts are partially oxidized. Sn_3O_4 is more oxidized, while still showing contributions of SnO, e.g. around 3.983 keV in **Figure 3.5a** or the pre-edge shoulder in **Figure 3.5b**. Contributions from metallic Sn can be excluded.

Suman et al. prepared nanobelt structures of all three tin oxides and compared their sensor performances [38]. For example, higher signals for NO_2, but lower signals for H_2 have been found for the novel materials at 200 °C.

On Sn_3O_4, comprehensive DRIFTS and work function changes measurements were performed to unravel the gas sensing mechanisms [BJR08],[BJR13]. One of the key findings is, that on Sn_3O_4 fewer OH groups will be formed upon exposure to humidity, because the surface is already highly hydroxylated in dry conditions. Moreover, in contrast to SnO_2, the amount of OH groups is not changed during exposure to CO, indicating different reaction partners for H_2O and CO. Regarding these findings, Sn_3O_4 qualifies as sensing material for applications with changing humidity backgrounds. SnO and Sn_3O_4 are both considered metastable and could be transformed into SnO_2 during prolonged operation at high temperature [39]. An assessment of these materials' long term stability is still pending.

Silicon Nanowires

Brophy et al. designed a set of silicon nanowire (SiNW) based gas sensors specifically for the detection of NO_2. NO_2 is well suited for detection at room temperature, because of its rather low bond dissociation energy, compared to other analytes such as CO [40].

Investigations on SiNWs pointed out a strong dependency on background humidity: The sensors show excellent response towards NO_2 with low limit of detection, however, in dry air, low response and poor recovery were observed [BJR10]. Therefore, the sensing mechanism is presumably based on a competition of O_2, H_2O, and NO_2 for the same adsorption sites. NO_2 dominates this competition and therefore disrupts the equilibrium between O_2 and H_2O. In dry air, there are no water adsorbates at the surface, which can be displaced to provide a sensor response. Moreover, without water as competitor, the desorption of NO_2 is slow and

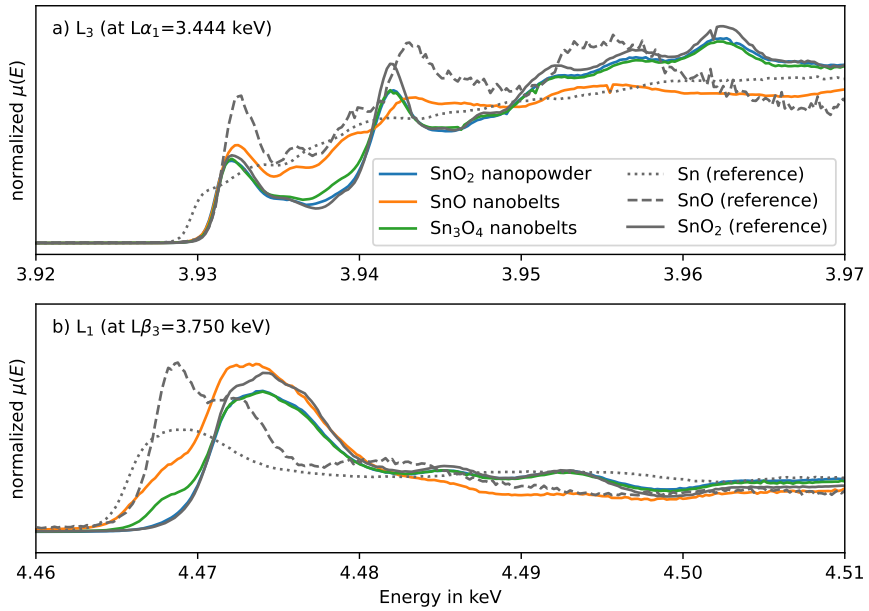

Figure 3.5: Sn HERFD-XANES of sensing layers and commercial Sn compounds, recorded at room temperature [37].

incomplete. Fortunately, a humidity level >10 % RH (at 20 °C), which is found in most application relevant conditions, enables satisfactory sensor performance. Other analytes that were tested (e.g. CO and ethanol) are not able to react at room temperature, making the SiNWs basically selective to NO_2.

3.2.2 Structure

How effectively the charge transfer of a chemical reaction is converted into a measurable change of resistance, highly depends on the structure of the sensing layer. As described in the introduction and illustrated in **Figure 1.3**, the overall resistance of a layer of large, spherical particles is often dominated by the barrier height at the grain boundaries and the unaffected bulk is neglected. For small spherical particles, however, the space charge layer may penetrate the entire cross section of the sphere. Therefore, not only

the barrier height decreases, but also the overall charge carrier concentration. It should be noted, that "small" in this context does not refer to the actual size of the grain, but to the ratio of its diameter and the material's Debye length. The latter controls the depth z_0 of the space charge layer.

An interesting model system to study the transduction and charge transport in a sensing layer is Sn_3O_4 nanobelts, due to their unconventional aspect ratio (15 nm × 150 nm × 30 µm). These can be approximated as single crystalline and therefore compact rectangular rods with uniform cross section that are connected at their long faces. Each rod-rod boundary can be treated as a potential barrier as found for spherical grains. Their shape introduces two peculiarities: On the one hand, a space charge layer building up radially can rather quickly affect the entire cross section and change the rod's bulk charge carrier density. On the other hand, their length does not justify ignoring their electrical resistance in axial direction. In fact, the results show, that the axial resistance of the rods outweighs the radial contact resistance due to potential barriers. (1.3) can be adjusted to model the correlation between band bending and resistance change of the Sn_3O_4 nanobelts:

$$\frac{R}{R_0} = \begin{cases} 1 + \sqrt{2} \cdot \frac{L_D}{D} \cdot \sqrt{e^{\frac{-eV_S}{kT}} + \frac{eV_S}{kT} - 1} & \text{for } \frac{eV_S}{kT} < 0 \text{ (upwards)} \\ 1 - \sqrt{2} \cdot \frac{L_D}{D} \cdot \sqrt{e^{\frac{-eV_S}{kT}} + \frac{eV_S}{kT} - 1} & \text{for } \frac{eV_S}{kT} \geq 0 \text{ (downwards)} \end{cases} \tag{3.11}$$

The relationship between band bending and resistance change according to (3.11) is illustrated in **Figure 3.6**. The higher the slope in this linearized representation, the more effective the transduction. For high ratios $L_D/D = 0.5$, i.e. the space charge layer penetrates the rods deeply, thus the resistance increases strongly under oxidizing conditions. For lower L_D/D, the unaffected core of the nanobelts limits the change of resistance, especially in oxidizing conditions.

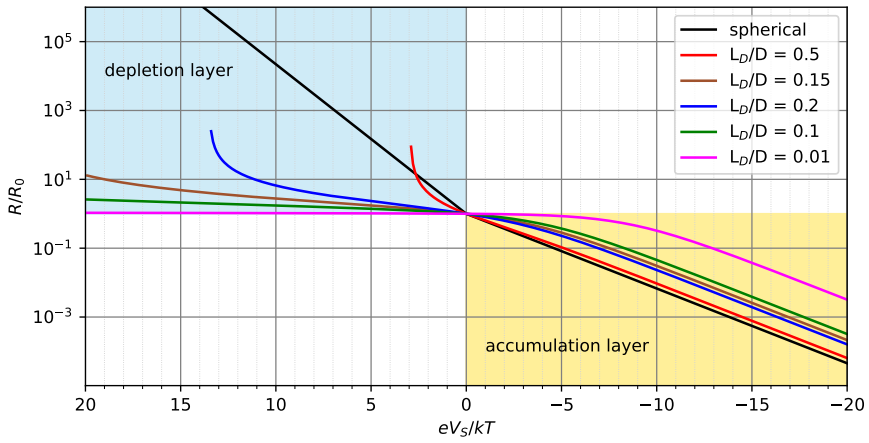

Figure 3.6: Calculated resistance change according to (3.11) with respect to band bending, expressed as eV_s/kT, of thin, compact layers for different ratios L_D/D

.

While these observations are interesting from an academic perspective, the general findings are relevant to the design of sensing layers: For good transduction the size and shape of primary particles must match their semiconductor properties. More specifically, the aspect ratio and size of the nanoparticles determines a certain concentration range where the induced band bending is translated into large resistance changes, i.e. where sensitivity is high. In conclusion, nanostructures can be tailored to solve specific analytic problems in this way.

3.2.3 Noble Metals

Noble metals are crucial components of SMOX gas sensors. Accordingly, they also provide a means for their improvement. Noble metals can be introduced as additives via loading or doping. They are also the default material of the electrodes.

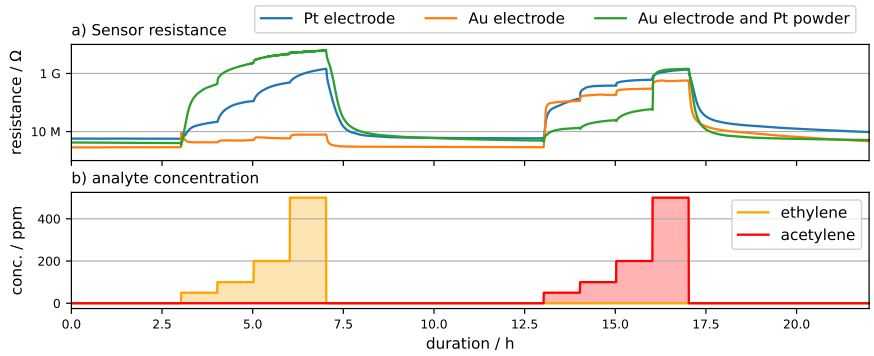

Figure 3.7: a) Resistance time series for $SmFeO_3$ sensors operated at 150 °C in an background of 10 % RH. b) Corresponding concentrations of ethylene and acetylene.

Electrodes

The electrode is an essential part of chemoresistive gas sensors. Prolonged operation in harsh conditions requires an inert and yet conductive material, hence, noble metals like Au or Pt are well suited candidates. However, beyond establishing an interface for charge transport, the electrode may introduce a (possibly rectifying) metal-semiconductor heterojunction, provide new reaction sites or may act as a catalyst.

For example, Alharbi et al. [10] demonstrated that the detection of ethylene using $LaFeO_3$ is possible in only combination with electrodes of Pt, not Au. Inspired by these results, the effect was investigated on differently designed $SmFeO_3$ sensors. The results presented in **Figure 3.7** not only confirm the need for Pt electrodes in order to detect ethylene, but also reveal its function. Ethylene is also detected on Au electrodes, if a small amount of Pt particles is added to the top of the sensing layer, separated from the charge transport. Therefore it is neither the interface, nor the heterojunction, but the catalytic properties which are responsible for this effect. Acetylene on the other hand can be detected with all three sensors with comparable signals. This indicates that the

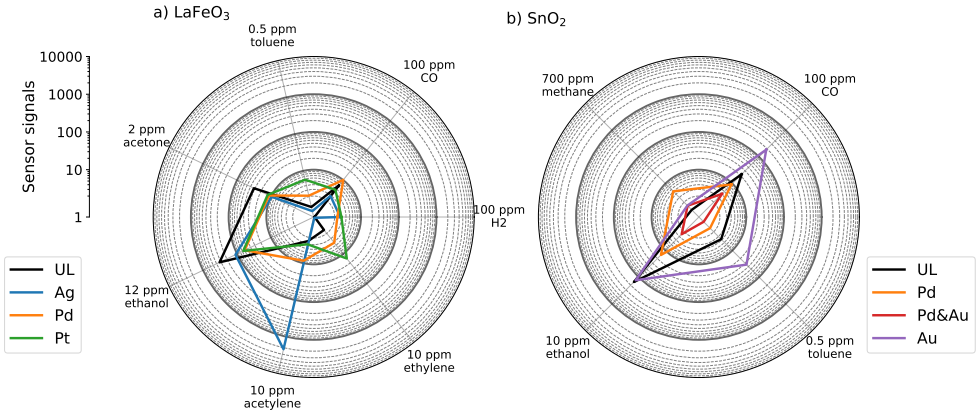

Figure 3.8: Sensor signals of loaded an unloaded SMOX sensors for different target gases. a) $LaFeO_3$ operated at 150 °C in 10% RH. b) SnO_2 operated at 300 °C in 50% RH.

relevant chemical reactions of acetylene take place on $SmFeO_3$, not Pt or Au.

Loadings

Loadings are the most powerful tool to change a SMOX sensor's selectivity. Two examples are given in **Figure 3.8**. $LaFeO_3$ was loaded with Ag, Pd, and Pt and each of the materials evoked a distinct selectivity pattern. Pt, as discussed in the previous section, could increase the response to ethylene, Pd the response to carbon monoxide, and Ag the response to acetylene. Noble metal alloys were the subject of another study [BJR02]. As shown in **Figure 3.8b**, the individual compounds and the alloy all affect the selectivity in a different way.

While the previous examples focused on the effect of different metals on the same SMOX, Staerz et al. demonstrated the distinct effect of Rh-loading on different SMOX [BJR01]. In all cases, oxidized Rh clusters were found to interact with the underlying SMOX electronically and change the conductance via Fermi level pinning. **Figure 3.9** shows that, despite the similarities, e.g.

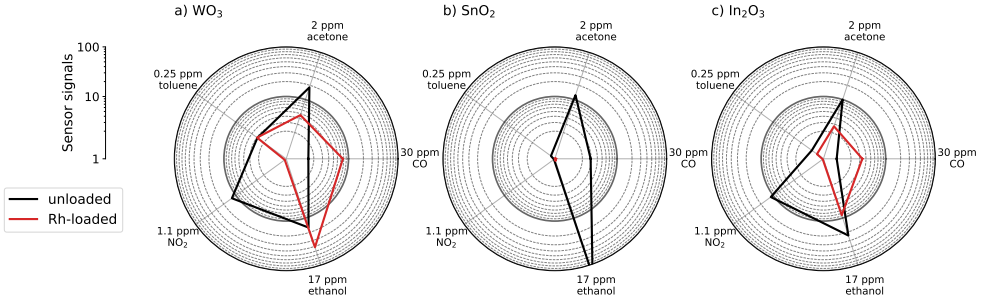

Figure 3.9: Sensor signals of loaded and unloaded SMOX sensors operated at 300 °C in 10% RH for different target gases. a) WO_3 (2.5%),°C in 10% RH. b) SnO_2 operated at 300 °C in 50% RH.

decreased response to NO_2 or increased response to CO, each material is affected in a unique way. Also, for SnO_2 with a loading of 0.5% (atomic) the overall response is nearly suppressed, while WO_3 still shows high signals at 2.5 %. Therefore, generalizing the findings of one loading to other SMOX is not possible.

A thorough study of the effect of size and concentration of the loading was conducted by Degler et. al [BJR12]. For this investigation, atomic layer deposition (ALD) was chosen as the loading method because it allows precise control of the amount of loading, starting from single ionic sites to nanoclusters. Besides, the deposition takes place on the entire surface accessible to the gas phase and the structure and composition of the WO_3 is not altered.

With the help of extensive spectroscopic investigations and CO as probe molecule, the effect of the loading's size can be explained as illustrated in **Figure 3.10**. Single Pt ions provide additional reaction sites for CO and increase the response. Small Pt clusters, can be fully oxidized and reduced by the atmosphere whereas for large clusters, an unaffected metallic core remains unchanged, shielding the WO_3 from the charge transfer at the Pt surface [BJR12].

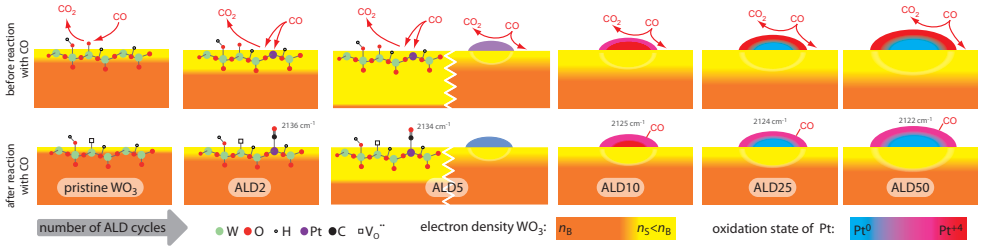

Figure 3.10: Schematic representation of the WO_3 sensing material with respect to the amount of Platinum deposited. Orange and yellow shades represent the local electron density. The top row illustrates the state of the surface and sites for the reaction of CO: Up to ALD5 the interaction with single oxygen and platinum sites is dominant, while at higher number of ALD cycles, the growth and composition of Pt-clusters is shown on a macroscopic scale. In the bottom row the effect of CO on both WO_3 and Pt is shown. Figure and caption are taken from [BJR12].

Doping

The materials in the previous section were prepared by adding noble metals on already synthesized SMOX powders or sensors, respectively. In order to incorporate the noble metal into the lattice, the additive can mixed with the precursor prior to calcination. Such a gel impregnation procedure was performed using $SnCl_4$ and $PtCl_4$ to yield Pt-doped SnO_2 [BJR04]. NAP-XPS was subsequently used to investigate the chemical state of Pt. Depending on the conditions, Pt was indeed oxidized or reduced, therefore acting as electron donor/acceptor for SnO_2. A comparison of the sensor properties of pristine, doped and loaded SnO_2 was not made, because the study was focused on the potential of NAP-XPS, not on the material itself [BJR04].

3.2.4 Light Activation

With the exception of SiNWs, the results presented in the previous chapters were all obtained at elevated temperature to provide

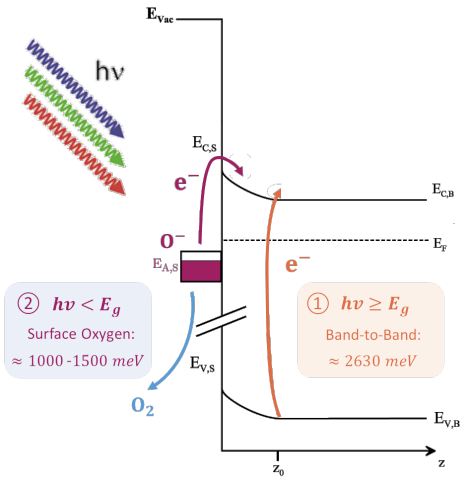

Figure 3.11: Schematic diagram of the WO_3 band structure and illustration of possible processes on illumination: Band-to-band excitation (1) and surface-state activation (2). The figure is taken from [BJR11].

the necessary energy for the chemisorption of molecules. A viable alternative is the addition of a light source, providing photons of a certain energy. The expected benefits can be summarized under two main aspects: Firstly, the replacement of a resistive heater by an LED promises a reduction in power consumption [28]. Also the mechanical construction and choice of materials is simplified by lowering the temperature of operation. Secondly, photo-activation enables entirely different reactions that are not possible with thermal activation or only take place at higher temperature. In other words, light provides another tool to change selectivity [24]. In contrast to the scalar temperature, at least two parameters (irradiance and photon energy) are required to describe a monochromatic light source (e.g. an LED). In other cases even the energy spectral density is required. On top of that, light gets adsorbed by SMOX, hence a non-homogeneous irradiance throughout the sensing layer is expected. Finally, one needs to consider the interaction of light with analyte molecules already in gas phase before interacting with the SMOX.

To understand the effect of light itself on SMOX, experiments on WO_3 under illumination were performed [BJR11]. **Figure 3.11** illustrates two possible processes: The excitation of charge carriers from the valence band to the conduction band ① as well as the clearing of surface related oxygen states ②. Since the effect is observed also with green light, whose photon energy is lower than the band gap, photodesorption of oxygen (②) was confirmed to be the more relevant process [41, 42]. Also on other materials, photons below the band gap of the materials lead to a decrease in resistance [BJR09]. The desorption of oxygen inevitably changes the surface coverage of the SMOX and its electron density. Any subsequent reactions of analytes are starting from a different state than under thermal activation.

This could be demonstrated by Wang et al. for the interaction of water vapor with the surface of WO_3 [BJR06]. Both the electrical resistance as well as the surface reactions were different at 340 °C without illumination and under illumination with blue light at room temperature.

Even though the baseline resistance at an intermediate temperature of 90 °C without illumination was similar to the one at room temperature with illumination, the reception of water vapor occurs differently.

Eventually, a systematic comparison of SnO_2, WO_3, In_2O_3 and ZnO under illumination at five different wavelengths was conducted by Junker et al. [BJR09]. The sensors were exposed to NO_2 and CO in different background humidities at 70 °C. The slightly higher temperature was selected to avoid detrimental effects of condensed water in the pores of the SMOX. For each of the materials, distinct peculiarities were discovered, e.g. for the detection of NO_2, shown in **Figure 3.12**: SnO_2 is strongly influenced by UV-light illumination. For In_2O_3 a minimum in NO_2 signals is found for moderate photon energies (blue light), whereas for ZnO the signals for NO_2 decrease with photon energy. Even though

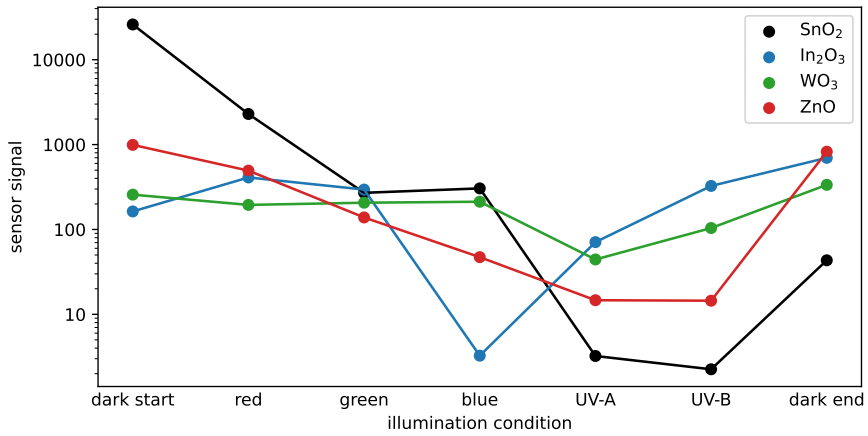

Figure 3.12: Sensor signals of different SMOX sensors operated at 70 °C in 30% RH exposed to 0.75 ppm NO_2 under illumination at different wavelengths [BJR09].

previous studies highlighted the mesmerizing photochemistry of WO_3, its performance was least affected by illumination.

3.3 Investigation Methods

To gain the insights presented in the previous chapters, different operando methods were used. *Operando* literally means "at work" [43] whereas *in-situ* (at place) only refers to conditions mimicking the applications. Operando investigations specifically on gas sensors require:

- defined gas atmosphere at ambient pressure
- heated sensing layer
- sensor readout (typically resistance)
- additional investigation (e.g. spectroscopy)
- exposure to light, if applicable

In-situ omits the electrical readout and sometimes also heating or the requirement for ambient pressure. The interpretation of the terms in-situ and operando varies between different fields of science. Unless stated otherwise, in this work the above mentioned criteria apply. A short overview on the methods used in this work and the experimental improvements is provided. Neither the list of experimental techniques, nor the presentation of the extracted information is complete.

3.3.1 Electrical Resistance

- Measured quantity: Resistance, impedance
- Derived information: Resistance change, I-V characteristics
- Instrumentation: Multimeter, Electrometer, Source-Measure-Unit

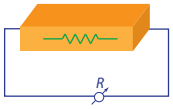

DC resistance is the most universal and most sensitive analytical method and is by definition the output quantity of a chemoresistive sensor. Multiple sensors can be investigated at once for efficient batch screening. Simple multimeters force constant current through the sensing layer and will measure the required voltage. For non-ohmic systems, that are sensitive to the polarization voltage, a reverse setup (force voltage – measure current) is required. Specialized equipment has to be used for accurate readout of very high resistances ($<$1GΩ). In addition, impedance measurements using alternating current at different frequencies can provide insights into capacitive elements (space charge layers) and charge carrier mobility.

During the investigation of light-activated gas sensors, a combination of the presence of condensed water due to low temperature

of operation and high polarization during DC resistance measurements, was found to be responsible for detrimental electrochemical processes [BJR09]. More specific, electrolysis of the sensing layer itself was observed. Also, permanent and pulsed polarization of the sensing layer affect the sensors differently.

3.3.2 Work Function Changes

- Measured quantity: Contact potential difference
- Derived information: Work function changes
- Instrumentation: Kelvin probe

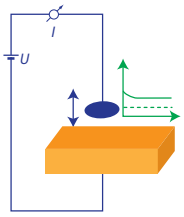

The Kelvin probe is able to measure *changes* in work function upon gas exposure. The work function Φ is the sum of band bending eV_S, electron affinity χ, and distance between Fermi level and conduction band edge $(E_C - E_F)_{bulk}$:

$$\Phi = eV_S + \chi + (E_C - E_F)_{bulk} \tag{3.12}$$

Combined work function changes and resistance measurements allow the separation of these parameters.

A direct comparison of experimental data and theoretical models was used to unravel the transduction in nanostructured Sn_3O_4 [BJR08].

3.3.3 UV-vis Spectroscopy

For the works discussed in this thesis, UV-vis spectroscopy has only been applied ex-situ for the determination of band gaps [BJR11]. However, it is possible to perform UV-vis spectroscopy

- Measured quantity: UV-vis diffuse reflection
- Derived information: Absorbance, band gap
- Instrumentation: UV-vis spectrometer with broad band light source, and diffuse reflectance optics

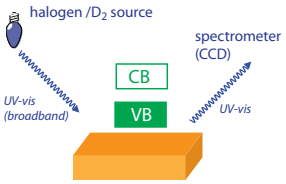

in diffuse reflectance geometry in operando, e.g. to monitor the surface reduction of SnO_2 [44].

3.3.4 Infrared Spectroscopy

- Measured quantity: Infrared diffuse reflection and absorbance
- Derived information: Changes of IR active surface species, lattice vibrations and gas phase molecules.
- Instrumentation: FTIR spectrometer with reflectance optics

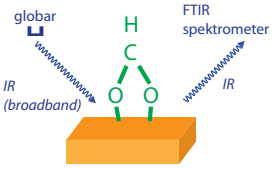

Diffuse reflectance infrared Fourier transformation spectroscopy (DRIFTS) is probably the most powerful tool in the investigation of gas sensing mechanisms. DRIFTS can monitor how different surface species are created and consumed during the exposure to different gases. Moreover, many metal–oxgen bonds of the SMOX lattice can be detected and conclusions on the reduction and oxidation of the surface can be drawn [BJR01],[BJR02],[BJR11]. Isotopically labeled gases help the identification of peaks due to their shift in wavenumbers [BJR07],[BJR13]. Gas phase molecules such as CO or CO_2 also

contribute to the absorption, adding more information about the reaction mechanism [BJR05].

The scope of DRIFTS was enhanced by combining light activation with operando investigations [BJR06].

3.3.5 X-ray Absorption Spectroscopy

- Measured quantity: X-ray absorption (via fluorescence)
- Derived information: Density of unoccupied states, oxidation state, environment of atoms
- Instrumentation: Synchrotron beamline with monochromator and total fluorescence detector or emission spectrometer

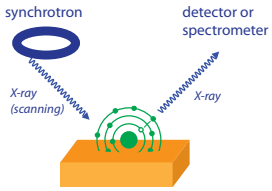

Synchrotron light sources with their highly specialized beamlines offer a vast selection of techniques, of which only a fraction has yet been applied to SMOX gas sensors. Under most circumstances, XAS is element-specific and therefore allows studying loadings independently of the SMOX. X-ray absorption near edge structure (XANES) can be used to determine the oxidation state of the loading's element during exposure to analyte gases [BJR12].

Another region of interest in absorbance spectra is the extended X-ray absorption near edge structure (EXAFS) region. Here, the emitted X-rays are scattered by neighboring atoms in the lattice. This can be transformed into a radial distribution of scattering atoms around the element of interest. In this way, one can distinguish between loadings present as oxide clusters or single atoms incorporated into the SMOX lattice [BJR01].

If the loading's edge of interest overlaps with an absorption edge of the SMOX (e.g. Pt Lα_1 and W Lβ_1), the X-ray fluo-

rescence is measured with an emission spectrometer as HERFD-XANES (high energy resolution fluorescence detection). While operando investigations are possible, the interaction of tender or hard X-rays with air is reduced as much as possible by using small measurement chambers and replacing N_2 with He.

Besides the characterization of noble metal additives, HERFD-XANES was applied to pristine SnO_2 [37].

3.3.6 Near Ambient Pressure X-ray Photoelectron Spectroscopy

- Measured quantity: Kinetic energy of photoelectrons
- Derived information: Binding energies, oxidation state, absolute work function
- Instrumentation: Photoelectron spectrometer with differentially pumped analyzer, preferably combined with synchrotron light source

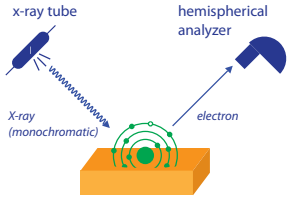

X-ray photoelectron spectroscopy (XPS) is a well-established, element specific surface analysis method. Limited by the mean free path of the photoelectrons, XPS only probes a few nanometers of the samples and is thus complementary to the previously presented, deeply penetrating XAS studies. Unfortunately, being a photon-in, electron-out technique, XPS requires UHV conditions. As a workaround, specialized analyzers with multiple pumping stages and a small inlet aperture in proximity to the sample were developed. In these near ambient pressure X-ray photoelectron spectrometers (NAP-XPS) the sample is typically kept at a pressure of a few millibars, with some setups going up to atmospheric pressure. Yet, in a low total pressure, the SMOX surface is in a different state than at ambient pressure, even if the partial pressure

of reactive analytes, e.g. oxygen is identical [BJR04]. NAP-XPS investigations can therefore only considered as an *indication* for the processes at ambient pressure.

3.3.7 Data Analysis

The data presented in the previous chapter was evaluated in a direct manner: An experiment was performed, raw data was transformed, visualized and then interpreted. Finally, the information of different experimental techniques was combined until conclusions could be drawn. This approach works well, if the objective of the experimental investigation is directly accessible with these methods. However, there are cases where this approach is not fruitful and more advanced methods for data analysis are required. In fact, at the interface of chemistry and statistics, the discipline of *chemometrics* i.e. "the application of statistics to the analysis of chemical data (from organic, analytical or medicinal chemistry) and design of chemical experiments and simulations" [13] can be found.

In the field of gas sensing, chemometrics is mainly used to extract the desired information from complex data sets, e.g. sensor arrays. An example of such a use case is the monitoring of hand disinfection processes in medical applications [45]: Here, convolutional neural networks are used to evaluate sensor data and to classify the disinfection process as "correct" or "incorrect".

In contrast to that, Junker et al. applied chemometric methods on a set of resistance data acquired using light activated gas sensors [BJR09]. Four different SMOX materials were systematically investigated in seven illumination conditions. First, only few obvious characteristics were found in the experimental data, but with the help of chemometrics, many more trends and correlations could be identified than initially expected.

Chapter 4

Conclusions

The overall goal of the studies presented is this work was to propose new strategies towards advanced chemoresistive gas sensors. Among the new materials, especially $LaFeO_3$ and $SmFeO_3$ are promising candidates due to their low temperature operation and inherent selectivity. Long term studies for these materials are promising. NiO is of interest because of its independence from humidity and its well-known chemical properties. While Sn_3O_4 and SiNWs are also promising materials, their long term stability still needs to be proven. Concerning noble metal loadings, rhodium turned out to be an interesting, so far less regarded element, while the Au-Pd alloy showed inferior performance, compared to the individual elements. ALD was introduced as a highly reproducible deposition method for gas sensors.

Experiments under illumination clearly showed the potential of light activation for decreased power consumption and tunable selectivity. However, because the processes of reception and transduction are fundamentally different from thermal activation, a considerable amount of research is required to reach the same level of understanding. Chemometric methods enable the extraction of additional information from experimental data.

Finally the benefits and versatility of operando investigations was demonstrated.

Chapter 5

Bibliography

Highlighted own Works

[BJR01] Anna Staerz, Inci Boehme, David Degler, Mounib Bahri, Dmitry E. Doronkin, Anna Zimina, Helena Brinkmann, Sina Herrmann, Benjamin Junker, Ovidiu Ersen, Jan-Dierk Grunwaldt, Udo Weimar, and Nicolae Barsan. Rhodium Oxide Surface-Loaded Gas Sensors. *Nanomaterials*, 8(11): 892, November 2018. ISSN 2079-4991. doi: 10.3390/nano8110892. URL https://www.mdpi.com/2079-4991/8/11/892.

[BJR02] Ghazal Tofighi, David Degler, Benjamin Junker, Sabrina Müller, Henning Lichtenberg, Wu Wang, Udo Weimar, Nicolae Barsan, and Jan-Dierk Grunwaldt. Microfluidically synthesized Au, Pd and AuPd nanoparticles supported on SnO_2 for gas sensing applications. *Sensors and Actuators B: Chemical*, 292:48-56, 2019. ISSN 0925-4005. doi: https://doi.org/10.1016/j.snb.2019.02.107. URL https://www.sciencedirect.com/science/article/pii/S0925400519303314.

[BJR03] David Degler, Benjamin Junker, Frank Allmendinger, Udo Weimar, and Nicolae Barsan. Investigations on

the Temperature-Dependent Interaction of Water Vapor with Tin Dioxide and Its Implications on Gas Sensing. *ACS Sensors*, 5(10):3207– 3216, October 2020. ISSN 2379-3694, 2379-3694. doi: 10. 1021/acssensors.0c01493. URL https://pubs.acs.org/doi/10.1021/acssensors.0c01493.

[BJR04] Benjamin Junker, Marco Favaro, David E Starr, Michael Hävecker, Udo Weimar, and Nicolae Barsan. NAP-XPS as a new tool for in-situ studies of SMOX gas sensors. *Journal of Physics D: Applied Physics*, 55(6):064002, February 2022. ISSN 0022- 3727, 1361-6463. doi: 10.1088/1361-6463/ac3283. URL https://iopscience.iop.org/article/10.1088/1361-6463/ac3283.

[BJR05] Abdulaziz Alharbi, Benjamin Junker, Mohammad Alduraibi, Ahmad Algarni, Udo Weimar, and Nicolae Bârsan. The role of different lanthanoid and transition metals in perovskite gas sensors. Sensors, 21(24), December 2021. ISSN 14248220. doi: 10.3390/s21248462. Publisher: MDPI.

[BJR06] Xiao-Xue Wang, Benjamin Junker, Carolin Ewald, Udo Weimar, Xin Guo, and Nicolae Barsan. Proof of Concept for Operando Infrared Spectroscopy Investigation of Light-Excited Metal Oxide- Based Gas Sensors. *The Journal of Physical Chemistry Letters*, 13(16):3631–3635, April 2022. ISSN 1948-7185, 1948-7185. doi: 10.1021/acs.jpclett.2c00480. URL https://pubs.acs.org/ doi/10.1021/acs.jpclett.2c00480.

[BJR07] Cristian E. Simion, Benjamin Junker, Udo Weimar, Adelina Stanoiu, and Nicolae Bârsan. Sensing mechanisms of

CO and H_2 with NiO material – DRIFTS investigations. *Sensors and Actuators B: Chemical*, 390:134028, 29 September 2023. ISSN 09254005. doi: 10.1016/j.snb.2023.134028. URL https://linkinghub.elsevier.com/retrieve/pii/S0925400523007438.

[BJR08] Pedro H. Suman, Benjamin Junker, Udo Weimar, Marcelo O. Orlandi, and Nicolae Barsan. Modeling the Conduction Mechanism in Chemoresistive Gas Sensor Based on Single-Crystalline Sn3 O4 Nanobelts: A Phenomenological In Operando Investigation. *ACS Sensors*, 9(1):149–156, January 2024. ISSN 2379- 3694, 2379-3694. doi: 10.1021/acssensors.3c01810. URL https://pubs.acs.org/doi/10.1021/acssensors.3c01810.

[BJR09] Benjamin Junker, Arne Kobald, Carolin Ewald, Peter Janoschek, Malte Schalk, Udo Weimar, Lutz Mädler, and Nicolae Bârsan. Multivariate Analysis of Light-Activated SMOX Gas Sensors. *ACS Sensors*, 9(3):1584–1591, March 2024. ISSN 2379-3694, 2379-3694. doi: 10.1021/acssensors.4c00078. URL https://pubs.acs.org/doi/10.1021/acssensors.4c00078.

[BJR10] Rachel Elizabeth Brophy, Benjamin Junker, Elham Aghabalei Fakhri, Hákon Örn Árnason, Halldór Guðfinnur Svavarsson, Udo Weimar, Nicolae Bârsan, and Andrei Manolescu. Ultra Responsive NO_2 silicon nanowires gas sensor. *Sensors and Ac- tuators B: Chemical*, 410:135648, July 2024. ISSN 09254005. doi: 10.1016/j.snb.2024.135648. URL https://linkinghub.elsevier.com/retrieve/pii/S0925400524003770.

[BJR11] Benjamin Junker, Xiao-Xue Wang, Udo Weimar, and Nicolae Bârsan. Operando DRIFTS Proof of Visible-Light-Activated Surface Reduction of WO3 :

Implication for Gas Sensing. *The Journal of Physical Chemistry C*, 129(21):9795–9800, May 2025. ISSN 1932-7447, 1932-7455. doi: 10.1021/acs.jpcc.5c01808. URL https://pubs.acs.org/doi/10.1021/acs.jpcc.5c01808.

[BJR12] David Degler, Ugur Geyik, Benjamin Junker-Reiss, Muhammad Hamid Raza, Patrick Amsalem, Norbert Koch, Blanka Detlefs, Nicola Pinna, Udo Weimar, and Nicolae Barsan. Investigation on the Structure–Function Relationship of Atomic- Layer-Deposited Platinum Additives on Tungsten Trioxide Gas Sensor Materials. *The Journal of Physical Chemistry C*, 129(34): 15301–15308, August 2025. ISSN 1932-7447, 1932-7455. doi: 10.1021/acs.jpcc.5c05000. URL https://pubs.acs.org/doi/10.1021/acs.jpcc.5c05000.

[BJR13] Pedro H. Suman, Benjamin Junker-Reiss, Udo Weimar, Marcelo O. Orlandi, and Nicolae Barsan. Unraveling the gas sensing mechanism of single-crystalline Sn_3O_4 nanobelts using operando DRIFT spectroscopy and isotopically labeled gases. *Sensors and Actuators B: Chemical*, 447:138909, January 2026. ISSN 09254005. doi: 10.1016/j.snb.2025. 138909. URL https://linkinghub.elsevier.com/retrieve/pii/S0925400525016855.

Bibliography

[1] Pravas Kumar Panigrahi, Basavaiah Chandu, and Nagaprasad Puvvada. Recent Advances in Nanostructured Materials for Application as Gas Sensors. *ACS Omega*, 9(3): 3092–3122, 2024. ISSN 2470-1343, 2470-1343. doi: 10.1021/acsomega.3c06533.

[2] Giovanni Neri. First Fifty Years of Chemoresistive Gas Sensors. *Chemosensors*, 3(1):1–20, 2015. ISSN 2227-9040. doi: 10.3390/chemosensors3010001.

[3] Ali Mirzaei, Salvatore Gianluca Leonardi, and Giovanni Neri. Detection of hazardous volatile organic compounds (VOCs) by metal oxide nanostructures-based gas sensors: A review. *Ceramics international*, 42(14):15119–15141, 2016.

[4] Avner Rothschild and Yigal Komem. The effect of grain size on the sensitivity of nanocrystalline metal-oxide gas sensors. *Journal of Applied Physics*, 95(11):6374–6380, 2004. ISSN 0021-8979. doi: 10.1063/1.1728314.

[5] Ghenadii Korotcenkov. The role of morphology and crystallographic structure of metal oxides in response of conductometric-type gas sensors. *Materials Science and Engineering: R: Reports*, 61(1):1–39, 2008. ISSN 0927-796X. doi: 10.1016/j.mser.2008.02.001.

[6] Wen-dong Zhou, Davoud Dastan, Xi-tao Yin, Shuai Nie, Saisai Wu, Qi Wang, and Jing Li. Optimization of gas sensing properties of n-SnO2/p-xCuO sensors for homogenous gases and the sensing mechanism. *Journal of Materials Science: Materials in Electronics*, 31(21):18412–18426, 2020. ISSN 0957-4522, 1573-482X. doi: 10.1007/s10854-020-04387-3.

[7] Huiwu Long, Yanqiong Li, Ke Chai, and Wen Zeng. Metal oxide semiconductor-based core-shell nanostructures for chemiresistive gas sensing: A review. *Sensors and Actuators B: Chemical*, 417:136183, 2024. ISSN 0925-4005. doi: https://doi.org/10.1016/j.snb.2024.136183.

[8] David Degler, Udo Weimar, and Nicolae Barsan. Current Understanding of the Fundamental Mechanisms of Doped and Loaded Semiconducting Metal-Oxide-Based Gas Sensing Materials. *ACS Sensors*, 4(9):2228–2249, 2019. ISSN 2379-3694, 2379-3694. doi: 10.1021/acssensors.9b00975.

[9] Shigenori Matsushima, Yasutake Teraoka, Norio Miura, and Noboru Yamazoe. Electronic Interaction between Metal Additives and Tin Dioxide in Tin Dioxide-Based Gas Sensors. *Japanese Journal of Applied Physics*, 27(10R):1798, 1988. ISSN 0021-4922, 1347-4065. doi: 10.1143/JJAP.27.1798.

[10] Abdulaziz A. Alharbi, Andre Sackmann, Udo Weimar, and Nicolae Bârsan. Essential role of electrode materials in ethylene and acetylene sensing selectivity for LaFeO3 based gas sensors. *Sensors and Actuators B: Chemical*, 353:131079, 2022. ISSN 0925-4005. doi: https://doi.org/10.1016/j.snb.2021.131079.

[11] T. Sauerwald, D. Skiera, and C.-D. Kohl. Selectivity enhancement of gas sensors using non-equilibrium polarisation effects in metal oxide films. *Applied Physics A*, 87(3):

525–529, 2007. ISSN 0947-8396, 1432-0630. doi: 10.1007/s00339-007-3980-2.

[12] Nicolas Dufour, Yoan Veyrac, Philippe Menini, Frédéric Blanc, Chabane Talhi, Bernard Franc, Christian Ganibal, Corinne Wartelle, and Khalifa Aguir. Increasing the sensitivity and selectivity of Metal Oxide gas sensors by controlling the sensitive layer polarization. In *2012 IEEE Sensors*, pages 1–4, Taipei, 2012. IEEE. ISBN 978-1-4577-1766-6 978-1-4577-1767-3. doi: 10.1109/ICSENS.2012.6411463.

[13] International Union of Pure and Applied Chemistry (IUPAC). Compendium of chemical terminology. 2025. doi: doi:10.1351/goldbook. URL `https://doi.org/10.1351/goldbook`.

[14] Zhiqiao Gao, Menglei Mao, Jiuwu Ma, Jincheng Han, Hengzhen Feng, Wenzhong Lou, Yixin Wang, and Teng Ma. Modeling of Chemiresistive Gas Sensors: From Microscopic Reception and Transduction Processes to Macroscopic Sensing Behaviors. *Chemosensors*, 13(7):227, 2025. ISSN 2227-9040. doi: 10.3390/chemosensors13070227.

[15] Taposhree Dutta, Tanzila Noushin, Shawana Tabassum, and Satyendra K. Mishra. Road Map of Semiconductor Metal-Oxide-Based Sensors: A Review. *Sensors*, 23(15):6849, 2023. ISSN 1424-8220. doi: 10.3390/s23156849.

[16] Nicolae Bârsan and Udo Weimar. Understanding the fundamental principles of metal oxide based gas sensors; the example of CO sensing with SnO2 sensors in the presence of humidity. *Journal of Physics: Condensed Matter*, 15 (20):R813–R839, 2003. ISSN 0953-8984, 1361-648X. doi: 10.1088/0953-8984/15/20/201.

[17] N. Bârsan, M. Hübner, and U. Weimar. Conduction mechanisms in SnO2 based polycrystalline thick film gas sensors exposed to CO and H2 in different oxygen backgrounds. *Sensors and Actuators, B: Chemical*, 157(2):510–517, 2011. ISSN 09254005. doi: 10.1016/j.snb.2011.05.011.

[18] Jong Myoung Choi, Joon Hyuk Byun, and Sang Sub Kim. Influence of grain size on gas-sensing properties of chemiresistive p-type NiO nanofibers. *Sensors and Actuators, B: Chemical*, 227:149–156, 2016. ISSN 09254005. doi: 10.1016/j.snb.2015.12.014.

[19] Takuya Suzuki, Andre Sackmann, Alexandru Oprea, Udo Weimar, and Nicolae Bârsan. Chemoresistive CO_2 Gas Sensors Based On $La_2O_2CO_3$: Sensing Mechanism Insights Provided by Operando Characterization. *ACS Sensors*, 5(8): 2555–2562, 2020. ISSN 2379-3694, 2379-3694. doi: 10.1021/acssensors.0c00882.

[20] Marcel Bouvet, Vicente Parra, Clémentine Locatelli, and Hui Xiong. Electrical transduction in phthalocyanine-based gas sensors: from classical chemiresistors to new functional structures. *Journal of Porphyrins and Phthalocyanines*, 13(01): 84–91, 2009.

[21] Ghenadii Korotcenkov, Vladimir Brinzari, and Moon-Ho Ham. Materials acceptable for gas sensor design: advantages and limitations. *Key Engineering Materials*, 780:80–89, 2018.

[22] Lutz Mädler, Thorsten. Sahm, Alexander Gurlo, Jan Dierk Grunwaldt, Nicolae Barsan, Udo Weimar, and Sotiris E. Pratsinis. Sensing low concentrations of CO using flame-spray-made Pt/SnO2 nanoparticles. *Journal of Nanoparticle Research*, 8(6):783–796, 2006. ISSN 13880764. doi: 10.1007/s11051-005-9029-6.

[23] Wen Jie Zhao, Dan Xu, Yin Sheng Chen, Xuan Wang, and Yun Bo Shi. A low-temperature micro hotplate gas sensor based on ALN ceramic for effective detection of low concentration NO2. *Sensors (Switzerland)*, 19(17), 2019. ISSN 14248220. doi: 10.3390/s19173719. Publisher: MDPI AG.

[24] Yanting Tang, Yunong Zhao, and Huan Liu. Room-temperature semiconductor gas sensors: challenges and opportunities. *ACS sensors*, 7(12):3582–3597, 2022.

[25] Artem Chizhov, Pavel Kutukov, Artyom Astafiev, and Marina Rumyantseva. Photoactivated processes on the surface of metal oxides and gas sensitivity to oxygen. *Sensors*, 23(3): 1055, 2023.

[26] Gulshan Verma, Anisha Gokarna, Hind Kadiri, Komla Nomenyo, Gilles Lerondel, and Ankur Gupta. Multiplexed Gas Sensor: Fabrication Strategies, Recent Progress, and Challenges. *ACS Sensors*, 8(9):3320–3337, 2023. ISSN 2379-3694, 2379-3694. doi: 10.1021/acssensors.3c01244.

[27] Arne Kobald, Udo Weimar, and Nicolae Bârsan. Towards understanding temperature modulated SMOX gas sensor arrays for outdoor air quality applications. *Sensors and Actuators B: Chemical*, 440:137879, 2025. ISSN 09254005. doi: 10.1016/j.snb.2025.137879.

[28] Jing Wang, Huchi Shen, Yi Xia, and Sridhar Komarneni. Light-activated room-temperature gas sensors based on metal oxide nanostructures: A review on recent advances. *Ceramics international*, 47(6):7353–7368, 2021.

[29] National Oceanic and Atmospheric Administration. The atmosphere. `https://www.noaa.gov/jetstream/atmosphere`, July 2024. URL `https:`

//www.noaa.gov/jetstream/atmosphere. Accessed: 2025-11-03.

[30] Kenji Tabata, Takashi Kawabe, Yoichi Yamaguchi, and Yousuke Nagasawa. Chemisorbed Oxygen Species over the (110) Face of SnO2. *Catalysis Surveys from Asia*, 7(4):251–259, 2003. ISSN 1571-1013, 1574-9266. doi: 10.1023/B:CATS.0000008164.21582.92.

[31] Susanne Wicker, Mathilde Guiltat, Udo Weimar, Anne Hémeryck, and Nicolae Barsan. Ambient Humidity Influence on CO Detection with SnO $_2$ Gas Sensing Materials. A Combined DRIFTS/DFT Investigation. *The Journal of Physical Chemistry C*, 121(45):25064–25073, 2017. ISSN 1932-7447. doi: 10.1021/acs.jpcc.7b06253.

[32] Katharina Großmann, Susanne Wicker, Udo Weimar, and Nicolae Barsan. Impact of Pt additives on the surface reactions between SnO2, water vapour, CO and H2; An operando investigation. *Physical Chemistry Chemical Physics*, 15 (44):19151–19158, 2013. ISSN 14639076. doi: 10.1039/c3cp52782d.

[33] Anna Staerz, Christoph Berthold, Tamara Russ, Susanne Wicker, Udo Weimar, and Nicolae Barsan. The oxidizing effect of humidity on WO3 based sensors. *Sensors and Actuators, B: Chemical*, 237:54–58, 2016. ISSN 09254005. doi: 10.1016/j.snb.2016.06.072. Publisher: Elsevier B.V.

[34] Abdulaziz A. Alharbi, André Sackmann, Udo Weimar, and Nicolae Bârsan. Acetylene- And Ethylene-Sensing Mechanism for LaFeO3-Based Gas Sensors: Operando Insights. *Journal of Physical Chemistry C*, 124(13):7317–7326, 2020. ISSN 19327455. doi: 10.1021/acs.jpcc.0c01052.

[35] Abdulaziz A. Alharbi, Andre Sackmann, Udo Weimar, and Nicolae Bârsan. A highly selective sensor to acetylene and ethylene based on LaFeO3. *Sensors and Actuators, B: Chemical*, 303, 2020. ISSN 09254005. doi: 10.1016/j.snb.2019.127204.

[36] Anupong Sukee, Abdulaziz A. Alharbi, Anna Staerz, Anurat Wisitsoraat, Chaikarn Liewhiran, Udo Weimar, and Nicolae Barsan. Effect of AgO loading on flame-made LaFeO3 p-type semiconductor nanoparticles to acetylene sensing. *Sensors and Actuators, B: Chemical*, 312, 2020. ISSN 09254005. doi: 10.1016/j.snb.2020.127990.

[37] David Degler, Blanka Detlefs, Carolin Ewald, Markus Fröhlich, Ugur Geyik, and Benjamin Junker. CH-6029: Operando investigation of the gas sensing mechanism of SnO2 materials by modulation excitiation HERFD-XAS at the Sn L1 edge, 2022.

[38] Pedro H. Suman, Anderson A. Felix, Harry L. Tuller, J. A. Varela, and Marcelo O. Orlandi. Comparative gas sensor response of SnO2, SnO and Sn3O4 nanobelts to NO2 and potential interferents. *Sensors and Actuators, B: Chemical*, 208:122–127, 2015. ISSN 09254005. doi: 10.1016/j.snb.2014.10.119.

[39] Tiantian Yin, Jaesung Lee, Elmira Moosavi-Khoonsari, and In-Ho Jung. Critical evaluation and the thermodynamic optimization of the Sn-O system. *Ceramics International*, 47(20):29267–29276, 2021. ISSN 02728842. doi: 10.1016/j.ceramint.2021.07.091.

[40] S.W. Mayer. Estimation of activation energies for nitrous oxide, carbon dioxide, nitrogen dioxide, nitric oxide, oxygen, and nitrogen reactions by a bond-energy method. *The Journal of Physical Chemistry*, 73(11):3941–3946, 1969.

[41] Luca Giancaterini, Seyed Mahmoud Emamjomeh, Andrea De Marcellis, E. Palange, Alessandro. Resmini, Umberto Anselmi-Tamburini, and Carlo Cantalini. The influence of thermal and visible light activation modes on the NO2 response of WO3 nanofibers prepared by electrospinning. *Sensors and Actuators B: Chemical*, 229:387–395, 2016. ISSN 09254005. doi: 10.1016/j.snb.2016.02.007.

[42] Chao Zhang, Abdelhamid Boudiba, Patrizia De Marco, Rony Snyders, Marie-Georges Olivier, and Marc Debliquy. Room temperature responses of visible-light illuminated WO3 sensors to NO2 in sub-ppm range. *Sensors and Actuators B: Chemical*, 181:395–401, 2013. ISSN 09254005. doi: 10.1016/j.snb.2013.01.082.

[43] Miguel A. Bañares. Preface. *Catalysis Today*, 126(1-2):1–2, 2007. ISSN 09205861. doi: 10.1016/j.cattod.2007.07.004.

[44] David Degler, Natascha Barz, Ulf Dettinger, Heiko Peisert, Thomas Chassé, Udo Weimar, and Nicolae Barsan. Extending the toolbox for gas sensor research: Operando UV/vis diffuse reflectance spectroscopy on SnO2-based gas sensors. *Sensors and Actuators, B: Chemical*, 224:256–259, 2016. ISSN 09254005. doi: 10.1016/j.snb.2015.10.040. Publisher: Elsevier.

[45] Stefanie Braun, Arne Kobald, Alexandru Oprea, Inci Boehme, Peter Bonanati, Udu Weimar, and Nicolae Barsan. Monitoring hand hygiene with commercial gas sensors: A pattern recognition approach. *Sensors and Actuators B: Chemical*, 352:131027, 2022.

Chapter 6

Acknowledgments and Funding

My sincere thanks goes to Nicolae Bârsan and Udo Weimar for having me in their research group for many years now. Despite the pandemics, I was able to visit many places, present my works at multiple conferences and meet many interesting people, both on travels and in Tübingen. There are so many things I was able to learn from Nicolae not only about sensors and semiconductor physics, but also about the mysterious nature of humans. His trust and friendship also encouraged me to accept new challenges like moving to California for half a year. To Udo, while not many words are required to work together in administration or teaching, we could talk for hours about trains, construction, technology and the Swabian way of life.

Furthermore I would like to thank all my recent and former colleagues in the research group for their help and their friendship. Especially Arne Kobald, my office buddy, best man, and "toxic twin" for our many discussions on electronics, software and just the right amount of pedantry to promote each other. Also I would like to thank Carolin Ewald for our constructive and complementing work during "Photologic".

Most of all, I am grateful for the unconditional support of my wife Hannah ⋆, and my parents Karin and Josef.

This work would not have been possible without the support and experience of many advisors, coworkers and collaboration partners. Special thanks goes to:

- Xiao-Xue Wang from University and Leibniz-IWT Bremen for many years of trustful collaboration in our research on light activated gas sensors and common activities in Tübingen and Bremen.

- David Degler from Hochschule München for sharing his skills in X-ray spectroscopy and scientific illustrating as well as for his guidance during all stages of my scientific career.

- Anna Staerz from Colorado School of Mines for her contagious enthusiasm and incredible passion about science. And of course for the warm welcome in Denver.

- Abdulaziz Alharbi from King Abdulaziz City for Science and Technology, Saudi Arabia, for his pioneering work on perovskites and the many discussions.

- Marco Favaro from the Helmholtz-Zentrum Berlin for his introduction to NAP-XPS and his selection of excellent Italian restaurants in Trieste.

- Cristian Simion from the Romanian National Institute of Materials Physics for his support in the nickel oxide investigations and for his friendship and good times outside the lab.

- Pedro Suman and Marcelo Orlandi for the opportunity to study their samples during the many recurring visits to Germany.

- Rachel Brophy for her SiNW samples and the good time at the sensor block course.

- Lutz Mädler and Malte Schalk from University and Leibniz-IWT Bremen for their contributions to the "Photologic" project.

- Alexandru Oprea not only for his sometimes genius experimental setups, but also for his support in their operation, even after his retirement.

- Alexander Haensch, André Sackmann and Peter Bonanati for their help with hardware and software issues.

- My fellow colleagues Ugur Geyik, Peter Janoschek, Tobias Köninger, Tamara Ruß and Leah Schynowski for their help whenever needed and for the fun times during and after work.

- David Baschnagel, Sarah Bieger, Noah Buth, Jihye Choi, Kenyatta Doumanas, Marco Flieg, Markus Fröhlich, Jan Hanenberg, Mandy Krott, Nils Rieger, Davina Nienhues and Sophia Westendorf, whose scientific results during their studies in our research group advanced the understanding of many topics related to my work.

- "My" Hiwis Daniel Dujmovic and Jan Hanenberg for their hands-on in the lab. Your thorough and reliable work brought many of my ideas to life.

Funding

We thankfully acknowledge:

- The Deutsche Forschungsgemeinschaft (DFG) for their funding of the Project "Investigation of porous nanoparticle structures under illumination for the application as gas sensors" (Photologic). Grant number 419896563 (`https://gepris.dfg.de/gepris/projekt/419896563`)

- The Berlin Joint Laboratory for Electrochemical Interfaces (BElChem), established between the Helmholtz-Zentrum Berlin (HZB) and the Fritz-Haber-Institut der Max-Planck-Gesellschaft (FHI-MPG), for the beamtime availability during the commissioning phase of the soft x-ray BElChem endstation (operating at the UE56-2/PGM1 beamline of the BESSY II synchrotron facility). BEl-Chem is supported by the Helmholtz Association through the Helmholtz Energy Materials Foundry (HEMF, GZ 714-48172-21/1).

- DESY (Deutsches Elektronen-Synchrotron, Hamburg, Germany), a member of the Helmholtz Association HGF, for the provision of experimental facilities. Parts of this research were carried out at PETRA III. Data was collected using P65 operated by DESY Photon Science. We would like to thank Edmund Welter and Matthias Hermann for assistance during the experiments. Beamtime was allocated for proposal I-20170680.

- The European Synchrotron Radiation Facility (ESRF) for the provision of synchrotron radiation facilities under proposal number CH-6029 (doi: 10.15151/ESRF-ES-650701946). We would like to thank the staff of ESRF's beamline ID26 for assistance and support during the beamtime.

Information on funding received by other authors can be found in the corresponding section of each publication.

Appendix: All Manuscripts

[BJR03], [BJR06], [BJR08], and [BJR09] are reprinted with permission from the respective ACS Journals. Copyright remains at the American Chemical Society.

[BJR02], [BJR07], and [BJR10] are reprinted from Sensors and Actuators B: Chemical. Copyright remains at Elsevier.

In lieu of [BJR04] the author's manuscript is attached. The publisher's version is available at `https://iopscience.iop.org/article/10.1088/1361-6463/ac3283`.

nanomaterials

MDPI

Article

Rhodium Oxide Surface-Loaded Gas Sensors

Anna Staerz [1], Inci Boehme [1], David Degler [2], Mounib Bahri [3], Dmitry E. Doronkin [4], Anna Zimina [4], Helena Brinkmann [1], Sina Herrmann [1], Benjamin Junker [1], Ovidiu Ersen [3], Jan-Dierk Grunwaldt [4], Udo Weimar [1] and Nicolae Barsan [1,*]

1 Institute of Physical and Theoretical Chemistry (IPTC), University of Tuebingen, Auf der Morgenstelle 15, D-72076 Tuebingen, Germany; anna.staerz@ipc.uni-tuebingen.de (A.S.); inci.can@ipc.uni-tuebingen.de (I.B.); helena.brinkmann@student.uni-tuebingen.de (H.B.); sina.herrmann@ipc.uni-tuebingen.de (S.H.); benjamin.junker@ipc.uni-tuebingen.de (B.J.); upw@ipc.uni-tuebingen.de (U.W.)

2 European Synchrotron Radiation Facility (ESRF), 71 Avenue des Martyrs, 38043 Grenoble, France; david.degler@esrf.fr

3 Institut de Physique et Chimie des Matériaux de Strasbourg (IPCMS), UMR 7504 CNRS-Université de Strasbourg, 23 rue du Lœss, F-67034 Strasbourg cedex 2, France; mounib.bahri@ipcms.unistra.fr (M.B.); ovidiu.ersen@ipcms.unistra.fr (O.E.)

4 Institute of Catalysis Research and Technology (IKFT) and Institute for Chemical Technology and Polymer Chemistry (ITCP), Karlsruhe Institute of Technology, Kaiserstr. 12, 76131 Karlsruhe, Germany; dmitry.doronkin@kit.edu (D.E.D.); anna.zimina@kit.edu (A.Z.); grunwaldt@kit.edu (J.-D.G.)

* Correspondence: nb@ipc.uni-tuebingen.de; Tel.: +49-(0)7071-29-78761

Received: 4 October 2018; Accepted: 25 October 2018; Published: 1 November 2018

Abstract: In order to increase their stability and tune-sensing characteristics, metal oxides are often surface-loaded with noble metals. Although a great deal of empirical work shows that surface-loading with noble metals drastically changes sensing characteristics, little information exists on the mechanism. Here, a systematic study of sensors based on rhodium-loaded WO_3, SnO_2, and In_2O_3—examined using X-ray diffraction, high-resolution scanning transmission electron microscopy, direct current (DC) resistance measurements, operando diffuse reflectance infrared Fourier transform (DRIFT) spectroscopy, and operando X-ray absorption spectroscopy—is presented. Under normal sensing conditions, the rhodium clusters were oxidized. Significant evidence is provided that, in this case, the sensing is dominated by a Fermi-level pinning mechanism, i.e., the reaction with the target gas takes place on the noble-metal cluster, changing its oxidation state. As a result, the heterojunction between the oxidized rhodium clusters and the base metal oxide was altered and a change in the resistance was detected. Through measurements done in low-oxygen background, it was possible to induce a mechanism switch by reducing the clusters to their metallic state. At this point, there was a significant drop in the overall resistance, and the reaction between the target gas and the base material was again visible. For decades, noble metal loading was used to change the characteristics of metal-oxide-based sensors. The study presented here is an attempt to clarify the mechanism responsible for the change. Generalities are shown between the sensing mechanisms of different supporting materials loaded with rhodium, and sample-specific aspects that must be considered are identified.

Keywords: gas sensors; surface-loading; DRIFT spectroscopy; X-ray absorption spectroscopy; Fermi-level pinning

1. Introduction

As the world becomes more automated and connected, sensors will play an increasing role. Gas sensors based on semiconducting metal oxides (SMOX) are a compact, inexpensive, sensitive,

and robust alternative to other detection methods. Over the last five decades, SMOX-based sensors were widely used for automated air flap control in cars and in domestic alarms for explosive gases [1,2]. A great deal of research is being done on the use of SMOX sensors in a wide array of applications. However, in order for SMOX-based sensors to be effectively used in the future, their sensitivity, selectivity, and stability must be increased [3]. Numerous different methods were examined in order to address these issues, ranging from the optimization of morphology to the use of composite materials based on metal oxides coupled with organics or silica [3–5]. Traditionally, these limitations were addressed through loading with noble metals [6]. Already in the 1960s, palladium was added to the first commercially available SnO_2-based sensor from Figaro Engineering [7,8]. Even today, most commercial sensors are not based on pure materials, but contain low quantities of noble-metal-oxide additives [8]. These additives are usually chosen based on empirically attained knowledge. However, in the late 1980s and early 1990s, Yamazoe and Morrison suggested two mechanisms, spillover and Fermi-level pinning, which could explain the effect of surface-loading on the sensor response; experimental results supporting the theories remain limited [9–11]. In the case of the spillover mechanism, the target/analyte molecule is adsorbed onto the noble-metal-oxide cluster which leads to a weakening of its molecular bond. The adsorbate is transferred onto the support material where the reaction takes place [12]. In the Fermi-level pinning mechanism, the gas detection reaction takes place on the surface of the noble metal cluster. The cluster electronically interacts with the base material and the contact pins the Fermi levels of both materials. If the work function of the noble-metal-oxide cluster is changed upon interacting with an analyte gas, the depletion layer in the base material caused by the contact is also affected. It was recently reported that the Fermi-level pinning mechanism explains the change in the sensing characteristics of WO_3 surface-loaded with oxidized rhodium clusters and the effect of oxidized platinum clusters on the surface of SnO_2 [13]. Here, a systematic study of three commonly used oxides for gas sensors, WO_3, SnO_2, and In_2O_3 [3], loaded with rhodium oxide clusters was done to examine the general validity of these findings. The response of the sensors to five chemically different and application-relevant gases was examined. The gases were picked in concentrations relevant for different applications. There is currently a large interest in detecting acetone in the breath as a means for diabetes monitoring [14]. For diabetes monitoring, an acetone concentration between 0.5 ppm and 2 ppm (0.001–0.005 mg/L) is relevant [14]. CO and NO_2 are both relevant pollutants found in automobile exhaust measurements [15]. Values between 30 ppm and 100 ppm (ca. 0.035–0.116 mg/L) are relevant for CO, and between 2 ppm and 10 ppm (0.004–0.019 mg/L) for NO_2 [16]. Often, however, indoor air is more polluted than outdoors. As people spend more and more time inside, governments and even the World Health Organization released guidelines regarding indoor air quality [17,18]. Indoor air quality is often diminished by the presence of volatile organic compounds due to outgassing of furniture and other household objects. The Canadian government, for example, set a short-term indoor air exposure limit of toluene at 4 ppm (0.015 mg/L) [18]. Ethanol is another volatile organic compound which metal-oxide-based gas sensors are known to respond well to. In total, these gases show high variation in their chemical characteristics and allowing their use in sensors for a wide array of relevant applications.

A full characterization of the samples was done using X-ray diffraction (XRD) and high-resolution scanning transmission electron microscopy (HR-STEM). In order to understand the effect of oxidized noble-metal surface clusters on sensing, operando diffuse reflectance infrared Fourier transform (DRIFT) spectroscopy and operando X-ray absorption spectroscopy (XAS) were used. The results show that the Fermi-level pinning mechanism accurately describes the effect of the clusters on sensing. This work indicates the general validity of the Fermi-level pinning mechanism for sensors based on oxygen-deficient *n*-type SMOX-containing surface noble-metal-oxide clusters. This finding is very significant, as the sensor characteristics of SMOX are often tuned using loading with noble metals.

Nanomaterials **2018**, *8*, 892 3 of 17

2. Materials and Methods

2.1. Sample Preparation

The loaded samples were prepared as described in Reference [19]. $SnO_2/WO_3/In_2O_3$ and $RhCl_3 \cdot xH_2O$ from Sigma Aldrich (Saint Louis, MI, USA) were stirred in deionized water at a pH value of 1.0 at 80 °C for 2 h and dried at 70 °C. The powders were calcined at 500 °C for 1 h. To ensure that the detected results were caused by the presence of the surface-loading and not due to the preparation procedure itself, the pure samples were also suspended in deionized water at a pH value of 1.0, which was set using a concentrated HCl solution. Then, the suspension was stirred at 80 °C for 2 h and the powders were dried at 70 °C and calcined at 500 °C for 1 h. The powders were deposited onto alumina substrates as described elsewhere [20]. More information regarding the loading can be found in the Table S1.

2.2. Direct Current (DC) Resistance Measurements

The measurements were performed using a Keithley 617 electrometer for WO_3 and SnO_2 and an Agilent 34972 multimeter for In_2O_3. Agilent E3630A and E3614A voltage sources were used to heat the sensors. The sensors were mounted in a homemade Teflon sensor chamber, and the various test gas concentrations in dry synthetic air were supplied using a computer-controlled gas-mixing system. As the standard for work done using gas sensors, the concentration of the target gas is given in ppm. The following relationship was used [21]:

$$\text{Gas Concentration (ppm)} = \frac{\text{Mole Volume}}{\text{Mole Mass}} \times \text{Gas Concentration}\left(\frac{\text{g}}{\text{m}^3}\right) = \frac{0.241\text{m}^3}{\text{Mole Mass}} \times \text{Gas Concentration}\left(\frac{\text{g}}{\text{m}^3}\right) \quad (1)$$

The sensors were measured at 300 °C. The sensor signal for reducing gases was calculated using the following Equation (2):

$$s = \frac{R_{\text{reference}}}{R_{\text{test gas}}} \quad (2)$$

In the case of oxidizing gases, the inverse relationship was used. The reference was the resistance measurement in dry synthetic air.

2.3. DRIFT Spectroscopy

For the operando DRIFT spectroscopy, a Vertex70v containing a narrow-band mercury cadmium telluride (MCT) detector (Bruker, Billerica, MA, USA) with a spectral resolution of 4 cm^{-1} was used. The sensors were mounted in a homemade chamber containing a KBr window. The sensors were heated to 300 °C, and the DC resistance was recorded simultaneously. Every 15 min, a single-channel spectrum was recorded during the gas exposure. To obtain the absorbance spectra, information about the surface reaction was provided with the target gas. The single-channel spectra taken under exposure to the target gases were referenced to the spectra taken under the carrier gas using Equation (3).

$$\text{Absorbance} = -\log\left(\frac{\text{single channel test gas}}{\text{single channel reference}}\right) \quad (3)$$

As previously reported, it is possible to estimate the band-bending caused by the presence of noble-metal-oxide surface-loadings from these measurements [13,22,23]. In N_2, the surface acceptor state related to the ionosorption of O_2 is considered negligible, and the relationship between resistance and surface band-bending (eV_S) for depletion layer limited charge transport can be estimated using the Equation (4) [13,22,23]:

$$eV_s = kT \cdot \ln\left(\frac{R_{\text{loaded}}}{R_{\text{pure}}}\right) \quad (4)$$

where k represents the Boltzmann constant, T is the temperature, R_{pure} is the resistance of the unloaded material, and R_{loaded} is the resistance of the loaded material in N_2.

2.4. XRD Measurements

XRD diffractograms were collected with a Philips X'Pert apparatus (PANalytical Spectris, Egham, UK). A monochromatic Cu Kα radiation source (λ = 1.540598 Å) was used. The diffractograms were recorded from a 2θ-ω angle of 25° to 45° with a step size of 0.01° at a rate of 0.01°/s. The XRD data were analyzed using the Match! 3 software (CRYSTAL IMPACT, Bonn, Germany).

2.5. X-ray Absorption Spectroscopy (XAS) Measurements

All X-ray absorption spectroscopy (XAS) experiments were recorded at beamline P65 at the PETRA III synchrotron radiation source (DESY, Hamburg, Germany). X-rays were provided by an undulator (11 periods, seventh harmonic, DESY, Hamburg, Germany); higher harmonics were rejected using Pt-coated mirror layers mounted before the monochromator, and the incident X-ray energy was selected using a double crystal monochromator with Si (311) crystals. Using slits, the beam size was set to 1.5 × 0.3 mm. X-ray absorption near-edge structure (XANES) and extended X-ray absorption fine structure (EXAFS) spectra were recorded at the Rh K-edge in fluorescence geometry using an energy-dispersive Vortex P80 detector. For operando XAS, the samples were placed in a homemade in situ cell, which allowed controlling the atmosphere and heating voltage, while simultaneously recording XAS and DC resistance of the sensor placed in the cell [24]. XAS data analysis was done using the ATHENA and ARTEMIS software form the IFEFFIT package (developed by Ravel and Newville from the US Naval Research Laboratory and the University of Chicago, for details see [25]). ATHENA was used for calibrating and normalizing all spectra, and for subtracting the background of the EXAFS. Fourier transformation (FT) of k^1, k^2, and k^3-weighted EXAFS was done in a k range of 2.5 $Å^{-1}$ to 10 $Å^{-1}$, using a Hanning window with a sill size of 1 $Å^{-1}$. Using ARTEMIS, EXFAS fitting was done by adjusting theoretical backscattering paths, which were obtained from FEFF 6.0 calculations (The FEFF Project, University of Washington, WA, USA, to experimental data using the least-squares method in R space (1 Å to 3.5 Å) [26].

2.6. Scanning Transmission Electron Microscopy

Scanning transmission electron microscopy (STEM) experiments were performed using a Cs-corrected JEM-2100F (JEOL Akishima, Tokyo, Japan) operated at 200 kV.

3. Results

3.1. Material Characterization

WO_3, SnO_2, and In_2O_3 are all oxygen-deficient *n*-type semiconductors that are commonly used for gas sensors. The sensors are typically operated between 200 °C and 500 °C. Here, in order to minimize the measurement variables, an operation temperature of 300 °C was selected.

XRD measurements were taken at room temperature for SnO_2 and In_2O_3, while that of WO_3 was taken at 300 °C (see Figure 1). For SnO_2, the tetragonal rutile structure was verified [27], and, as it only has one stable crystal structure, it can be assumed that the same structure exists at the operation temperature. As already reported in the case of WO_3, the sample is found to be in a mixed γ- and β-phase at 300 °C [28–30]. For In_2O_3, the cubic structure was verified by XRD [31]. This structure is stable until 800 °C, which is well above the operation temperature; thus, no change was anticipated [32]. Using the Debye-Scherrer equation, the crystallite diameters of the base materials were approximated as 30 nm for WO_3, 20 nm for SnO_2, and 40 nm for In_2O_3.

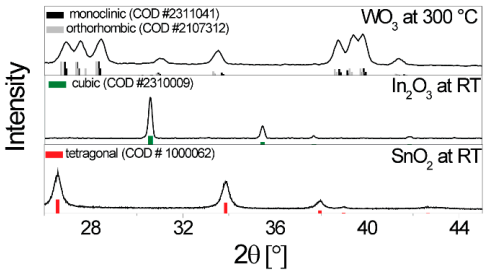

Figure 1. X-ray diffractograms taken of the sensitive layer on the sensors (SnO_2 and In_2O_3 at room temperature; WO_3 was recorded on a heated sensor). The reference patterns are from the Crystallography Open Database.

In HR-STEM images, however, it can be seen that the In_2O_3 clusters were larger than 100 nm, meaning that the crystallite size could not be accurately determined using the Debye-Scherrer equation [33]. The average size of the In_2O_3 clusters was approximately 300 nm. In the case of the SnO_2 sample, the grain size was between 7 nm and 25 nm. In the case of the WO_3 sample, the crystallite size varied between 25 nm and 65 nm. These findings are in line with the XRD measurements. The Rh-oxide loading is marked with yellow arrows in Figure 2. The STEM measurements revealed that, for loaded WO_3 and SnO_2, the rhodium-oxide particle size was between 1 nm and 2.5 nm with a good dispersion on the surface (Figure 2).

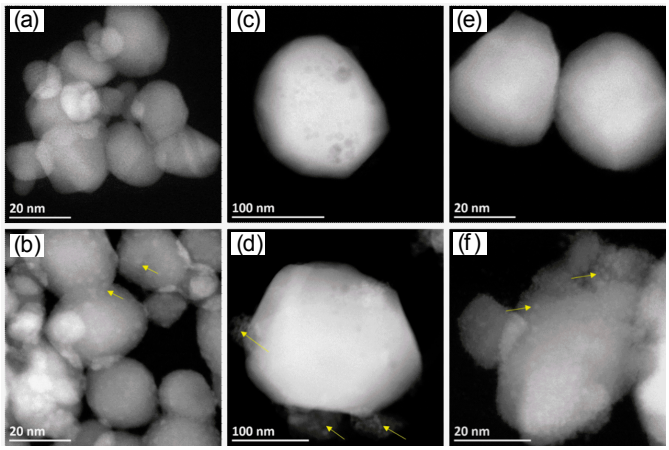

Figure 2. Scanning transmission electron microscopy (STEM) high-angle annular dark-field (HAADF) images of pure and Rh-loaded clusters on three different supports: SnO_2 (**a**) pure and (**b**) 3.00 at.% Rh-loaded SnO_2; In_2O_3 (**c**) pure and (**d**) 2.75 at.% Rh-loaded In_2O_3; WO_3 (**e**) pure and (**f**) 5.00 at.% Rh-loaded WO_3. Yellow arrows show the Rh_2O_3 particles and clusters.

For loaded In_2O_3, however, there were two kinds of structures: one with a high amount of Rh_2O_3 on a small amount of In_2O_3 (yellow arrow, Figure 3a), and the second with large crystals of In_2O_3 and a small quantity of rhodium oxides (Figure 2d; blue arrow Figure 3a; barely visible in Figure 3b). The high amount of Rh_2O_3 is shown as a layer formed around a highly crystalline small In_2O_3 grain (Figure 3c,d). Energy-dispersive X-ray spectroscopy (EDS) elemental mapping images support these findings (see Figure S1).

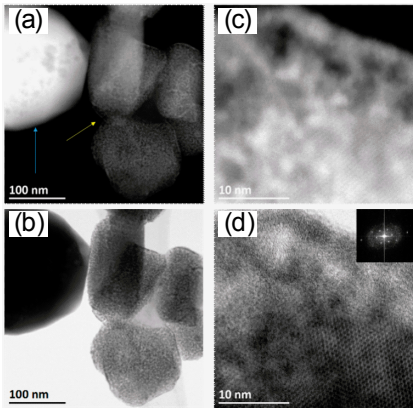

Figure 3. STEM images of 2.75 at.% Rh-Loaded In_2O_3. (**a**) STEM HAADF and (**b**) STEM bright-field (BF) images show two kinds of structures: low Rh-loaded (blue arrows) and high Rh-loaded (yellow arrow). (**c**) High-resolution (HR)-STEM HAADF and (**d**) HR-STEM BF images show high crystalline In_2O_3 and a rich Rh layer around In_2O_3. The inset in (**d**) is the fast Fourier transform (FFT) of the STEM BF image.

The XANES spectra, at room temperature, of all sensing materials and two reference compounds are shown in Figure 4. All three sensing materials showed similar XANES spectra which corresponded to the Rh_2O_3 reference compound, i.e., Rh was present as Rh^{3+}. Further information on the structure of the Rh loadings was gained through analysis of the EXAFS. The visual inspection of the FT EXAFS (Figure 4b) shows good agreement with Rh_2O_3 in the first coordination shell and, thus, confirms the presence of oxidized Rh structures. The strongly decreased magnitude of features related to the outer shells suggests a small size of the Rh loadings. Quantitative information on the Rh structure was obtained by fitting the calculated EXAFS based on Rh_2O_3 to the experimentally obtained EXAFS. The results of the best fits are shown in Table 1.

Table 1. Structural parameters obtained from fitted extended X-ray absorption fine structure (EXAFS). Coordination number, N; distance, R; Debye–Waller factor, σ^2; energy shift, δE_0; passive electron reduction factor, $S_0{}^2$; misfit, ρ.

Sample	Atom	N	R (Å)	σ^2 (10^{-3} Å^2)	$S_0{}^2$	δE_0 (eV)	ρ (%)
5.0 at.% Rh WO_3	O	6.0 [f]	2.02 ± 0.01	4.01 ± 1.75	0.72 ± 0.09	−2.10 ± 1.14	1.7
	Rh	2.0 [f]	3.09 ± 0.02	5.25 ± 2.52			
3.0 at.% Rh SnO_2	O	5.5 [f]	2.04 ± 0.01	3.22 ± 1.38	0.84 ± 0.08	−0.65 ± 0.94	1.1
	Rh	2.0 [f]	3.14 ± 0.03	4.39 ± 3.75			
	Rh	2.5 [f]	3.34 ± 0.03				
2.75 at.% Rh In_2O_3	O	5.5 [f]	2.04 ± 0.01	3.45 ± 1.18	0.72 ± 0.06	−1.14 ± 0.86	0.9
	Rh	1.5 [f]	3.15 ± 0.03	5.95 ± 4.41			
	Rh	1.5 [f]	3.38 ± 0.04				

[f] fixed.

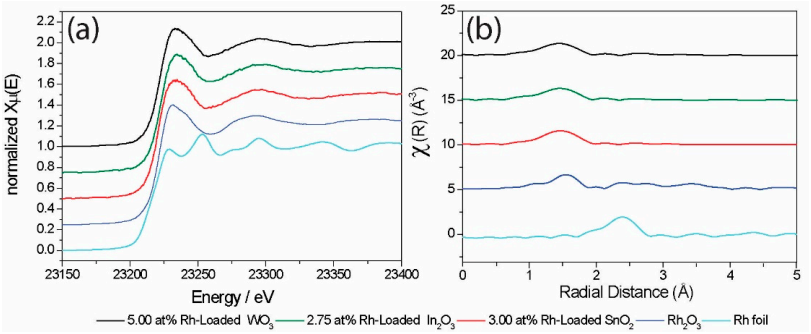

Figure 4. Rh K-edge X-ray absorption near-edge structure (XANES) spectra (**a**) and Fourier transform (FT) k^3-weigthed extended X-ray absorption fine structure (EXAFS) spectra (**b**) of Rh-loaded sensing materials (amplitude × 2), Rh_2O_3 reference (amplitude × 2), and Rh foil $\left(\frac{\text{amplitude}}{2}\right)$.

For the 5.0 at.% Rh-loaded WO_3 sample, the best EXAFS fit was obtained by a model with two coordination shells. The first shell consisted of six O atoms at a distance of 2.02 Å, while the second shell featured two Rh atoms at a distance of 3.09 Å. The coordination of Rh by six O atoms corresponds to the theoretical coordination number. The fitted Rh–O distance was shorter than expected for bulk Rh_2O_3 (2.04 Å), but still closer to that of Rh_2O_3 than the average W–O distance of the supporting WO_3 (1.93 Å). The coordination number of the second shell was smaller than the theoretical value of 3, and the obtained Rh–Rh distance was longer than the expected value of the corresponding shell in bulk Rh_2O_3 (2.99 Å). The introduction of additional Rh shells found for bulk Rh_2O_3 at either at 2.72 Å (N of bulk Rh_2O_3: 1.0) or 3.58 Å (N of bulk Rh_2O_3: 3.0) did not improve the fit model.

For the 3.0 at.% Rh-loaded SnO_2 and the 2.75 at.% Rh-loaded In_2O_3, the best fits were obtained by a model with three coordination shells. In both cases, the best fits were obtained by adjusting the coordination number of oxygen (first shell) to 5.5, which was smaller than the theoretical value of 6.0, but still matched an octahedral coordination of Rh by O. The fitted Rh–O distance (2.04 Å) was similar for both materials and corresponded to that of bulk Rh_2O_3. The second and third coordination shells were fitted by Rh atoms at distances of 3.14 and 3.34 Å for 3.0 at.% Rh-loaded SnO_2, and 3.15 and 3.38 Å for 2.75 at.% Rh-loaded In_2O_3. Considering the calculated errors, the second and third shells were within similar distances for both materials. The used coordination numbers (Table 1) were smaller than the theoretically expected value of 3.0 for each shell in bulk Rh_2O_3. The Rh-loaded In_2O_3 sample was fitted with significantly lower coordination numbers than the Rh-loaded SnO_2 sample.

All three materials were successfully fitted with fit models derived from Rh_2O_3. Thus, an incorporation of Rh into the lattice of the supporting oxide could be excluded. Rh-loaded SnO_2 and In_2O_3 showed a similar Rh_2O_3-like structure, and the decreased coordination numbers and high disorder of the second and third shells suggested a small size of Rh_2O_3 clusters on SnO_2 and In_2O_3. The coordination numbers of the second and third shells of an oxide decrease with decreasing particle size, e.g., as reported for NiO [34]. Thus, based on the coordination number, the Rh_2O_3 clusters on SnO_2 were expected to be larger than those on In_2O_3. For Rh-loaded WO_3, the quantitative analysis of the EXAFS showed a less Rh_2O_3-like structure. However, based on the Rh–O distance, which was still close to that of Rh_2O_3, and based on the presence Rh in the second coordination shell, the structure was assumed to still be Rh_2O_3-like. The shortened Rh–O distance, high disorder, low coordination number of the second shell, and atypical Rh–Rh distance suggested the presence of very small and highly disordered Rh_2O_3-like clusters on WO_3.

3.2. Resistance Measurements

The goal of the study was to understand how the presence of the oxidized noble-metal clusters changes sensing. In order to identify changes in the sensor characteristics, sensors based on the pure base material must show significant and stable responses. Although it is known that sensors based on

materials which are highly loaded with noble metals show responses at lower temperatures, the sensors based on pure base materials need a higher operation temperature. For this reason, the DC resistance measurements were conducted at 300 °C (see Figures 5 and 6). The sensor signals were calculated using Equation (2), and the results are shown in Figure 5. Although, for real world applications, the effect of humidity must be considered, the work here sought to understand the fundamental mechanism responsible for the change in sensor response. Thus, for the sake of simplicity, the sensor response measurements were done in dry air. In all three cases, the loading resulted in a drastic change of the sensing characteristics. It was previously reported in the 1990s, by Buedy et al., that loading with rhodium drastically changes the sensor response of SnO_2 [35]. The change in the sensing mechanism, as a result of loading WO_3 with Rh_2O_3 nanoclusters, was recently reported [13]. In this work, a surface-loading of 2.50 at.% was used, and, to corroborate the previous results, a similar loading level was selected here. Based on the crystallite size calculated from the XRD spectra, loadings of 2.75 at.% for In_2O_3 and 3.00 at.% for SnO_2 were selected in order to attain comparable surface-loadings. In both cases, however, the effect of the loading was more significant (negligible sensor responses to all gases) than for the WO_3 sample [36,37]. For these cases, a lower loading of 0.50 at.% was then additionally examined, while, for WO_3, a higher loading of 5 at.% was added. In the case of In_2O_3, the total surface area was much lower than expected from the XRD measurements (Figure 1), and from the large grains visible in the STEM images (Figure 2). This is a possible explanation for the stronger effect of loading on In_2O_3 (comparable results at much lower concentrations) in comparison to WO_3. Due to the large crystallite size of In_2O_3, the ratio of surface area to volume was much smaller than for SnO_2 and WO_3 (ca. 0.02 for In_2O_3, 0.22 for SnO_2, and 0.20 for WO_3). In the case of SnO_2, there was no identifiable microstructural reason for the stronger effect of the loading. This indicates that the different electronic properties of the base materials also play a role. The results for 2.50 at.% loaded WO_3 are similar to those previously reported on a differently prepared sample [13]. The 2.50 at.% loading led to the disappearance of the NO_2 response. Rh_2O_3 is a known catalyst for the oxidation of NO to NO_2, indicating it would be a poor sensing material for NO_2 [38]. The response to CO increased; CO is known to react with the lattice oxygen of Rh_2O_3 to form CO_2 [39]. The response to acetone decreased, and there was practically no change in the response to toluene. Here, it was additionally found that the response to ethanol increased. For sensors based on the 5.00 at.% loaded WO_3 sample, the response to all gases except ethanol became negligible.

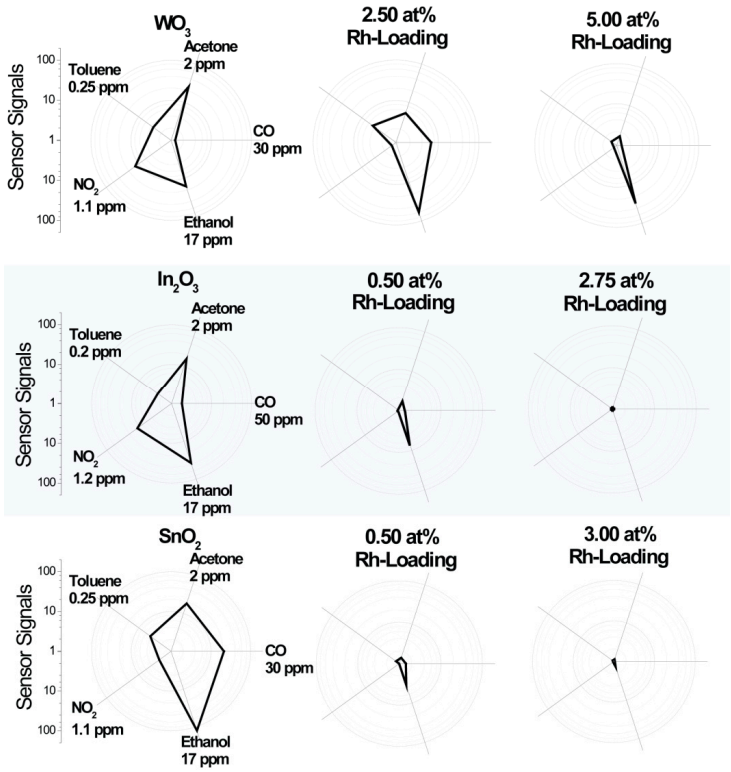

Figure 5. Signals of the sensors based on the different materials with various test gases in dry air at an operation temperature of 300 °C. The results are shown in a polar plot in order to highlight the general qualities of the sensors.

A very significant change in the sensing characteristics of In_2O_3 can already be seen for the 0.50 at.% loaded sample. Like WO_3, In_2O_3 is known to respond well to NO_2. This inherent characteristic of In_2O_3 disappeared as a result of the loading. Similar to the loaded WO_3 sample, the response to acetone decreased. The response to CO remained practically unchanged. The response of the 2.75 at.% to all gases was indeterminable. The effect of 0.50 at.% loading also had a significant effect on SnO_2. The sensor response was very similar to that of the 0.50 at.% loaded In_2O_3 sensor. The response of the 3 at.% loaded SnO_2 sample was negligible for all gases.

In order to examine the electronic coupling between the oxidized rhodium clusters and the host oxide, resistance measurements were conducted in N_2.

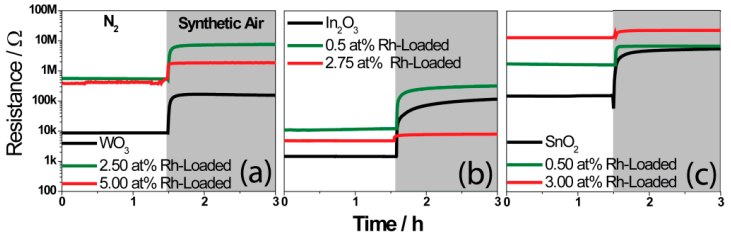

Figure 6. The resistances of the sensors, based on WO_3 (**a**), In_2O_3 (**b**), and SnO_2 (**c**), are shown in N_2 and dry synthetic air background (80% N_2 and 20% O_2).

The large increase of the resistance in nitrogen as a result of the loading indicates a strong electronic coupling between the surface clusters and the base material. The heterojunction resulted in a depletion layer which extended into the *n*-type base material, resulting in a higher resistance. Using the resistance

values in nitrogen (Figure 6) of the pure base materials and of the loaded materials, it is possible to calculate the band-bending caused by the noble-metal surface clusters [13,22]. The calculated band-bending of the Rh_2O_3 loaded materials are shown in Table 2. This was done using Equation (4).

Table 2. A list of the calculated band-bending values.

Material	Band-bending (meV)
2.50 at.% Rh-Loaded WO_3	ca. 198
5.00 at.% Rh-Loaded WO_3	ca. 200
0.50 at.% Rh-Loaded In_2O_3	ca. 105
2.75 at.% Rh-Loaded In_2O_3	ca. 98
0.50 at.% Rh-Loaded SnO_2	ca. 119
3.00 at.% Rh-Loaded SnO_2	ca. 222

In the presence of synthetic air, the resistance increased due to the adsorption of the oxygen. The pure materials all showed large changes in resistance (Figure 6). The effect of oxygen was lower for the loaded samples. While the oxidation of the Rh-clusters by atmospheric oxygen (dominant effect on loaded samples) would also lead to an increase in the resistance, it appears to be less effective than the direct oxidation of the base material (effect of atmospheric oxygen on the pure materials). Interestingly, for the WO_3 sample, the band-bending caused by the surface clusters was similar for the 2.50 at.% and the 5 at.% loaded samples. The effect of oxygen was, however, much more significant for the 2.50 at.% loaded sample [36]. One possible explanation is that the dispersion of the clusters was similar for the two samples, but the clusters on the 5.00 at.% sample were significantly larger. A similar situation was most probably true for In_2O_3. In the case of SnO_2, the calculated band-bending was significantly smaller for the lower loading versus the higher sample. The effect of atmospheric oxygen was also, however, lower for the higher-loaded sample. This could indicate that the clusters were larger but also more homogeneously dispersed in the case of the 3.00 at.% loaded sample. When comparing the results of the nitrogen and synthetic air measurements with the sensor response, it becomes clear that the reactivity to oxygen is correlated with the strength of the response to the test gases.

3.3. DRIFT Measurements

Following surface-loading with oxidized rhodium clusters, the responses of the different base materials became similar (see Figure 5). In order to examine how the presence of the surface additives unified the sensing characteristics, the interaction between the sensors and CO, an exemplary gas, was examined in greater detail. To examine the surface reactions, operando DRIFT spectroscopy was used. This method was proven to be a powerful tool [40]. In order to examine the role of the oxidized rhodium clusters in sensing and to induce a mechanism switch by reducing the clusters to their metallic state, the samples were exposed to different CO concentrations (between 25 ppm and 400 ppm) in a low-oxygen background (50 ppm O_2). The simultaneously obtained electrical measurements are shown in Figure 7.

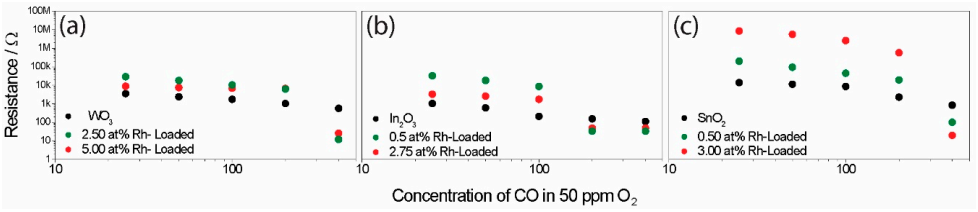

Figure 7. The change in resistance of the sensors, based on WO_3 (**a**), In_2O_3 (**b**), and SnO_2 (**c**), during exposure to different CO concentrations in a low-oxygen background, measured during the simultaneously measured diffuse reflectance infrared Fourier transform (DRIFT) spectroscopy, is plotted in log–log.

As expected, the sensor signals for the unloaded samples initially increased with higher concentrations, and, at higher concentrations, the sensitivity (the change in sensor response per ppm) decreased as a result of saturation (Figure 7). In the case of the loaded sample, there was a significant jump in the sensor response at higher CO concentrations (in the cases of WO_3 and SnO_2, this jump occurred between 200 ppm and 400 ppm, while, for indium, the jump occurred between 100 ppm and 200 ppm). The simultaneously acquired DRIFT spectra also showed a much higher absorbance at this point (Figure 8). It is known that the free-carrier absorption is proportional to the density of conduction electrons. For this reason, the resistance is inversely proportional to the absorbance, explaining the large change in the overall absorbance in the spectra taken under high CO concentrations [41]. In the 1960s, this phenomenon was examined in detail by Harrick for an oxidized silicon surface [42]. In addition, discrete adsorption bands in the DRIFT spectra provide information about the surface reactions responsible for the sensing at this point. In the case of pure WO_3 (Figure 8a), the exposure to CO determined the decrease of the W–O lattice bands at 2061 cm^{-1} and 1853 cm^{-1} [43]. This indicates the reduction of the material's surface.

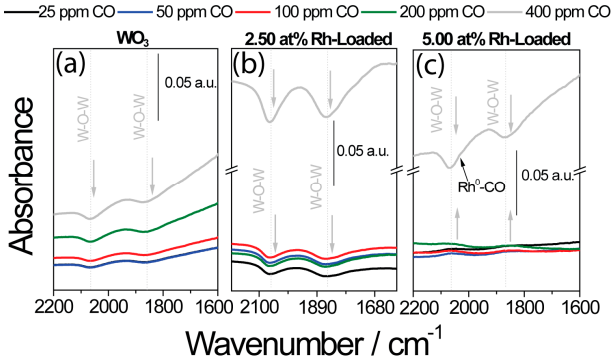

Figure 8. DRIFT spectra taken during exposure to different CO concentrations in low-oxygen (50 ppm O_2) backgrounds for (**a**) unloaded WO_3 sample, (**b**) 2.50 at.% Rh_2O_3 loaded WO_3, and (**c**) 5 at.% Rh_2O_3 loaded WO_3.

The sensing mechanism was different for 5 at.% loaded WO_3 (Figure 8c). Here, an increase of the W–O bands was visible for low CO concentrations. This finding was previously reported for Rh-loaded WO_3 during exposure to reducing gases such as acetone under normal sensing conditions [13]. As a result of the surface Rh_2O_3 clusters, the surface of WO_3 is highly depleted (see Table 2). As a result of the reaction between CO and the Rh_2O_3 clusters, electrons are released back into WO_3. With these electrons, WO_3 can react with atmospheric oxygen. This oxidation would, in turn, result in an increase in resistance. The mechanism changed as a result of exposure to 400 ppm, resulting in only the reduction of WO_3 being visible. This mechanism change was again correlated with the significant decrease in the resistance seen in the electrical measurements. In the DRIFT spectra of the 2.50 at.% loaded WO_3 sample, the reduction of WO_3 was visible even at low CO concentrations. Once the Rh_2O_3 cluster was reduced, however, CO reacted entirely with the base oxide, and the intensity of the decreasing bands attributed to the reduction of the WO_3 lattice was significantly heightened. This correlates with the stronger decrease in resistance detected in the electrical measurements.

The DRIFT spectra taken of the pure and loaded In_2O_3 samples showed a similar situation (Figure 9). The simultaneously acquired DRIFT spectra of pure In_2O_3 showed the reduction in the number of In–O bands centered at 1517 cm^{-1}, 1274 cm^{-1}, 1108 cm^{-1}, and 1022 cm^{-1}, which indicates the reduction of the surface by CO [37,44]. In the case of the highly loaded sample, the decrease in the number of In–O bands appeared only in higher CO concentrations (200 ppm and 400 ppm CO) [45]. In these concentrations, the jump in the sensor signal appeared. There was also an additional band centered at 2028 cm^{-1}, which was assigned to metallic rhodium carbonyls (Rh–CO) [37,44,46].

The DRIFT spectra of the loaded SnO_2 samples were more difficult to interpret, but showed a similar situation.

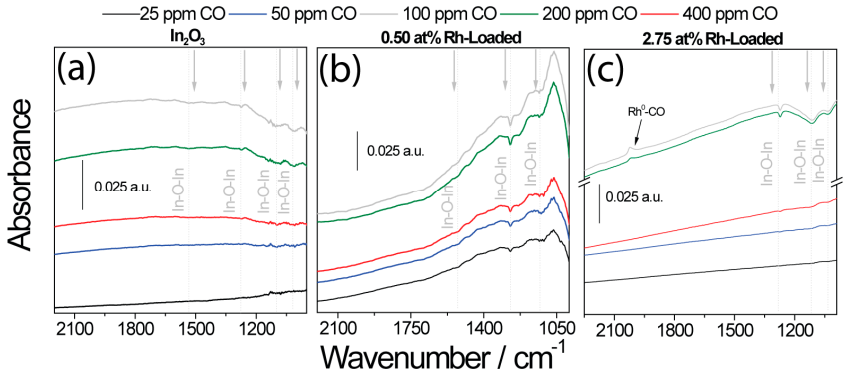

Figure 9. DRIFT spectra taken during exposure to different CO concentrations in low-oxygen (50 ppm O_2) backgrounds for (**a**) unloaded In_2O_3 sample, (**b**) 0.50 at.% Rh_2O_3 loaded In_2O_3, and (**c**) 2.75 at.% Rh_2O_3 loaded In_2O_3.

The DRIFT spectra of the sensors based on the SnO_2 samples are shown in Figure 10. It was previously reported that the reduction of the SnO_2 lattice by CO is the initial step of the surface reaction [47]. The formed CO_2 subsequently reacts with the SnO_2 surface to form carbonates. The DRIFT spectra taken of the pure SnO_2 sample were in line with this mechanism (Figure 10a). There were decreasing bands visible at 1060 cm^{-1} [48], 1120 cm^{-1} [48], and 1270 cm^{-1} [47], which were attributed to the lattice oxygen of SnO_2. The increasing bands at 1302 cm^{-1}, 1348 cm^{-1}, 1442 cm^{-1}, and 1561 cm^{-1} were attributed to surface carbonates [49]. In the case of the highly loaded sample (Figure 10c), there was no visible reduction of SnO_2 or carbonate formation during exposure to low CO concentrations.

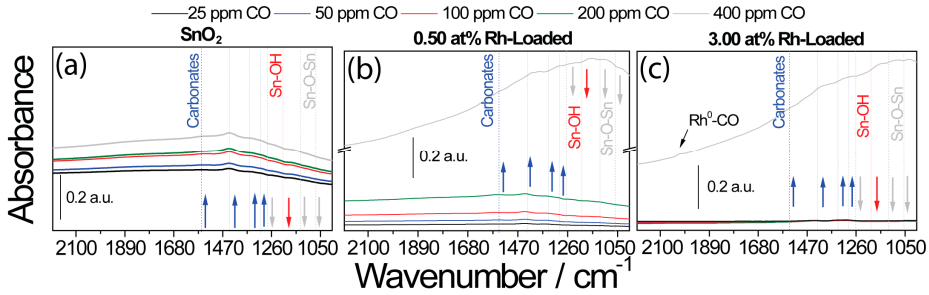

Figure 10. DRIFT spectra taken during exposure to different CO concentrations in low-oxygen (50 ppm O_2) backgrounds for (**a**) unloaded SnO_2 sample, (**b**) 0.50 at.% Rh_2O_3 loaded SnO_2, and (**c**) 3.00 at.% Rh_2O_3 loaded SnO_2.

In total, the DRIFT spectra provided good insight into how the presence of the Rh_2O_3 nanoclusters changed sensing. All three base oxides were reduced by the presence of CO in low-oxygen backgrounds. As expected, the sensitivity of the materials decreased with higher CO concentrations.

In the case of the highly loaded samples, the reduction of the base material only took place in high CO concentrations. This indicates that the reaction mechanism for each material was different at low CO concentration from that of the pure material.

3.4. X-ray Absorption Spectroscopy (XAS)

The DRIFT spectra predominantly provided insight into how the interaction between the base oxides and CO changed as a result of loading. In order to gain insight into how the Rh_2O_3 clusters

changed during sensing, operando XAS was used. Here, the sensors were again exposed to CO (between 25 ppm and 400 ppm CO) in low-oxygen (50 ppm) concentrations. XAS is an element-selective technique, and the shape of the XANES spectra is sensitive to the oxidation state and chemical surrounding of the absorbing element [50,51]. In order to study the behavior of Rh, the same measurements investigated by operando DRIFT spectroscopy of the higher-loaded samples were repeated, simultaneously recording XANES spectra at the Rh K-edge and the sensor response.

The electrical response (Figure 11) of the sensors was very similar to that attained during the DRIFT spectroscopy measurements (Figure 7). The loaded WO_3 and SnO_2 samples showed a significant resistance jump under exposure to 400 ppm CO. In the case of In_2O_3, the resistance jump was already visible during exposure to 200 ppm CO.

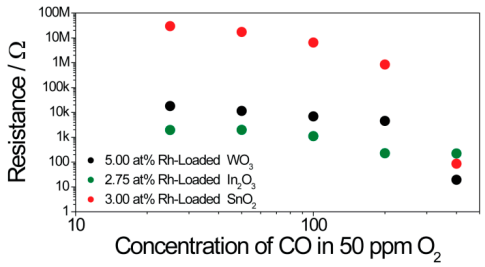

Figure 11. The change in resistance of the sensors during exposure to different CO concentrations in low-oxygen background, acquired during simultaneously measured X-ray absorption spectroscopy (XAS), is plotted in log-log.

For Rh-loaded WO_3 and SnO_2, the XANES spectra showed a change from Rh^{3+} to Rh^0 between 200 ppm and 400 ppm CO, and, for Rh-loaded In_2O_3, the change was already visible between 100 ppm and 200 ppm CO (Figure 12). The oxidation state change of Rh agreed well with the resistance jump and the distinct changes in the DRIFT spectra. Prior to the resistance jump, no indications of metallic Rh were visible in the XANES spectra, i.e., metallic Rh was only found in strongly reducing conditions, while, in oxygen-rich conditions, Rh was oxidized (Rh^{3+}). Here, it is important to note that, once the rhodium clusters were completely reduced to their metallic state, the sensors were irreversibly changed, i.e., the resistance in dry air did not return to the same value, and the color of the sensitive layer was different compared to that of a new sensor. In the case of normal operation conditions, the clusters were not reduced to their metallic state, and the sensor response showed good recovery (see XANES spectra recorded during exposure to CO in dry and humid synthetic air; Figure S2).

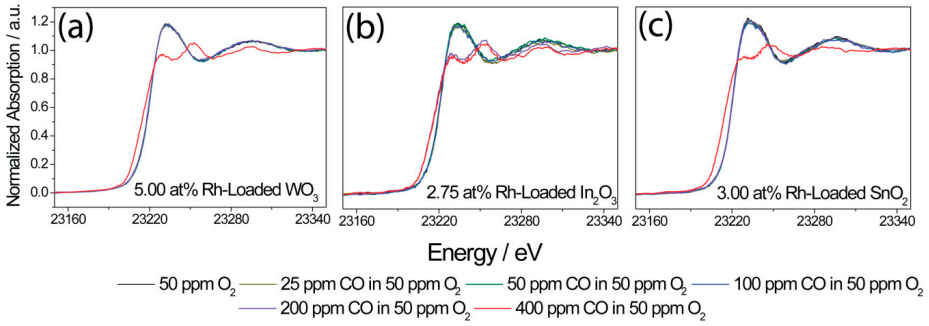

Figure 12. Rh K-edge XANES spectra of 5.00 at.% Rh-loaded WO_3 (**a**), 2.75 at.% Rh-loaded In_2O_3 (**b**), and 3.00 at.% Rh-loaded SnO_2 (**c**), recorded during different CO exposures in a low-oxygen background (50 ppm O_2) at 300 °C.

4. Discussion and Conclusion

It was found that, through surface-loading with oxidized rhodium clusters, it is possible to drastically change the sensing characteristics of WO_3, In_2O_3 and SnO_2. The three metal oxides, which are very commonly used for gas sensors, show very different responses in their pure states. The surface-loading with Rh resulted in more unified responses; none of the sensors responded to NO_2, while the response of all sensors to acetone decreased, and, at lower loadings, the response to CO was detectable. In all cases, the rhodium-loaded samples showed the highest responses to ethanol. It was previously reported that the Fermi-level pinning mechanism explains the change in the sensing characteristics of WO_3 surface-loaded with oxidized rhodium clusters, and also the effect of oxidized platinum clusters on the surface of SnO_2 [13].

In order to generally validate these findings, it was examined whether the change in sensor response of the three most commonly used materials as a result of Rh_2O_3 loading could be explained using the Fermi-level pinning mechanism. In all cases, the oxidized rhodium surface clusters caused a significant increase in the material's resistance in nitrogen, indicating significant electronic coupling between the clusters and the base material. By increasing the loading concentration, the effect of oxygen on the resistance of the materials was lowered and, in all cases, the response of the sensors decreased; this can be explained by the increase in the size of the Rh_2O_3 nanoclusters, limiting the charge transfer between the cluster and the base material during the reaction with the target gas. Using measurements in low-oxygen backgrounds, it was possible to identify the effect of the oxidation state of rhodium on the sensing mechanism. The XANES measurements revealed that, under normal sensing conditions, the surface rhodium clusters were oxidized. This was also true for measurements conducted at low CO concentrations in low-oxygen backgrounds. At higher CO concentrations, our results indicate that the clusters were reduced, and only metallic rhodium was present on the surface. A great deal of work was previously done on the interaction between rhodium and CO in catalysis [52,53]. The findings here are in line with those of Basini et al., who found that, at or above 300 °C, for rhodium clusters on various support oxides, only linear or bridged carbonyls were visible, indicative of Rh^0 [54]. In operando DRIFT spectra taken under the same conditions, the reduction of the base material could only be seen once the surface rhodium clusters were metallic. In the case of WO_3, the oxidation of the material was visible even in conditions where the rhodium clusters were still oxidized. This indicates that, in normal sensing conditions, when the rhodium clusters are oxidized (Figure S2), reactions between the rhodium clusters and the target gases are responsible for the sensor response. These findings are significant for the intentional tuning of sensors characteristics; the surface chemistry, and, as a result, the sensing characteristics of the sensor are dominated by the noble-metal loading. Although this was true for the three base materials, different loading levels were needed to attain similar results. This indicates that the base material still plays a role in the sensing mechanism. In order to verify this finding and examine it more closely, in the future, base materials with comparable crystallite size and morphology are needed. Hence, it is crucial that a preparation method is developed in which the Rh_2O_3 surface cluster size and dispersion are homogeneous among the different samples.

The work presented here provides significant evidence for the general validity of the Fermi-level pinning mechanism for sensors based on Rh_2O_3-loaded *n*-type oxides. For decades, sensors based on oxides loaded with noble metals were used in numerous applications. Although theories were developed to explain the changes in sensing characteristics as a result of the loading, experimental evidence is still scarce. The comprehensive study presented here is a crucial first step in understanding the effect of surface-loading. It identifies generalities between different supporting materials, as well as the additional sample-specific aspects that must be considered.

Supplementary Materials: The following are available online at http://www.mdpi.com/2079-4991/8/11/892/s1, Table S1: Concentrations used for the loading preparations, Figure S1: STEM images of 2.75 at.% Rh-Loaded In_2O_3. (a) STEM-HAADF (b) STEM-BF and EDS elemental mapping images (c), STEM images of 5 at.% Rh-Loaded WO_3. (d) STEM-HAADF (e) STEM-BF and EDS elemental mapping images (f), Figure S2: Rh K-edge XANES spectra

of 5 at.% Rh-loaded WO_3 (a), 2.75 at.% Rh-loaded In_2O_3 (b) and 3.00 at.% Rh-loaded SnO_2 (c), recorded during different CO exposure in dry syn. air at 300 °C.

Author Contributions: A.S. and I.B. contributed equally to this work; Conceptualization, N.B., U.W., O.E. and J.-D.G.; Formal analysis and experiments, A.S., I.B., D.D., M.B. and D.E.D.; Investigation, A.S., I.B., D.D., M.B., D.E.D., A.Z., H.B., S.H. and B.J.; Writing-original draft preparation, A.S., I.B., D.D. and M.B.; Writing-review and editing, A.S., D.D., J.-D.G. and N.B.; Supervision, N.B.

Funding: Parts of this research were carried out at PETRA III at DESY, a member of the Helmholtz Association (HGF), and we acknowledge the granted beamtime at beamline P65 and their financial support. Edmund Welter and Matthias Hermann (DESY) are thanked for their help during XAS measurements.

Conflicts of Interest: The authors declare no conflicts of interest.

References

1. Yamazoe, N. Toward innovations of gas sensor technology. *Sens. Actuator B Chem.* **2005**, *108*, 2–14. [CrossRef]
2. Chemical and Biochemical Sensors. *Ullmann's Encyclopedia of Industrial Chemistry*; Wiley VCH GmbH & Co KGaA. Posted September 29, 2016. Available online: https://doi.org/10.1002/14356007.b06_121.pub2 (accessed on 17 August 2018).
3. Hoa, N.D.; Duy, N.V.; El-Safty, S.A.; Hieu, N.V. Meso-/nanoporous semiconducting metal oxides for gas sensor applications. *J. Nanomater.* **2015**, *2015*. [CrossRef]
4. Lee, J.H. Gas sensors using hierarchical and hollow oxide nanostructures: Overview. *Sens. Actuator B Chem.* **2009**, *140*, 319–336. [CrossRef]
5. Hoa, N.D.; El-Safty, S.A. Highly sensitive and selective volatile organic compound gas sensors based on mesoporous nanocomposite monoliths. *Anal. Methods* **2011**, *3*, 1948–1956. [CrossRef]
6. Sun, Y.F.; Liu, S.B.; Meng, F.L.; Liu, J.Y.; Jin, Z.; Kong, L.T.; Liu, J.H. Metal oxide nanostructures and their gas sensing properties: A review. *Sensors* **2012**, *12*, 2610–2631. [CrossRef] [PubMed]
7. Neri, G. First Fifty Years of Chemoresistive Gas Sensors. *Chemosensors* **2015**, *3*, 1–20. [CrossRef]
8. Taguchi, N. Gas-Detecting Device. US3695848, 3 October 1972.
9. Yamazoe, N.; Kurokawa, Y.; Seiyama, T. Effects of Additives on Semiconductor Gas Sensors. *Sens. Actuators B* **1983**, *4*, 283–289. [CrossRef]
10. Morrison, S.R. Selectivity in semiconductor gas sensors. *Sens. Actuators* **1987**, *12*, 425–440. [CrossRef]
11. Yamazoe, N. New Approaches for improving semiconductor gas sensors. *Sens. Actuators B* **1991**, *5*, 7–19. [CrossRef]
12. Matsushima, S.; Teraoka, Y.; Miura, N.; Yamazoe, N. Electronic interaction between metal additives and tin dioxide in tin dioxide-based gas sensors. *JPN J. Appl. Phys.* **1988**, *27*, 1798–1802. [CrossRef]
13. Staerz, A.; Kim, T.-H.; Lee, J.-H.; Weimar, U.; Barsan, N. Nanolevel control of gas sensing characteristics via p–n heterojunction between Rh_2O_3 clusters and WO_3 crystallites. *J. Phys. Chem. C* **2017**, *121*, 24701–24706. [CrossRef]
14. Deng, C.; Zhang, J.; Yu, X.; Zhang, W.; Zhang, X. Determination of acetone in human breath by gas chromatography-mass spectrometry and solid-phase microextraction with on-fiber derivatization. *J. Chromatogr. B* **2004**, *810*, 269–275. [CrossRef]
15. Wiegelb, G.; Heitbaum, J. Semiconductor gas sensor for detecting NO and CO traces in ambient air of road traffic. *Sens. Actuators B* **1994**, *17*, 93–99. [CrossRef]
16. Nakagawa, H.; Okazaki, S.; Asakura, S.; Fukuda, K.; Akimoto, H.; Takahashi, H.; Shigemori, S. An automated car ventilation system. *Sens. Actuators B* **2000**, *65*, 133–137. [CrossRef]
17. Guidelines for indoor air quality. *WHO Regional Office for Europe*. 2010. Available online: http://www.euro.who.int/__data/assets/pdf_file/0009/128169/e94535.pdf (accessed on 21 July 2017).
18. Residential Indoor Air Quality Guidelines. *Government of Canada*. 2018. Available online: http://healthycanadians.gc.ca/healthy-living-vie-saine/environment-environnement/air/guidelines-lignes-directrices-eng.php#a1 (accessed on 16 October 2018).
19. Choi, K.-I.; Hwang, S.-J.; Dai, Z.; Kang, Y.C.; Lee, J.-H. Rh-catalyzed WO_3 with anomalous humidity dependence of gas sensing characteristics. *RSC Adv.* **2014**, *4*, 53130–53136. [CrossRef]
20. Wicker, S.; Guiltat, M.; Weimar, U.; Hémeryck, A.; Barsan, N. Ambient humidity influence on CO detection with SnO_2 gas sensing materials. A combined DRIFTS/DFT Investigation. *J. Phys. Chem. C* **2017**, *121*, 25064–25073. [CrossRef]

21. Harris, D.C. Measurements. In *Quantitative Chemical Analysis*, 7th ed.; China Lake: Kern County, CA, USA, 2007; pp. 13–15.
22. Degler, D.S.; Müller, A.; Doronkin, D.E.; Wang, D.; Grunwaldt, J.-D.; Weimar, U.; Barsan, N. Platinum loaded Tin dioxide: A model system for unravelling the interplay between heterogeneous catalysis and gas sensing. *J. Mater. Chem. A* **2018**. [CrossRef]
23. Bârsan, N.; Hübner, M.; Weimar, U. Conduction mechanisms in SnO_2 based polycrystalline thick film gas sensors exposed to CO and H_2 in different oxygen backgrounds. *Sens. Actuators B* **2011**, *157*, 510–517. [CrossRef]
24. Koziej, D.; Hübner, M.; Barsan, N.; Weimar, U.; Sikora, M.; Grunwaldt, J.-D. Operando X-ray absorption spectroscopy studies on Pd-SnO_2 based sensors. *Phys. Chem. Chem. Phys.* **2009**, *11*, 8620–8625. [CrossRef] [PubMed]
25. Ravel, B.; Newville, M. ATHENA, ARTEMIS, HEPHAESTUS: Data analysis for X-ray absorption spectroscopy using IFEFFIT. *J. Synchrotron Radiat.* **2005**, *12*, 537–541. [CrossRef] [PubMed]
26. Ravel, B. *Quantitative EXAFS Analysis*; van Bokhoven, J.A., Lamberti, C., Eds.; John Wiley & Sons, Ltd.: Chichester, UK, 2016; pp. 281–302.
27. Baur, W.H.; Khan, A. Rutile-type compounds. IV. SiO_2, GeO_2 and a comparison with other rutile-type structures. *Acta Crystallogr. B* **1971**, *27*, 2133–2139. [CrossRef]
28. Loopstra, B.O.; Boldrini, P. Neutron diffraction inverstigation of WO_3. *Acta Crystallogr. B* **1966**. [CrossRef]
29. Staerz, A.; Weimar, U.; Barsan, N. Understanding the Potential of WO_3 Based Sensors for Breath Analysis. *Sensors* **2016**, *16*, 1815. [CrossRef] [PubMed]
30. Salje, E. The Orthorhombic Phase of WO_3. *Acta Crystallogr. B* **1977**, *33*, 574–577. [CrossRef]
31. Marezio, M. Refinement of the crystal structure of In_2O_3. *Acta Crystallogr. B* **1966**, *20*, 723–728. [CrossRef]
32. Prewitt, C.T.; Shannon, R.D.; Rogers, D.B.; Sleight, A.W. The C rare earth oxide-corundum transition and crystal chemistry of oxides having the corundum structure. *Inorg. Chem.* **1969**, *8*, 1985–1993. [CrossRef]
33. Birkholz, M. *A Thin Film Analysis by X-ray Scattering*; Wiley-VCH Verlag: Weinheim, Germany, 2006.
34. Kuzmin, A.; Chaboy, J. EXAFS and XANES analysis of oxides at the nanoscale. *IUCrJ* **2014**, *1*, 571–589. [CrossRef] [PubMed]
35. Anton, M.; Buedy, B. The influence of rhodium on SnO_2-CO gas sensor. *Sens. Actuators B* **1994**, *19*, 500–501. [CrossRef]
36. Brinkmann, H. An Investigation of Rh_2O_3-Loaded n-Type Semiconducting Metal Oxide Sensors. Teacher's Thesis, University of Tuebingen, Tuebingen, Germany, 2017.
37. Herrmann, S. Eine untersuchung von Rh_2O_3 geladenen In_2O_3 Gassensoren. Teacher's Thesis, University of Tuebingen, Tuebingen, Germany, 2018.
38. Weiss, B.M.; Artioli, N.; Iglesia, E. Catalytic NO oxidation pathways and redox cycles on dispersed oxides of rhodium and cobalt. *ChemCatChem* **2012**, *4*, 1397–1404. [CrossRef]
39. Watson, P.R.; Somorjai, G.A. Interaction of carbon monoxide, carbon dioxide, and deuterium with rhodium oxide: its reduction and catalytic stability. *J. Phys. Chem.* **1982**, *20*, 3993–3996. [CrossRef]
40. Barsan, N.; Koziej, D.; Weimar, U. Metal oxide-based gas sensor research: How to? *Sens. Actuators B* **2007**, *121*, 18–35. [CrossRef]
41. Mijalković, S. Optical properties and photoelectric effects. In *Semiconductor Physical Electronics*; Li, S.S., Ed.; Springer: New York, NY, USA, 1997; Chapter 9; pp. 248–256.
42. Harrick, N.J. Optical spectrum of the semiconductor surface states from frustrated total internal reflections. *Phys. Rev.* **1962**, *125*, 1165–1170. [CrossRef]
43. Hübner, M.; Simion, C.E.; Haensch, A.; Barsan, N.; Weimar, U. CO sensing mechanism with WO_3 based gas sensors. *Sens. Actuators B* **2010**, *151*, 103–106. [CrossRef]
44. Can, I.; Weimar, U.; Barsan, N. Operando investigations of differently prepared In_2O_3-Gas sensors. *Proceedings* **2017**, *1*, 432. [CrossRef]
45. Boehme, I.; Herrmann, S.; Staerz, A.; Brinkmann, H.; Weimar, U. Understanding the sensing mechanism of Rh_2O_3 loaded In_2O_3. *Proceedings* **2018**, in press.
46. Hecker, W.C.; Rasband, P.B. Catalyst characterization using quantitative FTIR: CO on supported Rh. *J. Catal.* **1993**, *139*, 551–560.
47. Degler, D.; Wicker, S.; Weimar, U.; Barsan, N. Identifying the active oxygen species in SnO_2 based gas sensing materials: An operando IR spectrsocopy study. *J. Phys. Chem. C* **2015**, *119*, 11792–11799. [CrossRef]

48. Amalric Popescu, D.; Herrmann, J.-M.; Ensuque, A.; Bozon-Verduraz, F. Nanosized tin dioxide: Spectroscopic (UV–VIS, NIR, EPR) and electrical conductivity studies. *Phys. Chem. Chem. Phys.* **2001**, *3*, 2522–2530. [CrossRef]
49. Wicker, S. Influence of Humidity on the Gas Sensing Characteristics of SnO_2: DRIFTS Investigation of Different Base Materials and Dopants. Ph.D. Thesis, University of Tuebingen, Tuebingen, Germany, 2016.
50. De Groot, F. High-resolution X-ray emission and X-ray absorption spectroscopy. *Chem. Rev.* **2001**, *101*, 1779–1808. [CrossRef] [PubMed]
51. Kowalska, J.K.; Lima, F.A.; Pollock, C.J.; Rees, J.A.; DeBeer, S. A practical guide to high-resolution X-ray spectroscopic measurements and their applications in bioinorganic chemistry. *Isr. J. Chem.* **2016**, *56*, 803–815. [CrossRef]
52. Koningsberger, D.C.; Prins, R. *X-ray Absorption: Principles, Applications, Techniques of EXAFS, SEXAFS and XANES*; John Wiley & Sons: Hoboken, NJ, USA, 1987.
53. Grunwaldt, J.D.; Basini, L.; Clausen, B.S. In situ EXAFS study of Rh/Al_2O_3 catalysts for catalytic partial oxidation of methane. *J. Catal.* **2001**, *200*, 321–329. [CrossRef]
54. Basini, L.; Marchionna, M.; Aragno, A. Drift and mass spectroscopic studies on the reactivity of rhodium clusters at the surface of polycrystalline oxides. *J. Phys. Chem.* **1992**, *96*, 9431–9441. [CrossRef]

Supporting Information

Rhodium Oxide Surface-Loaded Gas Sensors

Anna Staerz [1], Inci Boehme [1], David Degler [2], Mounib Bahri [3], Dmitry E. Doronkin [4], Anna Zimina [4], Helena Brinkmann [1], Sina Herrmann [1], Benjamin Junker [1], Ovidiu Ersen [3], Jan-Dierk Grunwaldt [4], Udo Weimar [1] and Nicolae Barsan [1,*]

[1] Institute of Physical and Theoretical Chemistry (IPTC), University of Tuebingen, Auf der Morgenstelle 15, D-72076, Tuebingen, Germany; anna.staerz@ipc.uni-tuebingen.de (A.S.); inci.can@ipc.uni-tuebingen.de (I.B.); helena.brinkmann@student.uni-tuebingen.de (H.B.); sina.herrmann@ipc.uni-tuebingen.de (S.H.); benjamin.junker@ipc.uni-tuebingen.de (B.J.); upw@ipc.uni-tuebingen.de (U.W.)

[2] European Synchrotron Radiation Facility (ESRF), 71 Avenue des Martyrs, 38043 Grenoble, France; david.degler@esrf.fr

[3] Institut de Physique et Chimie des Matériaux de Strasbourg (IPCMS), UMR 7504 CNRS-Université de Strasbourg, 23 rue du Lœss, F-67034 Strasbourg cedex 2, France; mounib.bahri@ipcms.unistra.fr (M.B.); ovidiu.ersen@ipcms.unistra.fr (O.E.)

[4] Institute of Catalysis Research and Technology (IKFT) and Institute for Chemical Technology and Polymer Chemistry (ITCP), Karlsruhe Institute of Technology, Kaiserstr. 12, 76131 Karlsruhe, Germany; dmitry.doronkin@kit.edu (D.E.D.); anna.zimina@kit.edu (A.Z.); grunwaldt@kit.edu (J.-D.G.)

* Correspondence: nb@ipc.uni-tuebingen.de; Tel.: +49-(0)7071-29-78761

Table S1. Concentrations used for the loading preparations.

0.5 g of Base Material	M($RhCl_3*H_2O$) [g]	Loading Level
WO_3	0.0113 g	2.50 at.%
	0.0226 g	5.00 at.%
In_2O_3	0.0038 g	0.50 at.%
	0.0207 g	2.75 a.%
SnO_2	0.0035 g	0.50 at.%
	0.0208 g	3.00 at.%

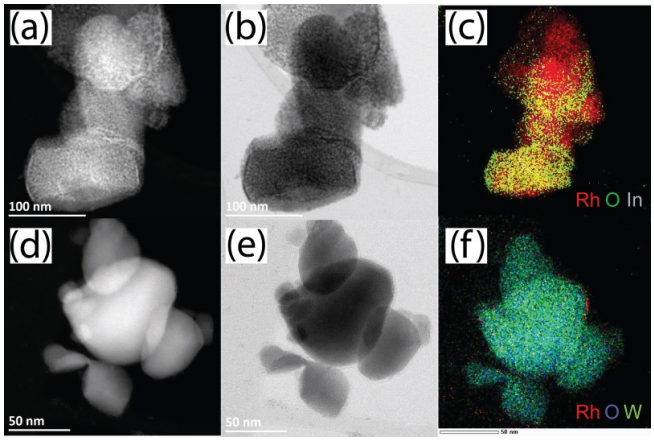

Figure S1. STEM images of 2.75 at.% Rh-Loaded In_2O_3. (**a**) STEM-HAADF (**b**) STEM-BF and EDS elemental mapping images (**c**), STEM images of 5 at.% Rh-Loaded WO_3. (**d**) STEM-HAADF (**e**) STEM-BF and EDS elemental mapping images (**f**).

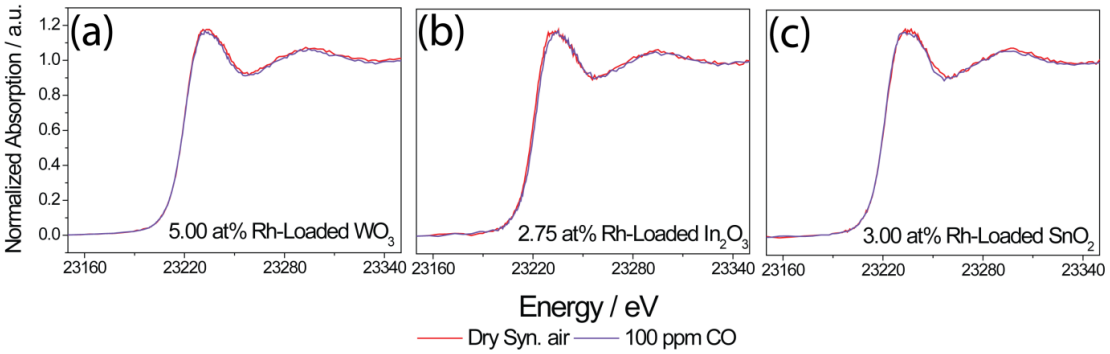

Figure S2. Rh K-edge XANES spectra of 5 at.% Rh-loaded WO_3 (**a**), 2.75 at.% Rh-loaded In_2O_3 (**b**) and 3.00 at.% Rh-loaded SnO_2 (**c**), recorded during different CO exposure in dry syn. air at 300 °C.

Sensors & Actuators: B. Chemical 292 (2019) 48–56

Contents lists available at ScienceDirect

Sensors and Actuators B: Chemical

journal homepage: www.elsevier.com/locate/snb

Microfluidically synthesized Au, Pd and AuPd nanoparticles supported on SnO_2 for gas sensing applications

Ghazal Tofighi[a,1], David Degler[b,1,2], Benjamin Junker[b], Sabrina Müller[a], Henning Lichtenberg[a,c], Wu Wang[d], Udo Weimar[b], Nicolae Barsan[b,*], Jan-Dierk Grunwaldt[a,c,**]

[a] Institute for Chemical Technology and Polymer Chemistry (ITCP), Karlsruhe Institute of Technology (KIT), Engesserstr. 20, D-76131 Karlsruhe, Germany
[b] Institute of Physical and Theoretical Chemistry and Centre for Light-Matter Interaction, Sensors & Analytics (LISA+), University of Tübingen, D-72076 Tübingen, Germany
[c] Institute of Catalysis Research and Technology (IKFT), Karlsruhe Institute of Technology (KIT), D-76344 Eggenstein-Leopoldshafen, Germany
[d] Institute of Nanotechnology (INT), Karlsruhe Institute of Technology (KIT), D-76344 Eggenstein-Leopoldshafen, Germany

ARTICLE INFO

Keywords:
Microfluidic synthesis
AuPd nanoalloy
Gold
Palladium
SnO_2
Gas sensor

ABSTRACT

Monometallic Au and Pd nanoparticles (NPs) and homogeneous AuPd nanoalloy particles were synthesized in a continuous flow of reactants ($HAuCl_4$, K_2PdCl_4, $NaBH_4$ and polyvinylpyrrolidone (PVP)) using a microfluidic reactor with efficient micromixers. The obtained ultrasmall NPs were subsequently deposited onto SnO_2 supports with different surface area (32.7 and 3.6 $m^2 g^{-1}$). Samples with 1.0 and 0.1 wt.% metal loading were prepared. After calcination at 380 °C for 1 h the supported NPs aggregated to some extent. SnO_2 supported AuPd nanoalloys with low (0.1 wt.%) metal loadings showed the smallest NP diameters (~ 5–7 nm) and the narrowest size distribution among the samples. The gas sensing performance of the materials was investigated at 300 °C in four different gas atmospheres containing either CO, CH_4, ethanol or toluene using dry and humid conditions. They exhibited a distinct variation in the response patterns and selectivity toward the test gases depending on composition and metal loading: Au increased the sensor signals compared to pristine SnO_2 in all cases and decreased the interference of water vapor; the supported Pd NPs showed a weak response to toluene, strong sensitivity in CO sensing and slightly better response in ethanol sensing in humid air compared to dry air. However, they showed a high selectivity toward CH_4 when used in dry air; AuPd alloy particles provided lower sensor signals compared to pristine SnO_2 and no remarkable CH_4 selectivity, in contrast to the Pd system. Operando diffuse reflectance infrared Fourier-transformed spectroscopy (DRIFTS) and DC-resistance measurements indicate a strong band bending in the case of Pd and AuPd NPs, whereas in the case of Au no band bending occured, indicating a strong electronic interaction between the support and Pd-containing NPs (Fermi-level control mechanism), and a weak electronic interaction between SnO_2 and Au NPs (spill-over mechanism).

1. Introduction

Gas sensing has become increasingly important in our society due to technical innovations and the higher living standard [1–4]. Semiconducting metal oxide (SMOX) based materials are widely applied in the field of gas sensing for safety, quality control and personnel protection. Their applications range from gas bottle leak detection [5] to air quality monitoring, e.g. air intake in cars [1,6].

Most SMOX sensors are based on SnO_2 which has proven to be one of the most inexpensive, best performing and most stable sensing materials for reducing gases [7,8]. The gas sensing mechanism in pristine SMOX is based on the reception of gases, i.e. a surface reaction changing the free charge carrier concentration at the surface, and transduction, which translates the changes in the charge carrier concentration into an electronic signal [1]. A detailed discussion of the fundamental gas sensing mechanism of SMOX is found elsewhere [9–11].

Pristine SMOX materials have excellent gas sensing properties in dry

* Corresponding author.
** Corresponding author at: Institute for Chemical Technology and Polymer Chemistry (ITCP), Karlsruhe Institute of Technology (KIT), Engesserstr. 20, D-76131 Karlsruhe, Germany.
E-mail addresses: nb@ipc.uni-tuebingen.de (N. Barsan), grunwaldt@kit.edu (J.-D. Grunwaldt).
[1] Ghazal Tofighi and David Degler contributed equally to this work.
[2] Present address: European Synchrotron Radiation Facility (ESRF), F-38043 Grenoble, France.

https://doi.org/10.1016/j.snb.2019.02.107
Received 14 July 2018; Received in revised form 21 January 2019; Accepted 22 February 2019
Available online 30 March 2019

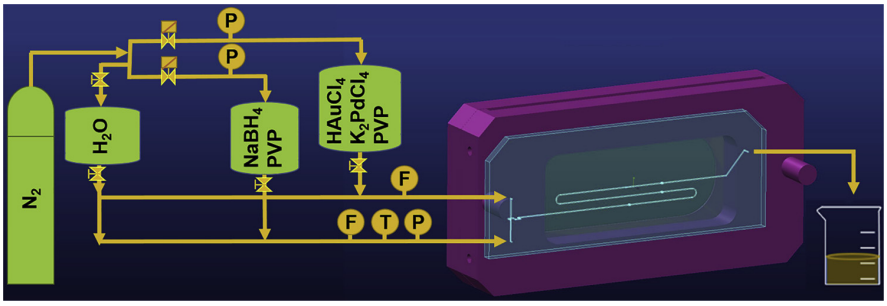

Fig. 1. Microfluidic apparatus for colloidal nanoparticle synthesis in continuous flow with reactant vessels and microfluidic chip (F, T and P: flowmeter, temperature sensor and pressure transducer). The microfluidic chip made of Si-glass bonded wafer is fixed in a stainless steel support frame.

air, but lack selectivity and long-term stability [11], and show a strong cross-interference of water vapor [9]. A solution to overcome these issues is the introduction of noble or transition metals in low concentration (0.1–2.0 wt%) into the sensing materials [12–15]. Additives can be present as dispersed nanoparticles (NPs), oxidized clusters, i.e. loadings, or as ions incorporated into the SnO_2 lattice, i.e. dopants. Depending on their chemical state, distribution and dispersion, the metal NPs either influence the reception (chemical properties) and/or transduction (electronic properties) of the base material [11,16]. When metallic NPs are present at the surface of the sensing materials, they are assumed to affect the chemical reaction of the target gas or gaseous reaction partners by activation of the gases at the NP surface and/or their subsequent spill-over to the SnO_2 surface (spill-over mechanism). If the metals are present as oxidized clusters, they are in close contact with the SMOX, affecting the chemical and electronic properties of the SnO_2, e.g. the Fermi-level of SnO_2 (Fermi-level control mechanism) [17–20].

A very good example for a dopant leading to spill-over in CO sensing is Au [21–23]. Generally, the Au loadings are found in metallic state on the surface of the SnO_2 sensing material and do not change the surface or bulk electronic properties of the SnO_2 [13,16,21,22,24]. In previous works, an oxygen-related spill-over sensitization was found for Au NPs on SnO_2 [22,23]. Combined work function and resistance measurements show no electronic interaction of Au and SnO_2 [22] and High Energy Resolution Fluorescence Detection X-ray Absorption Spectroscopy (HERFD-XAS) and Diffuse Reflectance Infrared Fourier-Transformed Spectroscopy (DRIFTS) indicate additional oxygen species on the surface of Au-loaded SnO_2 [25].

The second generally accepted sensitization mechanism is the Fermi-level control mechanism, which is expected for oxidized metal loading like in the case of Pt [19,26] or Pd [27,28] supported on SnO_2. If deposited onto SnO_2, Pd is present as clusters. Due to the close contact of the oxidized Pd with the SnO_2 base material an electronic coupling between the oxidized Pd and SnO_2 occurs. The strength of this coupling is determined by the stoichiometry of the noble metal loading, i.e. PdO. If PdO is partially reduced, the electronic coupling is altered and directly affects the charge transport in SnO_2 (transduction) and therefore the sensors' output signal [29].

With the knowledge that sensing materials loaded with monometallic Au or Pd as dopants lead to spill-over and the Fermi-level control sensing mechanism, respectively, it is intriguing to examine the effect of the two metals being combined as an alloy. Recently, Tofighi et al. [30,31] introduced an innovative method to produce monodisperse mono- and homogeneously mixed bimetallic nanocolloids in aqueous suspension in a one-step microfluidic synthesis process. The obtained NPs can be subsequently deposited onto metal oxide supports, i.e. materials attractive for catalysis and gas sensing. The aim of this study is to trigger the sensing properties, e.g. selectivity, by preparing noble metal NPs including well-mixed AuPd nanoalloys using a microfluidic reactor, to study their response with respect to various reducing gases and the dominant mechanism involved.

2. Materials and methods

2.1. Materials

$HAuCl_4 \cdot 3H_2O$ (Roth, 99.5% purity), K_2PdCl_4 (Alfa Aesar, 99.99% purity), polyvinylpyrrolidone (PVP, Sigma-Aldrich, average molecular weight 40 kDa), $NaBH_4$ (Sigma-Aldrich, 99.99% purity), H_2SO_4 (Sigma-Aldrich, 95% solution) were used without purification. $SnCl_4$ purchased from Merck was purified by distillation.

2.2. Microfluidic synthesis of Au, Pd and AuPd nanoparticles

The colloidal route for synthesis of ultrasmall Au, Pd and AuPd NPs using a microfluidic reactor was adopted from our previous reports [30,31] and Hayashi et al. [32]. An aqueous solution of metal precursors (7.5 mM) with 666 mg PVP was prepared for all samples with nominal molar Au:Pd ratios of 1:0, 1:1 and 0:1. $NaBH_4$ aqueous solution (37.5 mM) with 666 mg PVP was prepared as the reducing agent. These two solutions were poured separately into the corresponding vessels of the microfluidic setup (Fig. 1), which under 13 bar N_2 gas pressure generates a continuous and pulsation-free flow of reactants at high flow rates (2.6 L h^{-1} achieving 2400 Reynolds number). The pressurized reactants were injected into three cyclone micromixers for fast, efficient and homogeneous mixing in 2 ms (necessary for fast reduction reactions), and followed by a meandering microchannel for controlled nucleation and growth of NPs. Finally, the synthesized NPs were collected in a round-bottom flask placed in an ice/water bath and stirred for 1 h.

2.3. SnO_2 synthesis

SnO_2 with two different surface areas were synthesized by an aqueous sol-gel method with $SnCl_4$ as precursor [33]. The precipitated solid material was separated by centrifugation, washed several times and dried at 120 °C. Afterwards, the product was divided into two samples, one calcined at 450 °C (SnO_2-450) and the other at 1000 °C (SnO_2-1000) for 8 h under air leading to surface areas of 32.7 and 3.6 $m^2 g^{-1}$, respectively. Spectroscopic investigations by DRIFTS [34,35] and UV/vis-DRS [36] and electronic studies of the conduction mechanisms [37,38] for two base materials are reported elsewhere. The spectroscopic investigations reveal strong difference in the surface chemistry and optical band gap, while the electronic studies exhibit the same conduction mechanism for both materials, namely a depletion layer-controlled conduction involving grains with an unaffected bulk region.

2.4. Preparation of Au, Pd and AuPd nanoparticles supported on SnO_2

The metal NP solution produced in the microreactor was added to a suspension of 1 g SnO_2 in 80 mL water acidified with 10 mL H_2SO_4

solution (0.58 M) while stirring at room temperature for 1 h. After adsorption of the metal colloids on the support, the suspension was centrifuged three times (4500 rpm, 5 min each) and washed with water until pH 5–6 was achieved. Subsequently, the material was dried at 80 °C overnight. Afterwards, the samples were calcined at 380 °C for 1 h. This method was used to prepare sensor materials with 0.1 wt% and 1.0 wt% Au, Pd and AuPd supported on SnO_2-450 and SnO_2-1000, respectively.

2.5. Characterization of gas sensor materials

2.5.1. Gas sensor preparation and gas sensing measurements

Gas sensors were made by screen printing a paste, made from undoped or metal-doped SnO_2 powders and an organic binder (propanediol), on alumina substrates equipped with interdigitated Pt-electrodes and a backside heating meander (Pt) [39]. Gases were mixed using home-made gas dosing units with mass flow controllers, addition the diluted analyte gas to the carrier gas stream (synthetic air, 20.5 vol.% O_2) with a total flow of 250 sccm. Humidity levels were dosed by using evaporators filled with deionized water. All gases were supplied by Westfalen AG Münster. When measuring in N_2 atmospheres, the residual oxygen concentration in the gas flow was determined using a solid-state electrochemical oxygen sensor (Zirox SGM 400), which was placed downstream of the measured samples. The sensors were heated by applying a specific voltage and current to the backside heaters using a DC-powder supply (Agilent E3614 A) and adjusting the exact values according to the sensor's temperature calibration. All experiments were conducted at 300 °C. The sensor response (resistance R) was measured using a digital multimeter (Agilent 34410 A). All experiments were performed by measuring one sensor at a time to avoid downstream effects. For reducing gases the sensor signal was calculated as the ratio ($S = R_0 / R_{gas}$) of the baseline resistance (R_0) and the resistance during gas exposure (R_{gas}).

2.5.2. Electron microscopy

Electron microscopy was carried out using a scanning transmission electron microscope (STEM) with high angle annular dark-field detector (HAADF) and the composition of the samples was investigated by energy dispersive X-ray spectroscopy (EDX) using an EDAX S-UTW EDX detector in a FEI Titan 80–300 microscope operating at 300 kV. The gas sensor samples were directly dispersed on Cu grids coated with holey carbon film. Particle size statistics of the specimens were carried out on HAADF-STEM images by the ImageJ 1.49v software [40] assuming particles with ellipsoid shapes.

2.5.3. Diffuse reflectance FTIR spectroscopy

All FTIR spectra were recorded in diffuse reflectance geometry (DRIFTS) using a N_2-purged Bruker Equinox55 FT-IR spectrometer equipped with a six-mirror optic (Harrick Praying Mantis). The sensors were placed in a homemade operando cell [41], which was installed in the six-mirror optic. All single channel spectra were recorded with a resolution of 4 cm^{-1} and 1024 scans per spectrum. Absorbance spectra were calculated using Lambert-Beer's law, taking a single channel spectrum recorded in absence of CO, i.e. in dry or humid air, as reference [42]. Gas dosing, heating of sensors and electrical measurements were performed as described in 2.5.1.

3. Results and discussion

3.1. Gas sensing performances

The prepared gas sensors were tested at 300 °C in dry and humid air (50% r.h. at 25 °C) and the results are shown in Figs. 2–4 and Fig. S1. The gas sensing properties of the noble metal loaded SnO_2 samples differ from the corresponding pristine SnO_2 materials (shown in blue).

3.1.1. Au-loaded samples

In the case of SnO_2-1000, the presence of Au causes an enhancement of all sensor signals compared to the pristine material (Fig. 2a). By comparing the impact of water vapor on the sensing properties of pristine and Au-loaded SnO_2-1000, different observations are made. In case of CH_4 and ethanol similar trends are observed for both materials, namely a decrease in CH_4 signals and a slight increase in the ethanol signals in humid air. The presence of Au NPs strongly decreases the influence of humidity on the CO signal, which now causes only a minor decrease in the CO signal in humid air. In case of toluene, Au-loading enhances the toluene signals in humid air instead of decreasing them, as observed for pristine SnO_2-1000. These observations are in line with the expectations for the sensitization effect of Au NPs: The activation of oxygen by Au NPs and subsequent spill-over increase the reactivity of the SnO_2 surface and thus enhances the gas reception on SnO_2 with minor effects on the selectivity [22,23]. A similar pattern is found for Au NPs deposited on SnO_2-450 (Fig. 2b), but with two differences: Compared to pristine SnO_2 in dry air, the sensor signals for methane and toluene are respectively decreased by a factor of 1.8 and 2.5; probably due to the expected higher overall reactivity of the high-surface area SnO_2-450 with 1 wt.% Au loading. The effect of water vapor in the case of Au/SnO_2-450 and pristine SnO_2-450 is different quantitatively in the case of ethanol and qualitatively in the case of CO. The ethanol sensing signals of Au-/SnO_2-450 markedly increase, while for Au/SnO_2-1000 this increase is less pronounced. In the case of CO sensing, the presence of water vapor increases the signals of Au/SnO_2-450, while for Au/SnO_2-1000 a small decrease is observed. Since water vapor has different effects on the CO and EtOH sensing properties of both base materials (Fig. S2) and H_2O causes different chemical and electrical effects on both SnO_2 surfaces [34,43], the observations on the Au-loaded materials can be explained by different properties of the SnO_2 surfaces. With respect to the responses to the four tested gases, the effect of Au NPs on both SnO_2 materials follows a similar pattern (Fig. 2a,b), slightly affected by the properties of the base materials.

3.1.2. Pd-loaded samples

Compared to the Au-loaded SnO_2 sample, loading SnO_2 with Pd NPs (Fig. 3) has a different effect on the gas response patterns of the sensing materials. In the case of CO, both Pd-loaded materials show low sensor signals in dry air, which are - unlike those of pristine SnO_2 - increased in the presence of humidity. This behavior is well-known for noble metal oxide loaded SMOX. In the case of Pt-loaded SnO_2, it is explained by the interference of H_2O with the surface reduction by CO as well as the re-oxidation by O_2. In dry air neither reduction nor re-oxidation is hindered, and efficient re-oxidation prevents changes in the PtO_x composition, which would cause sensor signals. In humid air water vapor inhibits both reactions, but the inhibiting effect is stronger for the re-oxidation and, thus, the sensor signals increase compared to dry air, while the catalytic activity of the material decreases [26]. A strong difference between the CH_4 gas response of Au/SnO_2 and Pd/SnO_2 is observed. In dry air Pd/SnO_2 shows strong sensor signals for CH_4, which are decreased by the presence of water vapor, but remain rather high compared to the other sensing materials. Assuming that the activation of the less reactive CH_4 is limiting the methane sensing, a decrease in the CH_4 oxidation activity of PdO under humid conditions would explain the effect of water vapor on the CH_4 signals. And indeed, for PdO-based catalysts used for CH_4 oxidation a reduced activity is found under humid conditions [44]. Differences in ethanol sensing are also observed: Pd/SnO_2-1000 shows a slight increase of the ethanol signals in the presence of water vapor, while Pd/SnO_2-450 shows a slight decrease. These differences may arise from the different surface areas and Pd concentrations in the samples, or in case of ethanol sensing from an interaction with the support. Both Pd-loaded samples show weak response to toluene and are not significantly affected by water vapor.

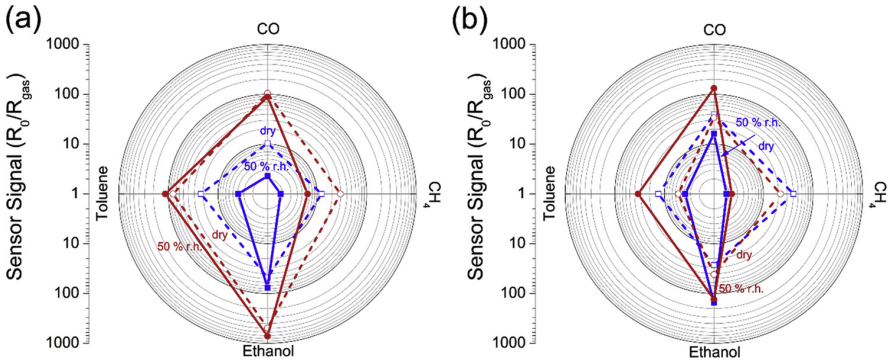

Fig. 2. Polar plot representation of the gas sensor signals for 50 ppm CO, 1000 ppm CH_4, 10 ppm ethanol and 500 ppb toluene in dry air (dashed lines/empty symbols) and 50% r.h. (straight line/filled symbols) of pristine SnO_2 (blue) and Au-loaded SnO_2 (red) at 300 °C. The sensor signals for the material based on SnO_2-1000 are shown in (a), the ones based on SnO_2-450 in (b). (For interpretation of the references to colour in this figure legend, the reader is referred to the web version of this article).

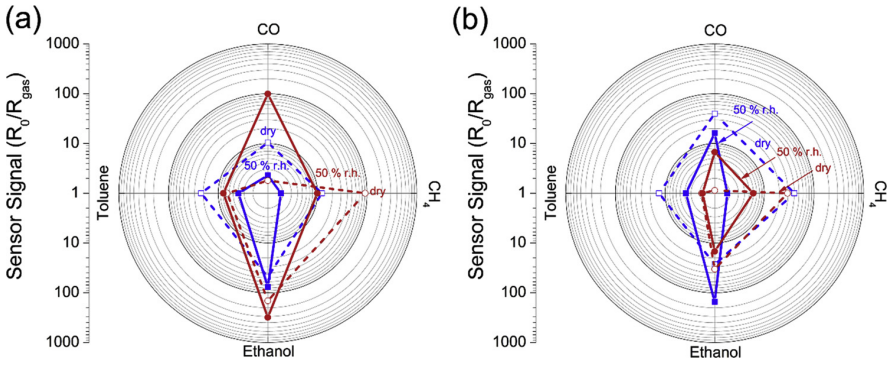

Fig. 3. Polar plot representation of the gas sensor signals for 50 ppm CO, 1000 ppm CH_4, 10 ppm ethanol and 500 ppb toluene in dry air (dashed lines/empty symbols) and 50% r.h. (straight line/filled symbols) of pristine SnO_2 (blue) and Pd-loaded SnO_2 (red) at 300 °C. The sensor signals for the material based on SnO_2-1000 are shown in (a), the ones based on SnO_2-450 in (b). (For interpretation of the references to colour in this figure legend, the reader is referred to the web version of this article).

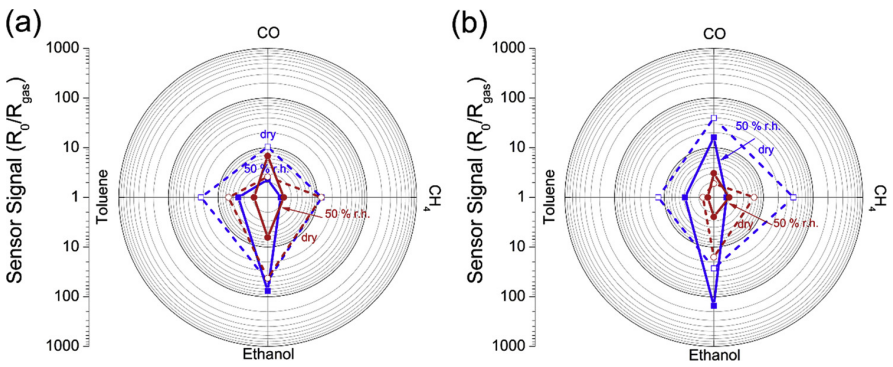

Fig. 4. Polar plot representation of the gas sensor signals for 50 ppm CO, 1000 ppm CH_4, 10 ppm ethanol and 500 ppb toluene in dry air (dashed lines/empty symbols) and 50% r.h. (straight line/filled symbols) of pristine SnO_2 (blue) and AuPd-loaded SnO_2 (red) at 300 °C. The sensor signals for the material based on SnO_2-1000 are shown in (a), the ones based on SnO_2-450 in (b). (For interpretation of the references to colour in this figure legend, the reader is referred to the web version of this article).

3.1.3. AuPd-loaded samples

AuPd NPs on SnO_2 (Fig. 4) show once again a different behavior compared to their monometallic systems. Compared to the undoped SnO_2, the AuPd nanoalloy shows lower sensor signals, with a different response pattern to the four gases, and a different susceptibility to water vapor. In the case of both pristine SnO_2 materials, water vapor causes a decrease in the CO signals, while the AuPd/SnO_2 materials provide increased signals. For ethanol the opposite effect compared to the Pd/SnO_2 samples is observed. The AuPd/SnO_2 materials show a strong decrease in the ethanol sensor signals in the presence of water vapor. Unlike Pd/SnO_2, AuPd/SnO_2 samples do not show a pronounced enhancement of the CH_4 sensor signals. The response to toluene remains low. The sensing properties of the AuPd NPs are more similar to those of Pd NPs, but show differences in the selectivity towards CH_4 and the effect of water vapor on the ethanol signals.

On both SnO_2 materials, Pd and AuPd NPs cause response patterns less dependent on the support material, but rather on the noble metal loading. This observation suggests that the gas reception is controlled by the AuPd or Pd NPs, respectively, i.e. the oxidation of the reducible analyte gases dominantly takes place on the noble metal NPs and the charge carrier concentration in SnO_2 is changed due to the electronic coupling of SnO_2 and the noble metal NPs (Fermi-level control). Thus, in the case of a Fermi-level control sensitization, the gas sensing properties, e.g. the selectivity, are defined by the catalytic properties of the noble metal loading, as the gas reception is shifted to the noble metal NPs. In the case of Pd (Fig. 3) and AuPd (Fig. 4) supported on SnO_2, the strong dependency of the sensing properties on the noble metal loadings shows that a Fermi-level controlled sensitization mechanism dominates, i.e. a strong electronic interaction of the noble metal clusters and SnO_2, rather than an activation of the SnO_2 surface, e.g. by a spill-over mechanism as in the case of Au clusters. In case of a spill-over sensitization by gold (Fig. 2), the nature of the support material plays an important role. When comparing the noble metal NPs supported on two differently prepared SnO_2 materials (with two different surface areas) with each other or with their corresponding pristine SnO_2 base materials, differences in the magnitude of the sensor signals maybe explained with differences in the concentration of reactive sites, which depends on noble metal loadings and the surface

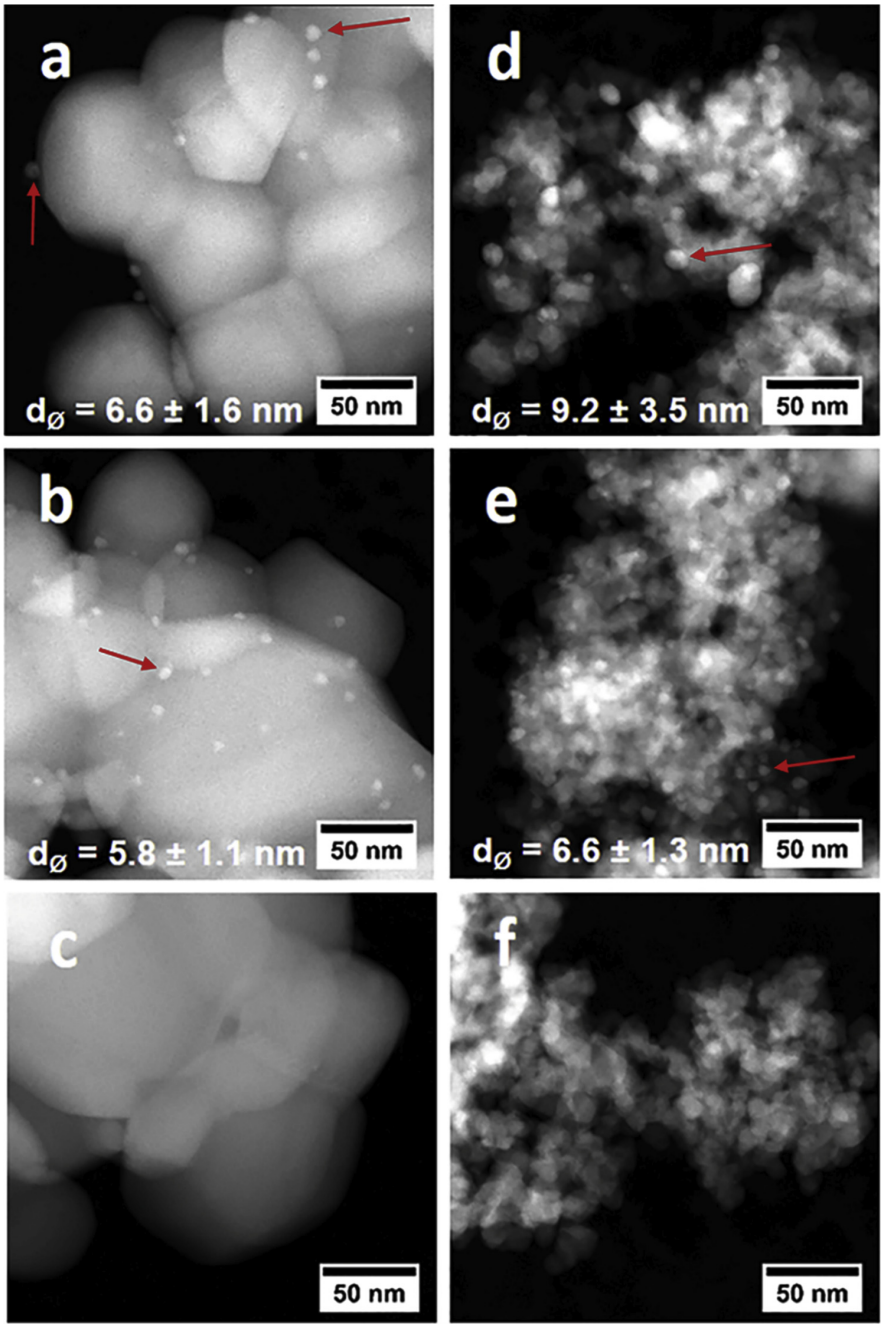

Fig. 5. STEM images of 0.1 wt.% (a) Au, (b) AuPd and (c) Pd supported on SnO_2-1000, and 1.0 wt.% (d) Au, (e) AuPd and (f) Pd supported on SnO_2-450 after gas sensing test at 300 °C. Red arrows indicate representatives of noble metal NPs. (For interpretation of the references to colour in this figure legend, the reader is referred to the web version of this article).

area of the SnO_2. Despite the strong differences in the magnitude of the sensor signals, it is important to note that all three noble metal loadings cause different response patterns to the test gases, i.e. have a different effect on the selectivity of the gas sensing materials. This is an interesting finding, demonstrating that it is possible to influence the selectivity of gas sensing materials by tuning the composition of the noble metal component.

3.2. Mechanistic investigations

The impact of additives in SMOX gas sensing materials is influenced by various factors; besides their chemical state, i.e. oxide or metal, and structure, their surface concentration has a large impact on the gas sensing properties. Both base materials have different material properties [34–36], but also different grain sizes [33]. In order to achieve a similar surface loading, the absolute loadings were adjusted by a factor similar to the difference in specific surface area. This allows us to discuss the impact of different additives as well as the role of the

Table 1
Sensor resistances in an inert atmosphere and the calculated initial band bending due to the noble metal dopants. Further details are given in the text.

Sample	Residual O_2 [ppm]	Resistance [Ω]	Band bending [meV]
SnO_2-1000			
undoped	1.7	1224	–
0.1 wt.% Au	1.7	2439	34
0.1 wt.% AuPd	1.7	24007	147
0.1 wt.% Pd	1.7	34100	164
SnO_2-450			
undoped	2.4	145	–
1.0 wt.% Au	2.4	647	74
1.0 wt.% AuPd	2.4	22505	249
1.0 wt.% Pd	2.4	36326	273

supporting SMOX properties on the basis of a similar additive surface concentration.

3.2.1. Structural analysis

The morphology and size distributions of the NPs from as prepared gas sensors were analyzed by STEM (Fig. 5 and S3). Size distributions were determined by measuring the diameters of several hundreds of NPs (Fig. S3). Samples with low noble metal loadings on supports with low surface area, i.e. 0.1 wt.% Au(Pd)/SnO_2-1000, exhibited small average diameters (5.8 and 6.6 nm, respectively). Moreover, the alloyed AuPd NPs show a smaller NP size compared to Au NPs. This effect was also reported earlier in our previous work [30] for such monometallic and bimetallic NPs supported on TiO_2; extended-X-ray absorption fine structure (EXAFS) showed that the surface of AuPd NPs after deposition on support material and drying was mostly dominated by segregated Palladium. The presence of both Au and Pd in one single nanoparticle of AuPd nanoalloy is also shown in STEM-EDX spectrum (Fig. S4). Due to low contrast in STEM image between oxidized Pd and the SnO_2 support in the calcined Pd/SnO_2 sample, the Pd NPs could not be clearly detected by electron microscopy (Fig. 5c,f), however the presence of Pd on SnO_2 was confirmed by EDX spectroscopy (Fig. S5 and S6). Previous studies on Pd-loaded SnO_2 gas sensing materials revealed that Pd is present as PdO on the SnO_2 surface [43,45] and remains oxidized during sensor operation [43,46].

The structural analysis by STEM and the analogy to NPs supported on SnO_2 suggest that for all doped materials the noble metals form clusters on the SnO_2 surface. To further understand the sensitization mechanism, the electrical and chemical impact of the dopants was studied by estimating the initial surface band bending in an inert atmosphere (pure N_2) and by operando DRIFTS, respectively.

3.2.2. Electronic effects of the loadings

Sensitization by a Fermi-level control mechanism requires an electronic coupling between the noble metal oxide and the supporting SnO_2 support. The electronic coupling will cause an initial band bending independent on adsorbed gases, i.e. also present in an inert atmosphere. Thus, by comparing the resistances of the noble metal loaded materials with the corresponding values for pristine SnO_2 allows estimating the initial band bending using the following equation [26,47], where eV_S is the initial band bending, k_BT the thermal energy, R_L is the resistance of the noble metal loaded samples in pure N_2, and R_P the resistance of pristine SnO_2 in pure N_2:

$$eV_S = k_BT \cdot ln\left(\frac{R_L}{R_P}\right)$$

The results of these calculations are summarized in Table 1. In addition to the initial band bending and the resistance in nitrogen, the residual oxygen content in the nitrogen atmosphere is shown. The high initial band bending for the samples loaded with Pd or AuPd NPs indicates a strong electronic coupling of SnO_2 and the NPs, while for the samples loaded with Au NPs a lower initial band bending is found. The low initial band bending for Au NPs is comparable with the expected error of this calculation, namely the thermal energy at 300 °C (49 meV), and can be explained by an increased adsorption of residual oxygen related to the expected O_2 spill-over by Au NPs. The calculated initial band bending for the noble metal loaded samples indicates that there is only an electronic coupling for the materials loaded with Pd or AuPd NPs, while in the case of Au NPs there is no strong electronic interaction

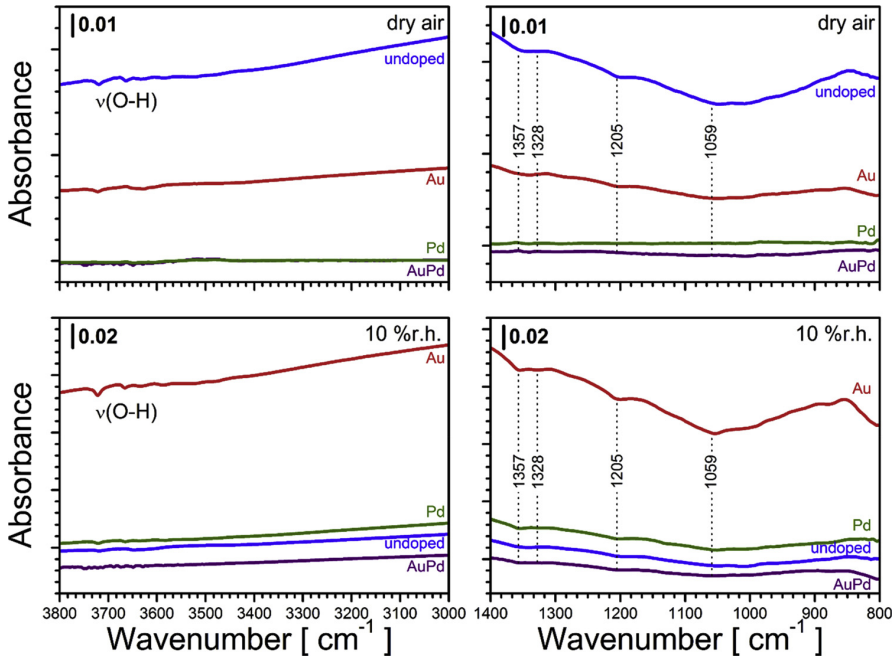

Fig. 6. Operando DRIFT spectra of SnO_2-1000 materials during sensing of 50 ppm CO in dry air (top) and in 10% r.h. (bottom). The spectral regions with the O—H stretch vibrations and the fingerprint region are respectively shown on the left and right side. All sensors were operated at 300 °C.

with the supporting SnO_2 support.

3.2.3. Chemical effects of the loadings

Changes in surface chemistry due to loading with noble metal NPs were investigated by operando DRIFTS spectroscopy using CO as reducing gas. On pristine SnO_2, the detection of CO consumes surface oxygen, causing a decrease in the Sn-O overtone vibrations between 1370 and 1330 cm^{-1} on both SnO_2 materials [34]. On SnO_2-1000 additional Sn-O overtone bands are reported at 1271, 1205, 1159 and 1059 cm^{-1} [34]. The decrease in surface oxygen concentration causes a subsequent decrease in surface hydroxyl groups, which are in equilibrium with surface oxygen [34,42]. The hydroxyl groups show several sharp O—H stretch vibrations between 3750 and 3450 cm^{-1}, one broad band of interacting OH groups (3600 to 2500 cm^{-1}) and the corresponding Sn—OH deformation vibrations (mainly below 1000 cm^{-1}) [34]. No adsorbed carbonyls are observed under dry or humid gas sensing conditions (50 ppm CO and 20.5 vol.% O_2). The DRIFTS spectra of all SnO_2-1000 materials during CO sensing are shown in Fig. 6. In dry air (Fig. 6, top), undoped SnO_2 bands related to surface oxygen and hydroxyl groups decrease as described above. In the case of the sample doped with Au NPs, a similar situation occurs. This indicates that gas reception takes place on the SnO_2 surface, while for the AuPd and Pd NPs loaded samples no changes in the SnO_2 surface are observed. For the latter case, this suggests that the gas reception does no longer take place on the SnO_2 surface, i.e. it is shifted to the AuPd or Pd NPs. In 10% r.h. (Fig. 6, bottom), the strongest change is observed for undoped SnO_2, which shows a lower impact on the SnO_2 surface species due to CO exposure. This correlates with the decreased CO signals in humid air (see Figs. 2–4) and is explained by the previously reported competition of CO and H_2O for the same surface oxygen species [34]. For the samples loaded with Au NPs, humidity does not cause a decrease, i.e. the material remains reactive in the presence of water vapor. This observation explains the low impact of water vapor on the CO sensor signals in humid air (Figs. 2–4). For the samples loaded with AuPd or Pd NPs, one observes a weak increase of surface oxygen and hydroxyl groups on SnO_2. This can be explained by a decreased reactivity of the noble metal NPs in humid air: As recently reported for Pt-loaded SnO_2, water can inhibit re-oxidation of the noble metal clusters and CO oxidation consumes oxygen from the SnO_2 surface [26]. In case of Pt loaded SnO_2, the PtO_x sensitized SnO_2 by a Fermi-level control mechanism and a decreased re-oxidation of the PtO_x clusters during sensing in humid air caused strong changes in the composition of the PtO_x clusters and, thus, a strong effect on the electronic interface of PtO_x and SnO_2, i.e. a stronger change in resistance. The DRIFT spectra of the AuPd and Pd loaded sample suggests that a similar situation as for Pt loaded SnO_2 occurs.

The samples based on SnO_2-450 show the same behavior, i.e. an increased reactivity of the SnO_2 surface for the samples loaded with Au NPs and a decreased interaction of CO with the SnO_2 surface in case of the samples loaded with AuPd or Pd NPs. The decreased interaction of CO with the SnO_2 surface indicates that the gas reception is shifted to the noble metal NPs. However, in dry air an increase in rooted hydroxyl groups (3600 to 3400 cm^{-1}), i.e. OH groups coordinated with two or three Sn ions [41], on the noble metal samples due to CO exposure is observed. This increase is most likely related to very small changes in the residual humidity in the gas flow due to mixing flows from two different channels and gas bottles.

3.3. Summary

Independent of the base materials, the gas sensing experiments (Figs. 2–4) along with the estimated values for initial band bending (Table 1) and operando DRIFTS results (Fig. 6 and Fig. S7) reveal similar effects for each noble metal loading:

- In case of Au NPs, there is no initial band bending due to the Au loading, i.e. there is no electronic coupling of Au and SnO_2. DRIFTS revealed, that Au enhances the reactivity of the SnO_2 surface. In line with previous works [22,23], these findings support an oxygen related spill-over sensitization for Au NPs.
- In case of AuPd and Pd NPs a strong initial band bending is found, i.e. there is a strong electronic interaction between SnO_2 and AuPd or Pd, respectively. The DRIFTS spectra of both materials show that the reaction of CO is no longer taking place on the SnO_2 surface and, thus, is shifted to the noble metal clusters. These findings suggest a sensitization by a Fermi-level control mechanism, as recently reported for Pt loaded SnO_2 or Rh loaded WO_3 [26,47].

The similarity between the AuPd and Pd doped sample suggests that a Fermi-level control mechanism determines the sensing properties of the alloy material. The absence of a spill-over sensitization is related to the deactivation of the oxide support by an initial band bending, e.g. as recently reported for Rh loaded WO_3 [47]. Thus, it is concluded, that in case of a sensitization by a Fermi-level control mechanism, a spill-over sensitization is absent or does not contribute to the gas reception. In the case of the Fermi-level control sensitization, the sensor signals depend on changes in the NP composition determined by the interplay of reduction and (re-) oxidation of the catalytically active sites on the NPs under certain conditions [26].

4. Conclusions and outlook

Colloidal monometallic Au and Pd NPs as well as AuPd nanoalloys were synthesized using a microfluidic reactor with efficient micromixers and then deposited on SnO_2 as support. The gas sensing measurements at 300 °C and especially the comparison of pure Au, AuPd alloy and pure Pd NPs supported on different SnO_2 substrates demonstrate that the gas sensing properties can be strongly influenced by the noble metal loading and its composition. The investigations on the sensitization mechanism of the materials revealed that for Au oxygen spill-over improves the sensing properties of the SnO_2 surfaces, whereas for the samples with Pd-containing loadings, i.e. AuPd or Pd NPs, a Fermi-level control sensitization mechanism is found to determine the sensing properties of the materials. Moreover, the catalytic reactions over the PdO_x-particles may strongly alter the sensing properties, e.g. for CO. The AuPd nanoalloy differs from the monometallic noble metal loadings and thus, systematically testing further alloy compositions is a promising approach to improve the selectivity of gas sensing materials. In addition to the alloy composition, further optimization of the noble metal concentration, support materials and operation temperature will enhance the potential of this promising type of noble metal NP based sensors.

Acknowledgements

The Virtual Institute VI-403 “In-situ Nano Imaging of Biological and Chemical Processes”, the BMBF (projects 05K10VK1, 05K13VK2), “Science and Technology of Nanosystems” Programme (432202) and KIT are gratefully acknowledged for financial support. Finally, we would like to appreciate the Karlsruhe Nano Micro Facility (KNMF), a Helmholtz research infrastructure at KIT, for providing STEM-EDX measurements.

Appendix A. Supplementary data

Supplementary material related to this article can be found, in the online version, at doi:https://doi.org/10.1016/j.snb.2019.02.107.

References

[1] N. Bârsan, G. Gauglitz, A. Oprea, E. Ostertag, G. Proll, K. Rebner, K. Schierbaum, F. Schleifenbaum, U. Weimar, Chemical and Biochemical Sensors, 1. Fundamentals.

Ullmann's Encyclopedia of Industrial Chemistry, (2012).
[2] S.A. Müller, D. Degler, C. Feldmann, M. Türk, R. Moos, K. Fink, F. Studt, D. Gerthsen, N. Bârsan, J.-D. Grunwaldt, Exploiting synergies in catalysis and gas sensing using noble metal-loaded oxide composites, ChemCatChem 10 (2018) 864–880.
[3] D. Briand, J. Courbat, Micromachined semiconductor gas sensors, in: R. Jaaniso, K. Tan (Eds.), Semiconductor Gas Sensors, Elsevier, 2013, pp. 220–260.
[4] J. Spannhake, A. Helwig, O. Schulz, G. Müller, Micro-fabrication of Gas Sensors, Solid State Gas Sensing, Springer, 2009, pp. 1–46.
[5] K. Ihokura, J. Watson, The Stannic Oxide Gas Sensor Principles and Applications, CRC press, 1994.
[6] G.D. Chansin, Printed and Flexible Sensors 2015-2025: Technologies, Players, Forecasts, IDTechEx Limited, (2015).
[7] D. Kohl, Surface processes in the detection of reducing gases with SnO_2-based devices, Sens. Actuators 18 (1989) 71–113.
[8] T. Sahm, W. Rong, N. Bârsan, L. Mädler, U. Weimar, Sensing of CH_4, CO and ethanol with in situ nanoparticle aerosol-fabricated multilayer sensors, Sens. Actuators B Chem. 127 (2007) 63–68.
[9] N. Bârsan, U. Weimar, Conduction model of metal oxide gas sensors, J. Electroceramic 7 (2001) 143–167.
[10] R. Jaaniso, O.K. Tan, Semiconductor Gas Sensors, Elsevier, 2013.
[11] H.W. Carvalho, D. Degler, N. Bârsan, J.-D. Grunwaldt, Y. Iwasawa, K. Asakura, M. Tada (Eds.), XAFS Techniques for Catalysts, Nanomaterials, and Surfaces, Springer, 2017, pp. 383–396.
[12] D. Kohl, The role of noble metals in the chemistry of solid-state gas sensors, Sens. Actuators B Chem. 1 (1990) 158–165.
[13] A. Cabot, J. Arbiol, J.R. Morante, U. Weimar, N. Bârsan, W. Göpel, Analysis of the noble metal catalytic additives introduced by impregnation of as obtained SnO_2 sol–gel nanocrystals for gas sensors, Sens. Actuators B Chem. 70 (2000) 87–100.
[14] N. Ma, K. Suematsu, M. Yuasa, T. Kida, K. Shimanoe, Effect of water vapor on Pd-loaded SnO_2 nanoparticles gas sensor, ACS Appl. Mater. Interfaces 7 (2015) 5863–5869.
[15] H.-J. Kim, J.-H. Lee, Highly sensitive and selective gas sensors using p-type oxide semiconductors: overview, Sens. Actuators B Chem. 192 (2014) 607–627.
[16] A. Cabot, A. Diéguez, A. Romano-Rodríguez, J. Morante, N. Bârsan, Influence of the catalytic introduction procedure on the nano-SnO_2 gas sensor performances: where and how stay the catalytic atoms? Sens. Actuators B Chem. 79 (2001) 98–106.
[17] M. Hübner, N. Bârsan, U. Weimar, Influences of Al, Pd and Pt additives on the conduction mechanism as well as the surface and bulk properties of SnO_2 based polycrystalline thick film gas sensors, Sens. Actuators B Chem. 171-172 (2012) 172–180.
[18] J. Rebholz, P. Bonanati, C. Jaeschke, M. Hübner, L. Mädler, U. Weimar, N. Bârsan, Conduction mechanism in undoped and antimony doped SnO_2 based FSP gas sensors, Sens. Actuators B Chem. 188 (2013) 631–636.
[19] D. Degler, H.W.P. de Carvalho, K. Kvashnina, J.-D. Grunwaldt, U. Weimar, N. Bârsan, Structure and chemistry of surface-doped Pt: SnO_2 gas sensing materials, RSC Adv. 6 (2016) 28149–28155.
[20] K. Großmann, S. Wicker, U. Weimar, N. Bârsan, Impact of Pt additives on the surface reactions between SnO_2, water vapour, CO and H_2; an operando investigation, Phys. Chem. Chem. Phys. 15 (2013) 19151–19158.
[21] G. Korotcenkov, V. Brinzari, L. Gulina, B. Cho, The influence of gold nanoparticles on the conductivity response of SnO_2-based thin film gas sensors, Appl. Surf. Sci. 353 (2015) 793–803.
[22] M. Hübner, D. Koziej, J.-D. Grunwaldt, U. Weimar, N. Bârsan, An Au clusters related spill-over sensitization mechanism in SnO_2-based gas sensors identified by operando HERFD-XAS, work function changes, DC resistance and catalytic conversion studies, Phys. Chem. Chem. Phys. 14 (2012) 13249–13254.
[23] D. Degler, S. Rank, S. Mueller, H.W. Pereira de Carvalho, J.-D. Grunwaldt, U. Weimar, N. Bârsan, Gold-loaded tin dioxide gas sensing materials: mechanistic insights and the role of gold dispersion, ACS Sens. 1 (2016) 1322–1329.
[24] C. Liu, Q. Kuang, Z. Xie, L. Zheng, The effect of noble metal (Au, Pd and Pt) nanoparticles on the gas sensing performance of SnO_2-based sensors: a case study on the {221} high-index faceted SnO_2 octahedra, CrystEngComm 17 (2015) 6308–6313.
[25] Y. Sakai, M. Kadosaki, I. Matsubara, T. Itoh, Preparation of total VOC sensor with sensor-response stability for humidity by noble metal addition to SnO_2, J. Ceram. Soc. Jpn. 117 (2009) 1297–1301.
[26] D. Degler, S.A. Müller, D.E. Doronkin, D. Wang, J.-D. Grunwaldt, U. Weimar, N. Bârsan, Platinum loaded tin dioxide: a model system for unravelling the interplay between heterogeneous catalysis and gas sensing, J. Mater. Chem. A 6 (2018) 2034–2046.
[27] N. Yamazoe, New approaches for improving semiconductor gas sensors, Sens. Actuators B Chem. 5 (1991) 7–19.
[28] S. Matsushima, Y. Teraoka, N. Miura, N. Yamazoe, Electronic interaction between metal additives and tin dioxide in tin dioxide-based gas sensors, Jpn. J. Appl. Phys. 27 (1988) 1798.
[29] M. Hübner, A. Sackmann, F. Gyger, C. Feldmann, P. Bockstaller, D. Gerthsen, U. Weimar, N. Bârsan, Location effect of Pd additives on the detection of reducing gases for nanoscale SnO_2 hollow spheres based gas sensors, Procedia Eng. 47 (2012) 208–211.
[30] G. Tofighi, A. Gaur, D.E. Doronkin, H. Lichtenberg, W. Wang, D. Wang, G. Rinke, A. Ewinger, R. Dittmeyer, J.-D. Grunwaldt, Microfluidic synthesis of ultrasmall AuPd nanoparticles with a homogeneously mixed alloy structure in fast continuous flow for catalytic applications, J. Phys. Chem. C 122 (2018) 1721–1731.
[31] G. Tofighi, H. Lichtenberg, J. Pesek, T.L. Sheppard, W. Wang, L. Schöttner, G. Rinke, R. Dittmeyer, J.-D. Grunwaldt, Continuous microfluidic synthesis of colloidal ultrasmall gold nanoparticles: in situ study of the early reaction stages and application for catalysis, React. Chem. Eng. 2 (2017) 876–884.
[32] N. Hayashi, Y. Sakai, H. Tsunoyama, A. Nakajima, Development of ultrafine multichannel microfluidic mixer for synthesis of bimetallic nanoclusters: catalytic application of highly monodisperse AuPd nanoclusters stabilized by poly (N-vinylpyrrolidone), Langmuir 30 (2014) 10539–10547.
[33] A. Diéguez, A. Romano-Rodríguez, J.R. Morante, J. Kappler, N. Bârsan, W. Göpel, Nanoparticle engineering for gas sensor optimisation: improved sol–gel fabricated nanocrystalline SnO_2 thick film gas sensor for NO_2 detection by calcination, catalytic metal introduction and grinding treatments, Sens. Actuators B Chem. 60 (1999) 125–137.
[34] D. Degler, S. Wicker, U. Weimar, N. Bârsan, Identifying the active oxygen species in SnO_2 based gas sensing materials: an operando IR spectrsocopy study, J. Phys. Chem. C 119 (2015) 11792–11799.
[35] S. Wicker, M. Guiltat, U. Weimar, A. Hémeryck, N. Barsan, Ambient humidity influence on CO detection with SnO_2 gas sensing materials, A combined DRIFTS/DFT investigation, J. Phys. Chem. C 121 (2017) 25064–25073.
[36] D. Degler, N. Barz, U. Dettinger, H. Peisert, T. Chassé, U. Weimar, N. Barsan, Extending the toolbox for gas sensor research: operando UV/vis diffuse reflectance spectroscopy on SnO_2-based gas sensors, Sens. Actuators B Chem. 224 (2016) 256–259.
[37] N. Bârsan, M. Hübner, U. Weimar, Conduction mechanisms in SnO_2 based polycrystalline thick film gas sensors exposed to CO and H_2 in different oxygen backgrounds, Sens. Actuators B Chem. 157 (2011) 510–517.
[38] J. Rebholz, C. Dee, U. Weimar, N. Barsan, A self-doping surface effect and its influence on the sensor performance of undoped SnO_2 based gas sensors, Procedia Engineer. 120 (2015) 83–87.
[39] N. Bârsan, U. Weimar, Understanding the fundamental principles of metal oxide based gas sensors; the example of CO sensing with SnO_2 sensors in the presence of humidity, J. Phys. Condens. Matter 15 (2003) R813.
[40] C.A. Schneider, W.S. Rasband, K.W. Eliceiri, NIH Image to ImageJ: 25 years of image analysis, Nat. Methods 9 (2012) 671–675.
[41] S. Harbeck, A. Szatvanyi, N. Bârsan, U. Weimar, V. Hoffmann, DRIFT studies of thick film un-doped and Pd-doped SnO_2 sensors: temperature changes effect and CO detection mechanism in the presence of water vapour, Thin Solid Films 436 (2003) 76–83.
[42] K. Grossmann, R.G. Pavelko, N. Bârsan, U. Weimar, Interplay of H_2, water vapor and oxygenat the surface of SnO_2 based gas sensors–An operando investigation utilizing deuterated gases, Sens. Actuators B Chem. 166 (2012) 787–793.
[43] D. Degler, H.W.P. de Carvalho, U. Weimar, N. Bârsan, D. Pham, L. Maedler, J.-D. Grunwaldt, Structure–function relationships of conventionally and flame made Pd-doped sensors studied by X-ray absorption spectroscopy and DC-resistance, Sens. Actuators B Chem. 219 (2015) 315–323.
[44] A.T. Gremminger, H.W.P. de Carvalho, R. Popescu, J.-D. Grunwaldt, O. Deutschmann, Influence of gas composition on activity and durability of bimetallic Pd-Pt/Al_2O_3 catalysts for total oxidation of methane, Catal. Today 258 (2015) 470–480.
[45] A.V. Marikutsa, M.N. Rumyantseva, D.D. Frolov, I.V. Morozov, A.I. Boltalin, A.A. Fedorova, I.A. Petukhov, L.V. Yashina, E.A. Konstantinova, E.M. Sadovskaya, Role of PdO_x and RuO_y clusters in oxygen exchange between nanocrystalline tin dioxide and the gas phase, J. Phys. Chem. C 117 (2013) 23858–23867.
[46] D. Koziej, M. Hübner, N. Bârsan, U. Weimar, M. Sikora, J.-D. Grunwaldt, Operando X-ray absorption spectroscopy studies on Pd-SnO_2 based sensors, Phys. Chem. Chem. Phys. 11 (2009) 8620–8625.
[47] A. Staerz, T.-H. Kim, J.-H. Lee, U. Weimar, N. Bârsan, Nanolevel control of gas sensing characteristics via p–n heterojunction between Rh_2O_3 clusters and WO_3 crystallites, J. Phys. Chem. C 121 (2017) 24701–24706.

Ghazal Tofighi received her M.Sc. in materials science and engineering in 2012 from Iran University of Science and Technology (IUST) and her PhD in chemistry in 2017 from the Karlsruhe Institute of Technology (KIT). She is specialized in microfluidic synthesis and characterization of nanoparticles including in situ spectroscopy.

David Degler received his diploma in chemistry in 2013 and his PhD in chemistry in 2017 from the University of Tübingen. He is currently researcher at the European Synchrotron Radiation Facility in Grenoble (France). His fields of interest are spectroscopy, gas sensing and operando methodology.

Benjamin Junker received his B.Sc. in chemistry in 2015 from the University of Tübingen. Currently he is a student coworker in the research group of Udo Weimar and Nicolae Barsan at the Department of Chemistry of the University of Tübingen. His research is focused on SnO_2 based gas sensors.

Sabrina Müller received her diploma in chemistry in 2010 and her PhD in chemical engineering in 2015 both from the Karlsruhe Institute of Technology. Since 2015 she was active as scientific researcher in the group of Prof. Grunwaldt at the Karlsruhe Institute of Technology. Her research focused on fundamental research of functionalized nanomaterials suitable as catalysts and/or gas sensors using spectroscopic and operando techniques.

Henning Lichtenberg obtained his diploma in physics in 2003 from the University of Hamburg and his PhD in physics from the University of Bonn in 2008. He afterwards worked as postdoctoral researcher at the Center for Advanced Microstructures and Devices (Louisiana State University) before joining Karlsruhe Institute of Technology

(KIT) in 2011. Since 2012 he is leading the group 'In-Situ Spectroscopy/Synchrotron Methods' at the Institute of Catalysis Research and Technology (KIT).

Wu Wang started as a PhD student from 2014 at Institute of Nanotechnology, Karlsruhe Institute of Technology. His fields of interest are advanced transmission electron microscopy, characterization of supported nanocatalysts, electron tomography and quantitative 3D image analysis.

Udo Weimar: received his diploma in physics in 1989, his PhD in chemistry in 1993 and his Habilitation in 2002 from the University of Tübingen. Since 2010 he is a full professor at the Department of Chemistry of the University of Tübingen. His research interest focuses on chemical sensors as well as on multicomponent analysis and pattern recognition.

Nicolae Barsan: received his diploma in Physics in 1982 from the Faculty of Physics of the Bucharest University and his PhD in Solid State Physics in 1993 from the Institute of Atomic Physics, Bucharest, Romania. Since 1995 he is a senior researcher at the Institute of Physical Chemistry of the University of Tübingen, where he is leading, together with Udo Weimar, the Gas Sensors Group.

Jan-Dierk Grunwaldt received his Ph.D. from ETH Zurich (1998), worked at the catalyst and chemical engineering company Haldor Topsøe A/S, and received his Habilitation in 2006 at ETH Zurich. After a full professorship at the Technical University of Denmark (Chair in chemical engineering and catalysis) he joined Karlsruhe Institute of Technology as full professor in chemical technology and catalysis in 2010, where he deals with synthesis, test and in-depth characterization of heterogeneous catalysts and functional materials such as sensors. He is also director at the Institute of Catalysis Research and Technology (KIT).

Supporting Information

Microfluidically Synthesized Au, Pd and AuPd Nanoparticles Supported on SnO_2 for Gas Sensing Applications

Ghazal Tofighi[a,1], David Degler[b,c,1], Benjamin Junker[b], Sabrina Müller[a], Henning Lichtenberg[a,d], Wu Wang[e], Udo Weimar[b], Nicolae Barsan[b,], and Jan-Dierk Grunwaldt[a,d,*]*

[a] Institute for Chemical Technology and Polymer Chemistry (ITCP), Karlsruhe Institute of Technology (KIT), Engesserstr. 20, D-76131 Karlsruhe, Germany

[b] Institute of Physical and Theoretical Chemistry and Centre for Light-Matter Interaction, Sensors & Analytics (LISA+), University of Tübingen, D-72076 Tübingen, Germany

[c] European Synchrotron Radiation Facility (ESRF), F-38043 Grenoble, France

[d] Institute of Catalysis Research and Technology (IKFT), Karlsruhe Institute of Technology (KIT), D-76344 Eggenstein-Leopoldshafen, Germany

[e] Institute of Nanotechnology (INT), Karlsruhe Institute of Technology (KIT), D-76344 Eggenstein-Leopoldshafen, Germany

* Corresponding authors: nb@ipc.uni-tuebingen.de; grunwaldt@kit.edu

Tel.: +49 721 608-42120

Fax: +49 721 608-44820

[1] Ghazal Tofighi and David Degler contributed equally to this work.

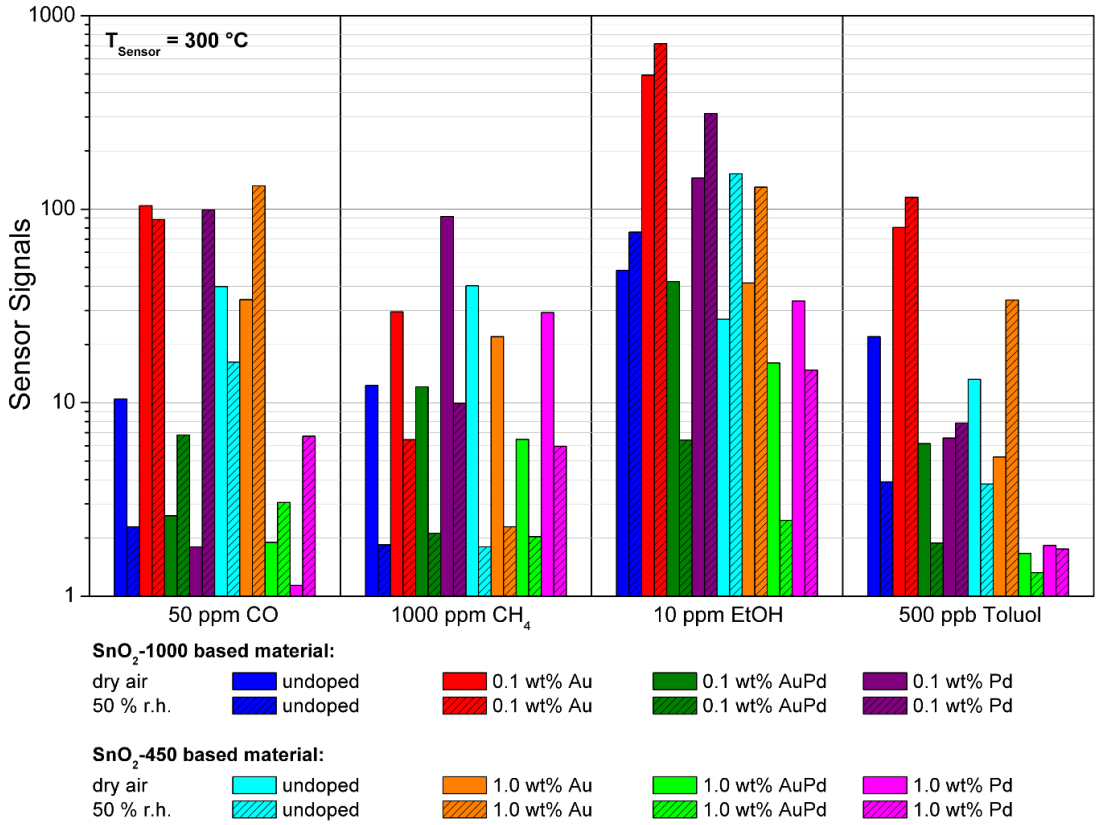

Fig. S1 Bar plot of the sensor signals for pristine and noble metal loaded gas sensing materials (see legend) in dry and humid air.

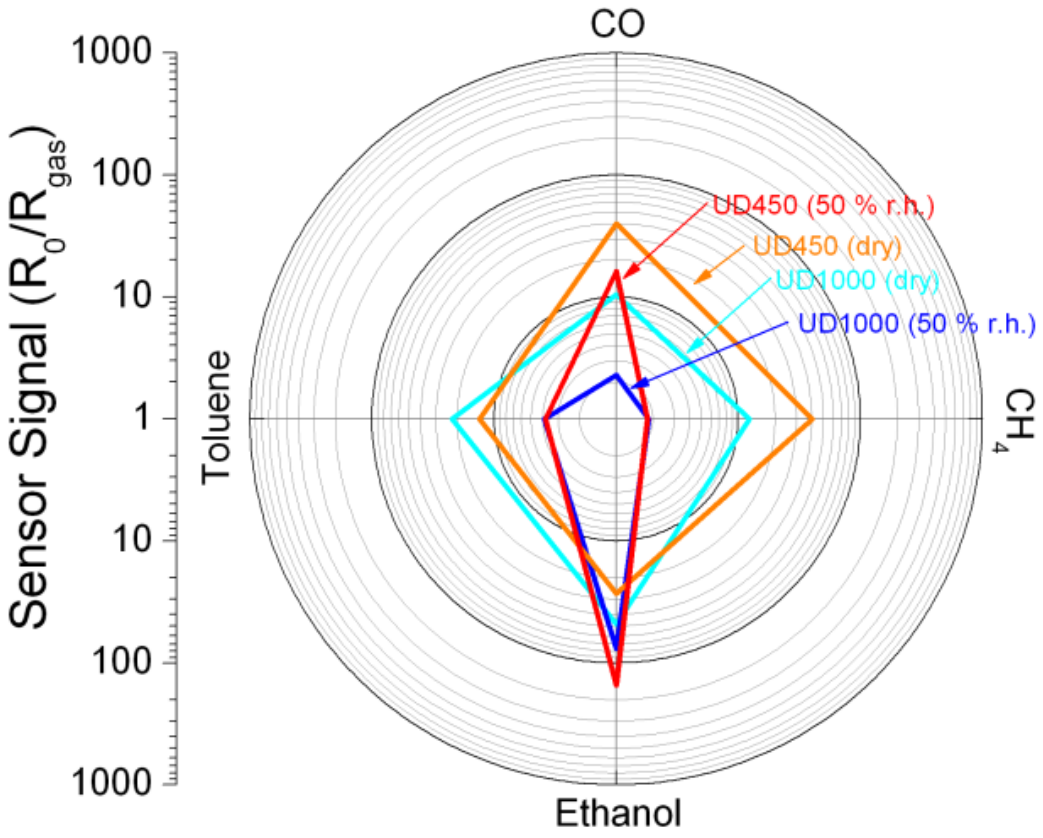

Fig. S2 Comparison of the gas sensing properties of the two differnt SnO_2 base materials measured at 300 °C in dry air (cyan / orange) and 50% r.h. (blue / red): SnO_2-1000 (cyan / blue) and SnO_2-450 (orange / red).

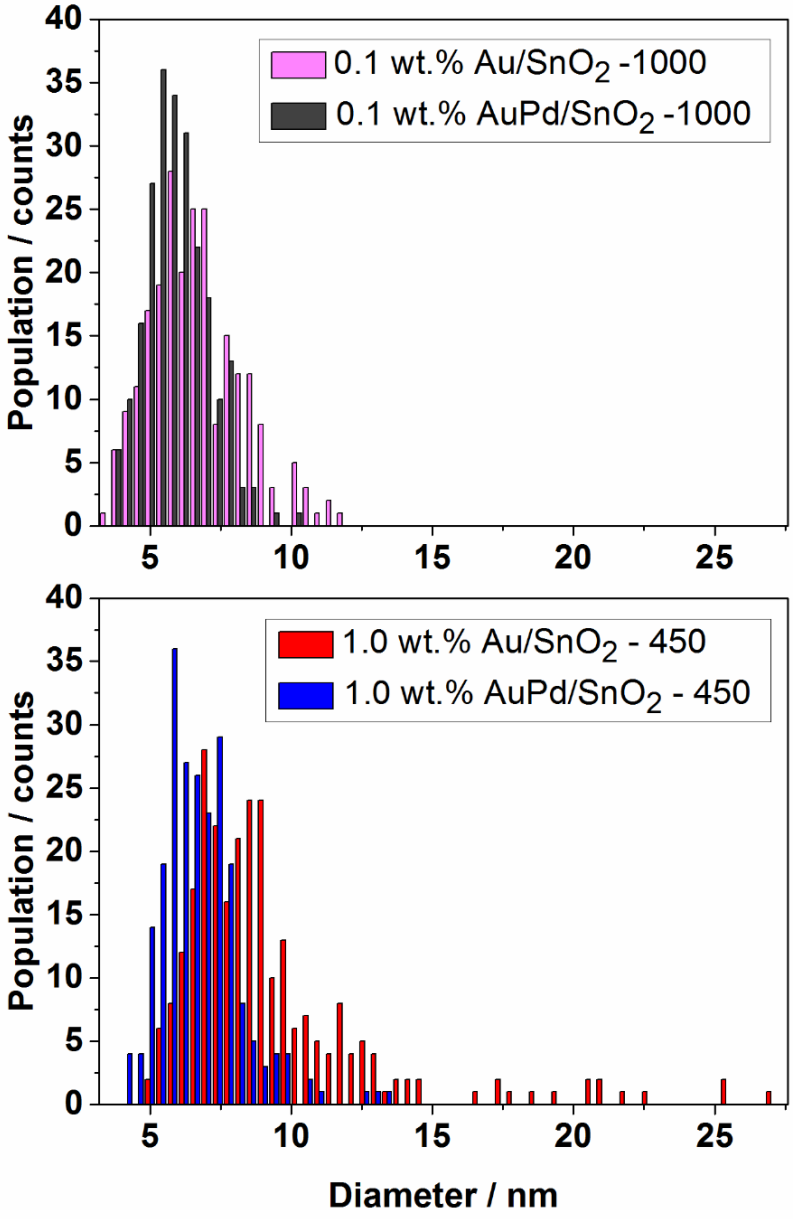

Fig. S3 Size distributions (based on HAADF-STEM images) of Au and AuPd NPs supported on SnO_2, measured after gas sensing tests at 300 °C.

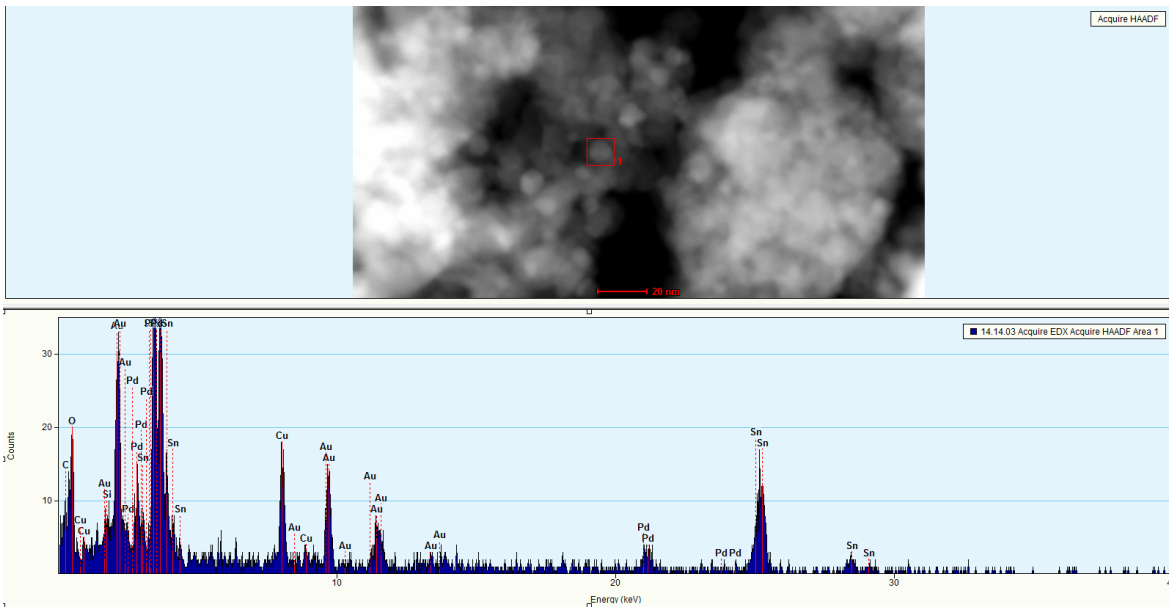

Fig. S4 STEM-EDX spectrum of a single nanoparticle in 1.0 wt.% AuPd/SnO_2-450 sample.

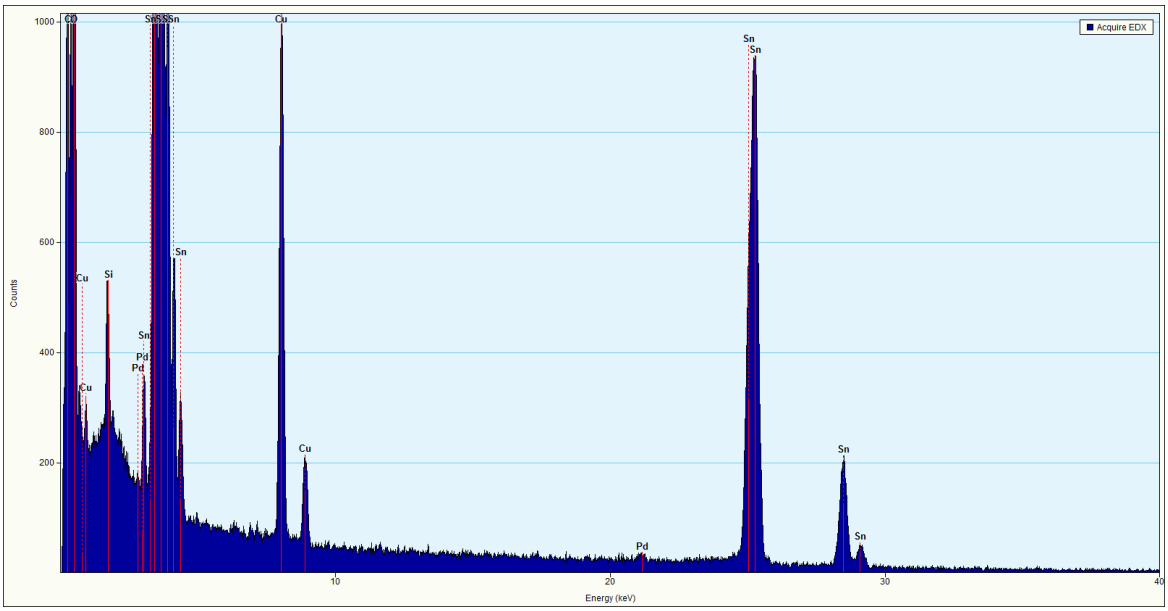

Fig. S5 STEM-EDX spectrum of 0.1 wt.% Pd/SnO_2-1000 sample.

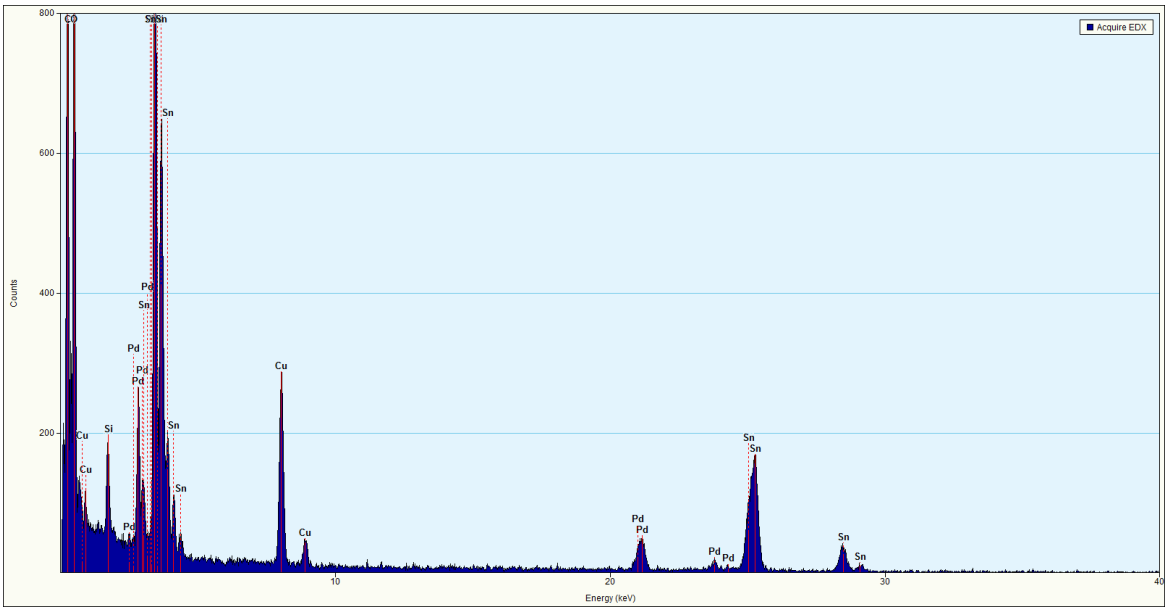

Fig. S6 STEM-EDX spectrum of 1.0 wt.% Pd/SnO_2-450 sample.

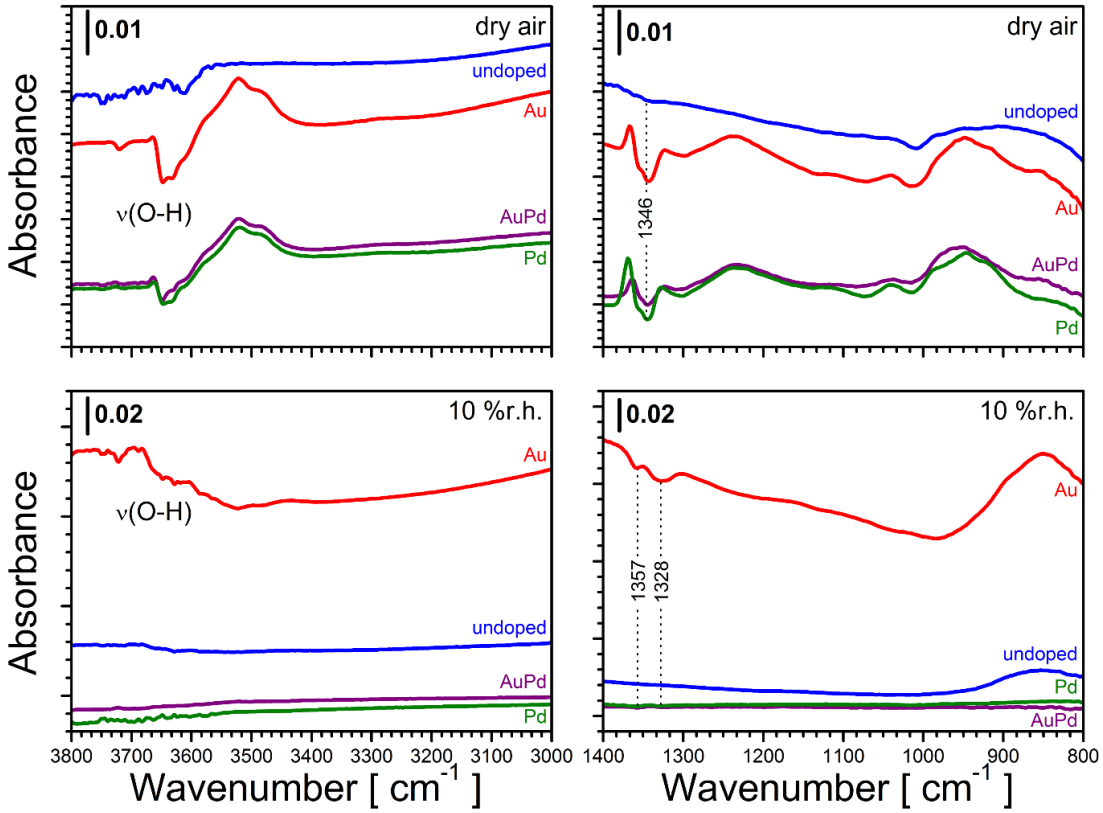

Fig. S7 Operando DRIFT spectra of SnO_2-450 materials during sensing of 50 ppm CO in dry air (top) and in 10% r.h. (bottom). The spectral regions with the O-H stretch vibrations and the fingerprint region are respectively shown on the left and right side. All sensors were operated at 300 °C.

ACS SENSORS

pubs.acs.org/acssensors Article

Investigations on the Temperature-Dependent Interaction of Water Vapor with Tin Dioxide and Its Implications on Gas Sensing

David Degler,* Benjamin Junker, Frank Allmendinger, Udo Weimar, and Nicolae Barsan

Cite This: ACS Sens. 2020, 5, 3207−3216 Read Online

ACCESS | Metrics & More | Article Recommendations | Supporting Information

ABSTRACT: This work presents an operando infrared spectroscopic study of the temperature-dependent water adsorption on pristine SnO_2 surfaces and discusses the possible implications on the oxygen ionosorption and gas-sensing mechanism. The impact of water on the sensor resistance, CO-sensing performance, and CO conversion was studied, and the obtained phenomenological results provide the basis for discussing the operando spectroscopic investigation findings. The provided information allows identification of three different water adsorption regimes ranging from physisorption and dominant associative adsorption to mainly dissociative water adsorption. In these regions, water has different impacts on the surface composition, sensor resistance, and gas-sensing performance.

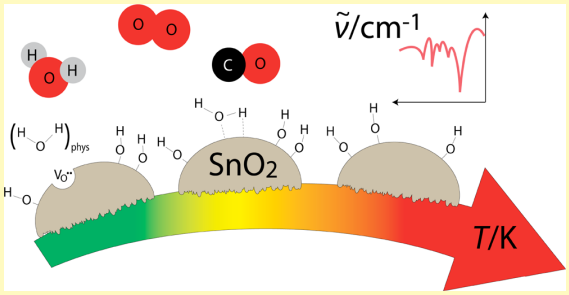

KEYWORDS: *SnO_2, gas sensor, water vapor, interference, temperature, mechanism, operando, IR spectroscopy*

Today, cost-efficient, small-sized, and easy-to-integrate SnO_2-based gas sensors are used in applications ranging from safety and process control over air quality measurements to medical ones.[1−4] Most of them are related to ambient air or other water vapor-containing environments, which makes humidity a highly significant interfering compound and as such, its role has been studied for the past decades.[5−13] Furthermore, humidity influences the aging of gas-sensing materials, e.g., by affecting the interaction with oxygen.[14]

Earlier studies are largely based on ex situ and surface science methods, thus leaving large gaps between investigation and application conditions and materials.[7,9,10,13] With increasing availability of in situ and operando IR spectroscopy, the effect of water vapor could be studied during sensor operation, further improving the understanding of the water-related surface chemistry of SnO_2.[5,8,11,12] The works carried out over the past decades identify two major influencing factors on the interaction of water vapor with SnO_2, namely, temperature and defect concentration in SnO_2. However, recent operando investigations mainly focus on the role of the SnO_2 properties, comparing differently prepared samples at one operation temperature, namely, 300 °C.[5,8,12] Although temperature was identified as an important factor by early works, a comprehensive operando study of the temperature dependency of the interaction of water vapor with SnO_2 is not available. A more detailed understanding of the role of water vapor is getting more relevant as SMOX-based gas sensors are increasingly operated at lower operation temperatures (<300 °C) or in temperature-cycled operation modes. This work will provide state-of-the-art experimental results and give a detailed discussion of the temperature dependency of water adsorption on SnO_2 gas-sensing materials.

1. MATERIALS AND METHODS

SnO_2 nanoparticles were obtained by an aqueous sol−gel process by dropwise adding $SnCl_4$ (Merck, purified by distillation) to a stirred aqueous ammonia solution (Riedel-deHaen) cooled down to 0 °C. After completing the addition of $SnCl_4$, the solution was stirred at room temperature for 30 min. The precipitate was separated by centrifugation, washed with deionized water until no chloride was found in the washing water, and dried at 120 °C. The obtained solid was ground using a shaker mill, calcined at 1000 °C for 8 h, and again ground. The as-prepared SnO_2 nanoparticles crystalize in the cassiterite structure show a low oxygen deficiency and have a size of around 100 nm.[15,16] Gas sensors were produced by screen printing a 1,2-propandiol-based SnO_2 paste onto planar Al_2O_3 substrates, which are equipped with interdigitated Pt electrodes on the front and a Pt heating meander on the backside.[17] The sensors were dried at 70 °C and thermally treated at stepwise varied temperatures (300, 400, 500, and 400 °C).

For all experiments in this study, a continuous gas flow (150 mL/min) was provided by gas mixing systems based on mass flow controllers. Different gas mixtures were obtained by mixing pre-diluted analyte gas (1000 ppm CO in dry synthetic air) and

Received: July 20, 2020
Accepted: September 11, 2020
Published: September 11, 2020

https://dx.doi.org/10.1021/acssensors.0c01493
ACS Sens. 2020, 5, 3207−3216

humidified and dry synthetic air (20.5% O_2 in N_2, purity of 99.999%). The experimentally achieved dry conditions had a residual humidity level of 10 ppm or lower. In the following discussion, these conditions will be referred to as low humidity. All gases and gas mixtures were supplied by Westfalen AG Münster. Humidified air was obtained using evaporators filled with deionized water (H_2O) or isotopically labelled water (D_2O, 99.9%). All relative humidity values are referred to 25 °C.

During the gas-sensing performance tests and the operando spectroscopy, the sensors were heated using an external power supply (Agilent E3630A), and the response of the gas sensors was recorded using a digital multimeter (Keithley 199 or Keithley 2000). Before each measurement, all sensors were maintained at the given operation temperature until a stable baseline was reached after 12−24 h. The sensor signals S were calculated as the ratio of the sensor resistance R_0 in reference conditions, e.g., pure air, and the resistance R_{gas} during CO or water exposure:

$$S = \frac{R_0}{R_{gas}}$$

The catalytic conversion of the prepared SnO_2 was studied in low-humidity background and humid air. To avoid an error due to the Pt electrodes and heater,[18] the measurement was done using plain SnO_2 powder. Therefore, 60 mg of the SnO_2 powder (~0.06 cm^3) was deposited onto quartz wool in a quartz tube, which was vertically placed in a tube furnace. For a given flow rate of 150 mL/min, the gas hourly space velocity was 150,000 h^{-1}. The temperature was increased stepwise, and the measurements were done after equilibration overnight. The exhaust of the setup was monitored by a photoacoustic gas analyzer (INNOVA 1312), and the catalytic conversion CC was calculated based on the residual CO concentration ($c_{CO,\,measured}$) referenced to a blank measurement ($c_{CO,\,blank}$):

$$CC = \left(1 - \frac{c_{CO,measured}}{c_{CO,blank}}\right) \cdot 100\%$$

Operando diffuse reflectance Fourier transform infrared spectroscopy (DRIFTS) was done using a commercial six-mirror optic (Harrick Praying Mantis) and a homemade gas sensor cell with a KBr window. All spectra were recorded on an FT-IR spectrometer (Bruker Vertex 70v) with an MCT mid-band detector and an external high-performance Globar. Each spectrum is an average of 512 scans and was measured with a spectral resolution of 1 cm^{-1}. Absorbance spectra were calculated as apparent absorbance using the spectra recorded in reference conditions (I_0):

$$A = -\log\left(\frac{I_{gas}}{I_0}\right)$$

Each reference spectrum was recorded directly prior to gas/vapor exposure, as reported in a previous work.[8]

Isotopically labelled water (D_2O) was used to provide further insights in the composition and chemistry of water-related surface species. H_2O exposure spectra show the changes on the surface of SnO_2 due to water exposure, including water-related and other surface species. Meanwhile, D_2O exposure spectra reveal water-related species are present prior the water exposure as decreased bands in the OH region and the ones presented in high humidity as increased bands in the OD region, especially the information on pre-existing hydroxyl groups is valuable. Additionally, steady-state H_2O−D_2O-exchange spectra, as shown in in the Supporting Information, were calculated using the H_2O spectra as a reference for the D_2O spectra.[8] These spectra show solely the isotopic exchange and, thus, allow the identification of water-related and other species, such as SnO_2 lattice overtones, by comparing to H_2O or D_2O spectra.

2. RESULTS AND DISCUSSION

Before discussing the temperature dependency of water adsorption on SnO_2 surfaces, it is beneficial to summarize the current gas reception mechanism of SnO_2, classify the different surface hydroxyl groups, and briefly discuss previous works describing water adsorption mechanisms.

The ionosorption of oxygen from the surrounding atmosphere results in a chemical equilibrium between adsorbed oxygen and surface oxygen vacancies (reaction R1). The detection of reducing gases, such as CO, is based on their reaction with surface oxygen, forming oxygen vacancies and corresponding oxidation products, here CO_2 (reaction R2). This interplay of cancelation and formation of oxygen vacancies traps and releases electrons from the conduction band, respectively, and thus changes the conductivity of the material by the formation of surface depletion or accumulation layers. A more detailed description of the gas-detection mechanism is given elsewhere.[19,20]

$$\frac{1}{2}O_2 + V_O^{2+} + 2e^- \leftrightharpoons O_O \quad \text{(R1)}$$

$$O_O + CO \rightarrow CO_2 + V_O^{2+} + 2e^- \quad \text{(R2)}$$

In order to study the reaction of water vapor on a molecular level, it is essential to distinguish different types of surface hydroxyl groups since the reactions leading to their formation have different effects on the sensing material's electronic properties.[5]

Earlier reports on hydroxyl groups on the MgO surface can be transferred to SnO_2.[21,22] In the case of low surface coverage, there is no interaction between single hydroxyl groups, and they can be considered as isolated. Different chemical environments are described most efficiently by the coordination number of the respective oxygen atom. In the two-dimensional representation given in Figure 1, the hydroxyl

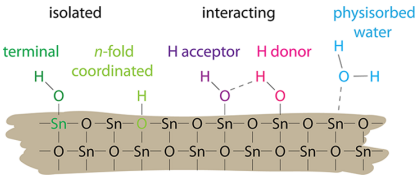

Figure 1. Two-dimensional representation of the SnO_2 surface covered with different types of hydroxyl groups as well as physisorbed water.

group on the left can be described as a onefold-coordinated or terminal hydroxyl group, whereas the adjacent hydroxyl group is two- or threefold coordinated or rooted.[20,21] The IR spectra of SnO_2-isolated terminal hydroxyl groups are generally observed as sharp bands at high wavenumbers of 3600 cm^{-1} and above, while isolated hydroxyl groups with higher coordination are expected at lower wavenumbers (<3600 cm^{-1}), depending on their coordination.[11,23,24]

Although this assignment is unambiguous for perfectly terminated single crystals of simple lattices, the surfaces of nanocrystalline SnO_2 reveal numerous defects such as vacancies, terraces, and out-of-plane and bridging atoms.[5,25,26] The variety of possible types of hydroxyl groups requires a more detailed description of their chemical bond situation, which is beyond the scope of this work.

With increased surface coverage, the interaction of hydroxyl groups in the form of hydrogen bonds, as illustrated in Figure 1, must be taken into account. Their vibrational frequency and hence the wavenumber in IR spectra are shifted depending on

https://dx.doi.org/10.1021/acssensors.0c01493
ACS Sens. 2020, 5, 3207−3216

whether the groups are acting as proton donors or acceptors.[24,27] Hydroxyl groups acting as a proton acceptor may still appear as redshifted sharp bands in IR spectra, while hydroxyl groups acting as a proton donor will no longer appear as sharp bands but rather contribute to a broad feature in the O−H-vibrational region.

For further discussion, hydroxyl groups will be distinguished between interacting and isolated hydroxyl groups, and the latter ones are divided into terminal (onefold coordinated) and rooted (two- or threefold coordinated) ones. Although this classification does not fully reflect all possible situations on SnO_2 surfaces, it is of practical use and provides sufficient detail to understand the experimental spectra.

On the SnO_2 surface, water is found as molecular or dissociated species.[13,28−30] Molecular water is either related to physisorbed water (reaction R3) or the stronger bound associatively adsorbed water, which interacts by H bonding with surface oxygen (reaction R4a) or surface hydroxyl groups (reaction R4b), where the adsorbed water molecule either acts as proton donor or acceptor, respectively.

$$H_2O_{gas} \leftrightharpoons H_2O_{phys} \quad (R3)$$

$$H_2O_{gas} + O_O \leftrightharpoons HO\cdots H\cdots O_O \quad (R4a)$$

$$H_2O_{gas} + (Sn - OH)_{Sn} \leftrightharpoons H_2O\cdots HO\cdots Sn_{Sn} \quad (R4b)$$

Dissociative adsorption of water involves surface oxygen and a surface site and results in the formation of hydroxyl groups. A general and simple description is shown in reaction R5: A proton of the water molecule is transferred to surface oxygen, forming a rooted hydroxyl group $(OH)_O$. The remaining atoms of the water molecule are adsorbed on a surface site, forming a terminal hydroxyl group $(OH)_S$.

$$H_2O_{gas} + O_O + S \leftrightharpoons (OH)_O + (OH)_S \quad (R5)$$

In order to understand the reducing effect of water, which is generally observed with SnO_2, the role of the surface site S has to be further specified, including the transfer of electrons between surface species and the semiconductor's bulk.

The first option we consider is the reaction of water with surface oxygen and two Sn sites resulting in the formation of two terminal hydroxyl groups and an oxygen vacancy, which, when ionized, injects two electros in the conduction band (reaction R6).[29] The second reaction results in the formation of a terminal and a rooted hydroxyl group (reaction R7). Rooted hydroxyl groups are considered to act as donors and, thus, inject one electron in the conduction band.[29] The third reaction involves an oxygen vacancy instead of Sn sites and results in the formation of two rooted hydroxyl groups and, thus, does not inject any additional electrons in the conduction band (reaction R8).[5] This reaction has no apparent net impact on the conductivity of SnO_2 but results in the formation of hydroxyl groups by dissociative water adsorption.

$$H_2O_{gas} + O_O + 2Sn_{Sn} \leftrightharpoons 2(Sn_{Sn}^{\delta+} - OH^{\delta-})_{Sn} + V_O^{2+} + 2e^- \quad (R6)$$

$$H_2O_{gas} + O_O + Sn_{Sn} \leftrightharpoons (Sn_{Sn}^{\delta+} - OH^{\delta-})_{Sn} + (OH)_O^+ + e^- \quad (R7)$$

$$H_2O_{gas} + O_O + V_O^{2+} + Sn_{Sn} \leftrightharpoons 2(OH)_O^+ \quad (R8)$$

The reducing effect of water may not only be related to the dissociative adsorption according to reactions R6 and R7, associatively adsorbed water molecules may directly act as an electron donor[28,30] or hinder the ionosorption of oxygen (reaction R1), e.g., by competing for the same surface sites, which are involved in oxygen ionosorption.[28,31]

This brief summary of water adsorption mechanisms shows the rather broad spectrum of possible reaction paths and as the adsorbed water species change with temperature, one may expect that different reactions and phenomena are dominant for a certain condition, having a different impact on SnO_2 and, finally, on the gas-sensing mechanism.

In order to experimentally determine the temperature-dependent impact of humidity on pristine SnO_2, the CO-sensing performance and CO conversion were studied in the temperature range 100−400 °C (Figure 2). Between 100 and

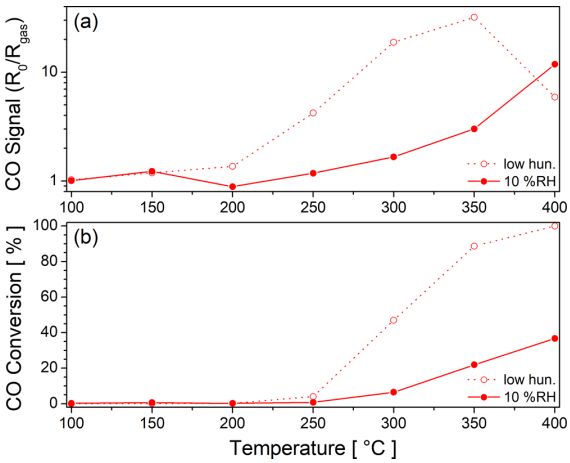

Figure 2. Temperature dependency of the (a) CO sensor signal and (b) CO conversion for 100 ppm CO in low humidity (<10 ppm H_2O) and 10% RH between 100 and 400 °C.

200 °C, there is almost no sensor signal for 100 ppm CO in low humidity (≤10 ppm) and humid conditions (10% RH). Surprisingly, at 200 °C in humid air, the sensor shows a resistance increase for CO, which is in fact a reducing gas and should cause a resistance decrease. This effect was repeatedly observed, i.e., has to be considered to be a real effect but was not further investigated here. Above 200 °C, the CO signals increase and reach a maximum around 350 °C in low humidity, while in humid air the increase does not reach a maximum within the investigated temperature range. At 400 °C, the CO signal in humid air is higher than the one in low humidity (400 °C) but does not exceed the overall maximum signal in low humidity (350 °C). The CO conversion is in line with the observed CO-sensing performance. Up to 200 °C, there is no conversion in low humidity or humid air. Above 200 °C, the CO conversion steeply increases in low humidity and reaches full conversion at 400 °C, while in humid air a less steep increase is observed, which is still below 50% conversion at 400 °C.

These phenomenological methods show a clear impact of humidity on the material's reactivity and gas-sensing performance, and the observations are in agreement with the proposed gas-sensing mechanism of pristine SnO_2, namely, formation and cancellation of oxygen vacancies due to the interplay of

https://dx.doi.org/10.1021/acssensors.0c01493
ACS Sens. 2020, 5, 3207−3216

oxygen and reducing gases (reactions R1 and R2).[16,32,33] As long as there is no CO conversion, there is no formation of oxygen vacancies and, thus, no gas-sensing effect. As soon as the CO conversion approaches full conversion, the cancelation of oxygen vacancies, i.e., re-oxidation of the surface, dominates, and less oxygen vacancies are present for a given CO concentration, consequently resulting in a lower sensor signal. Water vapor strongly decreases the reactivity of SnO_2 and thus, the gas-sensing effect, i.e., water vapor, interferes with the gas reception mechanism. However, the results shown in Figure 2 do not indicate whether the decreased reactivity originates from an interaction with the reactive oxygen species (active sites) or an inhibition of the interaction of CO with the active sites.

As the interaction of water with the surface itself is fundamental to its interfering effect, the electrical effect of water vapor exposure was also studied. Comparing the resistances in low humidity and humid air, and the calculated sensor signal for water vapor (Figure 3 and Figure S1) reveals

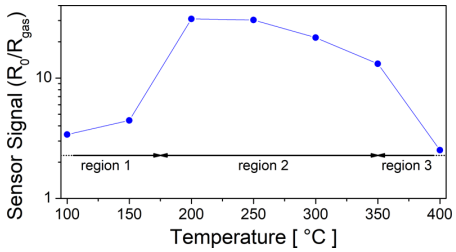

Figure 3. Sensor signal for 10% RH. The sensor resistance in low humidity (<10 ppm H_2O) and humid air are shown in Figure S1.

that between 100 and 400 °C, water acts as a reducing gas. The interaction with water vapor shows a strong temperature dependency, which can be divided into three regions. Up to 150 °C, water vapor has only a low impact on the sensor resistance (region 1); between 200 and 350 °C (region 2), it has a strong impact on the sensor resistance; and above 350 °C (region 3), its impact on the sensor resistance is drastically decreased. The transition from region 1 to region 2 correlates with an increasing dominance of the oxygen ionosorption on SnO_2, which causes the resistance increase between 150 and 250 °C (Figure S1).[20] For semiconductors, the resistance decreases with increasing temperature due to the thermal ionization of electronic states in the band gap; for an n-type SMOX like SnO_2, they are donor states situated below the conduction band. The sudden resistance increase is related to an additional process, namely, the formation of a surface electron depletion layer caused by oxygen ionosorption/oxygen vacancy cancellation.[20,30] This depletion layer controls the overall conductance of the porous gas-sensing layer.[20] The correlation of the increased dominance of oxygen ionosorption and the large impact of water vapor in the absence of CO indicates that the interfering effect of water vapor is strongly related to the active oxygen species or the ionosorption process and not to an inhibition of CO oxidation. With increasing temperature, the effect of water vapor decreases until it drastically drops above 350 °C (region 3). The steady decrease is assigned to the decreasing stability of adsorbed water species at higher temperatures and the steep drop with the onset of desorption of dissociatively adsorbed water[9,10] that strongly changes the surface composition and surface properties of SnO_2.

Based on these results, certain operation temperatures were selected for the operando DRIFTS. One temperature in region 1 right below the dominance of the oxygen ionosorption (150 °C), two temperatures in region 2, one showing the highest impact of water vapor before the steady decrease (250 °C) and one previously well studied (300 °C), and a temperature in region 3 (400 °C). Additionally, room temperature was included in the spectroscopic investigations.

The DRIFT spectrum of H_2O exposure at room temperature (Figure 4a, blue spectrum) is dominated by the increase in the broad band between 3600 and 2500 cm^{-1}, which corresponds to interacting OH groups. The band formed at 1637 cm^{-1} corresponds to the deformation vibration of physisorbed water molecules and, thus, indicates physisorption of water at room temperature.[13] The decreasing sharp bands between 3728 and 3480 cm^{-1} (O−H stretch vibrations) and decreasing bands below 1000 cm^{-1} (Sn−OH deformation vibrations) indicate a decrease of isolated OH groups due to water exposure. The DRIFT spectrum during D_2O exposure (Figure 4a, red spectrum) provides further insights due to the H−D shift of water-related surface species: The exchanged bands, i.e., decreased by D_2O exposure, correspond to the hydroxyl species present in low humidity; the newly formed bands correspond to the hydroxyl species present in humid air. This allows the identification of pre-existing hydroxyl groups, which show only a weak interaction with water vapor. The bands decreased by D_2O exposure show that at room temperature and in low humidity, the SnO_2 surface is covered with multiple isolated (3728−3480 cm^{-1}) and interacting (3600 to 2500 cm^{-1}) OH groups. Furthermore, the D_2O exposure reveals an additional Sn−OH deformation vibration at 1264 cm^{-1}, which is as such not affected by H_2O exposure.

The combined information of H_2O and D_2O exposures show that at room temperature, the SnO_2 surface is already covered with isolated and interacting hydroxyl groups in low humidity. The exposure of water vapor results in adsorption of molecular water, which interacts with the pre-existing OH groups and physisorption of water. The spectra do not indicate the formation of additional OH groups, i.e., no dissociative adsorption of water, at room temperature.

The spectra recorded at 150 and 250 °C (Figure 4b,c) show a continuous trend for the pre-existing OH groups and a similar impact of water vapor. At both temperatures, D_2O exposure shows that the intensity of the decreased bands in the OH region is lower than at room temperature, which further decreases with increasing temperature. This observation shows that the OH coverage in low humidity decreases with increasing temperature, but the same hydroxyl groups are observed between 150 and 250 °C, i.e., there is no substantial change in the water-related chemistry. However, the exposure of H_2O at these temperatures shows differences to room temperature. There is still a decrease in isolated OH groups due to water exposure (3726−3478 cm^{-1}), while there is no sign of physisorbed water at both temperatures and no (150 °C) or only little (250 °C) apparent change of the broad band, assigned to interacting hydroxyl groups.

The absence of physisorbed water at 150 °C and above is in good agreement with previous TPD studies, showing a maximum desorption of physisorbed water at 100 °C.[9,10] Thus, physisorption is not relevant for typical sensor operation temperatures (200−400 °C), and the interference of water

https://dx.doi.org/10.1021/acssensors.0c01493
ACS Sens. 2020, 5, 3207−3216

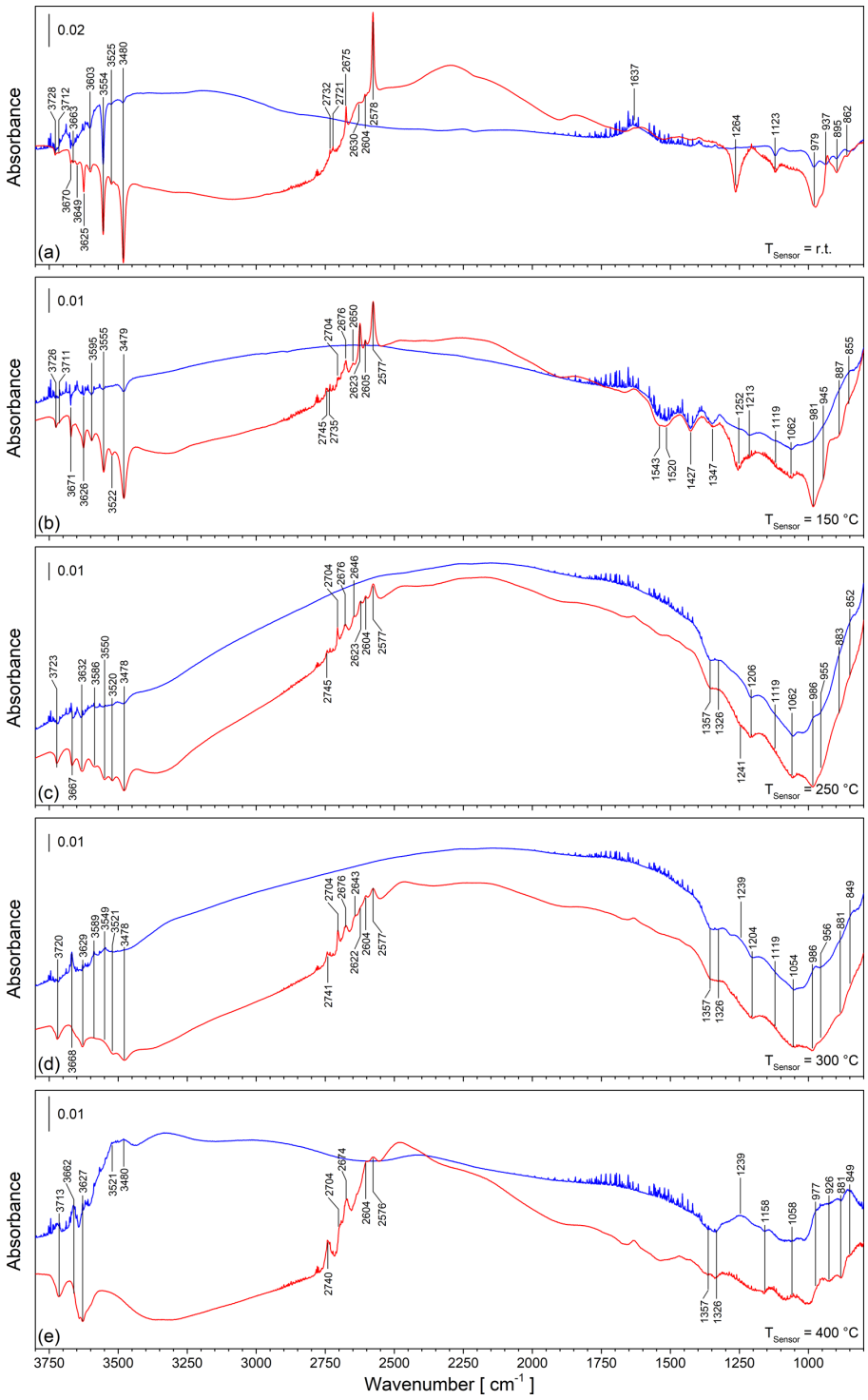

Figure 4. DRIFT spectra of 10% RH water exposure at (a) room temperature, (b) 150, (c) 250, (d) 300, and (e) 400 °C. H_2O exposure spectra are shown in blue, and D_2O spectra are shown in red. Corresponding H_2O−D_2O steady change exchange spectra are shown in Figure S2.

vapor should originate from associative (reaction R4a) and dissociative (reaction R5) adsorption. The lack of increasing isolated OH groups on the other hand suggests that there is no dissociative adsorption of water, which would result in the

https://dx.doi.org/10.1021/acssensors.0c01493
ACS Sens. 2020, 5, 3207−3216

ACS Sensors pubs.acs.org/acssensors Article

Table 1. Summary of the Water-Related IR Bands at Different Temperatures and the Impact of Water Vapor on These Bands[a]

		operation temperature				
wavenumber (cm^{-1})	assignment	r.t.	150 °C	250 °C	300 °C	400 °C
3728–3712	terminal OH stretch	P, –	P, –	P, –	P, –	P, +
3671–3662	terminal OH stretch	P, –	P, –	P, –	P, +	P, +
3649	terminal OH stretch	P, –				
3632–3625	terminal OH stretch	P, –	P, –	P, –	P, –	P, –
3603–3589	rooted OH stretch	P, –	P, –	P, =	N, +	
3555–3549	rooted OH stretch	P, –	P, =	P, –	N, +	
3525–3520	rooted OH stretch	P, –	P, =	P, –	P, –	N, +
3480–3478	rooted OH stretch	P, –	P, –	P, –	P, –	N, +
3600–2500	interacting OH stretch	P, +	P, =	P, –	P, +	P, +
1637	H_2O_{phys} deformation	N, +				
1264–1239	Sn–OH deformation	P, =	P, =	P, =	P, +	P, +
986–979	Sn–OH deformation	P, –	P, =	P, +	P, +	P, +
956–937	Sn–OH deformation	P, –	P, =	P, =		
896–881	Sn–OH deformation	P, –	P, =	P, +	P, =	P, –
862–849	Sn–OH deformation	P, –	P, =	P, +	P, +	P, +

[a]The bands are assigned according to previous reports.[5,8,27,34,35] P: pre-existing in low humidity, N: not pre-existing in low humidity, –: decreased by water vapor, +: increased by water vapor, and =: no apparent effect of water vapor. For the sake of readability, N, = is not shown.

formation of additional OH groups. The changes in the fingerprint region show additional bands, which are decreased by the exposure the water vapor. The H_2O–D_2O-exchange spectra (Figure S1b,c) show OH-group-related species, namely, Sn–OH deformation vibrations at 1252, 981, 945, 887, and 855 cm^{-1} for 150 °C and 1241, 986, 955, 883, and 852 cm^{-1} for 250 °C. The additionally decreasing bands in the H_2O spectra (Figure 4b,c, blue spectra) do not correspond to water-related species and are assigned to Sn–O overtones (1357–1326, 1213–1206, 1123–1119, and 1062 cm^{-1}) and Sn–O–Sn overtones (1543, 1520, and 1427 cm^{-1}); the latter are only observed at 150 °C.[33,34]

The decrease in bands assigned to oxygen surface species indicates an interaction of water vapor and surface oxygen and also an absence of newly formed OH groups, which would be indicated by additional O–H bands. This fact rules out a dominant contribution of dissociative adsorption. Consequently, associative water adsorption, i.e., water molecules interacting with pre-existing OH groups as well as surface oxygen, is dominant at 150 and 250 °C.

The spectra recorded at 300 °C (Figure 4d) show distinct differences to the spectra recorded at lower temperatures. The exposure of D_2O reveals fewer different pre-existing isolated OH groups (3720, 3668, 3629, 3521, and 3478 cm^{-1}) and the presence of interacting OH groups in low humidity. The exposure to H_2O has different effects on these pre-existing OH groups: The band at 3721 cm^{-1} is decreased, the band at 3668 cm^{-1} is increased, while the bands at 3629, 3521, and 3478 cm^{-1} show no changes. In addition, the exposure to H_2O results in the formation of isolated OH groups assigned to bands at 3589 and 3549 cm^{-1} and an increase in the broad band caused by interacting OH groups. The changes in the fingerprint region show a decrease in surface oxygen species (Sn–O overtones at 1357, 1326, 1204, 1119, and 1054 cm^{-1}) and increase in Sn–OH bands at 1239 and 986 cm^{-1}, while other Sn–OH bands show no apparent effect due to H_2O exposure.

The observations at 300 °C in low humidity are explained by the onset of recombination of surface OH groups to surface oxygen and water vapor,[9,10] which results in a lower concentration of pre-existing OH groups and the creation of free surface sites. In the presence of water vapor, these surface sites are available for the dissociative adsorption of water vapor (reaction R5) and result in an increased concentration of surface OH groups and a decrease in surface oxygen species. The increase in the surface concentration of OH groups results in a greater interaction between them, which gives rise to the bands assigned to interacting OH groups and correspondingly attenuate the bands of isolated OH groups. Thus, at 300 °C, dissociative adsorption becomes the dominant water adsorption process, although a contribution of associative water adsorption cannot be excluded because the latter would similarly attenuate bands of pre-existing OH groups and give an increase in the band assigned to interacting OH groups.

The D_2O exposure spectrum at 400 °C (Figure 4e, red spectrum) shows a strong decrease in pre-existing OH groups, which is indicated by fewer interacting OH groups (3600–2500 cm^{-1}) and the appearance of only three bands at 3713, (below) 3662, and 3627 cm^{-1} assigned to O–H stretch vibrations. The strongly decreased coverage with OH groups in low humidity originates from the now prevailing recombination of OH groups and subsequent desorption of H_2O with increasing temperature and continues the trend observed at 300 °C.

The exposure to water vapor at 400 °C (Figure 4e, blue spectrum) results in an overall increase in hydroxyl groups, as shown by the strongly increased intensity of the broad band assigned to interacting OH groups, new OH stretch bands (3521 and 3480 cm^{-1}), and an increasing Sn–OH deformation band (at 1239 cm^{-1}), indicating the formation of new OH groups. Pre-existing OH groups at 3627 cm^{-1} are attenuated, apparently due to the interaction with newly formed OH groups, while an increase in the bands around/above 3713 and at 3662 cm^{-1} is observed. The decrease in bands assigned to surface oxygen (1357, 1326, 1158, and 1058 cm^{-1}) along with a strong increase in surface OH groups is explained by dissociative adsorption (reaction R5) as the major process, resulting in a hydroxylated surface at 400 °C. While desorption studies[9,10] suggest that at 400 °C a majority of hydroxyl groups should be removed, the operando DRIFTS show that in humid air, i.e., in typical ambient-sensing conditions, water vapor still interacts with the surface, and hydroxyl groups are still present.

https://dx.doi.org/10.1021/acssensors.0c01493
ACS Sens. 2020, 5, 3207–3216

ACS Sensors pubs.acs.org/acssensors Article

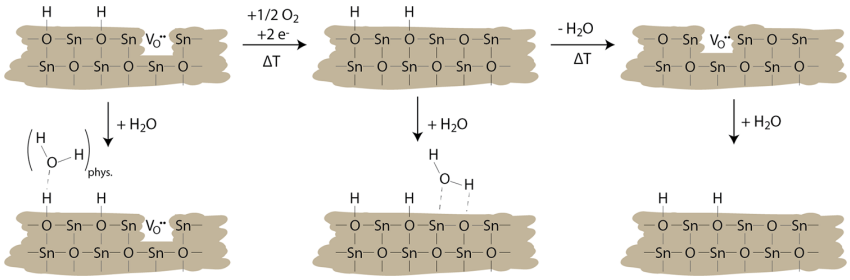

Figure 5. Schematic representation of the temperature-dependent surface chemistry of water on SnO_2; the situation in low humidity is shown on the top, and the one in humid air is at the bottom. At low temperatures, physisorption of water is dominant (left). "In an intermediate temperature range, physisorption is no longer possible and associative adsorption of water is the dominating interaction (center). The intermediate temperature range is marked by the increased dominance of oxygen ionosorption. At high temperatures, namely, after the recombination and desorption of hydroxyl groups in low humidity, dissociative adsorption of water is the main interaction with the SnO_2 surface (right).

The results of the operando DRIFTS investigations are summarized in Table 1, highlighting pre-existing (P) and not pre-existing (N) hydroxyl groups and the corresponding behaviors when the humidity level is increased, namely, an increase (+), decrease (−), or no apparent change (=) at the different operation temperatures. The water-related species on the SnO_2 surface show a clear temperature dependency. The absence of physisorbed water at elevated temperatures (T > 100 °C) and the recombination of OH groups above 250 °C are in good agreement with previous desorption studies.[9,10] In low humidity, the coverage with OH groups strongly decreases above 250 °C due to recombination of OH groups and subsequent H_2O desorption. In humid air, there is still a substantial OH coverage up to 400 °C, although it decreases with increasing temperature.

In conclusion, there are three major adsorption regimes for water, which are illustrated in Figure 5. At room temperature, physisorption of water is found to be the dominant process (Figure 5, left). In an intermediate temperature range, i.e., if the temperature is too high for physisorption but still too low to substantially cause a desorption of pre-existing OH groups, associative adsorption (Figure 5, center) is found to be the dominant process as additional dissociative adsorption is limited by large coverage with pre-existing OH groups and, thus, not substantial. At higher temperatures, more precisely after the onset of OH group recombination in low humidity, dissociative adsorption (Figure 5, right) becomes the dominant process in the presence of water vapor.

The recombination of OH groups is triggered by the operation temperature, but its onset is influenced by additional factors. At the same operation temperature (300 °C), SnO_2 materials with low defect concentrations may show still a strong contribution of associative adsorption, while for more defect-rich materials, dissociative adsorption is already the dominant process.[5,33] According to operando spectroscopy and theoretical calculations, this difference is due to a different concentration of surface oxygen vacancies, which have a strong influence to water adsorption and, thus, cause the differences between the SnO_2 materials measured at the same temperaure.[5] This work demonstrates that changes, which are observed for different materials measured at the same temperature, can be found for the same material measured at different temperatures, i.e., temperature as such is a key factor in the interaction with water vapor. Thus, it is expected to find similar temperature dependencies for different SnO_2 materials but with different transition temperatures for the different adsorption regimes (Figure 5). According to various authors, the main influencing factors are the stoichiometry of the SnO_2 surface/material, pre-existing OH groups, and the nature of predominant surface facets.[5−7,36]

Having identified the different water adsorption regimes, the key question is how these regimes are related with the electrical impact of water vapor and the gas-sensing properties. Although there are quantitative differences below 200 °C between the temperature screening (Figure 3) and the gas-sensing measurements made during operando spectroscopy (Figure S3), both measurements follow the same trend and, thus, allow their joint discussion.

Below 200 °C (region 1), water vapor has a low impact on the resistance and according to the operando DRIFT spectra, associative adsorption is the dominant process. Since there is no ionosorbed oxygen at these temperatures, the electrical effect cannot be explained by a direct reaction with or displacement of charged surface oxygen species. Thus, the electrical effect of water vapor is assigned to associatively adsorbed water acting as electron donors, as proposed by Heinrich and Cox.[28]

Water vapor has the strongest impact on the resistance between 200 and 350 °C (region 2). According to the operando DRIFT spectra (Figure 4a,b), associative adsorption is still found to be a dominant process; however, the spectra at 300 °C show already an increasing influence of dissociative water adsorption. The strong effect of water vapor can no longer be attributed to an electron donor state created by associatively adsorbed water, which, due to the destabilization of associatively adsorbed water with increasing temperature, should be even lower than that in region 1. Since the corresponding operando DRIFT spectra (Figure 4c,d) show no formation of new hydroxyl groups, dissociative adsorption mechanisms resulting in a surface reduction (reactions R6 and R7) can be excluded as well. However, since there is clearly a reduction of the surface, water has to influence the reactive oxygen species. The strong effect on the resistance and observed surface reduction has to be caused by the inhibition of oxygen ionosorption (reaction R1) by associatively adsorbed water. An inhibition of oxygen ionosorption would result in the surface reducing observed by DRIFTS, and that will have a significant impact on the sensor's resistance (Figure 3) and will also decrease the material's reactivity (Figure 2b).[28] All of that was experimentally observed and, by that, confirms an inhibition of ionosorption. Because the associative adsorption of water vapor decreases with increasing temper-

https://dx.doi.org/10.1021/acssensors.0c01493
ACS Sens. 2020, 5, 3207−3216

ature at higher temperatures, it is expected to see a lower impact of water vapor on the resistance and an improvement of the CO-sensing performance in humid air.

Above 350 °C (region 3), a different situation is found, which is characterized by the lowest impact of water vapor on the sensor resistance and the predominance of dissociative water adsorption (Figure 4e). Based on the experimental findings, one can conclude that it takes mainly place by a charge-neutral reaction (reaction R8) rather than a reducing reaction (reactions R6 and R7).

To sum up, the electronic effect of water vapor strongly depends on the nature of the interaction. Associative adsorption of water, as such, may only have a weak direct effect, acting as an electron donor. However, its indirect effect, namely, the inhibition of the oxygen ionosorption (reaction R1) has a very strong effect on the resistance. Dissociative adsorption (reaction R5) of water mostly takes place by a charge-neutral reaction (reaction R8), resulting in a low impact on the resistance. The dominant interaction is defined by the surface properties and operation temperature. There may be no clear-cut border between the adsorption regimes but rather a continuous transition.

As shown in Figure 2, water vapor does not only affect the resistance in the absence of reducing gases but has also a significant effect on the CO sensor signals as well as CO catalytic conversion. The sensor signals during the operando DRIFTS study (Figure S3) follow the same trend as observed during the initial screening (Figure 2a) and, thus, allow discussing the role of water-related surface species and the interaction of water with the surface for the detection of reducing gases.

The gas-sensing mechanism of pristine SnO_2 is based on the interplay of oxygen ionosorption (reaction R1), i.e., surface oxidation, and surface reduction (reaction R2). Water vapor and related surface species are able to influence both reactions. The ionosorption can be directly inhibited by molecular water blocking adsorption sites of molecular oxygen and be limited by water-forming rooted OH groups, i.e., consuming oxygen vacancies, and decreasing the number of sites available for ionosorption. Furthermore, the presence of OH groups on the surface hinders the interaction of CO with surface oxygen and prevents CO conversion (reaction R2) and, thus, the gas reception.[5] Based on these interference mechanisms, it is possible to describe the role of water vapor:

Until the occurrence of dominant oxygen ionosorption in low humidity at approximately 200 °C (region 1), the surface is widely covered with OH groups in low humidity and humid air. Up to this temperature, the lack of reactive oxygen species and presence of OH groups, which additionally hinder CO to react with the surface, prohibit any CO conversion and consequently CO sensing.

Temperatures between 200 and 350 °C (region 2) are characterized by feasible oxygen ionosorption in low humidity, still a substantial coverage with pre-existing OH groups and associative water adsorption as a major interaction of water with the SnO_2 surface. In low humidity, CO is converted to CO_2 (reaction R2), resulting in the formation of oxygen vacancies, which are not efficiently re-oxidized (reaction R1). This limits the surface reactivity and results in a measureable gas-sensing effect. With increasing temperature, more surface sites become available by increased ionosorption of oxygen and the recombination of OH groups, both resulting in a higher concentration of reactive oxygen. In humid air, the inhibition of oxygen ionosorption limits the concentration of reactive surface oxygen species, resulting in a strong electrical impact of water vapor, a decreased reactivity of the surface, and, thus, in low sensor signals.

Above 350 °C (region 3), the recombination of OH groups in low humidity results in a more reactive surface, which allows both reaction steps (reactions R1 and R2) to take place efficiently. Consequently, the efficient re-oxidation of the surface results in a lower oxygen vacancy concentration during CO exposure, i.e., lower sensor signals in low humidity, and high CO conversion as observed in the measurements (Figure 2). The presence of water vapor results in dissociative adsorption of water, which, as discussed above, takes place by a mainly charge-neutral reaction, having only a low impact on the resistance. As found at 400 °C, the presence of water and hydroxyl groups decreases the reactivity of the surface, while the obtained sensor signals are higher than those in low humidity at Figure 2. This effect is explained as follows: First, the surface still has reactive oxygen species, and CO is oxidized; however, either the partially restored surface OH groups or water molecules still hinder ionosorption. Compared to the corresponding low humidity conditions, the re-oxidation is limited, and in dynamic equilibrium during CO oxidation, a higher concentration of oxygen vacancies is formed, resulting in a higher sensor signal.

In conclusion, the interfering effect of water vapor is based on how its interaction affects the interplay of surface reduction and re-oxidation. Depending on temperature and other SnO_2 properties, the effect on this interplay ranges from hindering any surface reaction, overlimiting the available reactive oxygen species, to hindering re-oxidation in favor of an increased oxygen vacancy concentration. However, it should be stated that due to simple surface chemistry of CO and no direct involvement of OH groups in the gas reception, different trends are possible for gases and vapors.

3. SUMMARY AND OUTLOOK

Combining the information gained from different experimental techniques—gas sensing measurements, CO conversion measurements, and operando DRIFTS—performed at various operation temperatures allows the identification of three major temperature regions for the interaction with water vapor and its impact on gas sensing:

- Region 1: At temperatures below the occurrence of dominant ionosorption, water adsorption takes place by associative adsorption and, below 100 °C, by physisorption. Since, due to the lack of ionosorbed oxygen species, the material is not reactive, there is no possible impact on reactivity or CO sensing and no strong impact on the material's electrical resistance as such. The low impact on the material's electrical resistance is best explained by a weak donor effect of associatively adsorbed water.
- Region 2: At intermediate temperatures, namely, when oxygen ionosorption is dominant but below the onset of significant hydroxyl group desorption, water adsorption still takes place by associative adsorption. However, since the material is reactive, the presence of associatively adsorbed water inhibits oxygen ionosorption, having two major effects. First, the coverage with ionosorbed oxygen is decreased, resulting in an electrical resistance decrease in humid air with respect to low

https://dx.doi.org/10.1021/acssensors.0c01493
ACS Sens. 2020, 5, 3207−3216

humidity. Second, the lack of reactive oxygen species decreases the material's reactivity in humid air and, thus, the gas-sensing effect. Both effects steadily decrease with increasing temperatures.

- Region 3: At high temperatures, i.e., above the onset of hydroxyl desorption, water adsorption dominantly takes place by dissociative adsorption. In this region, water vapor has a weak impact on the sensor resistance, indicating that the dominant dissociative adsorption mechanism is rather charge neutral. Even after water adsorption, the surface remains reactive toward reducing gases, although less reactive than in low humidity at the same temperatures, and gas sensing is still possible in humid air.

There is rather no clear-cut separation between these three regions but rather a steady transition. Furthermore, there are no general transition temperatures for all SnO_2 materials. Pristine SnO_2 materials may show different surface facets and structures and, more importantly, a different oxygen vacancy concentration due to different synthesis methods and temperature treatments. Furthermore, the presence of additives, namely, dopants and loadings, has a significant effect on the interplay of oxygen ionosorption, water adsorption, and reactions with analyte gases. Future research should address these aspects, namely, by screening different operation temperatures during experimental investigations, as this study could only give a small, but decisive, insight in the temperature-dependent interaction of water vapor with SnO_2 surfaces and its effect on the gas-sensing properties.

■ ASSOCIATED CONTENT

Supporting Information

The Supporting Information is available free of charge at https://pubs.acs.org/doi/10.1021/acssensors.0c01493.

Additional spectra and the sensor performance during operando DRIFTS (PDF)

■ AUTHOR INFORMATION

Corresponding Author

David Degler − *Faculty of Industrial Technologies, Furtwangen University, D-78532 Tuttlingen, Germany;* orcid.org/0000-0002-2090-4715; Phone: +49 7461 1502-6783; Email: david.degler@hs-furtwangen.de

Authors

Benjamin Junker − *Institute of Physical and Theoretical Chemistry and Center for Light-Matter Interaction, Sensors & Analytics (LISA+), University of Tübingen, D-72076 Tübingen, Germany*

Frank Allmendinger − *Faculty of Industrial Technologies, Furtwangen University, D-78532 Tuttlingen, Germany*

Udo Weimar − *Institute of Physical and Theoretical Chemistry and Center for Light-Matter Interaction, Sensors & Analytics (LISA+), University of Tübingen, D-72076 Tübingen, Germany*

Nicolae Barsan − *Institute of Physical and Theoretical Chemistry and Center for Light-Matter Interaction, Sensors & Analytics (LISA+), University of Tübingen, D-72076 Tübingen, Germany;* orcid.org/0000-0001-6718-9889

Complete contact information is available at: https://pubs.acs.org/10.1021/acssensors.0c01493

Author Contributions

The manuscript was written through contributions of all authors. All authors have given approval to the final version of the manuscript.

Notes

The authors declare no competing financial interest.

■ REFERENCES

(1) Barsan, N.; Koziej, D.; Weimar, U. Metal Oxide-Based Gas Sensor Research: How To? *Sens. Actuators, B* **2007**, *121*, 18−35.

(2) Barsan, N.; Schierbaum, K.-D. *Gas Sensors Based on Conducting Metal Oxides*; 1st ed.; Korotcenkov, G., Ed.; Elsevier: Amsterdam, 2019.

(3) Jaaniso, R.; Tan, O. K. Semiconductor Gas Sensors. *Semicond. Gas Sens.* **2013**, *2*, 1−552.

(4) Neri, G. First Fifty Years of Chemoresistive Gas Sensors. *Chemosensors* **2015**, *3*, 1−20.

(5) Wicker, S.; Guiltat, M.; Weimar, U.; Hémeryck, A.; Barsan, N. Ambient Humidity Influence on CO Detection with SnO_2 Gas Sensing Materials. A Combined DRIFTS/DFT Investigation. *J. Phys. Chem. C* **2017**, *121*, 25064−25073.

(6) Batzill, M.; Bergermayer, W.; Tanaka, I.; Diebold, U. Tuning the Chemical Functionality of a Gas Sensitive Material: Water Adsorption on SnO_2(101). *Surf. Sci.* **2006**, *600*, 29−32.

(7) Gercher, V. A.; Cox, D. F. Water Adsorption on Stoichiometric and Defective SnO_2(110) Surfaces. *Surf. Sci.* **1995**, *322*, 177−184.

(8) Grossmann, K.; Pavelko, R. G.; Barsan, N.; Weimar, U. Interplay of H_2, Water Vapor and Oxygenat the Surface of SnO_2 Based Gas Sensors - An Operando Investigation Utilizing Deuterated Gases. *Sens. Actuators, B* **2012**, *166-167*, 787−793.

(9) Egashira, M.; Nakashima, M.; Kawasumi, S.; Selyama, T. Temperature Programmed Desorption Study of Water Adsorbed on Metal Oxides. 2. Tin Oxide Surfaces. *J. Phys. Chem.* **1981**, *85*, 4125−4130.

(10) Yamazoe, N.; Fuchigami, J.; Kishikawa, M.; Seiyama, T. Interactions of Tin Oxide Surface with O2, H2O and H2. *Surf. Sci.* **1979**, *86*, 335−344.

(11) Pavelko, R. G.; Daly, H.; Hardacre, C.; Vasiliev, A. A.; Llobet, E. Interaction of Water, Hydrogen and Their Mixtures with SnO2 Based Materials: The Role of Surface Hydroxyl Groups in Detection Mechanisms. *Phys. Chem. Chem. Phys.* **2010**, *12*, 2639−2647.

(12) Pavelko, R. G.; Choi, J. K.; Urakawa, A.; Yuasa, M.; Kida, T.; Shimanoe, K. H_2O/D_2O Exchange on SnO_2 Materials in the Presence of CO: Operando Spectroscopic and Electric Resistance Measurements. *J. Phys. Chem. C* **2014**, *118*, 2554−2563.

(13) Thornton, E. W.; Harrison, P. G. Tin Oxide Surfaces Part 1.-Surface Hydroxyl Groups and the Chemisorption of Carbon Dioxide and Carbon Monoxide on Tin(IV) Oxide. *J. Chem. Soc., Faraday Trans. 1* **1975**, *71*, 461−472.

(14) Suematsu, K.; Ma, N.; Watanabe, K.; Yuasa, M.; Kida, T.; Shimanoe, K. Effect of Humid Aging on the Oxygen Adsorption in SnO_2 Gas Sensors. *Sensors* **2018**, *18*, 254−211.

(15) Diéguez, A.; Romano-Rodríguez, A.; Morante, J. R.; Kappler, J.; Bârsan, N.; Göpel, W. Nanoparticle Engineering for Gas Sensor Optimization: Improved Sol-Gel Fabricated Nanocrystalline SnO_2 Thick Film Gas Sensor for NO_2 Detection by Calcination, Catalytic Metal Introduction and Grinding Treatments. *Sens. Actuators, B* **1999**, *60*, 125−137.

(16) Degler, D.; Barz, N.; Dettinger, U.; Peisert, H.; Chassé, T.; Weimar, U.; Barsan, N. Extending the Toolbox for Gas Sensor Research: Operando UV/Vis Diffuse Reflectance Spectroscopy on SnO_2-Based Gas Sensors. *Sens. Actuators, B* **2016**, *224*, 256−259.

(17) Bârsan, N.; Weimar, U. Understanding the Fundamental Principles of Metal Oxide Based Gas Sensors; the Example of CO Sensing with SnO_2 Sensors in the Presence of Humidity. *J. Phys. Condens. Matter* **2003**, *15*, R813.

https://dx.doi.org/10.1021/acssensors.0c01493
ACS Sens. 2020, 5, 3207−3216

(18) Kappler, J.; Tomescu, A.; Barsan, N.; Weimar, U. CO Consumption of Pd Doped SnO_2 Based Sensors. *Thin Solid Films* **2001**, *391*, 186−191.
(19) Degler, D.; Weimar, U.; Barsan, N. Current Understanding of the Fundamental Mechanisms of Doped and Loaded Semiconducting Metal Oxide-Based Gas Sensing Materials. *ACS Sens.* **2019**, *4*, 2228−2249.
(20) Barsan, N.; Weimar, U. Conduction Model of Metal Oxide Gas Sensors. *J. Electroceram.* **2001**, *7*, 143−167.
(21) Knözinger, E.; Jacob, K. H.; Singh, S.; Hofmann, P. Hydroxyl Groups as IR Active Surface Probes on MgO Crystallites. *Surf. Sci.* **1993**, *290*, 388−402.
(22) Chizallet, C.; Costentin, G.; Che, M.; Delbecq, F.; Sautet, P. Infrared Characterization of Hydroxyl Groups on MgO: A Periodic and Cluster Density Functional Theory Study. *J. Am. Chem. Soc.* **2007**, *129*, 6442−6452.
(23) Koziej, D.; Bârsan, N.; Hoffmann, V.; Szuber, J.; Weimar, U. Complementary Phenomenological and Spectroscopic Studies of Propane Sensing with Tin Dioxide Based Sensors. *Sens. Actuators, B* **2005**, *108*, 75−83.
(24) Tsyganenko, A. A.; Filimonov, V. N. Infrared Spectra of Surface Hydroxyl Groups and Crystalline Structure of Oxides. *J. Mol. Struct.* **1973**, *19*, 579−589.
(25) Jerdev, D. I.; Koel, B. E. Oxidation of Ordered Pt-Sn Surface Alloys by O_2. *Surf. Sci.* **2001**, *492*, 106−114.
(26) Sinner-Hettenbach, M.; Göthelid, M.; Weissenrieder, J.; von Schenck, H.; Weiß, T.; Barsan, N.; Weimar, U. Oxygen-Deficient SnO_2 (110): A STM, LEED and XPS Study. *Surf. Sci.* **2001**, *477*, 50−58.
(27) Koziej, D.; Thomas, K.; Barsan, N.; Thibault-Starzyk, F.; Weimar, U. Influence of Annealing Temperature on the CO Sensing Mechanism for Tin Dioxide Based Sensors-Operando Studies. *Catal. Today* **2007**, *126*, 211−218.
(28) Heinrich, V. E.; Cox, P. A. *The Surface Science of Metal Oxides*; 1 st ed.; Cambridge University Press: Cambridge, 1994.
(29) Kohl, D. Surface Processes in the Detection of Reducing Gases with SnO2-Based Devices. *Sens. Actuators* **1989**, *18*, 71−113.
(30) Morrison, S. R. Selectivity in Semiconductor Gas Sensors. *Sens. Actuators* **1987**, *12*, 425−440.
(31) Yamazoe, N.; Suematsu, K.; Shimanoe, K. Two Types of Moisture Effects on the Receptor Function of Neat Tin Oxide Gas Sensor to Oxygen. *Sens. Actuators, B* **2013**, *176*, 443−452.
(32) Elger, A. K.; Hess, C. Elucidating the Mechanism of Working SnO_2 Gas Sensors Using Combined Operando UV/Vis, Raman, and IR Spectroscopy. *Angew. Chem., Int. Ed.* **2019**, *58*, 15057−15061.
(33) Degler, D.; Wicker, S.; Weimar, U.; Barsan, N. Identifying the Active Oxygen Species in SnO_2 Based Gas Sensing Materials: An Operando IR Spectrsocopy Study. *J. Phys. Chem. C* **2015**, *119*, 11792−11799.
(34) Amalric-Popescu, D.; Bozon-Verduraz, F. Infrared Studies on SnO_2 and Pd/SnO_2. *Catal. Today* **2001**, *70*, 139−154.
(35) Harbeck, S.; Szatvanyi, A.; Barsan, N.; Weimar, U.; Hoffmann, V. DRIFT Studies of Thick Film Un-Doped and Pd-Doped SnO_2 Sensors: Temperature Changes Effect and CO Detection Mechanism in the Presence of Water Vapour. *Thin Solid Films* **2003**, *436*, 76−83.
(36) Santarossa, G.; Hahn, K.; Baiker, A. Free Energy and Electronic Properties of Water Adsorption on the SnO_2(110) Surface. *Langmuir* **2013**, *29*, 5487−5499.

https://dx.doi.org/10.1021/acssensors.0c01493
ACS Sens. 2020, 5, 3207−3216

Supporting Information: Investigations on the temperature dependent interaction of water vapor with tin dioxide and its implications on gas sensing

David Degler[1,*], Benjamin Junker[2], Frank Allmendinger[1], Udo Weimar[2] and Nicolae Barsan[2]

[1] Faculty of Industrial Technologies, Furtwangen University, D-78532 Tuttlingen, Germany

[2] Institute of Physical and Theoretical Chemistry and Centre for Light-Matter Interaction, Sensors & Analytics (LISA+), University of Tübingen, D-72076 Tübingen, Germany

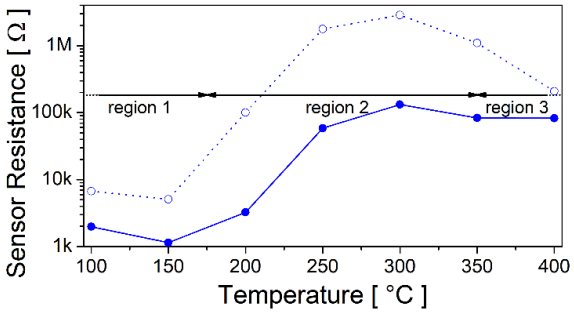

Figure S1. Sensor resistance in low humidity (< 10 ppm H2O) and humid air (10 %RH).

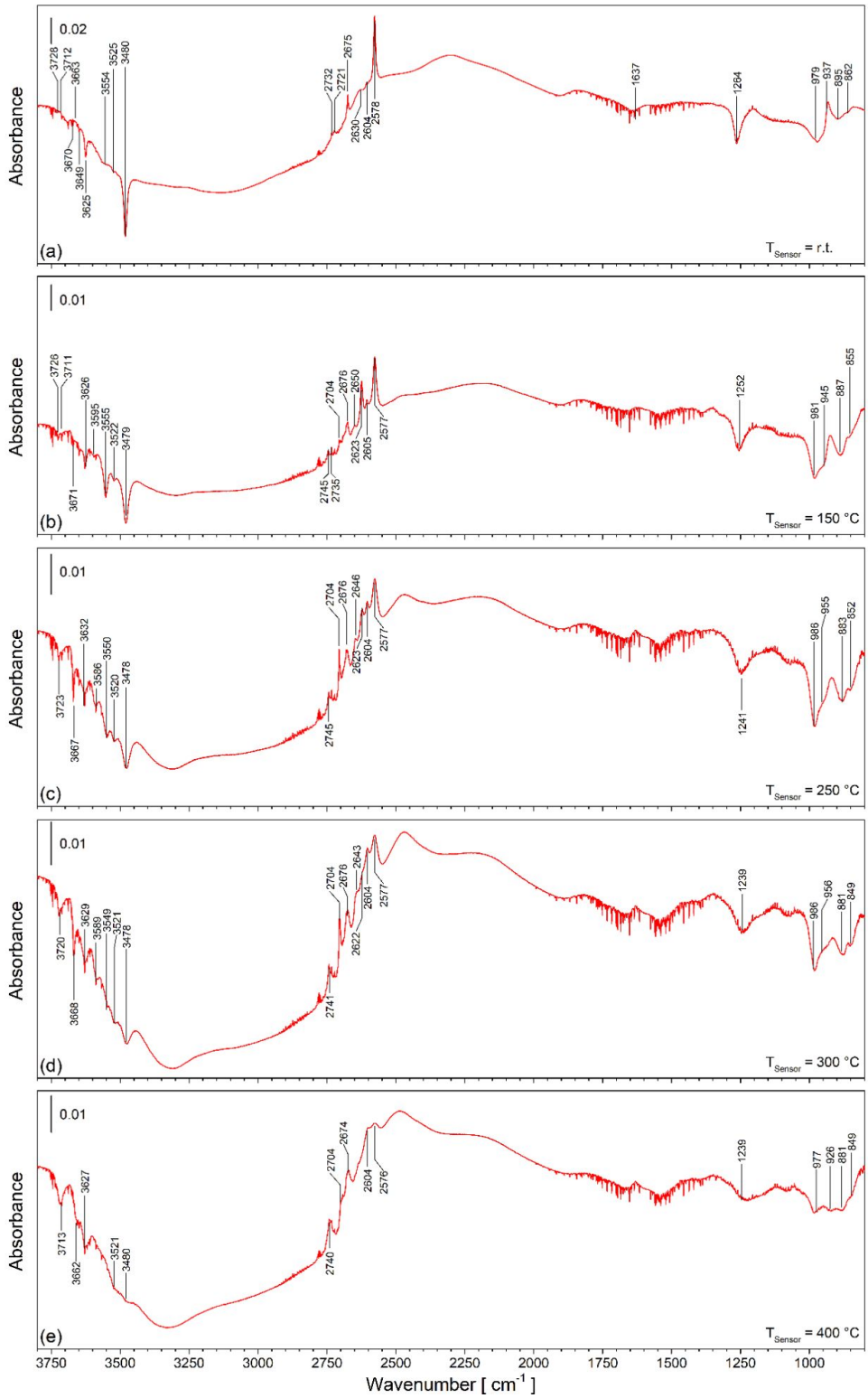

Figure S2. H_2O-D_2O steady change exchange spectra calculated from the H_2O and D_2O spectra shown in Figure 4 at room temperature (a), 150 °C (b), 250 °C (c), 300 °C (d) and 400 °C (e). These spectra provide a better overview of water-related species found on the SnO_2 surface during water exposure.

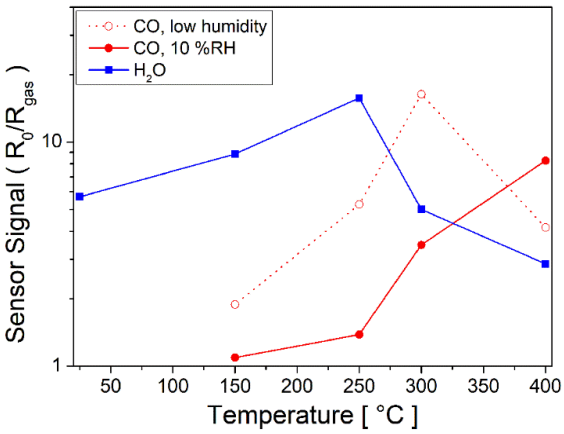

Figure S3. Sensor signals calculated from the resistance measurements during operando DRIFTS spectroscopy (Figure 4) for H_2O (blue), as well as for CO (red, empty symbols) in low humidty (< 10 ppm H_2O) and humid air (red, filled symbols).

IOP Publishing Journal Title
Journal **XX** (XXXX) XXXXXX https://doi.org/XXXX/XXXX

NAP-XPS as a new tool for in-situ studies of SMOX gas sensors

Benjamin Junker[1], Marco Favaro[2], David E. Starr[2], Michael Hävecker[3,4], Udo Weimar[1], Nicolae Barsan[1]

[1] Institute of Physical and Theoretical Chemistry (IPTC) and Center for Light-Matter Interaction, Sensors & Analytics (LISA+), University of Tuebingen, Auf der Morgenstelle 15, D-72076 Tuebingen, Germany
[2] Helmholtz-Zentrum Berlin für Materialien und Energie, Hahn-Meitner-Platz 1, D-14109 Berlin, Germany
[3] Max-Planck-Institut für Chemische Energiekonversion (MPI-CEC), Stiftstrasse 34-36, D-45470 Mülheim a.d. Ruhr, Germany
[4] Fritz-Haber-Institut der Max-Planck-Gesellschaft, Faradayweg 4-6, D-14195 Berlin, Germany

E-mail: nb@ipc.uni-tuebingen.de

Received xxxxxx
Accepted for publication xxxxxx
Published xxxxxx

Abstract

The development of near ambient pressure photoelectron spectroscopy (NAP-XPS) allows scientists to perform spectroscopic investigations of solid-gas interfaces at elevated pressures in a defined gas atmosphere. Due to the high surface sensitivity and element specificity, this technique promises to be a valuable and powerful tool in gas sensor research. A Pt doped SnO_2 sample was studied to explore a variety of phenomena in sensor research that can be addressed using NAP-XPS at a synchrotron. The change of several parameters, including chemical shifts, band bending, and valence band structure, could be oberserved in-situ and highlights the enormous potential of the method in this field. Furthermore, a series of DC resistance measurements has been performed to study the impact of pressure. The decrease of resistance at low pressure strongly indicates that both the electronic characteristics as well as the surface composition under the conditions of NAP-XPS are dissimilar to operando conditions at atmospheric pressure.

Keywords: NAP-XPS, gas sensor, operando spectroscopy, SnO_2, pressure gap

Introduction

Gas sensors are widely used for the detection of harmful, toxic or flammable gases in industrial and domestic applications. Since the first studies of Heiland et al. [1] and the successful development of a gas alarm as a consumer product by Taguchi [2], semiconducting metal oxides (SMOX) have garnered much interest for industrial use and research [3]–[5]. Although research has been conducted on a broad variety of materials such as SnO_2, ZnO, WO_3 etc., the detailed reaction mechanisms on most material – target gas combinations remain unclear. Such information is needed for the further development of this important technology.

A major drawback of using pure SMOX materials is their lack of selectivity. To overcome this problem SMOX-based sensor material is often modified with noble metal additives [6]–[8]. This can either be accomplished by doping where the additive is incorporated into the host SMOX lattice or by surface loading. Different synthesis routes can produce

different concentrations and distributions of the noble metal and which can lead to a broad range of sensing performance and different reaction mechanisms [9]–[11]

Fundamental studies that allow for sensor interrogation under operating conditions, as in the intended future application environment, and correlation with electrical measurements promise to be very illuminating with respect to the surface chemistry and active sites on the sensor material. Since these measurements are correlated with the electrical performance they provide a direct link to the application of the device despite being fundamental in nature. [4], [12], [13].

To understand the influence of the noble metal additive it is useful to study the additive independently of the base material. While established research methods such as DC resistance, AC impedance spectroscopy [14] or UV-vis spectroscopy [11], [15] are not capable of such differentiation, IR and Raman spectroscopies, in principle, can distinguish specific vibrational bands of the additive and the base material [16]. However, the low concentration of additives, as well as the need for spectroscopically detectable groups such as carbonyls, limit the extraction of relevant information. To overcome these limitations, element specific x-ray spectroscopies can be applied. The use of x-ray absorption near edge structure (XANES or NEXAFS) or extended x-ray absorption fine structure (EXAFS), is prevalent in gas sensor research to determine not only the oxidation state of single elements but also their local bonding, phase, and lattice parameters [10], [17], [18]. The drawback of such photon-in/photon-out methods is their lack of surface sensitivity. Depending on the photon energy and the detection mode, not only the bulk of the material in the sensitive layer but the whole sample including electrodes, substrates and attached electronic structures is probed.

XPS is a chemically precise, highly surface sensitive technique due to the short mean free paths of the photo-emitted electrons in solid materials. Despite the usefulness of XPS measurements in UHV for determining the chemical composition of deposited layers in sensor devices, UHV studies may not capture changes in surface chemical composition in the presence of an analyte gas. Such information is, however, vital for understanding how a sensor device functions. Near ambient pressure x-ray photoelectron spectroscopy (NAP-XPS), allows in-situ studies at total pressures of 1 mbar or above in specialized systems[19]. The unique combination of surface sensitivity, element specificity and elevated pressure operation makes NAP-XPS ideal for in-situ investigation of the chemical composition and mechanisms of surface processes central to the operation of a gas sensing device. [20]–[22].

We have conducted a combined NAP-XPS and DC resistance measurement study on a well-investigated and yet challenging Pt doped SnO_2 material. This system was chosen to be able to link the obtained results with published data and to further assess the future role of NAP-XPS experiments in sensor research [10], [17], [23]. The low concentration of 0.7 wt.-% Pt provides insight into the performance of the NAP-XPS method with an application relevant concentration of additives. In this case the platinum dopant is dispersed in the bulk of the material. Surface loaded samples with the same amount of additive would yield much higher signal intensities. Therefore, this challenging sample can be used as a benchmark for the application of NAP-XPS in sensor research. We expect that if measurements are successful on this sample that the majority of other gas sensor materials are able to be studied with NAP-XPS as well. Due to peak overlaps some material combinations will however be harder to investigate [16]

DC resistance measurements have been performed at various pressures to extrapolate the spectroscopic data to application relevant conditions. Combined with widely accepted theoretical models for conduction mechanisms in SMOX based gas sensors, the resistance changes are sufficient to evaluate the conditions in which the gas sensor is operating [24], [25].

Experimental

The tin dioxide raw material was synthesized as described in [26] by adding an aqueous ammonia solution to $SnCl_4$. Pt doping was achieved by adding $PtCl_4$ (0.7 wt.-% Pt with respect to SnO_2). The precipitate was washed using distilled water and calcined for 8 h at 1000 °C. The obtained powders were screen printed onto stainless steel plates using 1,2-propanediol and calcined at 500 °C. For DC resistance measurements, alumina substrates with interdigitated electrodes and platinum backside heaters as described in [14] were used instead of stainless steel plates.

Photoelectron spectroscopy (including NAP-XPS) was performed at beamline UE56-2/PGM1 [27] of the BElChem facility (Berlin Joint Lab for Electrochemical Interfaces) at the BESSY II synchrotron of Helmholtz Zentrum Berlin with the NAP-XPS end-station of the Fritz-Haber-Insitute. The end-station is equipped with a homebuilt differentially pumped analyzer (modified Specs Phoibos 150), for details see [28], [29] and references therein. The sample was heated using an NIR laser (LIMO GmbH). The photon energy of the horizontally polarized x-rays was set to 730 eV for O 1s, 685 eV for Sn 3d, 270 eV for Pt 4f, and 210 eV for the valence band spectra. The resulting kinetic energy of ~ 200 eV for all core-level and valence band spectra ensures comparable surface sensitivities with favorable photoionization cross sections. All spectra were recorded with an electron energy analyzer pass energy set to 20 eV, a dwell time of 0.2 s, and a step size of 0.05 eV. The beamline has been operated with its 1200 mm^{-1} grating and 180 µm exit slit. The energy

resolution of x-rays and analyzer combined is 260 to 460 meV, depending on the actual photon energy. For all experiments using a defined gas atmosphere, gases (Westfalen AG) with a purity of 5.0 or higher were used and fed into the NAP-XPS analysis chamber after passing through a gas mixing system. NAP-XPS was performed at a sample temperature of 300 °C, 1 mbar total gas pressure, in mixed gas atmospheres consisting of 80 vol.-% N_2 and 20 vol-% other gases (in the following discussion we will refer to these gas mixtures as e.g. "N_2 + He"). Before the NAP-XPS experiments, spectra were recorded in UHV ($p < 10^{-8}$ mbar) at room temperature in the same setup. Unless stated otherwise, signals from gas phase molecules have been suppressed by applying an anodic bias voltage of 90 V to the electrically isolated entrance aperture of the analyzer. After each adjustment of the monochromator the binding energy scale has been calibrated using the Au $4f_{7/2}$ peak of a gold foil (84.00 eV) that shares a common ground with the electron energy analyzer. Voigt profiles were used to fit XPS peaks. Data processing was done in Unifit2017.

For DC resistance measurements, the sample was mounted inside a stainless steel vacuum setup equipped with a gas mixing system similar to the one used in NAP-XPS. The resistance of the gas sensing layer was recorded using a Keithley 199 multimeter. The temperature of the sensor was calibrated against the resistance of the backside heater using an infrared pyrometer and a thermocouple. Gas composition and pressure were controlled with a gas mixing system and vacuum system comparable to the one used for the NAP-XPS experiment.

Results and discussion

Chemical composition and chemical shift

The surface stoichiometry of the pristine Pt-doped SnO_2 sensor was initially assessed acquiring a survey spectrum in UHV conditions at a photon energy of 840 eV (Figure S1). The survey spectrum shows the presence of Sn, O, Pt and C as contamination. Due to the low concentration the Pt 4f signal is extremely weak. During the exposure to CO a transport of Ni from stainless steel parts to the sample via carbonyls is possible, but no Ni was found in the analysis after the NAP-XPS experiments. In Figure 1 a-d Sn $3d_{5/2}$ spectra recorded in UHV as well as in different gas atmospheres are shown. The BE values of the single component between 486.6 and 486.8 eV indicate the presence of SnO_2 in all gas atmospheres. Fitting the spectra with two peaks or more was possible, however the components' distance was not in line with literature reports on Sn or SnO [30]–[32].

These results are supported by the O 1s spectra, given in Figure 1 e-h, which also show only one major component, assigned to O bound to Sn^{4+}. Several small components at higher binding energies can be assigned to surface adsorbates such as hydroxyl groups, oxygen ions or water [31], [33], [34].

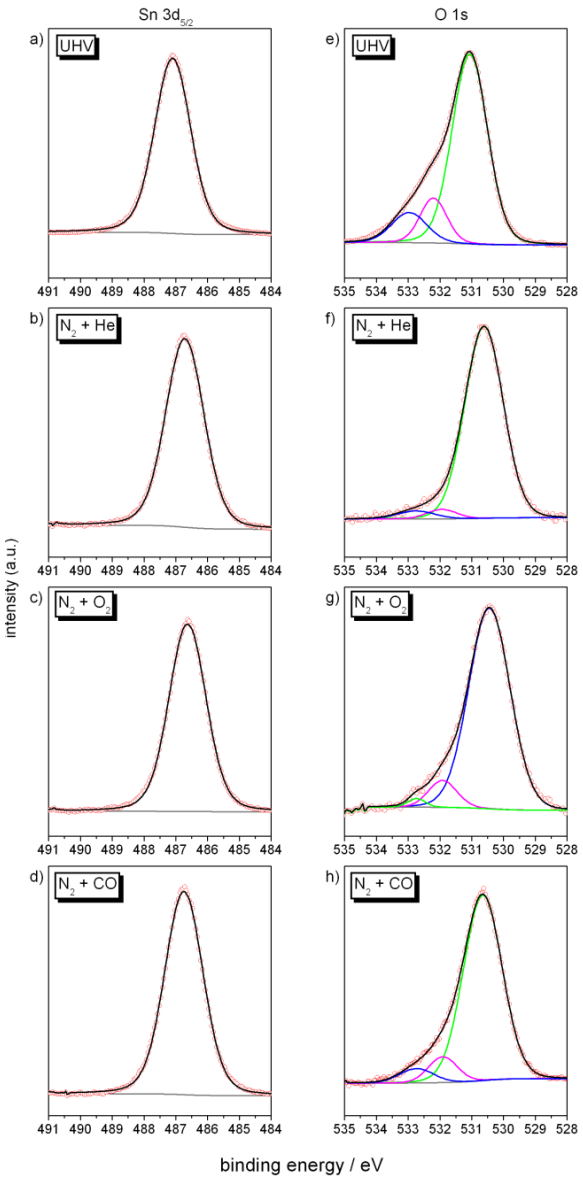

Figure 1: NAP-XPS spectra of the Sn $3d_{5/2}$ and O 1s and regions taken in UHV at room temperature (panels a and e) and in different atmospheres at 300 °C. For each spectrum the experimental data (circles) are fitted using a combined polynomial and Shirley type background and Voigt profiles (lines). Sn $3d_{5/2}$ spectra (a-d) were fitted with one component only. For O 1s (e-h) three components were used.

The binding energies of Sn $3d_{5/2}$ and O 1s main component are plotted in Figure 2. The binding energies of the two peaks are correlated. If charging was the cause of

these peak shifts, one would expect asymmetric and broadened core level peaks, which is not the case here. On top of that, charging of the sample is less likely to be observed in NAP-XPS, where gas molecules ionized close to the surface provide a source of electrons. Moreover, based on the experimentally determined conductivity of the sample, a higher possibility of charging is expected for the spectra in N_2 + O_2 gas atmosphere, yet, the binding energies in this condition are the lowest.

A shift of the Fermi level originating from the bulk, e.g. due to creation or annihilation of additional band gap states, has not been reported in literature and is likely to not be the source of the observed BE shifts [35]. Based on these observations we conclude that the correlated peak shifts are a result of surface band bending. With the assumption that the same depth is probed for both elements, we expect their binding energies to shift at the same value. The linear function shown in Figure 2 has a slope of 1 and an offset of 43.88 which is the mean of the differences in binding energy of O 1s and Sn $3d_{5/2}$ in each condition. For each point this graph lies within the error bars, given by the spectral resolution of the setup.

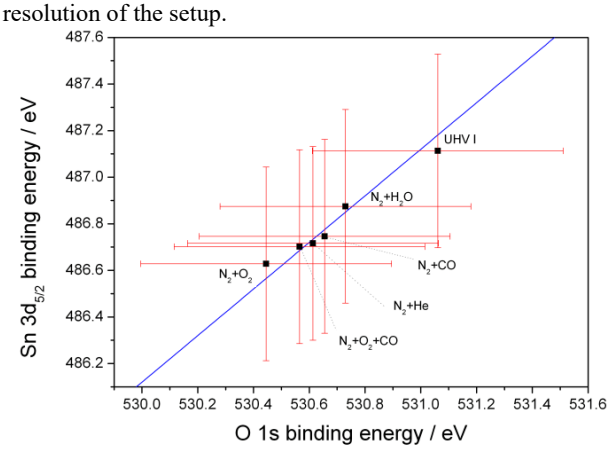

Figure 2: Binding energies of Sn $3d_{5/2}$ and O 1s in different atmospheres measured in-situ as well as spectra in UHV before the NAP-XPS experiments. The error bars are based on the spectral resolution of the setup. In blue the linear function y =x - 43.88 illustrates the expected binding energy shifts.

Noble metal characterization

The main focus of this study was put to the characterization of the platinum dopant. For Pt 4f, the adjacent Sn 4p peak as well as different backgrounds and the overall low signal intensity complicate the analysis of the spectra in this binding energy region. Still, an attempt was made to fit the spectra. While accuracy of the quantification is low, it can certainly be used to support the qualitative discussion in the following section. A fit of the spectrum in UHV taken at room temperature, given in Figure 3a, was possible using three components. It shows dominant contributions of metallic Pt^0 but also Pt^{2+} and Pt^{4+} can be identified. The binding energies and areas are summarized in Table 1. This spectrum reflects the condition of the sample after it was annealed in ambient air, making the coexistence of multiple oxidation states plausible. In contrast to Sn, the oxidation state of Pt depends on the surrounding gas atmosphere, as the spectra recorded at 300 °C in different atmospheres reveal.

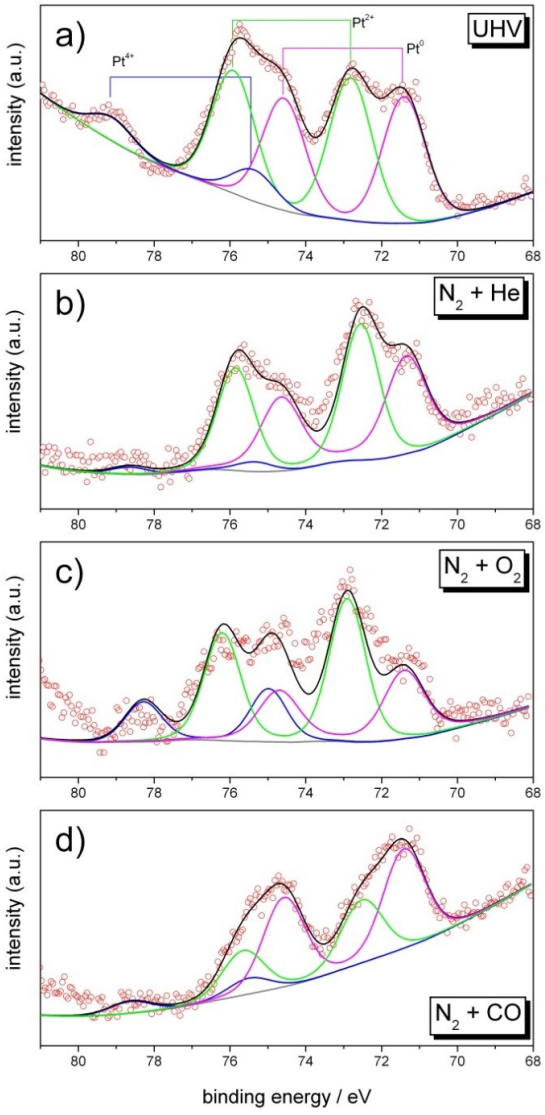

Figure 3: NAP-XPS spectra of the Pt 4f region taken at a photon energy of 270 eV in UHV at room temperature as well as in different gas atmospheres at 1 mbar at 300 °C. The experimental data (circles) are fitted using a combined polynomial and Shirley

type background and a three component fit. The areas of the components are given in Table 1

The situation in 80% N_2 + 20% He at 300°C (Figure 3b) shows a decrease of the Pt^{4+} component revealing a partial reduction of platinum, solely by heating the sample in an inert low-pressure atmosphere. In N_2+O_2 (Figure 3c), however, the intensity of the Pt^{2+} component is considerably higher than the one of the metallic component. Additionally, the intensity of Pt^{4+} is increased. In contrast, when introducing the reducing CO, the Pt^{4+} component drastically decreases and the metallic Pt becomes dominant (Figure 3d). The results indicate that the reaction of reducing gases affects the Pt oxidation state whereas the oxidation state of Sn is not influenced by the gas atmosphere. Further studies, including different concentrations of reducing gases and longer equilibration times may allow further insights into the interplay of additive and base material.

Table 1: Binding energies and relative area (Pt 4f doublet) of the peaks used in the fits shown in Figure 3. The binding energies are given for the UHV spectrum and may vary for the NAP-XPS spectra.

Component	BE in eV		Peak area in %			
	Pt $4f_{7/2}$	Pt $4f_{5/2}$	UHV	N_2+He	N_2+O_2	N_2+CO
Pt^0	*71.4*	*74.6*	*43*	*44*	*29*	*58*
Pt^{2+}	*72.8*	*75.9*	*47*	*52*	*52*	*33*
Pt^{4+}	*75.4*	*79.1*	*10*	*4*	*19*	*9*

The interaction of the noble metal additive may often be sufficiently described by two well-established mechanisms, namely the spillover and the Fermi-level control mechanisms [9], [36]. In the former, the target gas reacts on the additive and the reaction products spill over onto the SMOX where the actual reception reaction takes place. The oxidation state of the additive remains unchanged and the SMOX is reduced. For the Fermi level control mechanism, the chemistry completely takes place on the additive, changing its oxidation state. Because the additive and the SMOX are electronically coupled, the Fermi level of the supporting metal oxide is pinned by the Fermi level of the additive. The behavior of the sample in this study indicates that the active mechanism is the Fermi level control mechanism. The information depth (3λ) can be estimated around 1.9 nm using the TPP-2M formula [37]. Even though the determination of the Debye length of this specific material was not possible in previous experiments, a comparison with similar materials suggests that the volume of the origin of photoelectrons is significantly influenced by band bending [26]. While oxygen causes an increase in band bending and, thus, lowers the core level binding energies, reducing gases (CO, H_2O) decrease the band bending. These expectations are in line with the observed binding energy shifts [24], [25]. The spectrum recorded in UHV follows the same trend and was included in the fit.

Valence Band structure

A detailed analysis of the valence band structure has been performed. Unlike laboratory-based systems equipped with x-ray tubes and gas discharge lamps, the photon energy of 210 eV provides a probed depth comparable

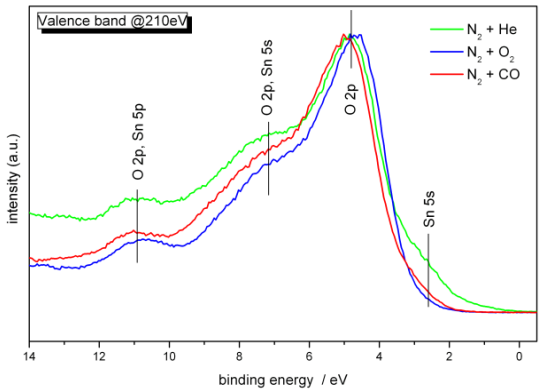

Figure 4: Spectra of the valence band region in different atmospheres at 300 °C. Gas phase peaks are suppressed by application of an anodic bias to the analyzer nozzle. The intensities have been normalized.

to that of the core level spectra presented above. The valence band spectra are presented in Figure 4. The main features could be attributed to O 2p, Sn 5p, and Sn 5s and their hybridized states [30], [33], [38]–[40]. The feature located around 3 eV is attributed to Sn 5s orbitals. The valence band is more sensitive to minor changes of the oxidation state of Sn that are not visible in the core level spectra [40]. However the situation is complicated by the fact that electronic states derived from C 2s and C 2p are expected in the same binding energy region [41], [42]. Especially in N_2 + He the amount of adventitious carbon on the sample is higher than after the treatment with N_2 + O_2, where no intensity is seen below 3 eV. The shift of the valence band maximum is in line with the shift in binding energy for Sn 3d and O1s core levels as discussed in the previous section.

In addition to the data presented, other well established methods in XPS can be applied to gas sensors, e.g. using different photon energies for different surface sensitivities, measuring at different sample angles or use a different polarization of the radiation. The determination of work function changes using gas phase peak shifts is another option in NAP-XPS [43], however it requires to have a clean surface for reliable results.

Differences compared to operando techniques

In order to investigate the effect of the pressure gap on the sensor's performance, DC resistance measurements were

performed at various pressures. Figure 5a shows the resistance of a sensor operated at 300 °C in dry air at various pressures. Additionally, the sensor has been exposed to pulses of 100 ppm and 200 ppm CO. As expected for an n-type SMOX based gas sensor, the resistance decreases during exposure to CO. The resistance in dry air (20.5 vol.-% O_2 in N_2) decreases with pressure.

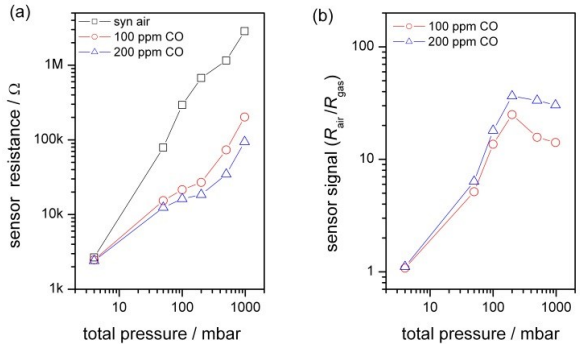

Figure 5: (a) Resistance of sensor sample at different pressures in pure dry air as well as with the addition of 100 and 200 ppm CO, respectively. (b) Sensor signals for CO exposure.

The gas phase oxygen is in equilibrium with oxygen adsorbed at the surface, which results in the localization of charge carriers and, thus, lower conductivity [25]. Decreasing the partial pressure of oxygen lowers the surface coverage and increases the conductivity. With the objective to mimic conditions similar to operando investigations, a reasonable approach might be to decrease the total pressure of the atmosphere while keeping the partial pressure of the reactive gases, i.e. oxygen, constant. Experimentally the sensor's resistances in nitrogen and dry air at atmospheric pressure and in pure O_2 at 200 mbar were compared (see Figure S2 in the supporting information). The resistance in the latter condition is lower by a factor of 2.3 and it can be concluded that the total pressure itself has a significant influence on the sensor performance. Further evidence is given by the comparison of the sensor resistance in pure nitrogen at atmospheric pressure and at 1 mbar, where it is lower by a factor of 8.3. These findings indicate that desorption of oxygen and the reduction of the sensing layer can be triggered by lowering the pressure as well as the partial pressure of oxygen.

The interplay of CO with the sensor surface follows an even more complicated model, since the reaction requires chemisorbed oxygen in order to form CO_2 [25]:

$$CO + O_S^{2-} \rightarrow CO_2 + 2e^- + S$$

The response towards CO can be described best by the sensor signal $S = \frac{R_{air}}{R_{CO}}$ which is defined as the resistance in dry air divided by the resistance during CO exposure. Above 100 mbar the signal is not much influenced by the pressure, but drastically decreases at lower pressures to finally approach a value of 1 at around 4 mbar, as illustrated in Figure 5b. To observe a response at pressures as low as in the NAP-XPS setup, much higher concentrations in the range of a few percent are required. Several reasons can be considered for this effect: First of all, the partial pressure of CO is lower at low pressure. Secondly, the coverage of the surface with oxygen as reaction partner is lower. And, finally, as a consequence of this there is a change in the conduction model. For SnO_2 gas sensors operated in air at atmospheric pressure each grain is expected to have an electron depletion layer at its surface. In nitrogen one can expect a flat band situation, unless doping or defects cause an initial band bending [24]. The decrease in resistance is caused by downwards band bending, that results in an accumulation layer controlled conduction mechanism. In the latter, the effect of additional electrons released by the reaction with CO will have a smaller effect on the conductivity (square root only) compared to a depletion layer mechanism controlled situation. These findings point out that pressure is an important factor for SMOX gas sensors and the pressure gap between NAP-XPS and operando conditions has to be taken into account.

Conclusions

In this study a selection of different tools and methods available in NAP-XPS, including analysis of elemental composition, chemical shift of single elements, band bending, and valence band spectroscopy, were used to gain insights into the sensing mechanism of a Pt-doped SnO_2 gas sensor. Even though it is possible to expose a SMOX gas sensor to certain gases, quench its chemical state by cooling it and then record photoelectron spectra in UHV, it cannot be ensured that during the quenching process the sample will not change again. Moreover, during the transfer into the spectrometer, carbon will be deposited at the surface and investigations that are sensitive to carbon contamination, e.g. valence band spectroscopy or work function changes won't be comparable between different samples. When operating the sensor at elevated temperatures in the presence of oxygen, carbon can be effectively removed from the surface by burning it. Such a cleaning procedure is expected to be helpful at the beginning of NAP-XPS experiments. By performing x-ray spectroscopy at the operating temperature in a defined gas atmosphere it was possible to observe changes in the oxidation state of platinum in-situ. A major drawback of the method is that, with the exception of a few specialized setups, it is not possible to perform these experiments at ambient pressure, i.e. truly in-operando [44], [45]. The DC resistance experiments performed over a wide range of pressure revealed, that the conductivity is very different between ambient pressure and the so called near-ambient pressure conditions. The electronic structure, surface

coverage and thus the reactivity are therefore also dissimilar. This effect of the pressure gap is expected for other materials as well. The power of NAP-XPS for gas sensor research lies in the possibility to study a gas sensor's behavior in-situ and to cautiously transfer the gained knowledge to observations made in real operando conditions. A simple, but very powerful tool for this transfer is to do simultaneous resistance measurements during NAP-XPS. While the setup used in this study didn't allow simultaneous resistance measurements, such experiments have been successfully performed in other setups [21], [46]. The progress in the development of spectrometers allows investigations at pressures at 1 bar and above using tender x-rays [44], [45]. These setups are very promising for gas sensor research. By eliminating the pressure gap, they in fact enable real *operando* investigations in the typical working conditions of SMOX materials.

Acknowledgements

We thankfully acknowledge the Berlin Joint Laboratory for Electrochemical Interfaces (BElChem), established between the Helmholtz-Zentrum Berlin (HZB) and the Fritz-Haber-Institut der Max-Planck-Gesellschaft (FHI-MPG), for the beamtime availability during the commissioning phase of the soft X-ray BElChem endstation (operating at the UE56-2/PGM1 beamline of the BESSY II synchrotron facility). BElChem is supported by the Helmholtz Association through the Helmholtz Energy Materials Foundry (HEMF, GZ 714-48172-21/1).

References

[1] G. Heiland, "Zum Einfluß von Wasserstoff auf die elektrische Leitfähigkeit an der Oberfläche von Zinkoxydkristallen," *Zeitschrift für Phys.*, vol. 148, no. 1, pp. 15–27, 1957.

[2] N. Taguchi, "Jpn. Patent 45-38200," S45-39200, 1962.

[3] N. Yamazoe, G. Sakai, and K. Shimanoe, "Oxide semiconductor gas sensors," *Catal. Surv. from Asia*, vol. 7, no. 1, pp. 63–75, 2003.

[4] N. Barsan, D. Koziej, and U. Weimar, "Metal oxide-based gas sensor research: How to?," *Sensors Actuators, B Chem.*, vol. 121, no. 1, pp. 18–35, 2007.

[5] S. R. Morrison, "Selectivity in semiconductor gas sensors," *Sensors and Actuators*, vol. 12, no. 4, pp. 425–440, 1987.

[6] A. Salehi, "Selectivity enhancement of indium-doped SnO2 gas sensors," *Thin Solid Films*, vol. 416, no. 1–2, pp. 260–263, 2002.

[7] A. V. Marikutsa, M. N. Rumyantseva, L. V. Yashina, and A. M. Gaskov, "Role of surface hydroxyl groups in promoting room temperature CO sensing by Pd-modified nanocrystalline SnO2," *J. Solid State Chem.*, vol. 183, no. 10, pp. 2389–2399, 2010.

[8] N. Yamazoe, Y. Kurokawa, and T. Seiyama, "Effects of additives on semiconductor gas sensors," *Sensors and Actuators*, vol. 4, no. C, pp. 283–289, 1983.

[9] D. Degler, U. Weimar, and N. Barsan, "Current Understanding of the Fundamental Mechanisms of Doped and Loaded Semiconducting Metal-Oxide-Based Gas Sensing Materials," *ACS Sensors*, vol. 4, pp. 2228–2249, 2019.

[10] M. Hübner *et al.*, "The Structure and Behavior of Platinum in SnO2-Based Sensors under Working Conditions," *Angew. Chemie Int. Ed.*, vol. 50, no. 12, pp. 2841–2844, Mar. 2011.

[11] L. K. Bagal, J. Y. Patil, I. S. Mulla, and S. S. Suryavanshi, "Influence of Pd-loading on gas sensing characteristics of SnO 2 thick films," *Ceram. Int.*, vol. 38, no. 6, pp. 4835–4844, 2012.

[12] M. A. Bañares, "Operando methodology: combination of in situ spectroscopy and simultaneous activity measurements under catalytic reaction conditions," *Catal. Today*, vol. 100, no. 1–2, pp. 71–77, Feb. 2005.

[13] A. Gurlo and R. Riedel, "In-situ- und Operando-Spektroskopie zur Untersuchung von Mechanismen der Gaserkennung," *Angew. Chemie*, vol. 119, no. 21, pp. 3900–3923, 2007.

[14] N. Bârsan and U. Weimar, "Understanding the fundamental principles of metal oxide based gas sensors; the example of CO sensing with SnO2 sensors in the presence of humidity," *J. Phys. Condens. Matter*, vol. 15, no. 20, pp. 813–839, 2003.

[15] D. Degler *et al.*, "Extending the toolbox for gas sensor research: Operando UV/vis diffuse reflectance spectroscopy on SnO2-based gas sensors," *Sensors Actuators, B Chem.*, vol. 224, pp. 256–259, 2016.

[16] A. Staerz *et al.*, "Direct Microscopic Proof of the Fermi Level Pinning Gas-Sensing Mechanism: The Case of Platinum-Loaded WO3," *J. Phys. Chem. Lett.*, vol. 11, no. 1, pp. 166–171, 2020.

[17] D. Degler, H. W. Pereira De Carvalho, K. Kvashnina, J. D. Grunwaldt, U. Weimar, and N. Barsan, "Structure and chemistry of surface-doped Pt:SnO2 gas sensing materials," *RSC Adv.*, vol. 6, no. 34, pp. 28149–28155, 2016.

[18] L. Mädler *et al.*, "Sensing low concentrations of CO using flame-spray-made Pt/SnO2 nanoparticles," *J. Nanoparticle Res.*, vol. 8, no. 6, pp. 783–796, 2006.

[19] D. E. Starr, Z. Liu, M. Hävecker, A. Knop-Gericke, and H. Bluhm, "Investigation of solid/vapor interfaces using ambient pressure X-ray photoelectron spectroscopy," *Chem. Soc. Rev.*, vol. 42, no. 13, pp. 5833–5857, 2013.

[20] K. A. Stoerzinger *et al.*, "Influence of LaFeO3 Surface Termination on Water Reactivity," *J. Phys. Chem. Lett.*, vol. 8, no. 5, pp. 1038–1043, 2017.

[21] M. Vorokhta *et al.*, "Investigation of gas sensing mechanism of SnO2 based chemiresistor using near ambient pressure XPS," *Surf. Sci.*, vol. 677, pp. 284–290, 2018.

[22] P. Hozák *et al.*, "New Insight into the Gas-Sensing Properties of CuOx Nanowires by Near-Ambient Pressure XPS," *J. Phys. Chem. C*, vol. 123, no. 49, pp. 29739–29749, 2019.

[23] A. Cabot, J. Arbiol, J. R. Morante, U. Weimar, N. Barsan, and W. Göpel, "Analysis of the noble metal catalytic additives introduced by impregnation of as obtained SnO2 sol–gel nanocrystals for gas sensors," *Sensors Actuators B*

Chem., vol. 70, pp. 87–100, 2000.

[24] N. Bârsan, M. Hübner, and U. Weimar, "Conduction mechanisms in SnO2 based polycrystalline thick film gas sensors exposed to CO and H2 in different oxygen backgrounds," *Sensors Actuators, B Chem.*, vol. 157, no. 2, pp. 510–517, 2011.

[25] N. Barsan and U. Weimar, "Conduction Model of Metal Oxide Gas Sensors," *J. Electroceramics*, vol. 7, pp. 143–167, 2001.

[26] M. Hübner, N. Bârsan, and U. Weimar, "Influences of Al, Pd and Pt additives on the conduction mechanism as well as the surface and bulk properties of SnO 2 based polycrystalline thick film gas sensors," *Sensors Actuators, B Chem.*, vol. 171–172, pp. 172–180, 2012.

[27] K. J. S. Sawhney *et al.*, "A novel undulator-based PGM beamline for circularly polarised synchrotron radiation at BESSY II," *Nucl. Instruments Methods Phys. Res. Sect. A Accel. Spectrometers, Detect. Assoc. Equip.*, vol. 390, no. 3, pp. 395–402, 1997.

[28] A. Nenning *et al.*, "Ambient pressure XPS study of mixed conducting perovskite-type SOFC cathode and anode materials under well-defined electrochemical polarization," *J. Phys. Chem. C*, vol. 120, no. 3, pp. 1461–1471, 2016.

[29] J. J. Velasco-Vélez *et al.*, "Atmospheric pressure X-ray photoelectron spectroscopy apparatus: Bridging the pressure gap," *Rev. Sci. Instrum.*, vol. 87, no. 5, 2016.

[30] J. M. Themlin, M. Chtaïb, L. Henrard, P. Lambin, J. Darville, and J. M. Gilles, "Characterization of tin oxides by x-ray-photoemission spectroscopy," *Phys. Rev. B*, vol. 46, no. 4, pp. 2460–2466, 1992.

[31] J. Szuber, G. Czempik, R. Larciprete, D. Koziej, and B. Adamowicz, "XPS study of the L-CVD deposited SnO2 thin films exposed to oxygen and hydrogen," *Thin Solid Films*, vol. 391, no. 2, pp. 198–203, 2001.

[32] J. F. Moulder, W. F. Stickle, P. E. Sobol, and K. D. Bomben, *Handbook of X-ray photoelectron spectroscopy: A reference book of standard spectra for identification and interpretation of XPS data*, 4th ed. Eden Prairie: Perkin-Elmer Corporation, 1992.

[33] Y. Nagasawa *et al.*, "Photoemission study of the interaction of a reduced thin film SnO2 with oxygen," *Surf. Sci.*, vol. 433, pp. 226–229, 1999.

[34] S. Kačiulis, G. Mattogno, A. Galdikas, A. Mironas, and A. Šetkus, "Influence of surface oxygen on chemoresistance of tin oxide film," *J. Vac. Sci. Technol. A Vacuum, Surfaces, Film.*, vol. 14, no. 6, pp. 3164–3168, 2002.

[35] T. Sahm, A. Gurlo, N. Bârsan, and U. Weimar, "Basics of oxygen and SnO2 interaction; work function change and conductivity measurements," *Sensors Actuators, B Chem.*, vol. 118, no. 1–2, pp. 78–83, 2006.

[36] S. Matsushima, Y. Teraoka, N. Miura, and N. Yamazoe, "Electronic interaction between metal additives and tin dioxide in tin dioxide-based gas sensors," *Jpn. J. Appl. Phys.*, vol. 27, no. 10 R, pp. 1798–1802, 1988.

[37] S. Tanuma, C. J. Powell, and D. R. Penn, "Calculations of electron inelastic mean free paths. V. Data for 14 organic compounds over the 50–2000 eV range," *Surf. interface Anal.*, vol. 21, no. 3, pp. 165–176, 1994.

[38] J. M. Themlin, R. Sporken, J. Darville, R. Caudano, J. M. Gilles, and R. L. Johnson, "Resonant-photoemission study of SnO2: Cationic origin of the defect band-gap states," *Phys. Rev. B*, vol. 42, no. 18, pp. 11914–11925, 1990.

[39] M. Batzill and U. Diebold, "The surface and materials science of tin oxide," *Prog. Surf. Sci.*, vol. 79, no. 2–4, pp. 47–154, 2005.

[40] P. De Padova, M. Fanfoni, R. Larciprete, M. Mangiantini, S. Priori, and P. Perfetti, "A synchrotron radiation photoemission study of the oxidation of tin," *Surf. Sci.*, vol. 313, no. 3, pp. 379–391, 1994.

[41] A. Bianconi, S. B. M. Hagström, and R. Z. Bachrach, "Photoemission studies of graphite high-energy conduction-band and valence-band states using soft-x-ray synchrotron radiation excitation," *Phys. Rev. B*, vol. 16, no. 12, pp. 5543–5548, 1977.

[42] M. Favaro *et al.*, "A synchrotron-based spectroscopic study of the electronic structure of N-doped HOPG and PdY/N-doped HOPG," *Surf. Sci.*, vol. 646, pp. 132–139, 2016.

[43] S. Axnanda *et al.*, "Direct work function measurement by gas phase photoelectron spectroscopy and its application on PbS nanoparticles," *Nano Lett.*, vol. 13, no. 12, pp. 6176–6182, 2013.

[44] P. Amann *et al.*, "A high-pressure x-ray photoelectron spectroscopy instrument for studies of industrially relevant catalytic reactions at pressures of several bars," *Rev. Sci. Instrum.*, vol. 90, no. 10, 2019.

[45] Y. Takagi *et al.*, "X-ray photoelectron spectroscopy under real ambient pressure conditions," *Appl. Phys. Express*, vol. 10, no. 7, pp. 7–11, 2017.

[46] M. Amati *et al.*, "Near ambient pressure photoelectron spectro-microscopy: from gas–solid interface to operando devices," *J. Phys. D. Appl. Phys.*, vol. 54, no. 20, p. 204004, 2021.

NAP-XPS as a new tool for in-situ studies of SMOX gas sensors – Supporting Information

Benjamin Junker[1], Marco Favaro[2], David E. Starr[2], Michael Hävecker[3,4], Udo Weimar[1], Nicolae Barsan[1]

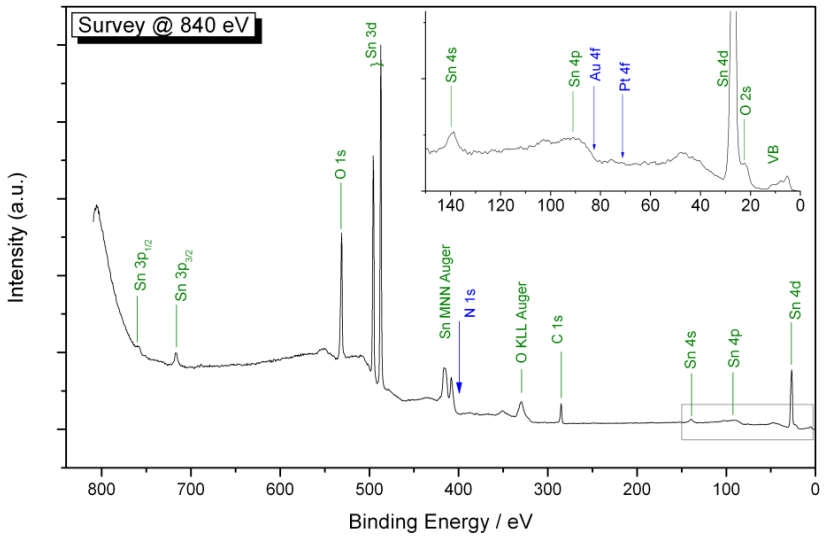

Figure S1: Survey spectrum of the sample in UHV at room temperature at the beginning of the experiments. The peaks of N 1s, Au 4f and Pt 4f orbitals are labelled for orientation only.

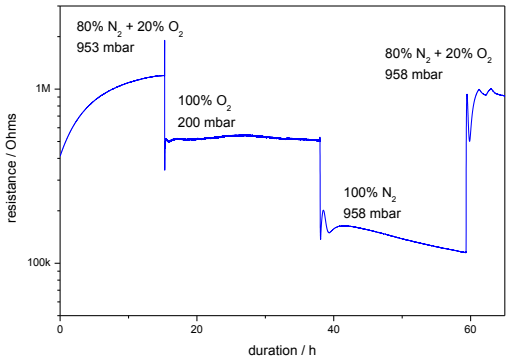

Figure S2: DC resistance measurement in different atmospheres at different pressures. The atmosphere composition and total pressure for each step are given in the graph. The temperature was kept at 300 °C.

sensors

MDPI

Article

The Role of Different Lanthanoid and Transition Metals in Perovskite Gas Sensors

Abdulaziz Alharbi [1,†], Benjamin Junker [2,3,†], Mohammad Alduraibi [4], Ahmad Algarni [1], Udo Weimar [2,3] and Nicolae Bârsan [2,3,*]

1 National Center for Nanotechnology and Semiconductors, King Abdulaziz City for Science and Technology (KACST), Riyadh 11421, Saudi Arabia; abharbi@kacst.edu.sa (A.A.); agarni@kacst.edu.sa (A.A.)
2 Institute of Physical and Theoretical Chemistry (IPTC), University of Tuebingen, Auf der Morgenstelle 15, D-72076 Tuebingen, Germany; benjamin.junker@ipc.uni-tuebingen.de (B.J.); upw@ipc.uni-tuebingen.de (U.W.)
3 Center for Light-Matter Interaction, Sensors & Analytics (LISA+), University of Tuebingen, Auf der Morgenstelle 15, D-72076 Tuebingen, Germany
4 Physics and Astronomy Department, College of Science, King Saud University, Riyadh 11451, Saudi Arabia; malduraibi@ksu.edu.sa
* Correspondence: nb@ipc.uni-tuebingen.de
† These authors contributed equally to this work.

Abstract: Beginning with $LaFeO_3$, a prominent perovskite-structured material used in the field of gas sensing, various perovskite-structured materials were prepared using sol–gel technique. The composition was systematically modified by replacing La with Sm and Gd, or Fe with Cr, Mn, Co, and Ni. The materials synthesized are comparable in grain size and morphology. DC resistance measurements performed on gas sensors reveal Fe-based compounds solely demonstrated effective sensing performance of acetylene and ethylene. Operando diffuse reflectance infrared Fourier transform spectroscopy shows the sensing mechanism is dependent on semiconductor properties of such materials, and that surface reactivity plays a key role in the sensing response. The replacement of A-site with various lanthanoid elements conserves surface reactivity of $AFeO_3$, while changes at the B-site of $LaBO_3$ lead to alterations in sensor surface chemistry.

Keywords: perovskites; gas sensor; DRIFTS; operando spectroscopy

Citation: Alharbi, A.; Junker, B.; Alduraibi, M.; Algarni, A.; Weimar, U.; Bârsan, N. The Role of Different Lanthanoid and Transition Metals in Perovskite Gas Sensors. *Sensors* **2021**, *21*, 8462. https://doi.org/10.3390/s21248462

Academic Editor: Marina N. Rumyantseva

Received: 12 November 2021
Accepted: 14 December 2021
Published: 18 December 2021

1. Introduction

Calcium titanate ($CaTiO_3$) was discovered in 1839 by German mineralogist Gustav Rose in the Ural Mountains (Russia). Perovskite material shares the same crystal structure as $CaTiO_3$, and was subsequently named in honor of the Russian mineralogist Lev Alekseevich von Perovskiy [1]. Perovskites have played a potentially significant role over many decades in various breakthrough technologies as innovative functional materials [1–3]. For example, in 1986, Bednorz and Müller discovered high-temperature superconductivity (HTSC) based on perovskite material (cuprate ceramics). They were jointly awarded the Noble Prize in Physics in 1987 for their discovery [4]. Moreover, manganite, another perovskite-structured material, shows a colossal magneto-resistive (CMR) phenomenon, which is crucial in spintronic applications [5]. In recent years, perovskites are rapidly becoming promising materials for inexpensive and high-efficiency photovoltaic cells [6–8].

In the gas sensors field, perovskites are promising candidate materials in gas sensor applications, due to their unique electrical and catalytic properties [9–15]. Owing to the general formula of perovskite, written as ABO_3, where the A-site cation bears a greater ionic radius than the B-site cation, this class of structures harbors a wide variety of possibilities for structure tailoring of oxides, i.e., by replacing A- and B-sites with different elements.

Among various target gases, the detection of hydrocarbons is extremely useful in a wide range of applications. For example, monitoring of dissolved gases (CH_4, C_2H_4, C_2H_2,

CO, CO_2, and H_2) in transformer oil provides beneficial information about transformer status [16,17]. Moreover, in agriculture, ethylene emissions indicate the maturity state of fruits; thus, detecting and controlling this gas is crucial for fruit ripening [18].

For the proper use and future development of selective gas sensors based on perovskite materials, it is essential to understand the sensing mechanism, including the molecular pathway of the reaction. However, few attempts were made to understand and systematically compare the underlying sensing mechanism of perovskites. For example, Arakawa and co-authors found a correlation between catalytic activity and the radius of A-site-element for $LnFeO_3$, where Ln is a lanthanoid element. In the case of $LnCrO_3$, however, the same correlation was unnoticeable. The effect of oxygen-binding energy with metal ions of perovskites on the gas-sensing mechanism was considered by the same group [19]. Furthermore, the influence of Ln elements and the surface composition of $LnFeO_3$ on sensing NO_2 was reported [20]. Subsequently, Siemons et al. used different lanthanoid elements (La, Pr, Nd, Sm, Eu, Gd, Tb, Dy, Ho, Er, Tm, Yb, and Lu) in $LnFeO_3$ and $LnCrO_3$ perovskite structures in order to investigate their gas-sensing properties of H_2, CO, NO, NO_2, and propylene via high-throughput impedance spectroscopy [21]. They noted a correlation between binding energy of oxygen to metal ions and gas sensing; the lower the binding energy, the greater the gas sensor signals (except for $LuFeO_3$). Recently, Gaskov and co-workers reported that modification of $LaCoO_3$ with Ag nanoparticles may lead to greater response and selectivity to H_2S compared with pure $LaCoO_3$. Additionally, they employed in situ infrared spectroscopy to study the chemical reactions of H_2S on the sensor's surface and observed an enhancement in H_2S chemisorption as a result of Ag nanoparticles present [22]. A summary of relevant material properties is given in Table 1.

Table 1. Properties of different perovskite materials.

Material	Bandgap	Conduction Type	Color
$LaCrO_3$	3.4 eV [23,24] 2.8 eV [25]	p-type [21] n-type [19]	dark green
$LaNiO_3$	metallic [23,26]	metallic p-type [27,28]	black
$LaCoO_3$	2.2 eV [29,30] 0.6 eV [23,31]	p-type [22] n-type [19]	black
$LaMnO_3$	0.7 eV [23,32] 0.33 eV [33]	p-type [34] n-type [19]	black
$LaFeO_3$	2.6 eV [35] 2.1 eV [23,36]	p-type [19,21]	light brown
$SmFeO_3$	2.2 eV [37]	p-type [21]	light brown
$GdFeO_3$	3.5 eV [38] 2.3 eV [39]	p-type [21]	brown

In our previous work, we used operando DRIFT spectroscopy to investigate the molecular pathway underlying the reaction of $LaFeO_3$ (LFO)-based sensors during ethylene and acetylene exposure. We demonstrated that the sensor response of LFO is associated with formation of surface formats as opposed to oxidation–reduction of the oxide surface [40].

This work aims to examine the validity of our novel mechanism for different perovskite compounds where La is replaced by other trivalent lanthanoid ions (Sm, Gd) or the transition metal ion Fe at the B-site is replaced by Cr, Mn, Ni, and Co. This systematic approach allows us to assess the role of both metals in the gas-sensing process. The sensing properties of all perovskite materials towards various hydrocarbons were examined. Moreover, operando DRIFT spectroscopy was used to investigate the molecular interaction between hydrocarbons and perovskite surfaces.

2. Experimental Details

2.1. Synthesis and Structural Characterization of Perovskites

Sol–gel technique was used to prepare $LaCrO_3$, $LaNiO_3$, $LaCoO_3$, $LaMnO_3$, $LaFeO_3$, $SmFeO_3$, and $GdFeO_3$ perovskite powders. Stoichiometric amounts of different metal nitrates were used as received, shown in Table 2, and dissolved using a (1:1) ratio of citric acid for each compound. Each mixture was then dissolved in deionized water. Following this, each solution was neutralized by adding ammonium hydroxide into the vigorously stirred precursor solution. The obtained gel was dried at 90 °C for 4 h. Finally, the powder was calcined at 600 °C for 2 h.

Table 2. Details of the raw materials used for sensitive materials preparation.

Perovskite Material	Metal Precursors
$LaCrO_3$	$La(NO_3)_3 \cdot 6H_2O$ (Fluka, (Buchs, Switzerland), Puriss. p.a., ≥99.0%) and $Cr(NO_3)_2.9H_2O$ (Sigma, (Buchs, Switzerland), Puriss. p.a., ≥99.0%)
$LaNiO_3$	$La(NO_3)_3 \cdot 6H_2O$ (Fluka, (Buchs, Switzerland), Puriss. p.a., ≥99.0%) and $Ni(NO_3)_2.6H_2O$ (Sigma, (Buchs, Switzerland), Puriss. p.a., ≥99.0%)
$LaCoO_3$	$La(NO_3)_3 \cdot 6H_2O$ (Fluka, (Buchs, Switzerland), Puriss. p.a., ≥99.0%) and $Co(NO_3)_2 \cdot 6H_2O$ (Sigma, (Buchs, Switzerland), Puriss. p.a., ≥99.0%)
$LaMnO_3$	$La(NO_3)_3 \cdot 6H_2O$ (Fluka, (Buchs, Switzerland), Puriss. p.a., ≥99.0%) and $Mn(NO_3)_2 \cdot 4H_2O$ (Sigma, (Buchs, Switzerland), Puriss. p.a., ≥99.0%)
$LaFeO_3$	$La(NO_3)_3 \cdot 6H_2O$ (Fluka, (Buchs, Switzerland), Puriss. p.a., ≥99.0%) and $Fe(NO_3)_3 \cdot 9H_2O$ (Fluka, (Buchs, Switzerland), Puriss. p.a., ≥99.0%)
$SmFeO_3$	$Sm(NO_3)_3 \cdot 6H_2O$ (Acros Organics, (Geel, Belgium), ≥99.9%) and $Fe(NO_3)_3 \cdot 9H_2O$ (Sigma Aldrich, (Buchs, Switzerland), ≥99.0%)
$GdFeO_3$	$Gd(NO_3)_3 \cdot 6H_2O$ (Aldrich, ≥99.9%) and $Fe(NO_3)_3 \cdot 9H_2O$ (Sigma Aldrich, (Buchs, Switzerland), ≥99.0%)

To confirm the perovskite phase formation of the prepared powders, X-ray diffractometers (MiniFlex 600, Rigaku, Tokyo, Japan and D8 discover, Bruker, Billerica, MA, USA) were used with nickel filtered Cu-Kα and Co-Kα radiation, respectively, in the diffraction range of 0° to 65°. Moreover, the morphologies of the perovskite powders were investigated using a field emission scanning electron microscope (FE-SEM, JEOL-7600F, Tokyo, Japan).

2.2. DC Measurements

Thick film sensors were prepared by screen printing the powders onto alumina substrates as described in [41]. Afterwards, the sensors were calcined at 500 °C to remove residual organic solvents in the paste. For DC resistance measurements, the sensors were mounted in a test chamber connected to a gas-mixing system. The resistive heater on the backside of each sensor substrate was individually calibrated with an infrared thermometer (KTR2300, Maurer, Kohlberg, Germany). The sensors were mounted in a PTFE measurement chamber and exposed to test gases in a background of 0%, 10%, and 50% relative humidity (measured at 25 °C) at operating temperatures of 150 °C and 250 °C. The sensors were exposed to concentrations of 50, 100, 200, and 500 ppm of methane, ethane, ethylene, and acetylene for 30 min. Analyte gases (Westfalen AG) were mixed with dry and humid air in a gas-mixing system equipped with mass flow controllers (Bronkhorst). The resistance was measured with a Keysight 34972A multimeter. The range of the device was increased as necessary by connecting a 100MOhm precision resistor in parallel to the sensor.

2.3. Operando DRIFT Spectroscopy

DRIFTS was performed on a Bruker Vertex 80 v spectrometer equipped with DLaTGS and MCT detectors. Absorbance spectra were calculated from the spectra which were recorded after two hours of the gas exposure referenced to the ones which were taken initially in clean air. DRIFTS experiments were performed on sensors as described above at 150 °C in dry air.

3. Results

3.1. Material Characterization

Figure 1 shows the XRD patterns of synthesized $LaCrO_3$, $LaNiO_3$, $LaCoO_3$ $LaMnO_3$, $LaFeO_3$, $SmFeO_3$, and $GdFeO_3$ materials. Due to our usage of two different X-ray sources, one with Cu and one with Co anode, we separated our XRD results into two figures, Figure 1a,b. Moreover, each figure contains its reference peaks, card no. JCPDS 37-1493 in Figure 1a and card no. ICSD 204,689 in Figure 1b. All samples show peaks related to perovskites structure.

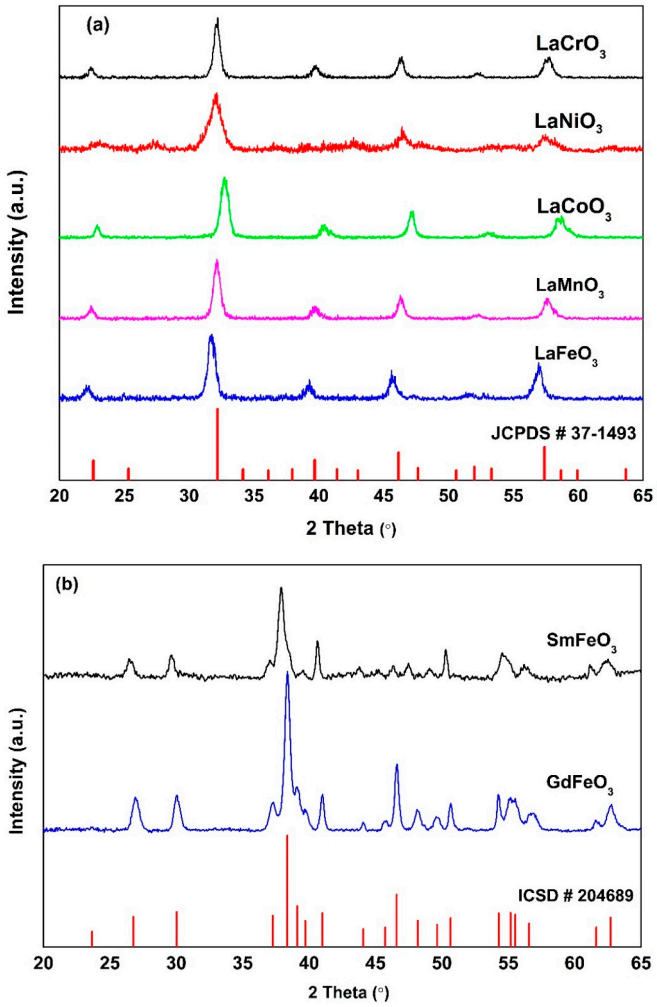

Figure 1. The XRD patterns of prepared perovskite materials using (**a**) Cu anode and (**b**) Co anode. The referenced peaks are indicated by red lines at the bottom.

The SEM images of the prepared perovskites are shown in Figure 2. All samples appear to contain nanoparticles with shapes of similar uniformity. The grain sizes range primarily between 50–100 nm diameter. XRD results confirm SEM findings indicating

the following grain sizes: $LaFeO_3$: 63 nm, $LaMnO_3$: 61 nm, $LaCoO_3$: 80 nm, $LaNiO_3$: 38 nm, $LaCrO_3$: 42 nm, $GdFeO_3$: 92 nm, and $SmFeO_3$: 101 nm. Fe-based compounds show less nanoparticle agglomeration and tend to form mesopores with greater ease than other compounds.

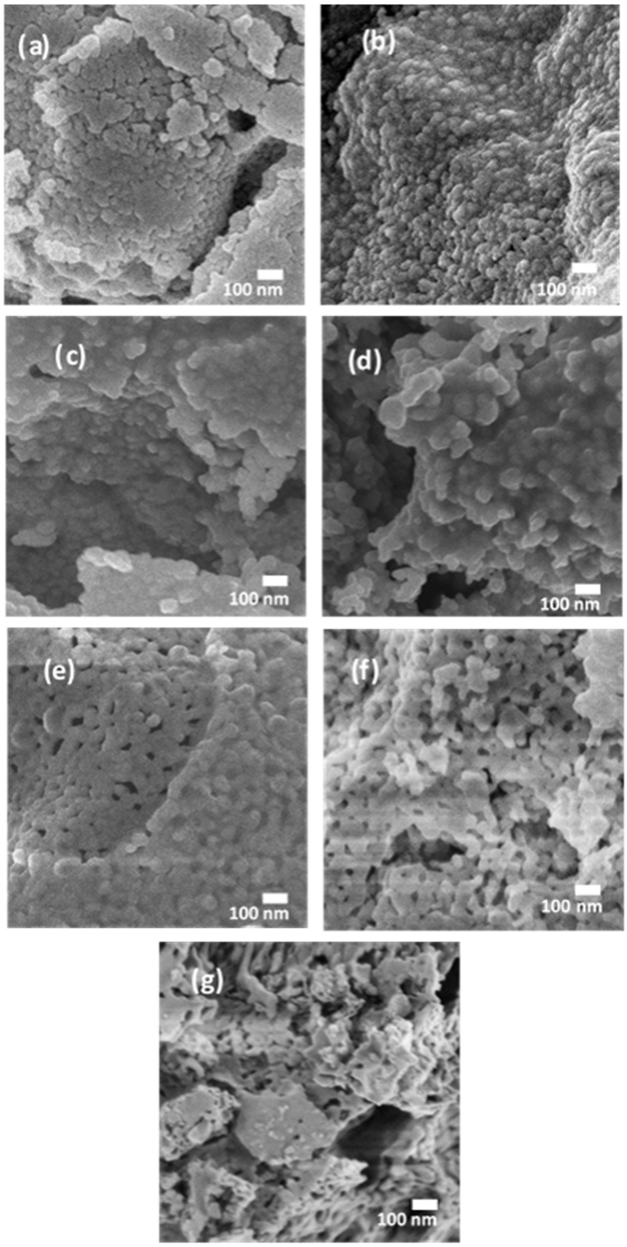

Figure 2. (**a**) $LaCrO_3$, (**b**) $LaNiO_3$, (**c**) $LaCoO_3$, (**d**) $LaMnO_3$, (**e**) $LaFeO_3$, (**f**) $SmFeO_3$ and (**g**) $GdFeO_3$.

3.2. Electrical Characterization

To determine whether the materials react as p-type or n-type semiconductors, sensors were equilibrated in dry nitrogen and subsequently exposed to dry air. The change in resistance is plotted in Figure 3a. The sensor signals (defined as $\frac{R_{nitrogen}}{R_{air}}$) range from 1.1 ($LaCoO_3$) to 89 ($GdFeO_3$). For all materials, a decrease in resistance was observed, except for $LaMnO_3$, where resistance increased (S = 0.98). This indicates all materials except

$LaMnO_3$ react as p-type semiconductors. The results are supported by at least one of the references given in Table 1.

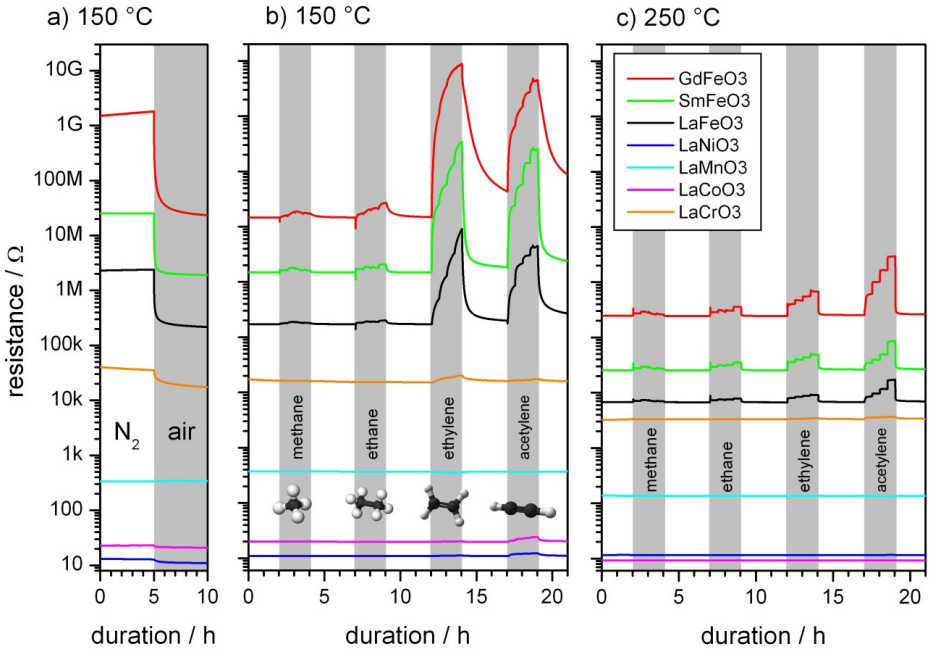

Figure 3. DC resistance measurements in dry air: (**a**) transition from nitrogen to air at 150 °C, (**b**) exposure different analyte gases at 150 °C, and (**c**) 250 °C. The shaded areas indicate periods, where the sensors were exposed to different concentrations of the analyte gases.

Figure 3b shows the resistance of gas sensors during exposure to different analyte gases in dry air at 150 °C. When La ions are replaced by Sm, the baseline resistance increases by a factor of 10, while replacing La with Gd increases the baseline resistance by another order of magnitude. When the Fe site is replaced by other transition metal ions, the opposite behavior is observed. For $LaCrO_3$ and $LaMnO_3$ the resistance is significantly decreased. For $LaCoO_3$ and $LaNiO_3$, the resistance ranges from 10 to 20 Ohms, which is comparable to the resistance of the metallic electrodes on the substrates.

The response to the analyte gases tested in this study varies substantially between Fe-based compounds and their counterparts. The response to saturated hydrocarbons methane and ethane is small for all materials. In contrast, ethylene and acetylene are clearly detected by all materials containing Fe, while the response is far lower for other materials. $LaMnO_3$ is the only material that shows a decrease in resistance upon contact with reducing gases. This is in keeping with findings of the oxygen exposure results. Interestingly, in the cases of $LaFeO_3$, $SmFeO_3$, and $GdFeO_3$, 30 min for one step of concentration was sufficient to reach equilibrium for acetylene, but not ethylene, even though the change in resistance is comparable. The reaction with acetylene is apparently faster at this temperature. At 250 °C (Figure 3b) the signals are smaller and the response is faster for all material–target gas combinations. For ethylene, this effect is more pronounced than acetylene. The baseline resistance is decreased for all materials except $LaNiO_3$. The low resistance in addition to the negative temperature coefficient of resistance represent properties of a metal rather than a semiconductor.

Figure 4 summarizes sensor signals for all investigated materials in different conditions. Methane remained undetected except for low signals from $GdFeO_3$ and $SmFeO_3$ sensors at 150 °C. Regarding ethane, the situation is similar, however the gas is detectable with the $LaFeO_3$ sensor and with greater sensor signals than methane. At 250 °C, a small sensor response may be observed with Fe-containing materials. For ethylene, sensor sig-

nals are greater by several orders of magnitude for Fe-containing materials. In a humid background, the sensor signals are smaller than in dry air. The sensor response to acetylene is more influenced by humidity than ethylene. This is due to dissociation of acetylene at the sensor surface being inhibited by the additional formation of OH groups, as demonstrated in our previous work [40]. The agreement of this study's data with earlier publications confirms reproducibility of the results [9]. Among other materials, only $LaCrO_3$ shows a response undiminished in a humid background. At greater temperatures the signals for ethylene are significantly decreased, particularly in humid air where only $GdFeO_3$ shows a response. For acetylene, the influence of humidity on materials containing Fe is more pronounced than for ethylene. With other materials showing a response, i.e., $LaCrO_3$, $LaCoO_3$, and $LaNiO_3$, the influence of humidity remains small.

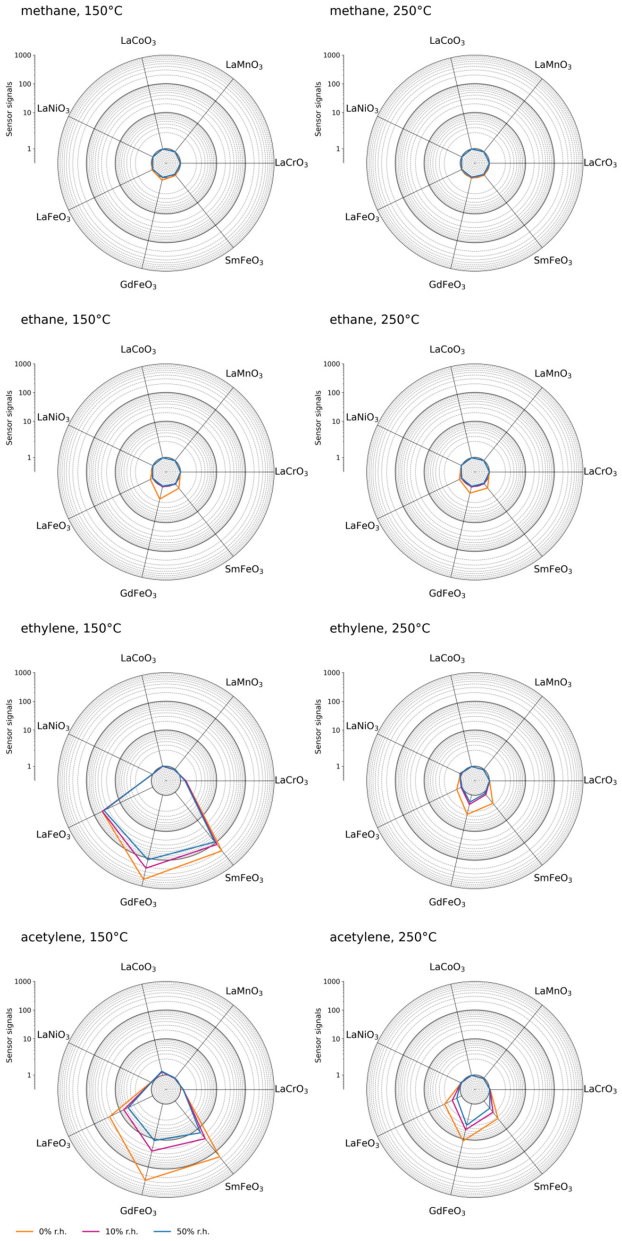

Figure 4. Sensor signals for exposure to 500 ppm of different gases at 150 °C (**left column**) and at 250 °C (**right column**).

These findings indicate Fe ions at the B-site of this class of materials play a key role in the gas-sensing mechanism, and that the occurrence of different surface reactions are expected, as observed from the different response of materials to acetylene and ethylene. The sensor response increases with baseline resistance of Fe-containing materials. The sensor signals of $LaNiO_3$ and $LaCoO_3$, however, reveal that a low baseline resistance does not necessarily exclude a response. A potential explanation for the differences among the sensor signals of Fe-containing materials may be their different morphology.

3.3. Surface Characterization

To compare the surface reactions on various materials, operando DRIFT spectroscopy was applied. The condition of 500 ppm of acetylene in dry air at 150 °C was chosen for comparison, as a majority of materials show a sensor signal. Additionally, the detection of acetylene is less influenced by the operating temperature and electrode material. The absorbance spectra with dry air as reference are presented in Figure 5. The presence of two bands at 2959 and 2850 cm^{-1}, together with 1580 and 1377 cm^{-1}, indicates the formation of formate species [40,42]. The two peaks at 2959 and 2850 cm^{-1} are attributed to C-H vibrations (asymmetric and symmetric), and the 1580 and 1377 cm^{-1} bands are associated with OCO vibrations (asymmetric and symmetric). The peak at 1430 cm^{-1} may be assigned to δ C-H [43,44]. Moreover, two small peaks in the OH region can be observed: a decreasing peak in around 3671 cm^{-1} indicates consumption of terminal OH groups.

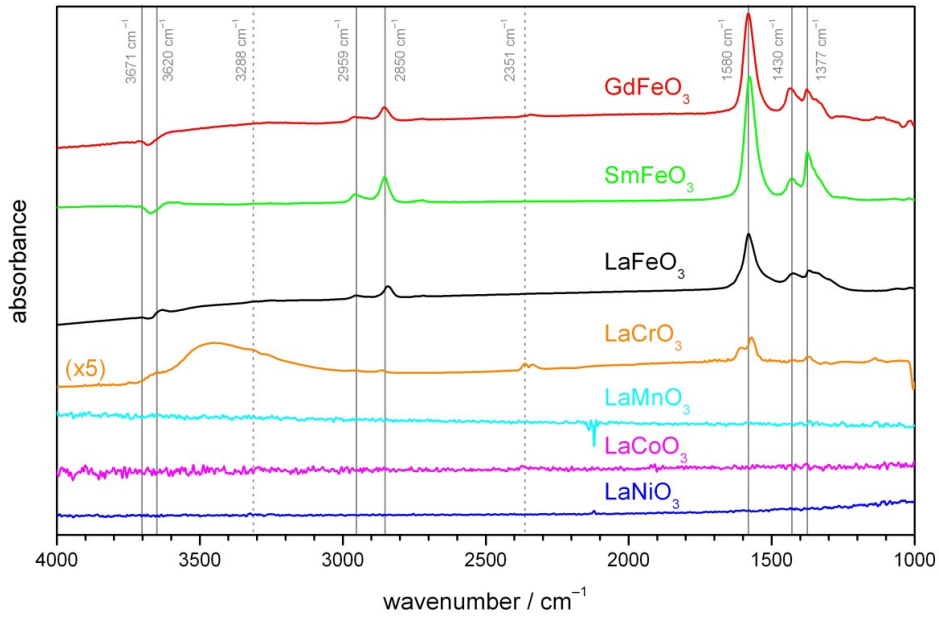

Figure 5. Absorbance DRIFT spectra of different materials at 150 °C. The spectra recorded after 2 h of exposure to 500 ppm acetylene were referenced to dry air. For increased visualization, the spectra are stacked and the magnitude of the spectrum of $LaCrO_3$ increases. The dashed lines mark the position of gas phase species.

These peaks are additionally present on $GdFeO_3$ and $SmFeO_3$, but with slightly different relative heights. Notably, the ratios of peaks in the OH region differ, indicating either a marginally different reaction or a different surface coverage prior to acetylene exposure. For $GdFeO_3$, gaseous CO_2 is visible around 2351 cm^{-1}. The situation concerning materials $LaMnO_3$, $LaCoO_3$, and $LaNiO_3$ is very different. Change at the surface cannot be observed. These materials exhibit low reflectance and the low intensity at the detector leads to high noise levels. A very different behavior is observed for $LaCrO_3$. The same formate peaks as seen with $LaFeO_3$ are observed, albeit at a much lower intensity. A broad band around 3400 cm^{-1} indicates the formation of interacting hydroxyl groups. Moreover,

the distinctive double band for gaseous CO_2 can clearly be seen at 2351 cm^{-1}. Based on our previous investigation [40], complete combustion of hydrocarbons, indicated by CO_2 formation in DRIFT spectra, is not generally accompanied by a strong sensor response. However, incomplete combustion of hydrocarbons, which can lead to the formation of formate species at the perovskite surface, playing a key role in effective gas sensing. As observable from DRIFT spectra, the complete combustion section of surface chemical reactions is more pronounced for LaCrO3 than Fe-based materials; therefore, the LaCrO3 sensors show a lower gas response.

Kremenic et al. investigated the catalytic properties of a series of $LaBO_3$ (B=Cr, Mn, Fe; Co, Ni) perovskites. In this series, $LaFeO_3$ bears the greatest tendency for absorption of isobutene, but the lowest for oxygen [45]. Moreover, the catalytic conversion of isobutene at temperatures comparable to our study was investigated. The lowest reaction rate for complete combustions for $LaFeO_3$ was observed, followed by $LaCrO_3$. The incomplete combustion was assessed by analyzing the amount of oxygenated organic compounds where the highest values were found for $LaCrO_3$ and $LaFeO_3$. These results support the assumption that the incomplete combustion of hydrocarbons and strong sensor performance is correlated.

The molecular orbitals (MO) with symmetry e_g centered at the B-site of the perovskite with the highest energy and e_g symmetry are populated by 0 (Cr^{3+}), 1 (Mn^{3+}, Co^{3+}, Ni^{3+}), or 2 (Fe^{3+}) electrons and interact differently with simple gas molecules such as CO, NO or O_2 [46]. The reaction sequence involves multiple intermediates, whose energies are dependent on the composition of the perovskite [47] The creation of formates requires preadsorbed oxygen, provided by oxygen in the gas phase. This is consistent with the finding that materials with greater signals to oxygen additionally show a better response to hydrocarbons. Moreover, we assume the reception of gas molecules investigated in this study relies on the transfer of electrons between molecular orbitals of the hydrocarbons and the B-site cations of the perovskite. The structure of the analyte gases used in this study is more complex than O_2 or CO. In contrast to methane and ethane, acetylene and ethylene contain additional π-MOs to interact with metals. A possible explanation for the high sensor signals of ethylene and acetylene may be interaction of these π-MOs with $d_{x^2-y^2}$ MO of the Fe centers. This orbital is occupied solely for $LnFeO_3$ [46]. This effect in combination with different reactivity to oxygen is suspected to be responsible for different sensing performances of materials with different B-sites. The exchange of La with Sm or Gd does not alter the number of electrons in MOs at the B-site. However, other factors such as ionic radii, electronegativity, magnetic properties, and differences in morphology of sensing layers may explain different sensor responses. Further research on surface chemistry and DFT calculations is planned to investigate the interplay between the perovskite surface, oxygen, and hydrocarbon molecules.

4. Conclusions

Lanthanoid-based perovskites present a promising class of materials for gas sensing due to their notable response to unsaturated hydrocarbons at low temperatures. As expected from the chemical properties of pure elements, exchanging different transition metal cations at the B-site drastically alters the electrical, chemical, and optical properties of the perovskite. Only Fe-based compounds showed clear sensor signals to acetylene and ethylene among other prepared perovskites. It appears from DRIFT spectra that surface reactivity, particularly the formation of formates, determines sensing behavior. In the case of $LaCrO_3$, which additionally showed clear surface reactivity, the lower response to acetylene may be attributed to complete combustion of gases. Therefore, the most promising element for gas-sensing applications at the B-site is iron. In addition, modifications on the A-site (lanthanoids) of Fe-based perovskites maintain overall gas-sensing properties.

Author Contributions: Conceptualization, A.A. (Abdulaziz Alharbi), B.J., N.B., U.W.; Investigation, A.A. (Abdulaziz Alharbi), B.J., M.A., A.A. (Ahmad Algarni); Writing—original draft preparation, A.A. (Abdulaziz Alharbi), B.J.; Writing—review and editing, A.A. (Abdulaziz Alharbi), B.J., M.A., N.B. All authors have read and agreed to the published version of the manuscript.

Funding: This research received no external funding.

Institutional Review Board Statement: Not applicable.

Informed Consent Statement: Not applicable.

Data Availability Statement: The data presented in this study are available on request from the corresponding author.

Conflicts of Interest: The authors declare no conflict of interest.

References

1. Ortega-San-Martin, L. Introduction to Perovskites: A Historical Perspective. In *Revolution of Perovskite. Materials Horizons: From Nature to Nanomaterials*; Arul, N.N.V., Ed.; Springer: Singapore, 2020; pp. 1–141.
2. Chakhmouradian, A.R.; Woodward, P.M. Celebrating 175 years of perovskite research: A tribute to Roger H. Mitchell. *Phys. Chem. Miner.* **2014**, *41*, 387–391. [CrossRef]
3. Belich, N.; Udalova, N.; Semenova, A.; Petrov, A.; Fateev, S.; Tarasov, A.; Goodilin, E. Perovskite Puzzle for Revolutionary Functional Materials. *Front. Chem.* **2020**, *8*, 1–9. [CrossRef] [PubMed]
4. Bednorz, K.A.; Müller, G.J. Possible highT c superconductivity in the Ba−La−Cu−O system. *Z. Phys. B-Condens. Matter* **1986**, *64*, 189–193. [CrossRef]
5. von Helmolt, K.; Wecker, R.; Holzapfel, J.; Schultz, B.; Samwer, L. Giant negative magnetoresistance in perovskitelike La 2/3 Ba 1/3 MnOx ferromagnetic films. *Phys. Rev. Lett.* **1993**, *71*, 2331–2333. [CrossRef] [PubMed]
6. Kojima, A.; Teshima, K.; Shirai, Y.; Miyasaka, T. Organometal Halide Perovskites as Visible-Light Sensitizers for Photovoltaic Cells. *J. Am. Chem. Soc.* **2009**, *131*, 6050–6051. [CrossRef] [PubMed]
7. Grätzel, M. The light and shade of perovskite solar cells. *Nat. Mater.* **2014**, *13*, 838–842. [CrossRef] [PubMed]
8. Snaith, P.; Hacke, J.H. Enabling reliability assessments of pre-commercial perovskite photovoltaics with lessons learned from industrial standards. *Nat. Energy* **2018**, *3*, 459–465. [CrossRef]
9. Alharbi, A.A.; Sackmann, A.; Weimar, U.; Bârsan, N. A highly selective sensor to acetylene and ethylene based on $LaFeO_3$. *Sens. Actuators B Chem.* **2020**, *303*, 127204. [CrossRef]
10. Sukee, A.; Alharbi, A.A.; Staerz, A.; Wisitsoraat, A.; Liewhiran, C.; Weimar, U. Effect of AgO loading on flame-made $LaFeO_3$ p-type semiconductor nanoparticles to acetylene sensing. *Sens. Actuators B Chem.* **2020**, *312*, 127990. [CrossRef]
11. Chen, Y.; Qin, H.; Wang, X.; Li, L.; Hu, J. Acetone sensing properties and mechanism of nano-$LaFeO_3$ thick-films. *Sens. Actuators B Chem.* **2016**, *235*, 56–66. [CrossRef]
12. Tong, Q.L.Y.; Zhang, Y.; Jiang, B.; He, J.; Zheng, X. Effect of Lanthanides on Acetone Sensing Properties of $LnFeO_3$ Nanofibers. *IEEE Sens. J.* **2017**, *17*, 2404–2410. [CrossRef]
13. Fan, K.; Qin, H.; Wang, L.; Ju, L.; Hu, J. CO_2 gas sensors based on La1−xSrxFeO$_3$ nanocrystalline powders. *Sens. Actuators B Chem.* **2013**, *177*, 265–269. [CrossRef]
14. Dai, Z.; Lee, C.-S.; Kim, B.-Y.; Kwak, C.-H.; Yoon, J.-W.; Jeong, H.-M.; Lee, J.-H. Honeycomb-like Periodic Porous $LaFeO_3$ Thin Film Chemiresistors with Enhanced Gas-Sensing Performances. *ACS Appl. Mater. Interfaces* **2014**, *6*, 16217–16226. [CrossRef]
15. Obayashi, H.; Sakurai, Y.; Gejo, T. Perovskite-type oxides as ethanol sensors. *J. Solid State Chem.* **1976**, *17*, 299–303. [CrossRef]
16. Duval, M. A review of faults detectable by gas-in-oil analysis in transformers. *IEEE Electr. Insul. Mag.* **2002**, *18*, 8–17. [CrossRef]
17. Dennison, J.C.; Trout, J.M. Transformer oil DGA monitoring technology study 2015. In Proceedings of the 2016 IEEE/PES Transmission and Distribution Conference and Exposition (T&D), Dallas, TX, USA, 3–5 May 2016; pp. 1–5.
18. Esser, B.; Schnorr, J.M.; Swager, T.M. Selective Detection of Ethylene Gas Using Carbon Nanotube-based Devices: Utility in Determination of Fruit Ripeness. *Angew. Chem. Int. Ed.* **2012**, *51*, 5752–5756. [CrossRef] [PubMed]
19. Arakawa, T.; Kurachi, H.; Shiokawa, J. Physicochemical properties of rare earth perovskite oxides used as gas sensor material. *J. Mater. Sci.* **1985**, *20*, 1207–1210. [CrossRef]
20. Aono, H.; Traversa, E.; Sakamoto, M.; Sadaoka, Y. Crystallographic characterization and NO_2 gas sensing property of $LnFeO_3$ prepared by thermal decomposition of Ln Fe hexacyanocomplexes, $Ln[Fe(CN)_6]\cdot nH_2O$, Ln = La, Nd, Sm, Gd, and Dy. *Sens. Actuators B Chem.* **2003**, *94*, 132–139. [CrossRef]
21. Siemons, M.; Leifert, A.; Simon, U. Preparation and Gas Sensing Characteristics of Nanoparticulate p-Type Semiconducting $LnFeO_3$ and $LnCrO_3$ Materials. *Adv. Funct. Mater.* **2007**, *17*, 2189–2197. [CrossRef]
22. Chumakova, V.; Marikutsa, A.; Rumyantseva, M.; Fasquelle, D.; Gaskov, A. Nanocrystalline $LaCoO_3$ modified by Ag nanoparticles with improved sensitivity to H2S. *Sens. Actuators B Chem.* **2019**, *296*, 126661. [CrossRef]
23. Arima, T.; Tokura, Y.; Torrance, J.B. Variation of optical gaps in perovskite-type 3d transition-metal oxides. *Phys. Rev. B* **1993**, *48*, 17006–17009. [CrossRef] [PubMed]

24. Polat, O.; Durmus, Z.; Coskun, F.M.; Coskun, M.; Turut, A. Engineering the band gap of $LaCrO_3$ doping with transition metals (Co, Pd, and Ir). *J. Mater. Sci.* **2018**, *53*, 3544–3556. [CrossRef]
25. Haas, O.; Ludwig, C.; Bergmann, U.; Singh, R.N.; Braun, A.; Graule, T. Electronic structure of La1-xSrxFeO$_3$. *Phys. Rev. B* **1996**, *54*, 7816–7822.
26. Guan, L.; Liu, B.; Jin, L.; Guo, J.; Zhao, Q.; Wang, Y.; Fu, G. Electronic structure and optical properties of $LaNiO_3$: First-principles calculations. *Solid State Commun.* **2010**, *150*, 2011–2014. [CrossRef]
27. Yannopoulos, L. A p-type semiconductor thick film gas sensor. *Sens. Actuators* **1987**, *12*, 263–273. [CrossRef]
28. Hwang, D.K.; Kim, S.; Lee, J.H.; Hwang, I.S.; Kim, I.D. Phase evolution of perovskite $LaNiO_3$ nanofibers for supercapacitor application and p-type gas sensing properties of LaOCl-NiO composite nanofibers. *J. Mater. Chem.* **2011**, *21*, 1959–1965. [CrossRef]
29. Michel, C.R.; López-Alvarez, M.A.; Martínez-Preciado, A.H.; Oleinikov, V. Ultraviolet Detection and Photocatalytic Activity of Nanostructured $LaCoO_3$ Prepared by Solution-Polymerization. *ECS J. Solid State Sci. Technol.* **2019**, *8*, Q9–Q14. [CrossRef]
30. Mukhopadhyay, S.; Finnis, M.W.; Harrison, N.M. Electronic structures and phonon free energies of $LaCoO_3$ using hybrid-exchange density functional theory. *Phys. Rev. B* **2013**, *87*, 34–36. [CrossRef]
31. Chainani, A.; Mathew, M.; Sarma, D.D. Electron-spectroscopy study of the semiconductor-metal transition in La1-xSrxCoO$_3$. *Phys. Rev. B* **1992**, *46*, 9976–9983. [CrossRef] [PubMed]
32. Smolin, S.Y.; Choquette, A.K.; Wilks, R.G.; Gauquelin, N.; Félix, R.; Gerlach, D.; May, S.J. Energy Level Alignment and Cation Charge States at the $LaFeO_3/LaMnO_3$ (001) Heterointerface. *Adv. Mater. Interfaces* **2017**, *4*, 1–8. [CrossRef]
33. Choi, W.S.; Jeong, D.W.; Jang, S.Y.; Marton, Z.; Seo, S.S.A.; Lee, H.N.; Lee, Y.S. $LaMnO_3$ Thin Films Grown by Using Pulsed Laser Deposition and Their Simple Recovery to a Stoichiometric Phase by Annealing. *J. Korean Phys. Soc.* **2011**, *58*, 569–574. [CrossRef]
34. Jha, P.; Sands, T.D.; Cassels, L.; Jackson, P.; Favaloro, T.; Kirk, B.; Zide, J.; Xu, X.; Shakouri, A. Cross-plane electronic and thermal transport properties of p-type $La0.67Sr0.33MnO_3/LaMnO_3$ perovskite oxide metal/semiconductor superlattices. *J. Appl. Phys.* **2010**, *112*, 63714. [CrossRef]
35. Scafetta, M.D.; Xie, Y.J.; Torres, M.; Spanier, J.E.; May, S.J. Optical absorption in epitaxial La1-xSrx FeO_3 thin films. *Appl. Phys. Lett.* **2013**, *102*, 081904. [CrossRef]
36. Tijare, S.N.; Joshi, M.V.; Padole, P.S.; Mangrulkar, P.A.; Rayalu, S.S.; Labhsetwar, N.K. Photocatalytic hydrogen generation through water splitting on nano-crystalline $LaFeO_3$ perovskite. *Int. J. Hydrog. Energy* **2012**, *37*, 10451–10456. [CrossRef]
37. Li, L.; Wang, X.; Zhang, Y. Enhanced visible light-responsive photocatalytic activity of $LnFeO_3$ (Ln = La, Sm) nanoparticles by synergistic catalysis. *Mater. Res. Bull.* **2014**, *50*, 18–22. [CrossRef]
38. Husain, S.; Keelani, A.O.; Khan, W. Influence of Mn substitution on morphological, thermal and optical properties of nanocrystalline $GdFeO_3$ orthoferrite. *Nano-Struct. Nano-Objects* **2018**, *15*, 17–27. [CrossRef]
39. Subramanian, Y.; Ramasamy, V.; Karthikeyan, R.J.; Srinivasan, G.R.; Arulmozhi, D.; Gubendiran, R.K.; Sriramalu, M. Investigations on the enhanced dye degradation activity of heterogeneous $BiFeO_3$–$GdFeO_3$ nanocomposite photocatalyst. *Heliyon* **2019**, *5*, e01831. [CrossRef]
40. Alharbi, A.A.; Sackmann, A.; Weimar, U.; Barsan, N. Acetylene-and Ethylene-Sensing Mechanism for $LaFeO_3$-Based Gas Sensors: Operando Insights. *J. Phys. Chem. C* **2020**, *124*, 7317–7326. [CrossRef]
41. Barsan, N.; Weimar, U. Understanding the fundamental principles of metal oxide based gas sensors; the example of CO sensing with SnO_2sensors in the presence of humidity. *J. Phys. Condens. Matter* **2003**, *15*, R813–R839. [CrossRef]
42. Liu, X.; Zhou, W.; Yang, Y.; Cheng, K.; Kang, J.; Zhang, L.; Zhang, G.; Min, X.; Zhang, Q.; Wang, Y. Design of efficient bifunctional catalysts for direct conversion of syngas into lower olefins via methanol/dimethyl ether intermediates. *Chem. Sci.* **2018**, *9*, 4708–4718. [CrossRef]
43. Busca, G.; Lamotte, J.; Lavalley, J.c.; Lorenzelli, V. FT-IR Study of the Adsorption and Transformation of Formaldehyde on Oxide Surfaces. *J. Am. Chem. Soc.* **1987**, *109*, 5197–5202. [CrossRef]
44. Cao, T.; You, R.; Zhang, X.; Chen, S.; Li, D.; Zhang, Z.; Huang, W. An in situ DRIFTS mechanistic study of CeO_2-catalyzed acetylene semihydrogenation reaction. *Phys. Chem. Chem. Phys.* **2018**, *20*, 9659–9670. [CrossRef] [PubMed]
45. Kremenić, G.; Nieto, J.M.L.; Tascón, J.M.D.; Tejuca, L.G. Chemisorption and catalysis on $LaMO_3$ oxides. *J. Chem. Soc. Faraday Trans. 1 Phys. Chem. Condens. Phases* **1985**, *81*, 939–949. [CrossRef]
46. Hwang, J.; Rao, R.R.; Giordano, L.; Katayama, Y.; Yu, Y.; Shao-Horn, Y. Perovskites in catalysis and electrocatalysis. *Science* **2017**, *358*, 751–756. [CrossRef] [PubMed]
47. Wang, Y.; Cheng, H.-P. Oxygen Reduction Activity on Perovskite Oxide Surfaces: A Comparative First-Principles Study of $LaMnO_3$, $LaFeO_3$, and $LaCrO_3$. *J. Phys. Chem. C* **2013**, *117*, 2106–2112. [CrossRef]

THE JOURNAL OF PHYSICAL CHEMISTRY LETTERS
A JOURNAL OF THE AMERICAN CHEMICAL SOCIETY

pubs.acs.org/JPCL Letter

Proof of Concept for Operando Infrared Spectroscopy Investigation of Light-Excited Metal Oxide-Based Gas Sensors

Xiao-Xue Wang, Benjamin Junker, Carolin Ewald, Udo Weimar, Xin Guo,* and Nicolae Barsan*

Cite This: J. Phys. Chem. Lett. 2022, 13, 3631−3635 Read Online

ACCESS | Metrics & More | Article Recommendations | Supporting Information

ABSTRACT: Light-excitation of semiconducting metal-oxide (SMOX)-based gas sensors is a promising means to lower their operation temperature, thereby reducing power consumption, which would allow for their broader application. Despite increased research interest in light-excited gas sensors, progress has been slow because of a lack of mechanistic understanding. Notably, significant differences between light-excitation and, the better understood, thermal-excitation mechanisms have been identified. Insights from operando spectroscopic studies have been key to understanding the surface chemistry that determines the performance of thermally activated SMOX, but they have not yet been performed on illuminated sensors. Here, for the first time, we demonstrate that it is possible to perform operando diffuse reflectance infrared Fourier transform (DRIFT) spectroscopy measurements on sensors under illumination. We demonstrate the benefits of the approach and show that under light illumination the splitting of water on the WO_3 surface is responsible for the increased resistance of the sensor during exposure to high humidity.

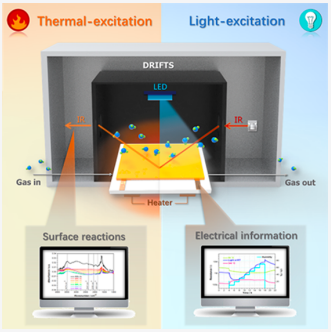

With the digitalization of daily life and rapid development of the Internet of Things, the demand for small, secure, cheap, sensitive, and selective gas sensors is projected to continuously increase.[1] Semiconducting metal-oxide (SMOX) gas sensors are inexpensive and simple to use and respond to a large number of gases, making them interesting for use in indoor air quality monitoring of smart buildings, mobile breath analyzers, and artificial intelligent olfaction.[2] However, usually, to activate both the sensing reactions on the surface and the desorption of reaction products, the concentration of free charge carriers must be increased. Therefore, the required excitation energy is typically provided in the form of heat. That is, the sensors are operated at temperatures around 300 °C.[3] A major advantage of lowering the necessary operation temperature would be a decrease in the power consumption of smart devices containing sensors. An alternative to heating would be to provide energy via illumination, potentially even allowing sensors to be operated at room temperature. As a result of the decreasing production costs of LEDs, light-excited gas sensors are becoming a viable option.

The potential of this method is clear by the ever-increasing number of research articles that report excellent gas-sensing performance of light-excited SMOX sensors.[4−12] In contrast to heated devices, little is known about the chemistry responsible for the signals of light-excited SMOX sensors. Although operando diffuse reflectance infrared Fourier transform spectroscopy (DRIFTS) has provided insights key to understanding the surface chemistry of heated samples, it had not previously been applied to light-excited sensors. Here, we demonstrate by performing operando DRIFTS on sensors under illumination that the chemistry of humidity on the WO_3 surface can be correlated with the sensor response under blue light illumination.

The motivation of this research is twofold. First, it is vital for a wide range of applications to understand how humidity affects the materials in the presence of light. This work provides a new method for the direct analysis of the light-excited gas−solid phase interactions. Second, it displays the ability to probe the mechanistic differences between the light and thermally excited gas sensors. This represents a crucial first step in the future unraveling of light-excited gas-sensing mechanisms.

For the interpretation of the results, our previous studies of the gas-sensing mechanism of WO_3 under thermal excitation are useful. We reported[13] that the effect of humidity (10% r.h.) on WO_3 depends on the operating temperatures. Considering operando DRIFT spectra, exhaust measurements, and DFT calculations, under 200 °C water vapor blocks the surface adsorption sites of atmospheric oxygen, namely, the oxygen vacancies. Therefore, in the presence of water molecules, the surface is less oxidized and the sensor resistance decreases. At high operation temperatures, above 250 °C, the water molecules adsorbed into the oxygen vacancies split, releasing hydrogen. This leads to an overall oxidation of the WO_3

Received: February 17, 2022
Accepted: April 14, 2022

https://doi.org/10.1021/acs.jpclett.2c00480
J. Phys. Chem. Lett. 2022, 13, 3631−3635

The Journal of Physical Chemistry Letters pubs.acs.org/JPCL Letter

surface, increasing the sensor resistance in the presence of humidity.

Figure 1 shows the effects of humidity exposure recorded in the three different operation modes. During the measurements,

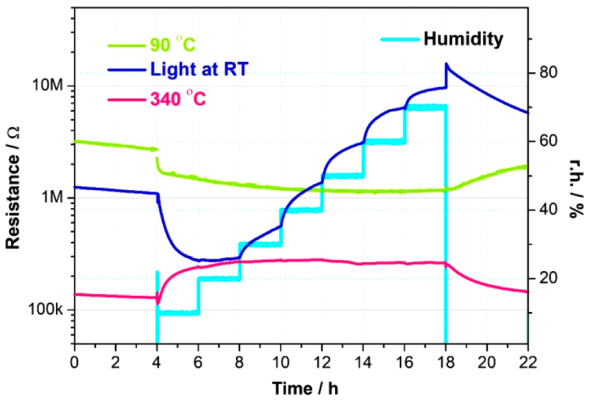

Figure 1. Resistance measurements of the WO_3 sensor under different humidities at different excitation conditions: RT under blue light; 90 and 340 °C in the dark.

the relative humidity, which is represented as light-blue lines in Figure 1, was increased from 0% up to 70% @25 °C in steps of 10% r.h. The dark-blue curve is the DC resistance of the WO_3 sensor operated at RT under illumination, the green curve is of a sensor operated at 90 °C, and the pink curve corresponds to a sensor operated at 340 °C.

As expected from our previous results, at 90 °C the sensor resistance decreases when the humidity increases and the opposite happens at 340 °C. Surprisingly, at RT with blue light illumination, although the sensor resistance decreases at low humidity levels (10% and 20% r.h. @25 °C), it starts to increase at higher levels and even exceeds the sensor resistance recorded in dry conditions when the relative humidity reaches 40%. This is an unexpected result because neither the operation temperature nor the illumination conditions changed; the only variable here is the humidity. In fact, increasing the humidity under illumination shows an analogous effect of increasing the operating temperature in dark conditions.

The electrical results are explained by the operando DRIFTS investigations. Their results are shown in Figure 2: panel a shows the measurements performed at RT under illumination; panel b gives the spectra recorded at 90 °C; panel c gives the spectra at 340 °C.

The spectral bands corresponding to the WO_3 surface species most strong influenced by humidity are marked in the spectra and the assignments are given in Table 1. Spectra taken in different humidity conditions are represented in distinct colors. To clearly depict the influence of increasing humidity, the reference spectrum is always the single-channel recorded in the preceding condition: for example, in the case of 10% r.h., the reference is recorded in dry conditions, while for the 20% r.h., the reference is recorded at 10% r.h., etc.

For the electrical effects, the most significant role is played by the lattice surface oxygen; the respective bands are centered at 1851, 2059, and 2341 cm^{-1}.[14] As already reported,[13] in dark conditions and at low (90 °C) operation temperature, the effect of the increase of water surface species is the decrease of

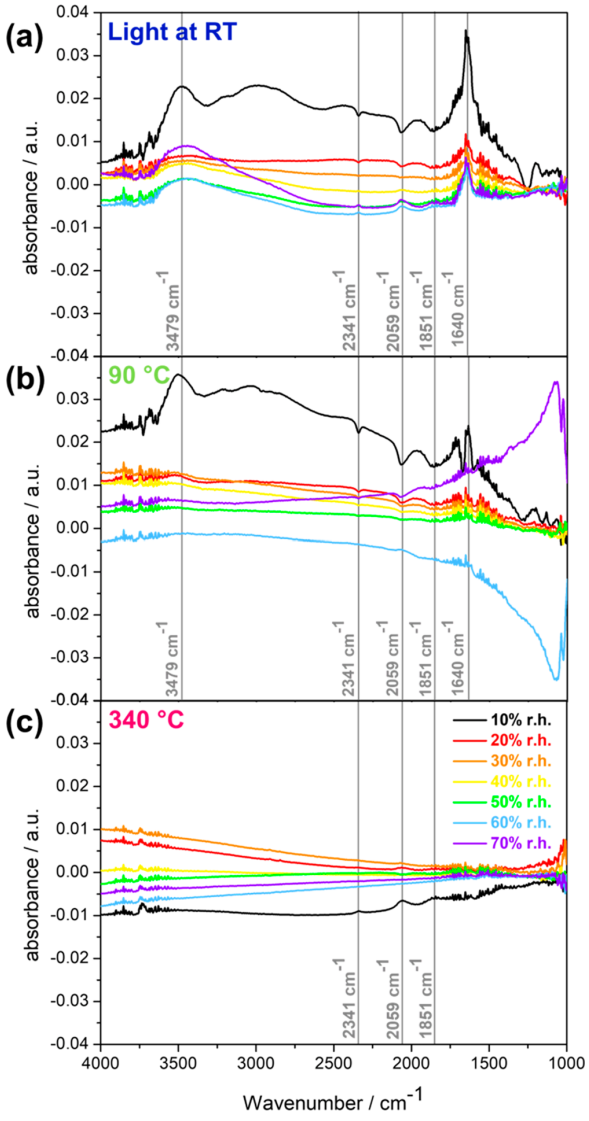

Figure 2. DRIFT spectra of the WO_3 sensor under different humidities (a) at RT under the blue light; (b) at 90 °C and (c) at 340 °C. The spectra were referenced to the spectrum which was recorded under former humidity conditions.

Table 1. Assignments of the Wavenumbers from Bands Related to Species Based on WO_3 with Humidity[14−16]

wavenumber (cm^{-1})		assigned vibration
3479	O−H	rooted, interacting
2341	W−O	surface lattice overtone
2059	W−O	surface lattice overtone
1851	W−O	surface lattice overtone
1640	$W-OH_2$	molecularly adsorbed water, bending vibration

the surface oxygens, which are replaced by adsorbed water molecules (band centered around 1640 cm^{-1}).[15] The broad band centered around 3479 cm^{-1}[16] corresponds to interacting hydroxyl groups. As indicated by the electrical and DRIFTS

https://doi.org/10.1021/acs.jpclett.2c00480
J. Phys. Chem. Lett. 2022, 13, 3631−3635

The Journal of Physical Chemistry Letters pubs.acs.org/JPCL Letter

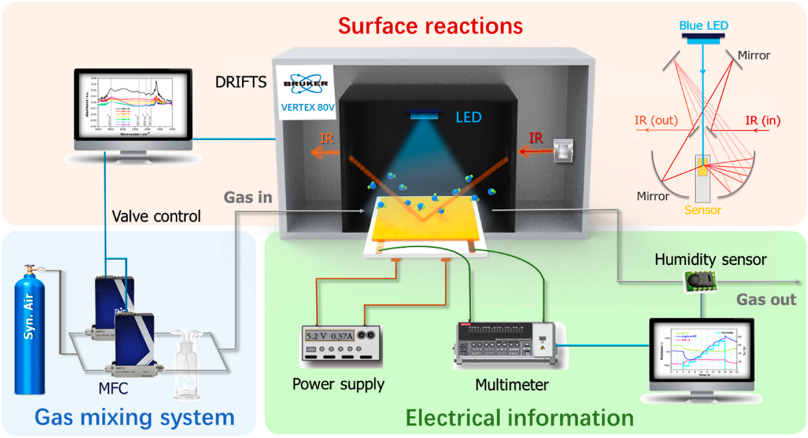

Figure 3. Schematic diagram of the experimental setup.

results, all surface processes seem to reach saturation around 40% r.h. This is seen as the resistance reaches a steady state while the W−O bands show very low changes (Figure 2b). In dark conditions and at high (340 °C) operation temperature, the increase of humidity determines an increase of the surface oxidation; no adsorbed molecular water or hydroxyl groups are present (Figure 2c). The DRIFTS results offer insights into the mechanism responsible for the effect of humidity on the resistance in the presence of light. Initially after exposure to low concentrations of water vapor there is a massive adsorption of molecular water (Figure 2a) and the concentration of surface lattice oxygen decreases (the W−O bands and the resistance decrease until 20% r.h.). Also at higher humidity levels water adsorption continues but is less strong. Between 30% r.h. and 40% r.h., the spectroscopic results, in line with the increase of the sensor resistance, indicate an oxidation of the surface (increasing W−O bands). Considering this finding, over a certain threshold concentration of humidity, blue light illumination results in the splitting of water on the WO_3 surface. The mechanism will be studied more closely in a follow-up study.

In conclusion, we were able to demonstrate that it is possible to perform operando DRIFT spectroscopy on illuminated gas sensors. In the specific example we provided, we have shown that it is possible to explain the electrical effect of water vapor on WO_3-based gas sensors that were exposed to blue light. This work opens up new avenues for the investigation of light-enhanced gas sensing that will support the advancement of this very promising research field.

EXPERIMENTAL METHODS

To realize the DRIFTS measurements under illumination, it is necessary to choose the proper light source and gas-sensing materials. For a first experiment, we decided to avoid the generation of electron−hole pairs, so the photon energy had to stay below the band gap of the chosen sensitive material. Also, in order to avoid interference with the operation of the DRIFTS system, the wavelength of the introduced light source had to be outside the detection range of the mercury cadmium telluride (MCT) detector (850−12000 cm^{-1}). As the gas-sensitive material we chose WO_3 (band gap 2.8 eV), and blue light (wavelength 460 nm, 2.7 eV) was used as the excitation source. We are aware that it is possible, because of the presence of various defects related to the different preparation methods employed for the synthesis of the materials, to have values of the band gap less than 2.8 eV. In fact, in the literature, values between 2.6 are 3.0 eV are reported.[17] This will make the future interpretation of the results more difficult and require additional experiments performed at higher and lower wavelengths (spanning from red light to UV).

We developed an experimental setup to acquire the electrical information and surface reactions of the sensor simultaneously, under different excitation conditions. The schematic diagram of the experimental setup is shown in Figure 3. The WO_3 sensors were mounted in a homemade gas chamber with a KBr window inside the DRIFTS system. A blue LED was placed inside the gas chamber to illuminate the sensing surface, and the mirrors for IR can also help blue light focus on the sensor surface. A constant flow rate of 200 mL/min was employed, and different levels of humidity (0−70% r.h. in synthetic air) were obtained using a bubbler with the help of a fully automated gas-mixing system. The sensors were illuminated or heated analogously to the DC resistance measurements, and operando DRIFT spectra were recorded simultaneously.

To fabricate the sensor samples, commercially available WO_3 nanopowder (Sigma-Aldrich; >100 nm) was ground with 1,2-Propanediol (Sigma-Aldrich; 99.5+% A.C.S. Reagent) using a mortar and pestle into a viscous paste which was screen-printed onto Al_2O_3 substrates (CeramTec GmbH, electrode gap 300 μm, front side Pt-electrodes and backside Pt-heater). The samples were dried overnight at 80 °C and then annealed for 10 min each at 400−500−400 °C with two 5 min steps to cool down in a tubular furnace (Heraeus ROK 6/30). Finally, a layer thickness of approximately 50 μm was attained.

The DC resistance measurements were performed with a Keithley 617 electrometer. A blue LED (460 nm, 2.7 eV, irradiance = 49.04 W/m^2) was applied to provide light illumination. An Agilent E3614A voltage source was used to heat the sensors via the backside heater.

The resistance measurements of the WO_3 sensors were carried out under three different conditions. The light-excited condition at room temperature (RT) was obtained by turning on the LED. Additionally, the sensors were operated at 90 °C without illumination; the reason is that at this temperature the baseline resistance was comparable to that under the blue light irradiance at room temperature, and in this way there is the

https://doi.org/10.1021/acs.jpclett.2c00480
J. Phys. Chem. Lett. 2022, 13, 3631−3635

The Journal of Physical Chemistry Letters pubs.acs.org/JPCL Letter

possibility to distinguish between the mere illumination effect of generating more free charge carriers and other possible contributions. Considering the typical operation temperature of WO_3 is between 200 and 400 °C, a higher operating temperature of 340 °C was selected for the thermally excited gas-sensing condition.

For the operando DRIFT spectroscopy, a Vertex 80v IR spectrometer containing a midband MCT detector (Bruker, Billerica, MA, USA) with a wavenumber limit of 850−12000 cm^{-1} and a spectral resolution of 4 cm^{-1} was used. Throughout the experiments, the whole sensitive layer (24.5 mm^2) was illuminated. A spot with a diameter of 2−3 mm in the center of the sensitive layer was probed by IR. Every 15 min a single-channel spectrum was recorded. To obtain the absorbance spectra, the single-channel spectra taken under exposure to the target gases were referenced to the spectra taken under the carrier gas using the relation suggested by Olinger and Griffiths:[18]

$$\text{absorbance} = -\log\left(\frac{\text{single-channel test gas}}{\text{single-channel reference}}\right) \quad (1)$$

Here, all spectra were attained by reference to the spectrum that was taken at the end of the former humidity condition.

■ ASSOCIATED CONTENT

Supporting Information

The Supporting Information is available free of charge at https://pubs.acs.org/doi/10.1021/acs.jpclett.2c00480.

Transparent Peer Review report available (PDF)

■ AUTHOR INFORMATION

Corresponding Authors

Xin Guo − *State Key Laboratory of Material Processing and Die & Mould Technology, Laboratory of Solid State Ionics, School of Materials Science and Engineering, Huazhong University of Science and Technology, Wuhan 430074, P.R. China;* orcid.org/0000-0003-1546-8119; Email: xguo@hust.edu.cn

Nicolae Barsan − *Institute of Physical and Theoretical Chemistry (IPTC) and Center for Light-Matter Interaction, Sensors & Analytics (LISA+), University of Tuebingen, 72076 Tuebingen, Germany;* orcid.org/0000-0001-6718-9889; Email: nb@ipc.uni-tuebingen.de

Authors

Xiao-Xue Wang − *State Key Laboratory of Material Processing and Die & Mould Technology, Laboratory of Solid State Ionics, School of Materials Science and Engineering, Huazhong University of Science and Technology, Wuhan 430074, P.R. China; Institute of Physical and Theoretical Chemistry (IPTC) and Center for Light-Matter Interaction, Sensors & Analytics (LISA+), University of Tuebingen, 72076 Tuebingen, Germany;* orcid.org/0000-0003-4581-537X

Benjamin Junker − *Institute of Physical and Theoretical Chemistry (IPTC) and Center for Light-Matter Interaction, Sensors & Analytics (LISA+), University of Tuebingen, 72076 Tuebingen, Germany;* orcid.org/0000-0002-2229-0534

Carolin Ewald − *Institute of Physical and Theoretical Chemistry (IPTC) and Center for Light-Matter Interaction, Sensors & Analytics (LISA+), University of Tuebingen, 72076 Tuebingen, Germany;* orcid.org/0000-0001-8367-7110

Udo Weimar − *Institute of Physical and Theoretical Chemistry (IPTC) and Center for Light-Matter Interaction, Sensors & Analytics (LISA+), University of Tuebingen, 72076 Tuebingen, Germany;* orcid.org/0000-0003-2354-0432

Complete contact information is available at: https://pubs.acs.org/10.1021/acs.jpclett.2c00480

Author Contributions

X.-X.W.: Conceptualization, Methodology, Investigation, Formal analysis, Writing−original draft. B.J.: Investigation, Writing− reviewing and editing. C.E.: Investigation, Writing−reviewing and editing. U.W.: Supervision. X.G.: Funding acquisition, Supervision, Writing−review and editing. N.B.: Project administration, Funding acquisition, Supervision, Writing−review and editing.

Notes

The authors declare no competing financial interest.

■ ACKNOWLEDGMENTS

This work was supported by the National Natural Science Foundation of China (NSFC Grant #61971202) and the Deutsche Forschungsgemeinschaft (DFG) - Projektnummer 419896563.

■ REFERENCES

(1) Evans, D. *Internet of Things How the Next Evolution of the Internet Is Changing Everything.*; Cisco Internet Business Solutions Group, 2011. http://www.cisco.com/web/about/ac79/docs/innov/IoT_IBSG_0411FINAL.pdf (accessed 2022-01-14).

(2) Bârsan, N.; Koziej, D.; Weimar, U. Metal Oxide-based Gas Sensor Research: How to? *Sens. Actuators B Chem.* **2007**, *121*, 18−35.

(3) Ihokura, K.; Watson, J. *The Stannic Oxide Gas Sensor Principles and Applications*; CRC Press: Boca Raton, FL, 1994.

(4) Lu, G.; Xu, J.; Sun, J.; Yu, Y.; Zhang, Y.; Liu, F. UV-Enhanced Room Temperature NO_2 Sensor using ZnO Nanorods Modified with SnO_2 Nanoparticles. *Sens. Actuators B Chem.* **2012**, *162*, 82−88.

(5) Park, S.; An, S.; Mun, Y.; Lee, C. UV-Enhanced NO_2 Gas Sensing Properties of SnO_2-Core/ZnO-Shell Nanowires at Room Temperature. *ACS Appl. Mater. Interfaces.* **2013**, *5*, 4285−4292.

(6) Zhou, Y.; Gao, C.; Guo, Y. UV Assisted Ultrasensitive Trace NO_2 Gas Sensing based on Few-Layer MoS_2 Nanosheet−ZnO Nanowire Heterojunctions at Room Temperature. *J. Mater. Chem. A* **2018**, *6*, 10286−10296.

(7) Park, S.; Sun, G.-J.; Jin, C.; Kim, H. W.; Lee, S.; Lee, C. Synergistic Effects of a Combination of Cr_2O_3-Functionalization and UV-Irradiation Techniques on the Ethanol Gas Sensing Performance of ZnO Nanorod Gas Sensors. *ACS Appl. Mater. Interfaces.* **2016**, *8*, 2805−2811.

(8) Bonaccorsi, L.; Malara, A.; Donato, A.; Donato, N.; Leonardi, S. G.; Neri, G. Effects of UV Irradiation on the Sensing Properties of In_2O_3 for CO Detection at Low Temperature. *Micromachines* **2019**, *10*, 338−349.

(9) Chinh, N. D.; Quang, N. D.; Lee, H.; Hien, T. T.; Hieu, N. M.; Kim, D.; Kim, C.; Kim, D. NO Gas Sensing Kinetics at Room Temperature under UV Light Irradiation of In_2O_3 Nanostructures. *Sci. Rep.* **2016**, *6*, 35066−35077.

(10) Li, H.-Y.; Yoon, J.-W.; Lee, C.-S.; Lim, K.; Yoon, J.-W.; Lee, J.-H. Visible Light Assisted NO_2 Sensing at Room Temperature by CdS Nanoflake Array. *Sens. Actuators B Chem.* **2018**, *255*, 2963−2970.

(11) Wang, X.-X.; Li, H.-Y.; Guo, X. Flexible and Transparent Sensors for ultra-low NO_2 Detection at Room Temperature under Visible Light Illumination. *J. Mater. Chem. A* **2020**, *8*, 14482−14490.

(12) Suh, J. M.; Eom, T. H.; Cho, S. H.; Kim, T.; Jang, H. W. Light-activated Gas Sensing: A Perspective of Integration with Micro-LEDs and Plasmonic Nanoparticles. *Mater. Adv.* **2021**, *2*, 827−844.
(13) Staerz, A.; Kobald, A.; Russ, T.; Weimar, U.; Hémeryck, A.; Bârsan, N. Thermal Water Splitting on the WO_3 Surface: Experimental Proof. *ACS Appl. Electron. Mater.* **2020**, *2*, 3254−3262.
(14) Staerz, A.; Berthold, C.; Russ, T.; Wicker, S.; Weimar, U.; Bârsan, N. The Oxidizing Effect of Humidity on WO_3 based Sensors. *Sens. Actuators B Chem.* **2016**, *237*, 54−58.
(15) Daniel, M. F.; Desbat, B.; Lassegues, J. C.; Gerand, B.; Figlarz, M. Infrared and Raman Study of WO_3 Tungsten Trioxides and WO_3, xH_2O Tungsten Trioxide Hydrates. *J. Solid State Chem.* **1987**, *67*, 235−247.
(16) Emiroglu, S.; Bârsan, N.; Weimar, U.; Hoffmann, V. In Situ Diffuse Reflectance Infrared Spectroscopy Study of CO Adsorption on SnO_2. *Thin Solid Films* **2001**, *391*, 176−185.
(17) Bamwenda, G. R.; Sayama, K.; Arakawa, H. The Effect of Selected Reaction Parameters on the Photoproduction of Oxygen and Hydrogen from a WO_3-Fe^{2+}-Fe^{3+} Aqueous Suspension. *J. Photochem. Photobiol., A* **1999**, *122*, 175−183.
(18) Olinger, J. M.; Griffiths, P. R. Quantitative Effects of an Absorbing Matrix on Near-Infrared Diffuse Reflectance Spectra. *Anal. Chem.* **1988**, *60* (21), 2427−2435.

https://doi.org/10.1021/acs.jpclett.2c00480
J. Phys. Chem. Lett. 2022, 13, 3631−3635

Sensors & Actuators: B. Chemical 390 (2023) 134028

Contents lists available at ScienceDirect

Sensors and Actuators: B. Chemical

journal homepage: www.elsevier.com/locate/snb

Sensing mechanisms of CO and H_2 with NiO material – DRIFTS investigations

Cristian.E. Simion [a,1], Benjamin Junker [b,1], Udo Weimar [b], Adelina Stanoiu [a], Nicolae Bârsan [b,*]

[a] Laboratory of Atomic Structures and Defects in Advanced Materials, National Institute of Materials Physics, Atomistilor 405A, 077125 Magurele, Romania
[b] Institute of Physical and Theoretical Chemistry and Center for Light-Matter Interaction, Sensors & Analytics (LISA+), University of Tübingen, 72076 Tübingen, Germany

ARTICLE INFO

Keywords:
NiO based gas sensors
Diffuse reflectance infrared Fourier transform spectroscopy
Sensing mechanism
In-field conditions
Operando spectroscopy, surface reactions

ABSTRACT

The response of nickel oxide gas sensors towards CO and H_2 and the underlying gas sensing mechanisms were investigated with special focus on the influence of ambient humidity interference. Surface reactions were tracked by using diffuse reflectance infrared Fourier transformation spectroscopy with simultaneous resistance measurements. The sensor response to both gases is barely influenced by the background humidity. Spectroscopic results reveal that the underlying processes at the surface are almost identical for CO and H_2 reception and similar to the effect of the removal of oxygen. Accordingly, the detection of the analytes is based purely on the reduction and oxidation of the oxide material instead of the formation of analyte specific surface species.

1. Introduction

Nickel oxide (NiO), which exhibits a p-type semiconductor behaviour due to its Ni^{2+} vacancies and O defects, did not receive much attention in the field of gas sensing based on semiconducting metal oxides [1,2]. A possible explanation can be its low sensor response to different target gases which could be due to the less efficient transduction of the surface changes into sensor signals specific to p-type materials [3]. Not all is bad, though; NiO stands out because of the unusual low impact of the humidity on its sensing performance, whose understanding is, despite its relevance, still in the early stages [4,5]. To date, different researchers gathered relevant insights. For instance, Gupta et al. showed that the sensitivity to relative humidity (r.h.) increases when the annealing temperature increases [6]. Such effect was attributed to the mesoporous structure, due to the specific surface to volume ratio increase. Additionally, the presence of surface hydroxyl groups was proved via thermal desorption spectroscopy, being stable up to 600 K on the non-polar NiO (100) surface, explaining the dual function of the semiconductor/catalyst junction, accordingly [7,8]. The benefit of the presence of humidity towards NO_2 detection was underlined without justifying the sensing mechanism behind [9]. In one of our publications we proposed a gas-surface interaction mechanism for CO detection in the presence of humidity, taking into account the role played by the surface hydroxyl groups [10]. The insights were underlined through complementary investigations such as: simultaneous electrical resistance changes and contact potential differences. In order to reveal the fundamental and applicative potential of NiO based gas sensors, herein we limit ourselves towards CO and H_2 as target gases.

Accordingly, Das et al. [11] have found that hydrogen interaction with various surface defects manifests as a key factor within the embrittlement process. Moreover, after NiO annealing process at 700–800 °C under high pressure of H_2, a subsequent lattice contraction takes place due to the rich formation of vacancies (e.g. one Ni vacancy is able to trap up to six H atoms) [12]. Out of DFT calculations, [13] it was possible to explain the appearance of two maxima within the thermal desorption spectra based on the hydrogen interactions with the surface oxygen vacancies.

In the work of Xu et al. [14] one can find that at least three hydrogen atoms are necessary to reduce the NiO material, with the subsequent presence of water in the gas phase.

With respect to the NiO surface reduction by H_2, experimental and theoretical studies showed that the reactivity towards H_2 can be ignored for the most common crystallographic face of NiO (100) [15]. Moreover, the migration of oxygen vacancies from bulk to the NiO surface is also possible upon H_2 exposure.

For CO, whose gas-surface interaction pathway, at least for SnO_2,

* Corresponding author.
E-mail address: nb@ipc.uni-tuebingen.de (N. Bârsan).
[1] These authors contributed equally.

https://doi.org/10.1016/j.snb.2023.134028
Received 31 March 2023; Received in revised form 12 May 2023; Accepted 24 May 2023
Available online 25 May 2023

seems to be quite straightforward different reports come to somehow different conclusions [16]. For instance, knowing that the distance between carbon and oxygen of 1.24 Å leads to a favorable reaction CO with NiO and keeping in mind that the Ni-O bond is only 1.54 Å, DFT calculations indicated the preference for CO adsorption on the oxygen site situated on the apex of the NiO nanocone [17]. Therefore, for optimal detection, the recommendation of the authors was to synthesize the NiO-sensitive material in nanocone morphology.

Self-consistent DFT-GGA calculations showed that carbon monoxide prefers the top, bridged, fcc and hcp sites of the Ni (111) metal ion-terminated polar surface [18]. Two additional observations deserve to be noted here, namely: when CO coverage is rather low ($\theta_{CO} = 0.05$ ML (monolayers)) the said molecule prefers three-fold sites for adsorption, exhibiting a stretching frequency of 1817 cm-1 while the CO coverage increases up to 0.57 ML, CO prefers the two-fold bridge or even the top site of the NiO material. In the work of Dey et.al. [19] there is a description related to the CO oxidation mechanism at the surface of NiO as catalyst. Thus, they have found that the surface oxidation process exhibits an exothermic nature when CO molecules are adsorbed at the surface, forming initially Ni^{2+}-CO complex, followed by CO-active oxygen interaction to obtain CO_2 in the gas phase. Additionally, it was found that the catalytic performances of NiO have an optimal crystal size. One of the reasons why the knowledge gathered so far is difficult to integrate is the lack of information acquired in operation conditions [20]. Even if NiO based gas sensors are not very sensitive their peculiar behavior makes them attractive candidates for integration into sensor arrays, where it is important to ensure different sensing performances. Because of that it is of general interest to understand their sensing mechanism. For this reason, in the present work, we explore fundamental NiO-sensing properties by performing simultaneous electrical resistance and operando diffuse reflectance infrared Fourier transform (DRIFT) spectroscopy. The aim is to elucidate CO and H_2 the NiO sensing mechanisms and the influence of humidity.

2. Experimental

2.1. Powder synthesis and sensor fabrication

The chemical synthesis route, involving a hydrothermal procedure was extensively described in our previous report [10]. Briefly, the hydrated inorganic precursor ($Ni(NO_3)_2$) was dissolved in an aqueous agent. As a complexing agent, ethylenediaminetetraacetic acid was used while ethylene glycol was added playing the role of structural targeting agent. The intermediate temperature of 180 °C for 24 h was used for the hydrothermal procedure. The final precipitate has been filtered and washed using water and ethanol and further calcined at 500 °C for 8 h.

The as-obtained NiO powder was mixed with an organic binder (α-terpineol) until a homogeneous paste was obtained. Afterwards, the paste was transferred onto commercial alumina substrates (Al_2O_3) via the screen-printing method. The substrates are provided with Pt electrodes on one side (responsible for reading the electrical resistance changes) and Pt heater on the opposite side (responsible for attaining the desired operating temperature). After drying over the night at room temperature, the final heat treatment was done progressively up to 500 °C ensuring adherence to the substrate and complete removal of the organic binder.

2.2. Resistance measurements and infrared spectroscopy

For the operando diffuse reflectance infrared Fourier transform spectroscopy (DRIFTS) experiments the sensor was mounted in a Vertex 70 v infrared spectrometer (Bruker) equipped with a six-mirror optics (Harrick Praying Mantis) and a gas tight sensor chamber with KBr windows that allows the sensor to be heated to 250 °C in a defined gas atmosphere. Reflectance spectra were acquired with a resolution of 4 cm^{-1} during 15 min intervals and the apparent absorbance spectra with respect to a certain reference condition were calculated by: $A = -\log (I/I_{ref})$. Simultaneously, DC resistance was measured with a Keithley 617 Electrometer in Ohms mode. All gases, including ^{13}C labelled CO and D_2 gas mixtures were provided by Westfalen AG and diluted to the targeted concentration in a gas mixing system by means of mass flow controllers. Relative humidity was provided in form of H_2O and D_2O vapors, respectively, and is measured at 25 °C. The sensor signals were calculated by the ratio of the resistance of the sensor in the presence and the absence of the analyte: $S = R_{gas}/R_{air}$. In case of O_2 the reciprocal value is used.

3. Results

3.1. Material characterization

The synthesized material has been thoroughly characterized by means of scanning electron microscopy (SEM), high-resolution transmission electron microscopy (HRTEM), energy dispersive X-ray spectroscopy (EDX) and X-ray powder diffraction (XRD). The SEM investigations have shown a homogeneous, porous sensing layer comprising spherical agglomerates with an average size around 1.4 μm. TEM and XRD revealed that they are formed of face-centered cubic (fcc) NiO crystallites with an averaged size around 19 nm and dominant (111) crystallographic planes. No additional phase was found [10].

3.2. Sensor performance

The sensing performance has been evaluated at the operating temperature of 250 °C (where the maximum in the sensor signal occurs), under atmospheres with different oxygen, r.h. and analyte concentrations (Fig. 1). When the atmosphere changes from dry nitrogen to dry air, i.e. 20.5% oxygen is introduced, the resistance of the material drops from 4470 to 3130 Ohms (S=1.43), which indicates that the material reacts as a p-type semiconductor.

Interestingly, and in line with previous results, the resistance change when going from dry air to air with 10% r.h. is extremely low (S=1.04) and, consequently, the ambient humidity does not have a significant impact on the sensor resistance like in the case of many other SMOX sensitive materials [21,22]. To describe this process, an electronically neutral reaction must be taken into account.

Both hydrogen and CO show satisfactory response in dry conditions with hydrogen yielding somewhat higher signals. Remarkably, in humid conditions the sensor signals are higher than in dry air. In nitrogen atmosphere, i.e. in the absence of oxygen the sensor signals are significantly higher.

The electrical evaluation alone does not provide information about specific surface sites interaction for oxygen and moisture, hence the sensor's surface was monitored with DRIFT spectroscopy during the exposure to the different gases to complete the experimental study.

3.3. Oxygen and water reactions: DRIFTS insights

For analyzing the effect of O_2 on NiO a DRIFT experiment was performed and the absorbance spectrum, with nitrogen as reference, was calculated. The spectrum (Fig. 2) reveals increasing bands at 1296, 1257, 980 and 1070 cm^{-1}.

The band at 1070 cm_{-1} can be attributed to O_2^- ions bound to Ni, while the aforementioned ones are assigned to Ni-O vibrations [23–25]. It is assumed, that oxygen is chemisorbed as a molecule on Ni-sites and captures one electron in this process:

$$O_2 + V_O^{\cdot\cdot} + e^- \rightarrow (V_O^{\cdot\cdot} - O_2^-)_O^{\cdot} \quad (1)$$

As illustrated in Fig. 3, the adsorbed oxygen molecules serve as a precursor to the filling of oxygen vacancies in a subsequent reaction:

$$(V_O^{\cdot\cdot} - O_2^-)_O^{\cdot} + V_O^{\cdot\cdot} + 3e^- \rightarrow 2O_O^{\times} \quad (2)$$

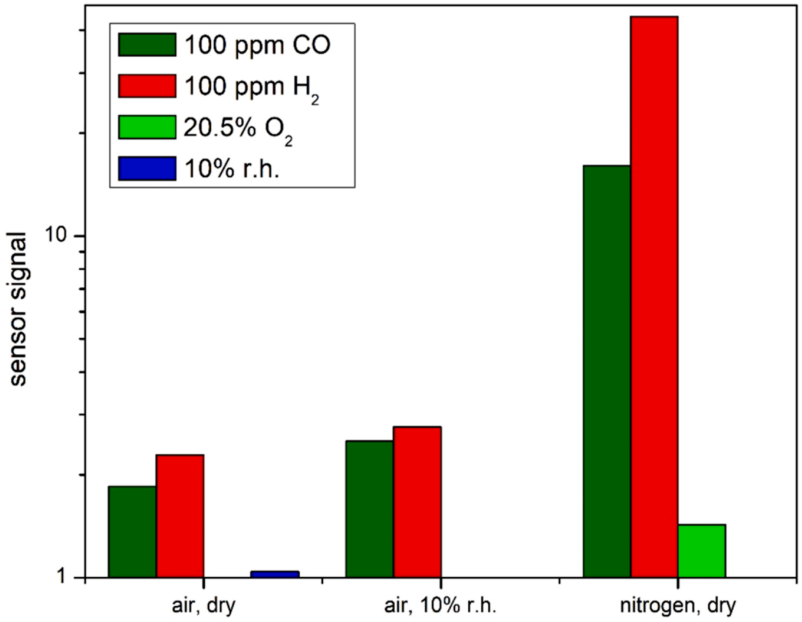

Fig. 1. Sensor signals for CO and H_2 in different background atmospheres. For comparison the sensor signals of O_2 in N_2 and the introduction of 10% relative humidity, measured at 25 °C, to dry air are shown as well.

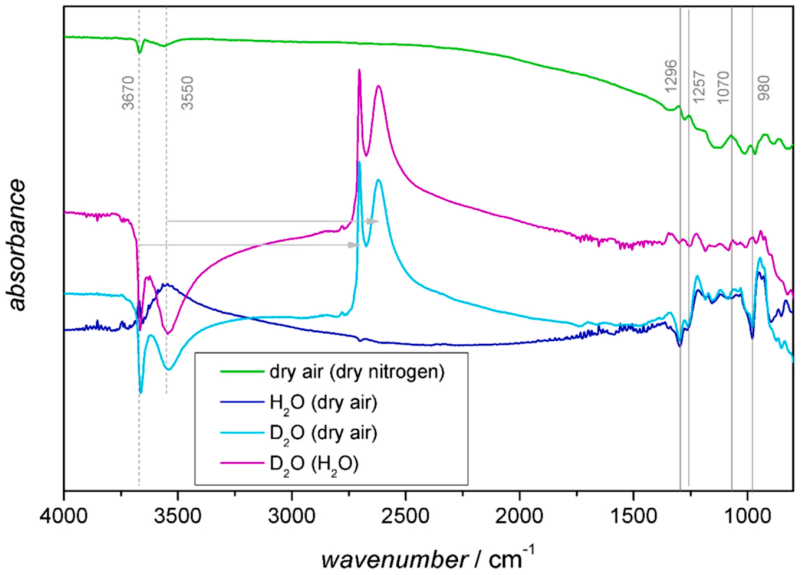

Fig. 2. DRIFT absorbance spectra of NiO at 250 °C during the exposure to air (20.5% O_2 in N_2) and water (in form of H_2O and D_2O vapors, both as 10% r.h. at 25 °C). The corresponding reference condition for each spectrum is given in parenthesis.

This process consumes additional three electrons. An additional feature in the spectra is two decreasing bands at 3670 and 3550 cm^{-1}. The sharp one centered at 3670 cm^{-1} can be attributed to an "isolated" OH group coordinated with three or less surrounding Ni atoms [26,27]. Both the defective NiO(100) and the Ni terminated NiO(111) surfaces offer suitable sites for this kind of isolated OH groups [7,25,26,28]. The broad band around 3550 cm^{-1} is attributed to "rooted" OH groups with a higher coordination number [23,25]. In the absence of oxygen, the equilibrium in (1) is more on the left side and more Ni-sites are available for the adsorption of OH groups. There is a competition of oxygen and OH groups for the same surface sites, which is also different from the case of, e. g. In_2O_3 and SnO_2 [29–31].

After the exposure of the surface to water vapor, the same two bands, which have been attributed to hydroxyl groups are increasing. The band at 3550 cm^{-1} is increasing more and indicates that water is adsorbed at oxygen vacancies with higher coordination for OH groups. It is of special interest that the bands assigned to Ni-O, are decreasing, but not the one at 1070 cm^{-1}. Even though both kinds of peaks are related to oxygen they need to be analyzed separately. The absence of a signal at 1070 cm^{-1} indicates that the surface coverage with O_2^- is unchanged and, consequently, oxygen and water do not compete for the same sites at the NiO surface. A competition with oxygen would also result in an

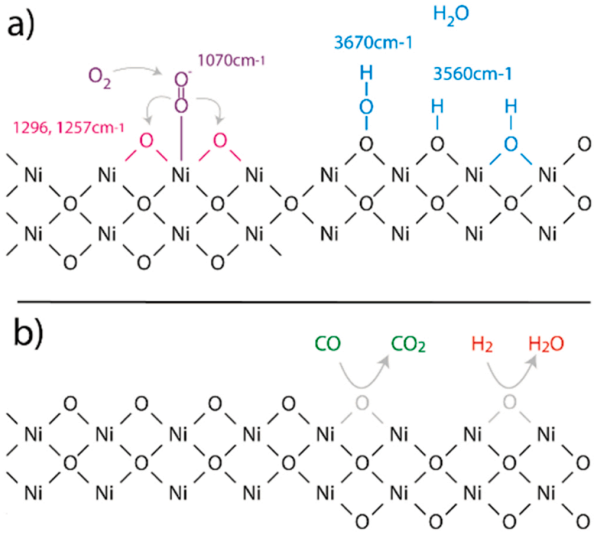

Fig. 3. Illustrations of reactions at the Ni(111) surface: a) adsorption and dissociation of O_2 (left) and possible reactions of H_2O (right). b) Oxidation of the surface by CO and hydrogen.

electrical effect by shifting (1) to the left side. On the other hand, if the decrease of Ni-O is interpreted as the removal or displacement of oxygen, one would expect a decrease of the aforementioned band as well, according to reaction (2). Hence, the decreasing bands for Ni-O vibrations at 1296, 1257 and 980 cm^{-1} should rather be interpreted as a conversion of surface hydrogen to hydroxyl groups. One option is the formation of two rooted hydroxyls:

$$V_O^{\cdot\cdot} + H_2O + O_O^{\times} \rightarrow 2OH_O^{\cdot} \quad (3)$$

Alternatively, the formation of a rooted and an isolated OH group has to be considered:

$$H_2O + O_O^{\times} \rightarrow OH_O^{\cdot} + (OH - Ni)_{Ni}{}' \quad (4)$$

The reaction does not capture or release any additional electrons and is in line with the negligible electrical effect.

In order to confirm the assignments in the spectra, the experiment has been repeated with D_2O vapor. The D_2O spectrum is referenced to the dry condition and, additionally, to the sample in the same concentration of H_2O. Not only are new OD groups formed (at 2703 and 2621 cm^{-1}), but also the preexisting OH groups ones are rapidly replaced by OD groups. The decrease of the band at 3670 cm^{-1} during the D_2O exchange is more intense compared to the increase during H_2O exposure and thus reveals that the surface is already covered with many isolated OH groups in dry conditions. Reports indicate that the NiO (111) surface, which is the dominant surface for our sample, is very reactive to OH groups [7,25].

3.4. CO and H_2 gas sensing: DRIFTS insights

Fig. 4 shows the DRIFT absorbance spectra for H_2 and CO. In addition, the inverted spectrum of the O_2 exposure, e.g. the spectrum in N_2 with air as reference, has been added. There are no other peaks to be identified for H_2 and CO than in the O_2 spectrum. Accordingly, the same kinds of surface reactions have to be considered. The DRIFTS acquired during the reaction with CO and H_2 – just like the electrical results – are very similar to each other, and are marked by the formation of OH groups. These findings are unexpected, especially since CO itself is not able to form OH groups whereas hydrogen could simply react with lattice oxygen:

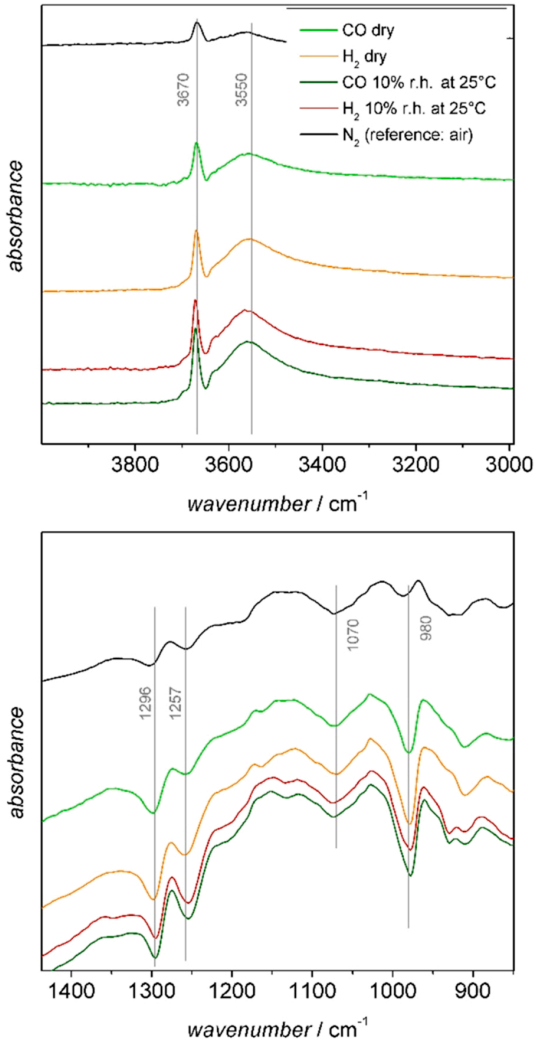

Fig. 4. DRIFT absorbance spectra of CO and H_2 in different background humidities. The reference is air with the same humidity. Additionally, a spectrum in N_2 with air as reference is shown.

$$H_2O + O_O^{\times} \rightarrow OH_O^{\cdot} + (OH - Ni)_{Ni}{}' \quad (5)$$

For other materials this direct reaction of hydrogen has been proposed by DRIFTS studies [31] but keeping in mind that the intensity of OH groups in the spectra during CO and H_2 reactions are similar, this is not considered to be relevant for NiO.

On top of that a decrease in Ni-O vibrations and Ni-$O_2^{\cdot}$ can be observed in all background atmosphere conditions (dry air, humid air, and dry N_2). It has to be noted that no additional peaks which may be linked to carbonate or carbonyl species could be observed during the reaction with CO. This observation is further backed up by experiments performed with isotopically labelled CO. The difference spectrum 12–13 C confirmed that there are no shifted peaks (except for the gas phase CO at 2140 cm^{-1} and CO_2 at 2340 cm^{-1}) and thus no species containing carbon atoms from CO that remain at the surface.

The reaction relevant for the reception of CO is the oxidation to CO_2 with lattice oxygen:

$$CO + O_O^{\times} \rightarrow CO_2 + V_O^{\cdot\cdot} + 2e^- \quad (6)$$

The process is illustrated in Fig. 3b. Immediately afterwards water is

reacting with the vacancy, as described in Eq. (4) to provide OH groups. For this reaction already the small amount of H_2O in the residual background humidity is sufficient. In total, the process can be described like this:

$$CO + H_2O + 2O_O^{\times} \rightarrow 2OH_O + CO_2 + 2e^- \quad (7)$$

In this way the reaction of CO creates new reactive sites for water vapor instead of competing for them, which is different as in the case of SnO_2, In_2O_3 or WO_3 [32]. The reaction of CO in air leads to more intense peaks and to higher sensor signals compared to the switch form air to nitrogen. An active reducing agent in the presence of air is apparently more effective than just the removal of oxygen from the atmosphere.

For the reaction with H_2 the formation of the same OH groups as for CO and similarly a decrease in Ni-O and Ni-O_2^- species can be observed with DRIFTS (Fig. 4). This suggests that the reaction with NiO is based on the reduction of the oxide:

$$H_2 + O_O^{\times} \rightarrow H_2O + V_O^{\cdot\cdot} + 2e^- \quad (8)$$

In dry N_2 background the sensor signals and the decrease of Ni-O_2^- and NiO are stronger than in air. In N_2 additional adsorption sites are available for OH groups that are otherwise blocked by oxygen ions and only in the absence of oxygen the H_2 can effectively shift the equilibrium towards OH groups without having a re-oxidation. The sensor signals for hydrogen are slightly higher in the presence of background humidity. This is remarkable, because one can conclude that H_2 and H_2O are not competing for the same sites, such as for example on SnO_2 [15]. The baseline resistance of the investigated NiO material is almost unaffected by water vapor, whose main reaction is the filling of oxygen vacancies with OH groups. This makes the material very different to other commonly used materials. On SnO_2, depending on the temperature, there is a strong competition between water and reducing gases for certain adsorption sites, which typically results in decreased sensor signals in humid conditions [33,34]. A competition of water and reducing gases for mutual reactive sites was also reported for In_2O_3 [24, 32], but in contrast to SnO_2, the formation of OH groups is more favored. The relationship of WO_3 however is ambiguous: At low temperatures there is a competition of water with oxygen for the same sites while at higher temperatures water can oxidize the surface by releasing its hydrogen atoms and in this way promote the reception of reducing gases in humid atmosphere [35]. For SnO_2 a correlation between the electrical effect of humidity and the formation of hydroxyl groups has been reported [15]. It is assumed that the same underlying mechanisms are responsible for the reception of water vapor on NiO, namely the conversion of surface oxygen to hydroxyl groups and the competition of H_2O and O_2 for different sites.

4. Conclusions

Nickel oxide showed good response to CO and H_2 in both dry and humid conditions. From DRIFTS results it is evident that O_2, H_2, and CO have very similar surface reactivity. Out of these findings we conclude that the reception on NiO is based purely on the reduction and oxidation of the material and not on the formation of specific ionic species at the surface. Moreover, it could be demonstrated that water has no reducing effect on NiO and that water is not competing for the same reaction sites as CO or H_2. All of these findings combined outline the special behavior of NiO compared to other commonly used SMOX.

Funding

This work was supported by the Romanian Ministry of Research, Innovation and Digitization, CNCS-UEFISCDI, through the projects PN-III-P4-ID-PCE-2020-0506 and PN-III-P4-PCE-2021-0384 within PNCDI III and Core Program of the National Institute of Materials Physics through the Project PC1- PN23080101.

CRediT authorship contribution statement

Cristian. E. Simion: Conceptualization, Investigation, Funding acquisition, Visualization, Writing – original draft. **Benjamin Junker:** Investigation, Visualization, Writing – original draft. **Udo Weimar:** Supervision. **Adelina Stanoiu:** Conceptualization, Supervision, Funding acquisition. **Nicolae Bârsan:** Supervision, Writing – review & editing.

Declaration of Competing Interest

The authors declare that they have no known competing financial interests or personal relationships that could have appeared to influence the work reported in this paper.

Data Availability

Data will be made available on request.

References

[1] P. Manojreddy, S. Itapu, J.K. Ravali, S. Sakkarai, Tuning the electrical parameters of p-NiOx-Based thin film transistors (TFTs) by pulsed laser irradiation, Condens. Matter 6 (2) (2021) 21, https://doi.org/10.3390/condmat6020021.
[2] T.P. Mokoena, H.C. Swart, D.E. Motaung, A review on recent progress of p-type nickel oxide based gas sensors: Future perspectives, J. Alloy. Compd. 805 (2019) 267–294, https://doi.org/10.1016/j.jallcom.2019.06.329.
[3] N. Barsan, C. Simion, T. Heine, S. Pokhrel, U. Weimar, Modeling of sensing and transduction for p-type semiconducting metal oxide based gas sensors, J. Electroceram. 25 (2010) 11–19, https://doi.org/10.1007/s10832-009-9583-x.
[4] R.L. Wilson, C.E. Simion, A. Stanoiu, A. Taylor, S. Guldin, J.A. Covington, C. J. Carmalt, C.S. Blackman, Humidity-Tolerant ultrathin NiO gas-sensing films, ACS Sens 5 (5) (2020) 1389–1397, https://doi.org/10.1021/acssensors.0c00172.
[5] Y. Wang, Y. Zhou, Recent progress on anti-humidity strategies of chemiresistive gas sensors, Materials 15 (24) (2022) 8728, https://doi.org/10.3390/ma15248728.
[6] P. Gupta, S. Maurya, N.K. Pandey, V. Verma, Structural, electrical and humidity sensing properties of nano-structured nickel oxide prepared by sol–gel method, J. Mater. Sci.: Mater. Electron. 32 (2021) 3529–3542, https://doi.org/10.1007/s10854-020-05099-4.
[7] D. Cappus, C. Xu, D. Ehrlich, B. Dillmann, C.A. Ventrice, K. Al Shamery, H. Kuhlenbeck, H.-J. Freund, Hydroxyl groups on oxide surfaces: NiO(100), NiO (111) and Cr_2O_3(111), Chem. Phys. 177 (2) (1993) 533–546, https://doi.org/10.1016/0301-0104(93)80031-4.
[8] K. Zhu, S.K. Frehan, G. Mul, A. Huijser, Dual role of surface hydroxyl groups in the photodynamics and performance of NiO-Based photocathodes, J. Am. Chem. Soc. 144 (24) (2022) 11010–11018, https://doi.org/10.1021/jacs.2c04301.
[9] I. Hotovy, V. Rehacek, P. Siciliano, S. Capone, L. Spiess, Sensing characteristics of NiO thin films as NO_2 gas sensor, Thin Solid Films 418 (1) (2002) 9–15, https://doi.org/10.1016/S0040-6090(02)00579-5.
[10] A. Stanoiu, C. Ghica, C.G. Mihalcea, D. Ghica, S. Somacescu, O.G. Florea, C. E. Simion, Effects of calcination temperature on CO-Sensing mechanism for NiO-Based gas sensors, Chemosensors 10 (5) (2022) 191, https://doi.org/10.3390/chemosensors10050191.
[11] N.K. Das, T. Shoji, T. Nishizumi, T. Fukuoka, T. Sugawara, R. Sasaki, T. Tatsuki, H. Yuya, K. Ito, K. Sakima, K. Tsutsumi, S. Ooki, Y. Sueishi, K. Takeda, First-principles calculations of hydrogen interactions with nickel containing a monovacancy and divacancies, https://ui.adsabs.harvard.edu/link_gateway/2017MRE.4g6505D/, Mater. Res. Express 4 (7) (2017), 076505, https://doi.org/10.1088/2053-1591/aa7afb.
[12] Y. Fukai, N. Okuma, Evidence of copious vacancy formation in Ni and Pd under a high hydrogen pressure, Jpn. J. Appl. Phys. 32 (9A) (1993) L1256–L1259, https://doi.org/10.1143/JJAP.32.L1256.
[13] D. Tanguy, Y. Wang, D. Connétable, Stability of vacancy-hydrogen clusters in nickel from first-principles calculations, Acta Mater. 78 (2014) 135–143, https://doi.org/10.1016/j.actamat.2014.06.021.
[14] Q. Xu, S. Cheah, Y. Zhao, Initial reduction of the NiO(100) surface in hydrogen, J. Chem. Phys. 139 (2013), 024704, https://doi.org/10.1063/1.4812824.
[15] J.A. Rodriguez, J.C. Hanson, A.I. Frenkel, J.Y. Kim, M. Pérez, Experimental and theoretical studies on the reaction of H_2 with NiO: role of O vacancies and mechanism for oxide reduction, J. Am. Chem. Soc. 124 (2) (2002) 346–354, https://doi.org/10.1021/ja0121080.
[16] S. Wicker, M. Guiltat, U. Weimar, A. Hémeryck, N. Barsan, Ambient humidity influence on CO detection with SnO_2 gas sensing materials. A combined DRIFTS/DFT investigation, J. Phys. Chem. C. 121 (45) (2017) 25064–25073, https://doi.org/10.1021/acs.jpcc.7b06253.
[17] V. Nagarajan, R. Chandiramouli, NiO nanocone as a CO sensor: DFT investigation, Struct. Chem. 25 (2014) 1765–1771, https://doi.org/10.1007/s11224-014-0451-1.
[18] Y. Bai, D. Kirvassilis, L. Xu, M. Mavrikakis, Atomic and molecular adsorption on Ni (111), Surf. Sci. 679 (2019) 240–253, https://doi.org/10.1016/j.susc.2018.08.004.

[19] S. Dey, N.S. Mehta, Oxidation of carbon monoxide over various nickel oxide catalysts in different conditions: A review, Chem. Eng. J. Adv. 1 (2020), 100008, https://doi.org/10.1016/j.ceja.2020.100008.
[20] N. Barsan, D. Koziej, U. Weimar, Metal-oxide based gas sensor research: How to? Sens, Actuators B: Chem. 121 (1) (2007) 18–35, https://doi.org/10.1016/j.snb.2006.09.047.
[21] B. Saruhari, R.L. Fomekong, S. Nahirmiak, Review: influences of semiconductor metal oxide properties on gas sensing characteristics, Front. Sens. 2 (2021), 657931, https://doi.org/10.3389/fsens.2021.657931.2.
[22] I. Bohme, U. Weimar, N. Barsan, Unraveling the surface chemistry of CO sensing with In_2O_3 based gas sensors, Sens. Actuators B: Chem. 326 (2021), 129004, https://doi.org/10.1016/j.snb.2020.129004.
[23] A.A. Davydov, Molecular Spectroscopy of Oxide Catalyst Surfaces, 690, Wiley, Chichester, 2003.
[24] M.M. Natile, A. Glisenti, Surface reactivity of NiO: interaction with methanol, Chem. Mater. 14 (12) (2002) 4895–4903, https://doi.org/10.1021/cm0211047.
[25] A.A. Tsyganenko, T.A. Rodionova, V.N. Filimonov, Infrared studies of low temperature adsorption of oxygen on NiO surface, React. Kinet. Catal. Lett. 11 (1979) 113–116, https://doi.org/10.1007/BF02074196.
[26] J.N. Kondo, T. Yuzawa, J. Kubota, K. Domen, C. Hirose, IRAS study of hydroxyl species on NiO/Ni(110): formation and isotope exchange reaction, Surf. Sci. 343 (1–2) (1995) 71–79, https://doi.org/10.1016/0039-6028(95)00812-8.
[27] B. Pejova, T. Kocareva, M. Najdoski, I. Grozdanov, A solution growth route to nanocrystalline nickel oxide thin films, Appl. Surf. Sci. 165 (4) (2000) 217–278, https://doi.org/10.1016/S0169-4332(00)00377-9.
[28] B. Liu, M. Wang, S. Liu, H. Zheng, H. Yang, The sensing reaction on the Ni-NiO (111) surface at atomic and molecule level and migration of electron, Sens. Actuators B: Chem. 273 (2018) 794–803, https://doi.org/10.1016/j.snb.2018.06.102.
[29] A. Gurlo, Interplay between O_2 and SnO_2: oxygen Ionosorption and spectroscopic evidence for adsorbed oxygen, Chem. Phys. Chem. 7 (10) (2006) 2041–2052, https://doi.org/10.1002/cphc.200600292.
[30] N. Yamazoe, K. Suematsu, K. Shimanoe, Two types of moisture effects on the receptor function of neat tin oxide gas sensor to oxygen, Sens. Actuators B: Chem. 176 (2013) 443–452, https://doi.org/10.1016/j.snb.2012.08.060.
[31] R.G. Pavelko, H. Daly, C. Hardacre, A.A. Vasiliev, E. Llobet, Interaction of water, hydrogen and their mixtures with SnO_2 based materials: the role of surface hydroxyl groups in detection mechanisms, Phys. Chem. Chem. Phys. 12 (2010) 2639–2647, https://doi.org/10.1039/B921665K.
[32] (a) A. Staerz, U. Weimar, N. Barsan, Current state of knowledge on the metal oxide based gas sensing mechanism, Sens. Actuators B: Chem. 358 (2022), 131531, https://doi.org/10.1016/j.snb.2022.131531;
(b) A.A. Tsyganenko, V.N. Filimonov, Infrared spectra of surface hydroxyl groups and crystalline structure of oxides, J. Mol. Struct. 19 (1973) 579–589, https://doi.org/10.1016/0022-2860(73)85136-1.
[33] D. Degler, S. Wicker, U. Weimar, N. Barsan, Identifying the active oxygen species in SnO_2 based gas sensing materials: an operando IR spectrsocopy study, J. Phys. Chem. C. 119 (21) (2015) 11792–11799, https://doi.org/10.1021/acs.jpcc.5b04082.
[34] D. Degler, B. Junker, F. Allmendinger, U. Weimar, N. Barsan, Investigations on the temperature-dependent interaction of water vapor with tin dioxide and its implications on gas sensing, ACS Sens 5 (10) (2020) 3207–3216, https://doi.org/10.1021/acssensors.0c01493.
[35] A. Staerz, A. Kobald, T. Russ, U. Weimar, A. Hémeryck, N. Barsan, Thermal water splitting on the WO_3 surface: experimental proof, ACS Appl. Electron. Mater. 2 (10) (2020) 3254–3262, https://doi.org/10.1021/acsaelm.0c00577.

Cristian Eugen Simion received his Ph.D. (2011) in Condensed Matter Physics from University of Bucharest-Faculty of Physics. Presently he is senior researcher in the Gas Sensors Group at the National Institute of Materials Physics, Bucharest-Magurele, Romania. His field of interest is metal oxides solid state gas sensors.

Benjamin Junker received his M.Sc. in chemistry from the University of Tübingen in 2020. Currently he is a Ph.D. student in the research group of Udo Weimar and Nicolae Bârsan. His research is focused on perovskite gas sensors and operando spectroscopy

Udo Weimar received his diploma in physics in 1989, his Ph.D. in chemistry in 1993 and his Habilitation in 2002 from the University of Tuebingen. Since 2010, he is a full professor in the Department of Chemistry at the University of Tuebingen. His research interest focuses on chemical sensors as well as on multicomponent analysis and pattern recognition.

Adelina Stanoiu received her Ph.D. (2007) in Condensed Matter Physics from University of Bucharest-Faculty of Physics. Presently she is the leader of the Gas Sensors Group as senior researcher at the National Institute of Materials Physics, Bucharest-Magurele, Romania. With more than 30 years of experience in the field, her scientific work focuses on both fundamental and experimental research in the field of gas sensors based on metal oxide semiconductors.

Nicolae Barsan received his diploma in Physics from the Faculty of Physics of the Bucharest University in 1982. In 1993 his received his Ph.D. in Solid State Physics from the Institute of Atomic Physics, Bucharest, Romania. Since 1995 he has been a senior researcher at the Institute of Physical Chemistry of the University of Tuebingen, where he and Udo Weimar lead the Gas Sensors Group.

ACS SENSORS

pubs.acs.org/acssensors Article

Modeling the Conduction Mechanism in Chemoresistive Gas Sensor Based on Single-Crystalline Sn_3O_4 Nanobelts: A Phenomenological In Operando Investigation

Pedro H. Suman,* Benjamin Junker, Udo Weimar, Marcelo O. Orlandi, and Nicolae Barsan*

Cite This: https://doi.org/10.1021/acssensors.3c01810 Read Online

ACCESS | Metrics & More | Article Recommendations | Supporting Information

ABSTRACT: Investigating the sensing mechanisms in semiconducting metal oxide (SMOx) gas sensors is essential for optimizing their performance across a wide range of potential applications. Despite significant progress in the field, there are still many gaps in comprehending the phenomenological processes occurring in one-dimensional (1D) nanostructures. This article presents the first insights into the conduction mechanism of chemoresistive gas sensors based on single-crystalline Sn_3O_4 nanobelts using the operando Kelvin Probe technique. From this approach, direct current (DC) electrical resistance and work function changes were simultaneously measured in different working conditions, and a correlation between the conductance and the surface band bending was established. Appropriate modeling was proposed, and the results revealed that the conduction mechanism in the single-crystalline one-dimensional nanostructures closely aligns with the behavior observed in single-crystalline epitaxial layers rather than in polycrystalline grains. Based on this assumption, relevant parameters were further estimated, including Debye length, concentration of free charge carriers, effective density of states in the conduction band, and position of the Fermi level. Overall, this study provides an effective contribution to understanding the role of surface chemistry in the transduction of the electrical signal generated from gas adsorption in single-crystalline one-dimensional nanostructures.

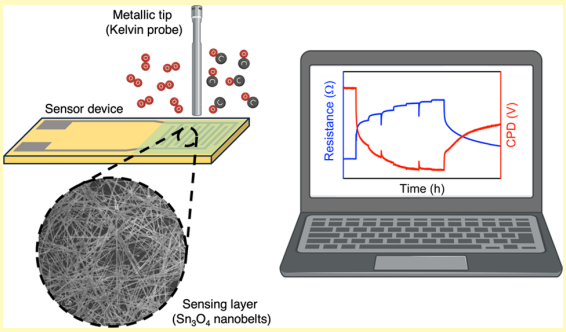

KEYWORDS: *tin oxide, Sn_3O_4, single-crystalline nanobelts, one-dimensional nanostructures, semiconducting metal oxide (SMOx), gas sensing, conduction mechanism*

The increasing demands of modern society have stimulated the rapid development of sensing technologies to address an extensive array of challenges and requirements. Chemoresistive gas sensors have emerged as operational devices capable of detecting numerous gaseous compounds by taking advantage of the unique electrical and chemical properties of semiconducting metal oxides (SMOx) used as active elements.[1−3] Their operating principles are based on the interplay of physical and chemical processes, essentially involving surface reactions and subsequent charge transfer dynamics (reception and transduction mechanisms, respectively). One prominent benefit of SMOx gas sensors is that they can be engineered through cost-effective and versatile approaches, offering excellent compatibility for miniaturization and reasonable energy consumption. These features enable their integration into state-of-the-art sensing platforms for applications in environmental monitoring, indoor air quality management, food industries, agriculture, and healthcare.[4−9]

Tin(IV) oxide (SnO_2) was a pioneering inorganic compound employed in sensitive layers of commercial solid-state chemical sensors.[10] Even today, it remains a key material for gas detection, along with ZnO, In_2O_3, and WO_3.[11−13] Among a wide range of other possible Sn_xO_y stoichiometries predicted by theoretical calculations,[14] Sn_3O_4 is a mixed-valence tin oxide (Sn^{2+}, Sn^{4+}, and O^{2-}) that exhibits n-type semiconductor behavior and an optical bandgap of approximately 2.7 eV.[15−17] Accordingly, the functionalities of Sn_3O_4 have been explored in many research fields.[18−24] In 2014, we reported the first results on the gas sensing properties of Sn_3O_4,[16] followed by a more detailed investigation focusing on NO_2 detection.[25] The studied material consists of single-crystalline layered Sn_3O_4 nanobelts, which grow along the (101) plane direction of the triclinic crystal system.[16] Additional cross-sectional analyses using high-resolution transmission electron microscopy (HRTEM) revealed the epitaxial stacking of multilayers oriented in the [010] direction. These

Received: August 30, 2023
Revised: November 20, 2023
Accepted: December 22, 2023

https://doi.org/10.1021/acssensors.3c01810
ACS Sens. XXXX, XXX, XXX−XXX

findings suggested that the exposed facets, containing a larger concentration of available surface sites for solid−gas interactions, align with the (010) plane. However, despite the outstanding sensing performance observed in the nanobelts and other Sn_3O_4 architectures,[26−28] fundamental concepts concerning the reception and transduction mechanisms are still incompletely understood and require further examination.

The Kelvin Probe (KP) method has been a powerful analytical tool to study the surface properties of SMOx materials under working conditions.[29−32] The sensing mechanism in porous sensing layers consisting of polycrystalline grains was thoroughly investigated using this technique, revealing that the oxygen concentration in the background controls the conduction across the channel.[33] The proposed model was extended to analyze the role of grain size[34] and additives (dopants/loadings from noble metals)[34,35] on the conduction of SnO_2-based gas sensors. Moreover, it was also applied to elucidate the lower sensor signals (S) observed in p-type semiconductors (CuO and Cr_2O_3) compared to n-type semiconductors with similar morphological characteristics and depletion/accumulation layer dimensions ($S_p \approx \sqrt{S_n}$).[36−38] Nevertheless, given that the validation of the existing models is limited to sensitive layers composed of polycrystalline grains, investigation of the sensing phenomena occurring in alternative architectures is demanded. One-dimensional (1D) nanostructures, including nanowires, nanotubes, and nanobelts, have been particularly attractive building blocks for manufacturing advanced gas sensing devices due to the high surface-to-volume ratio and confined electronic transport in one direction.[39−43] Consequently, a comprehensive examination of the conduction process at their interfaces becomes essential for optimizing their sensing properties.

In this context, this work presents a phenomenological investigation of the gas sensing mechanism in single-crystalline Sn_3O_4 nanobelts through operando work function measurements. Qualitative modeling of the transduction of electrical signals generated by gas adsorption was achieved by correlating variations in direct current (DC) electrical resistance with changes in surface band bending while exposing the sensor to different O_2 and CO concentrations in an N_2 background at 200 and 300 °C. To the best of our knowledge, this study reports the first examination of the conduction mechanism in one-dimensional Sn_3O_4 nanostructures under operating conditions. Therefore, a significant contribution to new concepts and materials in gas sensing technology is expected from our findings using this tin oxide with unusual surface stoichiometry and structure as the sensing material.

EXPERIMENTAL SECTION

Synthesis of Sn_3O_4 Nanobelts. Single-crystalline Sn_3O_4 nanobelts were synthesized using the carbothermal reduction method, following the optimized experimental parameters described in our earlier study.[16] In brief, a mixture of SnO_2 (Sigma-Aldrich, 99.9% purity) and carbon black (Union Carbide, >99% purity) was heated to 1135 °C in a tightly controlled synthesis environment within a tubular furnace. The carrier gas was established from a mixture of N_2 and O_2 with a specific ratio. The obtained material was analyzed using X-ray diffraction (XRD), field emission scanning electron microscopy (FESEM), high-resolution transmission electron microscopy (HRTEM), and adsorption−desorption experiments to determine the specific surface area employing the Brunauer−Emmett−Teller (BET) method. The results were discussed in detail in our previous works[16,44] and are summarized in Figure S1. XRD analyses revealed that the synthesized material grows from the triclinic structure of Sn_3O_4 (JCPDS card #16-0737), with a minor amount of the tetragonal phase of SnO_2 (JCPDS card #41-1445). SEM characterization showed that the Sn_3O_4 nanobelts maintain a homogeneous width of approximately 150 nm along their length, with the length on the order of tens of micrometers (average of 30 μm). Additionally, HRTEM analyses confirmed the single-crystalline nature of the Sn_3O_4 nanobelts, validating their phase through the interplanar distances and angles between the identified crystalline planes.

Sensor Fabrication. The sensing layer was fabricated by mixing the Sn_3O_4 nanobelts with 1,2-propanediol (Sigma-Aldrich, >99.5% ACS reagent) to form a homogeneous paste. The paste was then screen-printed onto Al_2O_3 substrates patterned with interdigitated platinum electrode arrays on the topside (300 μm Pt fingers spaced 300 μm apart; Ceramtec AG, Germany) and an independent platinum self-heating circuit on the backside. The sensor was dried overnight at 80 °C and subsequently annealed at 325 °C for 30 min to remove residual solvent and enhance the adherence and stability of the sensing layer.

Operando Work Function Measurements. The Kelvin Probe technique was employed for simultaneous DC electrical resistance and work function measurements, using an appropriate experimental setup (McAllister Technical Services; KP 6500).[29,45] A metallic reference electrode, composed of stainless steel coated with an insulating layer, was positioned at a distance d over the sensing layer and set to oscillate at 233 Hz in a noncontact mode. Changes in the contact potential difference (CPD) between the surface of the sensing layer and the reference electrode were measured as a function of gas composition. Simultaneously, the DC electrical resistance was recorded using a picoammeter/voltage source (Keithley 6487) by applying a constant polarization voltage of 0.2 V. A computer-controlled gas mixing system unit equipped with mass-flow controllers (MFC; Bronkhorst) and data acquisition cards provided the specified amount of the target gases into the test chamber, maintaining a total flow of 400 mL/min during the experiments. The sensor was equilibrated in dry N_2 for over 24h and subsequently exposed to stepwise increasing concentrations of O_2 (ranging from 200 to 205,000 ppm, each step lasting for 4 h) and CO (ranging from 35 to 250 ppm, each step lasting for 2 h) in a dry N_2 background. The heater of the sensors was connected to a power supply, and the operating temperatures were set at 200 and 300 °C.

The sensor signals for O_2 and CO were calculated from eqs 1 and 2, respectively.

$$S = \frac{R_{O_2}}{R_{N_2}} \tag{1}$$

$$S = \frac{R_{N_2}}{R_{CO}} \tag{2}$$

where R_{O_2} and R_{CO} are the resistances in the presence of the target gases (O_2 and CO) and R_{N_2} is the resistance in the background condition (N_2).

Assuming that the work function of the reference electrode is unaffected by the gas atmosphere inside the chamber, the relationship between the measured CPD data and the corresponding work function changes ($\Delta\Phi$) of the sensing layer was estimated from eq 3.

$$\Delta CPD = -\frac{\Delta\Phi}{e} \tag{3}$$

where e is the elementary electron charge.

The work function (Φ) of a semiconductor is expressed mathematically from the contribution of three components: the band bending (eV_S), the electron affinity (χ), and the difference in energy between the Fermi level and the conduction band into the bulk ($E_{C,b} - E_F$), as shown in eq 4. At the selected operating temperatures (200 and 300 °C), the thermal energy is not sufficiently high to promote gas reactions into the bulk. Since the gas−solid interactions are restricted to the sensing layer's surface, the bulk properties remain unaffected by the gas adsorption. Accordingly, the

https://doi.org/10.1021/acssensors.3c01810
ACS Sens. XXXX, XXX, XXX−XXX

ACS Sensors pubs.acs.org/acssensors Article

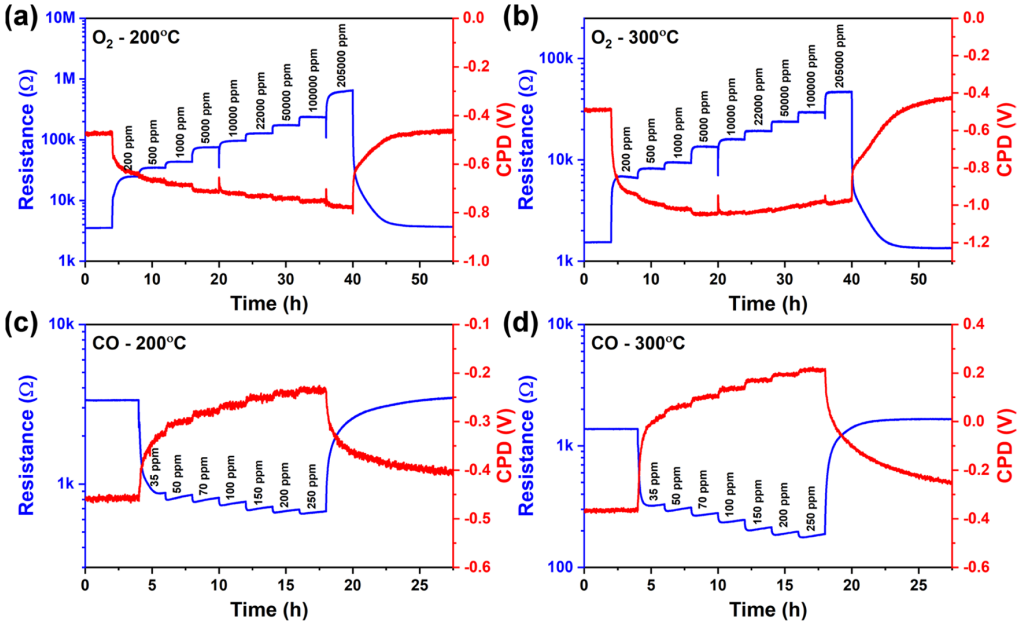

Figure 1. Simultaneous DC electrical resistance and contact potential difference (CPD) changes of the Sn_3O_4 nanobelts-based sensor under exposures to stepwise increasing concentrations of (a, b) O_2 and (c, d) CO in a dry N_2 background at 200 and 300 °C, respectively.

contribution of $\Delta(E_{C,b} - E_F)$ was neglected. Additionally, changes in electron affinity depend on the concentration of surface dipoles associated with hydroxyl groups originating from the water vapor adsorption. As the experiments were performed in a dry atmosphere (in fact, residual water vapor was <10 ppm) and assuming minor water vapor interference, the electron affinity is expected to remain constant during target gas exposures ($\Delta\chi = 0$). Therefore, the work function change is limited to the variation of the band bending (eV_S),[29,36] according to eq 5. Consequently, a relationship between the conductance and the surface band bending was established based on the obtained experimental data.

$$\Delta\Phi = e\Delta V_S + \Delta\chi + \Delta(E_{C,b} - E_F) \quad (4)$$

$$\Delta\Phi = e\Delta V_S \quad (5)$$

RESULTS AND DISCUSSION

Figure 1 shows the temporal evolution of the DC resistance (blue line) and CPD (red line) for the Sn_3O_4 nanobelts-based sensor at 200 and 300 °C. The measurements were performed as a function of stepwise increasing concentrations of O_2 (ranging from 200 to 205,000 ppm) and CO (ranging from 35 to 250 ppm) in a dry N_2 background. The results demonstrate that the presence of O_2 induced a simultaneous increase in resistance and a decrease in CPD at both operating temperatures (Figure 1a,b). Conversely, the resistance and CPD followed the opposite trend under CO exposures (Figure 1c,d). These findings are consistent with the previously reported n-type semiconductor behavior of the Sn_3O_4 nanobelts in synthetic dry air.[16,25] Although the absence of oxygen in the background led to relatively slow recovery kinetics, the Sn_3O_4 sensor exhibited a reversible response as the resistance recovered to its initial values following the last exposure steps to O_2 and CO. However, a slight upward drift in the CPD occurred at the end of the CO measurement. Notably, Figure 1b reveals an upward drift of the CPD after exposure to 5000 ppm of O_2 at 300 °C. This behavior was absent in second-run measurement, as shown in Figure S2. It is attributed to the use of a homemade instrument setup for recording the CPD data, which may provide a drifted signal in long-term measurements. The sensor signals and corresponding band bending changes were calculated as a function of the O_2 and CO concentrations, and the results are presented in Figure S3.

The detailed description of the surface chemistry is out of the scope of this work. Nevertheless, the general understanding of the reaction mechanisms for n-type semiconductors operating between 200 and 400 °C is described in terms of the ionosorption of O_2.[1,46,47] Initially, acceptor levels are created through the adsorption of oxygen molecules on available surface sites, typically oxygen vacancies in n-type semiconductors; the adsorption can be dissociative, and molecular and atomic oxygen are formed by capturing electrons from the conduction band.[1] Depending on the nature of the adsorption site and the atomic and molecular nature of the oxygen ions, some of them can also be incorporated into the surface lattice of the oxide, as demonstrated for SnO_2,[48] WO_3,[49] and In_2O_3.[50] The most important result is the localization of the delocalized free charge carriers and the resulting negative surface charging that leads to the appearance of a space-charge region and an increase in resistance due to upward band bending. The sensing mechanism of SMOx gas sensors for detecting reducing gases in a dry N_2 background differs from that under standard ambient conditions. In the presence of atmospheric oxygen, reducing gases, including CO, interact with preadsorbed oxygen, releasing trapped electrons back into the conduction band of the semiconductors. In this situation, water vapor is an interfering compound, acting as a reducing gas and playing a determining role in the reception mechanism. In an oxygen-free environment, preadsorbed oxygen species are absent, and the surface acceptor states related to oxygen ionosorption are assumed to be neglected. This condition

https://doi.org/10.1021/acssensors.3c01810
ACS Sens. XXXX, XXX, XXX−XXX

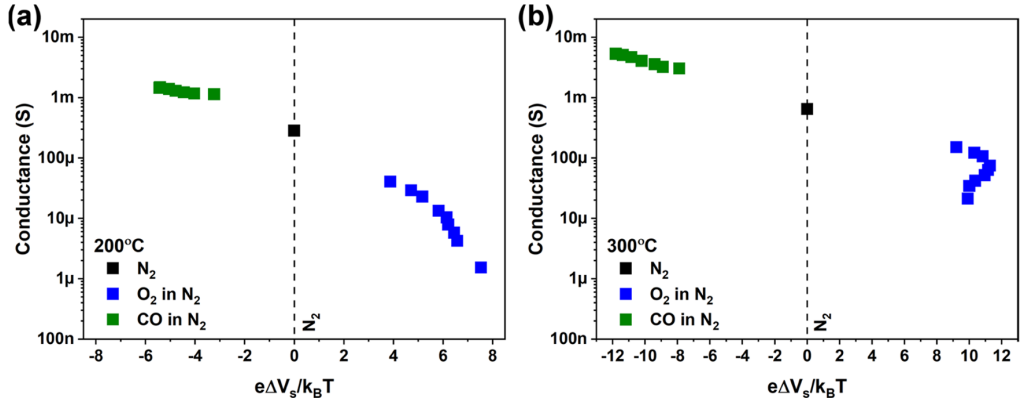

Figure 2. Correlation between the conductance and the associated changes in band bending, expressed in terms of the thermal energy (k_BT), for the Sn_3O_4 nanobelts-based sensor taken under exposures to different O_2 and CO concentrations in a dry N_2 background at (a) 200 °C and (b) 300 °C.

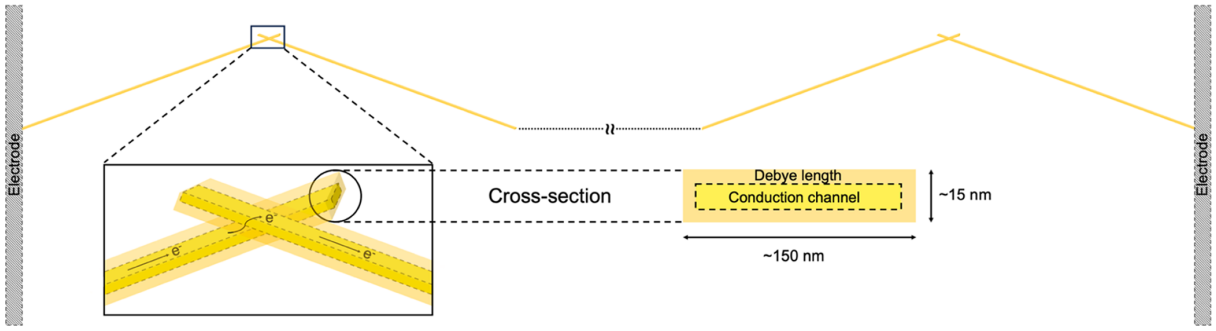

Figure 3. Schematic representation of the conducting channel consisting of connected Sn_3O_4 nanobelts between the interdigitated electrodes.

allows one to isolate the specific effects of CO adsorption on the conduction mechanisms without interference from oxygen and water vapor. The detection process takes place through the reduction of the material's surface, consuming lattice oxygen and generating oxygen vacancies ($V_0^{\bullet\bullet}$) and CO_2.[48,51] Electrons are injected into the conduction band, and the electrical resistance decreases due to the downward band bending.[48,51]

Figure 2 presents the relationship between the conductance and the corresponding changes in the band bending of the Sn_3O_4 nanobelts-based sensors at 200 and 300 °C. This correlation is shown in terms of the thermal energy (k_BT) from the data presented in Figure 1 and considering the reference point in the N_2 condition ($e\Delta V_s/k_BT = 0$). At 200 °C, the effect of O_2 adsorption on the band bending was stronger than that of CO adsorption. Examining the region during the O_2 exposures, a transition regime governing the conductance as a function of band bending was observed. An abrupt initial variation of the band bending occurred after the first pulse of O_2. Subsequently, the contribution of the O_2 adsorption to the conduction process was less effective for concentrations of up to 1000 ppm. Lastly, a relatively small change in the band bending led to a significant variation in the conductance above 1000 ppm of O_2 (from $e\Delta V_s/k_BT = 5.2$ at 200 °C). When the operating temperature was increased to 300 °C, an identical effect was found under the same experimental conditions. However, the transition regime was much more evident, as demonstrated by the sudden decrease in the conductance in the region above $e\Delta V_s/k_BT = 10.8$ at 300 °C.

Understanding the electronic transport path across the sensing layer is relevant for modeling the sensing mechanism in the Sn_3O_4 nanobelts-based sensors. The proposed model illustrated in Figure 3 depicts a conduction channel comprising multiple interconnected Sn_3O_4 nanobelts. Assuming these nanostructures as large and flat grains, the conduction between the interdigitated electrodes occurs initially through the core until the electrons reach their extremity. At the nanobelt−nanobelt junctions, the electrons must overcome the barriers to enable conduction through the core again.

The sensing mechanism in thick porous films, composed of connected polycrystalline grains, is basically described through the formation of intergranular back-to-back Schottky barriers. Upon exposure to the target gases, chemical reactions modulate the concentration of free charge carriers on the SMOx surface (n_s) by regulating the height of the barrier. In this situation, the electrical conductance (G) follows an exponential dependence on surface band bending (eV_S), as described in eq 6. Depending on the surrounding atmosphere, the conduction mechanism is controlled by either a depletion layer ($m = 1$; upward band bending) or an accumulation layer ($m \geq 2$; downward band bending) formed on the surface of the grain.

$$G \sim n_s \sim \exp\left(-\frac{eV_S}{mk_BT}\right) \tag{6}$$

On the other hand, the proposed model for the transduction function in single-crystalline/compact layer thin films[52]

https://doi.org/10.1021/acssensors.3c01810
ACS Sens. XXXX, XXX, XXX−XXX

ACS Sensors pubs.acs.org/acssensors Article

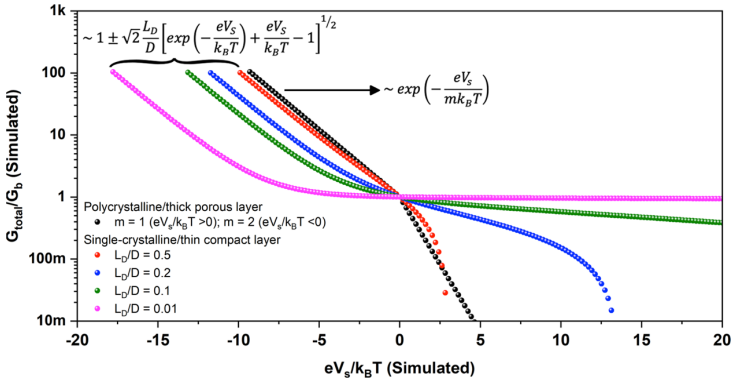

Figure 4. Simulated dependence between the normalized conductance and the associated changes in band bending, expressed in terms of the thermal energy (k_BT), according to the conduction models for the polycrystalline/thick porous layer and single-crystalline/thin compact layer for different values of m and L_D/D for the respective models.

postulates that the relationship between the conductance (G_{total}) and the band bending is expressed by eq 7. The signs "+" and "−" indicate a conduction mechanism controlled by an accumulation and a depletion layer, respectively.

$$G_{total} = G_b\left\{1 \pm \sqrt{2}\frac{L_D}{D}\left[\exp\left(-\frac{eV_S}{k_BT}\right)+\frac{eV_S}{k_BT}-1\right]^{1/2}\right\} \quad (7)$$

where G_b is the conductance in the bulk, L_D is the Debye length, D is the thickness, k_B is the Boltzmann constant, and T is the temperature.

Figure 4 illustrates the relationship between the normalized conductance (G_{total}/G_b) and the surface band bending for both proposed models, expressed in terms of the k_BT units. In the case of the polycrystalline/thick porous layer, the values of m = 1 and 2 were considered in eq 6 to cover the depletion and the accumulation regions, respectively. Conversely, the model for single-crystalline/compact layer thin films was examined in four scenarios, assuming the values of 0.5, 0.2, 0.1, and 0.01 for the Debye length-to-nanobelt thickness ratio (L_D/D) in eq 7.

It is apparent from Figures 2 and 4 that the conductance change of the Sn_3O_4 nanobelts follows a similar profile to that of single-crystalline/compact layers, particularly when L_D/D = 0.5 or 0.2 in Figure 4. Notably, a sudden change in the slope and a significant decrease in the conductance were found at high upward band bendings, revealing that the surface effect extends throughout the entire volume of the layer. The results further suggest that the nanobelt−nanobelt barrier does not play the most important role in the overall conduction and the sensing effect mainly originates from the nanobelts themselves. Therefore, the similarity in the conductance behavior as a function of the band bending indicates that the sensing phenomenon in the single-crystalline thin films and single-crystalline nanobelts may be comparable, differing only in the limited conduction in one direction of the nanobelts. Considering the lack of a proper model to describe the conduction process in one-dimensional nanostructures, the model proposed in eq 7 can be extended to fit the experimental results shown in Figure 2 for the Sn_3O_4 nanobelts.

To achieve an optimal fitting of the experimental data, initial upward band bendings (eV_S) of 0.16 and 0.44 eV were considered at 200 and 300 °C, respectively. Under this assumption, the energy bands are assumed to be intrinsically bent in N_2. Figure S4 illustrates the fitting curve of the experimental data shown in Figure 2 by shifting the reference point from N_2 to 50 ppm of CO at both operating temperatures. The initial band bendings reduced in the presence of CO, reaching the flat band condition when the sensor was exposed to 50 ppm of CO at both temperatures ($e\Delta V_s/k_BT$ = −4.03 and −8.9 at 200 and 300 °C, respectively, in Figure 2). At the flat band condition, the conductance of the sensing layer is around 1.2 mS at 200 °C and 3.2 mS at 300 °C, which means that the electrical resistance is around 0.83 and 0.31 kΩ, respectively. Consequently, two distinct electronic conduction regions were identified: a region where the conduction mechanism is controlled by an accumulation layer and a region where a depletion layer controls the conduction mechanism.

By fitting the curve with the model proposed in eq 7, the G_b and L_D/D parameters were extracted. The estimated bulk conductance was 1.2×10^{-3} S at 200 °C and 3.35×10^{-3} S at 300 °C. For an average thickness of Sn_3O_4 nanobelts of D = 15 nm, the Debye length was found to be 2.9 and 2.1 nm at 200 and 300 °C, respectively. The observation that $L_D < D$ reveals the existence of distinct electronic conduction regions in the material: a surface depletion region with a lower concentration of free charge carriers (electrons), leading to higher electrical resistance, and an unaffected bulk region with lower electrical resistance. In this way, the conduction through the core is modulated depending on the concentration of free charge carriers (electrons) resulting from the O_2 and CO adsorption. These results enable calculation of the bulk electron concentration in the conduction band (n_b) using eq 8 and assuming the Schottky approximation to be valid (i.e., the concentration of electrons in the depletion layer is negligible). The dielectric constant of Sn_3O_4 was considered to be ∼12, which is within the same range as that of SnO_2 (9−14)[7,53,54] and SnO (6−19).[7,55] The values of n_b were 3.2×10^{24} and 7.4×10^{24} m^{-3} at 200 and 300 °C, respectively.

$$L_D = \sqrt{\frac{k_BT\kappa\varepsilon_0}{e^2 n_b}} \quad (8)$$

where κ is the dielectric constant and ε_0 is the vacuum permittivity.

The position of the Fermi level relative to the bottom of the conduction band in the bulk ($E_{C,b} - E_F$) can be determined

https://doi.org/10.1021/acssensors.3c01810
ACS Sens. XXXX, XXX, XXX−XXX

ACS Sensors pubs.acs.org/acssensors Article

Table 1. Bulk Conductance (G_b), Debye Length (L_D), Bulk Electron Concentration in the Conduction Band (n_b), Effective Density of States in the Conduction Band (N_C), and the Position of the Fermi Level ($E_{C,b} - E_F$) Calculated for Sn_3O_4 Nanobelts-Based Sensor under Exposure to O_2 and CO in a Dry N_2 Background at 200 and 300 °C

temperature (°C)	initial eV_S (eV)	G_B (S)	L_D (nm)	n_b ($1/m^3$)	N_C ($1/m^3$)	$(E_{C,b} - E_F)$ (meV)
200	0.16	1.2×10^{-3}	2.9	3.2×10^{24}	4.4×10^{25}	107
300	0.44	3.35×10^{-3}	2.1	7.4×10^{24}	5.8×10^{25}	101

according to eq 9. Equation 10 gives the effective density of states in the conduction band (N_C) of the Sn_3O_4 nanobelts. For this calculation, the density-of-states effective mass (m^*) of Sn_3O_4 was $m^* = 0.918m_0$,[56] where m_0 is the free electron mass. Table 1 provides all of the results obtained from the fittings in Figure S4.

$$(E_{C,b} - E_F) = k_B T \ln\left(\frac{N_C}{n_b}\right) \tag{9}$$

$$N_C = \frac{1}{\sqrt{2}}\left(\frac{m^* k_B T}{\pi \hbar^2}\right)^{3/2} \tag{10}$$

where $\hbar$ is the reduced Planck's constant.

A summary of the surface and bulk contributions obtained from the experiments is presented in a schematic representation of the energy bands in a dry N_2 atmosphere (Figure 5).

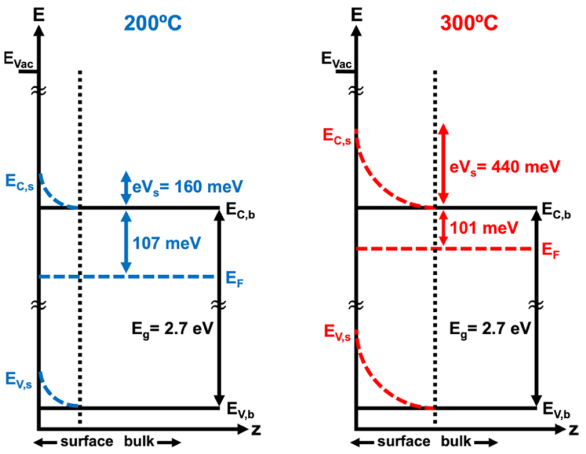

Figure 5. Schematic representation of the energy bands for the Sn_3O_4 nanobelts-based sensor illustrating the initial surface band bending and the position of the Fermi level in a dry N_2 atmosphere at 200 and 300 °C. E_C represents the bottom of the conduction band, E_F is the position of the Fermi level, and E_V is the valence band.

The position of the Fermi level was estimated to be located at 107 and 101 meV below the bottom of the conduction band at 200 and 300 °C, respectively. The initial band bendings of 0.16 and 0.44 eV at 200 and 300 °C, respectively, indicate a lower concentration of donors at the surface compared to the bulk. This effect is unrelated to the adsorption of O_2 on the surface of the Sn_3O_4 nanobelts, given that the measurements were performed in a dry N_2 environment. It is determined by an additional factor, possibly associated with the formation of surface electron acceptor due to the exchange of some Sn atoms from Sn^{4+} to Sn^{2+}, as observed in SnO_2.[57] The different magnitudes of the initial band bending at each operating temperature may be attributed to the distinct concentrations of acceptor states on the surface at 200 and 300 °C.

CONCLUSIONS

In this study, the sensing mechanism in chemoresistive gas sensors based on single-crystalline Sn_3O_4 nanobelts was investigated for the first time. By employing operando investigations through the Kelvin Probe technique, we were able to delineate the experimental conditions under which a shift in the conduction mechanism occurs from a depletion layer to an accumulation layer model. The results revealed the existence of an initial upward band bending in the absence of oxygen. In contrast, the flat band condition was reached under low concentrations of CO at both operating temperatures. We introduced an appropriate model to describe the conduction process in Sn_3O_4 nanobelts. The outcomes revealed that the sensing mechanism in these single-crystalline, one-dimensional nanostructures resembles the behavior observed in single-crystalline epitaxial layers more closely than in polycrystalline grains. Overall, this work provides insights into the conduction process responsible for the gas sensing properties of single-crystalline one-dimension nanostructures.

ASSOCIATED CONTENT

Supporting Information

The Supporting Information is available free of charge at https://pubs.acs.org/doi/10.1021/acssensors.3c01810.

Dependence of the sensor signals and band bending changes on the stepwise increasing concentrations of O_2 and CO at 200 and 300 °C (PDF)

AUTHOR INFORMATION

Corresponding Authors

Pedro H. Suman − *Institute of Physical and Theoretical Chemistry, University of Tübingen, D-72076 Tübingen, Germany; Department of Engineering, Physics and Mathematics, Institute of Chemistry, São Paulo State University (UNESP), 14800-060 Araraquara, Brazil*; Email: pedro.suman@unesp.br, phsuman@yahoo.com.br

Nicolae Barsan − *Institute of Physical and Theoretical Chemistry, University of Tübingen, D-72076 Tübingen, Germany*; orcid.org/0000-0001-6718-9889; Email: nb@ipc.uni-tuebingen.de

Authors

Benjamin Junker − *Institute of Physical and Theoretical Chemistry, University of Tübingen, D-72076 Tübingen, Germany*; orcid.org/0000-0002-2229-0534

Udo Weimar − *Institute of Physical and Theoretical Chemistry, University of Tübingen, D-72076 Tübingen, Germany*; orcid.org/0000-0003-2354-0432

Marcelo O. Orlandi − *Department of Engineering, Physics and Mathematics, Institute of Chemistry, São Paulo State University (UNESP), 14800-060 Araraquara, Brazil*

Complete contact information is available at: https://pubs.acs.org/10.1021/acssensors.3c01810

https://doi.org/10.1021/acssensors.3c01810
ACS Sens. XXXX, XXX, XXX−XXX

Author Contributions

The manuscript was written through contributions of all authors. All authors have given approval to the final version of the manuscript.

Notes

The authors declare no competing financial interest.

■ ACKNOWLEDGMENTS

The authors acknowledge the São Paulo Research Foundation (FAPESP) (grants #2019/26333-2, #2016/20808-0, #2013/07296-2, #2017/26219-0, and 2017/24839-0); the National Council for Scientific and Technological Development (CNPq) (grant #443138/2016-8); the Financier of Studies and Projects (FINEP) (contract #01.22.0291.00, reference #0083/21 and contract #01.18.0075.00, reference #0382/16); and the Coordination for the Improvement of Higher Education Personnel (CAPES) (grant #88887.469365/2019-00) for the financial support.

■ REFERENCES

(1) Barsan, N.; Weimar, U. Conduction Model of Metal Oxide Gas Sensors. *J. Electroceram.* **2001**, *7* (3), 143−167.
(2) Bârsan, N.; Huebner, M.; Weimar, U. Conduction Mechanism in Semiconducting Metal Oxide Sensing Films: Impact on Transduction. In *Semiconductor Gas Sensors*; Jaaniso, R.; Tan, O., Eds.; Woodhead Publishing, 2013; pp 35−63. DOI: 10.1533/9780857098665.1.35.
(3) Oprea, A.; Degler, D.; Barsan, N.; Hemeryck, A.; Rebholz, J. Basics of Semiconducting Metal Oxide-Based Gas Sensors. In *Gas Sensors Based on Conducting Metal Oxides: Basic Understanding, Technology and Applications*; Barsan, N.; Schierbaum, K., Eds.; Elsevier, 2018; pp 61−165. DOI: 10.1016/B978-0-12-811224-3.00003-2.
(4) Yamazoe, N. Toward Innovations of Gas Sensor Technology. *Sens. Actuators, B* **2005**, *108* (1−2), 2−14.
(5) Korotcenkov, G.; Cho, B. K. Metal Oxide Composites in Conductometric Gas Sensors: Achievements and Challenges. *Sens. Actuators, B* **2017**, *244*, 182−210.
(6) Barsan, N.; Schierbaum, K. *Gas Sensors Based on Conducting Metal Oxides: Basic Understanding, Technology and Applications*; Elsevier, 2018. DOI: 10.1016/C2016-0-00984-1.
(7) Orlandi, M. O. *Tin Oxide Materials: Synthesis, Properties, and Applications*; Elsevier, 2019.
(8) Suman, P. H. Electrical Properties of Tin Oxide Materials. In *Tin Oxide Materials*; Orlandi, M. O., Ed.; Elsevier, 2020; pp 41−60. DOI: 10.1016/b978-0-12-815924-8.00003-7.
(9) Staerz, A.; Weimar, U.; Barsan, N. Current State of Knowledge on the Metal Oxide Based Gas Sensing Mechanism. *Sens. Actuators, B* **2022**, *358*, No. 131531.
(10) Taguchi, N. Gas Detecting Device. U.S. Patent US3631436A1971.
(11) Krishna, K. G.; Umadevi, G.; Parne, S.; Pothukanuri, N. Zinc Oxide Based Gas Sensors and Their Derivatives: A Critical Review. *J. Mater. Chem. C* **2023**, *11* (12), 3906−3925.
(12) Majhi, S. M.; Navale, S. T.; Mirzaei, A.; Kim, H. W.; Kim, S. S. Strategies to Boost Chemiresistive Sensing Performance of In_2O_3-Based Gas Sensors: An Overview. *Inorg. Chem. Front.* **2023**, *10* (12), 3428−3467.
(13) Dong, C.; Zhao, R.; Yao, L.; Ran, Y.; Zhang, X.; Wang, Y. A Review on WO_3 Based Gas Sensors: Morphology Control and Enhanced Sensing Properties. *J. Alloys Compd.* **2020**, *820*, No. 153194.
(14) Wang, J.; Umezawa, N.; Hosono, H. Mixed Valence Tin Oxides as Novel van Der Waals Materials: Theoretical Predictions and Potential Applications. *Adv. Energy Mater.* **2016**, *6* (1), No. 1501190.
(15) Lawson, F. Tin Oxide-Sn_3O_4. *Nature* **1967**, *215* (5104), 955−956.
(16) Suman, P. H.; Longo, E.; Varela, J. A.; Orlandi, M. O. Controlled Synthesis of Layered Sn_3O_4 Nanobelts by Carbothermal Reduction Method and Their Gas Sensor Properties. *J. Nanosci. Nanotechnol.* **2014**, *14* (9), 6662−6668.
(17) Balgude, S. D.; Sethi, Y. A.; Kale, B. B.; Munirathnam, N. R.; Amalnerkar, D. P.; Adhyapak, P. V. Nanostructured Layered Sn_3O_4 for Hydrogen Production and Dye Degradation under Sunlight. *RSC Adv.* **2016**, *6* (98), 95663−95669.
(18) Huda, A.; Suman, P. H.; Torquato, L. D. M.; Silva, B. F.; Handoko, C. T.; Gulo, F.; Zanoni, M. V. B.; Orlandi, M. O. Visible Light-Driven Photoelectrocatalytic Degradation of Acid Yellow 17 Using Sn_3O_4 Flower-like Thin Films Supported on Ti Substrate (Sn_3O_4/TiO_2/Ti). *J. Photochem. Photobiol., A* **2019**, *376*, 196−205.
(19) Liu, Y. S.; Yamaguchi, A.; Yang, Y.; Abe, H.; Ueda, S.; Tanabe, T.; Miyauchi, M. Visible-Light-Induced CO_2 Reduction by Mixed-Valence Tin Oxide. *ACS Appl. Energy Mater.* **2021**, *4* (12), 13415−13419.
(20) Chen, L.; Yue, S.; Wang, J.; Chen, W.; Zhang, Y.; Xie, M.; Han, W. Overall Water Splitting on Surface-Polarized Sn_3O_4 through Weakening the Trap of Sn(II) to Holes. *Appl. Catal., B* **2021**, *299*, No. 120689.
(21) Xie, Q.; Zhu, Y.; Zhao, P.; Yang, C. A Strategic Co-Assembly of Carbon Nanotubes and Graphene on Hierarchical Flower-like Sn_3O_4 Clusters Aimed to Enhance Lithium Storage Capability. *J. Electroanal. Chem.* **2021**, *880*, No. 114898.
(22) Li, S.; Qin, F.; Peng, Q.; Liu, S.; Zhang, Z.; Zhang, D.; Liu, C.; Li, D.; Liu, J.; Qi, J.; Hu, Y.; Rong, Y.; Mei, A.; Han, H. Van Der Waals Mixed Valence Tin Oxides for Perovskite Solar Cells as UV-Stable Electron Transport Materials. *Nano Lett.* **2020**, *20* (11), 8178−8184.
(23) Yang, R.; Song, G.; Wang, L.; Yang, Z.; Zhang, J.; Zhang, X.; Wang, S.; Ding, L.; Ren, N.; Wang, A.; Yu, X. Full Solar-Spectrum-Driven Antibacterial Therapy over Hierarchical Sn_3O_4/PDINH with Enhanced Photocatalytic Activity. *Small* **2021**, *17* (39), No. 2102744.
(24) Morais, P. V.; Suman, P. H.; Schöning, M. J.; Siqueira, J. R.; Orlandi, M. O. Layer-by-Layer Film Based on Sn_3O_4 Nanobelts as Sensing Units to Detect Heavy Metals Using a Capacitive Field-Effect Sensor Platform. *Chemosensors* **2023**, *11* (8), 436.
(25) Suman, P. H.; Felix, A. A.; Tuller, H. L.; Varela, J. A.; Orlandi, M. O. Comparative Gas Sensor Response of SnO_2, SnO and Sn_3O_4 Nanobelts to NO_2 and Potential Interferents. *Sens. Actuators, B* **2015**, *208*, 122−127.
(26) Yang, X. Y.; Shi, Y. T.; Xie, K. F.; Wang, J. Y.; Wang, Y. F.; Zheng, Y.; Fang, S. M.; Zhang, Y. H. Engineering of In-Plane SnO_2-Sn_3O_4 Hierarchical Nanoflower Heterojunctions for Enhanced Formaldehyde Sensing. *Appl. Surf. Sci.* **2023**, *614*, No. 156110.
(27) Chen, D.; Yu, W.; Wei, L.; Ni, J.; Li, H.; Chen, Y.; Tian, Y.; Yan, S.; Mei, L.; Jiao, J. High Sensitive Room Temperature NO_2 Gas Sensor Based on the Avalanche Breakdown Induced by Schottky Junction in TiO_2-Sn_3O_4 Nanoheterojunctions. *J. Alloys Compd.* **2022**, *912*, No. 165079.
(28) Liu, J.; Wang, C.; Yang, Q.; Gao, Y.; Zhou, X.; Liang, X.; Sun, P.; Lu, G. Hydrothermal Synthesis and Gas-Sensing Properties of Flower-like Sn_3O_4. *Sens. Actuators, B* **2016**, *224*, 128−133.
(29) Oprea, A.; Bârsan, N.; Weimar, U. Work Function Changes in Gas Sensitive Materials: Fundamentals and Applications. *Sens. Actuators, B* **2009**, *142* (2), 470−493.
(30) Bârsan, N.; Weimar, U. Understanding the Fundamental Principles of Metal Oxide Based Gas Sensors; the Example of CO Sensing with SnO_2 Sensors in the Presence of Humidity. *J. Phys.: Condens. Matter* **2003**, *15* (20), R813−R839.
(31) Mazhar, M. E.; Faglia, G.; Comini, E.; Zappa, D.; Baratto, C.; Sberveglieri, G. Kelvin Probe as an Effective Tool to Develop Sensitive P-Type CuO Gas Sensors. *Sens. Actuators, B* **2016**, *222*, 1257−1263.
(32) D'Amico, A.; Di Natale, C.; Paolesse, R.; Mantini, A.; Goletti, C.; Davide, F.; Filosofi, G. Chemical Sensing Materials Characterization by Kelvin Probe Technique. *Sens. Actuators, B* **2000**, *70* (1−3), 254−262.

https://doi.org/10.1021/acssensors.3c01810
ACS Sens. XXXX, XXX, XXX−XXX

(33) Bârsan, N.; Hübner, M.; Weimar, U. Conduction Mechanisms in SnO_2 Based Polycrystalline Thick Film Gas Sensors Exposed to CO and H_2 in Different Oxygen Backgrounds. *Sens. Actuators, B* **2011**, *157* (2), 510−517.
(34) Rebholz, J.; Bonanati, P.; Jaeschke, C.; Hübner, M.; Mädler, L.; Weimar, U.; Barsan, N. Conduction Mechanism in Undoped and Antimony Doped SnO_2 Based FSP Gas Sensors. *Sens. Actuators, B* **2013**, *188*, 631−636, DOI: 10.1016/j.snb.2013.07.063.
(35) Hübner, M.; Bârsan, N.; Weimar, U. Influences of Al, Pd and Pt Additives on the Conduction Mechanism as Well as the Surface and Bulk Properties of SnO_2 Based Polycrystalline Thick Film Gas Sensors. *Sens. Actuators, B* **2012**, *171*−*172*, 172−180.
(36) Hübner, M.; Simion, C. E.; Tomescu-Stănoiu, A.; Pokhrel, S.; Bârsan, N.; Weimar, U. Influence of Humidity on CO Sensing with P-Type CuO Thick Film Gas Sensors. *Sens. Actuators, B* **2011**, *153* (2), 347−353.
(37) Pokhrel, S.; Simion, C. E.; Quemener, V.; Bârsan, N.; Weimar, U. Investigations of Conduction Mechanism in Cr_2O_3 Gas Sensing Thick Films by AC Impedance Spectroscopy and Work Function Changes Measurements. *Sens. Actuators, B* **2008**, *133* (1), 78−83.
(38) Barsan, N.; Simion, C.; Heine, T.; Pokhrel, S.; Weimar, U. Modeling of Sensing and Transduction for P-Type Semiconducting Metal Oxide Based Gas Sensors. *J. Electroceram.* **2010**, *25* (1), 11−19.
(39) Paghi, A.; Mariani, S.; Barillaro, G. 1D and 2D Field Effect Transistors in Gas Sensing: A Comprehensive Review. *Small* **2023**, *19* (15), No. 2206100.
(40) Tonezzer, M.; Thi Thanh Le, D.; Van Duy, L.; Hoa, N. D.; Gasperi, F.; Van Duy, N.; Biasioli, F. Electronic Noses Based on Metal Oxide Nanowires: A Review. *Nanotechnol. Rev.* **2022**, *11* (1), 897−925.
(41) Yang, B.; Myung, N. V.; Tran, T. T. 1D Metal Oxide Semiconductor Materials for Chemiresistive Gas Sensors: A Review. *Adv. Electron. Mater.* **2021**, *7* (9), No. 2100271.
(42) Wang, Z.; Zhu, L.; Sun, S.; Wang, J.; Yan, W. One-Dimensional Nanomaterials in Resistive Gas Sensor: From Material Design to Application. *Chemosensors* **2021**, *9* (8), 198.
(43) Suman, P. H.; Jorgetto, A. O.; Romeiro, F. C.; Felix, A. A.; Morais, P. V.; Melquíades, M. O.; Orlandi, M. O. 1D Hybrid Tin Oxide Nanostructures: Synthesis and Applications. In *1D Semiconducting Hybrid Nanostructures*; Kumar, A.; Aswal, D. K.; Joshi, N., Eds.; Wiley-VCH: Weinheim, 2023; pp 97−125. DOI: 10.1002/9783527837649.ch5.
(44) Orlandi, M. O.; Suman, P. H.; Silva, R. A.; Arlindo, E. P. S. Carbothermal Reduction Synthesis: An Alternative Approach to Obtain Single-Crystalline Metal Oxide Nanostructures. In *Recent Advances in Complex Functional Materials: From Design to Application*; Longo, E.; La Porta, F. A., Eds.; Springer, 2017; pp 43−67. DOI: 10.1007/978-3-319-53898-3_2.
(45) D'Amico, A.; Di Natale, C.; Paolesse, R.; Mantini, A.; Goletti, C.; Davide, F.; Filosofi, G. Chemical Sensing Materials Characterization by Kelvin Probe Technique. *Sens. Actuators, B* **2000**, *70* (1−3), 254−262.
(46) Morrison, S. R. *The Chemical Physics of Surfaces*, 1st ed.; Springer: New York, 1977.
(47) Gurlo, A. Interplay between O_2 and SnO_2: Oxygen Ionosorption and Spectroscopic Evidence for Adsorbed Oxygen. *ChemPhysChem* **2006**, *7* (10), 2041−2052.
(48) Degler, D.; Wicker, S.; Weimar, U.; Barsan, N. Identifying the Active Oxygen Species in SnO_2 Based Gas Sensing Materials: An Operando IR Spectrsocopy Study. *J. Phys. Chem. C* **2015**, *119* (21), 11792−11799.
(49) Hübner, M.; Simion, C. E.; Haensch, A.; Barsan, N.; Weimar, U. CO Sensing Mechanism with WO_3 Based Gas Sensors. *Sens. Actuators, B* **2010**, *151* (1), 103−106, DOI: 10.1016/j.snb.2010.09.040.
(50) Boehme, I.; Weimar, U.; Barsan, N. Unraveling the Surface Chemistry of CO Sensing with In_2O_3 Based Gas Sensors. *Sens. Actuators, B* **2021**, *326*, No. 129004, DOI: 10.1016/j.snb.2020.129004.
(51) Wicker, S.; Guiltat, M.; Weimar, U.; Hémeryck, A.; Barsan, N. Ambient Humidity Influence on CO Detection with SnO_2 Gas Sensing Materials: A Combined DRIFTS/DFT Investigation. *J. Phys. Chem. C* **2017**, *121* (45), 25064−25073.
(52) Simion, C. E.; Schipani, F.; Papadogianni, A.; Stanoiu, A.; Budde, M.; Oprea, A.; Weimar, U.; Bierwagen, O.; Barsan, N. Conductance Model for Single-Crystalline/Compact Metal Oxide Gas-Sensing Layers in the Nondegenerate Limit: Example of Epitaxial SnO_2(101). *ACS Sens* **2019**, *4* (9), 2420−2428, DOI: 10.1021/acssensors.9b01018.
(53) McAleer, J. F.; Moseley, P. T.; Norris, J. O. W.; Williams, D. E. Tin Dioxide Gas Sensors. Part 1. Aspects of the Surface Chemistry Revealed by Electrical Conductance Variations. *J. Chem. Soc., Faraday Trans. 1* **1987**, *83* (4), 1323−1346.
(54) Batzill, M.; Diebold, U. The Surface and Materials Science of Tin Oxide. *Prog. Surf. Sci.* **2005**, *79* (2−4), 47−154.
(55) Saji, K. J.; Tian, K.; Snure, M.; Tiwari, A. 2D Tin Monoxide-An Unexplored p-Type van Der Waals Semiconductor: Material Characteristics and Field Effect Transistors. *Adv. Electron. Mater.* **2016**, *2* (4), No. 1500453.
(56) Savioli, J.; Gavin, A. L.; Lucid, A. K.; Watson, G. W. The Structure and Electronic Structure of Tin Oxides. *Tin Oxide Mater.* **2020**, 11−39.
(57) Rebholz, J.; Dee, C.; Weimar, U.; Barsan, N. A Self-Doping Surface Effect and Its Influence on the Sensor Performance of Undoped SnO_2 Based Gas Sensors. *Procedia Eng.* **2015**, *120*, 83−87.

https://doi.org/10.1021/acssensors.3c01810
ACS Sens. XXXX, XXX, XXX−XXX

Supporting Information

Modeling the conduction mechanism in chemoresistive gas sensors based on single-crystalline Sn_3O_4 nanobelts: A phenomenological in operando investigation

Pedro H. Suman[†,‡,*], Benjamin Junker[†], Udo Weimar[†], Marcelo O. Orlandi[‡], Nicolae Barsan[†,*]

†Institute of Physical and Theoretical Chemistry, University of Tübingen, D-72076 Tübingen, Germany.

‡Department of Engineering, Physics and Mathematics, Institute of Chemistry, São Paulo State University (UNESP), 14800-060 Araraquara, Brazil.

*Corresponding author:

Dr. Pedro H. Suman (phsuman@yahoo.com.br; pedro.suman@unesp.br)

Dr. Nicolae Barsan (nb@ipc.uni-tuebingen.de)

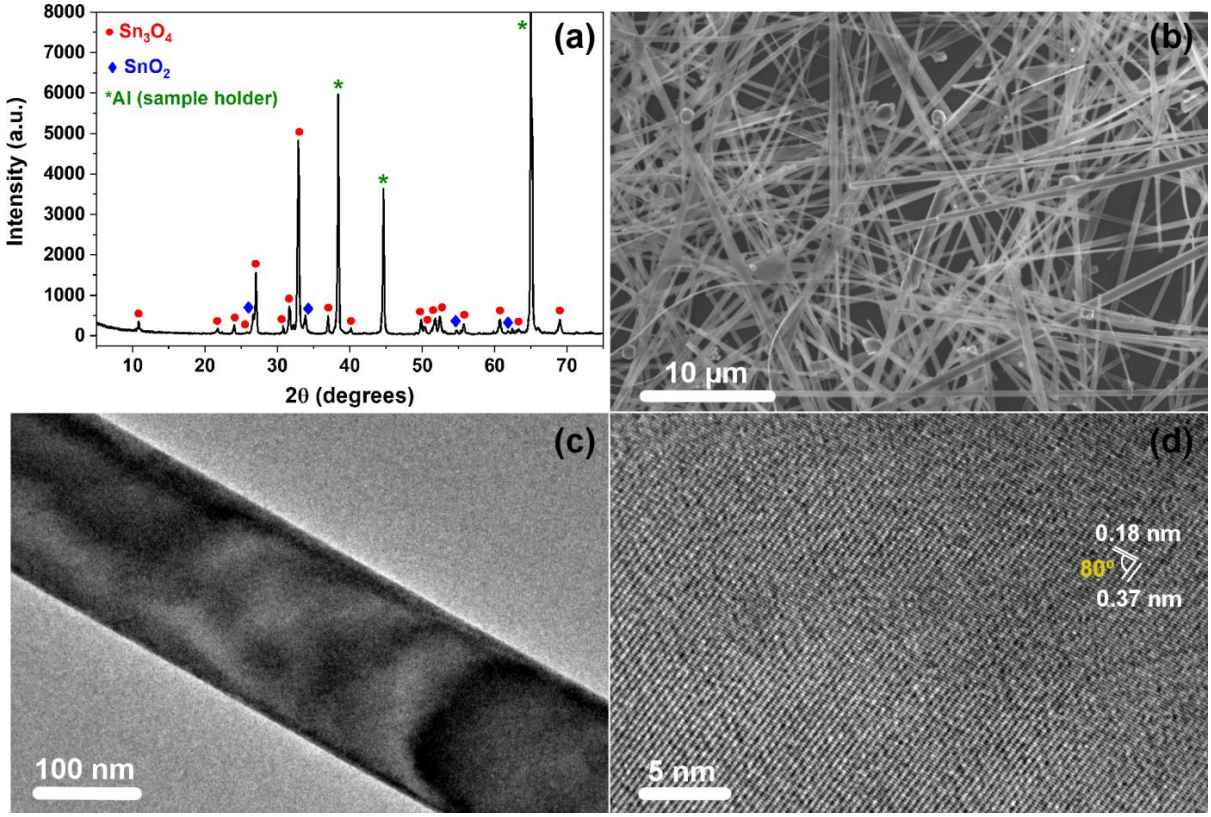

Figure S1. (a) XRD pattern, (b) SEM image, (c, d) TEM imagens of the Sn_3O_4 nanobelts.

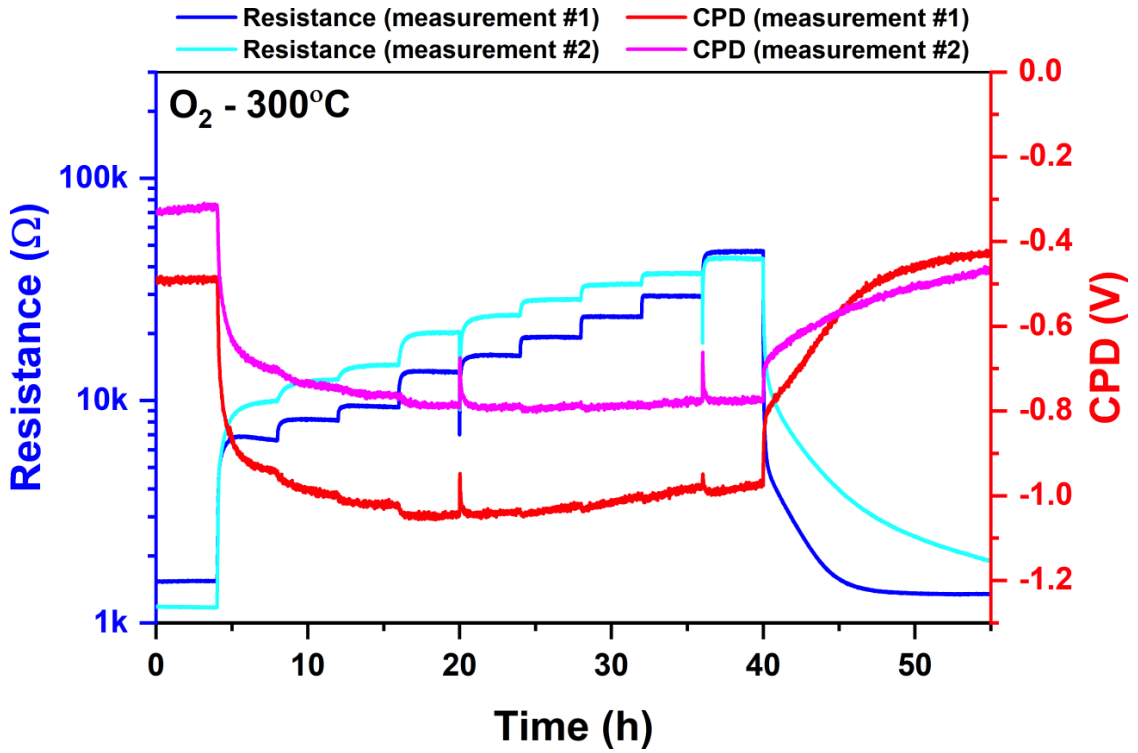

Figure S2. Simultaneous DC electrical resistance and contact potential difference (CPD) changes of two Sn_3O_4 nanobelts-based sensors under exposures to stepwise increasing concentrations of O_2 in a dry N_2 background at 300 °C.

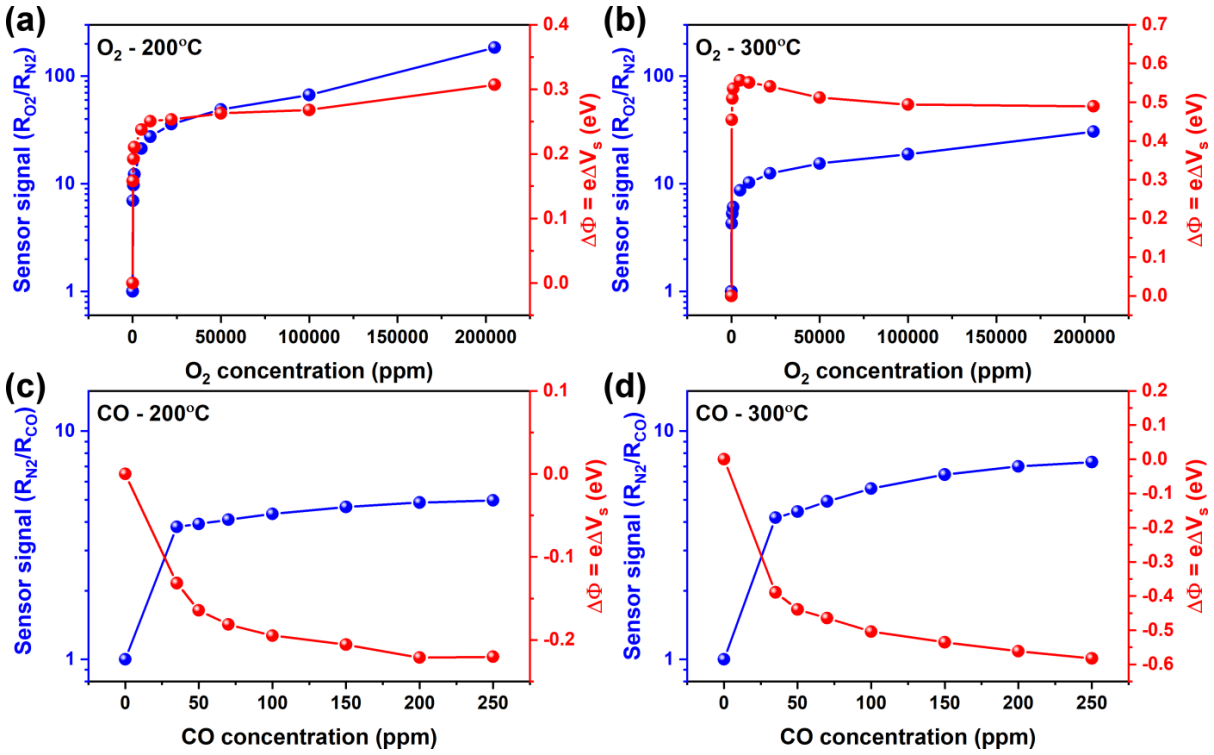

Figure S3. Corresponding sensor signals and band bending changes as a function of the stepwise increasing concentrations of (a, b) O_2 and (c, d) CO at 200 and 300 °C, respectively.

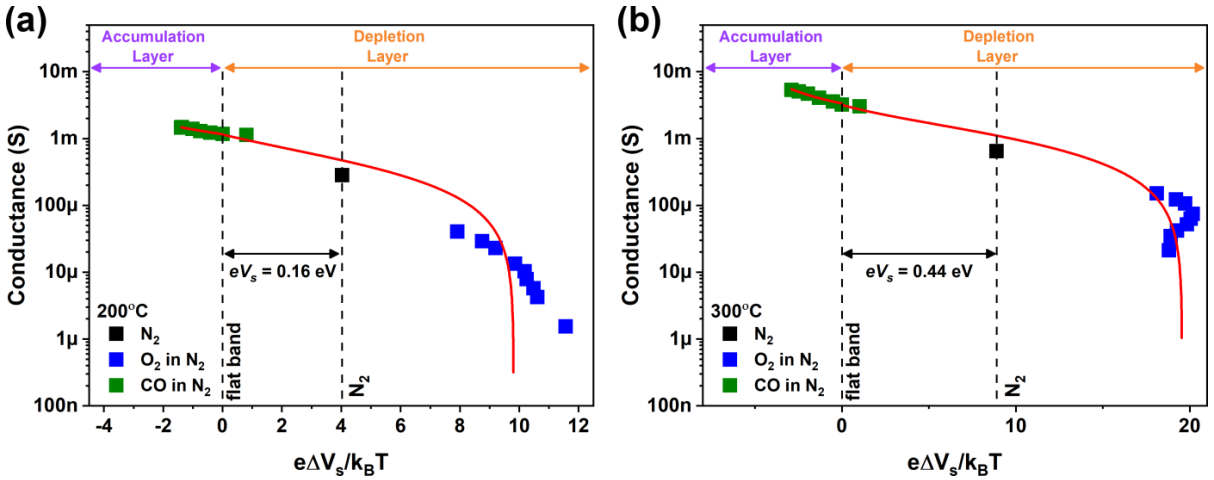

Figure S4. Fitting curve of the conductance as a function of the band bending, expressed in terms of the thermal energy (k_BT), for the Sn_3O_4 nanobelts-based sensor taken under exposures to different O_2 and CO concentrations in a dry N_2 background at (a) 200 °C and (b) 300 °C.

ACS SENSORS

pubs.acs.org/acssensors Article

Multivariate Analysis of Light-Activated SMOX Gas Sensors

Benjamin Junker, Arne Kobald, Carolin Ewald, Peter Janoschek, Malte Schalk, Udo Weimar, Lutz Mädler, and Nicolae Bârsan*

Cite This: *ACS Sens.* 2024, 9, 1584−1591 Read Online

ACCESS | Metrics & More | Article Recommendations | Supporting Information

ABSTRACT: Chemoresistive gas sensors made from SnO_2, ZnO, WO_3, and In_2O_3 have been prepared by flame spray pyrolysis. The sensors' response to CO and NO_2 in darkness and under illumination at different wavelengths, using commercially available LEDs, was investigated. Operation at room temperature turned out to be impractical due to the condensation of water inside the porous sensing layers and the irreversible changes it caused. Accordingly, for sensors operated at 70 °C, a characterization procedure was developed and proven to deliver consistent data. The resulting data set was so complex that usual univariate data analysis was intricate and, consequently, was investigated by correlation and principal component analysis. The results show that light of different wavelengths affects not only the resistance of each material, both under exposure to the target gases in humidity and in its absence, but also the sensor response to humidity and the target gases. It was found that each of the materials behaves differently under light exposure, and it was possible to identify conditions that need further investigations.

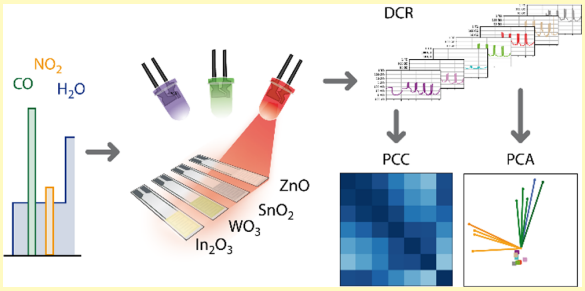

KEYWORDS: *gas sensors, light activation, photon energy, principal component analysis, chemometrics*

After the discovery of a change in electrical conductance on ZnO crystals under exposure to oxygen by Heiland et al.,[1] the combination of semiconducting metal oxides (SMOX) and gas sensing quickly garnered much attention. Since Taguchi launched the first commercial SMOX-based gas sensor for the detection of explosive gases in 1968, they have become widely popular. They operate based on the change in electrical conductance of the sensing layer, caused by reactions of the surface with gases that change the concentration of free charge carriers. These surface reactions are the main reason for high operating temperatures because they have certain activation energies which need to be overcome. At room temperature (RT) however, the thermal energy is so low that the surface reactions can take days to reach steady state with a target gas. Great attention is being placed on exploring alternatives to reduce the high power consumption of permanently heated sensors, with miniaturization in the form of micro electromechanical systems (MEMS), self-heating sensors, and sensor activation via light (photoconductance) being the most popular.[2]

While early demonstrations on SMOX sensors at RT with UV-light from large, expensive mercury and Xe-lamps were without any kind of advantage compared to high temperature operation,[3,4] the introduction of LEDs and their miniaturization changed this situation drastically, thus sparking an increased interest in this alternative activation. Because the approach of using high energy UV-LEDs has downsides, such as lack of selectivity, pricing of UV-LEDs, and the photolysis of some target gases, like NO_2,[5] the focus of research has shifted to light activation in the visible spectrum.[6−15]

Among the preparation routes for gas sensing materials, flame spray pyrolysis (FSP) offers some advantages such as simultaneous control of layer thickness, control of primary particle size, control of porosity, and the possibility of producing mixed oxide particles as well as heterojunctions.[16−21] Compared to conventionally screen-printed sensors, directly deposited FSP sensors have higher baseline resistance but offer higher sensor response, i.e., relative change in resistance, and in the context of light-activated sensors offer the advantage of high porosity which ensures that light can penetrate the entire layer and thus increases the photoresponse.[22−24]

Here, the electrical resistance of four SMOX materials, synthesized and deposited via FSP, was studied during exposure to CO and NO_2 in the presence of varying levels of relative humidity and during exposure to red, green, blue, UV, and deep-UV light. For comparison sake, the same data were collected in dark conditions before and after light

Received: January 12, 2024
Revised: February 21, 2024
Accepted: February 27, 2024
Published: March 7, 2024

https://doi.org/10.1021/acssensors.4c00078
ACS Sens. 2024, 9, 1584−1591

ACS Sensors pubs.acs.org/acssensors Article

Table 1. Precursor Solution and Distance *d* between the Flame Nozzle and Sample during the Spraying Process of Individual Materials

material	solvate	*c* in mol/L	solvent	*V* in mL	*d* in mm
WO_3	tungsten hexacarbonyl	0.1	tetrahydrofuran	100	300
In_2O_3	indium acetylacetonate	0.1	xylene	100	300
SnO_2	tin 2-ethyl-hexanoate	0.5	xylene	25	200
ZnO	zinc naphtenate	0.5	xylene	100	140

exposure. CO and NO_2 were chosen as representatives for reducing and oxidizing gases. Especially for sensor signals, besides the wavelength, the irradiance at the sensing layer is another important factor to consider.[25] However, the scope of this work is limited to a comparison of different materials.

That adds up to seven illumination conditions for four SMOX materials; a single measurement generated more than a week of electrical resistance data and around 30 weeks of data for the full experiment. The availability of such a large amount of data is a challenge for the traditional gas sensing evaluation. In this case, the feature space is simply too complex, so a multivariate data analysis was used for the interpretation. More precisely, principal component analysis (PCA) is applied to extract common features of the sensing materials and to understand the influence of the energy provided by light of different wavelengths on the four SMOX materials, each with a different bandgap. To the best of our knowledge, this is the first time that multivariate data analysis was applied to light-activated gas sensing.

EXPERIMENTAL SECTION

Sample Preparation. Flame spray pyrolysis was used for the fabrication of the sensors. For preparation of the precursors, the appropriate amount of chemicals was dissolved in the respective solvent, put into an ultrasonic bath for 10 min, and then checked for complete solution. During FSP synthesis methane flow was 1.5 L/min premixed with oxygen at 3.2 L/min. Dispersion oxygen was 5 L/min, and the nozzle was adjusted to give a pressure drop of 1.5 bar while atomizing the precursor flow of 5 mL/min. Table 1 summarizes the deposition conditions and precursor chemicals used for synthesis of the sensors. Further details on the setup and parameters can be found elsewhere.[26]

The sensors investigated in this work consist of an alumina substrate with interdigitated platinum electrodes.[27] The back side of the substrates is equipped with a resistive heating structure. For preparation of the flame made sensors, the sensor substrates were mounted in a temperature-controlled sample holder at different heights above the FSP nozzle to maintain the substrate temperature at approximately 120 °C during thermophoretic particle deposition. After deposition via FSP, the sensors were annealed in a tube furnace (ROK/A 6/60, Heraeus) at 400, 500, and 400 °C, for 10 min each, followed by a cooldown until RT is reached.

Powder Characterization. Powder X-ray diffraction (XRD) patterns were recorded for all samples on a diffractometer (Bruker D8 Discover), equipped with a Cu-tube producing Ni-filtered $K_{\alpha 1,2}$ radiation. The samples were placed in a 0.2 mm deep and 14 mm wide single crystalline holder. Diffraction patterns were taken from 5 to 135° 2θ and 1.5 s time steps without sample spin. X-ray results were evaluated using BRASS software[28] followed by Rietveld refinement to the respective ICSD database (see Table S2). The apparent crystallite sizes were estimated based on the Scherrer equation. The specific surface area (SSA) determination was performed using a nitrogen adsorption system (Quantachrome NOVA 4000e). All samples were degassed for 2 h at 200 °C in a vacuum before nitrogen adsorption measurement. The data were collected using 5-point adsorption isotherm in a pressure range of P/P_0 5×10^{-2} to 2×10^{-1} at 77 K in liquid nitrogen. BET diameters were calculated by the formula $d_{BET} = \frac{6}{\rho SSA}$ and therefore represent the Sauter diameter.

DC Resistance Measurements. The sensor performance was examined by DC resistance (DCR) measurements under different gas atmospheres. Synthetic air and CO and NO_2 mixtures were dosed from gas bottles (Westfalen AG) using a custom-made gas mixing system equipped with mass flow controllers and humidity was produced using distilled water filled bubblers. The sensor resistance was measured either directly with an electrometer (Keithley 6517B) or in parallel with 100 MΩ resistors (TE Connectivity), using a scanning multimeter (Agilent 34972A). The sensing performance was evaluated at a constant flow of 250 mL/min. During the experiments, the sensors were heated to 70 °C via DC power supplies and thus were temperature calibrated beforehand via an infrared pyrometer (KTR 1105-1, Maurer). The evaluated sensors are situated in a polytetrafluoroethylene (PTFE) measurement chamber, as shown in Figure S1 in the Supporting Information. LEDs are mounted in the side wall with a distance of 3 mm to the sensing layer. The entire active area of the sensing layer (5.1 × 1.6 mm) is covered by the main cone of light emitted by the LEDs. They are operated with a constant current source (Knight J152) set to 20 mA. The specifications of the LEDs are provided in Table S1 in the Supporting Information.

After an initial measurement in the dark, the sensors were exposed to red (631 nm), green (520 nm), blue (468 nm), UV (375 nm), and deep UV (dUV, 310 nm) light, followed by a measurement in the dark again. Two sensors of each material were investigated simultaneously and showed similar behavior; one of them was chosen for the evaluation. Commercial gas and humidity sensors are added downstream to monitor the correct operation of the system.

The finally established screening standard procedure is illustrated in Figure 1. After each sensor was allowed to reach a stable baseline in dry air, the experiment started with humidity ramps going up and down with 2 h for each step. Afterward the sensor is exposed to two pulses of CO (50 and 100 ppm) and two pulses of NO_2 (0.5 and 0.75 ppm). The test gas exposure is repeated in 10, 30, and 70% RH (relative humidity) at 25 °C. Afterwards, the humidity is decreased stepwise.

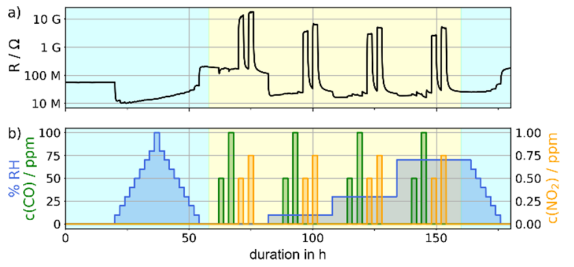

Figure 1. Standardized screening experiment for gas sensors under illumination at a sensor temperature of 70 °C. (a) DC resistance of WO_3 with blue light illumination. (b) Background humidity and gas concentrations. The blue shaded areas are referred to as "humidity sequences," whereas the yellow part represents the "analyte sequence".

Data Treatment. Before analyzing and comparing the different sensing materials and illumination conditions, the raw data are cleaned and collected in a table/matrix. The absolute timestamps of

https://doi.org/10.1021/acssensors.4c00078
ACS Sens. 2024, 9, 1584−1591

ACS Sensors pubs.acs.org/acssensors Article

the individual experiments are converted to relative timestamps, which are used as a common index. The raw resistances, which were acquired for more than 180 h with a sampling interval of 10 s, are resampled into 1 min bins using the median. The resulting matrix **X** has the shape (10,891 × 28) where the rows account for the observations, i.e., the 1 min intervals, and the columns represent the features or predictors. These are the resistances of the 28 experiments combining four sensing materials with 7 different illumination conditions each. Similarly, a matrix **Y** of the shape (10,891 × 3) is obtained describing the concentrations of CO, NO_2 and humidity for each of the observations, often called targets in regression or classification tasks. To obtain more meaningful results, the resistances and gas concentrations are logarithmized using the ln1p function, the natural logarithm of $(x + 1)$, to deal with the concentrations $c = 0$. For linear data, the results would be dominated by the conditions with extremely high resistance readings. Moreover, the calibration curve of SMOX sensors is known to be well described by an allometric function. It has to be noted, that no distinction is made between test gas exposure and recovery times and that only the resistance, not the response, is taken into account. Commonly, when considering a sensor array composed of the 28 experiments, a PCA is performed by diagonalization of the covariance matrix of mean-centered **X**, which has the shape (28 × 28) and describes the pairwise joint variability of any two experiments. The resulting transformation can then be used to reduce the original dimensionality and assess the ability of the sensor array to discriminate between the different gas concentrations or targets **Y**. Similarly, the Pearson correlation matrix—which is the covariance matrix where each pairwise covariance entry is weighted by two standard deviations—may be used to describe how the resistances of the experiments correlate with each other and the target gas concentrations. Here, a PCA is performed on the transpose of **X**, $\mathbf{X}^T$, considering the rows of **X**—the resistances of all experiments at a given time (and therefore in a given gas composition)—as features; and the columns—time series of each experiment—as observations. The results of the transformation are therefore governed by the covariance in relation to the time in the experiment, i.e., the gas composition. In other words, the PCA investigates how (well) the experiments can be characterized, differentiated or classified by the investigated gas exposure sequence.

RESULTS AND DISCUSSION

Material Characterization. Excess powder that was collected during the spraying process was used for XRD and BET analysis. The results are summarized in Table S2 in the Supporting Information. The layers are highly porous and uniform in morphology and thickness. XRD patterns together with the theoretically calculated values (Figure S2) as well as SEM images for all samples (Figure S3) are available in the Supporting Information. The particle diameters calculated from the BET range from 6.4 to 21.7 nm. The crystallite sizes, determined by XRD, are similar to the ones determined by BET. Thus, we conclude that the nanoparticles are monocrystalline particles. The thickness of the sensing layer was determined from SEM cross sections and is between 21.3 and 47 μm for the different materials. For each of the parameters, the four materials show values in the same order of magnitude and are eligible for quantitative comparison. Moreover, these parameters are similar to reports on gas sensing with flame made SMOX.[29,30]

Development of a Universal Screening Method. Initial direct current resistance experiments without additional heating revealed severe limitations of gas sensors operated at room temperature (covering a broad range of 20−25 °C). At these temperatures, water was found to be intercalated in the sensing layer and caused inconsistent results. This issue was overcome by elevating the temperature of operation to 70 °C which is high enough that no more detrimental effect of water could be observed experimentally. On top of that it was found that high polarization voltages in combination with physisorbed water can lead to a degradation of the sensing layer. Hence, instead of using an electrometer working with high polarization voltages across the sensing layer, a conventional multimeter in combination with a parallel resistor, which is necessary to evade the multimeter's limit of 120 MΩ was used. This constrains the voltage applied to the sensing layer to <5 V in all circumstances at the cost of limited accuracy at high resistances.

Material Screening. The raw data of all 28 experiments performed are plotted next to each other in Figure S4. The discussion of each experiment's individual features based on the raw data is outside the scope of this paper, but the most relevant commonalities and differences shall be highlighted: The response to the humidity ramps in the first stage of the experiment is stretching from almost none (e.g., ZnO with red light) to a decrease in resistance by a factor of more than 10,000 (SnO_2, UV). Even a change of direction with higher humidity can be observed (ZnO, UV). All material-illumination pairs except for some cases with SnO_2 respond to NO_2 with an increase in the resistance. The response to CO is a small decrease in resistance in most cases, but can result in an increase of resistance as well (ZnO, UV). Besides these special cases, the experiments are visually rather similar.

Correlation Analysis. As a first step in the investigation of the influence of light of different wavelengths on the sensing materials, the correlation between the sensor resistances (as ln1p) under different illumination conditions and gas concentrations was investigated. The correlation analysis is represented in form of a "heatmap," i.e., colored matrix of Pearson correlation coefficients in Figure 2. The expected

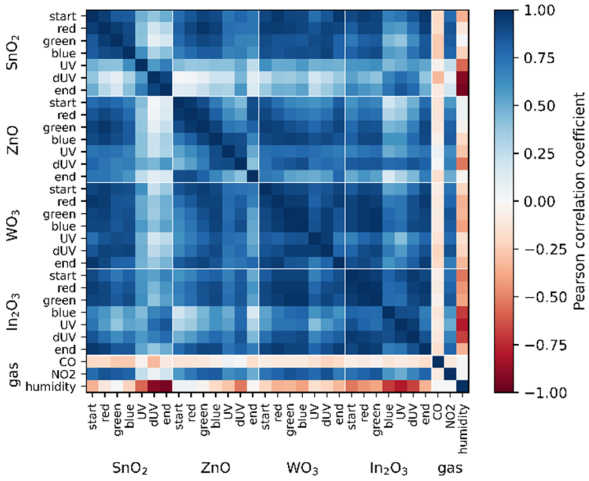

Figure 2. Correlation analysis of sensor resistance and gas concentrations (as ln1p) via the Pearson correlation coefficient.

behavior of the target gases on the n-type semiconductors is a decrease of resistance with the reducing gases CO and humidity (negative correlation of concentrations and resistance) and an increase of resistance through the oxidizing gas NO_2 (positive correlation).

When the correlation coefficients between different illumination conditions, including dark, are close to one for one material, this indicates a low influence of different

https://doi.org/10.1021/acssensors.4c00078
ACS Sens. 2024, 9, 1584−1591

wavelengths and even the presence of any illumination at all on the activation of one material. Such a situation can be found for WO_3 and, to a lesser extent, for In_2O_3.

For In_2O_3, blue, UV, and dUV light show a lower correlation with the rest of the data. While their correlation with CO and NO_2 is similar to those of the other conditions, the correlation with humidity is more negative. The raw data indeed show higher response to humidity for UV and dUV, but not for blue. For ZnO, the correlation between different illumination conditions is following the photon energy. This can be seen most easily for dark-start: The correlation coefficient decreases from red to dUV; dark-end is again highly correlated with dark-start. The raw data reveal a decrease in the mean resistance, as well as in sensor response for NO_2 with increasing photon energy. In the case of SnO_2 two clusters are formed, the first one includes dark-start, red, green, blue, and the second one UV, dUV and dark in the end. The two dark experiments have a correlation coefficient of only 0.50 and thus—unlike for ZnO with a much higher coefficient of 0.89—other reasons for the separation besides photon energy should be considered. A look into raw data explains the higher correlation of humidity and decreased correlation of NO_2 of the second group by an increased response to humidity and lower resistance during NO_2 exposure. In some cases, the material responds to NO_2 with a decrease in resistance, the signature of a reduction. Also, the baseline resistances in dry air are multiple decades higher than in the beginning, pointing to irreversible changes. The low photon energy group of SnO_2 is highly correlated with WO_3 and the lower photon energies of ZnO and In_2O_3. The higher photon energies, on the other hand, show some correlation with the high photon energies of In_2O_3, the commonality here is the increased response to humidity.

Principal Component Analysis. The analysis of correlation between the different conditions and target gas concentrations could unravel the most unique conditions in the test data set and, together with the raw data, provide explanations for the respective behavior. The data have been reduced to a 31×31 correlation matrix, where more than 82% of the resistance data is highly correlated ($P > 0.5$) and thus redundant. The introduction of a principal component analysis can further reduce the dimensions of the data set by a linear transformation of data. In contrast to the correlation analysis, the gas concentrations are excluded, and the PCA is performed on $\mathbf{X}^T$, where the observations are the 28 individual experiments and the features are the respective logarithmized resistances during gas exposure.

Figure 3a shows the PCA performed with data of the whole experiment, colored with respect to the material of the sensor. There is no formation of separate clusters between materials; however, the spread of SnO_2 seems to be orthogonal to the other three materials. In Figure 3b the same data are shown but color-coded by the illumination conditions. Green and blue and to some extent also red are forming the center of the scores plot without much variation. The extreme conditions (dark, UV, and dUV) are changing with the materials. Finally, in Figure 4a–d the scores of the same experiment are represented in separate panels for each material on the same scale for better comparison. Additionally, the loadings for PC1 to PC4 (principal component) are plotted against the factors, i.e. experiment time intervals.

The loadings (Figure 4e–h) give insight into the contributions to the PCs. The loadings for PC1 (weighted by their standard deviation) have approximately the same, negative contribution throughout the whole experiment. In other words: PC1 is representing the mean resistance of the whole experiment and experiments with higher mean resistance appear on the left side of the scores plot. The loadings for PC2 are less uniform. Overall, there is negative contribution for high humidity and positive contribution for low humidity. Therefore, PC2 is representing the resistance change due to humidity, i.e. for sensors with a high response to humidity, PC2 is positive and the scores are located more at the top of each plot. The loadings of PC3 are positive almost exclusively during NO_2 exposure and are also affected by the humidity. For PC4, the loadings are indistinct. The explained variance of the higher PCs is rather low, and the following discussion will be limited to PC1 and PC2.

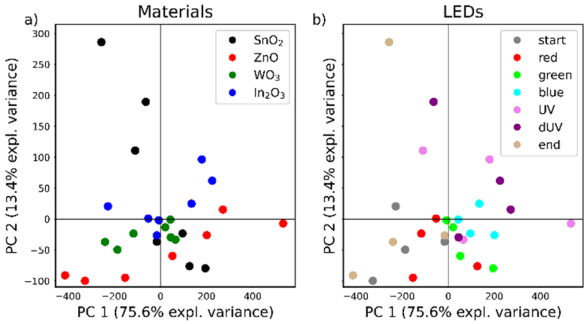

Figure 3. Scores plots of the PCA carried out on the logarithmized (ln1p) resistance time series $\mathbf{X}^T$. The data are colored by materials (a) and illumination conditions (b), where "start" and "end" refer to experiments conducted without illumination in the beginning and end of the experimental sequence, respectively.

The scores of In_2O_3, WO_3, and ZnO are mainly spread along PC1 with the photon energy increasing from left to right. Just in line with the observations of the correlation analysis, the scores for WO_3 are spread the least, supporting the idea of a limited influence of the presence of light, regardless of its wavelength. WO_3 forms two clusters. With dark and red being separated from the others, it is assumed that the photon energy of green light (520 nm, equals 2.38 eV) is already sufficient for the excitation of electrons between band gap states. In the humidity ramps at the beginning of the experiment, WO_3 shows the lowest response and leads to the least spread along PC2 as well.

For both PCs, the scores of In_2O_3 are further spread than those for WO_3 due to a higher influence of light on the mean resistance and the response to humidity. The latter is especially high for UV and dUV. The dark experiments are separated in both PCs, indicating irreversible changes.

While the correlation analysis showed similarities between SnO_2 and ZnO, their scores are mainly spread along PC1 and PC2, respectively. In this aspect, ZnO behaves more like WO_3 and In_2O_3. The sequence in PC1 follows the mean resistance but not the photon energy. Despite the lower photon energy, the mean resistance in UV is 13.8 times lower than that in dUV, which makes UV stand out in PC1. ZnO is the only material where the resistance starts to increase at higher humidities, which makes the interpretation of PC2 ambiguous. Undoubtedly, SnO_2 is the most unique material with the primary spread of its scores almost perpendicular to the others. In neither direction a trend of increasing photon energy is

https://doi.org/10.1021/acssensors.4c00078
ACS Sens. 2024, 9, 1584−1591

ACS Sensors pubs.acs.org/acssensors Article

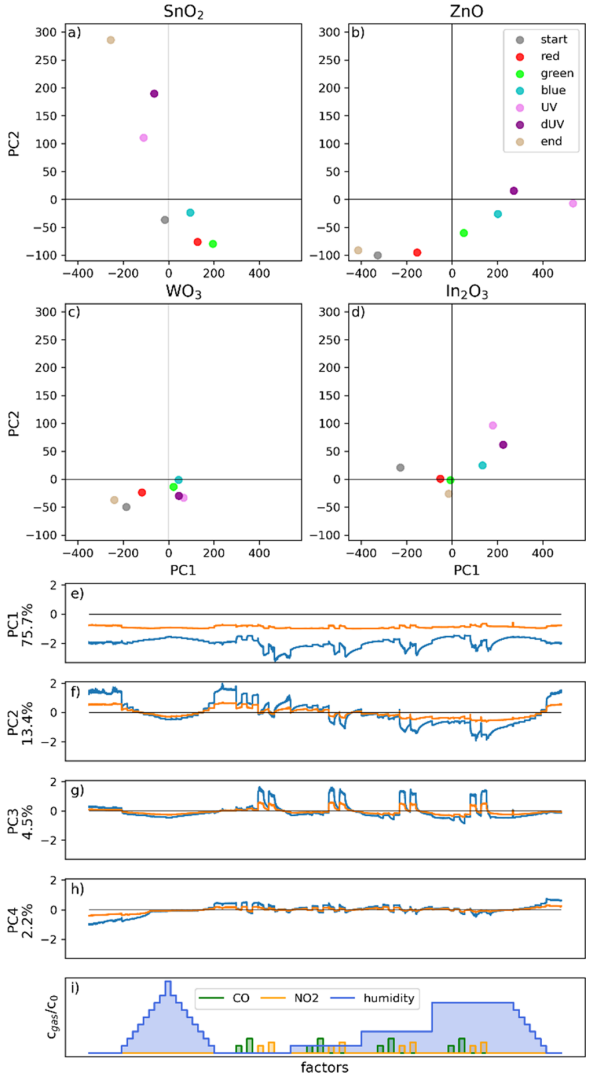

Figure 4. (a–d) Scores plots of the PCA carried out on the logarithmized (ln1p) resistance time series $\mathbf{X}^T$. Each panel shows the data points of one material colored according to the illumination during the experiment. (e–h) Loadings of the first four principal components (PCs). The horizontal black line represents $y = 0$. The blue loadings are weighted by the standard deviations of all experimental resistances and are displayed in the same panel in orange. The explained variance of each PC is added to the y-axis. (i) The qualitative sequence of the gas concentrations of CO, NO_2, and humidity corresponding to the loadings.

present. Among all of the materials investigated, its two dark conditions have the highest euclidean distance. As expected from the correlation analysis, two clusters containing the "early" experiments (dark-start, red, green, blue) and the "later" experiments (UV, dUV, dark-end), respectively, are formed. The separation happens along PC2 because of the highly increased response to humidity for the "late" conditions. The response to humidity is the property that makes SnO_2 very different from the other three materials.

Knowing that humidity plays a major role in the distinction of the materials, the data set was divided into two subsets: one containing the sections with varying humidity (in the beginning and in the end of each experiment), while the other one covered the middle section with exposure to target gases (see the areas marked in blue and yellow in Figure 1). A comparison of all scores is given in Figure 5.

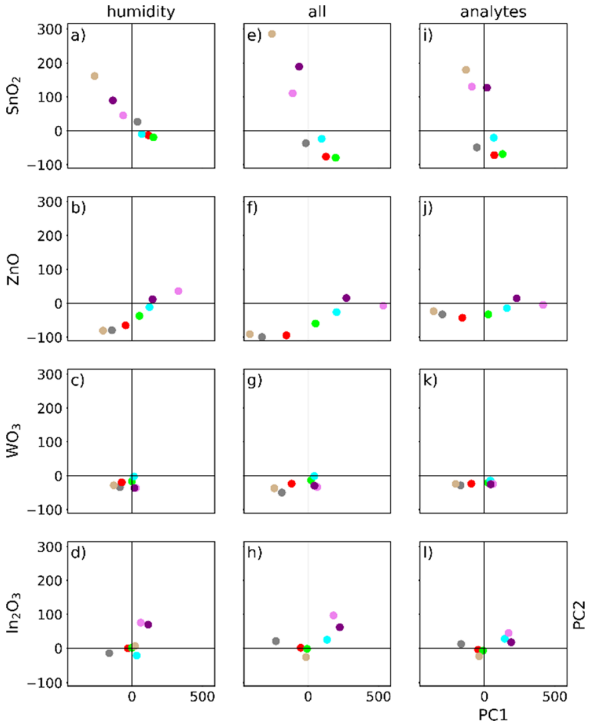

Figure 5. PCA of the humidity subset (a–d), whole data set (e–h), and analyte subset (i–l). In each row, one material is shown. All panels share the same scale.

Overall, the scores are quite similar between data sets, even for the two independent subsets. Similar to the PCA of all data, the loadings of the subsets (Figure S5) imply that PC1 represents the mean resistance, and PC2 is linked to humidity. In addition, there are negative loadings during NO_2 exposure in the analyte subset: High resistance during NO_2 exposure will decrease the scores of PC2.

In the humidity data set of SnO_2, the scores are spread along the angle bisector of PC1 and negative PC2 according to the photon energy (with the exception of both dark conditions). In contrast, the already discussed clusters along PC2 can be identified in the analyte subsets. The cause is an interplay of low resistance during NO_2 exposure in UV and dUV and the high impact of humidity on the baseline resistance for UV, dUV and dark-end. ZnO shows the most similarities between humidity, analytes, and the whole data set. The reason for this is probably the large variation of the resistance with the wavelength combined with a low response to humidity changes. PC1, representing the mean resistance, dominates. With WO_3 the scores of all PCAs are confined. There is almost no variation on PC2 for the analyte sequence but some more for humidity. The reason is that while the sensor response to humidity is dependent on the illumination, the response to NO_2 is almost constant. In the different PCAs for In_2O_3 blue light stands out: In the humidity subset it is next to the cluster

https://doi.org/10.1021/acssensors.4c00078
ACS Sens. 2024, 9, 1584–1591

of low photon energies, whereas in the analyte sequences the score for blue light is closer to UV and dUV.

Assessment of Individual Materials. Both the correlation matrix and PCA provide valuable information about commonalities and differences between the four materials. However, the PCA is dominated by the material changing the most during the experiments, and more subtle changes, e.g., for WO_3, are masked. In order to study the effect of the different illumination conditions on the four materials individually, independent PCAs on 7 × 10,891 matrices are performed. Figure 6 shows the scores of each PCA, and the corresponding loadings are available in Figure S6.

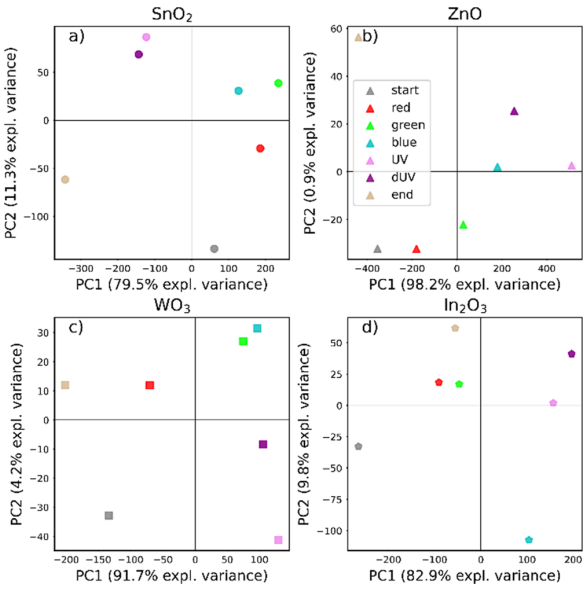

Figure 6. (a–d) Scores plots of PCAs, performed separately for each material. The panels do not share the same scale.

The scores of the PCA performed individually on SnO_2 form four clusters: dark-start, visible light, UV/dUV, and dark-end. In contrast to the comprehensive PCA, the loadings of PC1 change throughout the experiment (see Figure S6a). In a good approximation, PC1 represents the resistance of the first half of the experiment without the NO_2 sequences and explains the separation between dark-start and visible along PC1. Besides humidity, PC2 is characterized by negative loadings during NO_2 exposure. The extrema are dark-start with high resistance in NO_2 and the lowest value for PC2 and UV/dUV, where the inverse response leads to low resistance in NO_2. The other conditions are in between.

Except for the dark-end, the scores of ZnO are similar to the PCA of the whole data set, which identifies ZnO as the dominant material therein (see Figure S6f–i). Almost all variance is explained by PC1, representing the mean resistance.

Also, for WO_3 most of the variance can be explained by PC1, representing the mean resistance (see Figure S6k–n). The separation of red and dark materials from the other materials can be seen again. PC2 covers the response of the analytes.

In the case of In_2O_3 only 82,9% of the variance is explained by PC1 (representing the mean resistance; see Figure S6p). PC2 has negative loadings during high humidity and positive loadings for NO_2. The low resistance in NO_2 makes blue light stand out in PC2. In the case of dark-start, the higher resistance during the humidity ramps lowers the score for PC2. At the other end of PC2 are dUV (due to low resistance in humidity) and dark-end (high resistance during NO_2 exposure). The other materials are arranged in between. The special behavior of In_2O_3 under blue light was not identified immediately from the PCA of the whole data set and demonstrates the benefit of the individual investigation.

Sensor Signals. The analysis so far was based on the actual resistance at a specific point during the experiment, and thus the distinction between baseline and response was omitted. For the sensor performance, the actual sensor signals are of great interest, which requires a baseline resistance. The sensor signals S of selected conditions have been calculated in the following way:

$$S_{\mathrm{rh}} = \log_{10}\left(\frac{R_{0\%\mathrm{r.h.}}}{R_{50\%\mathrm{r.h.}}}\right)$$

$$S_{\mathrm{CO}} = \log_{10}\left(\frac{R_{\mathrm{air}}}{R_{100\mathrm{ppmCO}}}\right)$$

$$S_{\mathrm{NO_2}} = \log_{10}\left(\frac{R_{0.75\mathrm{ppmNO_2}}}{R_{\mathrm{air}}}\right)$$

In total, there are nine signals taken into account: One for for humidity (50% RH, extracted from the ramps at the beginning of each experiment), four for CO and four for NO_2 (each in 0, 10, 30, 70% RH). The signals are greater than one, except for cases where the response is in the opposite direction than expected for n-type semiconductors. The input matrix for the PCA has the shape 9 × 28 (sensor signals for 9 conditions and 28 combinations of illumination and material). The scores for each material are given in Figure 7, along with the loadings for each concentration. The loadings indicate that PC1 is mainly defined by the NO_2 signals, while PC2 covers CO and humidity. SnO_2 shows both the highest (dark-start) and the lowest (dUV, $S < 1$) signals for NO_2 and covers the whole range of PC1. ZnO and In_2O_3 exhibit the same relationship. WO_3 on the other hand has signals almost independent of the illumination, and thus the scores form one dense cluster. PC1 can explain 67.1% of the total variance and shows once again that among the materials and analytes in this study, NO_2 is dominant. PC2 (explained variance of 15.5%) on the other hand consists of the signals for humidity and CO. The upper section of PC2 is dominated by SnO_2, where especially the high photon energies stimulate a good response to these two gases. For ZnO the response to humidity and CO increases with photon energy. To these analytes, WO_3 responds uniformly as well, with the highest response from dUV. For In_2O_3 the combination for CO and humidity makes PC2 more complicated to interpret. Blue is separated from the remaining points due to its low response to both CO and NO_2. UV has low signals for CO, but reacts strongly to humidity, which brings it almost to the same PC2 value as dark-end or dUV, which reacts to both.

The way in which the scores are distributed allows one to draw some conclusions on the interaction of light and the sensor materials: The sensor signals of WO_3 are barely affected by light of any wavelength, much in contrast to SnO_2, whose response both to CO and NO_2 depends heavily on the illumination conditions. ZnO is less affected by the presence of

https://doi.org/10.1021/acssensors.4c00078
ACS Sens. 2024, 9, 1584–1591

ACS Sensors pubs.acs.org/acssensors Article

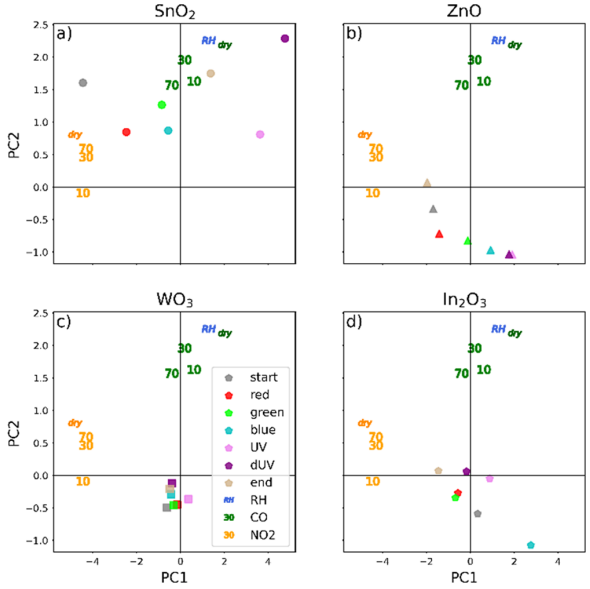

Figure 7. PCA was carried out on the extracted signals. Panels (a–d) show the scores as dots colored according the illumination during the experiment. The loadings of the signals for humidity (50% RH), CO and NO_2 (each in 0, 10, 30, and 70% RH) on the PCs are added as colored labels, corresponding to the background humidity.

light of any wavelength; however, unlike for SnO_2, the effect is more in line with the photon energy. In_2O_3 seems to have a minimum sensor performance around the wavelengths of UV and blue.

CONCLUSIONS

The results of this work revealed that gas sensing at room temperature can be severely affected by the presence of water inside the sensitive layer. Condensation of water from ambient humidity has to be considered or, as in the approach of this study, eliminated by raising the operating temperature. This discovery enabled a method for the systematic screening of four different gas sensing materials with seven illumination conditions, four background humidities, and two target gases. The yield is a reliable, meaningful, and comprehensive set of data for studying light-activated gas sensing.

In the toolbox of chemometrics, there are plenty of well-established methods for the analysis of big data sets. It was shown that methods of multivariate data analysis can be applied in a way that treats each material-illumination combination as a separate observation. Both correlation analysis and PCA helped to identify differences between the sensor materials and conditions, as well as to identify peculiarities among the combinations. To some extent, both methods could even deliver information about the origin of the trends identified. Chemometrics and the representation of raw data complement each other in the analysis.

It was demonstrated that light of different wavelengths has very different effects on the individual materials, ranging from barely affecting the sensor performance in the case of WO_3 to completely change the direction of response in the case of SnO_2. Also, the effects on the baseline resistance and on the response to analyte gases turned out to be independent of each other. Finally, the analysis helped to select special combinations of materials and wavelengths that are of interest for future investigations. For all materials except WO_3, the performance was changed after the light exposure, which makes long-term stability another topic that needs clarification.

ASSOCIATED CONTENT

Supporting Information

The Supporting Information is available free of charge at https://pubs.acs.org/doi/10.1021/acssensors.4c00078.

Technical data of LEDs, XRD, BET, and SEM characterization, and additional loadings for PCA data (PDF)

AUTHOR INFORMATION

Corresponding Author

Nicolae Bârsan − *Institute of Physical and Theoretical Chemistry and Center for Light-Matter Interaction, Sensors & Analytics (LISA+), University of Tübingen, 72076 Tübingen, Germany;* orcid.org/0000-0001-6718-9889; Email: nb@ipc.uni-tuebingen.de

Authors

Benjamin Junker − *Institute of Physical and Theoretical Chemistry and Center for Light-Matter Interaction, Sensors & Analytics (LISA+), University of Tübingen, 72076 Tübingen, Germany;* orcid.org/0000-0002-2229-0534

Arne Kobald − *Institute of Physical and Theoretical Chemistry and Center for Light-Matter Interaction, Sensors & Analytics (LISA+), University of Tübingen, 72076 Tübingen, Germany*

Carolin Ewald − *Institute of Physical and Theoretical Chemistry and Center for Light-Matter Interaction, Sensors & Analytics (LISA+), University of Tübingen, 72076 Tübingen, Germany;* orcid.org/0000-0001-8367-7110

Peter Janoschek − *Institute of Physical and Theoretical Chemistry and Center for Light-Matter Interaction, Sensors & Analytics (LISA+), University of Tübingen, 72076 Tübingen, Germany*

Malte Schalk − *Faculty of Production Engineering, University of Bremen, and Leibniz Institute for Materials Engineering IWT, 28359 Bremen, Germany*

Udo Weimar − *Institute of Physical and Theoretical Chemistry and Center for Light-Matter Interaction, Sensors & Analytics (LISA+), University of Tübingen, 72076 Tübingen, Germany;* orcid.org/0000-0003-2354-0432

Lutz Mädler − *Faculty of Production Engineering, University of Bremen, and Leibniz Institute for Materials Engineering IWT, 28359 Bremen, Germany;* orcid.org/0000-0002-7073-0733

Complete contact information is available at: https://pubs.acs.org/10.1021/acssensors.4c00078

Author Contributions

The manuscript was written through contributions of all authors. All authors have given approval to the final version of the manuscript.

Funding

This research has been supported by German Research Foundation (DFG project number 419896563).

Notes

The authors declare no competing financial interest.

https://doi.org/10.1021/acssensors.4c00078
ACS Sens. 2024, 9, 1584−1591

REFERENCES

(1) Heiland, G. *Zum Einfluss von Wasserstoff Auf Die Elektrisehe Leitfähigkeit an Der Oberfläche von Zinkoxydkristallen*; 1957; Vol. *148*, pp. 15−27.
(2) Majhi, S. M.; Mirzaei, A.; Kim, H. W.; Kim, S. S.; Kim, T. W. Recent Advances in Energy-Saving Chemiresistive Gas Sensors: A Review. *Nano Energy* **2021**, *79*, No. 105369.
(3) Camagni, P.; Faglia, G.; Galinetto, P.; Perego, C.; Samoggia, G.; Sberveglieri, G. Photosensitivity Activation of SnO2 Thin Film Gas Sensors at Room Temperature. *Sens. Actuators B Chem.* **1996**, *31* (1−2), 99−103.
(4) Saura, J. Gas-Sensing Properties of SnO2 Pyrolytic Films Subjected to Ultrviolet Radiation. *Sens. Actuators B Chem.* **1994**, *17* (3), 211−214.
(5) Pollack, I. B.; Lerner, B. M.; Ryerson, T. B. Evaluation of Ultraviolet Light-Emitting Diodes for Detection of Atmospheric NO2 by Photolysis - Chemiluminescence. *J. Atmospheric Chem.* **2010**, *65* (2−3), 111−125.
(6) Cao, K.; Cao, E.; Zhang, Y.; Hao, W.; Sun, L.; Peng, H. The Influence of Nonstoichiometry on Electrical Transport and Ethanol Sensing Characteristics for Nanocrystalline LaFexO3 - *δ* Sensors. *Sens. Actuators B Chem.* **2016**, *230*, 592−599.
(7) Deng, L.; Ding, X.; Zeng, D.; Tian, S.; Li, H.; Xie, C. Visible-Light Activate Mesoporous WO3 Sensors with Enhanced Formaldehyde-Sensing Property at Room Temperature. *Sens. Actuators B Chem.* **2012**, *163* (1), 260−266.
(8) Geng, Q.; He, Z.; Chen, X.; Dai, W.; Wang, X. Gas Sensing Property of ZnO under Visible Light Irradiation at Room Temperature. *Sens. Actuators B Chem.* **2013**, *188*, 293−297.
(9) Giancaterini, L.; Emamjomeh, S. M.; De Marcellis, A.; Palange, E.; Resmini, A.; Anselmi-Tamburini, U.; Cantalini, C. The Influence of Thermal and Visible Light Activation Modes on the NO2 Response of WO3 Nanofibers Prepared by Electrospinning. *Sens. Actuators B Chem.* **2016**, *229*, 387−395.
(10) Gulyaev, A. M.; Van, L. V.; Sarach, O. B.; Mukhina, O. B. Light-Enhanced Sensitivity of SnO2−x Gas Sensors. *Semiconductors* **2008**, *42* (6), 726−730.
(11) Gulyaev, A. M.; Van, L. V.; Sarach, O. B.; Mukhina, O. B. Increased Sensitivity and Selective Capacity of Gas Sensors Based on SnO2−x Films Exposed to Light-Emitting Diodes. *Meas. Technol.* **2008**, *51* (6), 694−698.
(12) Han, L.; Wang, D.; Cui, J.; Chen, L.; Jiang, T.; Lin, Y. Study on Formaldehyde Gas-Sensing of In2O3-Sensitized ZnO Nanoflowers under Visible Light Irradiation at Room Temperature. *J. Mater. Chem.* **2012**, *22* (25), 12915.
(13) Wang, X.-X.; Junker, B.; Ewald, C.; Weimar, U.; Guo, X.; Barsan, N. Proof of Concept for Operando Infrared Spectroscopy Investigation of Light-Excited Metal Oxide-Based Gas Sensors. *J. Phys. Chem. Lett.* **2022**, *13* (16), 3631−3635.
(14) Zhang, C.; Boudiba, A.; De Marco, P.; Snyders, R.; Olivier, M.-G.; Debliquy, M. Room Temperature Responses of Visible-Light Illuminated WO3 Sensors to NO2 in Sub-Ppm Range. *Sens. Actuators B Chem.* **2013**, *181*, 395−401.
(15) Zou, Z.; Qiu, Y.; Xu, J.; Guo, P.; Luo, Y.; Wang, C. Enhanced Formaldehyde Photoelectric Response on ZnO Film Illuminated with Visible Light. *J. Alloys Compd.* **2017**, *695*, 2117−2123.
(16) Blattmann, C. O.; Güntner, A. T.; Pratsinis, S. E. In Situ Monitoring of the Deposition of Flame-Made Chemoresistive Gas-Sensing Films. *ACS Appl. Mater. Interfaces* **2017**, *9* (28), 23926−23933.
(17) Großmann, K.; Kovács, K. E.; Pham, D. K.; Mädler, L.; Barsan, N.; Weimar, U. Enhancing Performance of FSP SnO2-Based Gas Sensors through Sb-Doping and Pd-Functionalization. *Sens. Actuators B Chem.* **2011**, *158* (1), 388−392.
(18) Kemmler, J. A.; Pokhrel, S.; Birkenstock, J.; Schowalter, M.; Rosenauer, A.; Bârsan, N.; Weimar, U.; Mädler, L. Quenched, Nanocrystalline In4Sn3O12 High Temperature Phase for Gas Sensing Applications. *Sens. Actuators B Chem.* **2012**, *161* (1), 740−747.
(19) Lyson-Sypien, B.; Radecka, M.; Rekas, M.; Swierczek, K.; Michalow-Mauke, K.; Graule, T.; Zakrzewska, K. Grain-Size-Dependent Gas-Sensing Properties of TiO2 Nanomaterials. *Sens. Actuators B Chem.* **2015**, *211*, 67−76.
(20) Minnermann, M.; Grossmann, H. K.; Pokhrel, S.; Thiel, K.; Hagelin-Weaver, H.; Bäumer, M.; Mädler, L. Double Flame Spray Pyrolysis as a Novel Technique to Synthesize Alumina-Supported Cobalt Fischer−Tropsch Catalysts. *Catal. Today* **2013**, *214*, 90−99.
(21) Teoh, W. Y.; Amal, R.; Mädler, L. Flame Spray Pyrolysis: An Enabling Technology for Nanoparticles Design and Fabrication. *Nanoscale* **2010**, *2* (8), 1324−1347.
(22) Degler, D.; Pereira De Carvalho, H. W.; Weimar, U.; Barsan, N.; Pham, D.; Mädler, L.; Grunwaldt, J.-D. Structure−Function Relationships of Conventionally and Flame Made Pd-Doped Sensors Studied by X-Ray Absorption Spectroscopy and DC-Resistance. *Sens. Actuators B Chem.* **2015**, *219*, 315−323.
(23) Kemmler, J.; Schopf, S. O.; Mädler, L.; Barsan, N.; Weimar, U. New Process Technologies for the Deposition of Semiconducting Metal Oxide Nanoparticles for Sensing. *Procedia Eng.* **2014**, *87*, 24−27.
(24) Xia, Y.; Zhou, L.; Yang, J.; Du, P.; Xu, L.; Wang, J. Highly Sensitive and Fast Optoelectronic Room-Temperature NO $_2$ Gas Sensor Based on ZnO Nanorod-Assembled Macro-/Mesoporous Film. *ACS Appl. Electron. Mater.* **2020**, *2* (2), 580−589.
(25) Espid, E.; Noce, A. S.; Taghipour, F. The Effect of Radiation Parameters on the Performance of Photo-Activated Gas Sensors. *J. Photochem. Photobiol. Chem.* **2019**, *374*, 95−105.
(26) Schalk, M.; Pokhrel, S.; Schowalter, M.; Rosenauer, A.; Mädler, L. Control of Porous Layer Thickness in Thermophoretic Deposition of Nanoparticles. *Materials* **2021**, *14* (9), 2395.
(27) Bârsan, N.; Weimar, U. *Understanding the Fundamental Principles of Metal Oxide Based Gas Sensors; the Example of CO Sensing with SnO 2 Sensors in the Presence of Humidity*; 2003; Vol. *15*, pp. 813−839.
(28) Birkenstock, J.; Fischer, R. X.; Messner, T. BRASS, the Bremen Rietveld Analysis and Structure Suite; In *Ninth European Powder Diffraction Conference*; Oldenbourg Wissenschaftsverlag, 2006; pp. 237−242. DOI: DOI: 10.1524/9783486992526-041.
(29) Güntner, A. T.; Pineau, N. J.; Pratsinis, S. E. Flame-Made Chemoresistive Gas Sensors and Devices. *Prog. Energy Combust. Sci.* **2022**, *90*, No. 100992.
(30) Samerjai, T.; Tamaekong, N.; Wetchakun, K.; Kruefu, V.; Liewhiran, C.; Siriwong, C.; Wisitsoraat, A.; Phanichphat, S. Flame-Spray-Made Metal-Loaded Semiconducting Metal Oxides Thick Films for Flammable Gas Sensing. *Sens. Actuators B Chem.* **2012**, *171−172*, 43−61.

SUPPORTING INFORMATION

Multivariate analysis of light-activated SMOX gas sensors

Benjamin Junker[1], Arne Kobald[1], Carolin Ewald[1], Peter Janoschek[1], Malte Schalk[2], Udo Weimar[1], Lutz Mädler[2], Nicolae Bârsan[1]*

[1] Institute of Physical and Theoretical Chemistry and Center for Light-Matter Interaction, Sensors & Analytics (LISA+), University of Tübingen, 72076 Tübingen, Germany.

[2] Faculty of Production Engineering, University of Bremen, and Leibniz Institute for Materials Engineering IWT, 28359 Bremen, Germany.

Table S1. Technical specifications of the LEDs used in this work. All data except the power consumption is extracted from the manufacturers' datasheets. Depending on the manufacturer, the intensity of the LEDs is either provided as intensity in cd or radiation power in W. Electrical power consumption was calculated as the product of the applied forward current (20 mA for each LED, Knick J152) and the measured voltage drop (forward voltage, Keithley 6517B).

LED color	manufacturer	product ID	wave-length nm	photon energy eV	viewing angle °	intensity cd	radiation power mW	power comsumption mW	package
red	Würth Elektronik	151054RS03000	631	2.0	30	5	-	40	T-1 3/4
green	RND Components	RND 135-00177	520	2.4	15	39	-	53	T-1 3/4
blue	RND Components	RND 135-00178	468	2.6	15	11	-	85	T-1 3/4
UV	Nichia	NSPU510CS	375	3.3	40	-	7,5	67	T-1 3/4
dUV	Roithner Laser Technik GmbH	DUV310_HL18M	310	4.0	24	-	1,2	99	TO18

Table S2. Overview of material characterization results of XRD, BET, and SEM analysis.

	XRD					BET		SEM
	d_{XRD}	phase, space group	ICSD	lattice constants a,b,c	ρ_{XRD}	SSA	d_{BET}	height
	nm	-	-	Å	g/cm³	m²/g	nm	µm
WO_3	11.0	ortho-rhombic P 1 21/N 1	836	7.396, 7.396, 7.645	7.31	59.39	14.1	21.3
In_2O_3	6.9	cubic I A -3	14387	10.112, 10.112, 10.112	7.13	130.96	6.4	25.0
SnO_2	8.4	tetragonal P 42/M N M	9163	4.735, 4.735, 3.185	7.01	69.51	12.4	37.5
ZnO	15.9	Wurtzite P 63 M C	162843	3.249, 3.249, 5.207	5.68	48.78	21.7	47.0

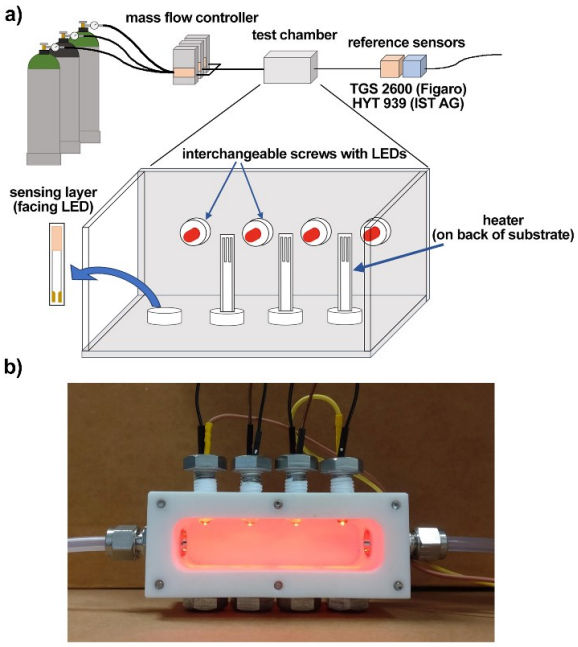

Figure S1 a) Measurement setup used for the characterization of the sensors consisting of gas mixing system, test chamber and reference sensors. Bottom left: Sensor substrate and placement of LEDs and sensors inside the measurement chamber. b) Cover of measurement chamber (bottom view) with LEDs mounted and operated in the side wall.

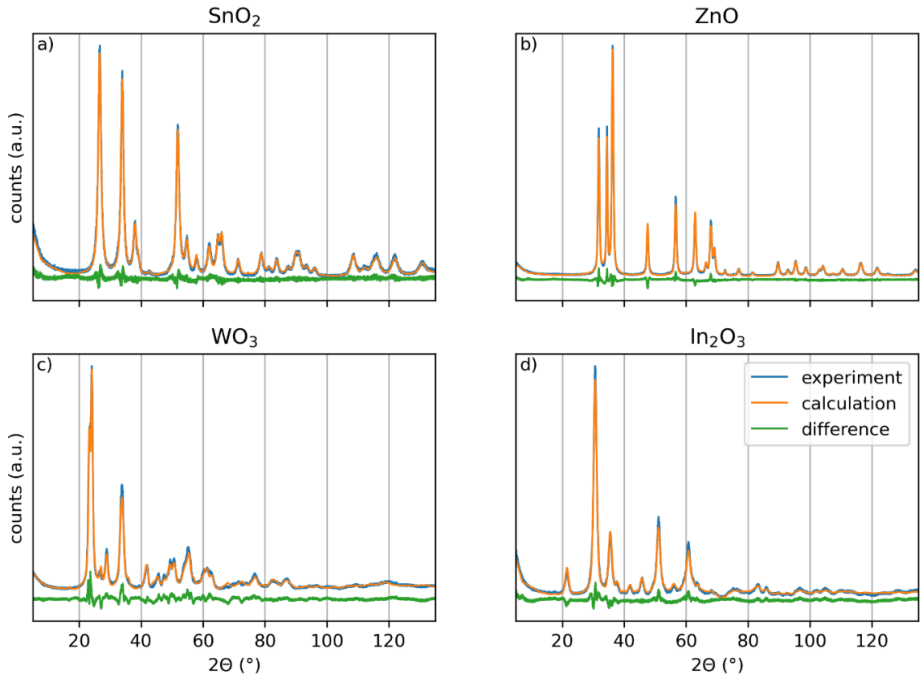

Figure S2 a)-d): XRD patterns of powder samples taken from sprays of respective powders. The experimental and calculated patterns match well and indicate correct phase fitting.

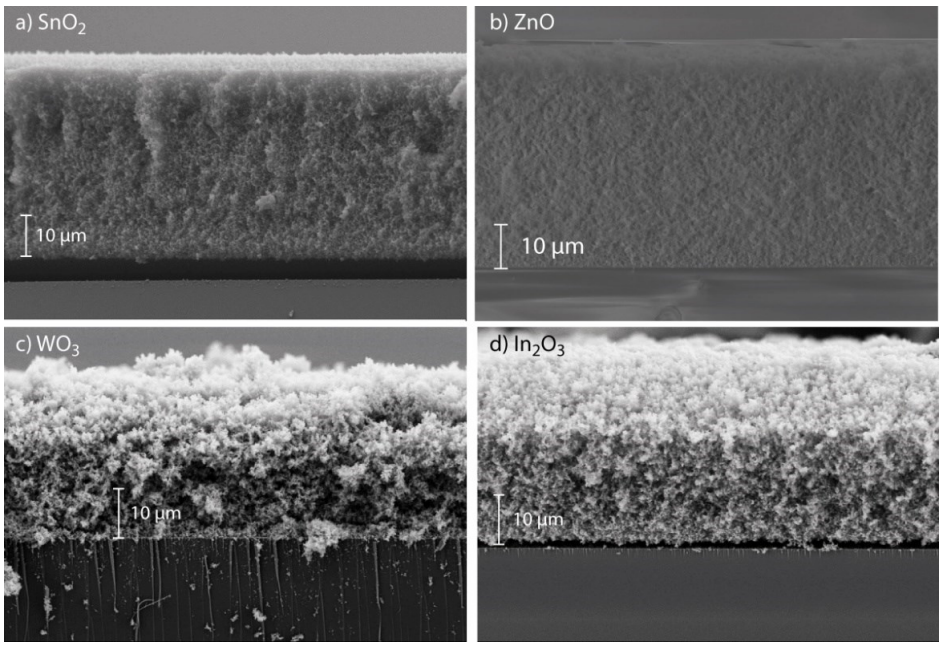

Figure S3 a)-d): SEM cross section of sensing layers deposited on glass slides along with the actual sensors. The dark area between sensing layer (top) and glass slide (bottom) on images (a) and (d) is due to partial detachment of the sensing layer from the substrate.

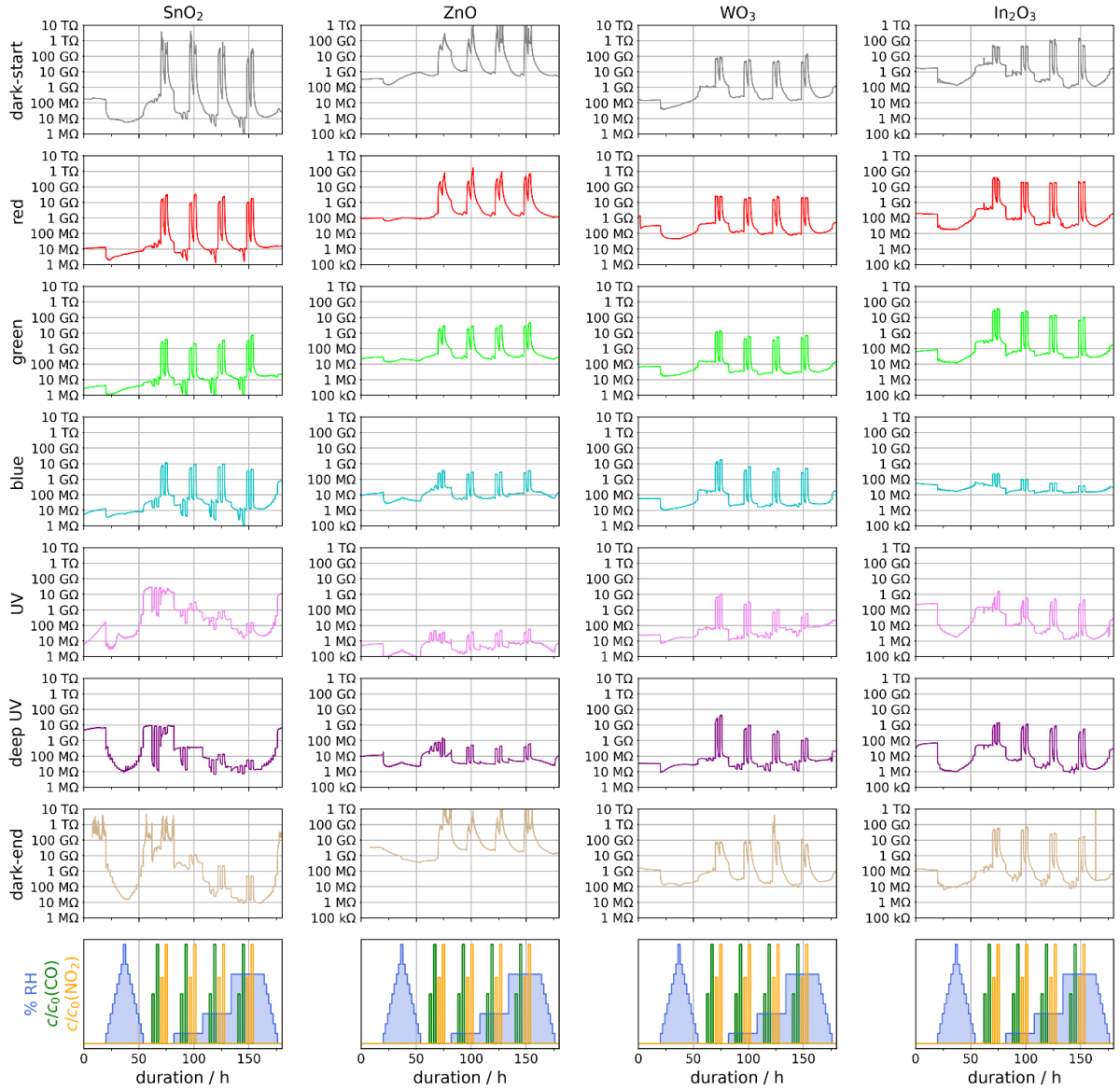

Figure S4: Results of material screening at 70 °C. The sensor resistance for each combination of material (columns) and illumination condi-tion (rows) is plotted versus duration. In the bottom row the concentrations of target gases and humidity are given.

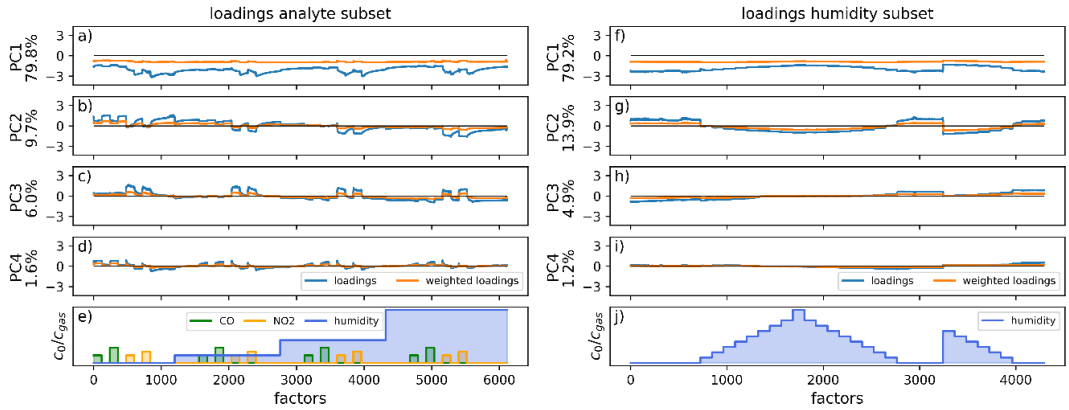

Figure S5: Loadings of PCAs performed on the data subsets of the analyte subsection (a-d) and humidity subsection (f-i). The horizontal balck line represents y=0. The explained variance of each PC is provided in the y-axis label. For easier orientation, the gas concentrations for each factor, i.e. time interval of the experiment, is plotted below the loadings (e,j).

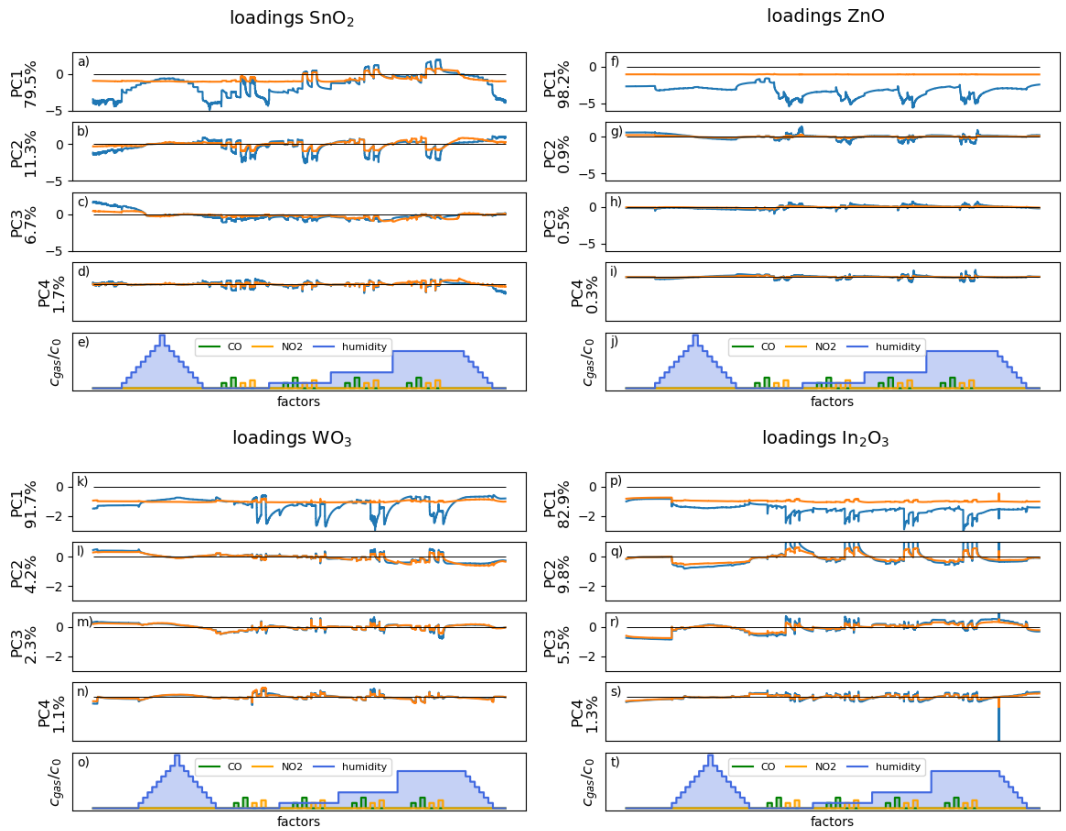

Figure S6 a)-t): Loadings of PCAs performed individually for each material. The horizontal black line represents y=0. The explained variance of each PC is provided in the y-axis label. For easier orientation, the gas concentrations for each factor, i.e. time interval of the experiment, is plotted below the loadings.

Sensors & Actuators: B. Chemical 410 (2024) 135648

Contents lists available at ScienceDirect

Sensors and Actuators: B. Chemical

journal homepage: www.elsevier.com/locate/snb

Ultra Responsive NO_2 silicon nanowires gas sensor

Rachel Elizabeth Brophy [a,*], Benjamin Junker [b,c], Elham Aghabalei Fakhri [a], Hákon Örn Árnason [a], Halldór Guðfinnur Svavarsson [a], Udo Weimar [b,c], Nicolae Bârsan [b,c], Andrei Manolescu [a]

[a] Department of Engineering, Reykjavík University, Menntavegur 1, Reykjavík, IS-102, Iceland
[b] Institute of Physical and Theoretical Chemistry, University of Tübingen, Auf der Morgenstelle 15, Tübingen, 72076, Germany
[c] Center for Light-Matter Interaction, Sensors & Analytics (LISA+), University of Tübingen, Auf der Morgenstelle 15, Tübingen, 72076, Germany

ARTICLE INFO

Keywords:
Gas sensor
Silicon nanowires
Humidity sensor
Nitrogen dioxide

ABSTRACT

Nitrogen dioxide (NO_2) is a hazardous gas emitted primarily from burning fossil fuels. When inhaled, it can have severe health implications, particularly for individuals with respiratory conditions such as asthma. It contributes to ground-level ozone formation, which can cause reduced lung function and increased susceptibility to respiratory infections. When in contact with water moisture in the air, NO_2 is easily oxidized into nitric acid (HNO_3), causing acid rain. Detection of NO_2 levels is therefore important for monitoring air quality and protecting public health. Among the possible technical solutions for gas sensing, silicon nanowires (SiNWs) have proven to be a promising candidate, partly due to their high sensitivity, low manufacturing cost, and ability to perform in various air qualities. This paper presents using SiNWs, fabricated by metal-assisted chemical etching, as a fast, accurate, sensitive, robust, and cost-effective NO_2 gas sensor. Our SiNWs gas sensor can experimentally detect 20 parts per billion (ppb) of NO_2 under a wide range of relative humidity. Our sensor shows ultra-high sensitivity with fast response and recovery time.

1. Introduction

Air pollutants can have detrimental effects on the environment as well as human health. One of the gases that have been of great concern is nitrogen dioxide (NO_2). It is released primarily from burning fossil fuels through power plants and automobiles and is considered one of the major pollutants in today's atmosphere. Exposure to it can cause respiratory infections, even at very low concentrations. Present healthy standards correspond to a 53 ppb annual average, with a one-hour daily maximum concentration of 100 ppb [1]. Whereas, OSHA defines the permissible exposure limit for NO_2 as 5 ppm at one time, or exposure to 1 ppm over 8 h [2]. Additionally, NO_2 contributes to the formation of acid rain when it reacts with water molecules to form HNO_3. It is, therefore, vitally important to monitor and measure the NO_2 concentration in a fast and accurate way.

Silicon nanowires (SiNWs), with their unique properties and versatile nature, have emerged as promising building blocks for various applications across different fields, ranging from solar cells and biosensors to thermoelectrics, as discussed in a very recent review article [3]. These nanoscale structures, typically ranging from a few to a few hundred nanometers in dimensions, can be integrated into transistors, memory devices, and sensors, enabling advancements in miniaturization and performance. This is mainly due to their large surface-to-volume ratio and high sensitivity of current–voltage (I–V) characteristics to the presence of surface states [4]. Although silicon-based gas sensors are already commonly used, the use of SiNWs offers the ability to increase the sensing surface, without increasing the physical size of the device.

Among the various existing methods to synthesize the SiNWs, metal-assisted chemical etching (MACE) is one of the simplest, and it offers the perspective of integration with microelectronics technologies at a lower cost with larger processable areas [5] and easy tuning of geometrical parameters [6]. Both disordered (random) [7] and ordered (periodic) [8] arrays of SiNWs can be obtained by MACE, and they can be fabricated in just two very simple wet-chemical steps. In particular, a recent study reported a sensor based on SiNWs that exhibited a change of electrical resistance of several percent upon exposure to human breath [9]. The presence of germanium (Ge) nanoparticles on the surface of the SiNWs (Ge:SiNWs) could further improve the sensitivity of such a sensor to humidity, and stabilize the baseline [10].

SiNWs used as an NO_2 gas sensor have been a research topic in recent years. In et al. [11] used periodic arrays of SiNWs covered with a periodic porous top electrode, and could detect down to 10 ppb NO_2 for relative humidity (r.h.) below 10%, whereas the detection level reported at higher humidity, such as 30%, was much higher, i.e. 500 ppb. More recently, Kwon et al. [12] used disordered arrays of SiNWs,

* Corresponding author.
E-mail address: rachel18@ru.is (R.E. Brophy).

https://doi.org/10.1016/j.snb.2024.135648
Received 18 December 2023; Received in revised form 28 February 2024; Accepted 14 March 2024
Available online 21 March 2024

and were able to detect 10 parts per million (ppm) of NO_2 at room temperature in dry conditions, but increasing the humidity to 40%–80% (typical atmospheric conditions) had a detrimental effect on their sensitivity. It was suspected that the humidity blocks the NO_2 from binding with the SiNWs, causing a decrease in the overall response, and to lessen this reaction, Qin et al. [13], placed an octadecyl trichlorosilane (OTS) layer within the sensor to block the access of the water molecules to the surface of the SiNWs. With this device, they could detect 50 ppb of NO_2 in the presence of 70% r.h.

In this paper we show that our sensor based on SiNWs does detect concentrations of NO_2 at least as low as 20 ppb at room temperature, at up to 80% r.h. Importantly, our sensor can be easily fabricated, with non-expensive chemicals and laboratory equipment. This allows for a more realistic application of the sensor, using a cheaper and simpler fabrication method than previously reported.

2. Experimental

The SiNWs were made from single-side polished, p-type (boron-doped), (100) Si-wafers with a thickness of 525 µm and resistivity ρ of 0.1 Ω cm to 0.5 Ω cm. A four-step MACE fabrication route was used to fabricate the samples. The route refers to the wet-etching of Si by means of noble metal particles or films present on the Si surface. We utilized silver nanoparticles (Ag-NPs) as our noble metal. Before the Ag-NPs deposition, the wafers were cleaned in an ultrasonic bath with acetone, methanol, and isopropanol, after which they were dipped in deionized water and dried with nitrogen (N_2) gas.

The first step includes the deposition of the Ag-NPs on top of the Si-wafer in an aqueous solution of 1.5 mM $AgNO_3$ and 3 M hydrofluoric acid (HF) for 1 min. The second step involves catalytic etching of the wafer in a diluted solution of HF and hydrogen peroxide (H_2O_2) for 20 min. The etching takes place at the metal-Si interface through a redox reaction, catalyzed by the Ag-NPs. This reaction injects holes (h^+) into the Si substrate's valence band, weakening chemical bonds, and enabling selective dissolution specifically at the metal-Si interface. With such selective etching, the Si touching the noble metal etches significantly faster (several orders) than uncovered Si, causing the metal to sink into the substrate and form pores (NWs). In the third step, the etching was halted by dipping the samples into de-ionized water, after which the Ag residual was removed with 60% nitric acid. Finally, two Au contacts are deposited on the top of the samples. A schematic of the fabrication process is shown in Fig. 1(a). The same fabrication process has also been used in other recent work from our group [7,14].

The SiNWs surface morphology shown in Fig. 2 was characterized by a field-emission scanning electron microscope, FE-SEM (ZEISS SUPRA 35). A top-view and a cross-section image of SiNWs obtained after 20 min etching time is seen. The top-view image reveals that the synthesized SiNWs form an interconnected structure that forms bundles at the tips of wires due to capillary forces being activated when extracting the samples out of the etching solution. Also, a uniform etching depth of 6 µm is evidenced in the cross-sectional image. In order to obtain the diameter of each nanowire, samples were partially cut using a razor blade to separate the wire area from the un-etched part of the Si wafer. The SEM image of the extracted wires revealed the diameter of wires being around 100 nm. It is important to note that the etching process can be variable, therefore characterization of each sample is imperative before testing.

A custom-made gas mixing system with mass-flow controllers (Tylan, Bronkhorst) was used to characterize the SiNWs as a gas sensor. The samples were placed in a measurement chamber made from polytetra fluoro ethylene (PTFE), to limit exposure to outside interactions. The electrical resistance was measured with a Multimeter (Keysight 34972A) in a four-wire configuration. The contact pads on the wafer were connected to copper wires using conductive silver paste (Plano), as illustrated in Fig. 1(b). Humidity was adjusted by sending a ratio of

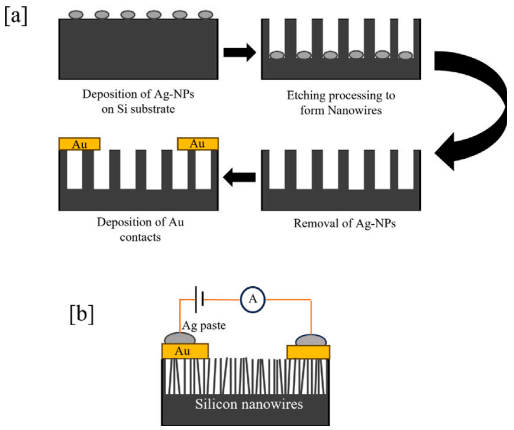

Fig. 1. Image (a) shows the four steps of the MACE process, beginning with the deposition of the Ag nanoparticles (shown as gray ovals) and ending with the deposition of the Au contacts. Image (b) shows the schematic of the final sensor device.

dry air through a vaporizer filled with deionized water, providing 100% r.h. (measured at 20 °C). To assess the sensor performance, a commercial humidity sensor (HYT939, IST AG) and a commercial air quality SMOX gas sensor (TGS2600, Figaro) were used. All experimental testing was completed at room temperature (20 °C).

3. Results and discussion

Our results demonstrate that the sensor based on SiNWs can work successfully as a humidity sensor and a NO_2 gas sensor. The behavior of the SiNW sensor as a humidity sensor was comparable to that of a commercial-grade humidity sensor. Fig. 3 shows the increase in resistance due to the rise in the relative humidity in the chamber. The relative humidity was tested by setting a baseline of 0% R.H for the first two hours. The humidity was then raised step-wise every half an hour until it reached 80% and then reduced step-wise back to 0% in the same manner. The resistance increased from 20 Ω at 0% R.H to 30 Ω at 80% R.H

To test the baseline steadiness, the next testing set included an increase of the humidity for 0.5 h, and then an immediate decrease back to 0% for the next 0.5 h. This testing was done six times. These results showed that the SiNW sensor has a steady baseline and a fast response time.

In the course of this study, the response of the SiNWs to NO_2 was tested extensively, both in the presence of humidity and without humidity. The sensor responded well to concentrations as low as 20 ppb of NO_2. The response and especially the recovery, however, was limited in dry conditions and became faster with increasing the background humidity, as shown in Fig. 4. The recovery was much faster in the presence of humidity already at 10% R.H, which is important for practical applications.

The baseline resistance shows a drift from 950 Ω to 1030 Ω at 50% humidity after 100 h of operation, this can be computed as only an 8% increase. However, we do not consider this a significant drift and future research can be done to reduce the drift further. In addition, the baseline resistance slightly depends on the sample details, such as randomness of the SiNWs, ohmic barriers at the contacts, etc., which at this stage are manually fabricated. More accurate or automatic control of the fabrication process is achievable, for future commercial purposes (see Fig. 5).

To determine the sensor's cross-sensitivity, a variety of common reducing gases was also tested on a separate sample, as can be seen in Fig. 6. No significant response was observed from any of them except for hydrogen, which produced a minor increase in resistance,

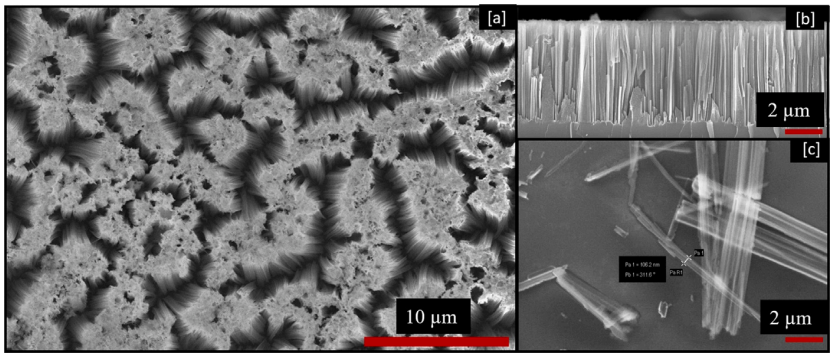

Fig. 2. SEM micrographs of SiNWs obtained by MACE after 20 min etching. Image (a) is the top view of the SiNWs. Image (b) is the cross-sectional analysis. Image (c) shows individual wire configurations on a broken surface.

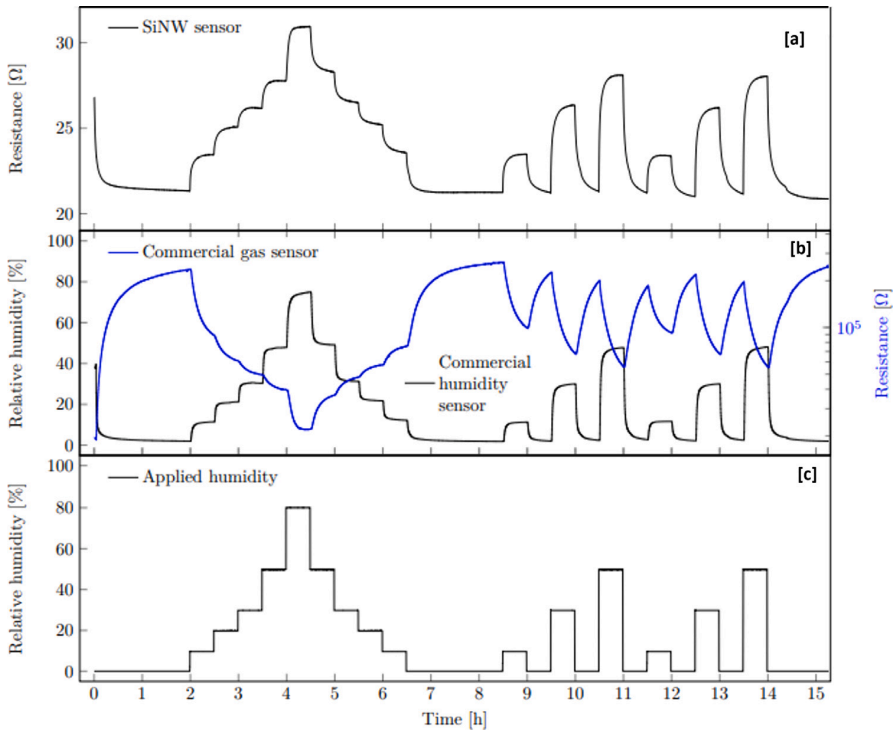

Fig. 3. Graph (a) shows the SiNW response to varying relative humidity concentrations. Graph (b) shows the response of the commercial humidity sensor HYT 939 and the commercial gas sensor TGS 2600. Graph (c) shows the actual set of relative humidity concentrations.

as shown in Fig. 6. In addition, we also tested the cross-sensitivity against SO_2, which showed no response, as well as O_3, which showed a small response, but needs further investigation before a conclusion can be made. In the presence of humidity, the resistance baseline was increased from 28 Ω to 30 Ω, without causing any detrimental effects on the sensitivity to NO_2.

Based on the above results, it can be concluded that the SiNWs system can detect both humidity and NO_2 with high sensitivity and high cross-sensitivity. We have also been able to prove reproducibility by testing different samples with similar sensitivity responses. While we could detect an experimentally controlled concentration of 20 ppb NO_2, it is obvious from Fig. 7 that the gradient of the signal, i.e. the sensitivity, at low concentrations is strong enough to allow the detection of even lower NO_2 concentrations in the presence of humidity.

Previous experimental work reported the detection of humidity with SiNWs using impedance spectroscopy measurements, as capacitance variations due to the presence of water molecules in the proximity of the nanowires [15,16]. Our understanding of the gas sensing mechanism involved in our experiments is based on the interaction of the SiNWs surface with atmospheric oxygen, which can occur at room temperature [17]. The SiNWs were made from a p-type wafer. The chemisorption of oxygen leads to increased hole concentration in the bulk, as electrons are localized at the surface as O_2- (superoxo) ions in a dynamic equilibrium. Water vapor will disturb this equilibrium by competing with oxygen molecules for suitable adsorption sites at the surface [18]. In contrast to oxygen, water molecules are probably only physisorbed and no charge transfer occurs at room temperature [19]. The observed increase in resistance due to humidity exposure is thus ascribed to a displacement of oxygen ions.

In contrast to H_2O, NO_2 can be ionosorbed at the surface already at room temperature. The interaction of NO_2 with the silicon surface has been reported as a formation of surface states that enable a charge

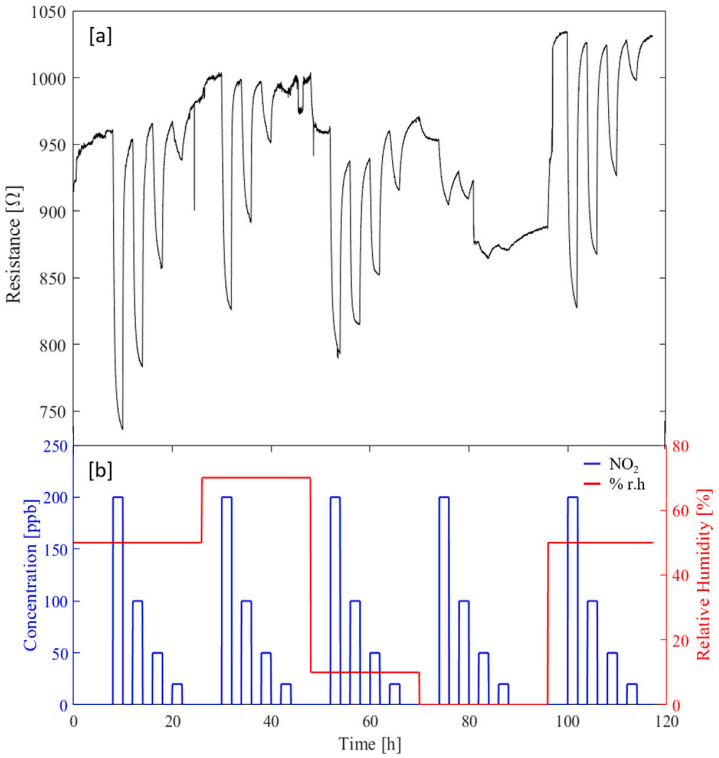

Fig. 4. (a) SiNW response to NO_2 in varying relative humidity concentrations. (b) concentration of NO_2 and background humidity, measured at 20 °C. The humidity was modified in several steps for more than 100 h.

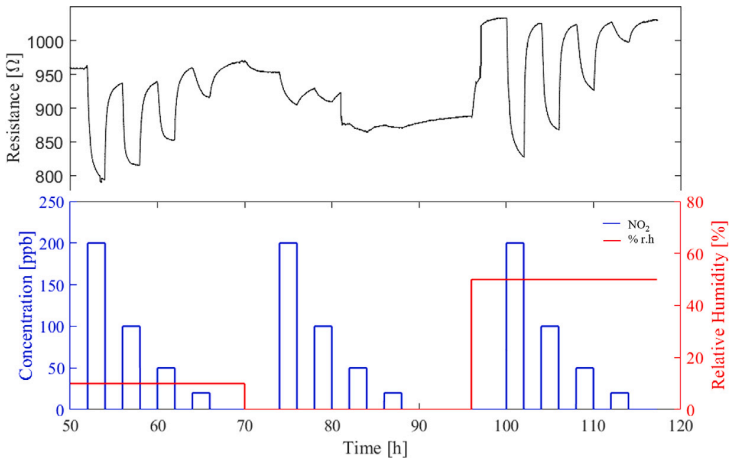

Fig. 5. Zoomed-in image of Fig. 2, showing the resistance with changing concentration of NO_2 and humidity after 50 h. During this time, the sensor has established stability.

transfer [20,21]. The result is the creation of additional holes and a decrease in resistance. The surface interacts much stronger with NO_2 than with H_2O or O_2 and will dominate in this competition. This suggested mechanism can also explain the higher sensor response in humidity compared to dry air: The more water is present at the surface before exposure to NO_2, the more can be displaced by NO_2. The other analytes are either not dissociated at room temperature, e.g. H_2, or their interaction is too weak to compete with O_2 for reactive sites.

4. Conclusion

Our experimental results show that p-doped silicon nanowires fabricated with the MACE method can be used as an inexpensive alternative to commercial humidity and NO_2 sensors. The lowest concentration of NO_2 detected under experimental control was 20 ppb. Unlike common NO_2 gas sensors, our SiNW gas sensors can operate at high humidity levels, allowing for more realistic applications. The highest sensitivity

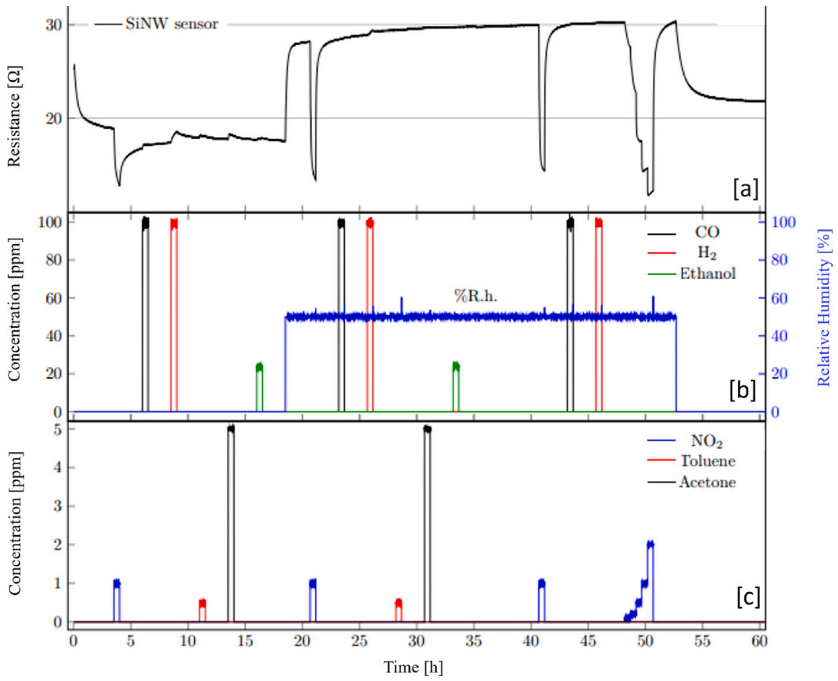

Fig. 6. Graph (a) shows the resistance variation in the SiNW sensor with changing the gas concentrations. Graphs (b) and (c) show the input concentrations of varying gases and relative humidity.

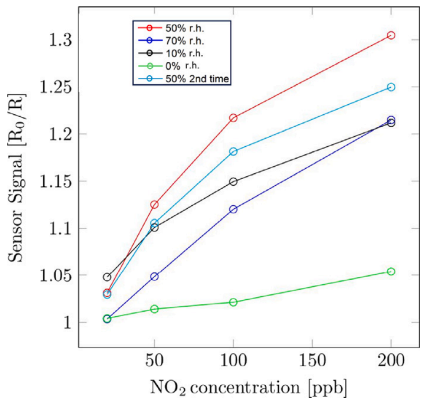

Fig. 7. Sensor signals of the SiNWs for different concentrations of NO_2 in different background levels of relative humidity.

to NO_2 was achieved for about 50% r.h., and the sensitivity dropped dramatically in the absence of humidity. The construction of the sensor device, outlined in the experimental section, is simple and easily reproducible. The experimental results suggest a sensing mechanism that is based on the dynamic equilibrium of the oxygen at the SiNWs surface, in the presence of water molecules, which proves to be very sensitive to the charge transfer from NO_2.

CRediT authorship contribution statement

Rachel Elizabeth Brophy: Writing – review & editing, Writing – original draft, Visualization, Methodology, Investigation, Formal analysis. **Benjamin Junker:** Writing – review & editing, Software, Methodology, Data curation. **Elham Aghabalei Fakhri:** Writing – review & editing, Writing – original draft, Methodology. **Hákon Örn Árnason:** Methodology, Conceptualization. **Halldór Guðfinnur Svavarsson:** Supervision. **Udo Weimar:** Project administration. **Nicolae Bârsan:** Resources, Project administration. **Andrei Manolescu:** Writing – review & editing, Supervision, Project administration.

Declaration of competing interest

The authors declare the following financial interests/personal relationships which may be considered as potential competing interests: Rachel Brophy reports financial support was provided by National Power Company of Iceland. Rachel Brophy reports financial support was provided by The Icelandic Centre for Research. If there are other authors, they declare that they have no known competing financial interests or personal relationships that could have appeared to influence the work reported in this paper.

Data availability

Data will be made available on request.

Acknowledgments

This work was supported by the Reykjavik University Research Fund (grant no. 222018), National Power Company of Iceland (Landsvirkjun) via the Sustainability Institute Forum (SIF) of Reykjavik University (grant no. 222075), and by the Icelandic Center for Research (Icelandic Research Fund grant no. 239987-051).

References

[1] USEPA, Integrated Science Assessment for Oxides of Nitrogen – Health Criteria, Technical Report, U.S. Environmental Protection Agency, 2016.
[2] Occupational Safety and Health Administration, Permissible Exposure Limits – Annotated Tables, Technical Report, OSHA, 2017.
[3] S. Raman, A.R. Sankar, M. Sindhuja, Advances in silicon nanowire applications in energy generation, storage, sensing, and electronics: A review, Nanotechnology 34 (18) (2023) 182001, http://dx.doi.org/10.1088/1361-6528/acb320.

[4] R. Plugaru, E. Fakhri, C. Romanitan, I. Mihalache, G. Craciun, N. Plugaru, H. Árnason, M. Sultan, G. Nemnes, S. Ingvarsson, H. Svavarsson, A. Manolescu, Structure and electrical behavior of silicon nanowires prepared by MACE process, Surfaces Interfaces 33 (2022) 102167, http://dx.doi.org/10.1016/j.surfin.2022.102167, URL https://www.sciencedirect.com/science/article/pii/S2468023022004357.

[5] C. Huo, J. Wang, H. Fu, X. Li, Y. Yang, H. Wang, A. Mateen, G. Farid, K.Q. Peng, Metal-assisted chemical etching of silicon in oxidizing HF solutions: Origin, mechanism, development, and black silicon solar cell application, Adv. Funct. Mater. 30 (52) (2020) 2005744, http://dx.doi.org/10.1002/adfm.202005744, URL https://onlinelibrary.wiley.com/doi/abs/10.1002/adfm.202005744. _eprint: https://onlinelibrary.wiley.com/doi/pdf/10.1002/adfm.202005744.

[6] A.A. Leonardi, M.J.L. Faro, A. Irrera, Silicon nanowires synthesis by metal-assisted chemical etching: A review, Nanomaterials 11 (2) (2021) 383, http://dx.doi.org/10.3390/nano11020383, URL https://www.mdpi.com/2079-4991/11/2/383.

[7] E. Fakhri, R. Plugaru, M.T. Sultan, T.H. Kristinsson, H.O. Árnason, N. Plugaru, A. Manolescu, S. Ingvarsson, H.G. Svavarsson, Piezoresistance characterization of silicon nanowires in uniaxial and isostatic pressure variation, Sensors 22 (17) (2022) 6340, http://dx.doi.org/10.3390/s22176340, URL https://www.mdpi.com/1424-8220/22/17/6340.

[8] H.G. Svavarsson, B.H. Hallgrimsson, M. Niraula, K.J. Lee, R. Magnusson, Large arrays of ultra-high aspect ratio periodic silicon nanowires obtained via top–down route, Appl. Phys. A 122 (2) (2016) 52, http://dx.doi.org/10.1007/s00339-015-9589-y, URL http://link.springer.com/10.1007/s00339-015-9589-y.

[9] R. Ghosh, M.S. Song, J.B. Park, Y. Tchoe, P. Guha, W. Lee, Y. Lim, B. Kim, S.W. Kim, M. Kim, G.C. Yi, Fabrication of piezoresistive Si nanorod-based pressure sensor arrays: A promising candidate for portable breath monitoring devices, Nano Energy 80 (2021) 105537, http://dx.doi.org/10.1016/J.NANOEN.2020.105537.

[10] E. Fakhri, M.T. Sultan, A. Manolescu, S. Ingvarsson, H.G. Svavarsson, Germanium coated silicon nanowires as human respiratory sensing device, in: 2022 International Semiconductor Conference, CAS, 2022, pp. 163–166, http://dx.doi.org/10.1109/CAS56377.2022.9934678, ISSN: 2377-0678.

[11] H.J. In, C.R. Field, P.E. Pehrsson, Periodically porous top electrodes on vertical nanowire arrays for highly sensitive gas detection, Nanotechnology 22 (35) (2011) 355501, http://dx.doi.org/10.1088/0957-4484/22/35/355501, Number: 35.

[12] Y.J. Kwon, A. Mirzaei, H.G. Na, S.Y. Kang, M.S. Choi, J.H. Bang, W. Oum, S.S. Kim, H.W. Kim, Porous Si nanowires for highly selective room-temperature NO_2 gas sensing, Nanotechnology 29 (29) (2018) 294001, http://dx.doi.org/10.1088/1361-6528/aac17b, URL https://iopscience.iop.org/article/10.1088/1361-6528/aac17b. Number: 29.

[13] Y. Qin, Y. Jiang, L. Zhao, Enhanced humidity resistance of porous SiNWs via OTS functionalization for rarefied NO_2 detection, Sensors Actuators B 283 (2019) 61–68, http://dx.doi.org/10.1016/j.snb.2018.12.013, URL https://linkinghub.elsevier.com/retrieve/pii/S0925400518321324.

[14] E. Fakhri, M.T. Sultan, A. Manolescu, S. Ingvarsson, H.G. Svavarsson, Application of p and n-type silicon nanowires as human respiratory sensing device, Sensors 23 (24) (2023) http://dx.doi.org/10.3390/s23249901, URL https://www.mdpi.com/1424-8220/23/24/9901.

[15] H. Li, J. Zhang, B. Tao, L. Wan, W. Gong, Investigation of capacitive humidity sensing behavior of silicon nanowires, Phys. E: Low-Dimens. Syst. Nanostruct. 41 (4) (2009) 600–604, http://dx.doi.org/10.1016/j.physe.2008.10.016, URL https://www.sciencedirect.com/science/article/pii/S1386947708004001.

[16] H. Taghinejad, M. Taghinejad, M. Abdolahad, A. Saeidi, S. Mohajerzadeh, Fabrication and modeling of high sensitivity humidity sensors based on doped silicon nanowires, Sensors Actuators B 176 (2013) 413–419, http://dx.doi.org/10.1016/j.snb.2012.09.062, URL https://www.sciencedirect.com/science/article/pii/S0925400512009756.

[17] H.Z. Massoud, The onset of the thermal oxidation of silicon from room temperature to 1000°C, Microelectron. Eng. 28 (1–4) (1995) 109–116, http://dx.doi.org/10.1016/0167-9317(95)00026-5, URL https://linkinghub.elsevier.com/retrieve/pii/0167931795000265.

[18] Y.H. Huang, T.Y. Yen, M.T. Shi, Y.H. Hung, W.T. Chen, C.H. Wu, K.M. Hung, K.Y. Lo, Competition between oxygen and water molecules on SiO2/P-doped Si surface: The electrical dipole evolution on water/oxygen-adsorbed oxide surface, Sensors Actuators B 376 (2023) 133011, http://dx.doi.org/10.1016/j.snb.2022.133011, URL https://linkinghub.elsevier.com/retrieve/pii/S0925400522016549.

[19] T. Morimoto, M. Nagao, J. Imai, The adsorption of water on SiO2, Al2O3, and SiO2·Al2O3. The relation between the amounts of physisorbed and chemisorbed water, Bull. Chem. Soc. Japan 44 (5) (1971) 1282–1288, http://dx.doi.org/10.1246/bcsj.44.1282, Publisher: The Chemical Society of Japan.

[20] E.A. Konstantinova, L.A. Osminkina, C.S. Sharov, V.Y. Timoshenko, P.K. Kashkarov, Influence of NO_2 molecule adsorption on free charge carriers and spin centers in porous silicon, Phys. Status Solidi (a) 202 (8) (2005) 1592–1596, http://dx.doi.org/10.1002/pssa.200461193, URL https://onlinelibrary.wiley.com/doi/10.1002/pssa.200461193.

[21] L. Boarino, C. Baratto, F. Geobaldo, G. Amato, E. Comini, A. Rossi, G. Faglia, G. Lérondel, G. Sberveglieri, NO2 monitoring at room temperature by a porous silicon gas sensor, Mater. Sci. Eng. B 69–70 (2000) 210–214, http://dx.doi.org/10.1016/S0921-5107(99)00267-6, URL https://linkinghub.elsevier.com/retrieve/pii/S0921510799002676.

Rachel Brophy received her M.Sc in Sustainable Energy from the University of Reykjavik in 2021. Currently, she is a Ph.D. student in the research groups with Andrei Manolescu and Halldór Svavarsson. Her reseach is focused on Molecular Dynamics of Perovskite solar cells, and experimental chemistry/physics.

Benjamin Junker received his M.Sc. in chemistry from the University of Tübingen in 2020. Currently, he is a Ph.D. student in the research group of Udo Weimar and Nicolae Bârsan. His research is focused on various types of gas sensors and operando spectroscopy

Elham Aghabalaei Fakhri received her Ph.D. in Applied Science and Engineering at Reykjavík University in 2023. Currently, she has a Post-Doctoral position at Reykjavík University where she is focusing on Silicon nanowires for healthcare purposes.

Hákon Örn Árnason received his Ph.D. in Applied Science and Engineering at Reykjavík University in 2023. His research focused on Silicon nanowires and experimental physics.

Halldor G. Svavarsson is a professor at Reykjavik University. He has a B.Sc. degree in chemistry from University of Iceland and an M.Sc. degree in mat. Science Eng. from the Technological University of Tampere, Finland. In 2003 he graduated with a Ph.D. degree in physics from the University of Iceland. His main research interest is in the field of silicon nano-nanostructures for sensing applications.

Udo Weimar received his diploma in physics in 1989, his Ph.D. in chemistry in 1993 and his Habilitation in 2002 from the University of Tübingen. Since 2010, he is a full professor in the Department of Chemistry at the University of Tübingen. His research interest focuses on chemical sensors as well as on multicomponent analysis and pattern recognition.

Nicolae Bârsan received his diploma in Physics from the Faculty of Physics of the Bucharest University in 1982. In 1993 his received his Ph.D. in Solid State Physics from the Institute of Atomic Physics, Bucharest, Romania. Since 1995 he has been a senior researcher at the Institute of Physical Chemistry of the University of Tübingen, where he and Udo Weimar lead the Gas Sensors Group.

Andrei Manolescu received his diploma in physics in 1983, and his Ph.D. in physics at the Institute of Atomic Physics, Bucharest University in 1992. Since 2008 he has worked at Reykjavík University where he is currently a Professor and Research Supervisor. His focus is on molecular dynamics and theoretical physics.

THE JOURNAL OF PHYSICAL CHEMISTRY C
A JOURNAL OF THE AMERICAN CHEMICAL SOCIETY

pubs.acs.org/JPCC Article

Operando DRIFTS Proof of Visible-Light-Activated Surface Reduction of WO_3: Implication for Gas Sensing

Benjamin Junker,[‡] Xiao-Xue Wang,[‡] Udo Weimar, and Nicolae Bârsan*

Cite This: J. Phys. Chem. C 2025, 129, 9795−9800 Read Online

ABSTRACT: The interaction of oxygen and water vapor with the surface of WO_3 gas sensors at elevated temperature is well understood. Alternative to heat, illumination with light of different wavelengths at low temperature provides the necessary activation energy for surface reactions. In this study, operando diffuse reflectance infrared Fourier transform spectroscopy (DRIFTS) was employed to investigate and compare the effects of illumination and thermal activation at the molecular level. Photodesorption of oxygen, even by photons with energies below the bandgap, was identified as the key process in light-activated gas sensing with WO_3. Furthermore, oxygen and water vapor were found to act as competitive analytes under illumination, highlighting the complex interplay of surface adsorption and desorption processes in light-activated sensing. The contrasts observed between light and heat activation are the probable reason for different selectivities.

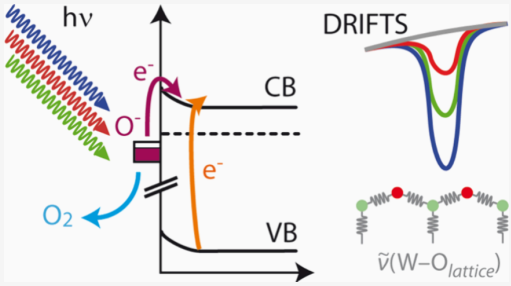

INTRODUCTION

Semiconducting metal oxides (SMOX) are widely employed in gas sensing applications due to their high sensitivity and broad applicability.[1] Conventional SMOX sensors rely on elevated temperatures to provide the activation energy necessary for surface reactions. However, illumination with visible or UV light has emerged as an alternative or additional means of providing the activation energy for chemical reactions. On top of decreased power consumption, the benefit of this mode of activation is the tuning of selectivity and sensitivity.[2,3] Despite growing interest in light-activated gas sensors, the fundamental mechanisms governing light-induced surface reactions remain incompletely understood.

A critical process in gas sensing is the interaction of SMOX surfaces with atmospheric oxygen. At elevated temperature, an equilibrium is established between atmospheric oxygen and chemisorbed oxygen species on the surface, involving the formation of a new chemical bond and charge transfer from the bulk to the adsorbate:

$$\frac{1}{2}O_2 + 2e^- + V_O^{\cdot\cdot} \rightleftharpoons O_O$$

Another crucial factor in light-activated gas sensing is humidity. Since photoactivated sensors typically operate at or near room temperature, ambient humidity plays a far more significant role than for thermally activated gas sensors, where elevated temperatures decrease water adsorption. Understanding how humidity interacts with the sensor surface under light exposure is therefore essential for optimizing the sensor performance. Despite several studies demonstrating that photodesorption of oxygen can occur even with sub-bandgap photon energies, the precise mechanistic details remain unclear.[4,5]

Under illumination, the contribution of photons to the activation energy for any reaction must be significant because the photon energy $h\nu$ of UV−vis light is significantly higher than any equivalent kT of thermal energy that is achieved at typical operation temperatures up to 400 °C.

Extensive studies using infrared spectroscopy, Raman spectroscopy, photoelectron spectroscopy, and DFT calculations have provided insights into the interaction of oxygen and other species.[6−10] However, many of the used conventional methods lack the ability to directly probe surface-bound species in operando conditions. Diffuse reflectance infrared Fourier transformation spectroscopy (DRIFTS) has proven to be a powerful tool for operando or in situ studies to investigate the reception, i.e., the chemical reactions of analyte molecules and charge transfer, in light-activated gas sensing.[11,12] In our previous work, we successfully introduced a light source into an operando DRIFTS system to investigate the role of humidity in light-activated WO_3 sensors and compare it with thermal excitation.[13] Our findings revealed significant differ-

Received: March 18, 2025
Revised: May 5, 2025
Accepted: May 7, 2025
Published: May 14, 2025

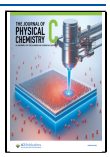

https://doi.org/10.1021/acs.jpcc.5c01808
J. Phys. Chem. C 2025, 129, 9795−9800

The Journal of Physical Chemistry C pubs.acs.org/JPCC Article

ences in the interaction of water vapor with the sensor surface under these two activation modes. However, spectroscopic insights into the impact of light exposure itself is lacking.

This study provides new fundamental insights into the effect of light in light-activated gas sensing, addressing critical knowledge gaps in the field. More importantly, DRIFTS provides direct spectroscopic evidence for these processes, offering an unprecedented level of detail in characterizing the adsorption−desorption dynamics of light-activated gas sensors.

MATERIALS AND METHODS

Commercial WO_3 nanopowder (Sigma-Aldrich Co., <100 nm particle size) was applied to alumina substrates with Pt electrodes via screen printing. Further details on the deposition process and sample treatment, as well as on the setup, can be found elsewhere.[14] The sensor was operated in a custom test chamber, equipped with gas connections, LED, electrical contacts, and a KBr window. Surface DRIFT spectra were recorded using Bruker Vertex 70v and Vertex 80v infrared spectrometers with diffuse reflectance optics (Praying Mantis, Harrick), while the resistance was measured using a HP34401A multimeter. The sensor was exposed to dry N_2 or dry synthetic air (20.5% O_2 in N_2, Westfalen AG) at a flow rate of 150 mL/min. Humidity (10% RH, at 20 °C) was introduced by diverting a fraction of the gas stream through a bubbler filled with deionized water. Experiments at 150 and 300 °C were always performed in the absence of light, and experiments under illumination were always performed at 70 °C. An experiment at 70 °C in the absence of light serves as a reference condition. Absorbance A was calculated from single channel spectra recorded right before and 2 h after the respective change in atmosphere composition as $A = -\log(I/I_0)$. For easier visual comparison, the absorbance of each spectrum was scaled by the dominant absolute value. The sensor response was quantified in terms of a sensor signal S, which is calculated using R_{dark}/R_{light}, R_{dry}/R_{humid}, or R_{air}/R_{N_2}.

The LEDs used in this study are referred to by their colors: Red (Würth Elektronik, 151054RS03000, λ = 631 nm, $h\nu$ = 2.0 eV), green (RND Components, RND 135−00177, 520 nm, 2.4 eV), blue (RND Components, RND 135−00178, 468 nm, 2.6 eV), UV-A (Nichia, NSPU510CS, 375 nm, 3.3 eV), and UV−B (Roithner Laser Technik GmbH, DUV310_HL18M, 310 nm, 4.0 eV). Each LED was placed inside the DRIFT reflectance optics at a distance of 1 cm from the sensing layer without blocking the IR beam path. The LED was separated from the sensor by a KBr window with a thickness of 3 mm and was operated at a constant forward current of 20 mA.

UV−vis diffuse reflectance spectroscopy was carried out on WO_3 powder, employing diffuse reflectance optics (Praying Mantis, Harrick), a broadband UV−vis lamp (DH-2000-Bal, Ocean Insight), and a single channel spectrometer (Maya2000 Pro, Ocean Insight). The spectrum was recorded at room temperature and referenced to $BaSO_4$ (97%, Alfa Aesar).

SCOPE OF CURRENT INVESTIGATIONS

As shown in Figure 1, two primary mechanistic hypotheses have been proposed in the literature to explain the role of light in light-activated gas sensing:[4,5]

1. Band-to-band activation mechanism: In this model, incident photons with energies equal to or greater than the bandgap of the semiconductor ($h\nu \geq E_g$) generate electron−hole pairs in the surface depletion layer. The photogenerated holes will be attracted to the negatively charged oxygen species (O^-, O^{2-}, O_2^-) and recombine with electrons, and the chemisorbed oxygen is released into the gas phase again.
2. Sub-bandgap surface-state activation mechanism: Light can excite electrons from oxygen-related surface states into the conduction band. The relevance of this process is underlined by the fact that photodesorption of oxygen is possible with photons whose energy is lower than the band gap of the semiconductor ($h\nu < E_g$).

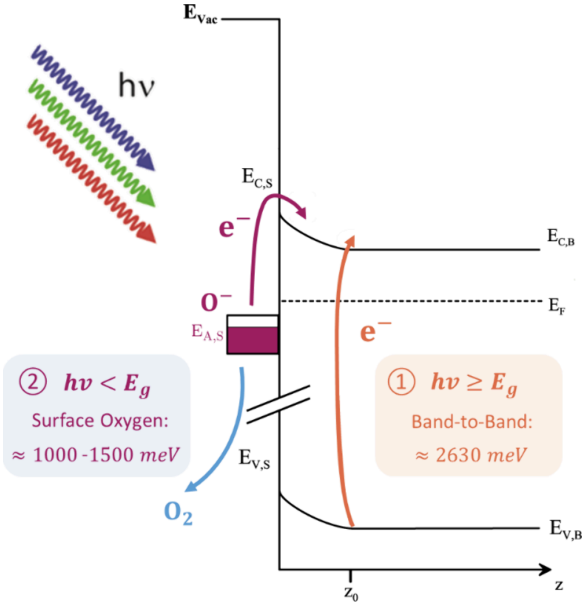

Figure 1. Schematic diagram of the WO_3 band structure and illustration of possible processes on illumination: band-to-band activation (1) and surface-state activation (2).

To distinguish between these mechanisms, WO_3 was applied as the model material in this study due to its well-defined optical properties, outstanding gas sensing properties, and established use in thermal gas sensing.[6,15] Moreover, WO_3 is particularly well-suited for this study due to its bandgap of ~2.63 eV, which corresponds to excitation by blue light (~475 nm).[16,17] By systematically varying illumination wavelengths that provide different photon energies—higher-energy UV light, bandgap-matched blue light, and lower-energy green and red light—and comparing the observed DRIFT spectra to those obtained under thermal activation, we aim to establish a direct correlation between photon energy and surface reaction dynamics. Additionally, we analyze the competitive adsorption of oxygen and water vapor under both conditions to better understand their influence on sensor performance. In previous studies, performing experiments at room temperature yielded results with poor stability and repeatability due the presence of large amounts of physisorbed water and incomplete recovery.[18] Therefore, in this study, the experiments were also conducted at 70 °C, which is still a rather low temperature than 150 and 300 °C.

RESULTS

The band gap was determined by UV−vis spectroscopy. The reflectance data underwent Kubelka−Munk transformation to

https://doi.org/10.1021/acs.jpcc.5c01808
J. Phys. Chem. C 2025, 129, 9795−9800

obtain the Tauc plot presented in Figure 2. Assuming a transitional value of m = 2, i.e., an indirect, allowed transition

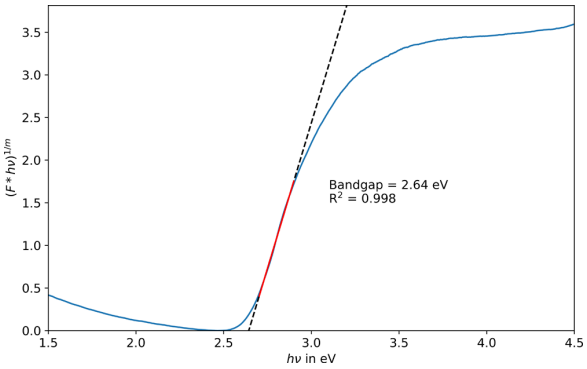

Figure 2. Tauc plot calculated from the WO_3 UV−vis absorbance spectrum.

from the valence band to the conduction band, a band gap value of 2.64 eV was obtained, which is in line with literature reports.[16,17] Therefore, the blue LED's photon energy (2.6 eV) almost exactly matches the optical bandgap of WO_3, while green and red lights are not capable of band-to-band excitation.

The change of the sensors' resistance on illumination, recorded simultaneously with the spectra, is presented in Figure 3a,b. The values are normalized by the last reading in

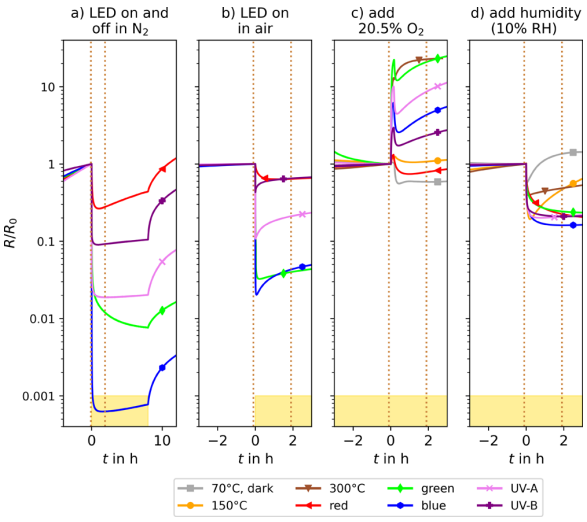

Figure 3. (a−d) Relative changes of sensor resistance during the experiments, normalized to the last reading in the reference condition. The dotted lines indicate the times at which the DRIFT spectra were recorded. For conditions involving illumination, yellow-shaded areas at the bottom of each plot indicate periods where the LED was operating.

darkness. The activation of each LED leads to a sudden decrease in resistance in N_2 and, to a lower extent, in air. In addition, the resistance changes during the transition from N_2 to air, i.e., the exposure to oxygen (Figure 3c), as well as during the exposure to 10% RH at 20 °C in a background of air (Figure 3d) are shown.

Figure 4 shows the resulting absorbance spectra for the exposure to light both in air and in N_2. The main features in

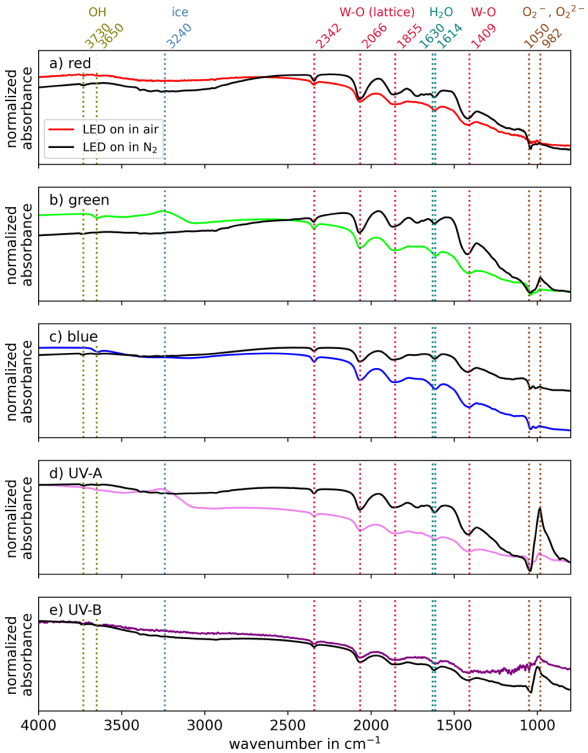

Figure 4. (a−e) DRIFT absorbance spectra for the exposure of WO_3 to light of different wavelengths at 70 °C in a nitrogen atmosphere (black lines) and in air (colored lines).

the spectra are the decreasing peaks at 2066, 1855, and 1409 cm^{-1}, which are assigned to the W−O vibrations.[9,19] Even though the decreasing peak at 2342 cm^{-1} behaves like the W−O related bands, it has been linked to trapped CO_2 originating from organic precursor molecules.[19] This is supported by a strong dependency of this peak's appearance on the preparation method.[6] The peaks at 1614 and 1630 cm^{-1} are assigned to adsorbed water molecules.[19] The assignment of all peaks is summarized in Table 1.

The fact that a decrease in W−O bands can be observed in all spectra presented in Figure 4 lets us draw the following conclusions: The photodesorption of oxygen is not limited to preadsorbed molecular oxygen species, like the superoxo ion, but applies also to lattice oxygen. This indicates an actual reduction of the oxide, at least superficially within the depth

Table 1. Assignment of Peaks in Infrared Spectra

wavenumbers (cm^{-1})	assignment
3730, 3650	OH groups
3240	ice on the IR detector[20]
2342	trapped CO_2[19]
2066, 1855, 1409	W−O vibrations[9,19]
1630	weakly bound water[19]
1614	strongly bound water[19]
1050	superoxide (O_2^-)[21−24]
982	peroxide (O_2^{2-})[21−25]

https://doi.org/10.1021/acs.jpcc.5c01808
J. Phys. Chem. C 2025, 129, 9795−9800

The Journal of Physical Chemistry C pubs.acs.org/JPCC Article

probed by DRIFTS. This reduction can be driven by photons whose photon energy is lower than the bandgap of WO_3. Therefore, the mechanism involving the excitation of charge carriers from surface states seems to be the dominant process, and the energy exceeding the band gap shows similar behavior.

The decrease in resistance observed for all wavelengths (Figure 3a) corroborates the spectral findings: As demonstrated by Giberti et al.,[26] the electrical effect in the absence of oxygen is much stronger because the reoxidation of the sample is limited. This is also reflected in the recovery after turning off the LEDs in a N_2 atmosphere (Figure 3a at 8 h), which is not only slower than the reduction but also incomplete. In a background of air (see Figure 3b), on the other hand, the photodesorption is opposed by the reaction with the atmospheric oxygen.

In addition to oxygen, water is also removed from the surface by the illumination. Water tends to be adsorbed without dissociation and with a rather low energy of around 1 eV, which can be provided by all LEDs.[10] Some differences between the different conditions can be observed in the OH region. The two most prominent OH groups at 3730 and 3650 cm^{-1} are both decreasing at a different ratio in different conditions. The peak at 3240 cm^{-1} is an artifact due the formation of ice on the infrared detector. Finally, two peaks at 1050 and 982 cm^{-1} are of special interest because their change is the highest upon UV illumination. The literature does not provide an assignment for these peaks; however, superoxide (O_2^-) and peroxide (O_2^{2-}) species are typically found in this wavenumber region.[21−25] While their vibrational frequencies vary a lot between different compounds, the peroxide species are usually found at lower wavenumbers. A hypothesis for the change of these peaks is that superoxide species at the surface (1050 cm^{-1}) are reduced to peroxides (982 cm^{-1}) by additional electrons that are in turn provided by illumination.

In further experiments, presented in Figure 5, the sensors were exposed to 20.5% oxygen in a background of dry nitrogen. Interestingly, without illumination or under illumination with red light, a slightly reducing effect is observed. Especially with red light, this is also reflected in the spectra by decreasing W−O bands and can be explained by the interference of humidity with the surface: Photons of red light provide enough energy for the physisorption of water molecules at the surface, as seen by the increasing peak at 1630 cm^{-1} and the surrounding vibrational fine structure of loosely adsorbed water molecules. Moreover, a decrease in W−O bands marks a competition between water and oxygen for the same absorption sites. The electrical effect is therefore most likely not due to the physisorption of water itself, but the hindrance of the adsorption of oxygen. Without illumination, at 70 °C, only changes related to water and OH groups can be seen in the spectra and the actual cause of resistance changes remains unknown. For all other LEDs, oxygen exposure yields an increase in resistance and an increase in W−O bands, along with the displacement of water. Exposure to humidity, on the other hand, leads to a decrease in W−O bands and increase in physisorbed water, again highlighting the competition between these two analytes. However, the spectra exhibit minor qualitative differences: The isolated OH groups at 3730 and 3650 cm^{-1} are changing in different ratios depending on the wavelength. Also, there is a shift in the wavenumber of physisorbed water from 1630 to 1614 cm^{-1}. A temperature-dependent shift of this peak has been assigned to weakly and strongly bound water molecules by Kanan et al.[19] This shift is

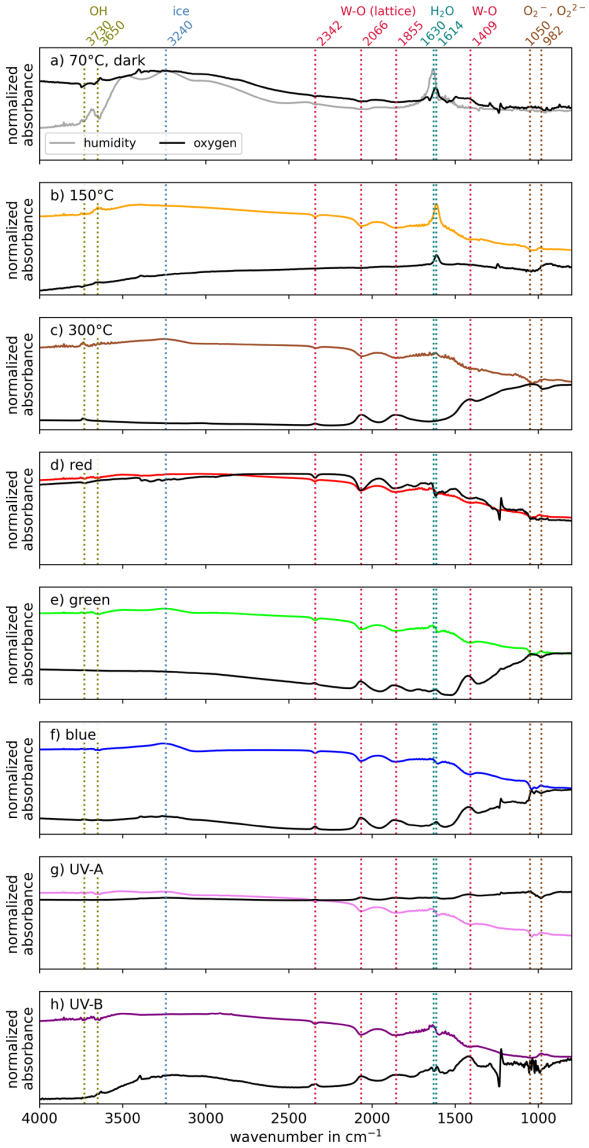

Figure 5. (a−h) DRIFT absorbance spectra for the exposure of WO_3 to 20.5% oxygen in dry nitrogen (black lines) and for the exposure to 10% RH@20 °C in air (colored lines). For (d−h), the exposure was carried out under illumination.

also present in our data recorded at 70 and 150 °C in the absence of light. We assume that light will modulate the strength of the physisorption of water in a similar way to temperature. The spectra recorded in the absence of light at 150 and 300 °C provide a means of comparison between illuminated and heated situations: In terms of W−O bands and the electrical response, the sensor operated at 150 °C behaves similar to the one at 70 °C under high-photon-energy illumination. However, the role of humidity is different: While illumination seems to hinder or even reverse the physisorption of water molecules, at 150 °C, their physisorption seems to be favored, as it can be seen in the spectrum for humidity exposure. Also, during exposure to oxygen, an increase at 1614 cm^{-1} is observed, indicating that

https://doi.org/10.1021/acs.jpcc.5c01808
J. Phys. Chem. C 2025, 129, 9795−9800

the adsorption of traces of water, probably from the oxygen supply, is more likely to happen than the reaction of oxygen itself. Finally, at 300 °C, the reaction with oxygen is dominant and leads to a substantial increase in W−O bands. Physisorbed water does not play a role anymore at this temperature. The electrical effect of water vapor is also the lowest in this condition.

CONCLUSIONS

The interaction between oxygen and WO_3 can be activated by both increased temperature and illumination. The highly equivalent results obtained under green and blue light illumination reveal that band-to-band excitation is less relevant than anticipated. Spectroscopic data indicate surface reduction, corroborating literature reports that identify the excitation of electrons from oxygen-related surface levels to the conduction band. Even in trace amounts, water vapor has been identified as an interferent in oxygen adsorption. Besides that, illumination enhances the reactivity of water vapor while increasing the temperature boosts the one of oxygen. Therefore, activation via illumination enables alternative reaction mechanisms with an impact on selectivity.

AUTHOR INFORMATION

Corresponding Author

Nicolae Bârsan − *Institute of Physical and Theoretical Chemistry (IPTC) and Center for Light-Matter Interaction, Sensors & Analytics (LISA+), University of Tübingen, Tübingen 72076, Germany; International Research Organization for Advanced Science and Technology (IROAST), Kumamoto University, Kumamoto 860-8555, Japan;* orcid.org/0000-0001-6718-9889; Email: nb@ipc.uni-tuebingen.de

Authors

Benjamin Junker − *Institute of Physical and Theoretical Chemistry (IPTC) and Center for Light-Matter Interaction, Sensors & Analytics (LISA+), University of Tübingen, Tübingen 72076, Germany;* orcid.org/0000-0002-2229-0534

Xiao-Xue Wang − *Institute of Physical and Theoretical Chemistry (IPTC) and Center for Light-Matter Interaction, Sensors & Analytics (LISA+), University of Tübingen, Tübingen 72076, Germany; Faculty of Production Engineering, University of Bremen, Bremen 28359, Germany; State Key Laboratory of Materials Processing and Die & Mould Technology, Laboratory of Solid State Ionics, School of Materials Science and Engineering, Huazhong University of Science and Technology, Wuhan 430074, P.R. China*

Udo Weimar − *Institute of Physical and Theoretical Chemistry (IPTC) and Center for Light-Matter Interaction, Sensors & Analytics (LISA+), University of Tübingen, Tübingen 72076, Germany;* orcid.org/0000-0003-2354-0432

Complete contact information is available at: https://pubs.acs.org/10.1021/acs.jpcc.5c01808

Author Contributions

‡These authors contributed equally. The manuscript was written through contributions of all authors. All authors have given approval to the final version of the manuscript. Benjamin Junker: Investigation, data analysis, visualization, writing of the manuscript. Xiao-Xue Wang: Sample preparation, methodology, investigation, data analysis, writing of the manuscript. Udo Weimar: Supervision. Nicolae Bârsan: Conceptualization, writing of the manuscript.

Notes

The authors declare no competing financial interest.

ACKNOWLEDGMENTS

The authors acknowledge the support of Peter Janoschek in performing UV−vis spectroscopy. This work is supported by the National Natural Science Foundation of China (No. 62401216).

ABBREVIATIONS

SMOX, Semiconducting Metal Oxide

REFERENCES

(1) Neri, G. First Fifty Years of Chemoresistive Gas Sensors. *Chemosensors* **2015**, *3* (1), 1−20.

(2) Majhi, S. M.; Mirzaei, A.; Kim, H. W.; Kim, S. S.; Kim, T. W. Recent Advances in Energy-Saving Chemiresistive Gas Sensors: A Review. *Nano Energy* **2021**, *79*, No. 105369.

(3) Wang, J.; Shen, H.; Xia, Y.; Komarneni, S. Light-Activated Room-Temperature Gas Sensors Based on Metal Oxide Nanostructures: A Review on Recent Advances. *Ceram. Int.* **2021**, *47* (6), 7353−7368.

(4) Giancaterini, L.; Emamjomeh, S. M.; De Marcellis, A.; Palange, E.; Resmini, A.; Anselmi-Tamburini, U.; Cantalini, C. The Influence of Thermal and Visible Light Activation Modes on the NO_2 Response of WO_3 Nanofibers Prepared by Electrospinning. *Sens. Actuators, B* **2016**, *229*, 387−395.

(5) Zhang, C.; Boudiba, A.; De Marco, P.; Snyders, R.; Olivier, M.-G.; Debliquy, M. Room Temperature Responses of Visible-Light Illuminated WO_3 Sensors to NO_2 in sub-ppm Range. *Sens. Actuators, B* **2013**, *181*, 395−401.

(6) Staerz, A.; Somacescu, S.; Epifani, M.; Kida, T.; Weimar, U.; Barsan, N. WO_3-Based Gas Sensors: Identifying Inherent Qualities and Understanding the Sensing Mechanism. *ACS Sensors* **2020**, *5* (6), 1624−1633.

(7) Bittencourt, C.; Landers, R.; Llobet, E.; Correig, X.; Calderer, J. The Role of Oxygen Partial Pressure and Annealing Temperature on the Formation of W O Bonds in Thin WO_3 Films. *Semicond. Sci. Technol.* **2002**, *17* (6), 522−525.

(8) Jin, H.; Zhou, H.; Zhang, Y. Insight into the Mechanism of CO Oxidation on WO_3(001) Surfaces for Gas Sensing: A DFT Study. *Sensors* **2017**, *17* (8), 1898.

(9) Hémeryck, A.; Barsan, N.; Staerz, A.; Kobald, A.; Russ, T.; Weimar, U. Thermal Water Splitting on the WO_3 Surface: Experimental Proof. *ACS Applied Electronic Materials* **2020**, *2* (10), 3254−3262.

(10) Albanese, E.; Di Valentin, C.; Pacchioni, G. H2 O Adsorption on WO_3 and WO_{3-x} (001) Surfaces. *ACS Appl. Mater. Interfaces* **2017**, *9* (27), 23212−23221.

(11) Inomata, Y.; Koga, K.; Shinkai, T.; Kida, T. Pt-Decorated ZnO Nanorods for Light-Assisted Ethanol Sensing and In Situ Analysis of the Sensing Mechanism under Light Irradiation. *ACS Appl. Mater. Interfaces* **2025**, *17* (1), 1399−1407.

(12) Wang, Z.; Wang, X.; Wang, H.; Chen, X.; Dai, W.; Fu, X. The Role of Electron Transfer Behavior Induced by CO Chemisorption on Visible-Light-Driven CO Conversion over WO_3 and $CuWO_4/WO_3$. *Applied Catalysis B: Environmental* **2020**, *265*, No. 118588.

(13) Wang, X.-X.; Junker, B.; Ewald, C.; Weimar, U.; Guo, X.; Barsan, N. Proof of Concept for Operando Infrared Spectroscopy Investigation of Light-Excited Metal Oxide-Based Gas Sensors. *J. Phys. Chem. Lett.* **2022**, *13* (16), 3631−3635.

(14) Schmitt, E. A.; Krott, M.; Epifani, M.; Suematsu, K.; Weimar, U.; Barsan, N. Volatile Organic Compound Sensing with WO_3 -Based Gas Sensors: Surface Chemistry Basics. *J. Phys. Chem. C* **2024**, *128* (4), 1633−1643.

(15) Epifani, M. Mechanistic Insights into WO_3 Sensing and Related Perspectives. *Sensors* **2022**, *22* (6), 2247.
(16) Strehlow, W. H.; Cook, E. L. Compilation of Energy Band Gaps in Elemental and Binary Compound Semiconductors and Insulators. *J. Phys. Chem. Ref. Data* **1973**, *2* (1), 163−200.
(17) Kwong, W. L.; Savvides, N.; Sorrell, C. C. Electrodeposited Nanostructured WO_3 Thin Films for Photoelectrochemical Applications. *Electrochim. Acta* **2012**, *75*, 371−380.
(18) Junker, B.; Kobald, A.; Ewald, C.; Janoschek, P.; Schalk, M.; Weimar, U.; Mädler, L.; Bârsan, N. Multivariate Analysis of Light-Activated SMOX Gas Sensors. *ACS Sens.* **2024**, *9* (3), 1584−1591.
(19) Kanan, S. M.; Lu, Z.; Cox, J. K.; Bernhardt, G.; Tripp, C. P. Identification of Surface Sites on Monoclinic WO_3 Powders by Infrared Spectroscopy. *Langmuir* **2002**, *18* (5), 1707−1712.
(20) Chesters, M. A.; McCash, E. M. The adsorption and reaction of methanol on oxidized copper(111) studied by Fourier transform reflection-absorption infrared spectroscopy. *Spectrochim. Acta, Part A* **1987**, *43*, 1625.
(21) Davydov, A. A.; Sheppard, N. T. *Molecular Spectroscopy of Oxide Catalyst Surfaces*; John Wiley & Sons, Ltd, 2003; Vol. *690*.
(22) Staerz, A.; Weimar, U.; Barsan, N. Current State of Knowledge on the Metal Oxide Based Gas Sensing Mechanism. *Sens. Actuators, B* **2022**, *358*, No. 131531.
(23) Caulfield, L.; Sauter, E.; Idriss, H.; Wöll, C. Tracking the Redox Properties of CeO_2 Powders by Infrared Spectroscopy: Monitoring the Defect States by O_2 Adsorption and the Ce^{3+} Spin−Orbit Transition. *J. Phys. Chem. C* **2025**, *129* (2), 1228−1233.
(24) Gurlo, A. Interplay between O_2 and SnO_2: Oxygen Ionosorption and Spectroscopic Evidence for Adsorbed Oxygen. *ChemPhysChem* **2006**, *7* (10), 2041−2052.
(25) Xu, J.; Zhang, T.; Sun, Y.; Fang, S.; Wu, Z.; Zhu, J.; Dai, L.; Liu, W.; Zhang, B.; Zhang, J.; et al. Insight into the Roles of Superoxide-Type (Mn(-O-)$_2$Mn), Bridge-Type (Mn-O-Mn), and Terminal-Type (Mn O) Oxygen Species on MnO_2 of Different Crystal Structures in CO Oxidation Using Operando TPR-DRIFTS-MS. *Applied Catalysis A: General* **2024**, *670*, No. 119519.
(26) Giberti, A.; Malagù, C.; Guidi, V. WO_3 Sensing Properties Enhanced by UV Illumination: An Evidence of Surface Effect. *Sens. Actuators, B* **2012**, *165* (1), 59−61.

https://doi.org/10.1021/acs.jpcc.5c01808
J. Phys. Chem. C 2025, 129, 9795−9800

THE JOURNAL OF PHYSICAL CHEMISTRY C
A JOURNAL OF THE AMERICAN CHEMICAL SOCIETY

pubs.acs.org/JPCC Article

Investigation on the Structure–Function Relationship of Atomic-Layer-Deposited Platinum Additives on Tungsten Trioxide Gas Sensor Materials

David Degler, Ugur Geyik, Benjamin Junker-Reiss, Muhammad Hamid Raza, Patrick Amsalem, Norbert Koch, Blanka Detlefs, Nicola Pinna, Udo Weimar, and Nicolae Barsan*

Cite This: J. Phys. Chem. C 2025, 129, 15301−15308

Read Online

ACCESS | Metrics & More | Article Recommendations | Supporting Information

ABSTRACT: Different Pt structures were deposited on WO_3 by using atomic layer deposition. The gas sensing properties, structures of the Pt loadings, and their influence on the gas detection mechanism were investigated using extensive material characterization and operando spectroscopies. The results show that, depending on the number of atomic layer deposition cycles, different Pt structures can be obtained, which influence the gas detection in different ways. The found structures range from predominantly ionic Pt sites over oxidic particles to partially oxidized metallic particles. It was found that single ion sites and small oxidic particles have the most effective influence on gas detection, whereas partially oxidized metal particles lead to a lower gas sensing performance.

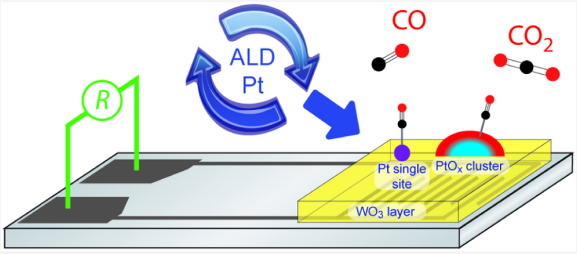

INTRODUCTION

Chemoresistive gas sensors based on semiconducting metal oxides (SMOX) are used in a wide variety of applications, ranging from air quality measurements over process control to health or safety applications.[1−3] The detection of the analyte gases takes place by different surface reactions and strongly depends on the nature of the SMOXs' surface properties, the analyte gas as such, and other gases present. For WO_3, these surface reactions range from the interplay of reduction and reoxidation of the SMOX surface by analyte gases like CO or H_2 to complex reactions involving dehydrogenation and partial oxidation, as observed for different volatile organic compounds.[4−8] If at least one step of these surface reactions involves a charge transfer between SMOX and reactive surface species, this interplay has a direct influence on the number of free charge carriers and, thus, on sensor resistance, i.e., the sensor signal.[2,9] Both the electrical properties of the SMOX bulk or surface and the reactivity of the surface can be strongly influenced by the deposition of noble metal additives at the surface. Their composition, structure, and distribution on the supporting SMOX have a significant influence on the gas sensing properties.[10,11] The structures of noble metal loadings range from individual atoms or ions, which can form a reactive center, to the introduction of separate noble metal phases that form a heterojunction. In addition to this size effect, the coverage of the SMOX and distribution of the noble metal loading also play an essential role. If there is too little noble metal present or if it is poorly distributed, this only has a local influence on the chemical and, in particular, electrical properties, i.e., it changes the reactivity, but not sufficiently the charge transport and thus the gas-sensitive properties.[11]

A difficulty in previous studies was to separate the influence of different synthesis methods on the nature and size of the noble metal additives and the SMOX as such from size-dependent changes in the gas sensing mechanism. In order to determine structure−function relationships, it is therefore of great importance to be able to obtain noble metal structures of different sizes using the same synthesis method. Thus, atomic layer deposition (ALD) was selected as the synthesis method of choice for this study, as it allows precise control over the deposition process and can be applied to already prepared gas sensors devices, i.e., eliminating possibly negative impacts of the sensing layer deposition on the noble metal additives, and focuses Pt deposition to regions accessible to the target and interfering gases.[12,13]

For this investigation targeting the effect of Pt surface additives, it makes sense to choose a target gas that has a simple surface chemistry. The logical choice is CO, whose surface chemistry on WO_3 is well understood.[6,7] Furthermore, unlike H_2, CO does not form hydroxyl groups. Also it does not undergo

Received: July 18, 2025
Revised: August 7, 2025
Accepted: August 7, 2025
Published: August 15, 2025

https://doi.org/10.1021/acs.jpcc.5c05000
J. Phys. Chem. C 2025, 129, 15301−15308

The Journal of Physical Chemistry C pubs.acs.org/JPCC Article

complex surface reactions, as is the case with volatile organic compounds.

MATERIALS AND METHODS

WO_3 nanoparticles were purchased from Sigma-Aldrich (Sigma-Aldrich Co., <100 nm particle size), and trimethyl-(methylcyclopentadienyl)platinum(IV) [(MeCp)Pt(IV)Me_3], 99%, was purchased from STREM Chemicals Inc. The gases for the synthesis (Ar, O_2, N_2) were sourced from Air Liquide, and all had a purity of 99.99%. For gas sensing and operando experiments, the carrier gases (synthetic air, N_2, or He) and high-purity test gas mixtures were obtained from Westfalen, with the exception of the experiments done at the synchrotron light source, where on-site available high-purity carrier gases and analyte mixtures were used.

Gas sensors were produced by screen-printing a 1,2-propanediol-based WO_3 paste onto planar Al_2O_3 substrates, which are equipped with interdigitated Pt electrodes on the front and a backside Pt heater.[14] The coated gas sensors were dried at 70 °C and calcined stepwise at 400, 500, and 400 °C for 10 min each. For X-ray absorption and X-ray photoelectron spectroscopies, special Al_2O_3 substrates with Au electrodes and a Pd/Ag-alloy heater were used to avoid Pt signals from the sensor substrate.

Pt loadings were deposited on WO_3 directly onto the calcined gas sensors. ALD was performed in a thermal ALD system by ARRADIANCE (GEMStar-XT). [(MeCp)Pt(IV)Me_3], contained in a stainless steel canister at 55 °C, and ultrahigh purity O_2 were used as metal precursor and counter-reactant/oxidant, respectively. The precursors were supplied using two separate supply lines maintained at 120 °C and 80 °C for the platinum precursor and oxygen, respectively. N_2 was used as a carrier gas and purging gas for the precursors to the reaction chamber, and to remove any of the excess reactants and byproducts, respectively. The temperature of the ALD reaction chamber was maintained at 265 °C during Pt deposition. The ALD cycle was adjusted as a pulse/exposure/purge sequence of 0.6/30/30 s and 0.3/35/50 s for (MeCp)Pt(IV) Me_3 and O_2, respectively. The nature, loading, and the particle size of the Pt species were controlled by changing the number of ALD cycles (2, 5, 10, 25, and 50). The samples are named ALD2, ALD5, ALD10, ALD25, and ALD50, respectively. The ALD process was followed by calcination at 300, 400, 500, and 400 °C for 10 min each.

X-ray photoelectron spectroscopy (XPS) measurements were performed using JPS-9030 (JEOL) and Phoibos 100 (SPECS) hemispherical analyzers in ultrahigh vacuum (UHV) setups (base pressure 5×10^{-10} mbar) and the Mg Kα radiation from dual anode X-ray sources.

High-angle annular dark-field scanning transmission electron microscopy (HAADF-STEM) was performed using a FEI Talos F200S scanning/transmission electron microscope operated at 200 kV. The analysis of the microscopy data was performed using Velox software, version 2.6, and *ImageJ* freeware.

For gas sensing and operando spectroscopy, gases were mixed and dosed using a homemade gas mixing system based on computer-controlled mass flow controllers. Relative humidity (RH) levels were adjusted by mixing humidified air from a bubbler filled with deionized water at 20 °C in the dry gas stream. Gas sensors were placed in dedicated measuring cells, and the heaters were connected to a power supply. The sensor resistance was recorded using a digital electrometer (Keithley 617).

X-ray absorption spectroscopy (XAS) was performed at X-ray absorption and emission spectroscopy beamline ID26 at the European Synchrotron Radiation Facility (ESRF) in Grenoble, France. The incident energy was selected using a double-crystal monochromator with a Si(111) crystal, with an energy resolution of 1.75 eV. High-energy-resolved fluorescence detection (HERFD) was used to record X-ray absorption near edge structure (XANES) spectra at the Pt L_3 edge (Pt $L_{\alpha 1}$ emission line) as a function of the incident energy using a Johann geometry X-ray emission spectrometer, equipped with four Ge crystal analyzers (Ge(660) reflection).[15] The use of HERFD is necessary to detect traces of Pt in the presence of W, as the overlap of the Pt $L_{\alpha 1}$ (9442 eV) and W $L_{\beta 1}$ (9472 eV) emission lines prevents other detection methods, due to the large excess of W in the WO_3 support. The HERFD-XANES spectra were evaluated using the Larch software package.[16]

Diffuse reflectance infrared Fourier transform spectroscopy (DRIFTS) was carried out on a Vertex 70v spectrometer (Bruker) equipped with a high-performance globar mid-IR source and a midband MCT detector. The sensors were placed in a homemade operando cell with a KBr window, which was fixed in a six-mirror optic (Praying Mantis by Harrick). DRIFT spectra were recorded with a resolution of 2 cm^{-1}. Absorbance spectra were calculated as described elsewhere.[17]

RESULTS AND DISCUSSION

The composition of the Pt species at the surface was studied by XPS (Figure 1). The growing surface coverage of Pt with an increasing number of ALD cycles can be observed by comparing the intensities of the W 5s peak of WO_3 at 79.4 eV and the Pt 4f peaks at lower binding energies. The assignments of the different Pt binding energies are given in Table 1.

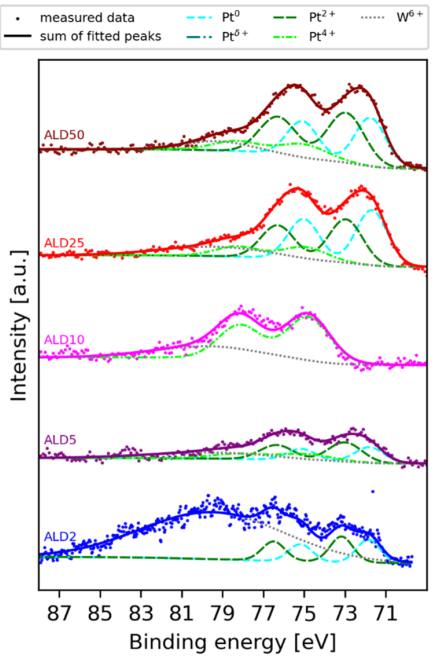

Figure 1. XP spectra of all Pt-loaded samples after calcination. The corresponding peak assignments are shown in Table 1. $Pt^{\delta+}$ was only found before calcination; see Figure S1.

https://doi.org/10.1021/acs.jpcc.5c05000
J. Phys. Chem. C 2025, 129, 15301−15308

Table 1. Assignment of Pt $4f_{7/2}$ Species Found by XPS

binding energy	species	assignment	references
71.1−71.3 eV	Pt^0	metallic Pt particles	18−22
72.0 eV	$Pt^{\delta+}$	single Pt atoms	23
72.7−73.0 eV	Pt^{2+}	single Pt ions	18,19,22
		partially oxidized Pt particles	19,20
74.8−75.0 eV	Pt^{4+}	Pt dioxide (PtO_2)	19,20

ALD2 shows the presence of a Pt^{2+} species, as well as metallic Pt. ALD5 shows a similar pattern of Pt^{2+} species and metallic Pt, but additionally a weak contribution of Pt^{4+}. ALD10 shows only the presence of Pt^{4+}. ALD25 and ALD50 show mainly metallic Pt and Pt^{2+} species with a contribution of Pt^{4+}.

To understand the impact of the calcination (400, 500, and 400 °C for 10 min each) on the Pt chemical state, i.e., the structure of the Pt loadings, additional spectra have been recorded prior to calcination (Figure S1). They clearly show different chemical states for the Pt surface species, depending on the number of ALD cycles. The change of single atom sites into other species due to calcination illustrates that single atom sites are not stable during sensor operation at 300 °C. Hence, a single treatment at an elevated temperature is required to obtain a sensor with a stable surface structure and, thus, performance.

To further investigate the morphology and microstructure of the Pt-loaded samples, HAADF-STEM was carried out before and after calcination. All micrographs of ALD2 (Figure 2) show

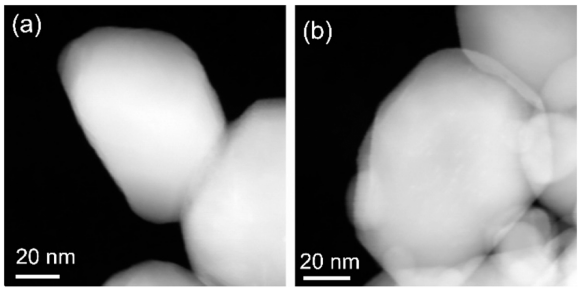

Figure 2. HAADF-STEM micrographs of ALD2 before (a) and after (b) calcination.

no phase that has segregated from the WO_3 particles, indicating the presence of single ionic Pt species, which are incorporated in the surface of WO_3, rather than metallic or oxidized Pt particles.[24]

For ALD5 to ALD50, electron microscopy reveals the presence of a separated phase both before (Figure S2) and after calcination (Figure 3), which is in agreement with the presence of fully metallic, fully oxidized, or partially oxidized Pt particles. The micrographs show that the WO_3 nanoparticles are uniformly covered with Pt clusters/particles, forming homogeneous particles at higher numbers of deposition cycles; the diameter of the Pt particles increases from around 1 nm for ALD5 to above 6 nm for ALD50. ALD50 shows agglomeration of the Pt particles, forming a quasi-continuous coverage of the supporting WO_3. This fine control of particle size is indeed one of the key features of the ALD method in combination with thermal treatment.[12,13]

As the chemical state of the Pt loadings is highly sensitive to the atmospheric composition and XPS and electron microscopy were done in vacuum, it is essential to probe the chemical state of the Pt loadings by an operando method, which allows to study the samples in realistic atmospheres and at typical operation conditions.[25] Thus, ALD2, ALD5, and ALD25 were selected to be further studied by operando XAS. Figure 4 shows the HERFD-XANES spectra of the three Pt-loaded WO_3 samples operated at 300 °C in the presence of 20% vol O_2 in a He background and reference spectra of Pt foil and PtO_2.

Comparing the Pt L_3 whiteline position of the ALD samples with the references clearly shows that on these samples, the loadings are present neither as metallic Pt nor as fully oxidized Pt^{4+}, but are rather found to be between the two references. In the literature, this is either assigned to Pt^{2+}, related to single Pt ions[18,22] or metallic Pt particles with an oxidized surface.[26] It is therefore not possible to distinguish between single Pt ions and partially oxidized particles using HERFD-XANES spectra. The differences in Pt L_3 whiteline intensities are expected to be real for ALD2 and ALD5, while for ALD25, the lower intensity may be caused by self-absorption due to the high Pt coverage. However, self-absorption should not affect the position of the whiteline and, thus, the interpretation of the spectra.

In summary, from the presented ex situ characterization, the following conclusions can be drawn.

- ALD2 presents Pt single ion sites at the WO_3 surface, as it is indicated by the applied X-ray spectroscopies and the absence of any segregated phase in the electron micrographs.
- ALD5 shows a separated solid phase in the electron micrographs and the presence of Pt^{4+} in the XP spectrum as well as a higher whiteline intensity in the HERFD-XANES spectra. This suggests the presence of single Pt ion sites as well as small oxidized Pt particles.
- ALD10 is expected to have only PtO_2 particles on the WO_3 surface, as only Pt^{4+} is found by XPS, and the electron micrographs show a separated phase
- ALD25 and ALD50 show very similar results, that is, a separate phase in the electron micrographs, which by XPS is assigned to both superficially oxidized Pt particles (Pt^0 and Pt^{2+}) and fully oxidized Pt (Pt^{4+}). The presence of partially oxidized Pt agrees with the HERFD-XANES spectra of ALD25.

Therefore, the following trend with an increasing number of ALD cycles can be determined. First, single Pt ion sites are formed on the surface (ALD2), followed by the coexistence of these single ion sites with very small, oxidized particles (ALD5), which then evolve into the dominant presence of entirely oxidized Pt particles (ALD10). However, further Pt deposition then leads to the formation of metallic particles that are superficially oxidized (ALD25 and ALD50).

The gas sensing performance at 300 °C of pristine and Pt-loaded WO_3 was studied for CO, acetone, toluene, NO_2, ethanol, and H_2 in different relative humidity backgrounds (5, 30, and 70% RH; see Figure S3). As shown in Figure 5, the presence of Pt on WO_3 significantly changes the response of the Pt-loaded materials toward the different analyte gases, namely, increasing the response to CO and H_2 in comparison to organic vapors like ethanol, toluene, and acetone. This is apparent when comparing the ratios of the sensor signals of CO and acetone (Figure S4). Pristine WO_3 shows by far a higher response to acetone than to CO. The highest ratio of the CO to acetone signal is observed for ALD5. The signal ratios of ALD2 are located between those of pristine WO_3 and ALD5. The other Pt-loaded samples, ALD10 to ALD50, show response ratios only slightly lower than the one of ALD5.

https://doi.org/10.1021/acs.jpcc.5c05000
J. Phys. Chem. C 2025, 129, 15301−15308

The Journal of Physical Chemistry C pubs.acs.org/JPCC Article

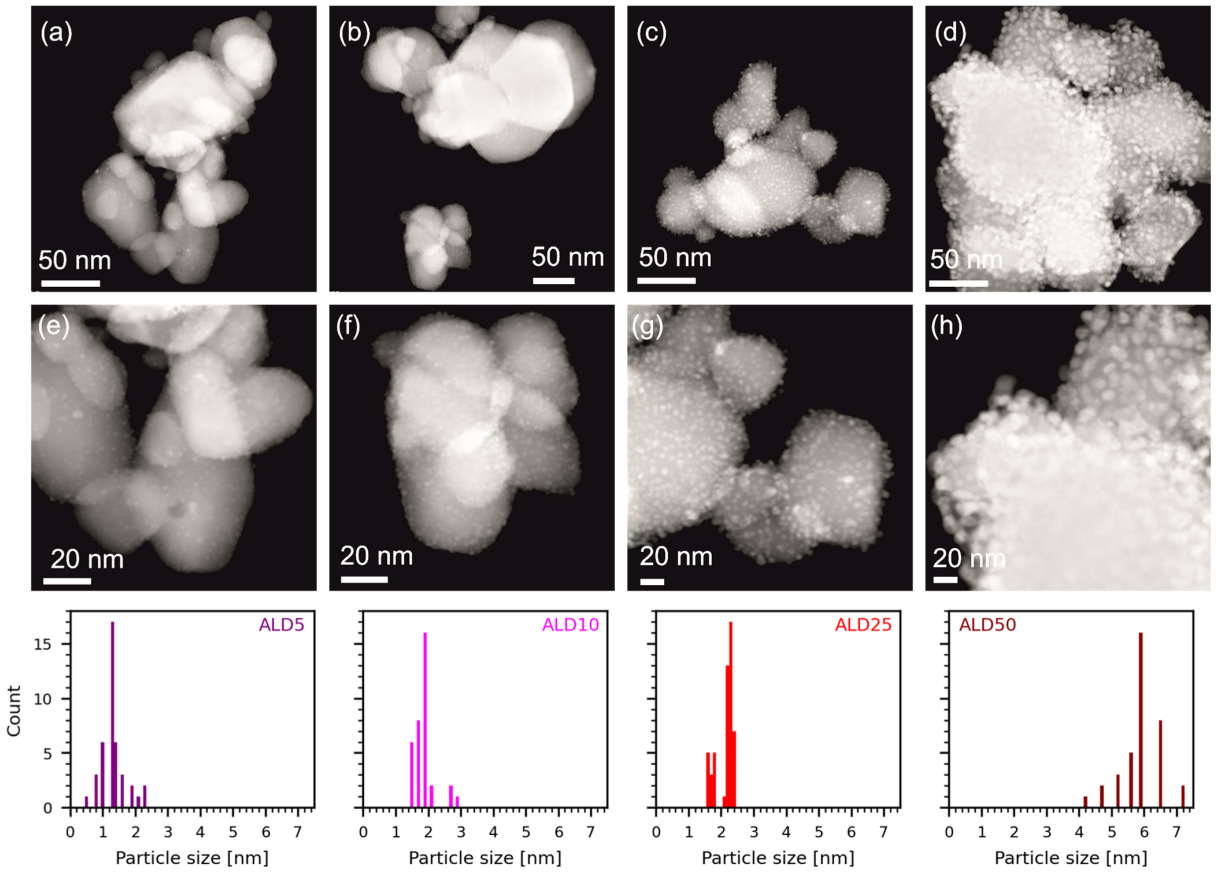

Figure 3. HAADF-STEM micrographs for ALD5 (a, e), ALD10 (b, f), ALD25 (c, g), and ALD50 (d, h) after calcination at different levels of magnification (top and middle rows) and the corresponding particle diameter distribution (bottom row). The HADDF-STEM micrographs before calcination are shown in Figure S2.

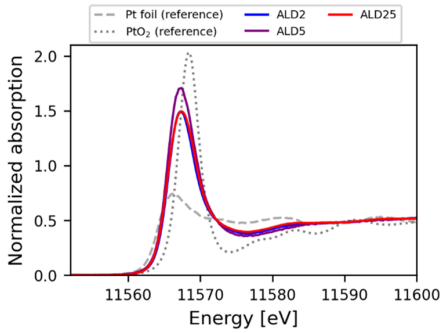

Figure 4. Pt L_3 HERFD-XANES spectra of ALD2 (blue), ALD5 (purple), and ALD25 (red) in 20%vol O_2 in He, at a sensor temperature of 300 °C and Pt foil (dashed) and PtO_2 (dotted) references at room temperature.

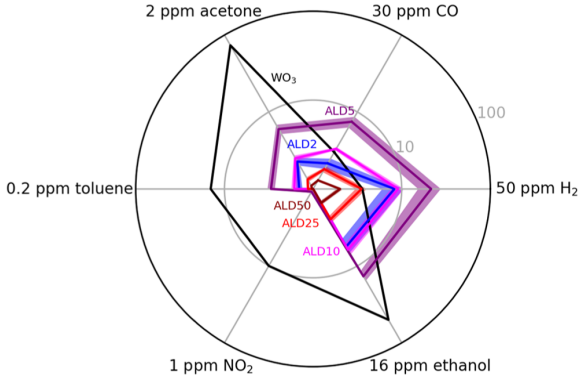

Figure 5. Sensor signals (R_{air}/R_{gas} or R_{NO2}/R_{air}) of pristine WO_3, ALD2, ALD5, ALD10, ALD25, and ALD50 in 5% RH and at a sensor temperature of 300 °C. The shaded areas for ALD-loaded sensors indicate error bars, calculated as the standard deviation of three independent samples. The gas sensing performance at different humidity levels is shown in Figure S3.

To gain further insight into the influence of the Pt loading on the electrical properties and the interaction with atmospheric oxygen, the resistances of all sensors were measured in pure N_2 and synthetic air at 300 °C (Figure 6, **top**). As previously reported, the presence of noble metal additives increases the sensor resistances measured in N_2 when compared to pristine SMOX, indicating a strong electronic coupling of the additives; the latter is due to electronic states related to single ion sites or Fermi-level coupling of additive clusters or particles at the SMOX surface.[11] ALD2 and ALD5 show the highest resistance in N_2, indicating the strongest electronic interaction of Pt loadings with WO_3. ALD10 shows a lower interaction, which is

https://doi.org/10.1021/acs.jpcc.5c05000
J. Phys. Chem. C 2025, 129, 15301−15308

The Journal of Physical Chemistry C pubs.acs.org/JPCC Article

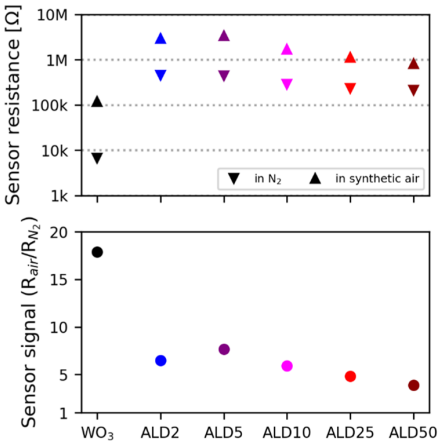

Figure 6. Sensor resistances in pure N_2 and synthetic air (top) and the calculated signals of ~20% O_2 (bottom) for WO_3 (black), ALD2 (blue), ALD5 (purple), ALD10 (magenta), ALD25 (red), and ALD50 (dark red) at a sensor temperature of 300 °C.

still higher than those of ALD25 and ALD50. This leads to the conclusion that the loadings from ALD2 to ALD5 and finally to ALD50 interact differently, which correlates with the different Pt structures found.

Based on the resistances in pure N_2 and synthetic air (Figure 6, **bottom**), sensor signals are calculated to quantify the effect of O_2. Pristine WO_3 shows the highest impact of the O_2 on the sensor resistance. Within the Pt-loaded samples, ALD5 presents the highest change in resistance due to the presence of oxygen, while ALD2, as well as ALD10 to ALD50, show lower O_2 signals, whereby ALD10 to ALD50 show a continuously decreasing trend. The trend seen for oxygen exposure correlates with the CO sensing performance of the Pt-loaded samples (Figure 5); that is expected since the detection of CO depends on its interaction of ionosorbed oxygen at the SMOX surface or additive structure, e.g., by its total or partial combustion.[6,7]

To further understand the observed trends with increasing number of ALD cycles, i.e., increasing Pt loading and changes in the nature of the Pt species, operando spectroscopic investigations were performed. ALD2, ALD5, and ALD25 were studied by operando XAS during CO sensing (Figure 7), and furthermore, all samples were studied by operando DRIFTS

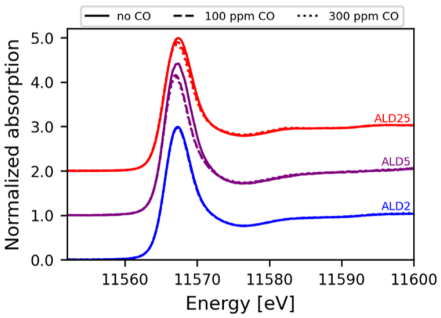

Figure 7. Operando Pt L_3 HERFD-XANES spectra of ALD2 (blue), ALD5 (purple), and ALD25 (red) in the absence of CO (solid line); 100 ppm of CO (dashed line) and 300 ppm of CO (dotted line) dosed in 20% O_2 in He at a sensor temperature of 300 °C. The recorded sensor signals are reported in Figure S5.

during CO sensing (Figure 8). The Pt L_3 HERFD-XANES spectra of ALD2 show no change upon exposure to 100 or 300

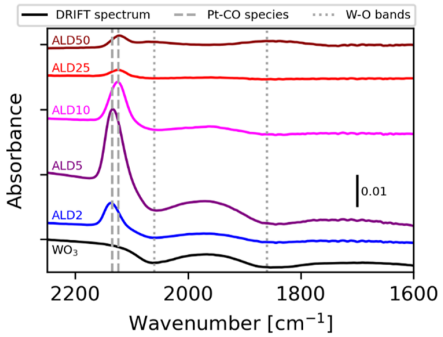

Figure 8. Operando DRIFT spectra of WO_3 (black), ALD2 (blue), ALD5 (purple), ALD10 (magenta), ALD25 (red), and ALD50 (dark red) for 100 ppm of CO dosed in dry air at a sensor temperature of 300 °C. The recorded sensor signals are reported in Figure S5.

ppm of CO. However, since still a change in resistance is observed (Figure S4), it can be assumed that single ion Pt sites are not changed during gas sensing and that the electrical effect stems from the reduction of the WO_3 surface instead. Indeed, an activation of lattice oxygen bound to Pt, as proposed for Pt-doped SnO_2, would explain the increased response to CO.[27] In contrast, ALD5 and ALD25 show a clear effect on the HERFD-XANES spectra: the whiteline is shifted to lower energies, and its intensity decreases due to Pt reduction, with this effect being more pronounced for ALD5. The distinct change in Pt L_3 whiteline suggests a significant change of the Pt loading by CO, which can be assigned to a reduction of oxidized Pt particles. The more pronounced reduction of Pt for ALD5 can be explained by the higher ratio of CO molecules with respect to the Pt sites at the surface as well as the better accessibility of Pt sites by gases on the smaller clusters of ALD5.

The understanding of the sensing is furthered by operando DRIFT spectroscopy. All recorded DRIFT spectra show two bands at 2060 and 1860 cm^{-1} (Figure 8, dotted gray lines) assigned to the W═O vibrational mode.[6] The decreasing W═O bands in pristine WO_3 indicate the reduction of the surface due to the oxidation of CO with lattice oxygen, as expected from previous reports.[6,7] This behavior is observed, to a lesser extent, for ALD2 and ALD5, further decreasing with increasing Pt loading, until for ALD50, an increase in the W═O bands, i.e., oxidation of the surface, is observed. The latter effect has been previously observed for highly noble metal-loaded SMOX and is explained by enhanced oxygen ionosorption, which is enabled by additional electrons released from the heterojunctions back into the SMOX.[28]

In addition to these, the Pt-loaded samples show bands that are assigned to the CO species adsorbed to Pt sites (Figure 8, dashed gray lines). ALD2 and ALD5 show bands at 2137 and 2134 cm^{-1}, indicating the presence of oxidized Pt^{2+} sites at the surface.[29] Based on the other material characterization, this band is assigned to the Pt single ion sites at the WO_3 surface. The DRIFT spectra of ALD10 to ALD50 present a band at 2123 to 2121 cm^{-1}, which can be assigned to CO adsorbed on ionic Pt species found in superficially oxidized metallic Pt particles supported on Al_2O_3.[30] None of the Pt-loaded samples show a band around 2066 cm^{-1} and, thus, the presence of any carbonyl species adsorbed to metallic Pt sites can be excluded.[30,31] The

https://doi.org/10.1021/acs.jpcc.5c05000
J. Phys. Chem. C 2025, 129, 15301−15308

The Journal of Physical Chemistry C pubs.acs.org/JPCC Article

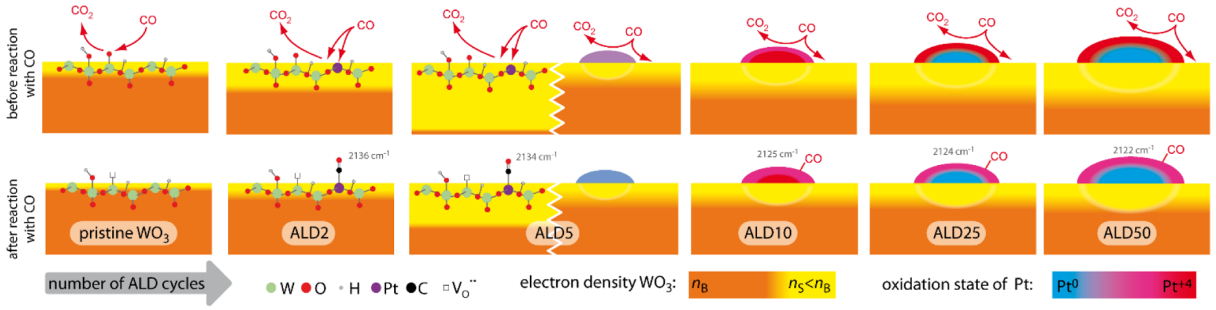

Figure 9. Schematic representation of the WO_3 sensing material with respect to the amount of platinum deposited. The orange-shaded areas correspond to regions with an electron density like in the bulk of WO_3 (n_b); the yellow shaded areas correspond to electron-depleted regions, i.e., the surface electron concentration being lower as in the bulk ($n_s < n_b$). The top row illustrates the state of the surface and sites for the reaction of CO: up to ALD5, the interaction with single oxygen and platinum sites is dominant, while at a higher number of ALD cycles, the growth and composition of Pt clusters is shown on a macroscopic scale. In the bottom row, the effect of CO on both WO_3 and Pt is shown.

analysis of the Pt carbonyl species observed by DRIFTS revealed the presence of two distinctly different Pt surface types: one clearly indicating the presence of Pt single sites at the surface in the case of ALD2 and ALD5, and another one for ALD10 to ALD50, where more reduced Pt species are found, e.g., as observed for oxidized sites on metallic particles. Furthermore, the trend observed with increasing Pt loading for the W═O bands suggests that, with increasing Pt coverage, less CO interacts with the WO_3, i.e., the surface chemistry is further shifted to the Pt loadings.

Based on the comprehensive material characterization and operando spectroscopic investigations, the structure and function of the different samples are summarized, as shown in Figure 9. For the lowest loading ALD2, Pt is solely present in the form of single ion sites, which play a double role. On the one hand, they are acceptor levels, which is indicated by the very significant increase of the resistance in N_2. The deficit of free electrons available results in fewer chemisorbed oxygen ions and, as a consequence of that, fewer reaction partners are available for the reaction with CO. This is manifested by the less pronounced decrease of the W═O bands when compared to the unloaded material. On the other hand, the Pt ion sites act as adsorption or reactive sites and only locally increase the reactivity of lattice oxygen, partially compensating for the aforementioned lower reactivity of the WO_3 surface for certain gases like CO or H_2.

ALD5 shows the coexistence of different Pt species. Material characterization by electron microscopy and operando HERFD-XANES clearly indicates the presence of oxidized Pt particles. In contrast, the operando DRIFT spectrum reveals the presence of single ion sites. Thus, in addition to the single ion Pt sites, small clusters are reduced by CO and, via electronic coupling (Fermi-level control), cause a decrease of the sensor resistance in the presence of reducing gases. ALD5 represents the case in which the two effects of the surface ionic sites and small oxidized clusters synergistically combine to increase the sensor performance.

Further increasing the Pt loading (ALD10) results in the surface being dominated by oxidized Pt particles, which are larger than those observed for ALD5. The efficiency of the sensitization by Fermi-level control decreases for larger particles, due to the nonreducible part of the particle at the particle-WO_3 interface shielding electronic changes of the Pt particle surface from the supporting WO_3.[11] In addition to the shielding, the decrease in sensor signals is also caused by the higher coverage of the surface with reactive Pt particles. Since the same amount of analyte reacts with more Pt sites, these are more easily reoxidized, which reduces the net change in particle composition and, thus, the gas sensing effect. Hence, the sensor signals are found to be lower than those for ALD5.

For even higher Pt loadings (ALD25 and ALD50), Pt forms predominantly metallic particles with an oxidized surface. The presence of a metallic core in the particles leads to even stronger electronic shielding, which hinders a Fermi-level-control mechanism and results in a further decrease in sensor signals. As with ALD10, the decrease in sensor signals is also favored by the increasing coverage of the surface with reactive Pt particles.

SUMMARY

ALD has been successfully used on already deposited SMOX gas sensing layers to form different Pt coverages, along with different Pt structures on WO_3. This clearly demonstrates the versatility of the ALD method for depositing noble metals onto metal oxide surfaces. ALD hence allows Pt to be efficiently deposited on the entire surface accessible to gases, thus potentially reducing the amount of noble metals required to change the gas sensing properties of the supporting SMOX.

In summary, three crucial aspects can be derived from this study for the role of noble metal additives in SMOX gas sensing materials:

- Single ion sites play a double role acting as electronic states, in the case of Pt ions in WO_3 as acceptor state, as well as local adsorption and reactions sites, which enhance the sensor response to certain gases.
- Fully oxidized and preferentially small clusters or particles generally exhibit good reactivity toward analyte gases and can effectively convert this reactivity into a change in resistance via the Fermi-level control mechanism and, thus, into a sensor signal.
- Partially oxidized metallic clusters may still be highly reactive; however, due to the shielding of the electronic interaction by the metallic core, a Fermi-level control mechanism is less effective or even no longer possible.

Hence, it can be concluded that the most effective sensitization of SMOX can be achieved by single ion sites or extremely small oxide particles. As shown for ALD5, the presence of single ion sites, an effective Fermi-level control mechanism, and a synergistic combination of both effects on the sensing properties are not mutually exclusive. Thus, an in-depth investigation of the transition from single Pt sites to clusters and

https://doi.org/10.1021/acs.jpcc.5c05000
J. Phys. Chem. C 2025, 129, 15301−15308

The Journal of Physical Chemistry C pubs.acs.org/JPCC Article

particles will be of great interest to enable the knowledge-based design of highly efficient SMOX gas sensor materials.

■ ASSOCIATED CONTENT

Supporting Information

The Supporting Information is available free of charge at https://pubs.acs.org/doi/10.1021/acs.jpcc.5c05000.

XP spectra recorded prior to calcination, STEM micrographs and particle size distribution before calcination, ratio of CO and acetone sensor signals for the studied samples, and sensor signals of CO for different operando methods (PDF)

■ AUTHOR INFORMATION

Corresponding Author

Nicolae Barsan − *Institute of Physical and Theoretical Chemistry (IPTC), University of Tuebingen, Tuebingen 72076, Germany; Center for Light-Matter Interaction, Sensors & Analytics (LISA+), University of Tuebingen, Tuebingen 72076, Germany; Faculty of Advanced Science and Technology (FAST), Kumamoto University, Kumamoto 860-8555, Japan;* orcid.org/0000-0001-6718-9889; Phone: +49 7071 29 78761; Email: nb@ipc.uni-tuebingen.de

Authors

David Degler − *Department of Applied Sciences and Mechatronics, University of Applied Science Munich, Munich 80335, Germany*

Ugur Geyik − *Institute of Physical and Theoretical Chemistry (IPTC), University of Tuebingen, Tuebingen 72076, Germany; Center for Light-Matter Interaction, Sensors & Analytics (LISA+), University of Tuebingen, Tuebingen 72076, Germany*

Benjamin Junker-Reiss − *Institute of Physical and Theoretical Chemistry (IPTC), University of Tuebingen, Tuebingen 72076, Germany; Center for Light-Matter Interaction, Sensors & Analytics (LISA+), University of Tuebingen, Tuebingen 72076, Germany;* orcid.org/0000-0002-2229-0534

Muhammad Hamid Raza − *Department of Chemistry, Center for the Science of Materials Berlin, Humboldt-Universität zu Berlin, Berlin 12489, Germany; Center for the Science of Materials Berlin, Humboldt-Universität zu Berlin, Berlin 12489, Germany; PVcomB, Helmholtz-Zentrum Berlin für Materialien und Energie GmbH (HZB), Berlin 12489, Germany;* orcid.org/0000-0003-0061-5139

Patrick Amsalem − *Institut für Physik and the Center for the Science of Materials Berlin, Humboldt-Universität zu Berlin, Berlin 12489, Germany;* orcid.org/0000-0002-7330-2451

Norbert Koch − *Institut für Physik and the Center for the Science of Materials Berlin, Humboldt-Universität zu Berlin, Berlin 12489, Germany;* orcid.org/0000-0002-6042-6447

Blanka Detlefs − *European Synchrotron Radiation Facility, Grenoble 38043, France;* orcid.org/0000-0002-9768-647X

Nicola Pinna − *Department of Chemistry, Center for the Science of Materials Berlin, Humboldt-Universität zu Berlin, Berlin 12489, Germany; Center for the Science of Materials Berlin, Humboldt-Universität zu Berlin, Berlin 12489, Germany;* orcid.org/0000-0003-1273-803X

Udo Weimar − *Institute of Physical and Theoretical Chemistry (IPTC), University of Tuebingen, Tuebingen 72076, Germany; Center for Light-Matter Interaction, Sensors & Analytics (LISA+), University of Tuebingen, Tuebingen 72076, Germany;* orcid.org/0000-0003-2354-0432

Complete contact information is available at: https://pubs.acs.org/10.1021/acs.jpcc.5c05000

Author Contributions

The manuscript was written through contributions of all authors. D.D. planned and evaluated the XANES investigations, merged the various results, and was responsible for writing the manuscript. U.G. prepared the pristine samples and planned, conducted, and evaluated the sensing performance, DRIFTS, and XANES investigations. B.J.-R. prepared and conducted XANES investigations and assisted in writing the manuscript. M.H.R. developed and optimized the Pt ALD process, deposited Pt on sensors, analyzed TEM data, and helped with XPS data analysis and discussion on sensing results. P.A. and N.K. measured and analyzed XPS data. B.D. was the local contact for the synchrotron-based measurements and supported all works carried out at the ESRF. N.P., U.W., and N.B. supervised the study. All authors contributed to the discussion of the results and the correction of the manuscript. All authors have given approval to the final version of the manuscript.

Notes

The authors declare no competing financial interest.

■ ACKNOWLEDGMENTS

The authors acknowledge the European Synchrotron Radiation Facility (ESRF) for the provision of synchrotron radiation facilities under proposal number CH-6029 (doi: 10.15151/ESRF-ES-650701946), and they would like to thank the staff of ESRF's beamline ID26 for assistance and support during the beamtime.

■ ABBREVIATIONS

ALD, atomic layer deposition
Cp, cyclopentadienyl
DRIFTS, diffuse reflectance infrared Fourier transform spectroscopy
HAADF-STEM, high-angle annular dark-field scanning transmission electron microscopy
HERFD, high-energy-resolved fluorescence detection
RH, relative humidity
SMOX, semiconducting metal oxide
XANES, X-ray absorption near edge structure
XAS, X-ray absorption spectroscopy
XPS, X-ray photoelectron spectroscopy

■ REFERENCES

(1) Barsan, N.; Koziej, D.; Weimar, U. Metal Oxide-Based Gas Sensor Research: How To? *Sens. Actuators, B* **2007**, *121* (1), 18−35.

(2) Yamazoe, N.; Sakai, G.; Shimanoe, K. Oxide Semiconductor Gas Sensors. *Catal. Surv. Asia* **2003**, 7 (1), 63−75.

(3) Neri, G. First Fifty Years of Chemoresistive Gas Sensors. *Chemosensors* **2015**, 3 (1), 1−20.

(4) Degler, D.; Wicker, S.; Weimar, U.; Barsan, N. Identifying the Active Oxygen Species in SnO2 Based Gas Sensing Materials: An Operando IR Spectrsocopy Study. *J. Phys. Chem. C* **2015**, *119* (21), 11792−11799.

(5) Sänze, S.; Hess, C. Ethanol Gas Sensing by Indium Oxide: An Operando Spectroscopic Raman-FTIR Study. *J. Phys. Chem. C* **2014**, *118* (44), 25603−25613.

https://doi.org/10.1021/acs.jpcc.5c05000
J. Phys. Chem. C 2025, 129, 15301−15308

(6) Hübner, M.; Simion, C. E.; Haensch, A.; Barsan, N.; Weimar, U. CO Sensing Mechanism with WO3 Based Gas Sensors. *Sens. Actuators, B* **2010**, *151* (1), 103−106.
(7) Staerz, A.; Somacescu, S.; Epifani, M.; Kida, T.; Weimar, U.; Barsan, N. WO3-Based Gas Sensors: Identifying Inherent Qualities and Understanding the Sensing Mechanism. *ACS Sens.* **2020**, *5* (6), 1624−1633.
(8) Schmitt, E. A.; Krott, M.; Epifani, M.; Suematsu, K.; Weimar, U.; Barsan, N. Volatile Organic Compound Sensing with WO3-Based Gas Sensors: Surface Chemistry Basics. *J. Phys. Chem. C* **2024**, *128* (4), 1633−1643.
(9) Barsan, N.; Weimar, U. Conduction Model of Metal Oxide Gas Sensors. *Growth (Lakeland)* **2001**, *7*, 143−167.
(10) Müller, S. A.; Degler, D.; Feldmann, C.; Türk, M.; Moos, R.; Fink, K.; Studt, F.; Gerthsen, D.; Bârsan, N.; Grunwaldt, J. D. Exploiting Synergies in Catalysis and Gas Sensing Using Noble Metal-Loaded Oxide Composites. *ChemCatChem* **2018**, *10* (5), 864−880.
(11) Degler, D.; Weimar, U.; Barsan, N. Current Understanding of the Fundamental Mechanisms of Doped and Loaded Semiconducting Metal-Oxide-Based Gas Sensing Materials. *ACS Sens.* **2019**, *4* (9), 2228−2249.
(12) Dendooven, J.; Ramachandran, R. K.; Solano, E.; Kurttepeli, M.; Geerts, L.; Heremans, G.; Rongé, J.; Minjauw, M. M.; Dobbelaere, T.; Devloo-Casier, K.; et al. Independent Tuning of Size and Coverage of Supported Pt Nanoparticles Using Atomic Layer Deposition. *Nat. Commun.* **2017**, *8* (1), No. 1074.
(13) Raza, M. H.; Movlaee, K.; Leonardi, S. G.; Barsan, N.; Neri, G.; Pinna, N. Gas Sensing of NiO-SCCNT Core−Shell Heterostructures: Optimization by Radial Modulation of the Hole-Accumulation Layer. *Adv. Funct. Mater.* **2020**, *30* (6), No. 1906874.
(14) Bârsan, N.; Weimar, U. Understanding the Fundamental Principles of Metal Oxide Based Gas Sensors; the Example of CO Sensing with SnO2 Sensors in the Presence of Humidity. *J. Phys.:Condens. Matter* **2003**, *15* (20), R813−R839.
(15) Glatzel, P.; Harris, A.; Marion, P.; Sikora, M.; Weng, T. C.; Guilloud, C.; Lafuerza, S.; ovezzi, M.; Detlefs, B.; Ducotté, L. The Five-Analyzer Point-to-Point Scanning Crystal Spectrometer at ESRF ID26. *J. Synchrotron Radiat.* **2021**, *28*, 362−371.
(16) Newville, M. Larch: An Analysis Package for XAFS and Related Spectroscopies. *J. Phys. Conf. Ser.* **2013**, *430* (1), No. 012007.
(17) Grossmann, K.; Pavelko, R. G.; Barsan, N.; Weimar, U. Interplay of H 2, Water Vapor and Oxygenat the Surface of SnO 2 Based Gas Sensors - An Operando Investigation Utilizing Deuterated Gases. *Sens. Actuators, B* **2012**, *166−167*, 787−793.
(18) Bera, P.; Priolkar, K. R.; Gayen, A.; Sarode, P. R.; Hegde, M. S.; Emura, S.; Kumashiro, R.; Jayaram, V.; Subbanna, G. N. Ionic Dispersion of Pt over CeO2 by the Combustion Method: Structural Investigation by XRD, TEM, XPS, and EXAFS. *Chem. Mater.* **2003**, *15* (10), 2049−2060.
(19) Park, J.; Lee, S.; Kim, H. E.; Cho, A.; Kim, S.; Ye, Y.; Han, J. W.; Lee, H.; Jang, J. H.; Lee, J. Investigation of the Support Effect in Atomically Dispersed Pt on WO3−x for Utilization of Pt in the Hydrogen Evolution Reaction. *Angew. Chem., Int. Ed.* **2019**, *58* (45), 16038−16042.
(20) Vovk, E. I.; Kalinkin, A. V.; Smirnov, M. Y.; Klembovskii, I. O.; Bukhtiyarov, V. I. XPS Study of Stability and Reactivity of Oxidized Pt Nanoparticles Supported on TiO2. *J. Phys. Chem. C* **2017**, *121* (32), 17297−17304.
(21) Shin, S.; Kim, J.; Park, S.; Kim, H. E.; Sung, Y. E.; Lee, H. Changes in the Oxidation State of Pt Single-Atom Catalysts upon Removal of Chloride Ligands and Their Effect for Electrochemical Reactions. *Chem. Commun.* **2019**, *55* (45), 6389−6392.
(22) Maurer, F.; Jelic, J.; Wang, J.; Gänzler, A.; Dolcet, P.; Wöll, C.; Wang, Y.; Studt, F.; Casapu, M.; Grunwaldt, J. D. Tracking the Formation, Fate and Consequence for Catalytic Activity of Pt Single Sites on CeO2. *Nat. Catal.* **2020**, *3* (10), 824−833.
(23) Chen, Y.; Ji, S.; Sun, W.; Chen, W.; Dong, J.; Wen, J.; Zhang, J.; Li, Z.; Zheng, L.; Chen, C.; et al. Discovering Partially Charged Single-Atom Pt for Enhanced Anti-Markovnikov Alkene Hydrosilylation. *J. Am. Chem. Soc.* **2018**, *140* (24), 7407−7410.
(24) Hübner, M.; Koziej, D.; Bauer, M.; Barsan, N.; Kvashnina, K.; Rossell, M. D.; Weimar, U.; Grunwaldt, J. D. The Structure and Behavior of Platinum in SnO2-Based Sensors under Working Conditions. *Angew. Chem., Int. Ed.* **2011**, *50* (12), 2841−2844.
(25) Degler, D. Trends and Advances in the Characterization of Gas Sensing Materials Based on Semiconducting Oxides. *Sensors (Switzerland)* **2018**, *18* (10), No. 3544.
(26) Gänzler, A. M.; Casapu, M.; Doronkin, D. E.; Maurer, F.; Lott, P.; Glatzel, P.; Votsmeier, M.; Deutschmann, O.; Grunwaldt, J. D. Unravelling the Different Reaction Pathways for Low Temperature CO Oxidation on Pt/CeO2 and Pt/Al2O3 by Spatially Resolved Structure-Activity Correlations. *J. Phys. Chem. Lett.* **2019**, *10* (24), 7698−7705.
(27) Degler, D.; Pereira De Carvalho, H. W.; Kvashnina, K.; Grunwaldt, J. D.; Weimar, U.; Barsan, N. Structure and Chemistry of Surface-Doped Pt:SnO2 Gas Sensing Materials. *RSC Adv.* **2016**, *6* (34), 28149−28155.
(28) Staerz, A.; Boehme, I.; Degler, D.; Bahri, M.; Doronkin, D. E.; Zimina, A.; Brinkmann, H.; Herrmann, S.; Junker, B.; Ersen, O.; et al. Rhodium Oxide Surface-Loaded Gas Sensors. *Nanomaterials* **2018**, *8* (11), 1−17.
(29) Ivanova, E.; Mihaylov, M.; Thibault-Starzyk, F.; Daturi, M.; Hadjiivanov, K. FTIR Spectroscopy Study of CO and NO Adsorption and Co-Adsorption on Pt/TiO2. *J. Mol. Catal. A:Chem.* **2007**, *274* (1−2), 179−184.
(30) Boubnov, A.; Gänzler, A.; Conrad, S.; Casapu, M.; Grunwaldt, J. D. Oscillatory CO Oxidation over Pt/Al2O3 Catalysts Studied by in Situ XAS and DRIFTS. *Top. Catal.* **2013**, *56* (1−8), 333−338.
(31) Meunier, F. C. Relevance of IR Spectroscopy of Adsorbed CO for the Characterization of Heterogeneous Catalysts Containing Isolated Atoms. *J. Phys. Chem. C* **2021**, *125* (40), 21810−21823.

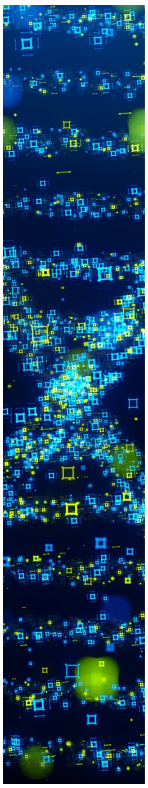

https://doi.org/10.1021/acs.jpcc.5c05000
J. Phys. Chem. C 2025, 129, 15301−15308

Investigation on the Structure-Function-Relationship of Atomic Layer Deposited Platinum Additives on Tungsten Trioxide Gas Sensor Materials

David Degler[1], Ugur Geyik[2,3], Benjamin Junker-Reiss[2,3], Muhammad Hamid Raza[4,5,6], Patrick Amsalem[7], Norbert Koch[7], Blanka Detlefs[8], Nicola Pinna[4,5], Udo Weimar[2,3] and Nicolae Barsan[2,3,8*]

[1] Department of Applied Sciences and Mechatronics, University of Applied Science Munich, Lothstrasse 34, 80335 Munich, Germany

[2] Institute of Physical and Theoretical Chemistry (IPTC), University of Tuebingen, Auf der Morgenstelle 15, 72076 Tuebingen, Germany

[3] Center for Light-Matter Interaction, Sensors & Analytics (LISA+), University of Tuebingen, Auf der Morgenstelle 15, 72076, Tuebingen, Germany

[4] Department of Chemistry Center for the Science of Materials Berlin, Humboldt-Universität zu Berlin, Brook-Taylor-Str. 2, 12489, Berlin, Germany

5Center for the Science of Materials Berlin, Humboldt-Universität zu Berlin, Brook-Taylor-Str. 2, 12489, Berlin, Germany

[6] PVcomB, Helmholtz-Zentrum Berlin für Materialien und Energie GmbH (HZB), Schwarzschildstrasse 3, 12489 Berlin, Germany

[7] Institut für Physik and the Center for the Science of Materials Berlin, Humboldt-Universität zu Berlin, 12489 Berlin, Germany

[8] European Synchrotron Radiation Facility, 71 avenue des Martyrs, CS 40220, 38043 Grenoble, France

[9] Faculty of Advanced Science and Technology (FAST), Kumamoto University, Kumamoto, 860-8555, Japan

Supporting information

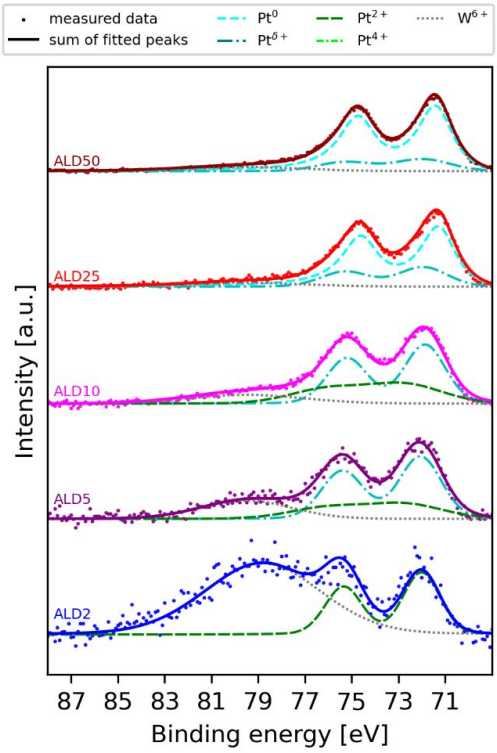

Figure S1: XP spectra of all Pt loaded samples before calcination. The corresponding peak assignments are shown in Table 1 in the main article.

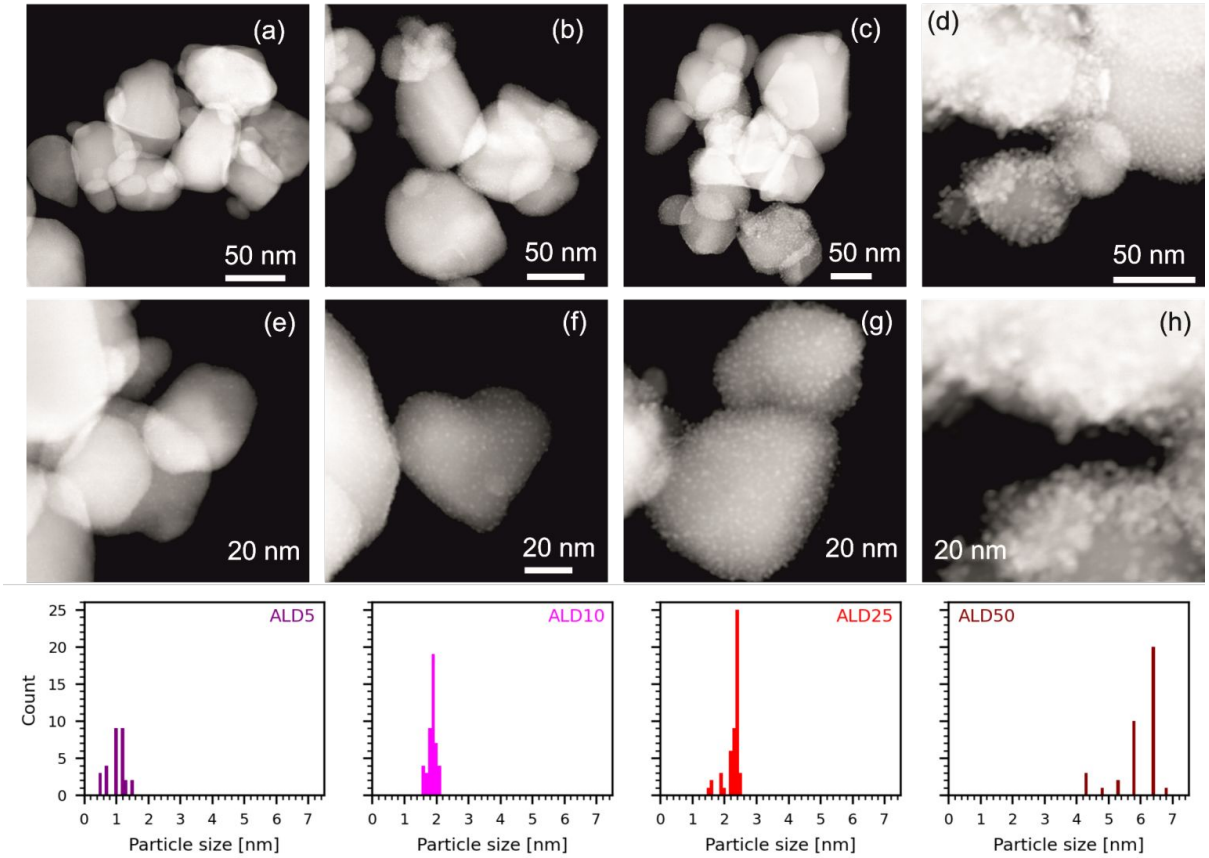

Figure S2: HAADF-STEM micrographs for ALD5 (a), ALD10 (b), ALD25 (c), and ALD50 (d) before calcination at different levels of magnification (top and middle row) and the corresponding particle diameter distribution (bottom row).

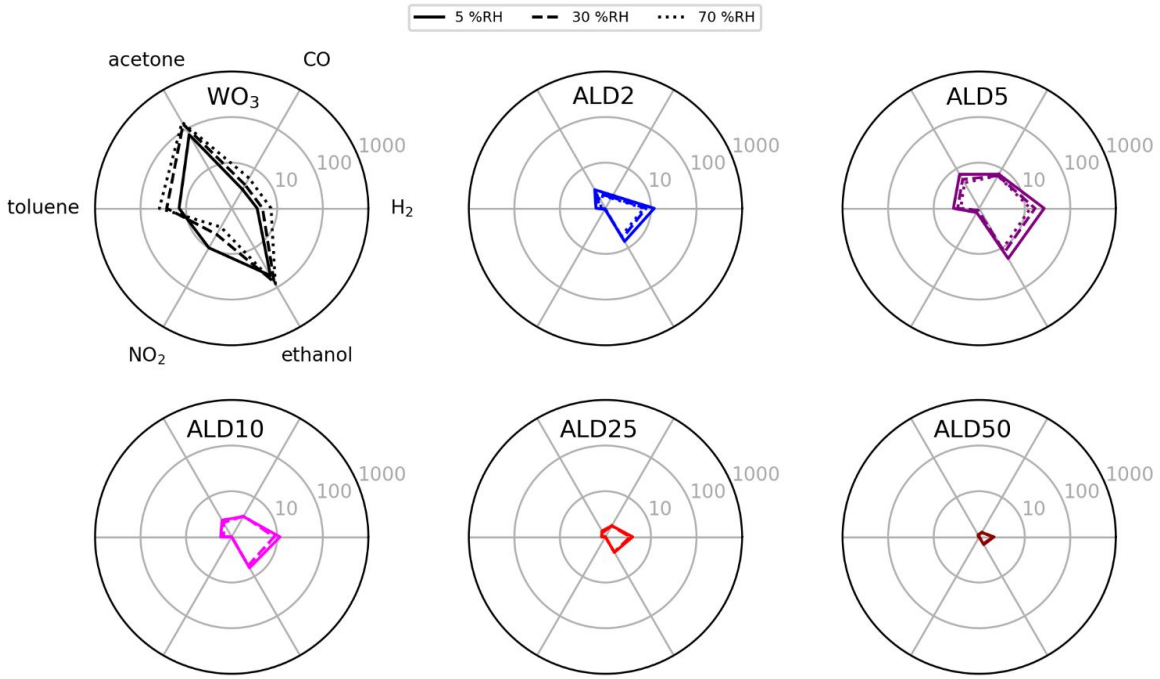

Figure S3: Sensor signals (Rair/Rgas, or RNO2/Rair) of pristine WO3, ALD2, ALD5, ALD10, ALD25, ALD50 for 30 ppm CO, 50 ppm H2, 16 ppm ethanol, 1 ppm NO2, 0.2 ppm toluene, 2 ppm acetone at a sensor temperature of 300 °C and in different humidity backgrounds (relative humidity, %RH): 5 %RH (solid line), 30 %RH (dashed line) and 70 %RH (dotted line)

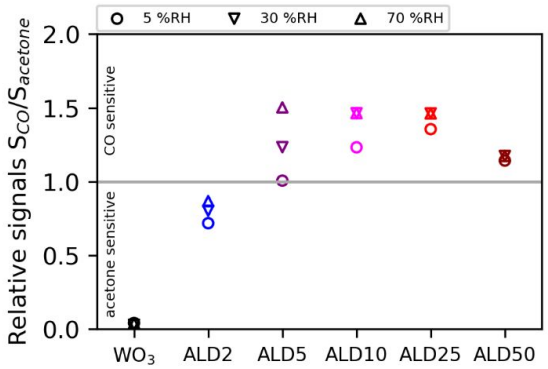

Figure S4: Ratio $S_{CO}/S_{acetone}$ of the sensor signals for 30 ppm CO to 2 ppm acetone in different humidity backgrounds.

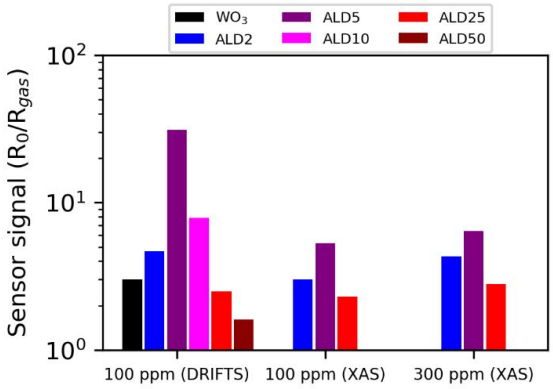

Figure S5: Comparison of sensor signals (R_{air}/R_{CO}) to CO in dry air obtained simultaneously to spectroscopic investigations.

Sensors & Actuators: B. Chemical 447 (2026) 138909

Contents lists available at ScienceDirect

Sensors and Actuators: B. Chemical

journal homepage: www.elsevier.com/locate/snb

Unraveling the gas sensing mechanism of single-crystalline Sn_3O_4 nanobelts using operando DRIFT spectroscopy and isotopically labeled gases

Pedro H. Suman [a,b,*], Benjamin Junker-Reiss [a], Udo Weimar [a], Marcelo O. Orlandi [b], Nicolae Barsan [a,c,*]

[a] Institute of Physical and Theoretical Chemistry (IPTC) and Center for Light-Matter Interaction, Sensors & Analytics (LISA+), University of Tübingen, Tübingen 72076, Germany
[b] Department of Physics and Mathematics, Institute of Chemistry, São Paulo State University (UNESP), Araraquara 14800-060, Brazil
[c] Faculty of Advanced Science and Technology (FAST), Kumamoto University, Kumamoto 860-8555, Japan

ARTICLE INFO

Keywords:
Tin oxide
Sn_3O_4
Nanobelts
One-dimensional (1D) nanostructures
Semiconducting metal oxide (SMOX)
Gas sensing mechanism
Operando DRIFT spectroscopy

ABSTRACT

While SnO_2 is a well-established benchmark semiconducting metal oxide (SMOX) for gas sensing applications, tin oxides with alternative oxidation states, such as Sn_3O_4 and SnO, remain underexplored. This study provides the first experimental evidence of the gas sensing mechanism for Sn_3O_4 using diffuse-reflectance infrared Fourier transform spectroscopy (DRIFTS) combined with simultaneous resistance measurements. From this approach, the interaction of Sn_3O_4 surface with O_2 and isotopically labeled gases, including H_2O/D_2O, H_2/D_2, and $^{12}CO/^{13}CO$ was examined in different operating conditions. O_2 exposure in an N_2 background revealed the formation of adsorbed molecular oxygen, which acts as a precursor for the subsequent healing of oxygen vacancies. H_2O/D_2O experiments showed minimal impact of water adsorption, indicating an initially hydroxylated Sn_3O_4 surface. Additionally, the dominant reaction mechanism between Sn_3O_4 and H_2O changes with temperature, and the presence of water vapor in the background significantly influences the H_2 and CO detection. Despite differing electrical effects, H_2/D_2 exchange demonstrated that identical hydroxyl species were formed at equivalent surface sites to those identified in the H_2O/D_2O studies. Besides, the interaction of H_2 with the Sn_3O_4 surface also follows different reaction pathways at 200 °C and 300 °C. DRIFTS spectra from $^{12}CO/^{13}CO$ experiments indicated the formation of carbonate species as intermediate products of CO oxidation; however, these species appear to have no direct influence on the sensing response. Overall, this work provides new insights into the surface chemistry and fundamental gas sensing mechanisms of single-crystalline Sn_3O_4 nanobelts.

1. Introduction

The demand for gas sensors with high sensitivity, selectivity, fast response, and long-term stability has increased significantly over recent decades. Accurate and reliable detection of gaseous substances under different operating conditions enables identifying hazardous compounds, real-time air quality tracking, optimizing industrial processes, and engineering portable sensing platforms. These capabilities are essential for applications in environmental monitoring, industrial safety, automotive emissions control, food supply chain management, agriculture, and medical diagnostics [1–6]. In this context, chemiresistive gas sensors based on semiconducting metal oxides (SMOX) are recognized as one of the most commercially viable solutions, owing to their robustness, simplicity, low cost, and versatility in detecting a wide range of gases [7–11]. The operation process of these devices occurs from the conversion of surface reactions (reception mechanism) into measurable electrical signals (transduction mechanism).

Stannic oxide (SnO_2) has been extensively studied as a benchmark SMOX material, demonstrating exceptional performance in detecting toxic and flammable gases under specific conditions [12–14]. Alternatively, tin oxides with other oxidation states, such as Sn_3O_4 and SnO, have exhibited noteworthy potential for sensing volatile organic compounds (VOCs), carbon monoxide, nitrogen oxides, hydrogen, and other gaseous species, positioning them as promising options for sensor development [15–23]. Sn_3O_4 is an outstanding representative of heterovalent tin oxides predicted by theoretical calculations, exhibiting a

* Corresponding authors at: Institute of Physical and Theoretical Chemistry (IPTC) and Center for Light-Matter Interaction, Sensors & Analytics (LISA+), University of Tubingen, Tubingen 72076, Germany.
E-mail addresses: pedro.suman@unesp.br, phsuman@yahoo.com.br (P.H. Suman), nb@ipc.uni-tuebingen.de (N. Barsan).

https://doi.org/10.1016/j.snb.2025.138909
Received 14 July 2025; Received in revised form 1 October 2025; Accepted 3 October 2025
Available online 3 October 2025

layered crystalline structure [24–26]. This structure, confirmed in our previous work by transmission electron microscopy (TEM) [19], arises from the alternating stacking of tin and oxygen atomic layers, maintained by weak van der Waals forces along the (010) plane. Experimentally, Sn_3O_4 is typically obtained via SnO disproportionation at temperatures below 500 °C, consistent with the Sn–O phase diagram [27,28]. Unlike the single-valence oxides SnO_2 and SnO, Sn_3O_4 exhibits a mixed-valence structure in which Sn^{2+} and Sn^{4+} coexist within the same lattice in a 2:1 ratio, $[(Sn^{2+})_2(Sn^{4+})O_4]$ [25]. This intrinsic feature confers unique redox process, enabling dynamic surface charge redistribution and reaction pathways inaccessible to conventional oxides, thus providing a unique platform to elucidate mixed-valence-mediated gas sensing mechanisms.

Despite growing interest in these unusual tin oxide stoichiometries, the fundamental mechanism underlying their detection properties remains unclear. Most previous studies have focused primarily on the sensing performance of Sn_3O_4-based materials, providing limited direct evidence of the surface chemistry involved [17,18,29–31]. This knowledge gap in the field persists because obtaining detailed molecular-level information on gas–surface interactions under operando conditions remains a significant challenge. In previous work, we provided the first insights into the transduction process of chemoresistive gas sensors based on single-crystalline Sn_3O_4 nanobelts using the operando Kelvin Probe technique [16]. This study examined the relationship between conductance and surface band bending, revealing a shift in the conduction mechanism from a partially depleted state to a fully depleted state. However, this study does not fully elucidate the surface chemistry and reaction pathways responsible for sensor responses under operating conditions. Therefore, a detailed investigation of Sn_3O_4 surface chemistry across varying temperatures, humidity levels, and gas concentrations is essential to advance understanding of the sensing mechanism.

To address this gap, operando diffuse reflectance infrared Fourier transform spectroscopy (DRIFTS) has demonstrated its effectiveness in elucidating reception dynamics under operating conditions [32–37]. This technique enables real-time monitoring of the vibrational wavenumbers of surface-active chemical species on the sensing layer while simultaneously measuring the corresponding electrical signals. The combination of operando DRIFTS with isotopic exchange experiments provides a complementary strategy for identifying reaction intermediates and examining the role of specific surface sites in gas sensing. Using isotopically labeled gases, adsorption and desorption processes of oxygen, water vapor, and other species can be tracked, offering relevant insights into the fundamental processes driving sensor responses.

This study aims to provide a comprehensive understanding of the gas sensing mechanism in chemoresistive gas sensors based on 1D single-crystalline Sn_3O_4 nanobelts, correlating DC resistance measurements with DRIFT spectroscopy. The surface reactivity of Sn_3O_4 nanobelts with O_2 and isotopically labeled gases (H_2O/D_2O, H_2/D_2, and $^{12}CO/^{13}CO$) was systematically examined under dynamic equilibrium conditions at different working temperatures, revealing novel insights into the surface chemistry and reaction pathways between Sn_3O_4 and gas molecules. The findings are expected to offer valuable guidance for the design of next-generation gas sensors with improved sensitivity, selectivity, and long-term stability for practical applications.

2. Experimental section

2.1. Synthesis of Sn_3O_4 nanobelts

The synthesis parameters used to produce single-crystalline Sn_3O_4 nanobelts, including temperature, synthesis time, and gas flow, were detailed in our previous work [19,38]. Briefly, the nanobelts were synthesized via carbothermal reduction from a powder mixture composed of SnO_2 (Sigma-Aldrich, 99.9 % purity) and carbon black (Union Carbide, > 99 % purity) in a molar ratio of 1.5:1 (SnO_2:C). This mixture was placed in a tubular furnace and heated to 1135 °C under a controlled N_2/O_2 atmosphere. Structural and morphological analyses revealed the formation of single-crystalline nanobelts with an average width of approximately 150 nm and lengths extending to several tens of micrometers. The nanobelts crystallize in the triclinic structure of Sn_3O_4 (JCPDS card #16–0737), with a minor presence of the tetragonal SnO_2 phase (JCPDS card #41–1445). A comprehensive discussion of the material's properties and characterization methods can be found elsewhere [19,39].

2.2. Sensor fabrication

Sn_3O_4 nanobelts were ground in a mortar with 1,2-propanediol (Sigma-Aldrich, 99.5 +% ACS reagent) to form a uniform paste, which was subsequently transferred onto alumina substrates using a screen-printing technique. These substrates were pre-patterned with interdigitated platinum (Pt) electrode arrays on the front side for electrical resistance measurements and an independent Pt heater on the backside to control the operating temperature of the sensors. Following deposition, the sensors were dried overnight at 80 °C and then annealed in a tubular furnace at 325 °C for 30 min to improve the adherence of the nanobelts and remove any residual solvent. This process produced a porous sensing layer approximately 50 μm thick.

2.3. Operando DRIFTS measurements

DRIFTS and DC resistance measurements were simultaneously performed to monitor surface reactions and their impact on the output electrical signals. The sensors were inserted in a custom-made sensing chamber containing a KBr window, which was mounted in a Praying Mantis Diffuse Reflection Accessory (Harrick Scientific Products). This system was coupled with a Fourier-transform infrared (FT-IR) spectrometer (Bruker; Vertex 70 v) equipped with a mid-band mercury-cadmium-telluride (MCT) detector. The DC electrical resistance was monitored with an electrometer (Keithley; 617), applying a constant polarization voltage of 0.2 V. The operating temperatures of the sensors were set to 200 °C and 300 °C using an Agilent U8001A DC power supply connected to the calibrated Pt heater located on the backside of the devices. These temperatures lie within the typical operating range of semiconducting metal oxide gas sensors (200–400 °C) and were chosen to probe distinct surface reactivity regimes dominated by molecular oxygen (200 °C) and atomic oxygen (300 °C) species [7,40–43]. Fig. 1 presents a schematic illustration of the experimental setup used for operando DRIFTS measurements.

Before the measurements, the spectrometer was pre-evacuated to remove residual compounds such as water and carbon dioxide, thereby minimizing spectral interferences. The desired atmospheric composition inside the sensing chamber was established using a computer-controlled gas mixing system equipped with mass-flow controllers (MFC) and data acquisition cards. This system also enabled the introduction of different relative humidity (R.H.) levels, relative to the temperature of 25 °C, into the carrier gas using evaporators filled with distilled water (H_2O). A constant total flow of 200 mL/min was maintained throughout the experiments. All gases and gas mixtures were supplied by Westfalen AG Münster. The sensors were equilibrated at the reference conditions for at least 24 h to ensure the stability of the baseline resistance.

The gas exposure protocol consisted of the following steps:

a. Exposure to 8000, 20,000, and 205,000 ppm O_2 in a dry N_2 background.
b. Subsequently, isotopic exchange experiments were performed under the following conditions:
   b.1. Exposures to 3, 5, and 10 % H_2O followed by 10 % D_2O in a background of dry synthetic air.

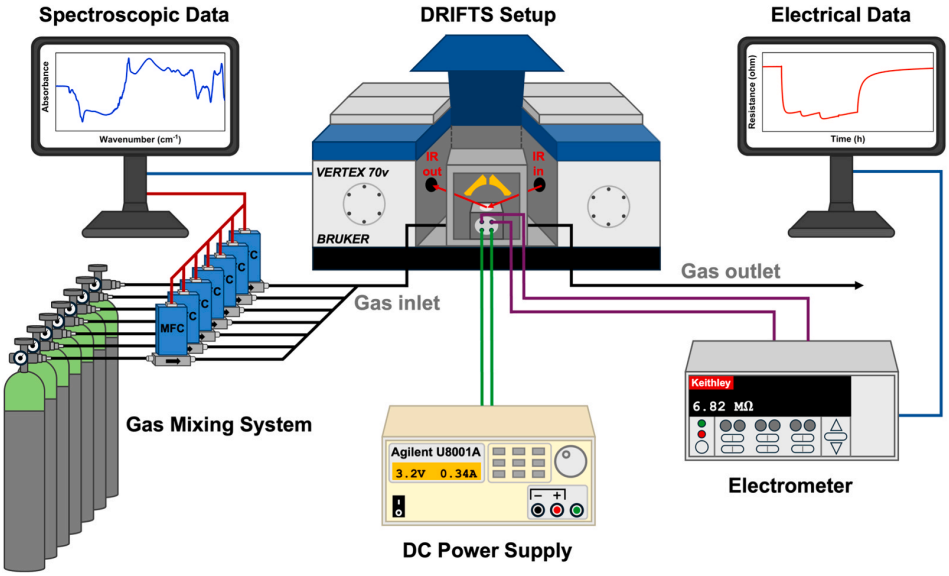

Fig. 1. Schematic illustration of the experimental setup used for operando DRIFTS measurements.

b.2. Exposures to 35, 100, and 500 ppm H_2 followed by 500 ppm D_2 in dry synthetic air and in synthetic air with 10 % H_2O (10 % R. H. at 25 °C).
b.3. Exposures to 35, 100, and 500 ppm ^{12}CO followed by 500 ppm ^{13}CO in dry synthetic air and in synthetic air with 10 % H_2O (10 % R.H. at 25 °C).

During the DRIFTS measurements, a single-channel spectrum (SCS) was continuously collected every 15 min. Each spectrum was generated by averaging 1024 sample scans within the spectral range from 800 to 4000 cm^{-1}, with a resolution of 4 cm^{-1}. Absorbance spectra (A) were calculated using OPUS software, referencing the intensity of the single-channel spectrum acquired under exposure to the target gases (I_{gas}) to the intensity of the single-channel spectrum taken under the reference conditions ($I_{reference}$). This relationship is shown in Eq. (1), proposed by Olinger and Griffiths [44].

$$Absorbance\ (A) = -\log\left(\frac{I_{gas}}{I_{reference}}\right) \quad (1)$$

The magnitude of the associated sensor responses to oxidizing and reducing gases was calculated from the simultaneous resistance measurements, according to Eqs. (2) and (3), respectively.

$$Sensor\ Signal\ (S) = \frac{R_{gas}}{R_0} \quad (2)$$

$$Sensor\ Signal\ (S) = \frac{R_0}{R_{gas}} \quad (3)$$

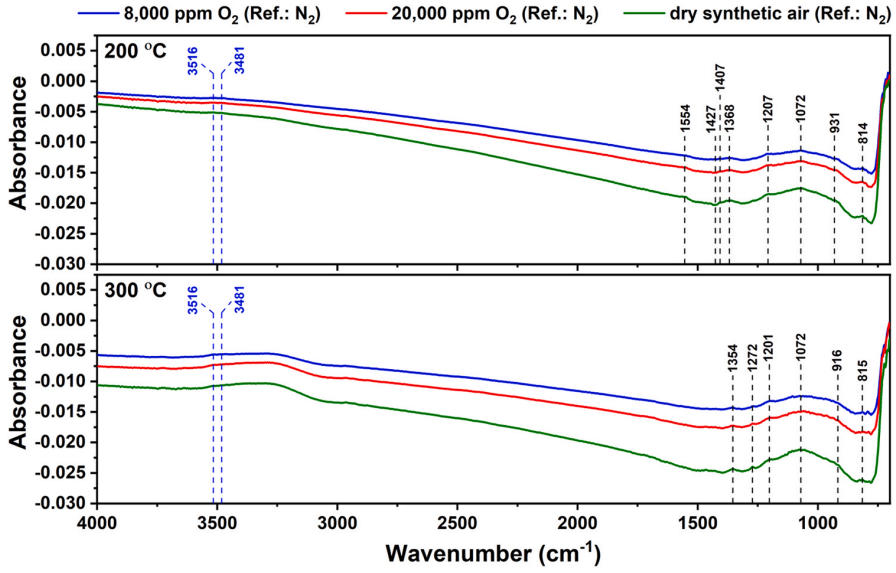

Fig. 2. DRIFT absorbance spectra of the Sn_3O_4 nanobelts-based sensor during exposure to 8000, 20,000, and 205,000 ppm O_2 (synthetic air) in dry N_2 at operating temperatures of 200 °C and 300 °C. The absorbance spectra were calculated using the single-channel spectrum recorded in dry N_2 as the reference.

where R_{gas} and R_0 represent the sensor resistances measured during exposure to the target and reference gases, respectively.

3. Results and discussion

The sensing mechanism of the Sn_3O_4 nanobelts was investigated using operando DRIFT spectroscopy to understand how surface reactions influence the sensor's properties. Under typical operating conditions, the presence of oxygen in the background plays a critical role in the performance of SMOX-based gas sensors. Therefore, the initial experiments focused on oxygen adsorption onto the Sn_3O_4 nanobelts. Fig. 2 presents the DRIFT absorbance spectra taken at 200 °C and 300 °C during stepwise exposures to 8000, 20,000, and 205,000 ppm O_2 in a dry N_2 background. The highest O_2 concentration corresponds to the composition of synthetic air, which was used as the reference gas in subsequent analyses. Additionally, Fig. S1 shows the simultaneously recorded DC resistance measurements, with gray bars indicating the conditions under which the DRIFT spectra were obtained. At both temperatures, a broadband centered around 1072 cm^{-1} was observed, accompanied by additional increasing bands at several wavenumbers: 814, 931, 1207, 1368, 1407, and 1554 cm^{-1} at 200 °C, and 815, 916, 1201, 1272, and 1354 cm^{-1} at 300 °C. A slightly decreasing band at 1427 cm^{-1} was also identified at 200 °C. It is important to note that assigning bands in the fingerprint region (<1500 cm^{-1}) to specific surface species is challenging due to the dominance of overlapping contributions from stretching vibrations of Sn–O bonds and their overtones, deformation vibrations of hydroxyl groups (Sn–OH), and stretching vibrations of carbonates and carboxylates (C═O).

A notable feature in the high-wavenumber region is the appearance of small increasing bands at 3516 and 3481 cm^{-1}, suggesting the formation of rooted hydroxyl groups [45,46]. However, in contrast to most metal oxides, such as SnO_2 [45,47], increasing the oxygen concentration does not significantly change the concentration of hydroxyl groups. These results provide novel experimental evidence distinguishing single-crystalline Sn_3O_4 nanobelts from conventional metal oxides. Furthermore, the data indicates that oxygen plays a limited role in surface reactions with water vapor, which will be further examined in the subsequent water exchange experiments discussed below. The presence of these hydroxyl species is attributed to the interaction between residual water vapor (<10 ppm H_2O; see Fig. S2 in the supplementary information of the study published by Boehme et al. [36]) in the synthetic air and adsorbed oxygen. Additionally, the broadband around 3300 cm^{-1} in the spectra at 300 °C is identified as an artifact resulting from ice formation on the detector, caused by a gradual vacuum loss over time [36].

The formation of oxygen species on the Sn_3O_4 surface is expected according to the ionosorption model [7,40,42]. This process occurs under chemical equilibrium between oxygen and active surface sites. From the perspective of the reception mechanism, it involves the formation and cancellation of chemical bonds between oxygen and the solid surface. In terms of transduction, adsorbed oxygen traps electrons from the semiconductor's conduction band, modulating the material's electrical conductivity. In n-type semiconductors, oxygen preferentially adsorbs at oxygen vacancies, which act as active adsorption sites for both atomic ($O_S^{-\alpha}$) and molecular ($O_{2,S}^{-\alpha}$) oxygen species [41–43]. Adsorbed molecular oxygen corresponds to chemisorbed species, often present as superoxide ions, that exist in dynamic equilibrium with the surrounding atmosphere and play a crucial role in catalytic and sensing reactions. These species are relatively less stable and may undergo transformations depending on the operating temperature. In contrast, lattice oxygen is incorporated into the crystal structure of the oxide, where it is more stable, occupies lower energy states, and participates in redox processes associated with the formation and healing of oxygen vacancies.

The broadband centered around 1072 cm^{-1} is attributed to the binding of tin with ionosorbed molecular oxygen (Sn–O_{2,S_i}^-), formed when oxygen adsorbs at an S_i site and captures electrons from the conduction band (Eq. (4)) [48–50]. These molecular oxygen species may exist in either ionized or non-ionized states and act as a precursor for the subsequent healing of a neighboring adsorption site S_j (Eq. (5)). This healing generates atomic oxygen species, which are incorporated into the surface lattice via metal–oxygen bonds (Sn–$O_{S_j}^{-\alpha}$), corresponding to the small increasing bands observed in the DRIFT absorbance spectra. Simultaneously, this process also results in the regeneration of an S_i site, maintaining the dynamic nature of surface oxygen chemistry. The charge state of chemisorbed oxygen ($\alpha = 1$ or 2) depends on the degree of ionization [7,40]. S_i and S_j represent distinct adsorption sites, likely associated with oxygen vacancies with different local environments and activation energies. Therefore, the overall mechanism entails a continuous process of formation and cancellation of oxygen vacancies. The broader shape of the 1072 cm^{-1} band at 200 °C and its slight narrowing at 300 °C suggests a higher concentration of molecular oxygen species at the lower temperature and a faster transition from molecular to atomic oxygen at the higher temperature. Furthermore, the small increasing bands identified in the fingerprint region of the absorbance spectra indicate that the formation of multiple atomic species at 200 °C and 300 °C is driven by distinct activation energies required to occupy different adsorption sites at each temperature. This finding highlights the temperature-dependent interaction between Sn_3O_4 and ionosorbed oxygen species.

$$O_2^{gas} + S_i + e^- \rightleftharpoons O_{2,S_i}^- \quad (4)$$

$$O_{2,S_i}^- + 2S_j + (2\alpha - 1)e^- \rightleftharpoons 2O_{S_j}^{-\alpha} + S_i \quad (5)$$

where O_2^{gas} represents the oxygen molecule from the air, S_i and S_j are surface sites available for oxygen chemisorption (typically oxygen vacancies), e^- is an electron in the conduction band at the surface.

The concentration of ionosorbed oxygen on the Sn_3O_4 surface determines the magnitude of resistance changes, which follow a function of the oxygen partial pressure. The resulting negative surface charging creates a space-charge region, inducing an upward band bending and increased resistance. This resistance increase during oxygen exposure is clearly observed in the DC resistance measurements recorded simultaneously with the DRIFT spectra (Fig. S1a), confirming the expected n-type semiconductor behavior for the Sn_3O_4 nanobelts [15,16,19,51]. At 200 °C, the resistance was approximately one order of magnitude higher than 300 °C (8.2 MΩ and 0.68 MΩ, respectively) after 2 h in dry synthetic air (205,000 ppm O_2). The corresponding sensor signals were 5.9, 8.8, and 26.1 at 200 °C and 4.5, 6, and 13.7 at 300 °C for 8000, 20,000, and 205,000 ppm O_2, respectively (Fig. S1b). These results indicate that oxygen adsorption has a more pronounced impact on the electrical response at 200 °C than at 300 °C. The observed difference can be attributed to a higher concentration of ionized donors at elevated temperatures, which enhances the availability of free electrons for conduction.

Water vapor is a well-known interfering compound in gas detection. To further investigate the reaction mechanism of the Sn_3O_4 nanobelts-based sensor, operando DRIFT spectroscopy was conducted using isotopic exchange experiments with water (H_2O) and deuterated water (D_2O). Upon exposure of the sensor surface to isotopically labeled water vapor, the vibrational bands associated with hydroxyl (OH) groups shift to lower wavenumbers due to the replacement of hydrogen atoms by deuterium. In contrast, the wavenumbers of bands related to Sn–O and C═O bonds remain unchanged. This experimental approach allows for the differentiation between the stretching vibrations of Sn–O bonds, including their overtones, and the deformation vibrations of hydroxyl groups (Sn–OH). Fig. 3 presents the DRIFT absorbance spectra of the Sn_3O_4 nanobelts-based sensor recorded at 200 °C and 300 °C during exposure to 10 % H_2O (blue curve), followed by direct isotopic exchange

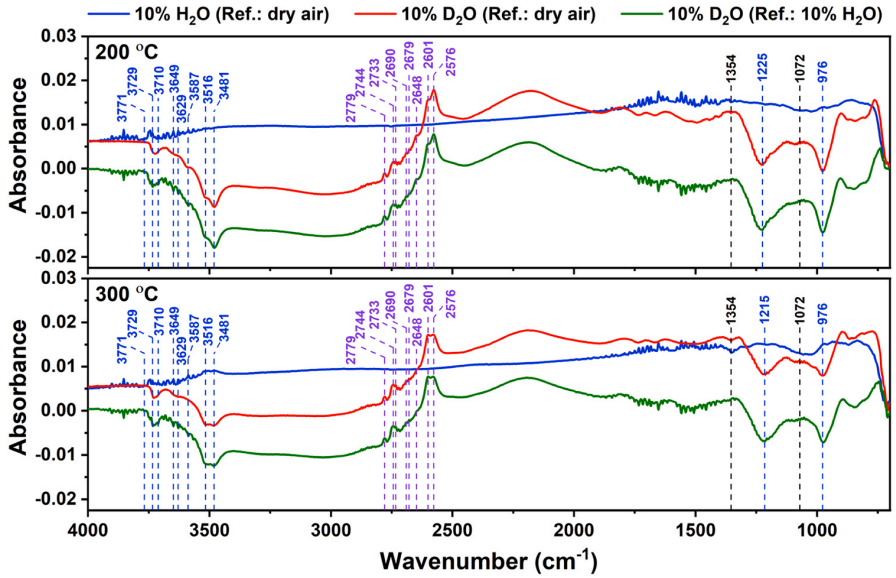

Fig. 3. DRIFT absorbance spectra of the Sn_3O_4 nanobelts-based sensor during exposure to 10 % H_2O, followed by the isotopic exchange to 10 % D_2O in dry synthetic air at operating temperatures of 200 °C and 300 °C. The absorbance spectra were calculated using single-channel spectra recorded in both dry synthetic air and synthetic air containing 10 % H_2O as references.

to 10 % D_2O (red curve) in synthetic air. In the presence of H_2O, the formation of OH groups was minimally visible at both operating temperatures. A slightly increased broadband was identified within the range from 2700 to 3600 cm^{-1}, corresponding to the stretching vibration of interacting hydroxyl (OH) groups [45]. Notably, deformation vibrations of physisorbed water were not detectable in the region around 1630 cm^{-1} at either 200 °C or 300 °C [37,52,53]. Moreover, a marginal decrease in the broadband between 900 and 1250 cm^{-1} (centered around 1072 cm^{-1}) and in the band at 1354 cm^{-1} was observed, representing the vibrations of Sn–O_2^- and Sn–$O^{-\alpha}$, respectively [54]. Such spectral changes indicate a decrease in the concentration of preexisting oxygen species, suggesting either a slight reduction of the Sn_3O_4 surface upon reaction with water vapor or a competition adsorption between oxygen and water vapor for the same adsorption sites. Similar band profiles with lower intensity were observed in spectra during exposures to 3 % and 5 % H_2O (Fig. S2). The weak impact of H_2O on the absorbance spectra reveals that the Sn_3O_4 surface is already hydroxylated under dry air conditions, but not fully saturated with water vapor. This effect arises from the trace levels of residual water vapor in the synthetic air. Furthermore, given the single-crystalline nature of the nanobelts, their surfaces exhibit a lower concentration of crystalline defects than polycrystalline grains. As a result, fewer active adsorption sites are available for the formation of hydroxyl groups, contrasting with SnO_2 surfaces where hydroxyl coverage usually varies more strongly with humidity levels [37,45,55].

The coverage of the Sn_3O_4 surface with preexisting OH groups in dry air is confirmed at both temperatures following the exchange reaction from 10 % H_2O to 10 % D_2O. During D_2O exposure, the absorbance spectra show a reduction in the concentration of OH species (negative bands in the OH region) along with a simultaneous increase in the concentration of OD species (positive bands in the OD region from 2000 cm^{-1} to 3000 cm^{-1}). These results indicate the replacement of OH groups with OD groups. Additionally, the DRIFTS spectra in Fig. 3 provide no evidence for the formation of new hydroxyl groups. The assigned OH and OD bands are shifted by a factor of approximately 0.736–0.74 (see Table 1), closely matching the theoretical factor of 0.737 for SnO_2 [45]. The decreasing bands in the IR spectral region above 3600 cm^{-1} (3771, 3729, 3710, 3649, and 3629 cm^{-1}) and below 3600 cm^{-1} (3587, 3516, and 3481 cm^{-1}) during D_2O exposure correspond to the stretching vibration of isolated terminal (one-fold-coordinated) and rooted (n-fold-coordinated) OH groups, respectively [45,46,54–60]. Although similar water-related species were observed at both operating temperatures, the intensity of the decreasing bands in the OH region after exposure to D_2O is lower at 300 °C compared to 200 °C. This trend suggests a higher degree of initial surface hydroxylation at 200 °C and a decrease in the concentration of preexisting OH groups on the Sn_3O_4 surface with increasing operating temperature due to a higher desorption rate. In addition, the decreasing bands in the fingerprint region of D_2O spectra (1225 and 976 cm^{-1} at 200 °C and 1215 and 976 cm^{-1} at 300 °C) correspond to the Sn–OH deformation vibrations. In contrast, the broadband centered around 1072 cm^{-1} and the band at

Table 1
Wavenumbers of the OH/OD vibration bands observed under H_2O/D_2O exposure on the Sn_3O_4 nanobelts-based gas sensor, along with their corresponding shift factors.

OH wavenumber (cm^{-1})	OD wavenumber (cm^{-1})	Shift (cm^{-1})	Assignment
3771	2779	0.736	ν(OH); isolated terminal
3729	2744	0.736	ν(OH); isolated terminal
3710	2733	0.737	ν(OH); isolated terminal
3649	2690	0.737	ν(OH); isolated terminal
3629	2679	0.738	ν(OH); isolated terminal
3587	2648	0.738	ν(OH); isolated rooted
3516	2601	0.74	ν(OH); isolated rooted
3481	2576	0.74	ν(OH); isolated rooted
3650–2700	–	–	ν(OH); interacting
1354	–	–	Sn–$O^{-\alpha}$
1225	–	–	Sn–OH
1072	–	–	Sn–O_2^-
976	–	–	Sn–OH

1354 cm^{-1} remain unshifted in D_2O, validating their assignment to the vibration of metal–oxygen bonds (Sn–O_2^- and Sn–$O^{-\alpha}$, respectively).

Experimental investigations have demonstrated a complex interplay between water molecules and the tin oxide surface, resulting in the formation of multiple possible hydroxyl groups [37]. In the temperature range of 200 °C to 350 °C, the electrical effects of water adsorption are primarily described in terms of dissociative adsorption of water [61]. In this process, water molecules react with surface oxygen and tin sites, producing either terminal and rooted hydroxyl groups (Eq. (6)) or terminal hydroxyl groups accompanied by the formation of oxygen vacancies (Eq. (7)). Rooted hydroxyl groups and oxygen vacancies act as surface donors, promoting electrons into the conduction band and increasing the electrical conductivity of the sensing layer [37,40]. Wicker et al. proposed an alternative reaction occurring in SnO_2 [47]. In this mechanism, H_2O interacts with surface oxygen and an oxygen vacancy (rather than with a tin site), generating two rooted hydroxyl groups (Eq. (8)). This replacement of oxygen vacancies with rooted hydroxyl groups does not inject electrons into the conduction band; consequently, it has no direct electrical effect on the conductivity of the sensing layer. Results from DRIFT spectra (Fig. 3) and electrical resistance measurements (Fig. S3) show that the formation of isolated hydroxyl groups is the dominant process taking place in Sn_3O_4 nanobelts at 200 °C, consistent with Eq. (6). However, the formation of rooted OH groups cannot be entirely excluded. Conversely, a higher concentration of rooted hydroxyl groups was observed at 300 °C, as evidenced by the bands at 3587, 3516, and 3481 cm^{-1}, indicating that their formation is the primary process. In light of this evidence and the limited role of oxygen in the reaction with water vapor, as discussed earlier, the mechanism described in Eq. (8) appears to be the dominant reaction pathway for H_2O interaction on the surface of Sn_3O_4 at 300 °C. Even though this reaction is electrically neutral, since it does not promote free electrons to the conduction band, it can still influence the resistance of the sensing layer. Water vapor can interact with the surface of the sensing layer by competing with oxygen for adsorption sites, hindering the oxygen ionosorption and suppressing the reoxidation [45,62]. As a result, the partial blocking of adsorption sites by water reduces the extent of electron trapping, decreasing the electrical resistance of the sensor as the humidity level increases [47].

$$H_2O^{gas} + Sn_{Sn} + O_O^{\times} \rightleftharpoons \left(Sn_{Sn}^{+} - OH^{-}\right) + (OH)_O^{+} + e^{-} \quad (6)$$

$$H_2O^{gas} + 2Sn_{Sn} + O_O^{\times} \rightleftharpoons 2\left(Sn_{Sn}^{+} - OH^{-}\right) + V_O^{++} + 2e^{-} \quad (7)$$

$$H_2O^{gas} + V_O^{++} + O_O^{\times} \rightleftharpoons 2(OH)_O^{+} \quad (8)$$

where Sn_{Sn} is a tin site on the surface, $O_O^{\times}$ is lattice oxygen, $\left(Sn_{Sn}^{+} - OH^{-}\right)$ is a terminal hydroxyl group, and $(OH)_O^{+}$ is a rooted hydroxyl group.

The systematic decrease in resistance with increasing H_2O concentration confirms the reducing nature of water on the Sn_3O_4 surface at both operating temperatures (Fig. S3), albeit through different reaction mechanisms. The calculated sensor signals were 11.6, 12.5, and 15 at 200 °C and 3.9, 4.2, and 4.8 at 300 °C for relative humidity levels of 3, 5, and 10 % H_2O, respectively. These results demonstrate that water adsorption induces a more substantial change in resistance at 200 °C than 300 °C, consistent with the trends observed during oxygen exposure. This behavior suggests that, at 200 °C, the dominant mechanism involves the dissociative adsorption of water, which releases electrons into the conduction band by forming terminal hydroxyl groups (as described in Eq. (6)). This process exerts a stronger effect on the overall electrical resistance than the blocking of oxygen adsorption caused by the formation of rooted hydroxyl groups at 300 °C (Eq. (8)).

To validate the results obtained from the H_2O/D_2O experiments, complementary isotopic exchange studies were performed using H_2/D_2, given that H_2 yields reaction products most analogous to those of water. Figs. 4 and 5 present the absorbance spectra recorded at 200 °C and 300 °C during exposure to 500 ppm H_2 (blue curve), followed by the direct isotopic exchange to 500 ppm D_2 (red curve) in synthetic dry air and synthetic air with 10 % R.H. at 25 °C, respectively. Figs. S4 and S5 show the simultaneously recorded DC resistance measurements. In dry synthetic air, the absorbance spectra at 200 °C and 300 °C (Fig. 4) exhibit band profiles similar to those observed in H_2O/D_2O exchange experiments. This similarity indicates that both exchange processes take place at equivalent sites and involve the same hydroxyl species on the surface of Sn_3O_4 nanobelts. Consistent with the water vapor experiments, the bands at 3587, 3516, and 3481 cm^{-1} exhibit superior intensity at 300 °C than at 200 °C, validating the increased concentration of rooted hydroxyl groups formed at higher temperatures. Additionally,

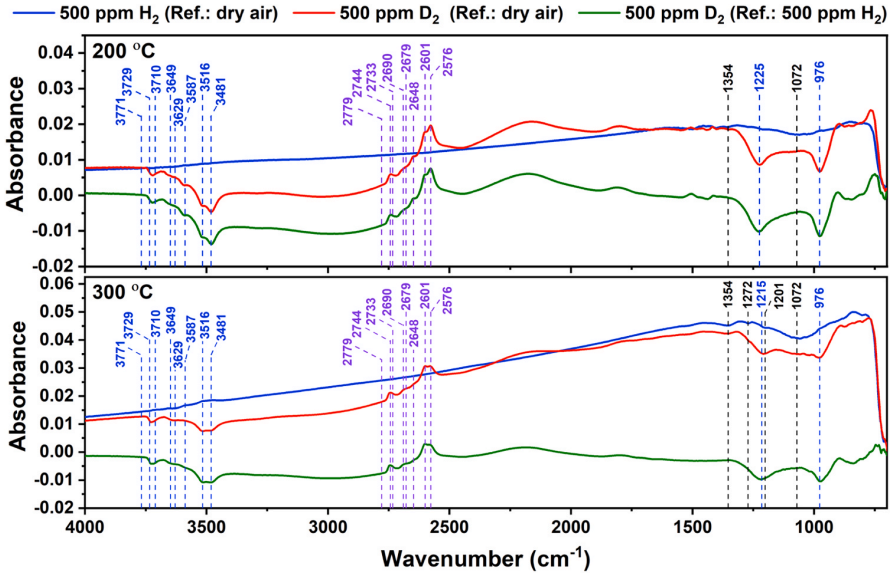

Fig. 4. DRIFT absorbance spectra of the Sn_3O_4 nanobelts-based sensor during exposure to 500 ppm H_2, followed by the isotopic exchange to 500 ppm D_2 in dry synthetic air at operating temperatures of 200 °C and 300 °C. The absorbance spectra were calculated using single-channel spectra recorded in both dry synthetic air and 500 ppm H_2 as references.

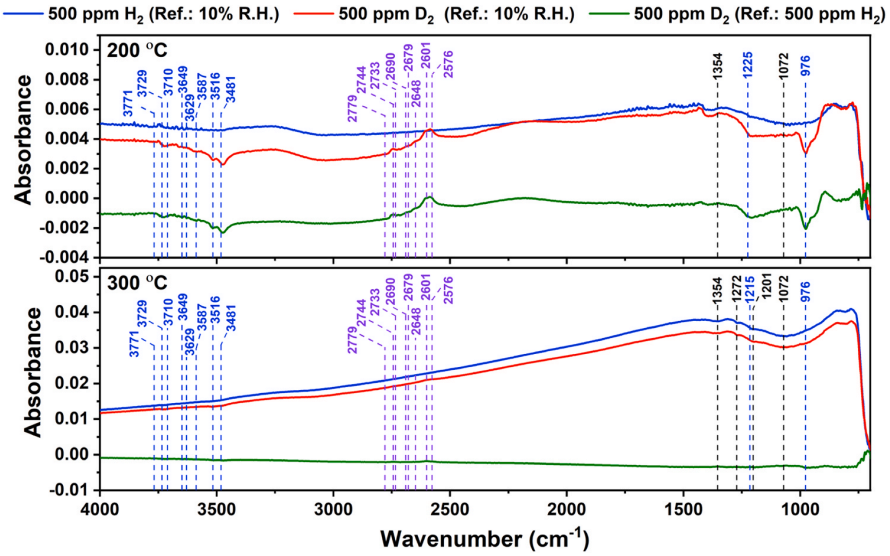

Fig. 5. DRIFT absorbance spectra of the Sn_3O_4 nanobelts-based sensor during exposure to 500 ppm H_2, followed by the isotopic exchange to 500 ppm D_2 in synthetic air with 10 % H_2O (10 % R.H. at 25 °C) at operating temperatures of 200 °C and 300 °C. The absorbance spectra were calculated using single-channel spectra recorded in both 10 % R.H. at 25 °C and 500 ppm H_2 as references.

experimental data confirmed the highly hydroxylated initial state of the Sn_3O_4 surface at 200 °C rather than 300 °C, matching the results obtained from the isotopic exchange of water vapor.

Under humid conditions (Fig. 5), the hydroxyl-related bands were significantly attenuated or absent at both temperatures. At 200 °C, isotopic exchange was notably weaker than in dry air, and no exchange occurred at 300 °C, indicating that surface interactions with water vapor dominate during H_2 exposure under humid conditions, effectively suppressing further isotopic exchange. Overall, H_2/D_2 exchange experiments revealed that no additional hydroxyl groups were created during H_2 exposure under either dry or humid conditions at 200 °C and 300 °C. In contrast, a clear decrease in the metal–oxide bonds ($Sn–O_2^-$ and $Sn–O^{-\alpha}$) signals was observed, as evidenced by the broadband centered around 1072 cm^{-1} and the band at 1354 cm^{-1} at both temperatures, and at 1272 cm^{-1} and 1201 cm^{-1} at 300 °C. This trend, consistent across all tested background atmospheres (dry and humid air) and operating temperatures, suggests a surface reduction process in agreement with the data from the water vapor exchange experiments. Similar band profiles with reduced intensity were also observed at lower H_2 concentrations (35 and 100 ppm), as shown in Figs. S6 and S7.

Results from electrical resistance measurements (Figs. S4 and S5) indicate that the sensor response to H_2 is influenced by the presence of humidity in the background and the operating temperature. Under dry conditions, the calculated sensor signals for 35, 100, and 500 ppm H_2 were 11.2, 18.6, and 36.8 at 200 °C, and 39.4, 53.5, and 83.1 at 300 °C, respectively. The sensor signals were significantly attenuated in humid environments (10 % R.H. at 25 °C), measuring 1.5, 2.0, and 3.6 at 200 °C and 7.3, 11.4, and 22.2 at 300 °C. Additionally, the baseline resistance was consistently higher in dry air than in humid air at both operating temperatures. These findings confirm the competition between oxygen and water vapor for the same active surface sites on the Sn_3O_4 surface, and demonstrate that, under humid conditions, H_2 and H_2O interact with mutual reaction partners. The spectroscopic data show a more pronounced decrease in metal–oxygen-related vibrational bands at 300 °C than at 200 °C under both dry and humid conditions. This result indicates a higher degree of surface reduction at the higher temperature, independently of the humidity level in the background, which is consistent with the enhanced sensor response observed in the electrical measurements to H_2. Based on spectroscopic and electrical data, the reaction mechanism underlying the reducing effect of H_2 on the Sn_3O_4 surface can be described according to Eqs. (9–11). At 200 °C, the dominant process involves the interaction of H_2 with surface oxygen species, forming H_2O and creating oxygen vacancies while releasing electrons into the conduction band (Eq. (9)). At 300 °C, the hydrogen dissociation and subsequent formation of rooted hydroxyl groups become the predominant processes. This dissociation occurs either through the reaction of H_2 with surface oxygen species (Eq. (10)) or via interaction with water produced from Eq. (9) (Eq. (11)). Importantly, the mechanism described in Eq. (10) results in simultaneous formation of rooted OH groups and electron release, which may explain the significantly higher sensor response to H_2 at 300 °C compared to 200 °C.

$$H_2^{gas} + O_O^{\times} \rightleftharpoons H_2O^{gas} + V_O^{++} + 2e^- \quad (9)$$

$$H_2^{gas} + 2O_O^{\times} \rightleftharpoons 2(OH)_O^{+} + 2e^- \quad (10)$$

$$H_2O^{gas} + V_O^{++} + O_O^{\times} \rightleftharpoons 2(OH)_O^{+} \quad (11)$$

Similar to H_2, carbon monoxide (CO) is a reducing gas detected through redox reactions on the SMOX surface. The interplay between CO and surface-adsorbed oxygen species leads to the formation and cancellation of oxygen vacancies, modulating the material's conductivity by trapping or releasing electrons in the conduction band. However, unlike H_2, the reaction products generated from CO exposure are not directly associated with OH groups. Therefore, understanding the interaction between the Sn_3O_4 surface and CO as a standard gas is crucial to elucidate fundamental aspects of detection mechanisms and, consequently, to advance gas sensing studies. Figs. 6 and 7 present DRIFT absorbance spectra taken at 200 °C and 300 °C during exposure to 500 ppm ^{12}CO (blue curve), followed by the direct isotopic exchange to 500 ppm ^{13}CO (red curve) in dry synthetic air and synthetic air with 10 % R.H. at 25 °C. The spectra reveal that COexposure leads to a decrease in the intensity of bands associated with metal–oxygen bonds ($Sn–O_2^-$ and $Sn–O^{-\alpha}$) at both operating temperatures and at both dry and humid conditions. This effect is particularly apparent in the broadband centered at 1072 cm^{-1}, attributed to molecular oxygen ($Sn–O_2^-$). Similar trends in the band intensities were observed during exposure to 35 and 100 ppm ^{12}CO in dry and humid conditions (Figs. S8 and S9, respectively). DRIFTS spectra also reveal that, in contrast to the typical

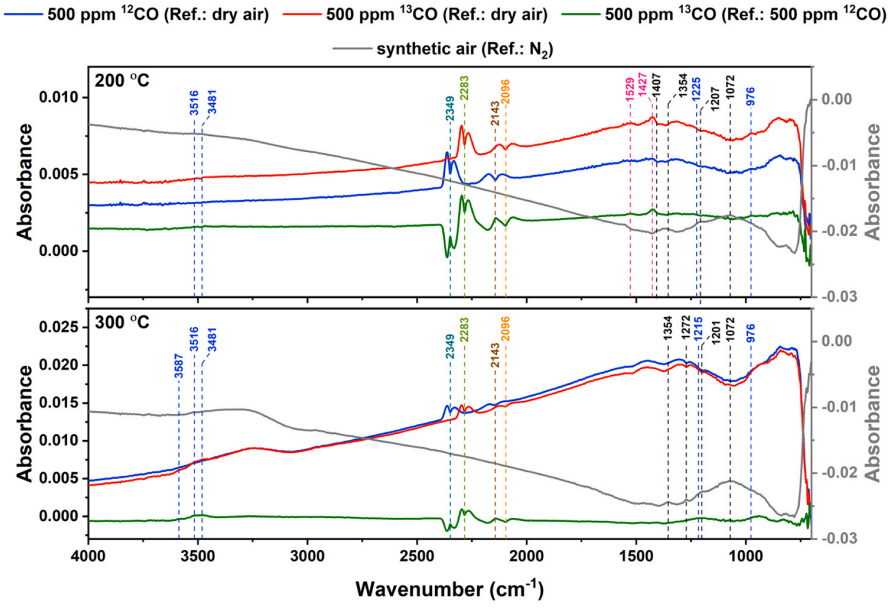

Fig. 6. DRIFT absorbance spectra of the Sn_3O_4 nanobelts-based sensor during exposure to 500 ppm ^{12}CO, followed by the isotopic exchange to 500 ppm ^{13}CO in dry synthetic air at operating temperatures of 200 °C and 300 °C. The absorbance spectra were calculated using single-channel spectra recorded in dry synthetic air and 500 ppm ^{12}CO as references.

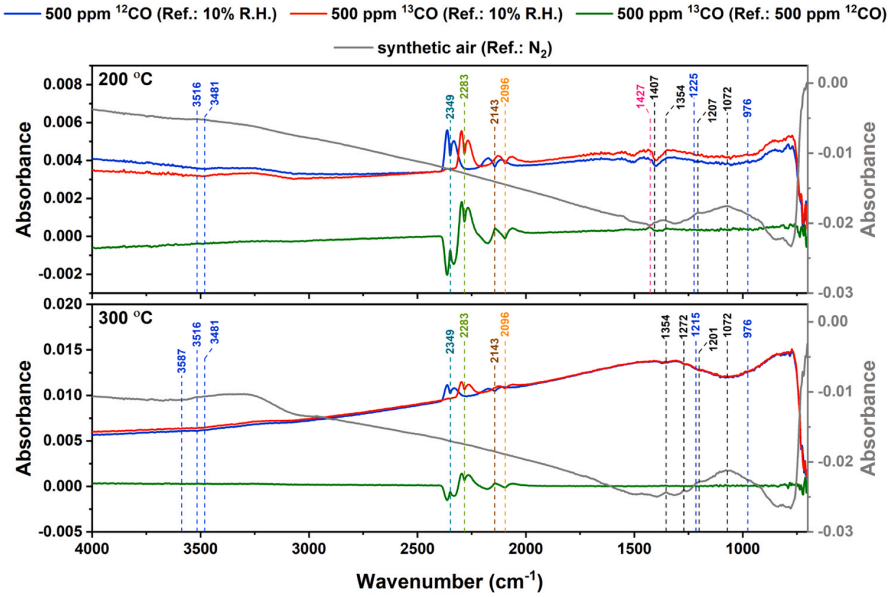

Fig. 7. DRIFT absorbance spectra of the Sn_3O_4 nanobelts-based sensor during exposure to 500 ppm ^{12}CO, followed by the isotopic exchange to 500 ppm ^{13}CO in synthetic air with 10 % H_2O (10 % R.H. at 25 °C) at operating temperatures of 200 °C and 300 °C. The absorbance spectra were calculated using single-channel spectra in 10 % R.H. at 25 °C and 500 ppm ^{12}CO as references.

behavior observed in SnO_2 materials [45,47,55], no decrease in the OH bands was detected under either dry or humid conditions. This result suggests that CO does not compete with H_2O for the same adsorption sites or reactive partners on the Sn_3O_4 surface. Therefore, the interaction of the Sn_3O_4 surface with OH groups is as strong as its interaction with CO, resulting in no apparent changes.

When CO is introduced, the Sn_3O_4 surface is reduced, indicating that adsorbed molecular oxygen (O_2^-) serves as a reservoir of reaction partners ($O^{-\alpha}$) for CO. This interaction creates additional oxygen vacancies/ oxygen adsorption sites, generates gaseous CO_2, and releases electrons into the conduction band at the surface (Eq. (12)). As a result, the material's resistance decreases (Figs. S10 and S11), as supported by the appearance of the band at 2349 cm^{-1} in the DRIFT spectra, corresponding to gaseous CO_2. The observed shift in the CO_2 band during isotopic exchange from 500 ppm ^{12}CO to 500 ppm ^{13}CO is 0.972, consistent with previous reports for SnO_2 [55]. As observed for H_2, the competition between oxygen species and water vapor for adsorption surface sites in humid conditions reduces the intensity of the decreasing

bands, thus limiting the extent of surface reduction, and weakens the electrical response, as evidenced by the lower sensor signals (Figs. S10 and S11).

In dry air, the calculated sensor signals for 35, 100, and 500 ppm ^{12}CO were 1.9, 2.3, and 3.9 at 200 ºC and 7.9, 10.4, and 16.1 at 300 ºC. The corresponding sensor signals in the humid environment (10 % R.H. at 25 ºC) were decreased to 1.3, 1.5, and 2.0 at 200 ºC and 2.2, 3.0, and 4.6 at 300 ºC, respectively. Consistent with data obtained during H_2 exposure, the reduction in the intensity of bands associated with metal–oxygen bonds was more pronounced at 300 °C than at 200 °C under both dry and humid conditions. This observation reveals a more significant surface reduction at elevated temperatures, regardless of humidity levels. Resistance measurements confirm these results, showing enhanced sensor responses to CO at 300 °C compared to 200 °C. Overall, the sensor response to CO is lower than that observed for H_2, aligning with the DRIFT spectra, which exhibit a slighter decrease in the intensity of bands related to metal–oxygen bonds during CO interaction compared to H_2 exposure. These findings suggest that CO removes a smaller concentration of adsorbed oxygen from the surface, resulting in lower sensor signals.

$$CO^{gas} + O_s^{-\alpha} \rightarrow CO_2^{gas} + \alpha e^- + S \quad (12)$$

Additionally, the DRIFTS spectra recorded in the presence of 500 ppm ^{13}CO at 200 °C show small peaks at 1427 and 1529 cm^{-1} in dry air and at 1427 cm^{-1} in 10 % R.H. at 25 °C (red curves in Figs. 6 and 7, respectively). These peaks indicate the formation of carbonate species ($CO_3^{-\alpha}$) adsorbed on the Sn_3O_4 surface. The presence of carbonate species has also been reported in some SnO_2-based gas sensors as well as in theoretical calculations; however, their occurrence strongly depends on the synthesis and treatment conditions of the sensing layer [45,55,56,63]. However, these species were absent in the spectra at 300 °C in either dry or humid air, suggesting that the formation or stability of these intermediates is temperature dependent. Previous studies using theoretical calculations [64,65] proposed that carbonates form as intermediate products in the reaction of molecular oxygen with CO (Eq. (13)) or from a subsequent reaction of CO_2 with atomic oxygen species (Eq. (14)). However, additional operando DRIFTS experiments involving CO_2 dosing in synthetic air, as performed by Degler et al. [55], are necessary to validate these mechanisms. Table 2 shows a summary of all vibrational species identified species during $^{12}CO/^{13}CO$ exposures.

$$CO^{gas} + O_{2,s}^{-\alpha} \rightarrow CO_3^{-\alpha} \rightarrow O_S^{-\alpha} + CO_2^{gas} \quad (13)$$

$$CO_2^{gas} + O_s^{-\alpha} \rightleftharpoons CO_3^{-\alpha} \quad (14)$$

4. Conclusion

This study provides the first experimental insights into the gas sensing mechanism of single-crystalline Sn_3O_4 nanobelts. By employing operando DRIFTS combined with resistance measurements, the interplay between surface chemistry and sensing behavior was elucidated. Results demonstrate that adsorbed molecular oxygen serves as a precursor for healing oxygen vacancies, creating reactive sites for subsequent interactions with H_2O, H_2, and CO. The minimal impact of water adsorption on the hydroxylated Sn_3O_4 surface in dry air, alongside the pronounced influence of water vapor on H_2 and CO detection, underscores the critical role of humidity in modulating gas sensing responses. Moreover, the primary reaction pathway between Sn_3O_4 and H_2O depends on the operating temperature. The H_2/D_2 exchange experiments revealed that H_2 exposure generates hydroxyl species on equivalent surface sites, further corroborating the interplay between H_2O and H_2 interactions. Additionally, the formation of carbonate species during CO oxidation, while detectable, does not directly influence the sensing response, indicating that the redox process dominates the detection mechanism for CO. Overall, this work advances the understanding of Sn_3O_4 as a promising alternative to traditional SMOX materials such as SnO_2. While this study clarifies the fundamental sensing behavior of Sn_3O_4, its limitations include the focus on specific gases and controlled laboratory conditions, which may not fully capture real-world complexities. Future studies should explore multi-gas environments, long-term stability, and device integration to further advance the development of Sn_3O_4 nanobelt-based sensors for selective and low-power gas sensing applications.

Table 2
Wavenumbers of the $^{12}C/^{13}C$ vibration bands observed under $^{12}CO/^{13}CO$ exposure on the Sn_3O_4 nanobelts-based gas sensor, along with their corresponding shift factors.

^{12}C wavenumber (cm^{-1})	^{13}C wavenumber (cm^{-1})	Shift (cm^{-1})	Assignment
2349	2283	0.972	CO_2^{gas}
2143	2096	0.978	CO^{gas}
(not observable)	1529	–	$CO_3^{-\alpha}$
(not observable)	1427	–	$CO_3^{-\alpha}$

CRediT authorship contribution statement

Pedro H. Suman: Writing – review & editing, Writing – original draft, Visualization, Validation, Methodology, Investigation, Formal analysis, Data curation, Conceptualization. **Benjamin Junker-Reiss:** Writing – review & editing, Investigation. **Nicolae Barsan:** Writing – review & editing, Supervision, Resources, Conceptualization. **Udo Weimar:** Resources. **Marcelo O. Orlandi:** Writing – review & editing, Supervision, Resources, Funding acquisition.

Declaration of Competing Interest

The authors declare that they have no known competing financial interests or personal relationships that could have appeared to influence the work reported in this paper.

Acknowledgments

This study was financed, in part, by the São Paulo Research Foundation (FAPESP), Brazil (Process Numbers #2019/26333–2, #2016/20808–0, #2013/07296–2, #2012/11139–7, #2017/26219–0, #2017/24839–0). The authors acknowledge the National Council for Scientific and Technological Development (CNPq) (Grant #443138/2016–8); the Financier of Studies and Projects (FINEP) (contract #01.22.0291.00, reference #0083/21 and contract #01.18.0075.00, reference #0382/16); and the Coordination for the Improvement of Higher Education Personnel (CAPES) (Grant #88887.936511/2024–00 and #88887.469365/2019–00) for the financial support.

Appendix A. Supporting information

Supplementary data associated with this article can be found in the online version at doi:10.1016/j.snb.2025.138909.

Data availability

Data will be made available on request.

References

[1] M. Tereshkov, T. Dontsova, B. Saruhan, S. Krüger, Metal oxide-based sensors for ecological monitoring: progress and perspectives, Chemosensors 12 (2024) 42, https://doi.org/10.3390/chemosensors12030042.
[2] T. Reis, P.C. Moura, D. Gonçalves, P.A. Ribeiro, V. Vassilenko, M.H. Fino, M. Raposo, Ammonia detection by electronic noses for a safer work environment, Sensors 24 (2024) 3152, https://doi.org/10.3390/s24103152.

[3] G. Benedetto, K.A. Mirica, Conductive framework materials for chemiresistive detection and differentiation of toxic gases, Acc. Chem. Res 57 (2024) 2775–2789, https://doi.org/10.1021/acs.accounts.4c00319.
[4] M. Nami, M. Taheri, I.A. Deen, M. Packirisamy, M.J. Deen, Nanomaterials in chemiresistive and potentiometric gas sensors for intelligent food packaging, TrAC Trends Anal. Chem. 174 (2024) 117664, https://doi.org/10.1016/j.trac.2024.117664.
[5] K. Muthumalai, N. Gokila, Y. Haldorai, R.T. Rajendra Kumar, Advanced wearable sensing technologies for sustainable precision agriculture – a review on chemical sensors, Adv. Sens. Res. 3 (2024) 2300107, https://doi.org/10.1002/adsr.202300107.
[6] Z.U. Abideen, W.U. Arifeen, Y.M.N.D.Y. Bandara, Emerging trends in metal oxide-based electronic noses for healthcare applications: a review, Nanoscale 16 (2024) 9259–9283, https://doi.org/10.1039/D4NR00073K.
[7] N. Barsan, U. Weimar, Conduction model of metal oxide gas sensors, J. Electroceram 7 (2001) 143–167, https://doi.org/10.1023/A:1014405811371.
[8] N. Yamazoe, Toward innovations of gas sensor technology, Sens Actuators B Chem. 108 (2005) 2–14, https://doi.org/10.1016/j.snb.2004.12.075.
[9] G. Korotcenkov, B.K. Cho, Metal oxide composites in conductometric gas sensors: achievements and challenges, Sens Actuators B Chem. 244 (2017) 182–210, https://doi.org/10.1016/j.snb.2016.12.117.
[10] A. Oprea, D. Degler, N. Barsan, A. Hemeryck, J. Rebholz, Basics of semiconducting metal oxide-based gas sensors, in: N. Barsan, K. Schierbaum (Eds.), Gas Sensors Based on Conducting Metal Oxides: Basic Understanding, Technology and Applications, Elsevier, 2018, pp. 61–165, https://doi.org/10.1016/B978-0-12-811224-3.00003-2.
[11] N. Barsan, K. Schierbaum, Gas sensors based on conducting metal oxides: basic understanding, technology and applications, Elsevier, 2018, https://doi.org/10.1016/C2016-0-00984-1.
[12] N. Taguchi, Gas detecting device, US3631436A, 1971.
[13] A. Staerz, T. Suzuki, U. Weimar, N. Barsan, SnO_2: the most important base material for semiconducting metal oxide-based materials, in: M.O. Orlandi (Ed.), Tin Oxide Materials, Elsevier, 2020, pp. 345–377, https://doi.org/10.1016/b978-0-12-815924-8.00012-8.
[14] Y. Kong, Y. Li, X. Cui, L. Su, D. Ma, T. Lai, L. Yao, X. Xiao, Y. Wang, SnO_2 nanostructured materials used as gas sensors for the detection of hazardous and flammable gases: a review, Nano Mater. Sci. 4 (2022) 339–350, https://doi.org/10.1016/j.nanoms.2021.05.006.
[15] P.H. Suman, A.A. Felix, H.L. Tuller, J.A. Varela, M.O. Orlandi, Comparative gas sensor response of SnO_2, SnO and Sn_3O_4 nanobelts to NO_2 and potential interferents, Sens Actuators B Chem. 208 (2015) 122–127, https://doi.org/10.1016/j.snb.2014.10.119.
[16] P.H. Suman, B. Junker, U. Weimar, M.O. Orlandi, N. Barsan, Modeling the conduction mechanism in chemoresistive gas sensor based on single-crystalline Sn_3O_4 nanobelts: a phenomenological in operando investigation, ACS Sens 9 (2024) 149–156, https://doi.org/10.1021/acssensors.3c01810.
[17] J. Hou, Z. Yang, Q. Rong, C. Zhang, C. Wang, Y. Guo, Au-decorated Sn_3O_4 nanoflower-based MEMS gas sensor for detecting ppb-level acetone, ACS Appl. Nano Mater. 7 (2024) 6506–6515, https://doi.org/10.1021/acsanm.4c00270.
[18] Y. Liu, S. Chen, B. Xiao, J. Chu, H. Wang, Y. Chen, T. Yao, A. Yang, X. Han, M. Rong, X. Wang, Ultra-large Sn_3O_4 nanosheets with Sn^{2+} defect for highly efficient hydrogen sensing, Sens Actuators B Chem. 401 (2024) 135025, https://doi.org/10.1016/j.snb.2023.135025.
[19] P.H. Suman, E. Longo, J.A. Varela, M.O. Orlandi, Controlled synthesis of layered Sn3O4 nanobelts by carbothermal reduction method and their gas sensor properties, J. Nanosci. Nanotechnol. 14 (2014) 6662–6668, https://doi.org/10.1166/jnn.2014.9356.
[20] P.H. Suman, A.A. Felix, H.L. Tuller, J.A. Varela, M.O. Orlandi, Giant chemo-resistance of SnO disk-like structures, Sens Actuators B Chem. 186 (2013) 103–108, https://doi.org/10.1016/j.snb.2013.05.087.
[21] M.S. Barbosa, P.H. Suman, J.J. Kim, H.L. Tuller, M.O. Orlandi, Investigation of electronic and chemical sensitization effects promoted by pt and pd nanoparticles on single-crystalline SnO nanobelt-based gas sensors, Sens Actuators B Chem. 301 (2019) 127055, https://doi.org/10.1016/j.snb.2019.127055.
[22] M.S. Barbosa, P.H. Suman, J.J. Kim, H.L. Tuller, J.A. Varela, M.O. Orlandi, Gas sensor properties of Ag- and Pd-decorated SnO micro-disks to NO_2, H_2 and CO: catalyst enhanced sensor response and selectivity, Sens Actuators B Chem. 239 (2017) 253–261, https://doi.org/10.1016/j.snb.2016.07.157.
[23] R.K. Rawat, A. Singh, P. Chauhan, Ordered mesoporous SnO micro sheets based highly sensitive and selective ethanol gas sensor, ECS J. Solid State Sci. Technol. 10 (2021) 097001, https://doi.org/10.1149/2162-8777/ac2324.
[24] A. Seko, A. Togo, F. Oba, I. Tanaka, Structure and stability of a homologous series of tin oxides, Phys. Rev. Lett. 100 (2008) 045702, https://doi.org/10.1103/PhysRevLett.100.045702.
[25] J. Wang, N. Umezawa, H. Hosono, Mixed valence tin oxides as novel van der waals materials: theoretical predictions and potential applications, Adv. Energy Mater. 6 (2016) 1501190, https://doi.org/10.1002/aenm.201501190.
[26] K. Govaerts, B. Partoens, D. Lamoen, Extended homologous series of Sn–O layered systems: a first-principles study, Solid State Commun. 243 (2016) 36–43, https://doi.org/10.1016/j.ssc.2016.06.006.
[27] F. Lawson, Tin oxide - Sn_3O_4, Nature 215 (1967) 955–956, https://doi.org/10.1038/215955a0.
[28] S. Cahen, N. David, J.M. Fiorani, A. Maître, M. Vilasi, Thermodynamic modelling of the O-Sn system, Thermochim. Acta 403 (2003) 275–285, https://doi.org/10.1016/S0040-6031(03)00059-5.
[29] J. Liu, C. Wang, Q. Yang, Y. Gao, X. Zhou, X. Liang, P. Sun, G. Lu, Hydrothermal synthesis and gas-sensing properties of flower-like Sn_3O_4, Sens Actuators B Chem. 224 (2016) 128–133, https://doi.org/10.1016/j.snb.2015.09.089.
[30] X. Li, F. Wang, J. Tu, H.U. Shah, J. Hu, Y. Li, Y. Lu, M. Xu, Synthesis and ethanol sensing properties of novel hierarchical Sn_3O_4 nanoflowers, J. Nanomater 2015 (2015) 980170, https://doi.org/10.1155/2015/980170.
[31] F. Yin, Y. Li, W. Yue, S. Gao, C. Zhang, Z. Chen, Sn_3O_4/rGO heterostructure as a material for formaldehyde gas sensor with a wide detecting range and low operating temperature, Sens Actuators B Chem. 312 (2020) 127954, https://doi.org/10.1016/j.snb.2020.127954.
[32] B. Junker, A. Kobald, C. Ewald, P. Janoschek, M. Schalk, U. Weimar, L. Mädler, N. Bârsan, Multivariate analysis of light-activated SMOX gas sensors, ACS Sens 9 (2024) 1584–1591, https://doi.org/10.1021/acssensors.4c00078.
[33] E.A. Schmitt, M. Krott, M. Epifani, K. Suematsu, U. Weimar, N. Barsan, Volatile organic compound sensing with WO_3-based gas sensors: surface chemistry basics, J. Phys. Chem. C. 128 (2024) 1633–1643, https://doi.org/10.1021/acs.jpcc.3c06954.
[34] C. Ewald, N. Saito, U. Weimar, N. Barsan, Role of potassium loading in ZnO-based gas sensors under NO_2 exposure – operando diffuse reflectance infrared Fourier transform spectroscopic study, Sens Actuators B Chem. 393 (2023) 134321, https://doi.org/10.1016/j.snb.2023.134321.
[35] T. Russ, Z. Hu, L. Li, L. Zhou, H. Liu, U. Weimar, N. Barsan, In operando investigation of the concentration dependent NO_2 sensing mechanism of Bi_2S_3 nanorods at low temperatures and the interference of O_3, ACS Sens 7 (2022) 3023–3031, https://doi.org/10.1021/acssensors.2c01319.
[36] I. Boehme, U. Weimar, N. Barsan, Unraveling the surface chemistry of CO sensing with In_2O_3 based gas sensors, Sens Actuators B Chem. 326 (2021) 129004, https://doi.org/10.1016/j.snb.2020.129004.
[37] D. Degler, B. Junker, F. Allmendinger, U. Weimar, N. Barsan, Investigations on the temperature-dependent interaction of water vapor with tin dioxide and its implications on gas sensing, ACS Sens 5 (2020) 3207–3216, https://doi.org/10.1021/acssensors.0c01493.
[38] P.H. Suman, M.O. Orlandi, Influence of processing parameters on nanomaterials synthesis efficiency by a carbothermal reduction process, J. Nanopart. Res. 13 (2011) 2081–2088, https://doi.org/10.1007/s11051-010-9964-8.
[39] M.O. Orlandi, P.H. Suman, R.A. Silva, E.P.S. Arlindo, Carbothermal reduction synthesis: an alternative approach to obtain single-crystalline metal oxide nanostructures, in: E. Longo, F. de, A. La Porta (Eds.), Recent Advances in Complex Functional Materials: From Design to Application, Springer, 2017, pp. 43–67, https://doi.org/10.1007/978-3-319-53898-3_2.
[40] S.R. Morrison. The Chemical Physics of Surfaces, 1st ed., Springer, New York, 1977. ⟨https://books.google.com.br/books?id=-ImzxxB-kSgC⟩.
[41] N. Yamazoe, J. Fuchigami, M. Kishikawa, T. Seiyama, Interactions of tin oxide surface with O_2, H_2O and H_2, Surf. Sci. 86 (1979) 335–344, https://doi.org/10.1016/0039-6028(79)90411-4.
[42] A. Gurlo, Interplay between O_2 and SnO_2: oxygen ionosorption and spectroscopic evidence for adsorbed oxygen, ChemPhysChem 7 (2006) 2041–2052, https://doi.org/10.1002/cphc.200600292.
[43] K.V. Sopiha, O.I. Malyi, C. Persson, P. Wu, Chemistry of oxygen ionosorption on SnO_2 surfaces, ACS Appl. Mater. Interfaces 13 (2021) 33664–33676, https://doi.org/10.1021/acsami.1c08236.
[44] J.M. Olinger, P.R. Griffiths, Quantitative effects of an absorbing matrix on near-infrared diffuse reflectance spectra, Anal. Chem. 60 (1988) 2427–2435, https://doi.org/10.1021/ac00172a022.
[45] K. Grossmann, R.G. Pavelko, N. Barsan, U. Weimar, Interplay of H_2, water vapor and oxygen at the surface of SnO_2 based gas sensors - an operando investigation utilizing deuterated gases, Sens Actuators B Chem. 166167 (2012) 787–793, https://doi.org/10.1016/j.snb.2012.03.075.
[46] S. Harbeck, A. Szatvanyi, N. Barsan, U. Weimar, V. Hoffmann, DRIFT studies of thick film un-doped and Pd-doped SnO_2 sensors: temperature changes effect and CO detection mechanism in the presence of water vapour, Thin Solid Films 436 (2003) 76–83, https://doi.org/10.1016/S0040-6090(03)00512-1.
[47] S. Wicker, M. Guiltat, U. Weimar, A. Hémeryck, N. Barsan, Ambient humidity influence on CO detection with SnO_2 gas sensing materials. A combined DRIFTS/DFT investigation, J. Phys. Chem. C. 121 (2017) 25064–25073, https://doi.org/10.1021/acs.jpcc.7b06253.
[48] T. Ueda, I. Boehme, T. Hyodo, Y. Shimizu, U. Weimar, N. Barsan, Effects of gas adsorption properties of an Au-loaded porous In_2O_3 sensor on NO_2-sensing properties, ACS Sens 6 (2021) 4019–4028, https://doi.org/10.1021/acssensors.1c01412.
[49] T. Yang, A. Hemeryck, S. Pokhrel, W. Chen, L. Mädler, U. Weimar, N. Barsan, HCHO sensing mechanism of $In_4Sn_3O_{12}$ revealed by DRIFTS and DFT, J. Phys. Chem. C. 127 (2023) 10499–10507, https://doi.org/10.1021/acs.jpcc.3c00686.
[50] C.E. Simion, B. Junker, U. Weimar, A. Stanoiu, N. Bârsan, Sensing mechanisms of CO and H_2 with NiO material – DRIFTS investigations, Sens Actuators B Chem. 390 (2023) 134028, https://doi.org/10.1016/j.snb.2023.134028.
[51] P.H. Suman, Electrical properties of tin oxide materials, in: M.O. Orlandi (Ed.), Tin Oxide Materials, Elsevier, 2020, pp. 41–60, https://doi.org/10.1016/b978-0-12-815924-8.00003-7.
[52] E.W. Thornton, P.G. Harrison, Tin oxide surfaces. Part 1. - surface hydroxyl groups and the chemisorption of carbon dioxide and carbon monoxide on tin(IV) oxide, J. Chem. Soc. Faraday Trans. 1 Phys. Chem. Condens. Phases 71 (1975) 461–472, https://doi.org/10.1039/F19757100461.
[53] M. Egashira, M. Nakashima, S. Kawasumi, T. Selyama, Temperature programmed desorption study of water adsorbed on metal oxides. 2. tin oxide surfaces, J. Phys. Chem. 85 (1981) 4125–4130, https://doi.org/10.1021/j150626a034.

[54] D. Amalric-Popescu, F. Bozon-Verduraz, Infrared studies on SnO_2 and Pd/SnO_2, Catal. Today 70 (2001) 139–154, https://doi.org/10.1016/S0920-5861(01)00414-X.
[55] D. Degler, S. Wicker, U. Weimar, N. Barsan, Identifying the active oxygen species in SnO_2 based gas sensing materials: an operando IR spectrsocopy study, J. Phys. Chem. C. 119 (2015) 11792–11799, https://doi.org/10.1021/acs.jpcc.5b04082.
[56] A. Davydov, Molecular spectroscopy of oxide catalyst surfaces, John Wiley & Sons, 2003, https://doi.org/10.1002/0470867981.
[57] R.G. Pavelko, H. Daly, M. Hübner, C. Hardacre, E. Llobet, Time-resolved DRIFTS, MS, and resistance study of SnO_2 materials: the role of surface hydroxyl groups in formation of donor states, J. Phys. Chem. C. 117 (2013) 4158–4167, https://doi.org/10.1021/jp312532u.
[58] A.K. Elger, C. Hess, Elucidating the mechanism of working SnO_2 gas sensors using combined operando UV/Vis, Raman, and IR spectroscopy, Angew. Chem. Int. Ed. 58 (2019) 15057–15061, https://doi.org/10.1002/anie.201908871.
[59] K.R. Hahn, A. Tricoli, G. Santarossa, A. Vargas, A. Baiker, First principles analysis of H2O adsorption on the (110) surfaces of SnO_2, TiO_2 and their solid solutions, Langmuir 28 (2012) 1646–1656, https://doi.org/10.1021/la204124p.
[60] C. Yang, Z. Li, J. Liu, Y. Zhang, H. Liang, J. Fang, X. Bai, T. Zhao, Hydroxylation and molecular adsorption behavior of SnO_2 (110) crystal plane, Mater. Res Bull. 150 (2022) 111787, https://doi.org/10.1016/j.materresbull.2022.111787.
[61] G. Heiland, D. Kohl, Physical and chemical aspects of oxidic semiconductor gas sensors, in: T. Seiyama (Ed.), Chemical Sensor Technology, Elsevier, 1988, pp. 15–38, https://doi.org/10.1016/b978-0-444-98901-7.50007-5.
[62] N. Yamazoe, K. Suematsu, K. Shimanoe, Two types of moisture effects on the receptor function of neat tin oxide gas sensor to oxygen, Sens Actuators B Chem. 176 (2013) 443–452, https://doi.org/10.1016/j.snb.2012.08.060.
[63] P. Bechthold, M.E. Pronsato, C. Pistonesi, DFT study of CO adsorption on Pd-SnO_2(110) surfaces, Appl. Surf. Sci. 347 (2015) 291–298, https://doi.org/10.1016/j.apsusc.2015.03.149.
[64] J.M. Ducéré, A. Hemeryck, A. Estève, M.D. Rouhani, G. Landa, P. Ménini, C. Tropis, A. Maisonnat, P. Fau, B. Chaudret, A computational chemist approach to gas sensors: modeling the response of SnO_2 to CO, O_2, and H_2O gases, J. Comput. Chem. 33 (2012) 247–258, https://doi.org/10.1002/jcc.21959.
[65] X. Wang, H. Qin, Y. Chen, J. Hu, Sensing mechanism of SnO_2 (110) surface to CO: density functional theory calculations, J. Phys. Chem. C. 118 (2014) 28548–28561, https://doi.org/10.1021/jp501880r.

Pedro H. Suman received his degree in Physics (2009), M.Sc. (2012), and Ph.D. (2016) in Materials Science and Engineering from São Paulo State University (UNESP). During his Ph.D., he was a visiting student in the research group of Prof. Tuller in the Department of Materials Science and Engineering at the Massachusetts Institute of Technology (MIT). He subsequently worked as a postdoctoral fellow in the group of Prof. Udo Weimar and Dr. Nicolae Bârsan at the University of Tübingen. He is currently a Temporary Professor at UNESP. His research interests include the synthesis of semiconducting metal oxides (SMOx), particularly one-dimensional (1D) nanostructures, for applications in chemical sensors, photodetectors, and field-effect transistors (FETs).

Benjamin Junker-Reiss received his M.Sc. in chemistry from the University of Tübingen in 2020. Currently, he is a Ph.D. student in the research group of Udo Weimar and Nicolae Bârsan. His research is focused on gas sensors and operando spectroscopy.

Udo Weimar received his diploma in physics in 1989, his PhD in chemistry in 1993 and his Habilitation in 2002 from the University of Tübingen. Since 2010, he is a full professor in the Department of Chemistry at the University of Tübingen. His research interest focuses on chemical sensors as well as on multicomponent analysis and pattern recognition.

Marcelo O. Orlandi is a physicist with a Ph.D. in Materials Science and Engineering from the Federal University of São Carlos (2005). He currently holds a full professorship at São Paulo State University (UNESP). Dr. Orlandi's research primarily focuses on the controllable growth and modeling of nanomaterials, as well as their application in sensor technologies. His additional areas of interest include charge transport in nanomaterials and photocatalysis. He has authored approximately 100 peer-reviewed publications, contributed to 8 book chapters, and serves as the editor of the most comprehensive reference on tin oxide materials. Dr. Orlandi is also the holder of two patents.

Nicolae Bârsan received his diploma in Physics from the Faculty of Physics of the Bucharest University in 1982. In 1993 his received his Ph.D. in Solid State Physics from the Institute of Atomic Physics, Bucharest, Romania. Since 1995 he has been a senior researcher at the Institute of Physical Chemistry of the University of Tübingen, where he and Udo Weimar lead the Gas Sensors Group.

Supplementary material

Unraveling the Gas Sensing Mechanism of Single-Crystalline Sn_3O_4 Nanobelts Using Operando DRIFT Spectroscopy and Isotopically Labeled Gases

Pedro H. Suman [a,b,], Benjamin Junker-Reiss [a], Udo Weimar [a], Marcelo O. Orlandi [b], Nicolae Barsan*

[a,c,*]

[a] Institute of Physical and Theoretical Chemistry (IPTC) and Center for Light-Matter Interaction, Sensors & Analytics (LISA+), University of Tübingen, Tübingen, 72076, Germany.

[b] Department of Physics and Mathematics, Institute of Chemistry, São Paulo State University (UNESP), Araraquara, 14800-060, Brazil.

[c] Faculty of Advanced Science and Technology (FAST), Kumamoto University, Kumamoto, 860-8555, Japan.

[*] Corresponding authors:

nb@ipc.uni-tuebingen.de (Nicolae Barsan)

pedro.suman@unesp.br and phsuman@yahoo.com.br (Pedro H. Suman)

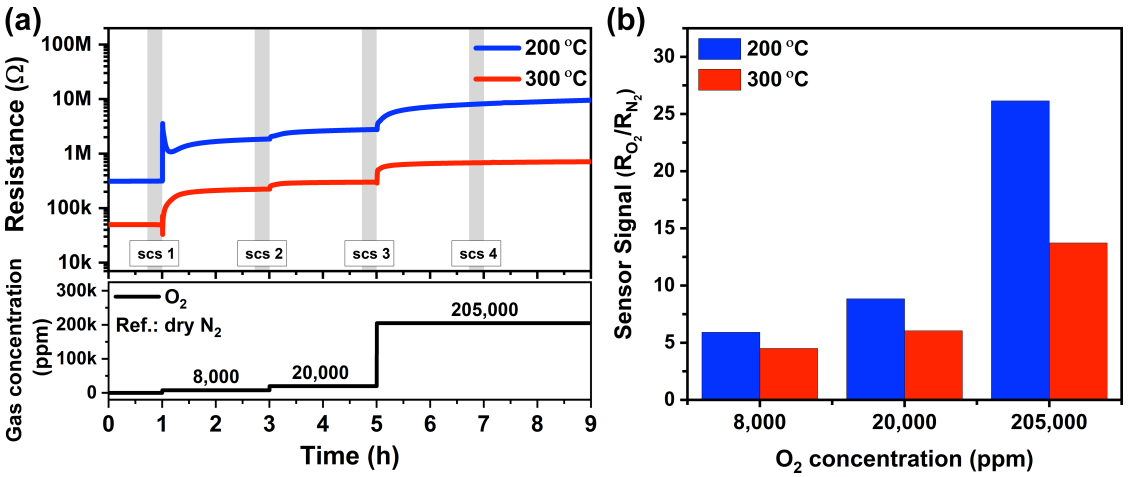

Fig. S1. (a) DC electrical resistance of the Sn_3O_4 nanobelts-based sensor during exposure to 8,000, 20,000, and 205,000 ppm O_2 (synthetic air) in dry N_2 at operating temperatures of 200 ºC and 300 ºC. The gray bars indicate the conditions under which the DRIFT spectra were recorded. (b) Corresponding sensor signals obtained from the data shown in (a).

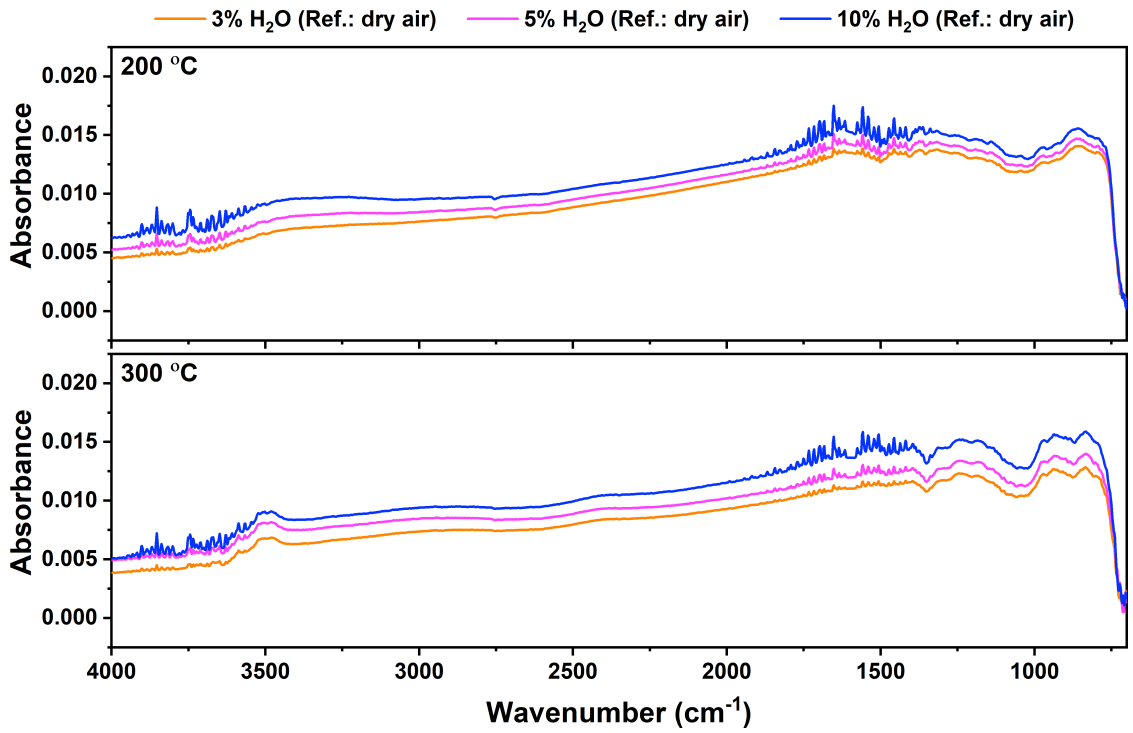

Fig. S2. DRIFT absorbance spectra of the Sn_3O_4 nanobelts-based sensor during exposure to 3, 5, and 10% H_2O at 25 ºC in dry synthetic air at operating temperatures of 200 ºC and 300 ºC. The absorbance spectra were calculated using the single-channel spectrum recorded in dry synthetic air as the reference.

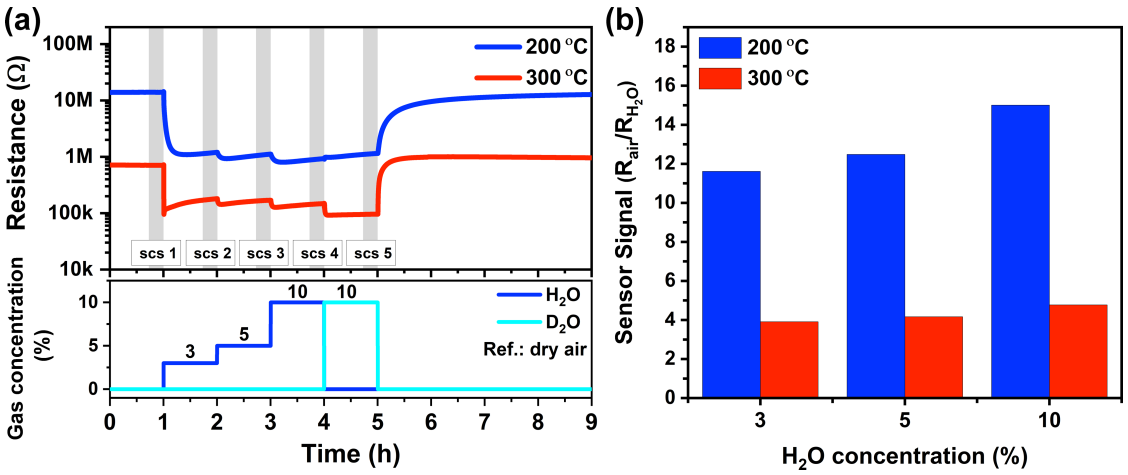

Fig. S3. (a) DC electrical resistance of the Sn_3O_4 nanobelts-based sensor during exposure to 3%, 5%, and 10% H_2O, followed by the isotopic exchange to 10% D_2O in dry synthetic air at operating temperatures of 200 ºC and 300 ºC. The gray bars indicate the conditions under which the DRIFT spectra were recorded. (b) Corresponding sensor signals to 3%, 5%, and 10% H_2O obtained from the data shown in (a).

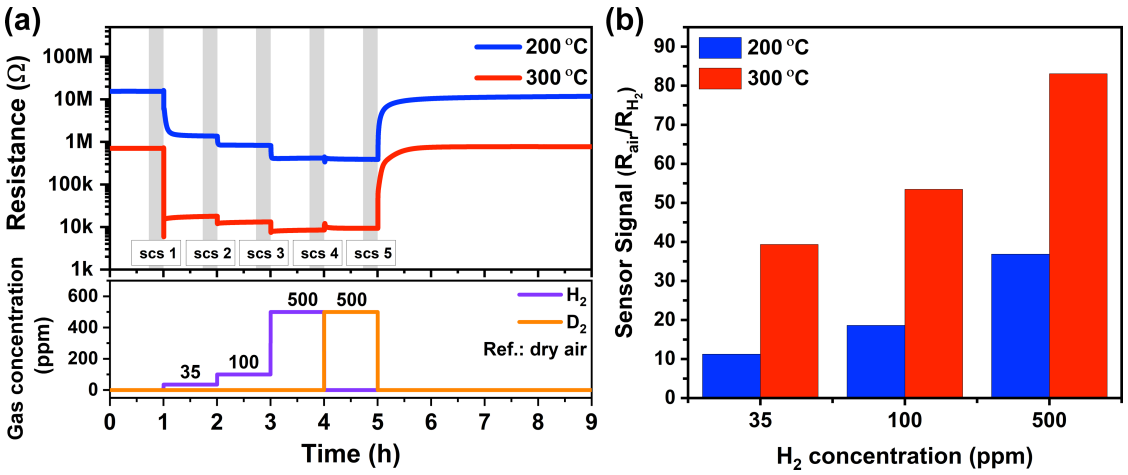

Fig. S4. (a) DC electrical resistance of the Sn_3O_4 nanobelts-based sensor during exposure to 35, 100, and 500 ppm H_2, followed by the isotopic exchange to 500 ppm D_2 in dry synthetic air at operating temperatures of 200 ºC and 300 ºC. The gray bars indicate the conditions under which the DRIFT spectra were recorded. (b) Corresponding sensor signals to 35, 100, and 500 ppm H_2 obtained from the data shown in (a).

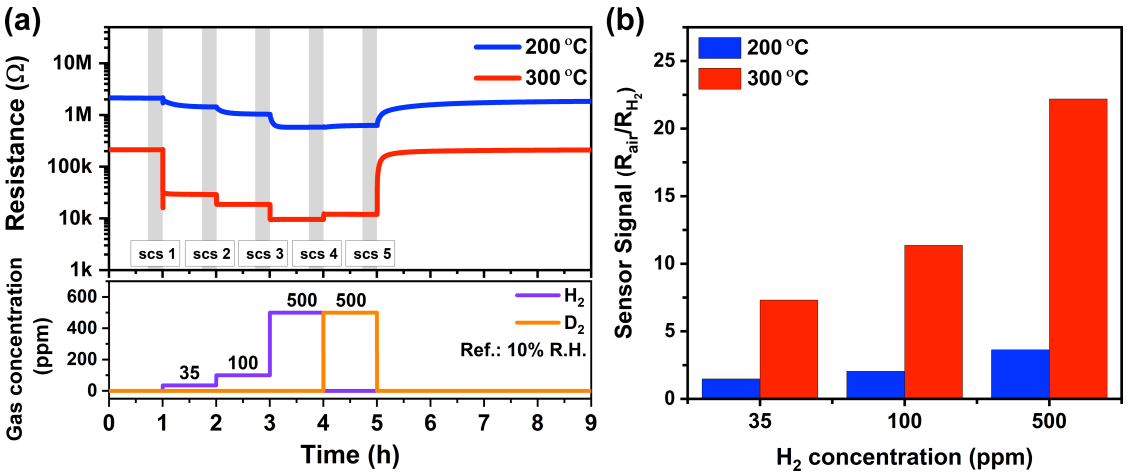

Fig. S5. (a) DC electrical resistance of the Sn_3O_4 nanobelts-based sensor during exposure to 35, 100, and 500 ppm H_2, followed by the isotopic exchange to 500 ppm D_2 in synthetic air with 10% H_2O (10% R.H. at 25 ºC) at operating temperatures of 200 ºC and 300 ºC. The gray bars indicate the conditions under which the DRIFT spectra were recorded. (b) Corresponding sensor signals to 35, 100, and 500 ppm H_2 obtained from the data shown in (a).

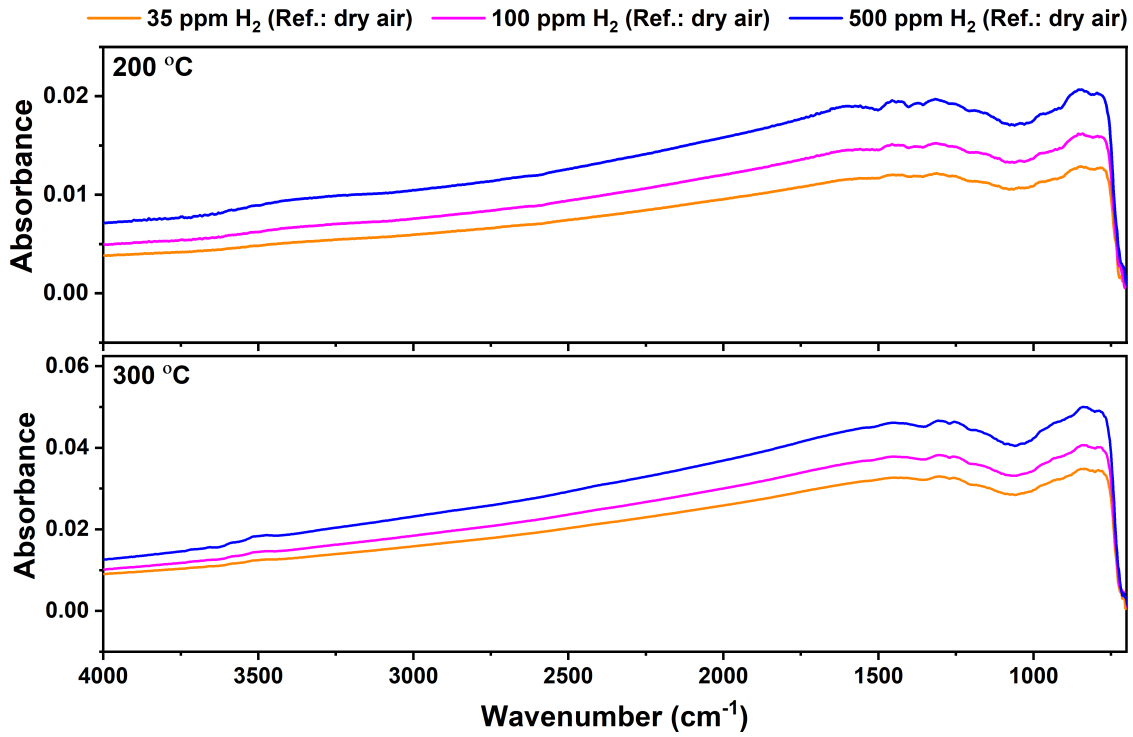

Fig. S6. DRIFT absorbance spectra of the Sn_3O_4 nanobelts-based sensor during exposure to 35, 100, and 500 ppm H_2 in dry synthetic air at operating temperatures of 200 ºC and 300 ºC. The absorbance spectra were calculated using the single-channel spectrum in dry synthetic air as the reference.

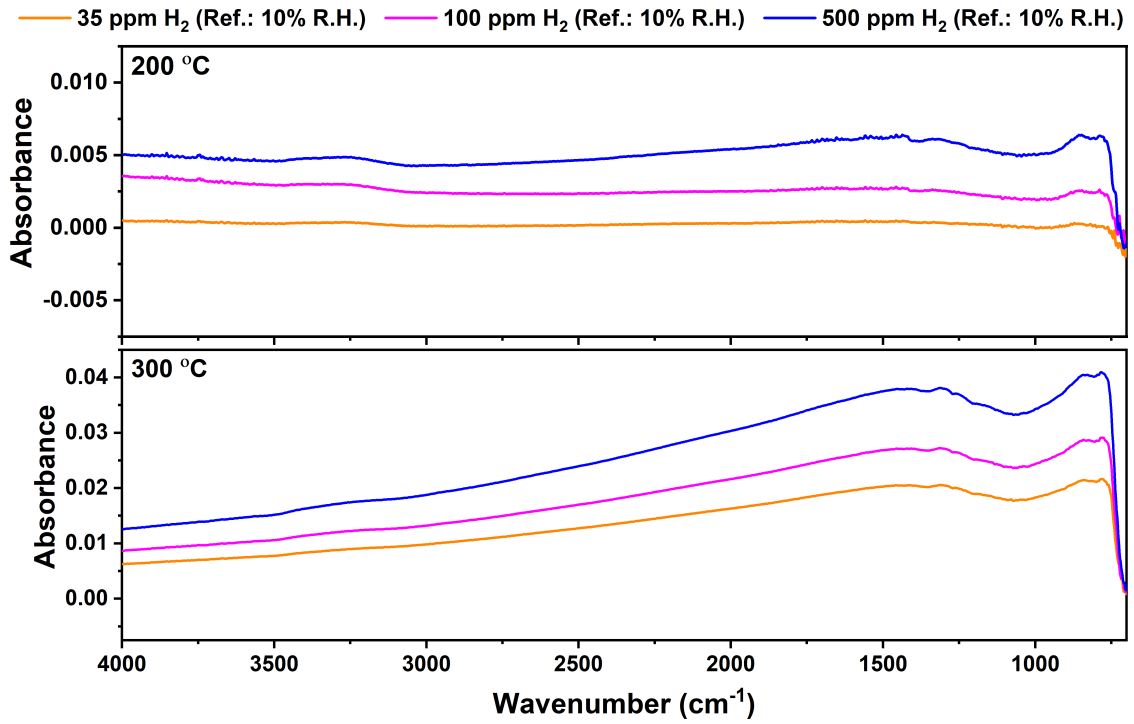

Fig. S7. DRIFT absorbance spectra of the Sn_3O_4 nanobelts-based sensor during exposure to 35, 100, and 500 ppm H_2 in synthetic air with 10% H_2O (10% R.H. at 25 ºC) at operating temperatures of 200 ºC and 300 ºC. The absorbance spectra were calculated using the single-channel spectrum in 10% R.H. at 25 ºC as the reference.

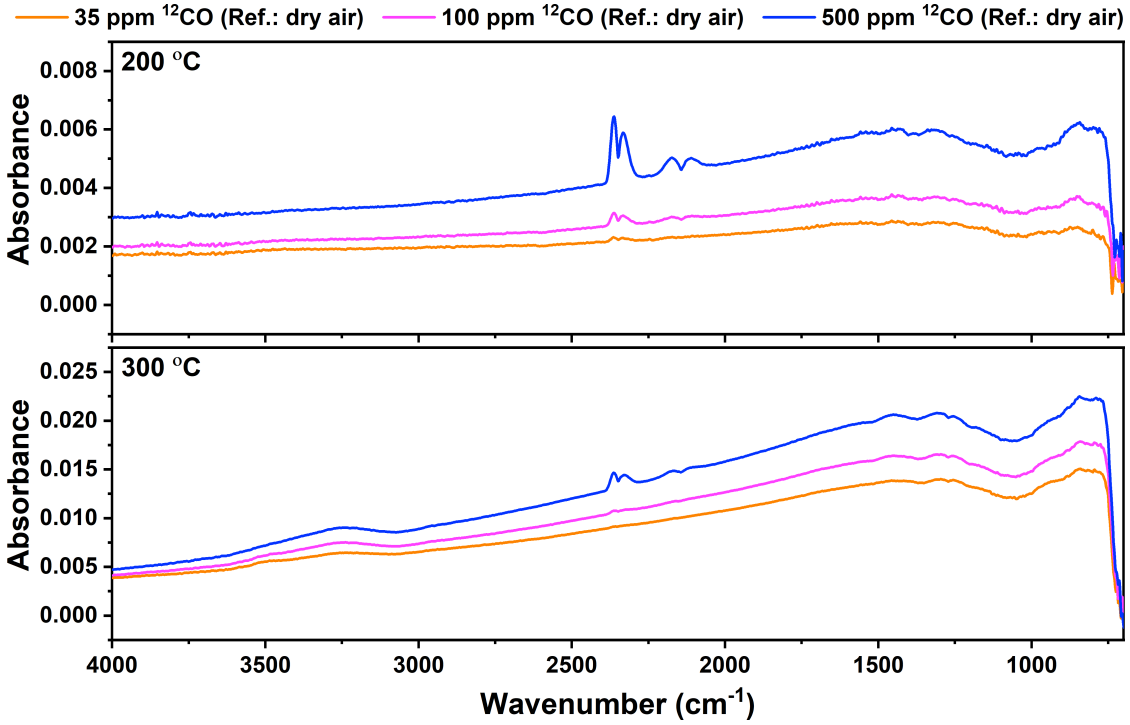

Fig. S8. DRIFT absorbance spectra of the Sn_3O_4 nanobelts-based sensor during exposures to 35, 100, and 500 ppm ^{12}CO in dry synthetic air at operating temperatures of 200 ºC and 300 ºC. The absorbance spectra were calculated using the single-channel spectrum in synthetic dry air as the reference.

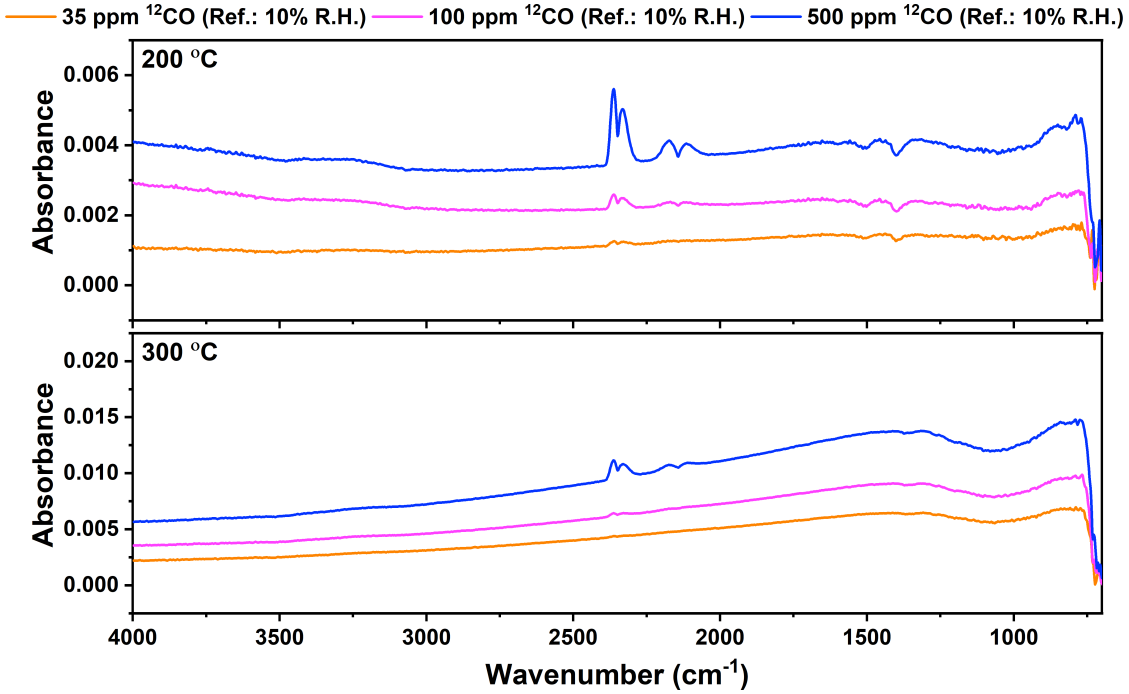

Fig. S9. DRIFT absorbance spectra of the Sn_3O_4 nanobelts-based sensor during exposures to 35, 100, and 500 ppm ^{12}CO in 10% H_2O (10% R.H. at 25 ºC) at operating temperatures of 200 ºC and 300 ºC. The absorbance spectra were calculated using the single-channel spectrum in 10% R.H. at 25 ºC as the reference.

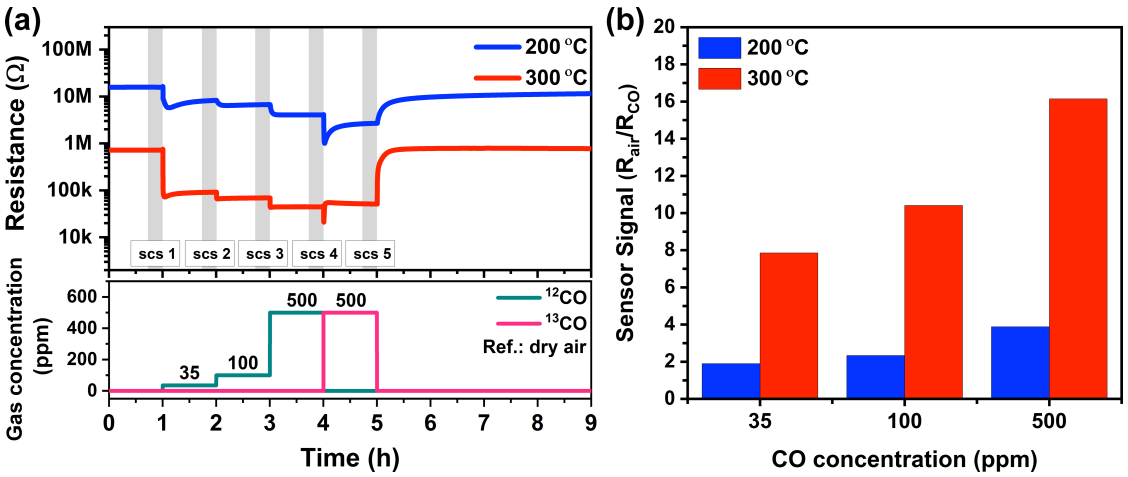

Fig. S10. (a) DC electrical resistance of the Sn_3O_4 nanobelts-based sensor during exposure to 35, 100, and 500 ppm ^{12}CO, followed by the isotopic exchange to 500 ppm ^{13}CO in dry synthetic air at operating temperatures of 200 ºC and 300 ºC. The gray bars indicate the conditions under which the DRIFT spectra were recorded. (b) Corresponding sensor signals to 35, 100, and 500 ppm ^{12}CO obtained from the data shown in (a).

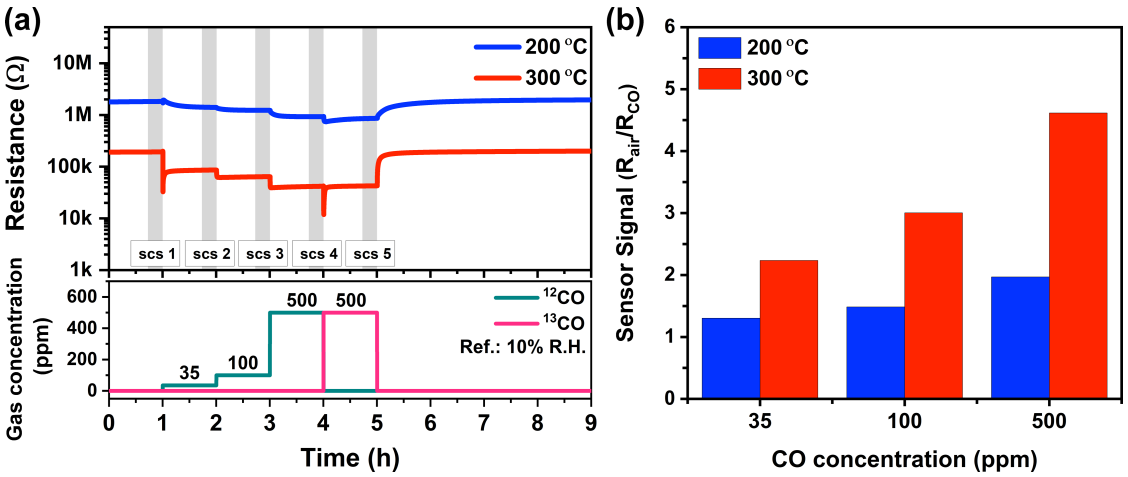

Fig. S11. (a) DC electrical resistance of the Sn_3O_4 nanobelts-based sensor during exposure to 35, 100, and 500 ppm ^{12}CO, followed by the isotopic exchange to 500 ppm ^{13}CO in synthetic air with 10% H_2O (10% R.H. at 25 ºC) at operating temperatures of 200 ºC and 300 ºC. The gray bars indicate the conditions under which the DRIFT spectra were recorded. (b) Corresponding sensor signals to 35, 100, and 500 ppm ^{12}CO obtained from the data shown in (a).